ACS SYMPOSIUM SERIES 1112

Functional Nanoparticles for Bioanalysis, Nanomedicine, and Bioelectronic Devices

Volume 1

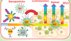
Nanoparticles
Luminescence
Raman
RELS

EDITED BY
Maria Hepel and Chuan-Jian Zhong

Downloaded by 89.163.35.42 on November 27, 2012 | http://pubs.acs.org
Publication Date (Web): November 26, 2012 | doi: 10.1021/bk-2012-1112.fw001

Functional Nanoparticles for Bioanalysis, Nanomedicine, and Bioelectronic Devices
Volume 1

In Functional Nanoparticles for Bioanalysis, Nanomedicine, and Bioelectronic Devices Volume 1; Hepel, M., et al.;
ACS Symposium Series; American Chemical Society: Washington, DC, 2012.

Downloaded by 89.163.35.42 on November 27, 2012 | http://pubs.acs.org
Publication Date (Web): November 26, 2012 | doi: 10.1021/bk-2012-1112.fw001

ACS SYMPOSIUM SERIES **1112**

Functional Nanoparticles for Bioanalysis, Nanomedicine, and Bioelectronic Devices
Volume 1

Maria Hepel, Editor
State University of New York at Potsdam
Potsdam, New York

Chuan-Jian Zhong, Editor
State University of New York at Binghamton
Binghamton, New York

Downloaded by 89.163.35.42 on November 27, 2012 | http://pubs.acs.org
Publication Date (Web): November 26, 2012 | doi: 10.1021/bk-2012-1112.fw001

Sponsored by the
ACS Division of Colloid and Surface Chemistry

American Chemical Society, Washington, DC

Distributed in print by Oxford University Press, Inc.

Downloaded by 89.163.35.42 on November 27, 2012 | http://pubs.acs.org
Publication Date (Web): November 26, 2012 | doi: 10.1021/bk-2012-1112.fw001

Library of Congress Cataloging-in-Publication Data

Functional nanoparticles for bioanalysis, nanomedicine, and bioelectronic devices
/ Maria Hepel, editor, State University of New York at Potsdam, Potsdam, New York,
Chuan-Jian Zhong, editor, State University of New York at Binghamton, Binghamton,
New York ; sponsored by the ACS Division of Colloid and Surface Chemistry.
pages cm. -- (ACS symposium series ; 1112)
Includes bibliographical references and index.
ISBN 978-0-8412-2775-0 (alk. paper)
1. Nanoparticles--Congresses. 2. Biotechnology--Congresses. I. Hepel, Maria, editor of compilation. II. Zhong, Chuan-Jian, editor of compilation. III. American Chemical Society. Division of Colloid and Surface Chemistry, sponsoring body.
TP248.25.N35F86 2012
660.6--dc23
2012041200

The paper used in this publication meets the minimum requirements of American National Standard for Information Sciences—Permanence of Paper for Printed Library Materials, ANSI Z39.48n1984.

Copyright © 2012 American Chemical Society

Distributed in print by Oxford University Press, Inc.

All Rights Reserved. Reprographic copying beyond that permitted by Sections 107 or 108 of the U.S. Copyright Act is allowed for internal use only, provided that a per-chapter fee of $40.25 plus $0.75 per page is paid to the Copyright Clearance Center, Inc., 222 Rosewood Drive, Danvers, MA 01923, USA. Republication or reproduction for sale of pages in this book is permitted only under license from ACS. Direct these and other permission requests to ACS Copyright Office, Publications Division, 1155 16th Street, N.W., Washington, DC 20036.

The citation of trade names and/or names of manufacturers in this publication is not to be construed as an endorsement or as approval by ACS of the commercial products or services referenced herein; nor should the mere reference herein to any drawing, specification, chemical process, or other data be regarded as a license or as a conveyance of any right or permission to the holder, reader, or any other person or corporation, to manufacture, reproduce, use, or sell any patented invention or copyrighted work that may in any way be related thereto. Registered names, trademarks, etc., used in this publication, even without specific indication thereof, are not to be considered unprotected by law.

PRINTED IN THE UNITED STATES OF AMERICA

Downloaded by 89.163.35.42 on November 27, 2012 | http://pubs.acs.org
Publication Date (Web): November 26, 2012 | doi: 10.1021/bk-2012-1112.fw001

Foreword

The ACS Symposium Series was first published in 1974 to provide a mechanism for publishing symposia quickly in book form. The purpose of the series is to publish timely, comprehensive books developed from the ACS sponsored symposia based on current scientific research. Occasionally, books are developed from symposia sponsored by other organizations when the topic is of keen interest to the chemistry audience.

Before agreeing to publish a book, the proposed table of contents is reviewed for appropriate and comprehensive coverage and for interest to the audience. Some papers may be excluded to better focus the book; others may be added to provide comprehensiveness. When appropriate, overview or introductory chapters are added. Drafts of chapters are peer-reviewed prior to final acceptance or rejection, and manuscripts are prepared in camera-ready format.

As a rule, only original research papers and original review papers are included in the volumes. Verbatim reproductions of previous published papers are not accepted.

ACS Books Department

In Functional Nanoparticles for Bioanalysis, Nanomedicine, and Bioelectronic Devices Volume 1; Hepel, M., et al.;
ACS Symposium Series; American Chemical Society: Washington, DC, 2012.

Downloaded by 89.163.35.42 on November 27, 2012 | http://pubs.acs.org
Publication Date (Web): November 26, 2012 | doi: 10.1021/bk-2012-1112.pr001

Preface

Current applications of nanotechnology span from new materials for energy production or conversion (including photovoltaics, fuel cells, etc.), to a variety of consumer products and novel pharmacological formulations, and expand now extensively to biomedical research, medical diagnostics and therapy. In this book, a comprehensive overview of the progress achieved in the development of functional nanoparticles for novel bioanalytical techniques and assays, enhancement of medical diagnostic imaging, and a variety of cancer treatment therapies is presented, and future trends of nanotechnology applications in these areas are evaluated. Particular emphasis is placed on the functionalization of metal, semiconductor and insulator nanoparticles for targeting cancer cells, delivering drugs and chemotherapeutic agents, preventing or reducing body inflammation response, averting biofouling and cytotoxicity, and enabling cell membrane crossing. Progress in the development of nanoparticles enhancing the diagnostic imaging is discussed in detail and this includes nanoparticles for Magnetic Resonance Imaging (MRI), Computed Tomography (CT) scan, megasonic imaging, and novel photoacoustic and Raman imaging. The image enhancing nanoparticles enable precise in-surgery viewing of tumors aiding surgical tumor removal in such complex cases as the brain tumor neuroblastoma, requiring ultra-precise incisions to remove cancer protrusions. Among novel imaging techniques, the Raman imaging provides distinctive features, such as chemical identification and multiplexing capabilities. It is noteworthy that Raman imaging is only possible owing to the extraordinary signal amplification enabled by the interaction of laser light with functionalized gold or silver nanoparticles administered to the targeted tissue. On the other hand, the interaction of nanoparticles with electromagnetic fields is also a key element in radiotherapy, photodynamic therapy, and hyperthermal cancer destruction. In these treatments, the nanoparticles specially optimized for efficient absorbance of electromagnetic irradiation are administered to a body, either locally to a tumor tissue or systemically into the blood stream when targeting had been developed so that the nanoparticles can recognize the tumor and accumulate in it. The tuning of nanoparticles to achieve absorbance of electromagnetic radiation at a specific wavelength in UV, visible, or NIR spectral region, requires an in-depth knowledge of optical and electronic properties of nanoparticles. Several Chapters are devoted to the synthesis and analysis of particles' size and shape dependencies of optoelectronic properties. In the case of gold and silver nanoparticles, the main absorption of electromagnetic energy in the visible region is due to the excitation of a collective oscillation of surface free electrons which is called the surface plasmon resonance. The optical property depends on the nanoparticle size, shape, surface, interparticle spacing, and the medium. Very strong effect on the absorption frequency has been observed with different aspect ratios of the nanorods. Interesting properties of fluorescent semiconductor core-shell nanoparticles, their broad across-the-spectrum size-dependent absorbance tunability, biocompatible functionalization, and biomedical applications are the focus of several Chapters.

The book covers comprehensively the two new trends of the recent development: (i) the theranostic multimodality (where theranostics = therapy + diagnostics), which combines two important nanocarrier functionalities: therapeutic drug delivery and enhanced diagnostics (e.g. by adding imaging-enhancement markers), and (ii) the race for the development of nanoparticle-enhanced biosensors which can serve as a useful, inexpensive, and easy-to-operate bioelectronic device in patients point-of-care.

Since the field of functional nanoparticles is rapidly expanding, with new discoveries reported every year, we hope that a wide audience will find this book very attractive as a source of valuable information concerning the synthesis of nanoparticles, their functionalization, and construction of biosensors and bioelectronic devices. We truly hope that researchers, students, medical doctors, and other professional workers will find the two volumes of this large collection of intriguing ideas, new data, and future developments, as a useful source to build on in further studies.

Maria Hepel

Chuan-Jian Zhong

Downloaded by 89.163.35.42 on November 27, 2012 | http://pubs.acs.org
Publication Date (Web): November 26, 2012 | doi: 10.1021/bk-2012-1112.pr001

Downloaded by UNIV DE SHERBROOKE on November 27, 2012 | http://pubs.acs.org
Publication Date (Web): November 26, 2012 | doi: 10.1021/bk-2012-1112.ot001

Editors' Biographies

Maria Hepel

Maria Hepel received the M.S. and Ph.D. degrees in chemistry from Jagellonian University in Krakow, Poland. She was a postdoctoral fellow at SUNY Buffalo. From 1985, she worked as the Faculty at the State University of New York at Potsdam where she is now a Distinguished Professor and Chair of the Department of Chemistry. She published over 144 papers, 25 chapters in books, and has made over 400 presentations at the international, national and regional symposia. She organized several symposia and has been the program chair of the 2010 North-East Regional Meeting of ACS. Her current research interests include DNA intercalation sensors, piezoimmunosensors, sensors for biomarkers of oxidative stress, fluorescence energy transfer (FRET and NSET), DNA-hybridization biosensors, photovoltaics, and electrochromic devices. She won the SUNY Potsdam President's Award for Excellence in Research and Creative Endeavor in 1995 and 2001, the SUNY Chancellor's Award for Excellence in Teaching in 1998 and SUNY Chancellor's Award for Research in 2003. She received the Northeast Region Award for Achievements in the Chemical Sciences at the Rochester Meeting NERM 2012 of the American Chemical Society.

Chuan-Jian Zhong

Chuan-Jian Zhong is Professor of Chemistry at State University of New York at Binghamton. He was Max-Planck-Society postdoctoral fellow at Fritz Haber Institute after receiving his Ph.D. at Xiamen University in 1989, and continued his postdoctoral work at University of Minnesota in 1991. He was associate scientist at Iowa State University/DOE-Ames Laboratory before joining the SUNY Binghamton faculty in 1998. His research interests include analytical and materials chemistry, catalysis, electrochemistry, and emerging fields of nanotechnology, focusing on challenging issues in chemical sensing and biomolecular recognition, and in green energy production, conversion and storage. He received NSF Career Award, SUNY Chancellor's Award for Excellence in Scholarship and Creative Activities, SUNY Innovation, Creation and Discovery Award, and 3M Faculty Research Award. He is the author of over 170 peer-reviewed research articles, the inventor of 11 U.S. patents, and has given over 100 invited talks at national/international conferences and university/industry/national lab seminars.

In Functional Nanoparticles for Bioanalysis, Nanomedicine, and Bioelectronic Devices Volume 1; Hepel, M., et al.;
ACS Symposium Series; American Chemical Society: Washington, DC, 2012.

Downloaded by 89.163.35.42 on November 27, 2012 | http://pubs.acs.org
Publication Date (Web): November 26, 2012 | doi: 10.1021/bk-2012-1112.ch001

Chapter 1

Biomolecule/Nanoparticle Hybrid Systems for Bioanalysis and Nanomedicine

Ronit Freeman, Bilha Willner, and Itamar Willner*

Institute of Chemistry, Center for Nanoscience and Nanotechnology,
The Hebrew University of Jerusalem, Jerusalem 91904, Israel
***E-mail: willnea@vms.huji.ac.il. Fax: +972-2-652-77-15.**
Tel.: +972-2-658-52-72

Metallic nanoparticles (NPs) and semiconductor quantum dots (QDs) exhibit unique photophysical, electronic and catalytic properties. The present article summarizes several paradigms developed in our laboratory for the use of semiconductor QDs and metal NPs for the *in vitro* and intracellular bioanalytical applications. Special emphasis is directed to the use of the different systems for future nano-medicine. Different photophysical mechanisms are implemented for the application of QDs for bioanalysis including fluorescence resonance energy transfer (FRET), electron transfer quenching, and chemiluminescence resonance energy transfer (CRET). The different mechanisms are used to develop analytical assays for enzymes, analysis of DNA, and the detection of aptamer-substrate complexes. Specifically, the development of multiplexed analysis schemes, and the amplified detection of DNA through the enzymatic recycling of the target-analyte are addressed.

The plasmonic properties of metal NPs are utilized to develop optical bioanalytical platforms. This is addressed with the biocatalytic growth of Au NPs and the colorimetric detection of enzyme activities and their substrates such as alcohol dehydrogenase, glucose oxidase and tyrosinase. The aggregation of Au NPs and the resulting color change, as a result of interparticle coupling of the localized plasmons of the individual Au NPs is implemented to develop different sensing platforms. This is addressed with the detection of DNA and

In Functional Nanoparticles for Bioanalysis, Nanomedicine, and Bioelectronic Devices Volume 1; Hepel, M., et al.;
ACS Symposium Series; American Chemical Society: Washington, DC, 2012.

of Pb^{2+}-ions, using the Pb^{2+}-dependent DNAzyme. Also, the coupling between the localized plasmon of Au NPs and the surface plasmon wave associated with surfaces is implemented to develop amplified surface plasmon resonance (SPR) analysis schemes for DNA aptamer-substrate complexes and Hg^{2+}-ions.

Finally, Nile-blue-functionalized semiconductor QDs are used to detect the 1,4-dihydronicotinamide adenine dinucleotide (phosphate), NAD(P)H, cofactor. The sensing of the cofactor is applied to follow the intracellular metabolism of HeLa cancer cells, and to probe anti-cancer drugs (taxol). Similarly, the NADH-mediated growth of Cu on Au NPs is used to follow biocatalytic transformations by plasmon resonance Rayleigh scattering spectroscopy of single metallic NPs using dark-field microscopy. Upon the incorporation of the NPs in HeLa cancer cells, the intracellular metabolism could be followed at the single-NP level, and the effect of anti-cancer drugs on cell metabolism was followed.

Downloaded by 89.163.35.42 on November 27, 2012 | http://pubs.acs.org
Publication Date (Web): November 26, 2012 | doi: 10.1021/bk-2012-1112.ch001

Introduction

Metal nanoparticles (NPs) or semiconductor nanoparticles (quantum dots, QDs) exhibit unique optical, electronic and catalytic properties that are derived from their nano-dimensions. For example, metal NPs exhibit localized plasmons with size-controlled excitation energy gaps that reveal unique optical features such as plasmon-enhanced fluorescence or Raman spectra, inter-particle plasmon coupling effects, or longitudinal plasmonic excitons of non-symmetrical NPs. Similarly, semiconductor QDs reveal size-controlled absorption and luminescence properties. Biomolecules such as enzymes, antigen-antibodies, or DNA exhibit nanoscale dimensions. Hence, the integration of biomolecules with metal NPs or semiconductor QDs may lead to nanostructures that combine the recognition and catalytic properties of the biomolecules with the unique electronic, optical and catalytic functions of the NPs and QDs (*1*–*5*). These bio-hybrid nanostructures may, then, be implemented as functional material for bioanalytical and nano-medical applications. Indeed, several review articles have addressed the progress in the area and discussed the future perspectives of the field (*1*, *4*, *6*–*9*). The present chapter aims to introduce some of our studies that apply semiconductor QDs and metallic NPs for optical and electronic sensing and discuss the implementation of these systems in bioanalysis and nano-medicine.

Bioanalytical Application of Semiconductor QDs

Semiconductor QDs exhibit unique optical properties reflected by size-controlled fluorescence, high luminescence quantum yields, narrow luminescence spectra, large Stokes shifts, and high stability against photobleaching (*10*–*15*). These optical features, particularly, the sized-controlled luminescence of the QDs turn these nanomaterials to be ideal labels of biomolecules for the multiplexed analysis of biosensing events. Indeed, numerous studies applied QDs as fluorescent labels for biosensing events such as the multiplexed analysis of pathogens (*16*) or DNAs (*17*). Nonetheless, biomolecules enable the application of the biomolecule/QDs hybrid systems to probe the dynamics of biorecognition events or of biocatalytic transformations by more complex photophysical mechanisms, or to harness the combined functions of the biomolecule-QDs hybrids to develop novel bioanalytical platforms. Figure 1 schematically outlines the different photophysical mechanisms that will be applied to develop the different QDs bioanalytical platforms. The photo-excitation of the QDs yields an electron-hole pair that upon radiative recombination yields the size-controlled luminescence. Provided that the bio-recognition event or the biocatalytic process lead to the labeling of the composite with an acceptor fluorophore exhibiting absorbance spectral overlap with the luminescence of the QDs (Figure 1(A)), the fluorescence resonance energy transfer process (FRET) could follow the dynamics of the catalytic reactions. The fluorescence resonance energy process (FRET) involves the dipole-dipole interaction between a donor and an acceptor, where the FRET probability, assuming a two point-like random distribution of the dipole, decreases with distance by the sixth power. This turns the FRET efficiency, E, to be very sensitive to the distance, r, separating the donor-acceptor couple, (where R_0 is the Förster radius), Eq. 1. The Förster radius R_0 is calculated by Eq. 2, where K^2 is a parameter that depends on the relative orientation of the dipoles, and gains a value between 0 and 4 (for two randomly oriented dipoles the value of K^2 is 2/3). QY_D corresponds to the luminescence quantum yield of the donor fluorophore, n is the refractive index of the medium, and J(λ) represents the overlap integral that provides a quantitative measure for the donor-acceptor spectral overlap. The overlap integral is calculated by Eq. 3, where $\varepsilon_A(\lambda)$ is the extinction coefficient of the acceptor and $F_D(\lambda)$ is the normalized emission spectrum.

$$E = \frac{R_0^6}{R_0^6 + r^6} \qquad \text{(Eq. 1)}$$

$$R_0 = \sqrt[6]{\frac{8.8\times10^{-25} K^2 QY_D J(\lambda)}{n^4}} \qquad \text{(Eq. 2)}$$

$$J(\lambda) = \int_0^\infty \varepsilon_A(\lambda) F_D(\lambda) \lambda^4 d\lambda \qquad \text{(Eq. 3)}$$

$$E = \frac{nR_0^6}{nR_0^6 + r^6} \qquad \text{(Eq. 4)}$$

Downloaded by 89.163.35.42 on November 27, 2012 | http://pubs.acs.org
Publication Date (Web): November 26, 2012 | doi: 10.1021/bk-2012-1112.ch001

Downloaded by 89.163.35.42 on November 27, 2012 | http://pubs.acs.org
Publication Date (Web): November 26, 2012 | doi: 10.1021/bk-2012-1112.ch001

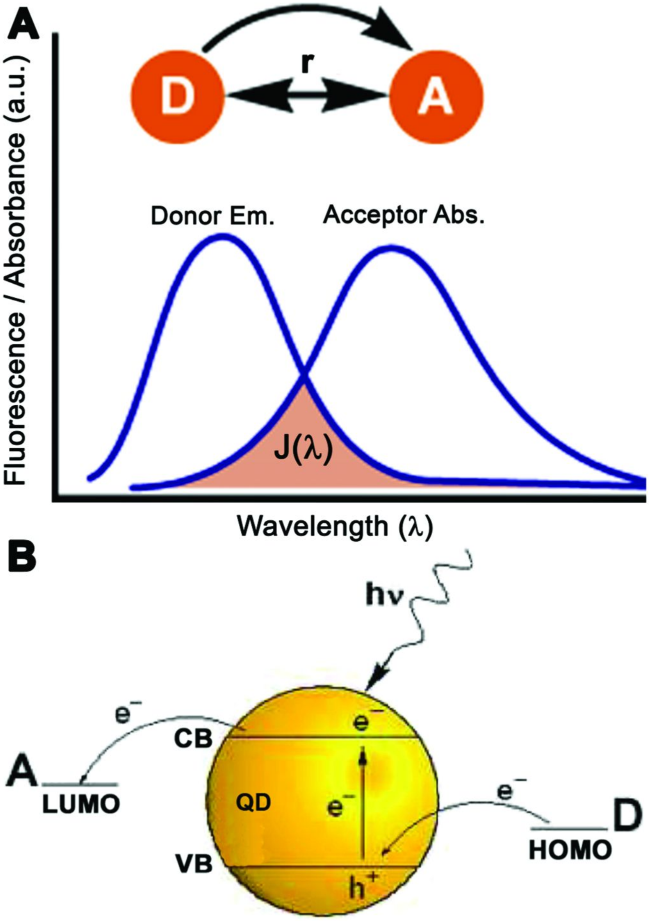

Figure 1. (A) Spectral overlap between the emission and absorption spectra of the donor-acceptor pair. (B) Electron transfer routes quenching semiconductor quantum dots by electron acceptor or electron donor units.

Typical Förster distances separating the donor and the acceptor range between 2 and 8 nm. FRET signals are detectable up to about twice the Förster distance separating the donor-acceptor pair. If, however, the acceptor unit is tethered to n×donor sites, the FRET efficiency increases and is given by Eq. 4. Alternatively, the biomolecule/QDs conjugates may be labeled by a biocatalyst that yields chemiluminescence. Provided that the spectral features of the resulting chemiluminescence overlap the excitation energy of the QDs, the chemiluminescence resonance energy transfer (CRET) might trigger-on the luminescence of the QDs and yield an optical readout signal for the sensing process. Similarly, the labeling of the recognition complex with an electron

Downloaded by 89.163.35.42 on November 27, 2012 | http://pubs.acs.org
Publication Date (Web): November 26, 2012 | doi: 10.1021/bk-2012-1112.ch001

acceptor unit (or electron donor) that exhibits energy levels that accept electrons from the conduction band level of the QDs (or donates electrons to the valence band holes of the QDs) may introduce an electron transfer (ET) path that quenches the luminescence of the QDs, Figure 1(B). The electron transfer (ET) quenching of photoexcited QDs is a versatile useful photophysical mechanism to follow spatially-restricted close interactions between electron donor-acceptor sites. The photoexcited QDs might participate in electron transfer via two general routes outlined in Figure 1(B). The photoexcitation of the QDs yields an electron-hole pair in the conduction band and valence band of the QDs. In the presence of an electron acceptor (A), exhibiting a LUMO energy level more positive than the conduction band potential, electron transfer quenching of the conduction band electrons to the acceptor units occurs. Similarly, in the presence of an electron donor (D) exhibiting a HOMO level that is less positive than the valence band potential, electron transfer from the donor to the holes associated with the valence band proceeds.

The two electron transfer routes deplete either the conduction band electrons or the valence band holes, thus prohibiting the recombination of the electron-hole pairs on the photoexcited QDs. Provided that the electron-hole recombinant process leads to the generation of luminescence, any of the competitive electron transfer reactions leads to the quenching of the luminescence of the QDs. The rate of electron transfer between the QDs and an electron acceptor (or an electron donor and the QDs) is given by Eq. 5 where R_0 and R represent the van-der Waals distance and the real distance separating the donor-acceptor pair, respectively, β is the electronic coupling constant, ΔG_0 is the free energy change associated with the electron transfer process, and λ is the reorganization energy accompanying the electron transfer process

$$K_{et} = \left(\frac{4\pi^2}{h}\right) T_{DA}^{\circ\ 2}\, e^{-\beta(R-R_0)} \frac{1}{\sqrt{4\pi\lambda K_B T}}\, e^{-(\Delta G^\circ+\lambda)^2/4\lambda K_B T} \qquad \text{(Eq. 5)}$$

The use of these three photophysical mechanisms for different bioanalytical and nanomedical applications will be exemplified.

The protein kinases are a large family of enzymes that modulate the activity of proteins by phosphorylation. They regulate the majority of cellular pathways, especially those involved in signal transduction (*18*, *19*). One of the most versatile of the protein kinases is casein kinase II (CK-2), a serine/threonine-selective protein kinase that is involved in signal transduction, transcriptional control, apoptosis, cell cycle and more (*20*). Aberrant activity of CK-2 has been implicated in a number of diseases. For example, both reduced amount and reduced activity of CK-2 were found in neurons of patients with Alzheimer's disease (*21*, *22*). On the other hand, elevated amounts of CK-2 were found in various types of cancer (*23*). It also plays a major role in the life cycle of HIV-1, and it has been found that CK-2 is a selective target of HIV-1 transcriptional inhibitors (*24*). Therefore, quantifying CK-2 activity from different tissue samples, and having a method for screening for CK-2 inhibitors are of great interest to the medical community.

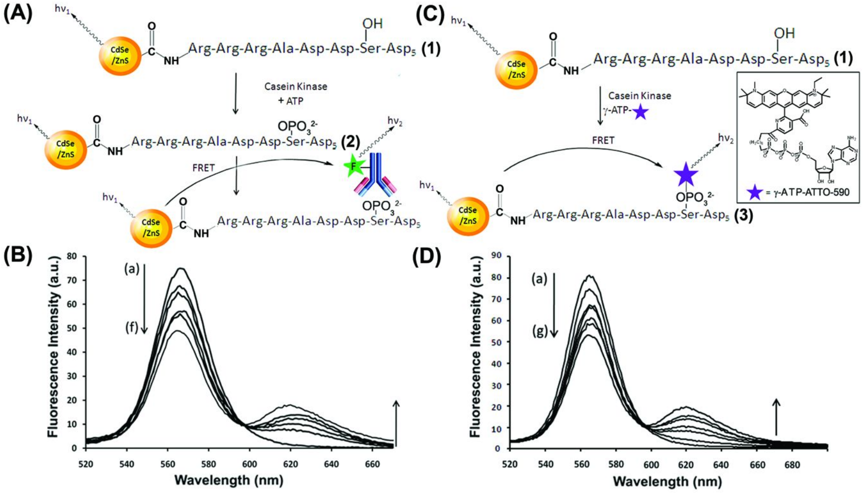

Figure 2. Probing the activity of casein kinase (CK-2) using CdSe/ZnS QDs and the FRET mechanism: (A) Through the application of a dye-labeled antibody that binds to the phosphorylated peptide. (B) Time-dependent FRET spectra upon analyzing CK-2, 1 Unit, according to (A). Spectra were recorded at time intervals of 8 min. (C) Analyzing CK-2 through the biocatalyzed phosphorylation of the peptide with the dye-labeled ATP and implementing the FRET process as readout mechanism. (D) Time-dependent FRET spectra upon analyzing CK-2, 1 Unit according to (C). Spectra were recorded at time intervals of 7 min. Reproduced with permission from reference (25). Copyright (2010) (American Chemical Society).

Figure 2(A) outlines the FRET-based detection of the activity of CK-2 by the labeling of an antibody with an acceptor-dye and following the FRET process within an immuno-complex formed between the labeled antibody and the CK-2-generated phosphorylated product associated with the QDs (*25*). CdSe/ZnS QDs were modified with the serine-containing peptide, (**1**). The CK-2-catalyzed phosphorylation of the peptide by ATP yielded (**2**). The Atto-590-labeled antibody that binds specifically to the phosphorylated peptide (**2**) was then linked to the modified QDs, and the FRET process between the QDs and the Atto-590 acceptor dye was used to follow the activity of CK-2. Figure 2(B) depicts the time-dependent luminescence features of the system. The quenching degree of the luminescence of the QDs was ca. 40%. Similarly, the interaction of the (**1**)-functionalized QDs with Atto-590-modified adenosine triphosphate, Atto-590-ATP, in the presence of CK-2, yielded the Atto-590-labeled phosphorylated peptide, (**3**), Figure 2(C). The FRET process between the QDs and the acceptor fluorophore enabled, then, to follow the phosphorylation reaction. Figure 2(D) shows the time-dependent luminescence changes of the system. As the CK-2 biocatalyzed phosphorylation of (**1**) is prolonged the FRET process is intensified, and this is reflected by the decrease in the luminescence of the QDs at

Downloaded by 89.163.35.42 on November 27, 2012 | http://pubs.acs.org
Publication Date (Web): November 26, 2012 | doi: 10.1021/bk-2012-1112.ch001

Downloaded by 89.163.35.42 on November 27, 2012 | http://pubs.acs.org
Publication Date (Web): November 26, 2012 | doi: 10.1021/bk-2012-1112.ch001

λ_{max} = 560 nm and the enhanced fluorescence of Atto-590 at λ_{max} = 620 nm. These results are consistent with the time-dependent increase of the phosphorylated reaction product.

CdSe/ZnS were, also, applied to follow NAD(P)$^+$-dependent enzymes, using a FRET mechanism (*26*). The QDs were functionalized with the redox-active Nile-Blue, NB$^+$, dye molecules, Figure 3(A). In the oxidized state, the NB$^+$ (**4**) quenches the luminescence of the QDs by a FRET mechanism with an energy-transfer quenching efficiency of around 90%, yet the reduction of the dye by the 1,4-dihydronicotinamide adenenine dinucleotide(phosphate), NAD(P)H, yielded the colorless reduced dye NBH, (**5**) that could not quench the QDs by the FRET mechanism. Accordingly, the rate of NB$^+$ reduction was controlled by the concentration of the NAD(P)H cofactor, and the luminescence of the QDs reflected the concentration of the reduced cofactor. The successful sensing of the NAD(P)H cofactors by the NB$^+$-functionalized QDs was, then, used to follow NAD$^+$-dependent enzymes and their substrates, such as the alcohol dehydrogenase AlcDH, and ethanol as substrate, Figure 3(B). The AlcDH-catalyzed oxidation of ethanol to acetaldehyde is accompanied by the reduction of NAD$^+$ to NADH. Since the concentration of NADH is controlled by the substrate concentration (ethanol), the resulting luminescence of the QDs, is related directly to the concentration of ethanol.

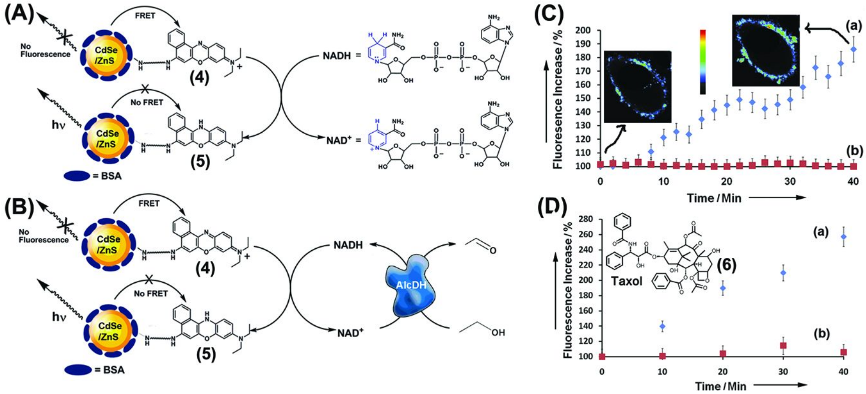

Figure 3. (A) Optical detection of NADH by Nile-Blue-functionalized CdSe/ZnS QDs. (B) Fluorescence analysis of ethanol by the NAD$^+$-dependent alcohol dehydrogenase and the Nile-Blue-functionalized semiconductor QDs. (C) Time-dependent luminescence changes of HeLa cancer cells modified with Nile-Blue-functionalized CdSe/ZnS QDs upon activation of intracellular metabolism (NADH generation) with: (a) D-glucose; (b) L-glucose. (D) Time-dependent luminescence changes of HeLa cancer cells modified with Nile-Blue-functionalized QDs, where (a) HeLa cells treated with D-glucose; (b) HeLa cells were pre-treated with Taxol and then with D-glucose. Reproduced with permission from reference (26). Copyright (2009) (Wiley-VCH).

Downloaded by 89.163.35.42 on November 27, 2012 | http://pubs.acs.org
Publication Date (Web): November 26, 2012 | doi: 10.1021/bk-2012-1112.ch001

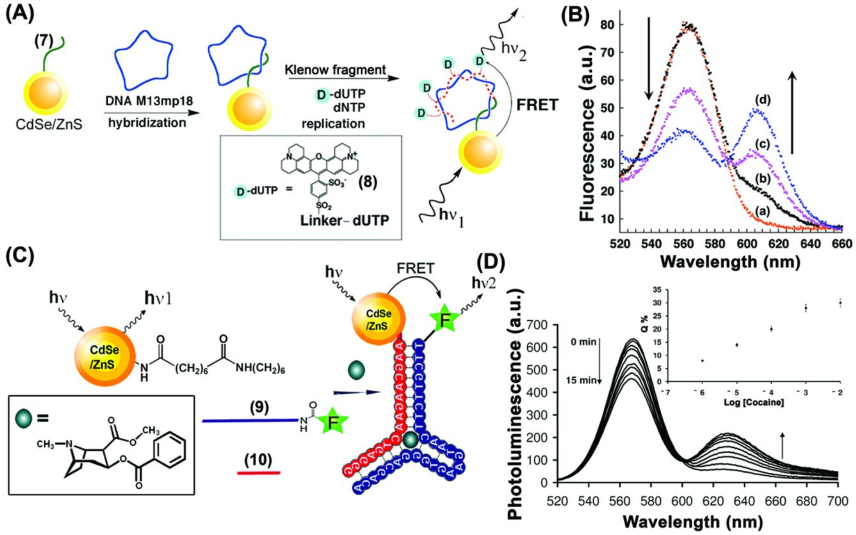

Figure 4. (A) FRET-based analysis of M13 phage DNA by probe nucleic acid-functionalized QDs that bind the analyte and subsequently replicate the analyte in the presence of polymerase and the dNTPs mixture that includes Texas-Red-functionalized dUTP. (B) Time-dependent FRET spectra following the replication process (a) before addition of Texas-Red-labeled-dUTP and (b-d) after 1, 30, and 60 min of replication. (C) Analysis of cocaine by QD/dye aptamer subunits and implementation of the FRET mechanism. (D) Time-dependent FRET spectra corresponding to the dynamics of the self-assembly of the cocaine-aptamer subunits and demonstrating intracomplex FRET process, according to (C). Inset: Calibration curve corresponding to the luminescence quenching degree of the QDs by different concentrations of cocaine. (A) and (B) were reproduced with permission from reference (27). Copyright (2003) (American Chemical Society). (C) and (D) were reproduced with permission from reference (33). Copyright (2009) (Royal Society of Chemistry).

Besides the ability to follow the activities of NAD^+-dependent enzymes, and to sense their substrates, the NB^+-modified CdSe/ZnS QDs were used to probe intracellular metabolic processes, and specifically, to screen drugs that could control cellular disorders that affect intracellular metabolic pathways (*26*). This was exemplified by probing the metabolic pathways in HeLa cancer cells, and demonstrating the optical detection of the anticancer Taxol drug on the cancer cell metabolism, by applying the NB^+-functionalized QDs as optical labels. Realizing that the NAD(P)H cofactor is a key intermediate in the cell metabolism, the intracellular monitoring of NAD(P)H levels provides a quantitative measure for the cell metabolism. Accordingly, the NB^+-modified CdSe/ZnS QDs were incorporated into HeLa cancer cells cultured under starvation. The living cells were then subjected to the addition of D-glucose as a nutrient that triggered-on the cell metabolism. This was evident by the rapid formation of NAD(P)H and the time-dependent increase in the luminescence generated by the cells, Figure 3(C), curve (a). For comparison, the non-native L-glucose nutrient did not affect the cell metabolism and did not increase the luminescence of the cells, Figure 3(C), curve (b). The ability to follow the activation of the HeLa cells metabolic pathways by the modified QDs was further implemented to characterize the inhibition of the cell metabolism by the anti-cancer drug, Taxol, (**6**), Figure 3(D). In these experiments the QDs-containing cells were cultured under starvation in the absence and presence of the Taxol, and the cells were subsequently subjected to D-glucose to activate the cell metabolism. While in the absence of Taxol, (**6**), the intracellular metabolism was activated, as evident by the increase in the luminescence intensities of the QDs, Figure 3(D), curve (a), the luminescence originating from the Taxol-treated cell remained low, Figure 3(D), curve (b). These results demonstrate that the NB^+-functionalized QDs hold future promise in the area of nanomedicine and drug screening. As many diseases are reflected by intracellular metabolic disorders, the rapid evaluation of the effects of drugs on the cells could lead to useful drug screening.

The luminescence properties of semiconductor QDs, and the FRET mechanism, were also used to develop nucleic acid-based sensing platforms. This will be exemplified with the detection of DNA and the design of aptamer-based sensors. Figure 4(A) depicts the schematic detection of the M13 phage DNA by QDs, using the FRET mechanism (*27*). The CdSe/ZnS QDs were functionalized with the nucleic acid (**7**) that is complementary to a sequence domain of the target analyte. Hybridization of the M13 phage to the probe nucleic acid (**7**), associated with the QDs, was then followed by replication of the analyte in the presence of polymerase and the dNTPs mixture that included Texas-Red-modified dUTP, (**8**). The incorporation of the Texas-Red dye into the replicated DNA resulted in the FRET process from the QDs to the dye units. Figure 4(B) shows the time-dependent enhancement of the fluorescence of the Texas-Red units, and the concomitant decrease in the luminescence of the QDs, (ca. 50% quenching) as the replication proceeds.

Nucleic acids that recognize proteins or low-molecular-weight substrates (aptamers) attract growing interest as functional sensing materials (*28–30*). The Systematic Evolution of Ligands by Exponential Enrichment (SELEX) process enables the effective selection of specific nucleic acid sequences that specifically recognize the respective substrates (*31*, *32*). We found that the cleavage of the aptamer sequences into subunits still allows the assembly of the subunits and the target analyte into the supramolecular aptamer-substrate complex. This principle was implemented to develop FRET-based aptasensor system and is exemplified with the development of a fluorescence-based cocaine aptasensor (*33*), Figure 4(C). The anti-cocaine aptamer sequence was cleaved into the two subunits (**9**) and (**10**). The subunit (**9**) was covalently linked to the Atto-590-fluorophore and subunit (**10**) was covalently linked to the CdSe/ZnS QDs. While in the absence of the cocaine the two subunits lack energetic stabilization of the aptamer structure (and, thus, no FRET between the QDs and the fluorophore occurs), the addition of cocaine stabilizes the supramolecular aptamer subunits-cocaine complex, resulting in the FRET process in the self-assembled nanostructure.

Downloaded by 89.163.35.42 on November 27, 2012 | http://pubs.acs.org
Publication Date (Web): November 26, 2012 | doi: 10.1021/bk-2012-1112.ch001

This FRET process enables the probing of the time-dependent assembly of the cocaine-subunits complex with a quenching degree of ca. 30%, Figure 4(D). Furthermore, as the formation of the supramolecular complex is favored as the concentration of cocaine increases, the fluorescence of the system at a fixed time-interval of assembly of the nanostructure provides a quantitative signal for the concentration of cocaine, Figure 4(D), inset. This system enabled the analysis of cocaine with a detection limit that corresponded to 1×10^{-6} M.

The use of the electron transfer (ET) quenching mechanism of the semiconductor quantum dots for bioanalytical applications requires that the energy levels of the electron-acceptor quencher or the electron-donor quencher will be positioned positively to the conduction-band level, or negatively to the valence-band energy level, respectively, to allow electron transfer between the photogenerated electron/hole pair and the acceptor/donor counterparts. These electron transfer processes compete with the radiative electron-hole recombination process, thus leading to the quenching of the luminescence of the QDs.

Downloaded by 89.163.35.42 on November 27, 2012 | http://pubs.acs.org
Publication Date (Web): November 26, 2012 | doi: 10.1021/bk-2012-1112.ch001

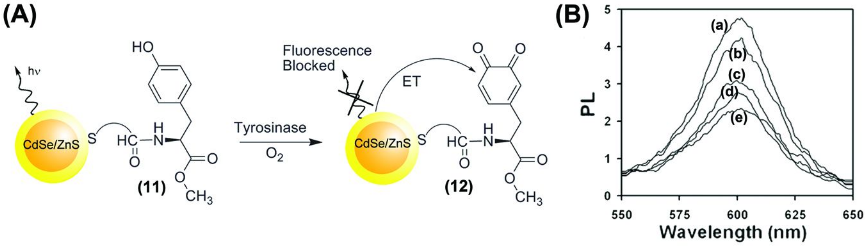

Figure 5. (A) Analysis of tyrosinase by methylester-tyrosine-functionalized QDs using an electron transfer quenching mechanism. (B) Time-dependent electron-transfer quenching of the luminescence of the QDs by the tyrosinase-generated dopaquinone units after (a) 0 min, (b) 0.5 min, (c) 2 min, (d) 5 min, and (e) 10 min. Reproduced with permission from reference (34). Copyright (2006) (American Chemical Society).

The ET quenching was used to develop an optical sensing platform for tyrosinase (*34*). This enzyme is over-expressed in melanoma cancer cells and is considered as a biomarker for these cells (*35*). CdSe/ZnS QDs were functionalized with the tyrosine methyl ester substrate, (**11**). In the presence of tyrosine and oxygen, the L-tyrosine residues are oxidized to L-DOPA, and subsequently to the dopaquinone residues, (**12**), Figure 5(A). The quinone products act as ET quenchers of the QDs, thus leading to the quenching of the luminescence of the QDs. Figure 5(B) depicts the time-dependent decrease of the luminescence of the QDs (the fluorescence intensity decreased by 45%), as the tyrosinase-catalyzed oxidation of the capping layer of the QDs proceeds.

Downloaded by 89.163.35.42 on November 27, 2012 | http://pubs.acs.org
Publication Date (Web): November 26, 2012 | doi: 10.1021/bk-2012-1112.ch001

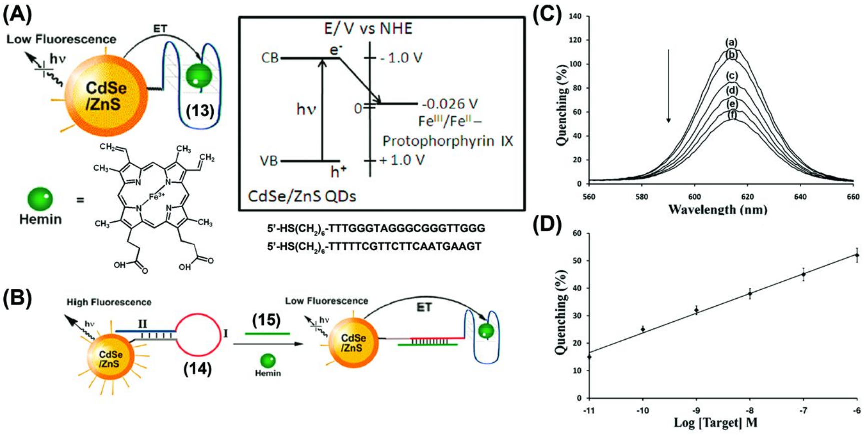

*Figure 6. (A) Electron transfer quenching of the luminescence of CdSe/ZnS QDs by the hemin/G-quadruplex. The appropriate energy levels diagram of the components is provided. (B) Analysis of the DNA strand (**15**) by a hairpin probe (**14**) that is associated with CdSe/ZnS QDs and includes in its stem region the "caged" sequence of the G-quadruplex. The opening of the hairpin by the analyte leads to the self-assembly of the hemin/G-quadruplex that quenches via electron transfer the luminescence of the QDs. (C) Time-dependent quenching of the luminescence of the QDs upon analyzing the target DNA, (15), 1 µM. (D) Calibration curve corresponding to the luminescence quenching degree by different concentrations of the analyte DNA, (**15**). (Quenching data were recorded after a fixed time-interval of 45 minutes). Reproduced with permission from reference (41). Copyright (2010) (American Chemical Society).*

A second example for using the ET quenching mechanism for developing QDs-based sensors involves the coupling of the QDs to hemin/G-quadruplex that has been recently extensively used as a biocatalytic label (DNAzyme) for amplifying different biorecognition events (*36–38*) or to follow enzyme-mediated transformations (*39*). Also, the hemin/G-quadruplex was used as an electrocatalyst for the amplified electrochemical detection of DNA or aptamer-substrate complexes (*40*). The hemin/G-quadruplex exhibits quasi-reversible redox function that turns the complex as a potential ET quencher of QDs, Figure 6(A). Indeed, we demonstrated that the surface associated with hemin/G-quadruplex, (**13**), quenches the luminescence of the QDs. This property was used to develop different fluorescent nucleic acid-based sensors (*41*). This is exemplified in Figure 6(B) with the development of DNA sensors. The hairpin nucleic acid structure (**14**) was linked to CdSe/ZnS QDs. The single-stranded loop, domain I, contained the recognition sequence for the target DNA, while domain II, being a part of the duplex stem region, consisted of the G-quadruplex sequence. The caging of the G-quadruplex sequence in the stem region prohibited the formation of hemin/G-quadruplex and resulted in the luminescent QDs. Hybridization of the analyte DNA (**15**) to the loop of the hairpin resulted in its opening, allowing the assembly of the hemin/G-quadruplex acting as ET quencher of the QDs. The time-dependent quenching of the luminescence of the QDs, Figure 6(C), reflects the rate of opening of the hairpin and self-assembly of the hemin/G-quadruplex quencher units. As the population of the hairpins, and thus, the hemin/G-quadruplex quenchers, are controlled by the concentration of the analyte DNA, the degree of quenched QDs (up to 55% quenching) relates to the concentration of the analyte (**15**), Figure 6(D), thus allowing the quantitative analysis of the target DNA. This concept was, further, implemented to detect aptamer-substrate complexes by using pre-tailored hairpin structures that include in their loop region the respective aptamer sequences (*41*). Also, the enzyme telomerase was assayed through the telomerization of the enzyme primer and assaying the resulting hemin/telomeric G-quadruplexes through the quenching of the QDs (*42*).

A further mechanism for the implementation of semiconductor QDs for optical biosensing has involved the chemiluminescence resonance energy transfer (CRET) process. The hemin/G-quadruplex acts as a horseradish peroxidase mimicking DNAzyme (*43*) that catalyzes the oxidation of luminol by H_2O_2 with the concomitant generation of chemiluminescence (λ= 420 nm) (*44*). This property of the hemin/G-quadruplex was applied to develop luminescent QDs-based DNA sensor based on the CRET mechanism (*45*), Figure 7(A). The CdSe/ZnS QDs were functionalized with the hairpin nucleic acid, (**16**), that includes in the single-stranded loop the recognition sequence of the target analyte DNA, (**17**), and in the stem region, the G-quadruplex sequence in a "caged" inactive configuration. Upon opening of the hairpin by the analyte the G-sequence is released and it assembles into the catalytic hemin/G-quadruplex nanostructure. The DNAzyme-catalyzed oxidation of luminol by H_2O_2 yields chemiluminescence in the vicinity of the QDs and this provides the radiative energy for the excitation of the QDs. That is, the CRET process activated by the generation of the hemin/G-quadruplex DNAzyme results in the internal excitation of the QDs and their luminescence as a result of the radiative recombination of the electron/hole pair. The CRET efficiency was determined to be ca. 15%. As the population of the open hairpins of (**16**), and the accompanying content of hemin/G-quadruplex units relate to the concentration of the target DNA, (**17**), the resulting CRET signal of the QDs is controlled by the concentration of the DNA analyte, Figure 7(B). This method was extended for the multiplexed, simultaneous analysis of three different target DNA, (**17**), (**18**) and (**19**). Three different-sized QDs emitting at, λ_{em} = 620 nm; λ_{em} = 560 nm, and, λ_{em} = 490 nm, were functionalized with the three different hairpins (**16**), (**20**) and (**21**). Each of these hairpins included in the single-stranded loop region a different recognition sequence for the analytes (**17**), (**18**) and (**19**), respectively, while the stem region of all hairpin structures included the "caged", inactive, G-quadruplex sequence. In the presence of any of the analytes the respective hairpin was opened, and the resulting hemin/G-quadruplex DNAzyme stimulated the CRET process to the respective QDs, leading to the luminescence characteristic to the QDs to which the probe hairpin was associated, Figure 7(C). The interaction of the mixture of

Downloaded by 89.163.35.42 on November 27, 2012 | http://pubs.acs.org
Publication Date (Web): November 26, 2012 | doi: 10.1021/bk-2012-1112.ch001

the three different-sized QDs with all three analytes resulted in the activation of the luminescence of all of the QDs, demonstrating the multiplexed analysis of the analytes using the CRET signal as an internal local light source for the excitation of the QDs.

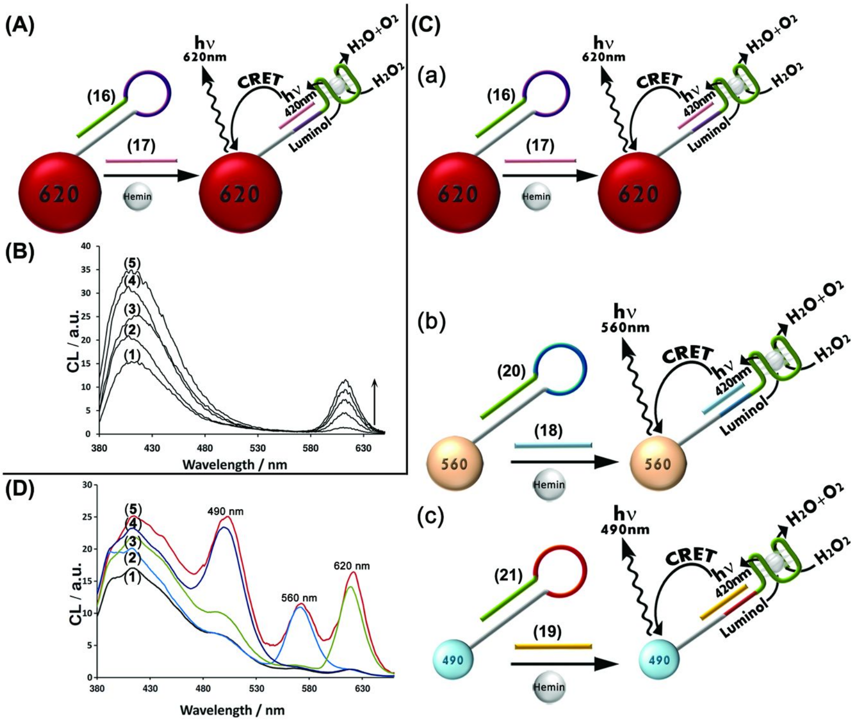

*Figure 7. (A) Analysis of a DNA strand, (**17**), using hairpin-functionalized QDs that include in their stem region the "caged" G-quadruplex sequence. Opening of the hairpin by the target DNA assembles the hemin/G-quadruplex catalyst that leads to chemiluminescence resonance energy transfer (CRET) to the QDs and to the activation of the luminescence of the QDs. (B) CRET luminescence signals of the (**16**)-functionalized QDs upon analyzing variable concentrations of (**17**) according to (A). (C) Multiplexed analysis of three different analytes (**17**), (**18**) and (**19**) by different sized QDs functionalized each with appropriate hairpin probes for analyzing the targets by the CRET mechanism. (D) CRET signals upon the multiplexed analysis of (**17**), (**18**) and (**19**) by the different sized QDs modified each with the appropriate hairpin, according to (C): (1) in the absence of the analytes; (2) in the presence of (**18**); (3) in the presence of (**19**); (4) in the presence of (**17**); (5) in the presence of all three analytes (**17**), (**18**) and (**19**). Reproduced with permission from reference (45). Copyright (2011) (American Chemical Society).*

Downloaded by 89.163.35.42 on November 27, 2012 | http://pubs.acs.org
Publication Date (Web): November 26, 2012 | doi: 10.1021/bk-2012-1112.ch001

Downloaded by 89.163.35.42 on November 27, 2012 | http://pubs.acs.org
Publication Date (Web): November 26, 2012 | doi: 10.1021/bk-2012-1112.ch001

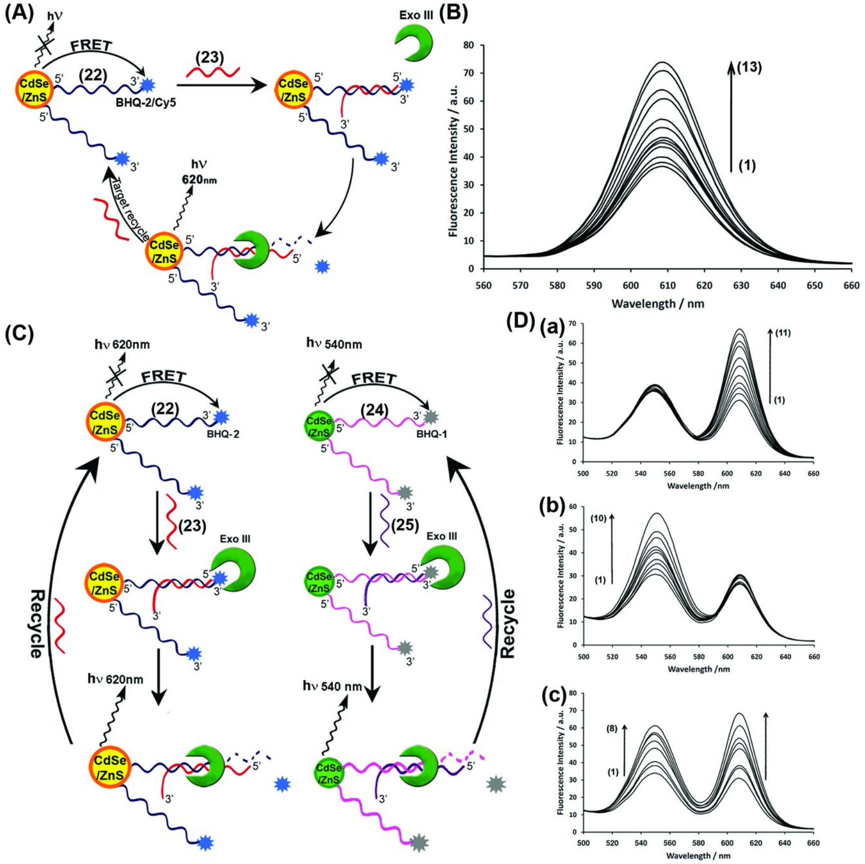
(A)
hν
FRET
CdSe /ZnS
(22)
5'
3'
BHQ-2/Cy5
(23)
Exo III
Target recycle
hν 620nm
(B)
Fluorescence Intensity / a.u.
Wavelength / nm
(13)
(1)
(C)
hν 620nm
hν 540nm
FRET
(22)
(24)
BHQ-2
BHQ-1
(23)
(25)
Exo III
Recycle
hν 540 nm
(D)
(a)
(11)
(1)
(b)
(10)
(1)
(c)
(8)
(1)
Fluorescence Intensity / a.u.
Wavelength /nm

*Figure 8. (A) Amplified analysis of the target DNA, (**23**), using Exo III as target-regeneration catalyst and quencher-functionalized particles as optical labels. (B) Time-dependent luminescence changes of the QDs upon the amplified analysis of (**23**), using Exo III as an amplifying catalyst, according to (A). Spectra were recorded at time intervals of 10 minutes. (C) Multiplexed analysis of two different DNA strands (**23**) and (**25**), using different-sized functionalized QDs and Exo III as amplification biocatalyst. (D) Time-dependent luminescence changes upon the multiplexed amplified analysis of the two DNA targets (**23**) and (**25**) according to (C): (a) In the presence of the QDs mixture and upon interaction with 1nM of (**24**), Spectra were recorded at time intervals of 10 min. (b) In the presence of the QDs mixture and upon interaction with 1nM of (**22**). Spectra were recorded at time intervals of 12 min. (c) In the presence of the QDs mixture and upon interaction with 1nM of both targets (**22**), and (**24**). Spectra were recorded at time intervals of 15 min. Reproduced with permission from reference (46). Copyright (2011) (American Chemical Society).*

The amplification of biosensing events is one of the challenging goals in bioanalytical science. An interesting approach to amplify the recognition events at modified semiconductor surfaces and to develop amplified optical QDs-based sensors (and multiplexed sensors) has included the application of Exonuclease III, Exo III (*46*). This enzyme specifically stimulates the hydrolytic "digestion" of the 3′-end of the nucleic acid strand being in a duplex structure with the complementary strand. (It should be noted that Exo III does not affect the 3′-end of single-stranded nucleic acids). Accordingly, the Exo III-amplified optical detection of an analyte DNA by the semiconductor QDs is depicted in Figure 8(A). The QDs were functionalized with the nucleic acid (**22**) that is labeled at its 3′-end with a black-hole quencher unit, BHQ-2, and it includes the recognition sequence for its hybridization with the analyte, (**23**). The luminescence of the QDs is quenched by the black-hole-modified quencher units through a FRET mechanism. The hybridization of the analyte DNA, (**23**), with the probe nucleic acid, in the presence of Exo III, results in the hydrolytic digestion of the probe nucleic acid, (**22**), leading to the release of the quencher units, and of the analyte DNA. As a result, the released nucleic acid hybridizes with another quencher-labeled probe strand associated with the QDs and this activates the Exo III digestion of the resulting duplex. Thus, the interaction of the analyte (**23**) with the (**22**)-functionalized QDs, in the presence of Exo III, leads to the regeneration of the analyte, and to the release of many quencher units as a result of one recognition event. The time-dependent increase in the luminescence of the QDs upon the Exo III-catalyzed regeneration of the analyte (**23**) is shown in Figure 8(B). The system enabled the analysis of (**23**) with a detection limit that corresponded to 1 pM. The system was further implemented for the multiplexed analysis of two different analytes, Figure 8(C). Two different sized QDs were functionalized with two different quencher-functionalized nucleic acids, (**22**) and (**24**), that act as probes for the analytes (**23**) and (**25**), respectively. Upon treatment of the QDs mixture with the different analytes, in the presence of Exo III, the luminescence of the QDs could be selectively activated by the analytes and the concomitant activation of the luminescence of the two-sized QDs by a mixture of the analytes was demonstrated, Figure 8(D).

Downloaded by 89.163.35.42 on November 27, 2012 | http://pubs.acs.org
Publication Date (Web): November 26, 2012 | doi: 10.1021/bk-2012-1112.ch001

Optical Biosensing with Metallic NPs

Metallic nanoparticles exhibit unique electrical, catalytic and optical properties (*47–50*). The charge-transport properties of metallic NPs were extensively used to electrically wire redox proteins with electrodes and to develop amperometric biosensors and biofuel cell elements (*51–57*). Similarly, electrocatalytic metallic NPs, e.g., Pt NPs were used as labels for the development of amplified electrochemical sensors (*58*, *59*). Isolated metal nanoparticles exhibit distinct, size-controlled energy levels. Subjecting the NPs to an external electric field of light induces a polarization of the conduction band electrons associated with the NPs, creating surface plasmon oscillation. This surface plasmon oscillation might lead to interparticle plasmonic coupling in a collective ensemble of NPs. While isolated metal nanoparticles exhibit size-controlled plasmon excitonic absorbance spectra, the coupling of plasmons in collective

NPs assemblies lead to a red-shifted absorbance. The surface plasmonic oscilation may also couple the surface plasmon waves associated with bulk metallic surfaces, leading to the polarization of the surface waves. The unique optical properties of nanometer-sized metallic NPs provide a broad spectrum of exciting opportunities for bioanalytical and biomedical applications (*60–63*). For example, the photoexcitation of Au NPs results in a localized heat source that was implemented to kill cancer cells or to separate duplex structures of DNA (*64–72*). Nonetheless, most exciting applications of plasmonic metallic NPs rest on the possibility to control the spectral plasmonic features by the size and shape of the NPs, to implement unique interparticle plasmonic coupling phenomena and utilize plasmonic surface spectroscopy for sensing (*73–79*), such as surface enhanced fluorescence (*80*) or surface enhanced Raman spectroscopy (*81*, *82*), and to use NPs-controlled Rayleigh scattering process to follow biorecognition events on the NPs (*83*). These unique features of metallic nanoparticles will be exemplified with several applications in the area of bioanalysis and nanomedicine.

Downloaded by 89.163.35.42 on November 27, 2012 | http://pubs.acs.org
Publication Date (Web): November 26, 2012 | doi: 10.1021/bk-2012-1112.ch001

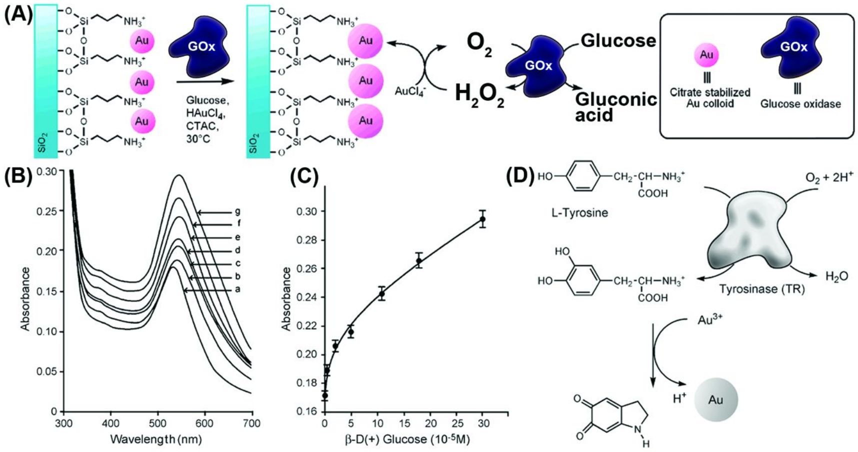
(A)
SiO2
Si
NH3+
Au
GOx
Glucose, HAuCl4, CTAC, 30°C
AuCl4-
O2
H2O2
Glucose
Gluconic acid
Citrate stabilized Au colloid
Glucose oxidase
(B)
Absorbance
Wavelength (nm)
g
f
e
d
c
b
a
0.30
0.25
0.20
0.15
0.10
0.05
0
300
400
500
600
700
(C)
Absorbance
β-D(+) Glucose (10-5M)
0.30
0.28
0.26
0.24
0.22
0.20
0.18
0.16
0
5
10
15
20
25
30
(D)
L-Tyrosine
Tyrosinase (TR)
O2 + 2H+
H2O
Au3+
H+
Au
HO
CH2-CH-NH3+
COOH
N
H

Figure 9. (A) Schematic analysis of glucose through the glucose-oxidase-mediated growth of Au NPs on glass supports. (B) Absorbance changes upon analyzing different concentrations of glucose, according to (A): (a) 0 M; (b) 5 µM; (c) 20 µM; (d) 50 µM; (e) 110 µM; (f) 180 µM; (g) 300 µM. (C) Calibration curve corresponding to the absorbance of the enlarged Au NPs upon analyzing different concentrations of glucose through the growth of Au NP, according to (A), for a fixed time-interval of 10 minutes. (D) Analysis of tyrosinase through the enzyme-mediated oxidation of L-DOPA and the growth of Au nanoparticles. (A) to (C) were reproduced with permission from reference (85). Copyright (2005) (American Chemical Society). (D) was reproduced with permission from reference (87). Copyright (2005) (American Chemical Society).

In Functional Nanoparticles for Bioanalysis, Nanomedicine, and Bioelectronic Devices Volume 1; Hepel, M., et al.;
ACS Symposium Series; American Chemical Society: Washington, DC, 2012.

Enzymes were found to act as effective catalysts for the growth of metal NPs (*84*). For example, glucose oxidase, GOx, catalyzes the oxidation of glucose by oxygen to yield gluconic acid and hydrogen peroxide (*85*). The resulting hydrogen peroxide was found to act as reducing agent that mediated the reduction of $AuCl_4^-$ to Au NPs in the presence of Au NPs seeds as catalysts. The enlargement of the Au NPs by the biocatalytic reaction could be followed by the increase in the plasmon absorbance of the resulting Au NPs. Figure 9(A) depicts schematically the biocatalyzed GOx-mediated increase of Au NPs associated with a glass support. The Au NPs catalytic seeds were linked to an aminopropylsilylated glass surface, and the biocatalyzed oxidation of glucose yields H_2O_2 that reduced $AuCl_4^-$ to Au resulting in the enlargement of the particles. The catalytic growth of the surface-confined Au NPs was then followed spectroscopically, Figure 9(B). As the time-interval of the biocatalytic growth was prolonged, the plasmon absorbance of the NPs was intensified. Aside from the red-shift of the plasmon absorbance of the NPs that is consistent with the growth of the NPs as the biocatalytic process was prolonged, a new absorbance band at 620 nm was observed at longer time-intervals of the biocatalytic enlargement of the NPs. This phenomenon is visible to the naked eye with a color transition from red to blue that is attributed to interparticle coupling of the localized plasmons that is facilitated upon enlargement of the NPs on the surface, bringing the NPs into close proximities. Since the growth of the Au NPs is controlled by the concentration of H_2O_2, the enlargement of the NPs and the absorbance changes is related to the concentration of glucose in the samples, Figure 9(C).

Other enzymes also reveal biocatalytic activities toward the growth of metallic NPs. For example, the hydrolysis of p-aminophenol phosphate by alkaline phosphatase yields the p-aminophenol product, a hydroquinone-type reducing agent that was found to reduce Ag^+-ions to Ag° on catalytic Au NPs seeds (*86*). Similarly, tyrosinase, an enzyme over-expressed in melanoma cancer cells oxidizes tyrosine-containing substrates to the L-DOPA derivatives. The resulting L-DOPA (o-hydroquinone derivatives) reduces $AuCl_4^–$ salts to form Au° NPs, Figure 9(D). For example, L-tyrosine was hydroxylated by tyrosinase/O_2 to form the L-DOPA component. The product reduced, then, $AuCl_4^-$ to form Au NPs (*87*). Also, 1,4-dihydronicotinamide adenine dinucleotide (phosphate), NAD(P)H was found to act as a reducing agent for the synthesis of Au NPs, and the process was used to analyze the substrates of NAD^+-dependent enzymes (*88*, *89*). For example, the NAD^+-dependent enzyme lactate dehydrogenase mediates the oxidation of lactate to pyruvate with the concomitant generation of the NADH cofactor. The NADH cofactor reduces Au NPs seeds to Au NPs through the NADH-stimulated reduction of $AuCl_4^-$, and then deposits Au on the NPs seeds. The plasmon absorbance of the Au NPs provided, then, a physical readout signal for the growth of the NPs and the content of NADH. As the concentration of NADH upon the biocatalyzed oxidation of lactate, in the presence of NAD^+/lactate dehydrogenase, is controlled by the concentration of the substrate (lactate), the plasmon absorbance of the resulting Au NPs related directly to the concentration of the substrate (*89*).

Downloaded by 89.163.35.42 on November 27, 2012 | http://pubs.acs.org
Publication Date (Web): November 26, 2012 | doi: 10.1021/bk-2012-1112.ch001

The aggregation of Au NPs results in the inter-particle electronic plasmon coupling. This phenomenon is accompanied by depletion of the localized NPs plasmon absorbance, and the formation of a red-shifted interparticle plasmonic exciton absorbance (*90*, *91*). This process is characterized by a red-to-blue transition upon the aggregation of the NPs. Numerous sensing platforms were developed based on the aggregation (or de-aggregation) of Au NPs and the accompanying color changes as reporting signal for the sensing events (*92–95*). As an example, NPs that were functionalized with two kinds of nucleic acids, which were complementary to two segments of an analyte DNA, were hybridized with the analyte DNA. This led to the aggregation of the NPs and to the formation of a red-shifted interparticle plasmon absorbance of the nanoparticles aggregates (*96*, *97*).

Downloaded by 89.163.35.42 on November 27, 2012 | http://pubs.acs.org
Publication Date (Web): November 26, 2012 | doi: 10.1021/bk-2012-1112.ch001

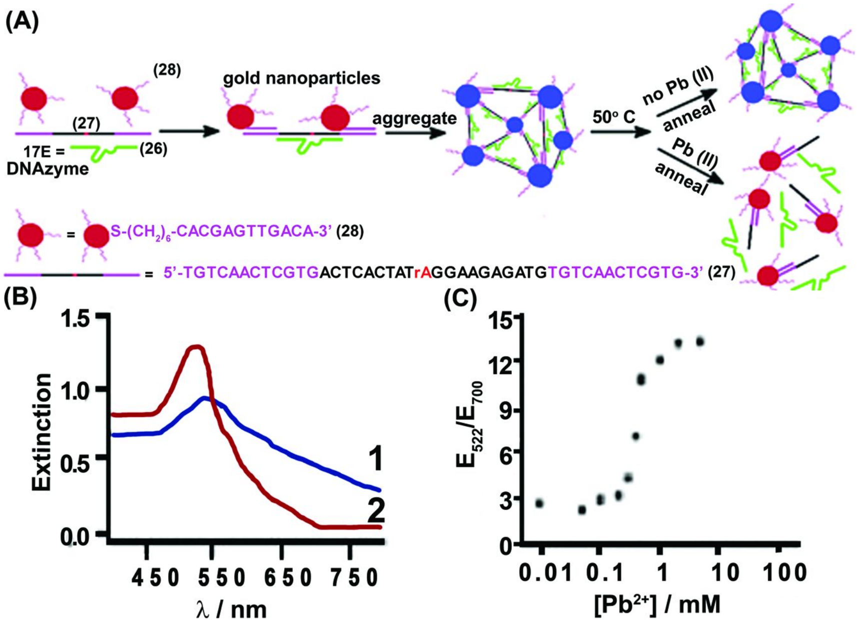

Figure 10. (A) Analysis of Pb^{2+}-ions through the Pb^{2+}-dependent DNAzyme cleavage of aggregated Au NPs, and the generation of separated single Au NPs. (B) Absorption spectra corresponding to: (1) The DNA-crosslinked Au NPs aggregate; (2) The separated single Au NPs after cleavage of the aggregate by the Pb^{2+}-dependent DNAzyme, $[Pb^{2+}]$ = 5 mM. (C) Calibration curve corresponding to the spectral changes of the aggregated Au NPs (presented as the ratio of monomer absorbance/aggregate absorbance) after cleavage of the aggregate generated in the presence of different concentrations of Pb^{2+} ions. Reproduced with permission from reference (101). Copyright (2007) (American Chemical Society).

Downloaded by 89.163.35.42 on November 27, 2012 | http://pubs.acs.org
Publication Date (Web): November 26, 2012 | doi: 10.1021/bk-2012-1112.ch001

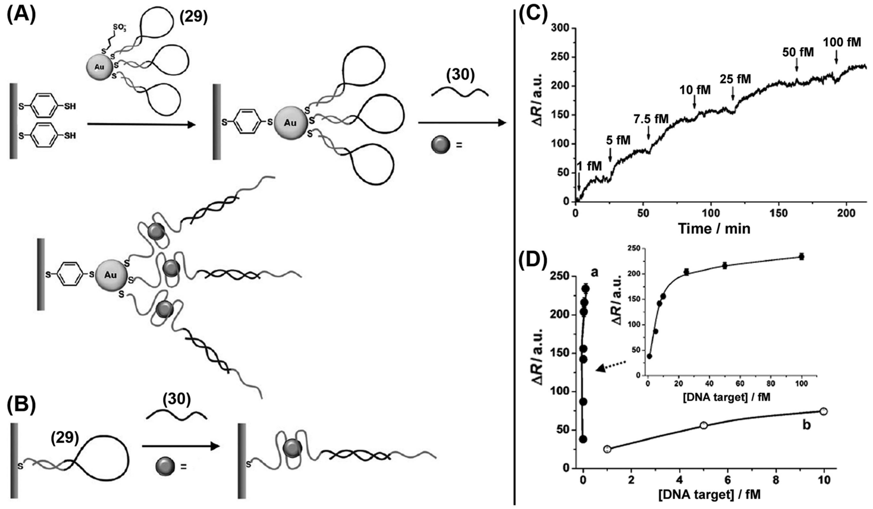

Figure 11. (A) Amplified surface plasmon resonance (SPR) detection of DNA using hairpin-functionalized nucleic acids assembled on Au surfaces as target-capturing probes, and the formation of a hemin/G-quadruplex label and the coupling between the localized plasmon of the Au NPs and the surface plasmon wave as amplification path. (B) SPR detection of the garget DNA by a hairpin probe linked directly to the Au surface that yields the hemin/G-quadruplex, but lacks the amplifying Au NPs. (C) Sensogram corresponding to the reflectance changes at θ =61.5°, observed upon analyzing different concentrations of the target DNA according to (A). (D) Calibration curves corresponding to: (a) The reflectance changes upon analyzing different concentrations of the target DNA according to (A); (b) The reflectance changes upon analyzing different concentrations of the target DNA according to (B). Reproduced with permission from reference (40). Copyright (2011) (Wiley-VCH).

An alternative approach based on the de-aggregation of metallic NPs, involved the use of nucleic acid-cleaving DNAzymes. DNAzymes exhibiting nucleic acid cleavage activities, in the presence of added cofactors, have been elicited and used for the specific scission of DNA sequences. For example, nucleic acid sequences that specifically bind Pb^{2+}, Mg^{2+}, Cu^{2+} or UO^{2+} ions (*98–101*), or histidine (*102*) were found to yield supramolecular structures that cleave specific DNA sequences. Using these properties, pre-designed nucleic acid sequences were tethered to the DNAzyme structures to yield functional units for the amplified detection of the cofactors, or alternatively, for target DNA/RNA units. One approach (*103*), included the use of the Pb^{2+}-dependent RNA-cleaving DNAzyme 17E (**26**) as a biocatalyst that stimulated the de-aggregation of Au nanoparticles through a cleavage process, thus providing a colorimetric sensor for Pb^{2+} ions, Figure 10 (A). The nucleic acid (**27**) included the RNA cleavage site and the base sequences that hybridize with the Pb^{2+}-dependent DNAzyme 17E (**26**). To the 3′ and 5′ ends of the cleavable nucleic acid were tethered nucleic acid sequences complementary to the nucleic acid, (**28**)-functionalized Au nanoparticles. The Au nanoparticles were then aggregated by the bridging cleavable nucleic acid (**27**), while the DNAzyme was hybridized with the single-stranded domain of (**27**). Bridging of the Au nanoparticles by the nucleic acid (**27**) resulted in the formation of an Au nanoparticles aggregate, reflected by the blue color (λ = 700 nm) of the system as a result of an interparticle coupled plasmon. Addition of Pb^{2+} activated the DNAzyme, resulting in the scission of (**27**) at the RNA nucleobase. This resulted in the separation of the cleaved units from the Au nanoparticles, leading to the de-aggregation of the particles that exhibited the red color (λ =522 nm) characteristic to the individual Au nanoparticles, Figure 10(B). The extent of de-aggregation of the gold nanoparticles and thus the color changes of the system, were controlled by the concentration of Pb^{2+} ions. The system enabled the detection of Pb^{2+} with a sensitivity that corresponded to 5×10^{-7} M.

Downloaded by 89.163.35.42 on November 27, 2012 | http://pubs.acs.org
Publication Date (Web): November 26, 2012 | doi: 10.1021/bk-2012-1112.ch001

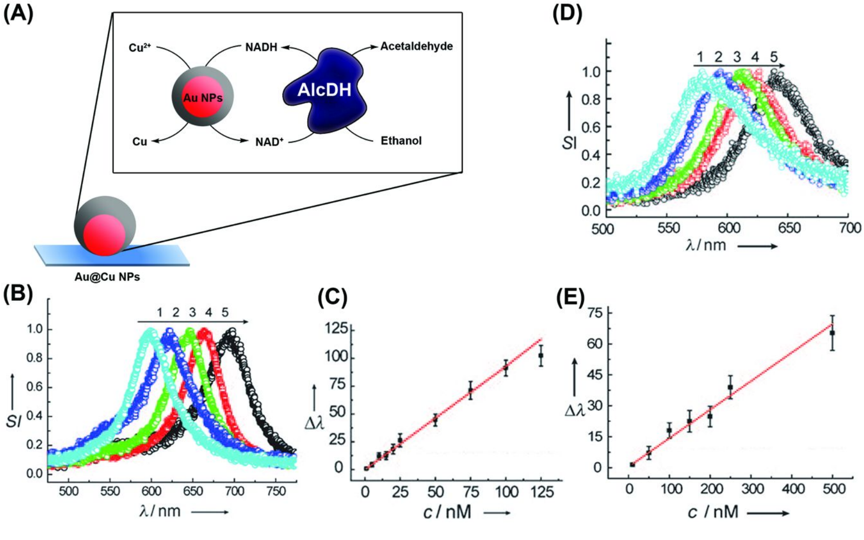

Figure 12. (A) Scehmatic NADH-mediated deposition of Cu on Au NPs and the application of the process for monitoring the alcohol dehydrogenase (AlcDH)-catalyzed oxidation of ethanol. (B) The PRRS spectra of Au@Cu core-shell nanoparticles upon interaction with different concentrations of NADH for a fixed time interval of 2 hours: (1) 25 nM; (2) 50 nM; (3) 75 nM; (4) 100 nM. (C) The derived calibration curve corresponding to the shift of the PRRS spectra at different concentration of NADH for a single Au NP. (D) The PRRS spectra of a single Au NP upon interaction with different concentrations of ethanol for a fixed time interval of 30 minutes, in the presence of NAD^+, AlcDH and $CuCl_2$. (E) The derived calibration curve corresponding to the shift in the PRRS spectra of a single Au NP at different concentrations of ethanol. Reproduced with permission from reference (114). Copyright (2011) (Wiley-VCH).

Downloaded by 89.163.35.42 on November 27, 2012 | http://pubs.acs.org
Publication Date (Web): November 26, 2012 | doi: 10.1021/bk-2012-1112.ch001

Surface plasmon resonance (SPR) provides a versatile technique to monitor dielectric changes occurring at thin metal surfaces, e.g., Au or Ag, that exhibit a surface plasmonic wave (*62*, *63*). This method was extensively used to follow biorecognition events on metal surfaces such as the formation of antigen-antibody complexes (*104*, *105*), receptor-substrate binding interactions and more (*59*, *106*, *107*). Amplification of SPR sensing events was demonstrated by labeling of the biorecognition complexes with high-molecular-weight labels such as liposomes (*108*) or latex particles (*109*) that introduce substantial changes in the dielectric properties at the sensing interface. These labels were used to amplify DNA recognition events. An important method to amplify SPR sensing methods included the coupling of the localized plasmon of metallic NPs, e.g., Au or Ag with the surface plasmon wave. It was found that this coupling phenomenon leads to substantial shifts in the surface plasmon resonance spectrum (*63*), and, thus, minute changes in the dielectric properties of the sensing interface, as a result of the sensing events, may be recognized by the SPR shifts. Indeed, Au NPs labeled with nucleic acids were used to amplify DNA detection on Au surfaces using a "sandwich assay" (*106*). The amplified SPR detection of DNA using the combined application of Au NPs and hemin as a dielectric modifier probe is presented in Figure 11(A) (*40*). A Au coated glass slide was modified with Au NPs (13 nm), and the metallic NPs were functionalized with the hairpin nucleic acid nanostructures (**29**). The hairpin structure included in its loop region the recognition sequence for the target DNA and in its "stem" region a domain corresponding to a part of a G-quadruplex forming sequence. The stability of the duplex stem region prohibits the formation of the G-quadruplex. In the presence of the analyte DNA that hybridizes with the loop, the hairpin structure is opened resulting in the "uncaging" of the G-quadruplex sequence and its self-assembly to the G-quadruplex. The hemin binds effectively to the G-quadruplex and this result in a substantial change in the dielectric properties of the interface. The dielectric changes of the surface upon analyzing the target DNA, (**30**) are then probed by SPR and amplified by the electronic coupling between the Au NPs linked to the Au surface. The amplified SPR detection of DNA was further confirmed by comparing the analytical performance of the Au NPs system to the analogous hairpin configuration on a flat Au surface that lacks the amplifying Au NPs, Figure 11(B). The sensogram corresponding to the reflectance changes of the system, at a constant angle upon the sensing of different concentrations of the target DNA are displayed in Figure 11(C). Control experiments showed that in the absence of hemin, or a nucleic acid probe that does not form the hemin/G-quadruplex, these reflectance changes are not observed. These results imply that formation of the hemin/G-quadruplexes is, indeed, essential to amplify the sensing of (**30**). Figure 11(D), curve (a), shows the derived calibration curve for analyzing (**30**) by the Au NPs composite. The detection limit for sensing (**30**) corresponded to 1 fM. For comparison, the calibration curve corresponding to the analysis of (**30**) on the flat Au surface is displayed in Figure 11(D), curve (b). The detection limit for the SPR analysis of (**30**) by the flat (**29**)-functionalized surface, that lacked the NPs, corresponded to 1 pM. A control experiment where Pt NPs substituted the Au NPs on the Au surface confirmed that enhanced sensitivity in the Au NPs system did not originate from a higher surface density of the hairpin probes, (**29**), on the sensing surface. The surface coverage of (**30**) on the Au NPs and Pt NPs was almost identical yet the sensitivity of detection of (**30**) by the (**29**)-modified Pt NPs linked to the Au support was very similar to the sensitivity for analyzing (**30**) on the flat Au surface, lacking the Au NPs. This result was attributed to the fact that the Pt NPs lack a localized plasmon exciton that couples to the surface plasmon wave, and hence, the amplification mechanism for sensing of (**30**) is prohibited. Accordingly, the impressive sensitivity observed for the analysis of (**30**) by the (**29**)-functionalized Au NPs associated with the Au surface was attributed to the amplification of the dielectric change, generated by the resulting hemin/G-quadruplexes through the electronic coupling between the local plasmonic excitons associated with the NPs and the surface plasmon wave. The system revealed selectivity, and one-, two-, or three base mutations in the target DNA (**30**) were easily discriminated. Furthermore, the amplification principle was further extended to develop aptamer-substrate sensor systems or ion-sensing (Hg^{2+}) sensing platform by designing and immobilizing hairpin nanostructures on the Au NPs that are being opened by the aptamer substrate or Hg^{2+} ions and self-assemble the respective hemin/G-quadruplexes labels (*40*).

A further plasmonic effect that was implemented for sensing, and for monitoring intracellular metabolic processes involved plasmon resonance Rayleigh scattering spectroscopy (PRRS) of single metallic NPs using dark-field microscopy (DFM). Recent studies have implemented DFM to characterize the size, shape, composition, and chemical environments of plasmonic NPs (*110–113*). The PRRS method was specifically applied for developing sensing platforms and to probe intracellular transformations at the single NP level (*114*). The 1,4-dihydronicotinamide adenine dinucleotide cofactor (NADH) was found to catalyze the reduction of Cu^{2+} ions on Au NPs to yield Au/Cu core-shell composites. The PRRS spectra of the resulting core-shell particles are dominated by the sizes and dielectric properties of the composite. Figure 12(A) shows the schematic NADH-mediated deposition of Cu on Au NPs and the application of the process for monitoring the alcohol dehydrogenase (AlcDH)-catalyzed oxidation of ethanol and for the sensing of ethanol. The PRRS spectra of the core-shell Cu/Au nanoparticles generated by different concentrations of NADH, and growth of the particles after a fixed time-interval of 2 hours are shown in Figure 12(B), together with the respective calibration curve, Figure 12(C). As the growth of the core-shell Au/Cu NPs is prolonged, the PRRS spectra are red-shifted, and the peak-scattering peak shifted by ca. $\Delta\lambda_{max}$ = 100 nm (from 590 nm of the Au NPs to 700 nm). As the red-shift scattering peak revealed linear correlation with the concentration of NADH the system could be used to follow biocatalytic transformations that include NAD^+-dependent enzymes, and to sense quantitatively their substrates. This is exemplified in Figure 12(D) with the analysis of ethanol in the presence of NAD^+ and alcohol dehydrogenase, AlcDH. The biocatalyzed oxidation of ethanol leads to the formation of NADH that reduces Cu^{2+} ions to the Cu-coated Au NPs. The resulting red-shift of the PRRS spectra are then controlled by the concentration of NADH that is directly related to the concentration of ethanol. Figure 12(D) shows the red-shifted PRRS spectra of a single Au NP interacted with a NADH-generating solution consisting of NAD^+/AlcDH/Cu and variable concentrations of ethanol for a fixed time-interval

Downloaded by 89.163.35.42 on November 27, 2012 | http://pubs.acs.org
Publication Date (Web): November 26, 2012 | doi: 10.1021/bk-2012-1112.ch001

of 30 minutes. As the concentration of ethanol increases a higher red-shift $\Delta\lambda_{max}$ in the PRRS spectrum peak is observed, consistent with the formation of higher concentration of NADH in the reaction medium and enhanced deposition of the Cu shell on the Au NPs core. Figure 12(E) depicts the resulting calibration curve demonstrating the analysis of ethanol at a single NPs level.

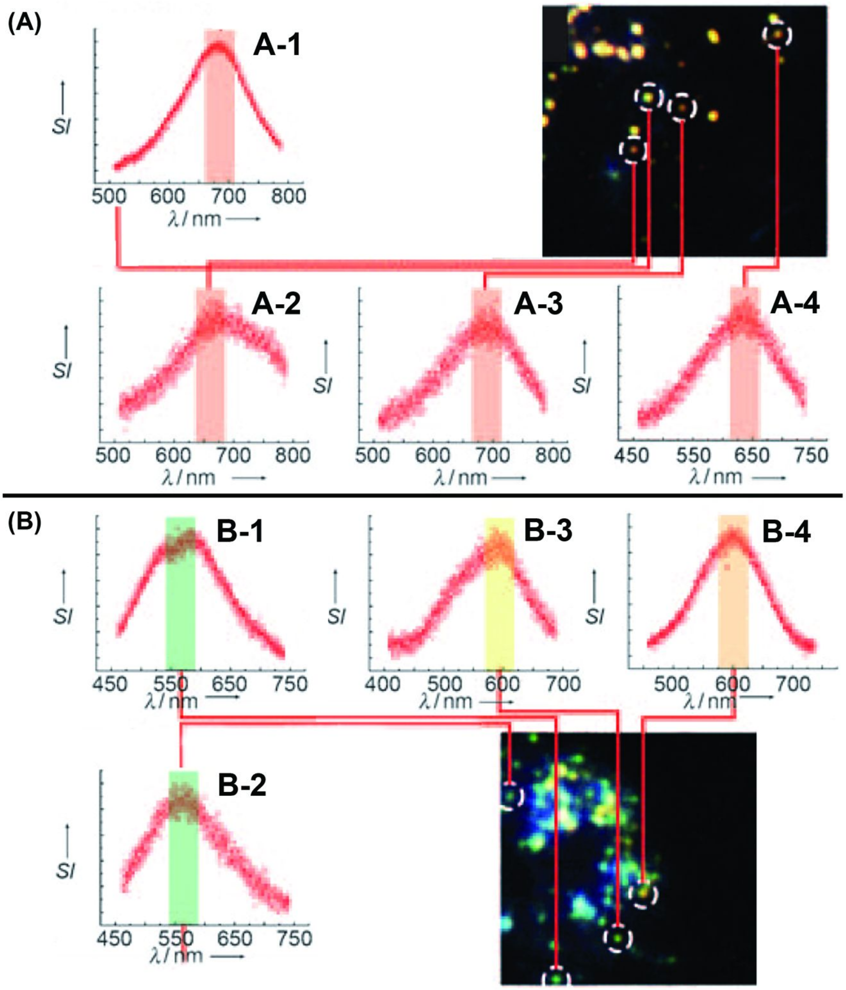

Figure 13. (A) A DFM image of a HeLa cell containing AuNPs after incubation with $CuCl_2$, in the absence of taxol. A-1 to A-4: the scattering spectra of different Au@Cu core-shell NPs in a living HeLa cell. (B) A DFM image of a HeLa cell containing AuNPs that was pre-treated with Taxol, (10 µM), and then with $CuCl_2$. B-1 to B-4: the scattering spectra of different AuNPs in a living HeLa cell. Reproduced with permission from reference (114). Copyright (2011) (Wiley-VCH).

Downloaded by 89.163.35.42 on November 27, 2012 | http://pubs.acs.org
Publication Date (Web): November 26, 2012 | doi: 10.1021/bk-2012-1112.ch001

Downloaded by 89.163.35.42 on November 27, 2012 | http://pubs.acs.org
Publication Date (Web): November 26, 2012 | doi: 10.1021/bk-2012-1112.ch001

The successful detection of the NADH cofactor through the NADH mediated reduction of Cu^{2+} on Au NPs and the probing of the formation of the Au/Cu core-shell particles by means of PRRS spectroscopy was adapted to follow intracellular metabolic pathways. This method was further used to identify the known inhibiting activity of the anti-cancer drug Taxol, (**6**), on the metabolism of cancer cells, as a general approach for drug-screening. The NADH cofactor is a key intracellular ingredient formed in the cell metabolic pathway. Accordingly, the Au NPs were incorporated into HeLa cancer cells and the cells were characterized by bright-field microscopy and dark-field microscopy upon incubation in buffer solution that included $CuCl_2$. While the cell-incorporated Au NPs revealed at t = 0 a characteristic PRRS peak at ~590, after three hours of reaction in the presence of the Cu^{2+}, the PRRS spectra of individual Au NPs shifted to 660-680 nm, Figure 13(A), consistent with the formation of the Au/Cu core-shell NPs in the cells as a result of cell metabolism. In turn, it is well established that the treatment of HeLa cancer cells with Taxol inhibits the cell metabolism. This phenomenon was confirmed by the incorporation of the Au NPs into the Taxol pre-treated HeLa cells and their subsequent interaction with Cu^{2+} ions, Figure 13(B). The inhibition in the cell metabolism retards the formation of the NADH cofactor, leading to the inefficient reduction of the Cu^{2+} ions on the Au NPs. Accordingly, the PRRS spectra of the individual Au NPs are almost unchanged and their peak scattering bands appear in the region 560-600 nm characteristic to the base NPs. These results indicate that the PRRS spectra of single Au NPs provide an effective tool to probe the intracellular metabolism, and the method holds great promise in nano-medicine as a drug-screening tool.

Conclusions and Perspectives

Substantial progress has been demonstrated in the past decade in the implementation of semiconductor QDs and metallic NPs for bioanalytical application. Semiconductor QDs have been successfully used to follow enzyme activities, gene analysis, antigen-antibody complexes, and aptamer-substrate complexes. Different photophysical mechanisms have been used in these analytical platforms including the fluorescence resonance energy transfer (FRET), electron transfer quenching, and chemiluminescence resonance energy transfer (CRET) processes. Besides the unique photophysical properties of semiconductor QDs (high luminescence quantum yield, photostability, large Stoke’s shifts and narrow luminescence band) the size-controlled luminescence features of semiconductor QDs, turn the QDs as ideal optical materials for developing multiplexed analysis assays. In this context, the recently reported chemiluminescence resonance energy transfer (CRET), - based multiplexed luminescence analysis of different DNAs (*45*), hold great promise as it demonstrates the optical analysis of genes without external irradiation. A serious limitation in using the QDs as labels for bioanalytical applications, specifically for medical applications, is, however, the limited sensitivity of the QDs-based systems. This is particularly important for the ultrasensitive detection of DNA biomarkers, using nucleic acid-functionalized QDs, or peptide/protein biomarkers using aptamer-modified QDs, due to the low concentrations of the biomarkers in biological fluids. The development of amplified detection schemes with semiconductor QDs is at its infancy. Impressive improvement of the QDs-based detection of DNA or aptamer substrate complexes was recently demonstrated by coupling an enzyme (exonuclease III) as a biocatalyst for the regeneration of the analyte. In fact, the amplified detection of DNA, aptamer-protein complexes, and ions using enzymes (*115*, *116*), and particularly DNAzymes (*39*, *117*, *118*), was significantly advanced in the recent years. The conjugation of such biocatalytic cycles to semiconductor QDs holds great promise for the future application of the QDs for the multiplexed, ultrasensitive, detection of biomarkers of clinical diagnostics significance.

While the development of generic QD-based sensing platform is quite-well established, the practical implementation of the systems in nano-medicine is scarce. The possibilities to detect biocatalytic biomarkers for certain diseases such as telomerase or tyrosinase for cancer cells and the detection of casein kinase as a marker for cancer cells or the Alzheimer's disease were demonstrated, but the practical utilization of these systems beyond the basic scientific level needs to be established. In this context, the future development of QDs-based aptasensor for biomarkers holds great promise. The protocols for eliciting aptamers against peptides/proteins are well established. Similarly, amplified QDs-based aptasensors were developed, and thus, the combination of new aptamers and QDs sensing platforms provides promising, yet challenging, means for the multiplexed analysis of biomarkers. Most of the systems discussed in the present chapter have implemented "clean" analytical enviroments. Naturally, the application of "real" biological samples, such as blood or urine, is anticipated to reveal non-specific adsorption phenomena and perturbance of the analytical platforms. Numerous studies have addressed means to minimize non-specific binding events (*119–125*). Thus, presumably, the further modification of the capping layers of the QDs will be required to adapt the systems for sensing real biological samples. Furtheremore, the cytotoxicity of the QDs-based nanosensors needs to be addressed in any future in vivo applications. This subject raised some controversy reports (*126–129*), and remains a challenge for future research.

The application of metallic NPs for bioanalytical applications was significantly advanced in the past fifteen years. Different analytes, particularly genes, proteins and toxic metal ions were analyzed by the analyte-induced aggregation/deaggregation of metallic NPs and the accompanying spectral changes. Several commercial enterprises are making efforts to bring these scientific developments into clinical, analytical practice. Similarly, the impressive sensitivities demonstrated with surface plasmon resonance (SPR) sensors upon the labeling of the recognition events with Au nanoparticles represent a major advance in analytical science that merits further developments. The amplified surface plasmon resonance detection of bio-analytes through the coupling between the localized plasmon of metallic nanoparticles (Au, Ag) and the surface plasmon wave represents a fundamental paradigm for ultrasensitive detection. In fact, amplified sensing through metal NPs plasmonic effects is a rapidly progressing area, and different optical methods such as surface enhanced resonance Raman spectroscopy (SERS), surface enhanced fluorescence spectroscopy (SEFS) and

Downloaded by 89.163.35.42 on November 27, 2012 | http://pubs.acs.org
Publication Date (Web): November 26, 2012 | doi: 10.1021/bk-2012-1112.ch001

plasmon resonance Rayleigh scattering spectroscopy (PRRS) are anticipated to find important application in the development of bioanalytical assays for biomarkers.

While ingenious *in vitro* bioanalytical assays using semiconductor QDs or metallic NPs were developed, the use of the QDs and NPs for probing intracellular processes, and particularly, for *in vivo* sensing is at its infancy. Numerous studies demonstrated the incorporation of semiconductor QDs or metallic NPs into cells and biological tissues, and the application of these nanomaterials for imaging the cells/tissues. Albeit these studies revealed methodologies to guide the nanoscale materials into cells/tissues and to microscopically monitor the nanostructures, the real scientific challenges are ahead of us. The implementation of semiconductor QDs and metallic NPs for probing metabolic pathways, and to follow intracellular signal transduction mechanisms, are important scientific goals. Specifically, the use of functional QDs or NPs for the *in vivo* detection of biomarkers will attract substantial future research efforts. In this context, the demonstration that functionalized semiconductor QDs follow intracellular metabolism in cancer cell and may be used to probe anti-cancer drugs indicate the future possibilities of these systems for drug screening. Also, the successful time-dependent detection of intracellular metabolism by following the intracellular growth of core-shell metal nanoparticles using dark-field microscopy suggests that dynamic intracellular reactions may be followed at the single particle level.

Downloaded by 89.163.35.42 on November 27, 2012 | http://pubs.acs.org
Publication Date (Web): November 26, 2012 | doi: 10.1021/bk-2012-1112.ch001

Acknowledgments

Parts of this research were supported by NanoSensoMach (ERC) Advanced Grant No. 267574 under the EC FP7/2007-2013 program and by the Israel Science Foundation.

References

1. Katz, E.; Willner, I. *Angew. Chem., Int. Ed.* **2004**, *43*, 6042–6108.
2. Niemeyer, C. M. *Angew. Chem., Int. Ed.* **2001**, *40*, 4128–4158.
3. Gu, H. W.; Xu, K. M.; Xu, C. J.; Xu, B. *Chem. Commun.* **2006**, 941–949.
4. Baron, R.; Willner, B.; Willner, I. *Chem. Commun.* **2007**, 323–332.
5. Willner, I.; Basnar, B.; Willner, B. *FEBS J.* **2007**, *274*, 302–309.
6. Medintz, I. L.; Uyeda, H. T.; Goldman, E. R.; Mattoussi, H. *Nat. Mater.* **2005**, *4*, 435–446.
7. Chan, W. C. W.; Maxwell, D. J.; Gao, X. H.; Bailey, R. E.; Han, M. Y.; Nie, S. M. *Curr. Opin. Biotechnol.* **2002**, *13*, 40–46.
8. Somers, R. C.; Bawendi, M. G.; Nocera, D. G. *Chem. Soc. Rev.* **2007**, *36*, 579–591.
9. Gill, R.; Zayats, M.; Willner, I. *Angew. Chem., Int. Ed.* **2008**, *47*, 7602–7625.
10. Alivisatos, A. P. *Science* **1996**, *271*, 933–937.
11. Nirmal, M.; Brus, L. *Acc. Chem. Res.* **1999**, *32*, 407–414.
12. Wu, X. Y.; Liu, H. J.; Liu, J. Q.; Haley, K. N.; Treadway, J. A.; Larson, J. P.; Ge, N. F.; Peale, F.; Bruchez, M. P. *Nat. Biotechnol.* **2003**, *21*, 41–46.

13. Brus, L. *Appl. Phys. A* **1991**, *53*, 465–474.
14. Grieve, K.; Mulvaney, P.; Grieser, F. *Curr. Opin. Colloid Interface Sci.* **2000**, *5*, 168–172.
15. Alivisatos, P. *Nat. Biotechnol.* **2004**, *22*, 47–52.
16. Goldman, E. R.; Clapp, A. R.; Anderson, G. P.; Uyeda, H. T.; Mauro, J. M.; Medintz, I. L.; Mattoussi, H. *Anal. Chem.* **2004**, *76*, 684–688.
17. Gerion, D.; Chen, F. Q.; Kannan, B.; Fu, A. H.; Parak, W. J.; Chen, D. J.; Majumdar, A.; Alivisatos, A. P. *Anal. Chem.* **2003**, *75*, 4766–4772.
18. Nishizuka, Y. *Nature* **1984**, *308*, 693–698.
19. Manning, G.; Whyte, D. B.; Martinez, R.; Hunter, T.; Sudarsanam, S. *Science* **2002**, *298*, 1912–1934.
20. Ahmed, K.; Davis, A. T.; Wang, H. M.; Faust, R. A.; Yu, S. H.; Tawfic, S. *J. Cell. Biochem.* **2000**, *35*, 130–135.
21. Flajolet, M.; He, G.; Heiman, M.; Lin, A.; Nairn, A. C.; Greengard, P. *Proc. Natl. Acad. Sci. U.S.A.* **2007**, *104*, 4159–4164.
22. Hanger, D. P.; Byers, H. L.; Wray, S.; Leung, K. Y.; Saxton, M. J.; Seereeram, A.; Reynolds, C. H.; Ward, M. A.; Anderton, B. H. *J. Biol. Chem.* **2007**, *282*, 23645–23654.
23. Critchfield, J. W.; Coligan, J. E.; Folks, T. M.; Butera, S. T. *Proc. Natl. Acad. Sci. U.S.A.* **1997**, *94*, 6110–6115.
24. Houseman, B. T.; Huh, J. H.; Kron, S. J.; Mrksich, M. *Nat. Biotechnol.* **2002**, *20*, 270–274.
25. Freeman, R.; Finder, T.; Gill, R.; Willner, I. *Nano Lett.* **2010**, *10*, 2192–2196.
26. Freeman, R.; Gill, R.; Shweky, I.; Kotler, M.; Banin, U.; Willner, I. *Angew. Chem., Int. Ed.* **2009**, *48*, 309–313.
27. Patolsky, F.; Gill, R.; Weizmann, Y.; Mokari, T.; Banin, U.; Willner, I. *J. Am. Chem. Soc.* **2003**, *125*, 13918–13919.
28. Willner, I.; Zayats, M. *Angew. Chem., Int. Ed.* **2007**, *46*, 6408–6418.
29. Shlyahovsky, B.; Li, D.; Weizmann, Y.; Nowarski, R.; Kotler, M.; Willner, I. *J. Am. Chem. Soc.* **2007**, *129*, 3814–3815.
30. Ho, H. A.; Leclerc, M. *J. Am. Chem. Soc.* **2004**, *126*, 1384–1387.
31. Tuerk, C.; Gold, L. *Science* **1990**, *249*, 505–510.
32. Ellington, A. D.; Szostak, J. W. *Nature* **1990**, *346*, 818–822.
33. Freeman, R.; Li, Y.; Tel-Vered, R.; Sharon, E.; Elbaz, J.; Willner, I. *Analyst* **2009**, *134*, 653–656.
34. Gill, R.; Freeman, R.; Xu, J.-P.; Willner, I.; Winograd, S.; Shweky, I.; Banin, U. *J. Am. Chem. Soc.* **2006**, *128*, 15376–15377.
35. Angeletti, C.; Khomitch, V.; Halaban, R.; Rimm, D. L. *Diagn. Cytopathol.* **2004**, *31*, 33–37.
36. Weizmann, Y.; Beissenhirtz, M. K.; Cheglakov, Z.; Nowarski, R.; Kotler, M.; Willner, I. *Angew. Chem., Int. Ed.* **2006**, *45*, 7384–7388.
37. Xiao, Y.; Pavlov, V.; Niazov, T.; Dishon, A.; Kotler, M.; Willner, I. *J. Am. Chem. Soc.* **2004**, *126*, 7430–7431.
38. Li, D.; Shlyahovsky, B.; Elbaz, J.; Willner, I. *J. Am. Chem. Soc.* **2007**, *129*, 5804–5805.
39. Willner, I.; Shlyahovsky, B.; Zayats, M.; Willner, B. *Chem. Soc. Rev.* **2008**, *37*, 1153–1165.

Downloaded by 89.163.35.42 on November 27, 2012 | http://pubs.acs.org
Publication Date (Web): November 26, 2012 | doi: 10.1021/bk-2012-1112.ch001

Downloaded by 89.163.35.42 on November 27, 2012 | http://pubs.acs.org
Publication Date (Web): November 26, 2012 | doi: 10.1021/bk-2012-1112.ch001

40. Pelossof, G.; Tel-Vered, R.; Liu, X. Q.; Willner, I. *Chem.−Eur. J.* **2011**, *17*, 8904–8912.
41. Sharon, E.; Freeman, R.; Willner, I. *Anal. Chem.* **2010**, *82*, 7073–7077.
42. Sharon, E.; Freeman, R.; Riskin, M.; Gil, N.; Tzfati, Y.; Willner, I. *Anal. Chem.* **2010**, *82*, 8390–8397.
43. Travascio, P.; Witting, P. K.; Mauk, A. G.; Sen, D. *J. Am. Chem. Soc.* **2001**, *123*, 1337–1348.
44. Pavlov, V.; Xiao, Y.; Gill, R.; Dishon, A.; Kotler, M.; Willner, I. *Anal. Chem.* **2004**, *76*, 2152–2156.
45. Freeman, R.; Liu, X.; Winner, I. *J. Am. Chem. Soc.* **2011**, *133*, 11597–11604.
46. Freeman, R.; Liu, X.; Willner, I. *Nano Lett.* **2011**, *11*, 4456–4461.
47. Mulvaney, P. *Langmuir* **1996**, *12*, 788–800.
48. Wilcoxon, J. P.; Abrams, B. L. *Chem. Soc. Rev.* **2006**, *35*, 1162–1194.
49. McConnell, W. P.; Novak, J. P.; Brousseau, L. C.; Fuierer, R. R.; Tenent, R. C.; Feldheim, D. L. *J. Phys. Chem. B* **2000**, *104*, 8925–8930.
50. Murphy, C. J.; San, T. K.; Gole, A. M.; Orendorff, C. J.; Gao, J. X.; Gou, L.; Hunyadi, S. E.; Li, T. *J. Phys. Chem. B* **2005**, *109*, 13857–13870.
51. Xiao, Y.; Patolsky, F.; Katz, E.; Hainfeld, J. F.; Willner, I. *Science* **2003**, *299*, 1877–1881.
52. Zayats, M.; Katz, E.; Baron, R.; Willner, I. *J. Am. Chem. Soc.* **2005**, *127*, 12400–12406.
53. Zayats, M.; Willner, B.; Willner, I. *Electroanalysis* **2008**, *20*, 583–601.
54. Willner, I.; Willner, B. *Trends Biotechnol.* **2001**, *19*, 222–230.
55. Willner, B.; Katz, E.; Willner, I. *Curr. Opin. Biotechnol.* **2006**, *17*, 589–596.
56. Heller, A. *Acc. Chem. Res.* **1990**, *23*, 128–134.
57. Willner, I. *Science* **2002**, *298*, 2407–2408.
58. Polsky, R.; Gill, R.; Kaganovsky, L.; Willner, I. *Anal. Chem.* **2006**, *78*, 2268–2271.
59. Golub, E.; Pelossof, G.; Freeman, R.; Zhang, H.; Willner, I. *Anal. Chem.* **2009**, *81*, 9291–9298.
60. Homola, J. *Chem. Rev.* **2008**, *108*, 462–493.
61. Phillips, K. S.; Cheng, Q. *Anal. Bioanal. Chem.* **2007**, *387*, 1831–1840.
62. Lyon, L. A.; Musick, M. D.; Smith, P. C.; Reiss, B. D.; Pena, D. J.; Natan, M. J. *Sens. Actuators, B* **1999**, *54*, 118–124.
63. Agarwal, G. S.; Gupta, S. D. *Phys. Rev. B* **1985**, *32*, 3607–3611.
64. Govorov, A. O.; Richardson, H. H. *Nano Today* **2007**, *2*, 30–38.
65. Jain, P. K.; El-Sayed, I. H.; El-Sayed, M. A. *Nano Today* **2007**, *2*, 18–29.
66. Murphy, C. J.; Gole, A. M.; Stone, J. W.; Sisco, P. N.; Alkilany, A. M.; Goldsmith, E. C.; Baxter, S. C. *Acc. Chem. Res.* **2008**, *41*, 1721–1730.
67. Huang, X. H.; El-Sayed, I. H.; Qian, W.; El-Sayed, M. A. *J. Am. Chem. Soc.* **2006**, *128*, 2115–2120.
68. Han, G.; You, C. C.; Kim, B. J.; Turingan, R. S.; Forbes, N. S.; Martin, C. T.; Rotello, V. M. *Angew. Chem., Int. Ed.* **2006**, *45*, 3165–3169.
69. Radt, B.; Smith, T. A.; Caruso, F. *Adv. Mater.* **2004**, *16*, 2184–2189.
70. Skirtach, A. G.; Dejugnat, C.; Braun, D.; Susha, A. S.; Rogach, A. L.; Parak, W. J.; Mohwald, H.; Sukhorukov, G. B. *Nano Lett.* **2005**, *5*, 1371–1377.

Downloaded by 89.163.35.42 on November 27, 2012 | http://pubs.acs.org
Publication Date (Web): November 26, 2012 | doi: 10.1021/bk-2012-1112.ch001

71. Skirtach, A. G.; Javier, A. M.; Kreft, O.; Koehler, K.; Alberola, A. P.; Moehwald, H.; Parak, W. J.; Sukhorukov, G. B. *Angew. Chem., Int. Ed.* **2006**, *45*, 4612–4617.
72. Pissuwan, D.; Valenzuela, S. M.; Cortie, M. B. *Trends Biotechnol.* **2006**, *24*, 62–67.
73. Dreaden, E. C.; Alkilany, A. M.; Huang, X. H.; Murphy, C. J.; El-Sayed, M. A. *Chem. Soc. Rev.* **2012**, *41*, 2740–2779.
74. Sperling, R. A.; Parak, W. J. *Philos. Trans. R. Soc. London, Ser. A* **2010**, *368*, 1333–1383.
75. Baptista, P.; Pereira, E.; Eaton, P.; Doria, G.; Miranda, A.; Gomes, I.; Quaresma, P.; Franco, R. *Anal. Bioanal. Chem.* **2008**, *391*, 943–950.
76. Boisselier, E.; Astruc, D. *Chem. Soc. Rev.* **2009**, *38*, 1759–1782.
77. Sperling, R. A.; Rivera gil, P.; Zhang, F.; Zanella, M.; Parak, W. J. *Chem. Soc. Rev.* **2008**, *37*, 1896–1908.
78. Jain, P. K.; Lee, K. S.; El-Sayed, I. H.; El-Sayed, M. A. *J. Phys. Chem. B* **2006**, *110*, 7238–7248.
79. Liz-Marzan, L. M. *Langmuir* **2006**, *22*, 32–41.
80. Han, X. X.; Kitahama, Y.; Tanaka, Y.; Guo, J.; Xu, W. Q.; Zhao, B.; Ozaki, Y. *Anal. Chem.* **2008**, *80*, 6567–6572.
81. Bantz, K. C.; Meyer, A. F.; Wittenberg, N. J.; Im, H.; Kurtulus, O.; Lee, S. H.; Lindquist, N. C.; Oh, S.-H.; Haynes, C. L. *Phys. Chem. Chem. Phys.* **2011**, *13*, 11551–11567.
82. Vo-Dinh, T.; Wang, H.-N.; Scaffidi, J. *J. Biophotonics* **2010**, *3*, 89–102.
83. Li, Y.; Jing, C.; Zhang, L.; Long, Y.-T. *Chem. Soc. Rev.* **2012**, *41*, 632–642.
84. Willner, I.; Baron, R.; Willner, B. *Adv. Mater.* **2006**, *18*, 1109–1120.
85. Zayats, M.; Baron, R.; Popov, I.; Willner, I. *Nano Lett.* **2005**, *5*, 21–25.
86. Basnar, B.; Weizmann, Y.; Cheglakov, Z.; Willner, I. *Adv. Mater.* **2006**, *18*, 713–718.
87. Baron, R.; Zayats, M.; Willner, I. *Anal. Chem.* **2005**, *77*, 1566–1571.
88. Xiao, Y.; Pavlov, V.; Levine, S.; Niazov, T.; Markovitch, G.; Willner, I. *Angew. Chem., Int. Ed.* **2004**, *43*, 4519–4522.
89. Shlyahovsky, B.; Katz, E.; Xiao, Y.; Pavlov, V.; Willner, I. *Small* **2005**, *1*, 213–216.
90. Myroshnychenko, V.; Rodriguez-Fernandez, J.; Pastoriza-Santos, I.; Funston, A. M.; Novo, C.; Mulvaney, P.; Liz-Marzan, L. M.; Garcia de Abajo, F. J. *Chem. Soc. Rev.* **2008**, *37*, 1792–1805.
91. Ghosh, S. K.; Pal, T. *Chem. Rev.* **2007**, *107*, 4797–4862.
92. Giljohann, D. A.; Seferos, D. S.; Daniel, W. L.; Massich, M. D.; Patel, P. C.; Mirkin, C. A. *Angew. Chem., Int. Ed.* **2010**, *49*, 3280–3294.
93. Thaxton, C. S.; Georganopoulou, D. G.; Mirkin, C. A. *Clin. Chim. Acta* **2006**, *363*, 120–126.
94. Lin, Y.-W.; Huang, C.-C.; Chang, H.-T. *Analyst* **2011**, *136*, 863–871.
95. Li, D.; Wieckowska, A.; Willner, I. *Angew. Chem., Int. Ed.* **2008**, *47*, 3927–3931.
96. Storhoff, J. J.; Lazarides, A. A.; Mucic, R. C.; Mirkin, C. A.; Letsinger, R. L.; Schatz, G. C. *J. Am. Chem. Soc.* **2000**, *122*, 4640–4650.

97. Storhoff, J. J.; Elghanian, R.; Mucic, R. C.; Mirkin, C. A.; Letsinger, R. L. *J. Am. Chem. Soc.* **1998**, *120*, 1959–1964.
98. Breaker, R. R.; Joyce, G. F. *Trends Biotechnol.* **1994**, *12*, 268–275.
99. Tang, J.; Breaker, R. R. *Proc. Natl. Acad. Sci. U.S.A.* **2000**, *97*, 5784–5789.
100. Liu, J.; Brown, A. K.; Meng, X.; Cropek, D. M.; Istok, J. D.; Watson, D. B.; Lu, Y. *Proc. Natl. Acad. Sci. U.S.A.* **2007**, *104*, 2056–2061.
101. Liu, J.; Lu, Y. *J. Am. Chem. Soc.* **2007**, *129*, 9838–9839.
102. Roth, A.; Breaker, R. R. *Proc. Natl. Acad. Sci. U.S.A.* **1998**, *95*, 6027–6031.
103. Liu, J. W.; Lu, Y. *J. Am. Chem. Soc.* **2003**, *125*, 6642–6643.
104. Lyon, L. A.; Musick, M. D.; Natan, M. J. *Anal. Chem.* **1998**, *70*, 5177–5183.
105. Mauriz, E.; Calle, A.; Lechuga, L. M.; Quintana, J.; Montoya, A.; Manclus, J. J. *Anal. Chim. Acta* **2006**, *561*, 40–47.
106. He, L.; Musick, M. D.; Nicewarner, S. R.; Salinas, F. G.; Benkovic, S. J.; Natan, M. J.; Keating, C. D. *J. Am. Chem. Soc.* **2000**, *122*, 9071–9077.
107. Zayats, M.; Pogorelova, S. P.; Kharitonov, A. B.; Lioubashevski, O.; Katz, E.; Willner, I. *Chem.−Eur. J.* **2003**, *9*, 6108–6114.
108. Wink, T.; van Zuilen, S. J.; Bult, A.; van Bennekom, W. P. *Anal. Chem.* **1998**, *70*, 827–832.
109. Kubitschko, S.; Spinke, J.; Bruckner, T.; Pohl, S.; Oranth, N. *Anal. Biochem.* **1997**, *253*, 112–122.
110. Anker, J. N.; Hall, W. P.; Lyandres, O.; Shah, N. C.; Zhao, J.; Van Duyne, R. P. *Nat. Mater.* **2008**, *7*, 442–453.
111. Lal, S.; Link, S.; Halas, N. J. *Nat. Photonics* **2007**, *1*, 641–648.
112. Eustis, S.; El-Sayed, M. A. *Chem. Soc. Rev.* **2006**, *35*, 209–217.
113. Huang, X.; Jain, P. K.; El-Sayed, I. H.; El-Sayed, M. A. *Nanomedicine* **2007**, *2*, 681–693.
114. Zhang, L.; Li, Y.; Li, D.-W.; Jing, C.; Chen, X.; Lv, M.; Huang, Q.; Long, Y.-T.; Willner, I. *Angew. Chem., Int. Ed.* **2011**, *50*, 6789–6792.
115. Baldrich, E.; Acero, J. L.; Reekmans, G.; Laureyn, W.; O'Sullivan, C. K. *Anal. Chem.* **2005**, *77*, 4774–4784.
116. Niu, S. Y.; Jiang, Y.; Zhang, S. S. *Chem. Commun.* **2010**, *46*, 3089–3091.
117. Lu, N.; Shao, C. Y.; Deng, Z. X. *Chem. Commun.* **2008**, 6161–6163.
118. Zhang, X. B.; Kong, R. M.; Lu, Y. *Metal Ion Sensors Based on DNAzymes and Related DNA Molecules*; Cooks, R. G., Yeung, E. S., Eds.; Annual Reviews: Palo Alto, 2011; Vol. 4, pp 105−128.
119. Choi, H. S.; Liu, W.; Misra, P.; Tanaka, E.; Zimmer, J. P.; Ipe, B. I.; Bawendi, M. G.; Frangioni, J. V. *Nat. Biotechnology* **2007**, *25*, 1165–1170.
120. Breus, V. V.; Heyes, C. D.; Tron, K.; Nienhaus, G. U. *ACS Nano* **2009**, *3*, 2573–2580.
121. Susumu, K.; Mei, B. C.; Mattoussi, H. *Nat. Protoc.* **2009**, *4*, 424–436.
122. Susumu, K.; Uyeda, H. T.; Medintz, I. L.; Pons, T.; Delehanty, J. B.; Mattoussi, H. *J. Am. Chem. Soc.* **2007**, *129*, 13987–13996.
123. Yu, W. W.; Chang, E.; Falkner, J. C.; Zhang, J.; Al-Somali, A. M.; Sayes, C. M.; Johns, J.; Drezek, R.; Colvin, V. L. *J. Am. Chem. Soc.* **2007**, *129*, 2871–2879.
124. Gerion, D.; Pinaud, F.; Williams, S. C.; Parak, W. J.; Zanchet, D.; Weiss, S.; Alivisatos, A. P. *J. Phys. Chem. B* **2001**, *105*, 8861–8871.

Downloaded by 89.163.35.42 on November 27, 2012 | http://pubs.acs.org
Publication Date (Web): November 26, 2012 | doi: 10.1021/bk-2012-1112.ch001

125. Zhang, Y.; Clapp, A. *Sensors* **2011**, *11*, 11036–11055.
126. Kirchner, C.; Liedl, T.; Kudera, S.; Pellegrino, T.; Javier, A. M.; Gaub, H. E.; Stolzle, S.; Fertig, N.; Parak, W. J. *Nano Lett.* **2005**, *5*, 331–338.
127. Hoshino, A.; Fujioka, K.; Oku, T.; Suga, M.; Sasaki, Y. F.; Ohta, T.; Yasuhara, M.; Suzuki, K.; Yamamoto, K. *Nano Lett.* **2004**, *4*, 2163–2169.
128. Derfus, A. M.; Chan, W. C. W.; Bhatia, S. N. *Nano Lett.* **2004**, *4*, 11–18.
129. Soenen, S. J.; Demeester, J.; De Smedt, S. C.; Braeckmans, K. *Biomaterials* **2012**, *33*, 4882–4888.

Downloaded by 89.163.35.42 on November 27, 2012 | http://pubs.acs.org
Publication Date (Web): November 26, 2012 | doi: 10.1021/bk-2012-1112.ch001

Downloaded by UNIV DE SHERBROOKE on November 27, 2012 | http://pubs.acs.org
Publication Date (Web): November 26, 2012 | doi: 10.1021/bk-2012-1112.ch002

Chapter 2

Functionalisation, Characterization, and Application of Metal Nanoparticles for Bioanalysis

I. A. Larmour, K. Faulds, and D. Graham*

**Centre for Molecular Nanometrology, Pure and Applied Chemistry,
University of Strathclyde, 295 Cathedral Street, Glasgow, G1 1XL, U.K.
*E-mail: duncan.graham@strath.ac.uk**

The explosion of nanotechnology research has led to significant advances in many fields. In this chapter we investigate the use of metallic nanoparticles in bioanalysis applications focussing specifically on their functionalisation and characterization. These funcationalized nanoparticles can find use with a wide range of analytical techniques however we will focus primarily on their use in surface plasmon resonance and surface enhanced Raman spectroscopy (SERS) applications.

Introduction

Nanometer sized entities have been around since the beginning of time but as is often the case it takes a label before a field is born and widespread interest is taken by the scientific community. You may imagine that "nanotechnology" was born upon Feynman giving his historic speech "There's plenty of room at the bottom" but this merely pointed out the potential of the very small, it did not contain the word nanotechnology (*1*). The first use of that particular word was by Taniguchi at a conference in 1974 (*2*). Finally the field had a name and an explosion of research was observed under the banner of "nanotechnology".

The prefix "nano" has been applied to almost every imaginable research field and the general population is becoming increasingly comfortable with its existence, even to the point that "nanoscience" can now be used to market products. Nanotechnology is starting to deliver benefits in many fields and this chapter focuses on those benefits that metallic nanoparticles can yield in bioanalysis.

In Functional Nanoparticles for Bioanalysis, Nanomedicine, and Bioelectronic Devices Volume 1; Hepel, M., et al.;
ACS Symposium Series; American Chemical Society: Washington, DC, 2012.

Nanoparticles can be made from a myriad of different materials and come in all shapes and sizes (*3*, *4*). When materials are confined to nanometer scaled structures their properties can change significantly. For example gold nanoparticles possess surface plasmon resonances (SPR) in the visible region of the electromagnetic spectrum due to the oscillation of conduction electrons (*5*). The wavelength at which the plasmon appears is dependent on the size of the nanoparticle which red-shifts as the nanoparticle size increases, as shown in Figure 1 (*6*, *7*). These collective electron oscillations can be tuned and shaped by careful preparation of the nanostructure (*8*) and used in a variety of analytical applications (*9*) including surface enhanced Raman spectroscopy (SERS) (*10*).

Downloaded by UNIV DE SHERBROOKE on November 27, 2012 | http://pubs.acs.org
Publication Date (Web): November 26, 2012 | doi: 10.1021/bk-2012-1112.ch002

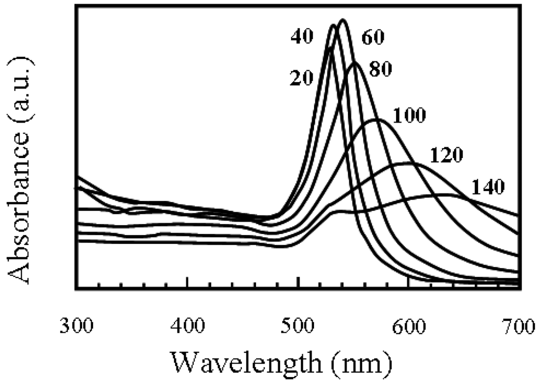

Figure 1. UV-Vis absorbance profiles of different sized spherical gold nanoparticles, the numbers against each trace relate to the diameter of the nanoparticles in nanometers. (Adapted with permission from reference (7). Copyright 1998 Academic Press.)

It is clearly necessary to narrow down the “nano” area of research related material for this chapter. Therefore, we have chosen to focus on metallic nanoparticles that are suitable for use in SERS applications and to a lesser extent SPR applications. Although SERS has been demonstrated for a wide variety of metals (*11*) the vast majority of research is based on silver and gold nanoparticles, which are also suitable for SPR applications due to their absorbance at visible wavelengths.

Metallic nanoparticles are most commonly prepared by the reduction of metal salts by reducing agents (*12*) such as; sodium borohydride (*13*, *14*), tri-sodium citrate (*15*), hydroxylamine (*16*) and ethylenediaminetetraacetic acid (*17*). Introduction of either suitable capping agents (*18–20*) or illumination by narrow wavelength light (*21–24*) during the synthesis can direct nanoparticle growth producing rods, wires or even plates. Once prepared, these nanoparticles can be immediately used for the detection of biomolecules by SERS.

Downloaded by UNIV DE SHERBROOKE on November 27, 2012 | http://pubs.acs.org
Publication Date (Web): November 26, 2012 | doi: 10.1021/bk-2012-1112.ch002

Biomolecule Detection Using As Prepared Nanoparticles

Intrinsic Detection

Direct, intrinsic detection of biomolecules by SERS is possible. For this the biomolecule of interest is adsorbed onto the surface of the nanoparticles and an aggregating agent added. Simple inorganic salts, i.e. NaCl, can be used to aggregate the nanoparticles before laser illumination and detection of the SERS signal. Aggregation leads to the plasmons on the individual nanoparticles coupling together to create “hot spots”, which are areas of intense electromagnetic field that significantly increases the observed signal (*25–28*). Proteins (*29*), nucleotides (*30*, *31*) and enzymes (*32*, *33*) have all been intrinsically detected using nanoparticles. Although intrinsic detection of pure biomolecule solutions is possible it becomes a significant challenge to detect a specific biomolecule in a complex solution such as serum, whole blood or even *in vivo*. This is due to the abundance of other biomolecules that compete to bind to the surface, often to the detriment of the biomolecule of interest. In addition to the surface binding competition, biomolecule adsorption to a metallic surface can disrupt the natural configuration of the biomolecule thus destroying its bioactivity (*34*). Therefore an alternative detection approach is desirable.

Extrinsic Detection

In this approach the biomolecule can be labeled with a dye molecule that produces a strong Raman signal. These dyes tend to be large aromatic molecules that carry a positive charge which is electrostatically attracted to the negatively charged nanoparticles. In this way dye labeled DNA, which is negatively charged due to the phosphates, can be detected by mixing with silver or gold colloid (*35–37*). Unfortunately this requires the labeling of the biomolecule of interest before SERS detection which is impractical in many experimental situations (*38*).

Alternatively, biomolecules can be detected due to their action on a chemical substrate which is then detected by SERS. An example of this is the detection of peroxidase enzymes which turnover the weak Raman scatterer *o*-phenylenediamine into azoaniline which produces an intense Raman response (*39*). Other enzymes can be detected when unique substrates are prepared. These substrates consist of a Raman active dye which is normally surface seeking but which has been masked by the attachment to the dye of a molecule that can act as a substrate for specific enzymes. Importantly the link between enzyme substrate and dye is cleaveable, i.e. when the enzyme acts on the substrate part, the dye is released (*40*, *41*). The dye is then free to attach to the metallic nanoparticles and produce a SERS signal. This signal generation can be monitored over time and the kinetics of individual (*42*, *43*) and multiple enzymes obtained simultaneously (*44*). Although this approach of releasing SERS active dyes works extremely well for enzymes it will not work for all classes of biomolecules.

It is clear from the discussion so far that nanoparticles in their native form can be used to detect biomolecules in specific, well controlled, circumstances. However, this approach is severely limited and is not the universal nor easily applicable method that would be suitable for routine bioanalysis. Therefore the nanoparticles must be funcationalized to create a system that does meet these requirements.

Biomolecule Detection Using Functionalized Nanoparticles

What is required to detect biomolecules using nanoparticles? Such a simple question but as with everything in science the answer is much more complicated and starts with “it depends”. Ultimately a unique signal must be detected, in the case of SPR the nanoparticles themselves produce an absorbance profile which is dependent on the size and aggregation state of the particles. However, in SERS we need to introduce a specific reporter molecule, much like those that were unmasked by the action of an enzyme.

It should be possible to detect biomolecules in a wide range of situations including buffers, serum, whole blood, cells and tissues. In all these situations high salt concentrations exist and this can lead to the undesired and irreversible aggregation of the nanoparticles. Therefore some form of stabilization of the native nanoparticles will be required. Thus stable nanoparticles with unique signatures, which are dependent on the incorporated reporter molecule, have been developed (*45*, *46*). These are often referred to as nanotags.

However, these nanotags are not capable of biomolecule detection, although they can be injected *in vivo* and monitored (*47*). For true biomolecule detection they need to be functionalized with a biorecognition site, e.g. antibodies (*48*). Biofunctionalized nanotags can then be considered as active sensors for specific biomolecules.

Nanoparticles must therefore be functionalized in such a way that they contain the three necessary constituents; reporter, stabilizer and biorecognition site. The remainder of this chapter is focused on how nanoparticles are functionalized to include these three constituents and more importantly how we can characterize the prepared substrates to ensure they have been successfully functionalized. Finally we present several examples of the use of these functionalized nanoparticles in biomolecular detection.

Downloaded by UNIV DE SHERBROOKE on November 27, 2012 | http://pubs.acs.org
Publication Date (Web): November 26, 2012 | doi: 10.1021/bk-2012-1112.ch002

Functionalization

Reporter Molecules

The first functionalization that must be incorporated onto the nanoparticle is a molecule that can act as a reporter. This molecule must have a large Raman cross-section and as such will produce an intense Raman/SERS spectrum. A huge library of dyes has been developed for fluorescence applications and many of these can be utilized in a SERS application. This is due to the well known quenching effect of metallic nanoparticles (*8*) which removes the broad fluorescence signal and leaves the sharp Raman peaks visible as demonstrated in Figure 2 (*49*).

Downloaded by UNIV DE SHERBROOKE on November 27, 2012 | http://pubs.acs.org
Publication Date (Web): November 26, 2012 | doi: 10.1021/bk-2012-1112.ch002

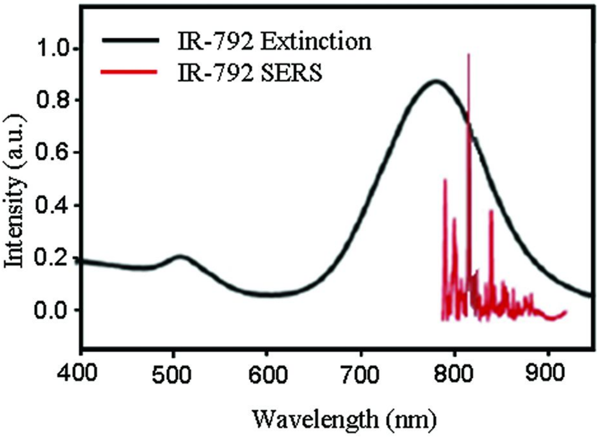

Figure 2. Fluorescence and SERRS of IR-792 dye showing the broad and narrow signals respectively. The SERRS spectrum was recorded using 785 nm laser excitation. (Reproduced with permission from reference (49). Copyright 2009 Wiley-VCH.)

Nanotags with various different fluorescent and non-fluorescent dye molecules have been demonstrated, some of their chemical structures are shown in Figure 3 (*49–51*). These molecules tend to interact with the surface through electrostatic interactions, however for improved stability it would be beneficial if they were attached via covalent bonds. This approach minimizes desorption and orientational fluctuations of the reporter molecule (*52*).

Covalent attachment can be achieved by using thiol terminated small molecules or by designing unique surface complexing dye molecules. These unique molecules have been based around a benzotriazole moiety which provides the surface complexing functionality. Formation of an azo with concomitant control of substituents produces a library of molecules with intense and unique SERS spectra, some of which are shown in Figure 4 (*53*).

Stabilization

To protect the reporter molecules and the nanoparticles from the harsh biological environment they may be introduced to, it is necessary to provide them with some armor. This can be a layer of molecules which attach to the nanoparticle surface and provide a densely packed structure which prevents other species from reaching the nanoparticle surface. There are two main types of species that can be used for this protective role; polyethylene glycols (PEG) and silica.

Downloaded by UNIV DE SHERBROOKE on November 27, 2012 | http://pubs.acs.org
Publication Date (Web): November 26, 2012 | doi: 10.1021/bk-2012-1112.ch002

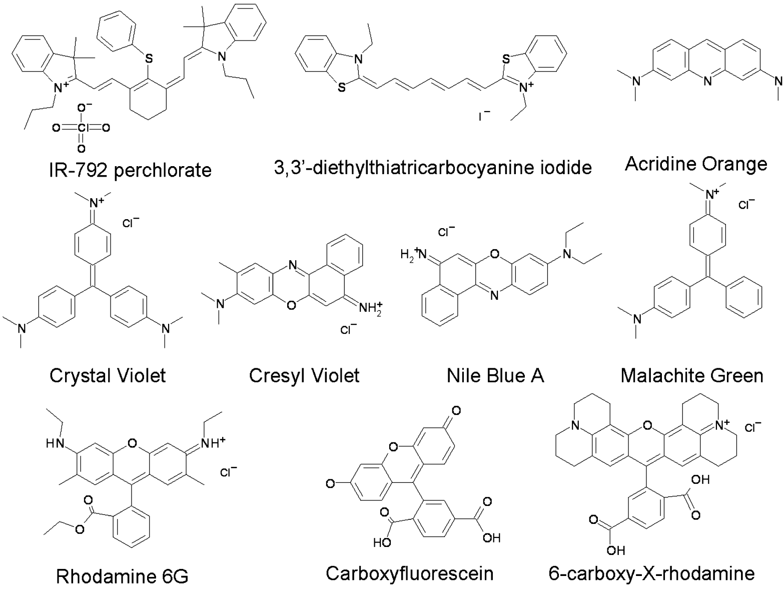
IR-792 perchlorate
3,3'-diethylthiatricarbocyanine iodide
Acridine Orange
Crystal Violet
Cresyl Violet
Nile Blue A
Malachite Green
Rhodamine 6G
Carboxyfluorescein
6-carboxy-X-rhodamine

Figure 3. Structures of common dye molecules used in nanotags.

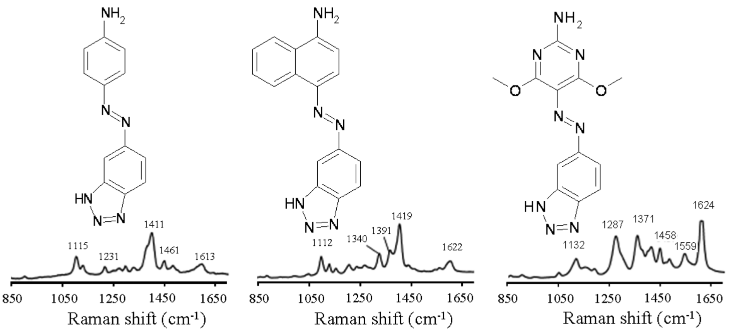

Figure 4. Three different benzotriazole monoazo dyes which differ in their substituents and thus produce distinct SERS spectra. (Adapted with permission from reference (53). Copyright 2002 Royal Society of Chemistry.)

In the case of polyethylene glycols, these tend to be attached via thiol functionality (*54*, *55*) and can be compared to thiol terminated alkane self-assembled monolayers (SAMs), which can themselves be used to control the functionality of the nanoparticles (*56*). Interestingly, a substantially longer PEG will not result in a significantly thicker surface coating than a short PEG due to its twisted structure. This clearly has benefits for improved stability due to the denser coating that it provides (*56*). The use of thiol PEGs also allows the nanoparticle to be functionalized with a reporter molecule before addition of the PEG. This wraps the nanoparticle without complete loss of the reporter molecule ensuring a SERS signal can still be obtained (*57*).

Silica can also be grown around the nanoparticle to produce a shell which isolates the core and exterior chemistries (*58*). Importantly the silica is optically transparent which is a significant bonus when recording optical signals. Generally a silica shell is grown by first activating the surface of the nanoparticle with (3-aminopropyl)trimethoxysilane (APTMS) which provides siloxy groups ready for silicate ion addition. Sodium silicate is then introduced to form an initial shell before ethanol is added to promote the controlled precipitation of silica and thus grow the shell (*59*).

Although PEGs and silica are the main routes for the stabilization of nanoparticles, other methods such as polymer encapsulation can also be carried out where layer-by-layer assembly is utilized (*19*, *60*). These coatings not only protect the nanoparticle from attack, but also prevent the reporter molecule from desorbing which would lead to a loss of the SERS signal. They also minimize non-specific binding of proteins and prevent uncontrollable aggregation in the biological environment (*61*).

Downloaded by UNIV DE SHERBROOKE on November 27, 2012 | http://pubs.acs.org
Publication Date (Web): November 26, 2012 | doi: 10.1021/bk-2012-1112.ch002

Biofunctionalization

In bioanalysis it is best to use a secondary biomolecule that will specifically target the primary biomolecule of interest. This requires the attachment of the secondary sensing biomolecule to the nanoparticle. It is important to note that the attached biomolecule is not itself being detected but is a tool to target the molecule of interest.

Some biomolecules will naturally bind to the surface of metallic nanoparticles, e.g. cytochrome c will bind through the lysine-rich heme pocket (*62*) while single stranded DNA (ssDNA) adsorption has recently been shown to be a result of hydrophobic effects (*63*). Although this approach can biofunctionalize nanoparticles the adsorbed molecule can be susceptible to dissociation and therefore covalent linkages should be favored. In the case of ssDNA, this is achieved by the extensive use of thiol modified DNA strands (*64–67*). Thiol modification of lactose can also be achieved by reaction with a heterobifunctional PEG containing thiol and acetal groups (*68*).

However, a single thiol-Ag/Au bond can dissociate and therefore developments have been made to increase the number of anchoring points used to attach the biomolecule. In the case of thiols, thioctic acid (*69*) and trithiol anchoring groups (*70*) have been prepared. An increasing number of surface anchoring points increases the stability of the system, particularly with respect to temperature, without affecting the subsequent hybridization properties of the DNA (*69*, *70*). Increasing the number of anchoring points is a universal approach and multiple thiol functionalities have been added to carbohydrate (*71*) and biotin ligands (*72*).

Downloaded by UNIV DE SHERBROOKE on November 27, 2012 | http://pubs.acs.org
Publication Date (Web): November 26, 2012 | doi: 10.1021/bk-2012-1112.ch002

Thioctic acid has also been used to produce nitrilotriacetic acid (NTA) coated nanoparticles. These were prepared by using 1-ethyl-3-[3'-(dimethylamino)propyl]carbodiimide (EDC)/*N*-hydroxysuccinimide (NHS) chemistry to couple an amino-nitrilotriacetic-Co(II) complex to thioctic acid. This allows any His tagged protein to bind to the nanoparticle (*73*). If acetylene functionality is present on the surface of the nanoparticle then "click" chemistry can be used. In this instance copper-catalyzed alkyne-azide coupling can be used to functionalize the surface with biomolecules such as folate and biotin (*74*).

Assembly of the Nanoparticle Biosensor

So far we have considered the functionalisation of nanoparticles with each component separately; reporter, stabilizer and biomolecular recognition. However, all these individual parts will compete for space on the nanoparticle surface. Unfortunately this means that the maximum signal that can be generated from the reporter molecules will be less than ideal, as the surface coverage will not be at the maximum. In an ideal situation, one molecule would incorporate all three components; a surface complexing unit (for nanoparticle attachment), a dye to act as a reporter, a polymer sequence to impart stability to the nanotag and terminal functionality to allow the attachment of biomolecules.

The ability of benzotriazoles to act as a reporter molecule and surface complexing group has already been mentioned. Unfortunately, the first set of benzotriazoles that were developed (*53*), while being excellent SERS standards, could not be used for further functionalisation due to an insufficient level of nucleophilicity which prevented them from reacting further with common electrophiles. Therefore a range of benzotriazoles with a nucleophilic amine group were prepared; some of which are shown in Figure 5. These dyes retained the high level of unique SERS fingerprints but allowed for subsequent biomolecule conjugation (*75*).

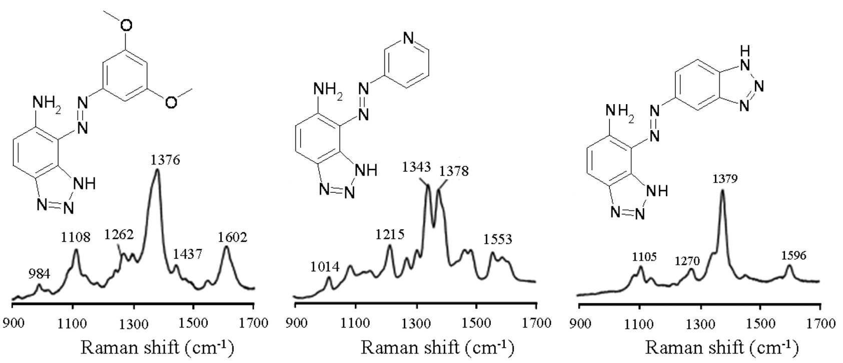

Figure 5. Benzotriazole dyes with a reactive nucleophilic amine suitable for further conjugation and their respective SERS spectra. (Adapted with permission from reference (75). Copyright 2004 Royal Society of Chemistry.)

Downloaded by UNIV DE SHERBROOKE on November 27, 2012 | http://pubs.acs.org
Publication Date (Web): November 26, 2012 | doi: 10.1021/bk-2012-1112.ch002

Alternatively, McKenzie *et al.* utilized a lysine core to prepare their trifunctional ligands (*76*). The two amines were functionalized with Boc and Fmoc respectively, which allowed the controlled addition of a PEG onto the carboxylic acid group, a reporter molecule onto the Fmoc protected amine and thioctic acid onto the Boc protected amine using adapted peptide coupling chemistry (*76*). Meanwhile, a carboxylic acid terminated PEG was incorporated into a trifunctional ligand by Wrzesien and Graham. They found that use of 4-(4,6-dimethoxy-1,3,5-triazin-2-yl)-4-methylmorpholinium chloride (DMT MM) allowed the bioconjugation reaction to occur in water and was an inexpensive and more efficient alternative to the more common EDC/NHS coupling chemistry (*77*). Meanwhile Schlücker *et al.* have used self-assembled monolayers of small aromatic thiols as the building blocks for their nanotags based around thiobis(2-nitrobenzoic acid) (*78*). The small molecules acted as efficient Raman reporters and were functionalized with different lengths of PEG molecules, where the longer PEG spacers were used for subsequent bioconjugation producing erinaceous nanoparticles.

For the stabilization of nanoparticles, PEG is a convenient molecule to incorporate into multi-functional ligands as it is capable of decreasing non-specific binding of biological molecules (*79*, *80*). However other options are available such as synthetic copolymers of styrene and maleic anhydride which are functionalized with a surface seeking reporter molecule such as a benzotriazole (*81*). In this case, the reporter molecule produces a hydrophobic side chain of the polymer, while the carboxylic acid groups produce a hydrophilic side chain as well as sites for further functionalisation, Figure 6. The functionalized polymer can therefore wrap the nanoparticles with many anchoring points since there are multiple benzotriazole molecules on each polymeric strand (*81*).

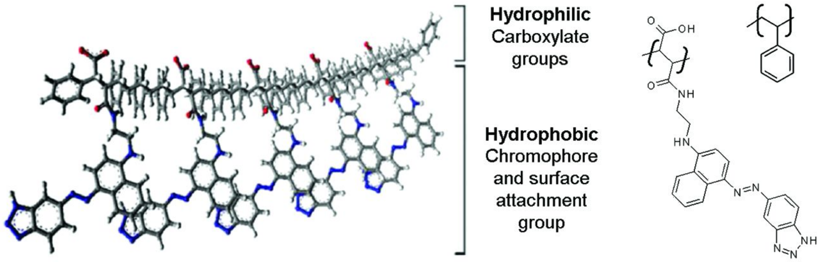

Figure 6. Schematic of a polymer dye. Oxygen atoms are highlighted in red and nitrogen atoms in the bonding group are in blue. Chemical structures of the two copolymers; styrene and functionalized maleic anhydride are shown on the right. (Adapted with permission from reference (81). Copyright 2008 Royal Society of Chemistry.)

Benzotriazole molecules have also been modified to be suitable as precursors for silica growth by removing the need for APTMS to be co-mixed with the reporter molecule on the nanoparticle surface (*82*). This is in contrast to Schlücker *et al.* who developed a similar approach using modified mercaptobenzoic acid derivatives functionalized with silica precursors for the same result (*83*). The mercaptobenzoic acid derivatives formed a self-assembled monolayer on the nanoparticle surface and acted as small molecule Raman reporters and the grown silica shell was terminated with amino groups ready for reaction with a bifunctional PEG spacer that had a biomolecule at the other end, therefore creating erinaceous nanoparticles (*84*).

Clearly incorporation of all the required functionality into one molecule maximizes the expression of all constituents. An increase in SERS signal cannot be generated beyond monolayer coverage, therefore complete coverage of a nanoparticle by a stabilizing polymer ensures there are no gaps for other molecules to attack the core while also minimizing non-specific binding. A complete shell also produces an exterior chemistry rich in functional groups primed for bioconjugation, maximizing the efficiency and success of the coupling reactions. Although the functionalisation of the nanoparticles by the required species has already been discussed, how can we characterize the nanoparticle to ensure the functionalisation process has been successful? In the next section we explore the techniques that are used to confirm the functionalisation of the nanoparticles.

Characterization

There are many techniques which can be used to study the functionalisation of nanoparticles but perhaps the easiest methods make use of the surface plasmon resonance of the nanoparticles themselves. If nanoparticles are coated with biomolecules, PEG or anything other than the surface chemistry resulting from their synthesis, their optical and physical properties will change. Upon addition of a surface species the SPR absorbance band can shift due to the change in refractive index immediately surrounding the nanoparticle. Alternatively, and easier to observe, is the increased stability after functionalisation with respect to aggregating agents. Simple salts (*85*) or organothiols (*69*, *86*) can be used to induce aggregation of the nanoparticles which is observed as a red-shift of the absorbance profile. If substantial aggregation occurs then the change can be seen by eye, gold nanoparticles change from red to blue while silver nanoparticles change from yellow to brown. Complete flocculation of the nanoparticles is also possible leaving a colorless solution behind. Use of UV-Vis absorbance spectroscopy is a comparative technique since aggregation can be induced for almost all functionalized nanoparticles irrespective of the presence of stabilizing coatings. Therefore, the observation of an increased time of stability, before the onset of aggregation, indicates that the surface has been successfully functionalized.

If nanoparticles have been functionalized with different DNA strands they can be coupled together with a complementary strand. In this case aggregation should not occur when a non-target sequence is present but should if the target sequence is present (*87*). The formation of DNA induced clusters can also be observed by subsequent transmission electron microscopy (TEM) studies where the distance can be controlled by the length of the complementary strand (*88*). This is a clear

Downloaded by UNIV DE SHERBROOKE on November 27, 2012 | http://pubs.acs.org
Publication Date (Web): November 26, 2012 | doi: 10.1021/bk-2012-1112.ch002

indication of functionalisation since formation of dimers or trimers would not occur if the nanoparticle had not been successfully functionalized. High resolution TEM studies can also be used to visualize nanoparticle ligands themselves (*89*).

Quantitative fluorescence measurements are one of the best ways to investigate the success of surface functionalisation with biomolecules. There are two main ways that this can be done; firstly the removal of a fluorescently labeled biomolecule that is conjugated to the nanoparticle and secondly the hybridization of a fluorescently labeled ssDNA to a nanoparticle conjugated sequence before its removal and measurement. In the first approach mercaptoethanol or dithiothreitol are used to displace the bound ligand shell. The resultant fluorescence, which is no longer quenched by the metallic surface is then measured (*90*, *91*). Alternatively an enzyme hydrolysis method, using trypsin or DNase I, can be employed to release the biomolecule while leaving the surface linker intact (*92*).

If the use of a labeled biomolecule is not desired, in the case of DNA, it is possible to quantify the hybridization efficiency of the surface bound DNA molecules without destroying the prepared nanotag. This involves the hybridization of a labeled complementary sequence to the DNA on the nanoparticle surface. After removal of excess labeled probe, the probe can be liberated and the fluorescence measured, as shown schematically in Figure 7. This has the benefit of returning the functionalized nanotag unharmed for further experimentation (*93*).

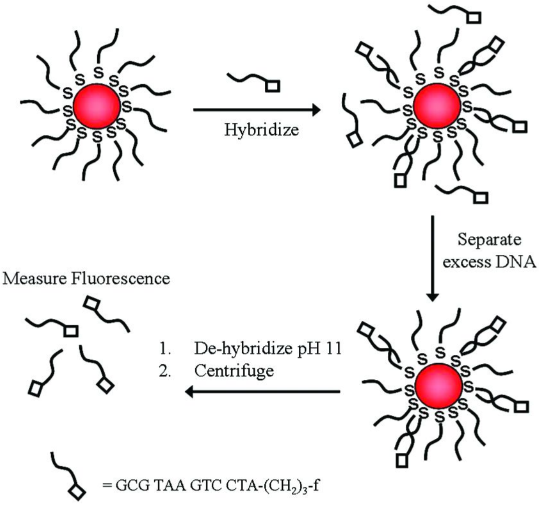

Figure 7. Quantification of DNA hybridization efficiency on a nanoparticle, the fluorescent label (□) is 5′-fluoroscein. (Reproduced with permission from reference (93). Copyright 2000 American Chemical Society.)

Functionalisation with enzymes also provides a method for confirming that a conjugation was successful. Essentially, the enzyme is allowed to turn over a substrate to form a product. The product can then be detected by the most

Downloaded by UNIV DE SHERBROOKE on November 27, 2012 | http://pubs.acs.org
Publication Date (Web): November 26, 2012 | doi: 10.1021/bk-2012-1112.ch002

Downloaded by UNIV DE SHERBROOKE on November 27, 2012 | http://pubs.acs.org
Publication Date (Web): November 26, 2012 | doi: 10.1021/bk-2012-1112.ch002

appropriate analytical method. If an enzyme has been attached, as observed by the appropriate analytical technique, but no turnover of the reactant is observed then it is likely that the conjugation reaction has caused the enzyme to become inactive (*94–96*).

Although we are interested in preparing SERS active nanotags that are suitable for bioanalysis applications, SERS can also tell us about the functionalisation of the nanoparticles. A simple demonstration of this is in the monitoring of the formation of a mixed SAM where both constituents are Raman active. Plotting of the relative peak intensities can show whether the SAM being formed on the nanoparticle is of the same ratio as the solution mixture, i.e. if the binding affinities of the two species are the same (*97*). SERS can also indicate when a reporter molecule has desorbed, since the signal will disappear. This has been used to demonstrate the superior quality of chemisorbed reporters over physisorbed reporters (*98*). Comparing the Raman spectrum of the reporter to the SERS spectrum after addition to the nanoparticle can also provide information about the orientation of the reporter molecule on the surface of the nanoparticle (*99*). This is due to the selection rules involved in the SERS process and observing which vibrations are selectively enhanced will indicate the molecular orientation with respect to the surface.

Other techniques that have been used to characterize functionalized nanoparticles include; Fourier transform infrared (FTIR) spectroscopy and solid-state nuclear magnetic resonance (SSNMR) which can provide information about the structure of the ligands attached to the nanoparticle but cannot quantifying the amount (*100*, *101*). Electron spin resonance (ESR) spectroscopy has been used to probe the organization of mixed SAMs on nanoparticles (*102*). Thrombin digestion has been used to remove peptides from the surface of nanoparticles followed by analysis using gel electrophoresis (*103*). Differential scanning calorimetry, contact-angle measurements, thermal desorption mass spectrometry (*104*), X-ray photoelectron spectroscopy (XPS), electron energy loss spectroscopy (EELS), circular dichroism (CD) and inductively coupled plasma – mass spectrometry (ICP-MS) have also been used to probe the functionalisation of nanoparticles (*105*).

It is important to note that, although a vast range of analytical techniques have been used to probe nanoparticle functionalisation, many of them only indicate that something has been attached to the surface. For example, there can be an indication that an Au-S bond has formed at the surface. If peptides are under investigation then it may not be possible to definitively state whether they are chemically bound to the ligand shell or non-specifically bound. The characterization that is currently undertaken is the best available and with the use of multiple techniques it can be confidently stated that nanoparticles have been functionalized.

However, even in the case where the analytical technique is providing a "quantitative" result it must be regarded with caution. This is due to the fact that the methods are all based on averaged statistics, specifically the colloid concentration is assumed from UV-Vis spectroscopy but this is dependent on the extinction co-efficient chosen which is in itself a function of the size of the nanoparticles and the refractive index of the material at its surface. The fluorescence signal also contains an error and therefore an average functionalisation of 5 DNA molecules

In Functional Nanoparticles for Bioanalysis, Nanomedicine, and Bioelectronic Devices Volume 1; Hepel, M., et al.;
ACS Symposium Series; American Chemical Society: Washington, DC, 2012.

Downloaded by UNIV DE SHERBROOKE on November 27, 2012 | http://pubs.acs.org
Publication Date (Web): November 26, 2012 | doi: 10.1021/bk-2012-1112.ch002

per colloid could actually mean that there are nanoparticles in the solution with 10's of DNA strands and others with none.

Currently there is no method to definitively state how many biomolecules have been added to a single nanoparticle, although absolute concentrations of colloid solutions can be measured which may improve the estimates somewhat (*106*). This is one of the major challenges facing the research community; to develop a technique that can measure the biofunctionalisation of individual nanoparticles and thus create a true picture of the solution as a whole. Considering how assays are being reduced to ever smaller scales, the variation in the functionalisation between individual nanoparticles will become ever more important (*107*).

Applications

Localized Surface Plasmon Resonance Applications

Detection methods based on localized surface plasmon resonances (LSPRs) depend on the difference in optical absorbance between an unaggregated and aggregated nanoparticle solution. Therefore, the analyte of interest must cause either an aggregation or deaggregation of the nanoparticle solution for a change to be observed and the analyte detected.

In the case of DNA based detection the introduction of a DNA sequence of interest causes the nanoparticles to aggregate (*108*). This is due to the nanoparticles being functionalized with the complementary strands to the target. A 3-dimensional polymer network of nanoparticles is created upon cross-linking of the particles which leads to a red-to-purple color change in gold nanoparticles. The degree of color change can be tuned by the length of the complimentary DNA strands used to functionalize the nanoparticles, the longer the strands the smaller the change between aggregated and unaggregated states (*109*).

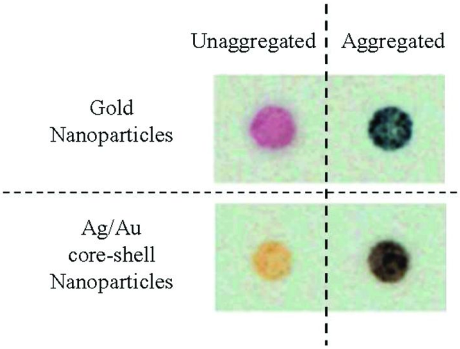

Figure 8. The color change observed between unaggregated and aggregated nanoparticles. (Adapted with permission from reference (111). Copyright 2001 American Chemical Society.)

Unfortunately, due to the broad absorbance bands in UV-Vis spectroscopy the number of targets that can be investigated in one solution simultaneously is limited. To overcome this it is possible to use different sized gold nanoparticles (which will have different absorbance profiles) and attach them to a surface using the target sequence to hybridize the nanoparticle to the surface (*110*).

Alternatively, silver core – gold shell nanoparticles can be used as a secondary nanoparticle probe. The silver core provides a different optical response to the gold nanoparticles, changing from yellow to brown/black upon aggregation as shown in Figure 8 (*111*). We will return to multiplexed DNA detection in the surface enhanced Raman spectroscopy section where we will show that the achievable multiplex can be significantly improved.

Glucose detection is clearly a very important consideration for those suffering from diabetes and LSPR based detection methods have been developed. One example is the use of glucose oxidase functionalized gold nanoparticles that aggregate in the presence of glucose molecules leading to the standard red to purple color change (*112*). However, an aggregated to unaggregated system has been developed that uses dextran coated gold nanoparticles. In this system the nanoparticles are aggregated using concanavalin A (Con A) and the introduction of glucose leads to competitive binding with the Con A resulting in the dextran coated nanoparticles no longer being aggregated, as shown in Figure 9 (*113*). Changing the size of the gold nanoparticles or the concentrations of dextran and Con A allows the available glucose detection range to be tuned (*114*).

Downloaded by UNIV DE SHERBROOKE on November 27, 2012 | http://pubs.acs.org
Publication Date (Web): November 26, 2012 | doi: 10.1021/bk-2012-1112.ch002

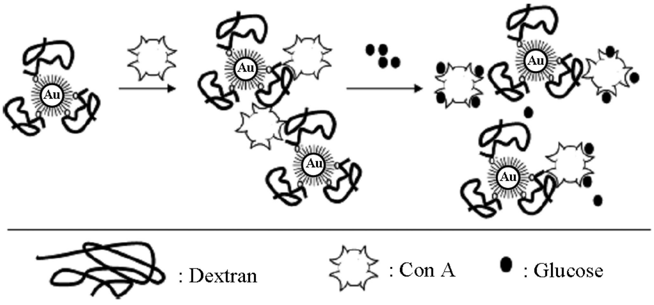

Figure 9. Schematic of the aggregated to unaggregated glucose sensing system. (Reproduced with permission from reference (113). Copyright 2005 American Chemical Society.)

SPR based techniques utilizing functionalized nanoparticles and the unaggregated to aggregated response has also been used to detect anti-protein A (*115*), homocysteine (*116*), platelet-derived growth factors (*117*) and enzymes such as proteases (*118*) and kinases (*119*). In the case of endonucleases, the system can be used to probe inhibitor activity (*120*). Two batches of gold nanoparticles were functionalized with complementary thiol terminated DNA strands. When mixed, the nanoparticles hybridize and in the presence of endonuclease the hybridized DNA strands are digested and the nanoparticle solution becomes red, i.e. unaggregated. This digestion does not happen in the presence of strong endonuclease inhibitors as demonstrated in Figure 10 (*120*).

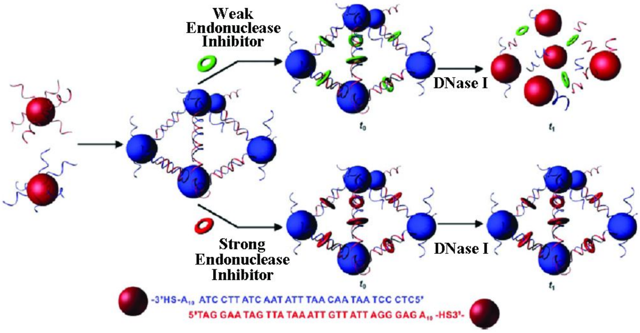
Weak
Endonuclease
Inhibitor
DNase I
t_0
t_1
Strong
Endonuclease
Inhibitor
DNase I
t_0
t_1
-3'HS-A_{10} ATC CTT ATC AAT ATT TAA CAA TAA TCC CTC5'
5'TAG GAA TAG TTA TAA ATT GTT ATT AGG GAG A_{10} -HS3'-

Figure 10. Functionalized nanoparticles to probe endonuclease inhibitors, analyzed by LSPR. (Reproduced with permission from reference (120). Copyright 2007 Wiley-VCH.)

LSPR techniques can give a clear colorimetric response, often observable by eye, for specific analytes provided the nanoparticles are correctly functionalized. However, due to the broad nature of the absorbance response, the ability to multiplex is severely limited. There is also a problem of false positives occurring since aggregation in real biological systems could be caused by undesired species (*121*). One way to combat these shortfalls is to modify the system and base it around a surface enhanced Raman spectroscopy (SERS) detection method.

Surface-Enhanced Raman Spectroscopy Applications

DNA has been labeled with a benzotriazole dye and shown to give a strong SERS signal when combined with silver nanoparticles and aggregated with salt (*122*). However, it is obvious that since the benzotriazole dyes have surface complexing domains the nanoparticles can be prepared and used to detect complementary DNA sequences, i.e. a DNA molecule causes the aggregation rather than being induced by salt addition. In this approach one set of nanoparticles can be prepared with a specific DNA sequence and a label while a second batch of nanoparticles is prepared with a different sequence, but no dye. When the target sequence is introduced the mixture of the two nanoparticles will aggregate and “turn on” the SERS signal (*123*). To maximize the signal both nanoparticles can be functionalized with the reporter dye or with different dyes to produce a multiplexed response to allow determination of the exact hybridization event that has occurred (*87*).

This approach to DNA detection is generic and can be used to detect sequences that are specific to diseases (*124*, *125*). The greatest benefit of this approach over LSPR and fluorescence based methods is its multiplexing ability (*126*) which is demonstrated in Figure 11. Due to the unique fingerprint signatures that are built into the nanoparticle probes this technique can also remove false-positives and false-negatives (*127*).

Downloaded by UNIV DE SHERBROOKE on November 27, 2012 | http://pubs.acs.org
Publication Date (Web): November 26, 2012 | doi: 10.1021/bk-2012-1112.ch002

Downloaded by UNIV DE SHERBROOKE on November 27, 2012 | http://pubs.acs.org
Publication Date (Web): November 26, 2012 | doi: 10.1021/bk-2012-1112.ch002

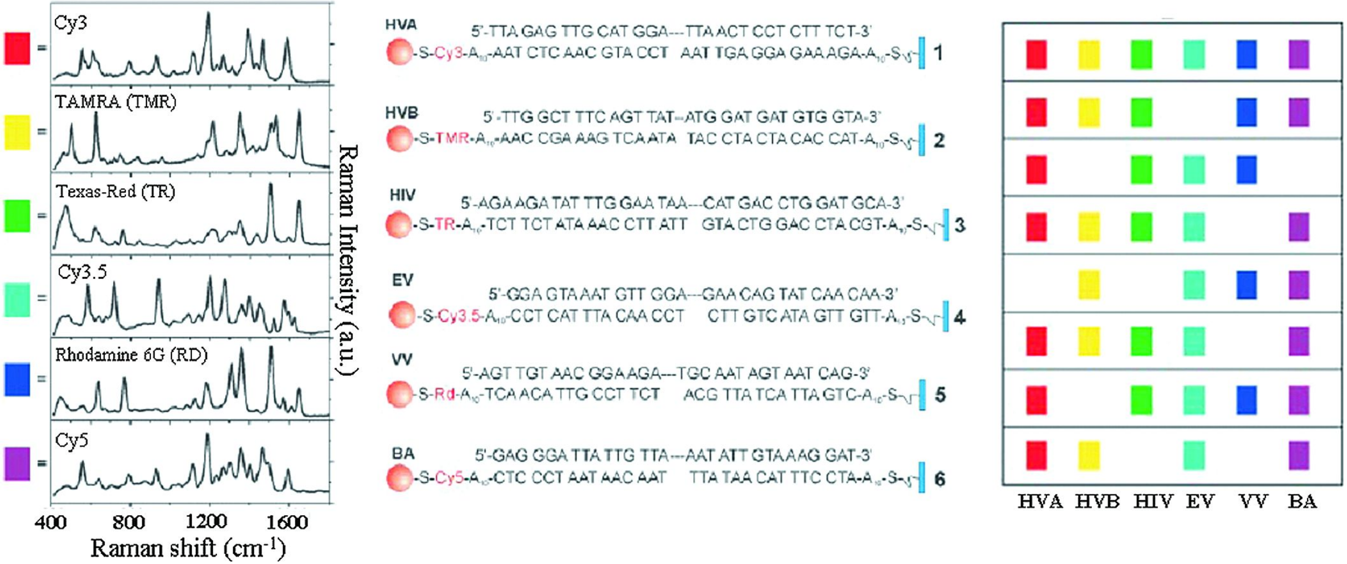

Figure 11. Multiplexed detection of six DNA sequences specific to 5 viruses and 1 bacterium, the panel on the right shows no false-positives or false-negatives from various mixtures. The targets were; HVA – hepatitis A virus, HVB – hepatitis B virus, HIV – human immunodeficiency virus, EV – Ebola virus, VV – variola virus (smallpox) and BA – Bacillus anthracis. (Adapted with permission from reference (127). Copyright 2002 AAAS.)

Different sugars are readily identifiable from their spectral fingerprint regions using Raman spectroscopy (*128*). To increase the sensitivity and specificity of the detection system SERS based methods have been developed. Glucose sensing by SERS is possible with a simple partition system (*129*), but a much more specific approach has been reported that uses a complex functionalized nanoparticle system (*130*). This complex system is based on a bienzyme functionalized nanoparticle; a glucose oxidase (GOD) – horseradish peroxidase (HRP) couple. Glucose and oxygen interact with the GOD which produces hydrogen peroxide which is then consumed by the HRP along with the SERS "silent" substrate *o*-phenylenediamine. The HRP converts the substrate into azoaniline which has a strong SERS response and can be detected (*130*). This is a nice demonstration of the ability to multifunctionalize the surface of a nanoparticle to produce a biological sensor.

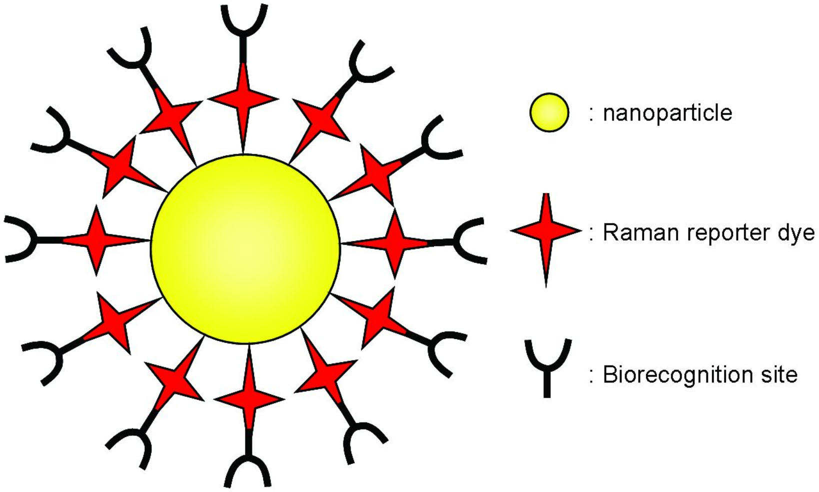

Figure 12. Generic SERS nanotag, all the constituents can be changed, i.e. the nanoparticle can be silver or gold, the reporter dye and biorecognition sites are all variable to create a large library of nanotags.

In the previous sections we have discussed the preparation of functionalized nanoparticles for SERS detection. These functionalized nanoparticles are generic in nature as shown in Figure 12 (*131*) and changes within the biorecognition species will change the species which can be detected while the fundamental workings of the assay will not change. Therefore assays have been developed to detect a range of biologically relevant species such as calcitriol, the 1,25-dihydroxy metabolite of vitamin D_3, of which a deficiency is linked to renal disease, and an excess linked to hypercalcemia (*132*). Other species include proteins (*133*), cancer markers such as prostate-specific antigen (PSA) (*134*) and mucin protein MUC4 (*135*) as well as viral pathogens (*136*) including the lysate of M. *avium* subspecies *paratuberculosis* (*137*).

In Functional Nanoparticles for Bioanalysis, Nanomedicine, and Bioelectronic Devices Volume 1; Hepel, M., et al.; ACS Symposium Series; American Chemical Society: Washington, DC, 2012.

Downloaded by UNIV DE SHERBROOKE on November 27, 2012 | http://pubs.acs.org
Publication Date (Web): November 26, 2012 | doi: 10.1021/bk-2012-1112.ch002

SERS assays using functionalized nanoparticles can be generally improved by optimizing some experimental parameters. To minimize nonspecific binding the assay can be carried out on a rotating substrate (*138*). This introduces fluid flows within the solution that bring the functionalized nanoparticles to the surface quicker, this reduces the time required for the assay and, more importantly, reduces the amount of nonspecific binding making the assay more sensitive (*138*). The nanoparticles that form the core of the functionalized nanoparticles can be replaced by gold cubes. These structures lead to greater focusing of the electromagnetic radiation at the vertices which produces a more intense SERS signal and again improves the sensitivity of the assay (*139*).

All the above examples detected biological molecules of interest, however functionalized nanoparticles can also be used to detect cells and species within cells (*140*, *141*). Johne's disease can devastate dairy herds and is caused by *Mycobacterium avium* subspecies *paratuberculosis* whose lysate has been detected using functionalized nanoparticles (*137*). However, the cells can also be detected directly by targeting a specific membrane protein, the sensitivity is significantly improved due to the fact that the membrane protein is shed from the cell, therefore the protein is detected in the sample as well as on the surface of the cell (*142*).

Functionalized nanotags have also been used to detect two different kinds of cancer cells. The nanotags were functionalized with antibodies against two different epidermal growth factor receptors which are over expressed in certain cancers (*143*), different reporter molecules allowed the differentiation of the cells.

Downloaded by UNIV DE SHERBROOKE on November 27, 2012 | http://pubs.acs.org
Publication Date (Web): November 26, 2012 | doi: 10.1021/bk-2012-1112.ch002

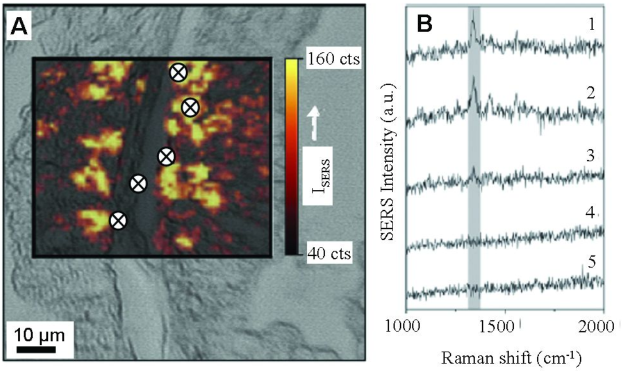

Figure 13. Prostate tissue section mapping using SERS nanotags functionalized with anti-p63 antibody. A) White light image and overlaid false color map based on the intensity of the 1340 cm^{-1} nitro stretching band from the reporter molecule. B) Raw spectra from the marked points in A. (Reproduced with permission from reference (144). Copyright 2011 Royal Society of Chemistry.)

Beyond single cell levels, nanotags can be used to map tissue samples. Schütz *et al.* functionalized their nanotags with anti-p63 antibodies so they could detect the tumor suppressor p63 in prostate biopsies as shown in Figure 13 (*144*). They found that the suppressor was only abundant in the basal epithelium of benign prostate tissues and not in other areas of the tissue (*144*). Although this tissue mapping was done on the surface of a section, the future potential of the technique is clear.

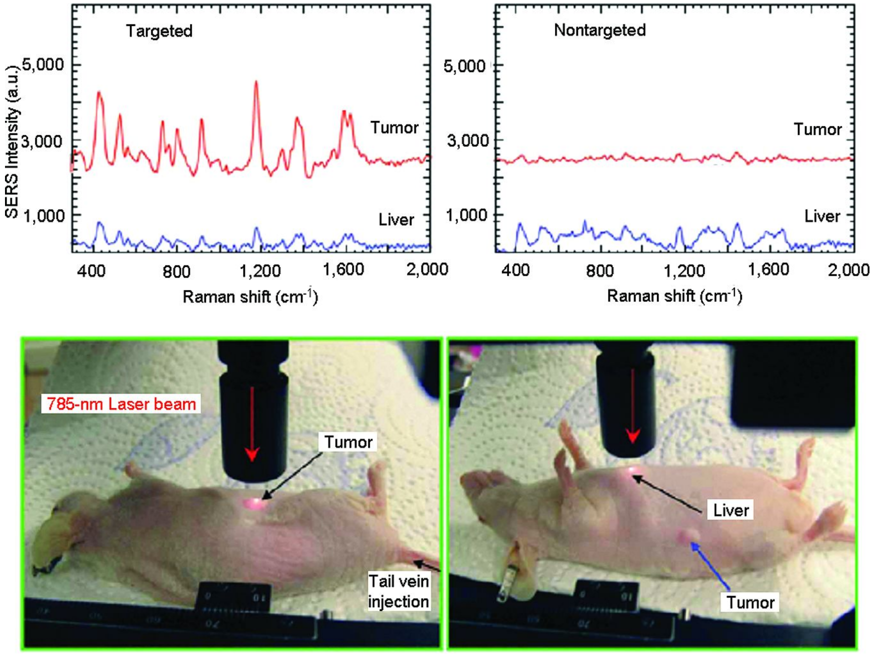

Figure 14. In vivo imaging of ScFv-antibody functionalized nanotag with a 785 nm laser and 2 second spectral integration. The spectra show that the functionalized nanotags primarily accumulate at the tumor site while nonfunctionalized nanotags accumulate in the liver. (Reproduced with permission from reference (57). Copyright 2008 Nature Publishing Group.)

Functionalized nanotags have also been used for *in vivo* detection of tumors within live mice. Qian *et al.* functionalized their nanotags with a single-chain variable fragment (ScFv) antibody that binds to the epidermal growth factor receptors (EGFR) of the tumor (*57*). This approach led to strong SERS signals being recorded from the tumor site while unfunctionalized nanotags were only recorded in the liver, Figure 14, where nanotags will naturally bioaccumulate before removal (*47*). Currently, nanotags for *in vivo* applications are being developed to be multi-modal, i.e. they can be detected by multiple techniques,

Downloaded by UNIV DE SHERBROOKE on November 27, 2012 | http://pubs.acs.org
Publication Date (Web): November 26, 2012 | doi: 10.1021/bk-2012-1112.ch002

such as magnetic resonance imaging and photoacoustic imaging (*145*, *146*). The SERS modality of the nanotags can be used alongside the other approaches to visualize tumors before surgery. However, the main benefit of SERS is the ability to help guide intraoperative surgery by indicating when the tumor has been completely removed (*146*). The superior sensitivity of the nanotags, with their many reporter molecules generating the signal, can indicate the presence of cancerous foci which are not visible to the naked eye (*146*), this has clear benefits for tumor surgery and ultimately improved patient outcomes.

Conclusions

In this chapter we have considered the functionalisation of metallic nanoparticles for bioanalysis. While the functionalisation of the particles is well established and many different routes exist to achieve it, the characterization of the produced nanoparticles is still somewhat lacking. Although many analytical techniques exist to interrogate the species on a nanoparticle surface, no methods exist that are capable of stating definitively how many molecules are on an individual nanoparticle. This is mainly due to the fact that the methods are bulk methods and thus rely on an estimate of nanoparticle concentration taken from UV-Vis absorbance measurements which leads to a range of values for the number of molecules on the surface.

Although the absolute characterization of the nanotags may be lacking this has not held back the development of the applications. Detection of DNA and other biological analytes is now well established and simple changes in the building blocks of the nanotag, i.e. the biorecognition unit, can create specificity for almost any target. However, there are two main challenges that remain to be met; firstly the assays must be applied to real world samples and not idealized laboratory samples, i.e. the detection should be carried out in whole blood or other sample media. The second challenge is the detection of species *in vivo*. We have already mentioned some *in vivo* papers within this chapter but these were simple demonstrations of a yes-no variety, i.e. were the tags present? The challenge is to detect SERS nanotags at depth within larger organisms, which will involve the use of special detection techniques such as spatially offset Raman spectroscopy (SORS) (*147*).

SORS allows signals at different depths in opaque media to be detected and minimizes the influence of surface species. It has already been combined with nanotags and its multiplexing ability demonstrated through 20 mm of porcine tissue (*148*). The next big advance will be the ability to map nanotags within a body in 3-dimensions. If this can be achieved then a multitude of different nanotags can be introduced to the body, each with a specific fingerprint and targeted at individual biological species and thus many different diseases can be tested for simultaneously. Both these challenges can only be met with the development of new detection approaches and tools. As this chapter has demonstrated, the functionalized nanoparticles to achieve this already exist.

Downloaded by UNIV DE SHERBROOKE on November 27, 2012 | http://pubs.acs.org
Publication Date (Web): November 26, 2012 | doi: 10.1021/bk-2012-1112.ch002

References

1. Feynman, R. P. *Eng. Sci.* **1960**, *23*, 22–36.
2. Taniguchi, N. Proceedings of the International Conference of Production Engineering, Tokyo, 1974; pp 18−23.
3. Xia, Y.; Xiong, Y. J.; Lim, B.; Skrabalak, S. E. *Angew. Chem., Int. Ed.* **2009**, *48*, 60–103.
4. Chen, H. M.; Liu, R.-S. *J. Phys. Chem. C* **2011**, *115*, 3513–3527.
5. Jain, P. K.; Huang, X.; El-Sayed, I. H.; El-Sayed, M. A. *Acc. Chem. Res.* **2008**, *41*, 1578–1586.
6. Bell, S. E. J.; McCourt, M. R. *Phys. Chem. Chem. Phys.* **2009**, *11*, 7455–7462.
7. Yguerabide, J.; Yguerabide, E. E. *Anal. Biochem.* **1998**, *262*, 137–156.
8. Le Ru, E. C.; Etchegoin, P. G. *Principles of Surface-Enhanced Raman Spectroscopy and related plasmonic effects*; Elsevier: Amsterdam, Netherlands, 2009; 663 pages.
9. Larmour, I. A.; Graham, D. *Analyst* **2011**, *136*, 3831–3853.
10. McNay, G.; Eustace, D.; Smith, W. E.; Faulds, K.; Graham, D. *Appl. Spectrosc.* **2011**, *65*, 825–837.
11. Tian, Z.-Q.; Ren, B.; Wu, D.-Y. *J. Phys. Chem. B* **2002**, *106*, 9463–9483.
12. Larmour, I. A.; Faulds, K.; Graham, D. *J. Raman Spectrosc.* **2012**, *43*, 202–206.
13. Brust, M.; Fink, J.; Bethell, D.; Schiffrin, D. J.; Kiely, C. *J. Chem. Soc.-Chem. Commun.* **1995**, 1655–1656.
14. Brust, M.; Walker, M.; Bethell, D.; Schiffrin, D. J.; Whyman, R. *J. Chem. Soc., Chem. Commun.* **1994**, 801–802.
15. Lee, P. C.; Meisel, D. *J. Phys. Chem.* **1982**, *86*, 3391–3395.
16. Leopold, N.; Lendl, B. *J. Phys. Chem. B* **2003**, *107*, 5723–5727.
17. Heard, S. M.; Grieser, F.; Barraclough, C. G.; Sanders, J. V. *J. Colloid Interface Sci.* **1983**, *93*, 545–555.
18. Alexander, K. D.; Skinner, K.; Zhang, S.; Wei, H.; Lopez, R. *Nano Lett.* **2010**, *10*, 4488–4493.
19. McLintock, A.; Hunt, N.; Wark, A. W. *Chem. Commun.* **2011**, *47*, 3757–3759.
20. Xu, L.; Kuang, H.; Wang, L.; Xu, C. *J. Mater. Chem.* **2011**, *21*, 16759–16782.
21. Huang, X.; Qi, X.; Huang, Y.; Li, S.; Xue, C.; Gan, C. L.; Boey, F.; Zhang, H. *ACS Nano* **2010**, *4*, 6196–6202.
22. Jin, R. C.; Cao, Y. C.; Hao, E. C.; Metraux, G. S.; Schatz, G. C.; Mirkin, C. A. *Nature* **2003**, *425*, 487–490.
23. Stamplecoskie, K. G.; Scaiano, J. C. *J. Am. Chem. Soc.* **2010**, *132*, 1825–1827.
24. Larmour, I. A.; Argueta, E. A.; Faulds, K.; Graham, D. *J. Phys. Chem. C* **2012**, *116*, 2677–2682.
25. Le Ru, E. C.; Etchegoin, P. G.; Meyer, M. *J. Chem. Phys.* **2006**, *125*, 204701.
26. Le Ru, E. C.; Meyer, M.; Blackie, E.; Etchegoin, P. G. *J. Raman Spectrosc.* **2008**, *39*, 1127–1134.
27. McMahon, J. M.; Li, S.; Ausman, L. K.; Schatz, G. C. *J. Phys. Chem. C* **2011**, *116*, 1627–1637.

Downloaded by UNIV DE SHERBROOKE on November 27, 2012 | http://pubs.acs.org
Publication Date (Web): November 26, 2012 | doi: 10.1021/bk-2012-1112.ch002

28. Martin, L. C.; Larmour, I. A.; Faulds, K.; Graham, D. *Chem. Commun.* **2010**, *46*, 5247–5249.
29. Kahraman, M.; Sur, Ì.; Culha, M. *Anal. Chem.* **2010**, *82*, 7596–7602.
30. Bell, S. E. J.; Sirimuthu, N. M. S. *J. Am. Chem. Soc.* **2006**, *128*, 15580–15581.
31. Papadopoulou, E.; Bell, S. E. J. *J. Phys. Chem. C* **2010**, *114*, 22644–22651.
32. Larmour, I. A.; Faulds, K.; Graham, D. *Chem. Sci.* **2010**, *1*, 151–160.
33. Copeland, R. A.; Fodor, S. P. A.; Spiro, T. G. *J. Am. Chem. Soc.* **1984**, *106*, 3872–3874.
34. Rospendowski, B. N.; Kelly, K.; Wolf, C. R.; Smith, W. E. *J. Am. Chem. Soc.* **1991**, *113*, 1217–1225.
35. Hering, K. K.; Möller, R.; Fritzsche, W.; Popp, J. *ChemPhysChem* **2008**, *9*, 867–872.
36. Graham, D.; Mallinder, B. J.; Whitcombe, D.; Smith, W. E. *ChemPhysChem* **2001**, *2*, 746–748.
37. Fruk, L.; Grondin, A.; Smith, W. E.; Graham, D. *Chem. Commun.* **2002**, 2100–2101.
38. Douglas, P.; McCarney, K. M.; Graham, D.; Smith, W. E. *Analyst* **2007**, *132*, 865–867.
39. Dou, X.; Takama, T.; Yamaguchi, Y.; Yamamoto, H.; Ozaki, Y. *Anal. Chem.* **1997**, *69*, 1492–1495.
40. Ingram, A. M.; Stirling, K.; Faulds, K.; Moore, B. D.; Graham, D. *Org. Biomol. Chem.* **2006**, *4*, 2869–2873.
41. Ingram, A.; Stokes, R. J.; Redden, J.; Gibson, K.; Moore, B.; Faulds, K.; Graham, D. *Anal. Chem.* **2007**, *79*, 8578–8583.
42. Moore, B. D.; Stevenson, L.; Watt, A.; Flitsch, S.; Turner, N. J.; Cassidy, C.; Graham, D. *Nat. Biotechnol.* **2004**, *22*, 1133–1138.
43. Ingram, A.; Byers, L.; Faulds, K.; Moore, B. D.; Graham, D. *J. Am. Chem. Soc.* **2008**, *130*, 11846–11847.
44. Ingram, A.; Moore, B. D.; Graham, D. *Bioorg. Med. Chem. Lett.* **2009**, *19*, 1569–1571.
45. Rodriguez-Lorenzo, L.; Krpetic, Z.; Barbosa, S.; Alvarez-Puebla, R. A.; Liz-Marzan, L. M.; Prior, I. A.; Brust, M. *Integr. Biol.* **2011**, *3*, 922–926.
46. Cui, Y.; Zheng, X.-S.; Ren, B.; Wang, R.; Zhang, J.; Xia, N.-S.; Tian, Z.-Q. *Chem. Sci.* **2011**, *2*, 1463–1469.
47. Zavaleta, C. L.; Smith, B. R.; Walton, I.; Doering, W.; Davis, G.; Shojaei, B.; Natan, M. J.; Gambhir, S. S. *Proc. Natl. Acad. Sci. U.S.A.* **2009**, *106*, 13511–13516.
48. Keren, S.; Zavaleta, C.; Cheng, Z.; de la Zerda, A.; Gheysens, O.; Gambhir, S. S. *Proc. Natl. Acad. Sci. U.S.A.* **2008**, *105*, 5844–5849.
49. von Maltzahn, G.; Centrone, A.; Park, J. H.; Ramanathan, R.; Sailor, M. J.; Hatton, T. A.; Bhatia, S. N. *Adv. Mater.* **2009**, *21*, 3175–3180.
50. Larmour, I. A.; Faulds, K.; Graham, D. *J. Phys. Chem. C* **2010**, *114*, 13249–13254.
51. Lutz, B. R.; Dentinger, C. E.; Nguyen, L. N.; Sun, L.; Zhang, J.; Allen, A. N.; Chan, S.; Knudsen, B. S. *ACS Nano* **2008**, *2*, 2306–2314.

Downloaded by UNIV DE SHERBROOKE on November 27, 2012 | http://pubs.acs.org
Publication Date (Web): November 26, 2012 | doi: 10.1021/bk-2012-1112.ch002

52. McHugh, C. J.; Docherty, F. T.; Graham, D.; Smith, W. E. *Analyst* **2004**, *129*, 69–72.
53. McAnally, G.; McLaughlin, C.; Brown, R.; Robson, D. C.; Faulds, K.; Tackley, D. R.; Smith, W. E.; Graham, D. *Analyst* **2002**, *127*, 838–841.
54. Zhang, F.; Skoda, M. W. A.; Jacobs, R. M. J.; Dressen, D. G.; Martin, R. A.; Martin, C. M.; Clark, G. F.; Lamkemeyer, T.; Schreiber, F. *J. Phys. Chem. C* **2009**, *113*, 4839–4847.
55. Zhang, F. J.; Dressen, D. G.; Skoda, M. W. A.; Jacobs, R. M. J.; Zorn, S.; Martin, R. A.; Martin, C. M.; Clark, G. F.; Schreiber, F. *Eur. Biophys. J. Biophys. Lett.* **2008**, *37*, 551–561.
56. Sperling, R. A.; Parak, W. J. *Philos. Trans. R. Soc. London, Ser. A* **2010**, *368*, 1333–1383.
57. Qian, X. M.; Peng, X. H.; Ansari, D. O.; Yin-Goen, Q.; Chen, G. Z.; Shin, D. M.; Yang, L.; Young, A. N.; Wang, M. D.; Nie, S. M. *Nat. Biotechnol.* **2008**, *26*, 83–90.
58. Mulvaney, S. P.; Musick, M. D.; Keating, C. D.; Natan, M. J. *Langmuir* **2003**, *19*, 4784–4790.
59. Ung, T.; Liz-Marzan, L. M.; Mulvaney, P. *Langmuir* **1998**, *14*, 3740–3748.
60. Yang, M. X.; Chen, T.; Lau, W. S.; Wang, Y.; Tang, Q. H.; Yang, Y. H.; Chen, H. Y. *Small* **2009**, *5*, 198–202.
61. Shkilnyy, A.; Souce, M.; Dubois, P.; Warmont, F.; Saboungi, M. L.; Chourpa, I. *Analyst* **2009**, *134*, 1868–1872.
62. Keating, C. D.; Kovaleski, K. M.; Natan, M. J. *J. Phys. Chem. B* **1998**, *102*, 9404–9413.
63. Nelson, E. M.; Rothberg, L. J. *Langmuir* **2011**, *27*, 1770, 1777.
64. Lim, D.-K.; Jeon, K.-S.; Kim, H. M.; Nam, J.-M.; Suh, Y. D. *Nat. Mater.* **2010**, *9*, 60–67.
65. Lim, D. K.; Kim, I. J.; Nam, J. M. *Chem. Commun.* **2008**, *44*, 5312–5314.
66. Fabris, L.; Dante, M.; Nguyen, T. Q.; Tok, J. B. H.; Bazan, G. C. *Adv. Funct. Mater.* **2008**, *18*, 2518–2525.
67. Niemeyer, C. M.; Burger, W.; Peplies, J. *Angew. Chem., Int. Ed.* **1998**, *37*, 2265–2268.
68. Otsuka, H.; Akiyama, Y.; Nagasaki, Y.; Kataoka, K. *J. Am. Chem. Soc.* **2001**, *123*, 8226–8230.
69. Dougan, J. A.; Karlsson, C.; Smith, W. E.; Graham, D. *Nucleic Acids Res.* **2007**, *35*, 3668–3675.
70. Li, Z.; Jin, R.; Mirkin, C. A.; Letsinger, R. L. *Nucleic Acids Res.* **2002**, *30*, 1558–1562.
71. Karamanska, R.; Mukhopadhyay, B.; Russell, D. A.; Field, R. A. *Chem. Commun.* **2005**, 3334–3336.
72. Sastry, M.; Lala, N.; Patil, V.; Chavan, S. P.; Chittiboyina, A. G. *Langmuir* **1998**, *14*, 4138–4142.
73. Abad, J. M.; Mertens, S. F. L.; Pita, M.; Fernandez, V. M.; Schiffrin, D. J. *J. Am. Chem. Soc.* **2005**, *127*, 5689–5694.
74. Krovi, S. A.; Smith, D.-D.; Nguyen, S.-B. T. *Chem. Commun.* **2010**, *46*, 5277–5279.

Downloaded by UNIV DE SHERBROOKE on November 27, 2012 | http://pubs.acs.org
Publication Date (Web): November 26, 2012 | doi: 10.1021/bk-2012-1112.ch002

Downloaded by UNIV DE SHERBROOKE on November 27, 2012 | http://pubs.acs.org
Publication Date (Web): November 26, 2012 | doi: 10.1021/bk-2012-1112.ch002

75. Enright, A.; Fruk, L.; Grondin, A.; McHugh, C. J.; Smith, W. E.; Graham, D. *Analyst* **2004**, *129*, 975–978.
76. McKenzie, F.; Ingram, A.; Stokes, R.; Graham, D. *Analyst* **2009**, *134*, 549–556.
77. Wrzesien, J.; Graham, D. *Tetrahedron* **2012**, *68*, 1230–1240.
78. Jehn, C.; Kustner, B.; Adam, P.; Marx, A.; Strobel, P.; Schmuck, C.; Schlucker, S. *Phys. Chem. Chem. Phys.* **2009**, *11*, 7499–7504.
79. Murphy, C. J.; Gole, A. M.; Stone, J. W.; Sisco, P. N.; Alkilany, A. M.; Goldsmith, E. C.; Baxter, S. C. *Acc. Chem. Res.* **2008**, *41*, 1721–1730.
80. Walkey, C. D.; Olsen, J. B.; Guo, H.; Emili, A.; Chan, W. C. W. *J. Am. Chem. Soc.* **2011**, *134*, 2139–2147.
81. Cormack, P. A. G.; Hernandez-Santana, A.; Prasath, R. A.; McKenzie, F.; Graham, D.; Smith, W. E. *Chem. Comm.* **2008**, *44*, 2517–2519.
82. Rocks, L.; Faulds, K.; Graham, D. *Chem. Commun.* **2011**, *47*, 4415–4417.
83. Schutz, M.; Kustner, B.; Bauer, M.; Schmuck, C.; Schlucker, S. *Small* **2010**, *6*, 733–737.
84. Kustner, B.; Gellner, M.; Schutz, M.; Schoppler, F.; Marx, A.; Strobel, P.; Adam, P.; Schmuck, C.; Schlucker, S. *Angew. Chem., Int. Ed.* **2009**, *48*, 1950–1953.
85. Storhofff, J. J.; Elghanian, R.; Mirkin, C. A.; Letsinger, R. L. *Langmuir* **2002**, *18*, 6666–6670.
86. Vangala, K.; Ameer, F.; Salomon, G.; Le, V.; Lewis, E.; Yu, L.; Liu, D.; Zhang, D. *J. Phys. Chem. C* **2012**, *116*, 3645–3652.
87. Graham, D.; Thompson, D. G.; Smith, W. E.; Faulds, K. *Nat. Nanotechnol.* **2008**, *3*, 548–551.
88. Alivisatos, A. P.; Johnsson, K. P.; Peng, X.; Wilson, T. E.; Loweth, C. J.; Bruchez, M. P.; Schultz, P. G. *Nature* **1996**, *382*, 609–611.
89. Wang, Y.; Neyman, A.; Arkhangelsky, E.; Gitis, V.; Meshi, L.; Weinstock, I. A. *J. Am. Chem. Soc.* **2009**, *131*, 17412–17422.
90. Maus, L.; Spatz, J. P.; Fiammengo, R. *Langmuir* **2009**, *25*, 7910–7917.
91. Hurst, S. J.; Lytton-Jean, A. K. R.; Mirkin, C. A. *Anal. Chem.* **2006**, *78*, 8313–8318.
92. McKenzie, F.; Steven, V.; Ingram, A.; Graham, D. *Chem. Comm.* **2009**, *45*, 2872–2874.
93. Demers, L. M.; Mirkin, C. A.; Mucic, R. C.; Reynolds, R. A.; Letsinger, R. L.; Elghanian, R.; Viswanadham, G. *Anal. Chem.* **2000**, *72*, 5535–5541.
94. Gole, A.; Dash, C.; Ramakrishnan, V.; Sainkar, S. R.; Mandale, A. B.; Rao, M.; Sastry, M. *Langmuir* **2001**, *17*, 1674–1679.
95. Gole, A.; Dash, C.; Soman, C.; Sainkar, S. R.; Rao, M.; Sastry, M. *Bioconjugate Chem.* **2001**, *12*, 684–690.
96. Gole, A.; Vyas, S.; Phadtare, S.; Lachke, A.; Sastry, M. *Colloids Surf., B* **2002**, *25*, 129–138.
97. Stewart, A.; Bell, S. E. J. *Chem. Commun.* **2011**, *47*, 4523–4525.
98. Sirimuthu, N. M. S.; Syme, C. D.; Cooper, J. M. *Chem. Commun.* **2011**, *47*, 4099–4101.
99. Porter, M. D.; Lipert, R. J.; Siperko, L. M.; Wang, G.; Narayanana, R. *Chem. Soc. Rev.* **2008**, *37*, 1001–1011.

100. Shaw, C. P.; Middleton, D. A.; Volk, M.; Levy, R. *ACS Nano* **2012**, *6*, 1416–1426.
101. Badia, A.; Gao, W.; Singh, S.; Demers, L.; Cuccia, L.; Reven, L. *Langmuir* **1996**, *12*, 1262–1269.
102. Gentilini, C.; Franchi, P.; Mileo, E.; Polizzi, S.; Lucarini, M.; Pasquato, L. *Angew. Chem., Int. Ed.* **2009**, *48*, 3060–3064.
103. Duchesne, L.; Wells, G.; Fernig, D. G.; Harris, S. A.; Levy, R. *ChemBioChem* **2008**, *9*, 2127–2134.
104. Hostetler, M. J.; Wingate, J. E.; Zhong, C.-J.; Harris, J. E.; Vachet, R. W.; Clark, M. R.; Londono, J. D.; Green, S. J.; Stokes, J. J.; Wignall, G. D.; Glish, G. L.; Porter, M. D.; Evans, N. D.; Murray, R. W. *Langmuir* **1998**, *14*, 17–30.
105. Olmedo, I.; Araya, E.; Sanz, F.; Medina, E.; Arbiol, J.; Toledo, P.; Alvarez-Lueje, A.; Giralt, E.; Kogan, M. J. *Bioconjugate Chem.* **2008**, *19*, 1154–1163.
106. Wark, A. W.; Stokes, R. J.; Darby, S. B.; Smith, W. E.; Graham, D. *J. Phys. Chem. C* **2010**, *114*, 18115–18120.
107. Irvine, E. J.; Hernandez-Santana, A.; Faulds, K.; Graham, D. *Analyst* **2011**, *136*, 2925–2930.
108. Thaxton, C. S.; Georganopoulou, D. G.; Mirkin, C. A. *Clin. Chim. Acta* **2006**, *363*, 120–126.
109. Elghanian, R.; Storhoff, J. J.; Mucic, R. C.; Letsinger, R. L.; Mirkin, C. A. *Science* **1997**, *277*, 1078–1081.
110. Taton, T. A.; Lu, G.; Mirkin, C. A. *J. Am. Chem. Soc.* **2001**, *123*, 5164–5165.
111. Cao, Y.; Jin, R.; Mirkin, C. A. *J. Am. Chem. Soc.* **2001**, *123*, 7961–7962.
112. Radhakumary, C.; Sreenivasan, K. *Anal. Chem.* **2011**, *83*, 2829–2833.
113. Aslan, K.; Lakowicz, J. R.; Geddes, C. D. *Anal. Chem.* **2005**, *77*, 2007–2014.
114. Aslan, K.; Lakowicz, J. R.; Geddes, C. D. *Anal. Biochem.* **2004**, *330*, 145–155.
115. Thanh, N. T. K.; Rosenzweig, Z. *Anal. Chem.* **2002**, *74*, 1624–1628.
116. Sun, S.-K.; Wang, H.-F.; Yan, X.-P. *Chem. Commun.* **2011**, *47*, 3817–3819.
117. Huang, C.-C.; Huang, Y.-F.; Cao, Z.; Tan, W.; Chang, H.-T. *Anal. Chem.* **2005**, *77*, 5735–5741.
118. Guarise, C.; Pasquato, L.; De Filippis, V.; Scrimin, P. *Proc. Natl. Acad. Sci. U.S.A.* **2006**, *103*, 3978–3982.
119. Wang, Z.; Levy, R.; Fernig, D. G.; Brust, M. *J. Am. Chem. Soc.* **2006**, *128*, 2214–2215.
120. Xu, X. Y.; Han, M. S.; Mirkin, C. A. *Angew. Chem., Int. Ed.* **2007**, *46*, 3468–3470.
121. Hirsch, L. R.; Jackson, J. B.; Lee, A.; Halas, N. J.; West, J. *Anal. Chem.* **2003**, *75*, 2377–2381.
122. Graham, D.; Brown, R.; Smith, W. E. *Chem. Commun.* **2001**, 1002–1003.
123. McKenzie, F.; Faulds, K.; Graham, D. *Nanoscale* **2010**, *2*, 78–80.
124. Graham, D.; Faulds, K.; Thompson, D.; Mackenzie, F.; Stokes, R.; Macaskill, A. *Biochem. Soc. Trans.* **2009**, *37*, 441–444.
125. Graham, D.; Stevenson, R.; Thompson, D. G.; Barrett, L.; Dalton, C.; Faulds, K. *Faraday Discuss.* **2011**, *149*, 291–299.
126. Dougan, J. A.; Faulds, K. *Analyst* **2012**, *137*, 545–554.

Downloaded by UNIV DE SHERBROOKE on November 27, 2012 | http://pubs.acs.org
Publication Date (Web): November 26, 2012 | doi: 10.1021/bk-2012-1112.ch002

127. Cao, Y. W. C.; Jin, R. C.; Mirkin, C. A. *Science* **2002**, *297*, 1536–1540.

128. Larmour, I. A.; Faulds, K.; Graham, D. *Anal. Methods* **2010**, *2*, 1230–1232.

129. Yuen, J. M.; Shah, N. C.; Walsh, J. T.; Glucksberg, M. R.; Van Duyne, R. P. *Anal. Chem.* **2010**, *82*, 8382–8385.

130. Wu, Z. S.; Zhou, G. Z.; Jiang, J. H.; Shen, G. L.; Yu, R. Q. *Talanta* **2006**, *70*, 533–539.

131. Ni, J.; Lipert, R. J.; Dawson, G. B.; Porter, M. D. *Anal. Chem.* **1999**, *71*, 4903–4908.

132. Dufek, E. J.; Ehlert, B.; Granger, M. C.; Sandrock, T. M.; Legge, S. L.; Herrmann, M. G.; Meikle, A. W.; Porter, M. D. *Analyst* **2010**, *135*, 2811–2817.

133. Cao, Y. C.; Jin, R. C.; Nam, J. M.; Thaxton, C. S.; Mirkin, C. A. *J. Am. Chem. Soc.* **2003**, *125*, 14676–14677.

134. Grubisha, D. S.; Lipert, R. J.; Park, H. Y.; Driskell, J.; Porter, M. D. *Anal. Chem.* **2003**, *75*, 5936–5943.

135. Wang, G.; Lipert, R. J.; Jain, M.; Kaur, S.; Chakraboty, S.; Torres, M. P.; Batra, S. K.; Brand, R. E.; Porter, M. D. *Anal. Chem.* **2011**, *83*, 2554–2561.

136. Driskell, J. D.; Kwarta, K. M.; Lipert, R. J.; Porter, M. D.; Neill, J. D.; Ridpath, J. F. *Anal. Chem.* **2005**, *77*, 6147–6154.

137. Yakes, B. J.; Lipert, R. J.; Bannantine, J. P.; Porter, M. D. *Clin. Vaccine Immunol.* **2008**, *15*, 227–234.

138. Driskell, J. D.; Uhlenkamp, J. M.; Lipert, R. J.; Porter, M. D. *Anal. Chem.* **2007**, *79*, 4141–4148.

139. Narayanan, R.; Lipert, R. J.; Porter, M. D. *Anal. Chem.* **2008**, *80*, 2265–2271.

140. Ochsenkuhn, M. A.; Jess, P. R. T.; Stoquert, H.; Dholakia, K.; Campbell, C. J. *ACS Nano* **2009**, *3*, 3613–3621.

141. Syme, C. D.; Sirimuthu, N. M. S.; Faley, S. L.; Cooper, J. M. *Chem. Commun.* **2010**, *46*, 7921–7923.

142. Yakes, B. J.; Lipert, R. J.; Bannantine, J. P.; Porter, M. D. *Clin. Vaccine Immunol.* **2008**, *15*, 235–242.

143. Maiti, K. K.; Samanta, A.; Vendrell, M.; Soh, K.-S.; Olivo, M.; Chang, Y.-T. *Chem. Commun.* **2011**, *47*, 3514–3516.

144. Schutz, M.; Steinigeweg, D.; Salehi, M.; Kompe, K.; Schlucker, S. *Chem. Commun.* **2011**, *47*, 4216–4218.

145. Yigit, M. V.; Zhu, L.; Ifediba, M. A.; Zhang, Y.; Carr, K.; Moore, A.; Medarova, Z. *ACS Nano* **2010**, *5*, 1056–1066.

146. Kircher, M. F.; de la Zerda, A.; Jokerst, J. V.; Zavaleta, C. L.; Kempen, P. J.; Mittra, E.; Pitter, K.; Huang, R.; Campos, C.; Habte, F.; Sinclair, R.; Brennan, C. W.; Mellinghoff, I. K.; Holland, E. C.; Gambhir, S. S. *Nat. Med.* **2012**, in press, DOI:10.1038/nm.2721.

147. Stone, N.; Faulds, K.; Graham, D.; Matousek, P. *Anal. Chem.* **2010**, *82*, 3969–3973.

148. Stone, N.; Kerssens, M.; Lloyd, G. R.; Faulds, K.; Graham, D.; Matousek, P. *Chem. Sci.* **2011**, *2*, 776–780.

Downloaded by UNIV DE SHERBROOKE on November 27, 2012 | http://pubs.acs.org
Publication Date (Web): November 26, 2012 | doi: 10.1021/bk-2012-1112.ch002

Downloaded by NORTH CAROLINA STATE UNIV on November 27, 2012 | http://pubs.acs.org
Publication Date (Web): November 26, 2012 | doi: 10.1021/bk-2012-1112.ch003

Chapter 3

Tailoring Quantum Dot Interfaces for Improved Biofunctionality and Energy Transfer

Joshua Zylstra, Rabeka Alam, Hyunjoo Han, Robert P. Doyle, and Mathew M. Maye*

Department of Chemistry, Syracuse University,
Syracuse, New York 13244, U.S.A.
***E-mail: mmmaye@syr.edu**

Over the past decade quantum dots (qdots) have emerged as a premier biological labeling tool due to their unique photophysical properties. In order to take advantage of these properties, a lot of surface chemistry design work needs to take place due to the need of phase transfer to aqueous buffers, as well as the need to preserve both photophysical and colloidal stability. This chapter first briefly reviews a number of functionalization strategies available to researchers, and then focuses on our groups strategy. In particular, the use the amino acid L-histidine to facilitate both phase trasfer, ligand exchange, as well as direct biological functionalization. The binding mechanism and properties of the histidine-capping at the qdots is reviewed, as well as the use of resonance energy transfer (FRET and BRET) to probe the abiotic-biotic interface.

Introduction

The synthetic methodology for colloidal nanoparticles, such as for semiconductive quantum dots (qdots), is an interesting combination of organic and inorganic wet-chemical reactions, with solid-state high temperature annealing, nucleation and growth, and epitaxial deposition (*1*–*5*). Since the seminal synthetic reports (*1*, *2*) the knowledge base for qdot synthesis and the remarkable final photophysical properties has grown considerably (*1*–*6*). Today, the qdots can be made highly crystalline (e.g. Wurtzite or ZincBlende) and highly monodisperse. These qdots have a core-shell architecture like many other nanomaterials, where

In Functional Nanoparticles for Bioanalysis, Nanomedicine, and Bioelectronic Devices Volume 1; Hepel, M., et al.;
ACS Symposium Series; American Chemical Society: Washington, DC, 2012.

Downloaded by NORTH CAROLINA STATE UNIV on November 27, 2012 | http://pubs.acs.org
Publication Date (Web): November 26, 2012 | doi: 10.1021/bk-2012-1112.ch003

the inorganic core is surrounded by a dense shell of hydrophobic self-assembled monolayers (e.g. TOPO) (*6*). This encapsulation plays a number of roles, one of which is related to stability, while the other promotes the utility of the qdots. Thus, understanding and optimizing the surface chemistry at the organic encapsulating shells is thus a prominent area of colloidal research (*5–11*). In particular, the design and implementation of chemical functionalization at qdot interfaces to promote biological functionalization as well as resonance energy transfer (RET) is a key component for using qdots as biological sensors (*8*, *9*, *11–20*).

These functionalization protocols often occur in multiple steps, and typically require rendering the interface as hydrophilic (*7–14*). The functionality change must protect the inorganic core from degradation (e.g. loss of quantum yield) (*21*, *22*), but also provide solubility in modest ionic strengths. Ideally, this interface would also be readily exchanged by additional ligands or biomaterials (*11–20*), and provide a soft-binding to the qdot interface or organic encapsulation, and not alter surface electronics, such as the introduction of electron or hole traps (*21*, *22*). Generally speaking, one of two general approaches are used to achieve these goals. These include the use of monolayer exchange at the qdot interface, and the polymer wrapping of alkyl-capped qdots. Table 1 summarizes a number of recent advances in these pursuits.

The monolayer exchange class utilizes place exchange between the incoming ligand, typically thiolated, and displaces the initial alkyl monolayers, typically trioctylphosphine oxide (TOPO) or alkyl amines. One advantage that this approach has is the potential for smaller hydrodynamic diameters (D_h) of the product. But a trade off to this is often a decreased QY, due direct binding to the qdot interface. These protocols include the use of short-chain mercapto acids (*23*), thiolated dendrimers (*24*), as well as other functional moieties that utilize thiol for attachment (*25–27*). Multidentate ligands, such as the dithiol dihydrolipoic acid (DHLA), have also been used extensively for both phase exchange (*14–22*, *28*, *29*) as well as an anchor for further modification (*30–33*).

Table 1. Molecules used to ligand exchange or wrapp quantum dots (qdots)

Mercaptoacetic Acid	(*9*)
Mercaptopropinoic Acid	(*17*, *34–37*)
Thiol-β-D-Lactose	(*26*)
Monothiol Peg derivatives	(*28*, *38*)
Cysteine	(*39*)
Dendron	(*24*, *40*)
Thiolated DNA	(*17*, *34*, *36*, *37*, *41–43*)
Phosphonic Acidic Acid	(*44*)
1,4-Benzenedithiol	(*25*)

Continued on next page.

Table 1. (Continued). Molecules used to ligand exchange or wrapp quantum dots (qdots)

5-mercaptomethyltetrazole	(*27*)
His-tagged DNA	(*43*, *45*)
Glutathione	(*46–48*)
Histidine	(*41*, *49*, *50*)
DHLA	(*14–16*, *29*)
DHLA-PEG	(*29*, *32*, *45*, *51–53*)
DHLA-Tween	(*54*)
DHLA–sulphobetaine	(*55*)
Bis-DHLA–PEG conjugate	(*29*)
Aminated polymers	(*56–58*)
RAFT Polymer	(*59*, *60*)
DHLA–albumin	(*61*)
Cystine functionalized Polyaspertic acid	(*62*)
Bisthiol-g-polyethylene glycol	(*37*, *63*, *64*)
Peptides	(*65–67*)
DTT	(*68*)
Block Copolymers	(*9*, *69*)
Poly(maleic anhydride) Block Copolymers	(*25*, *70*, *71*)
Polymer Capsules	(*25*, *72*)
Calixarene derivatives	(*73*)
Phospholipids	(*33*, *74*)
β-Cyclodextrin	(*75*)
Silica encapsulation	(*76–78*)
Biotinylated Polymer	(*18*)
DNA Adsorption	(*79*, *80*)

Downloaded by NORTH CAROLINA STATE UNIV on November 27, 2012 | http://pubs.acs.org
Publication Date (Web): November 26, 2012 | doi: 10.1021/bk-2012-1112.ch003

The second class of qdot phase transfer and functionalization protocols is the polymer wrapping method (*9*, *27–33*, *69–71*). This protocol is particularly important for a number of reasons. First, it often allows for the preservation of QY, owing in large part to the hydrophobic anchoring of the amphiphilic polymer to the original surface encapsulation. However actual QY values are known to fluctuate from batch to batch. Because of the multilayer nature of the wrapping, and the potential to add polyethyleneglycol (PEG) units, the polymer wrapped qdots are often stable at a wide range of pH and ionic strengths. A drawback to this is often seen by the increased D_h, which is thought to limit some biocompatibility.

Once rendered hydrophilic and phase transfered, these qdots are often functionalized with biomacromolecules, which has facilitated the study of novel biomimetic assembly approaches (*81–89*), where cross-linking reactions between qdots mimic biological recognition or biological material itself (*90–97*). For example, the DNA-mediated assembly of nanomaterials, such as gold nanoparticles, is established (*98–109*), and this strategy has recently been broadened by devising new functionalization strategies for programming qdots with similar DNA-mediated reactivity (*110–114*), were oligonucleotide functionaliztion is achieved using classical carbodiimide (EDC) coupling chemistry (*115*), polyhistidine peptide DNA assembly (*18*), and biotin-avidin recognition (*92*, *93*). Once functionalized, the interface can be probed using the Förster (or Fluorescence) resonance energy transfer (FRET) method, where the qdot is the fluorescent donor, and a fluorophore acceptor is attached in proximity by a DNA linkage. A number of DNA-qdot FRET studies have been performed (*18*, *43*, *45*, *47*, *116*). Moreover, an additional RET design exists where the qdot performs as the energy acceptor. The seminal work in this area has been performed by Rao and co-workers (*117–121*), who first showed that bioluminescent enzymes mutated from *R. reniformis luciferase* (Luc8) can be conjugated to qdots via EDC coupling (*117*). In the presence of the substrate colenterazine, the qdot accepts the excited state energy of Luc8 via the non-radiative pathway known as bioluminescence resonance energy transfer (BRET).

In this chapter, we review our recent success in the synthesis, phase transfer, and biofunctionalization of qdot interfaces for utility in biomimetic self-assembly and energy transfer. We first describe a modular phase transfer approach that utilizes a small molecule and amino acid L-histidine (His, **2**) to readily ligand exchange the dense hydrophobic shells at CdSe/ZnS qdot interfaces. We then characterize this unique interface via 1D ^{1}H NMR, and 2D NOESY and DOESY ^{1}H NMR. We then show that this **2**-modified interface can be readily displaced by polyhistidine tagged proteins that perform DNA-mediated self-assembly, and undergo highly efficient FRET and BRET.

I. Histidine-Mediated Phase Transfer Protocol and Analysis

The general strategy employed for qdot phase transfer and further modification is illustrated in scheme 1. First, CdSe/ZnS core/shell qdots were synthesized via standard organometallic methods with slight modification (*122–124*). To initiate phase transfer to buffers, an excess of **2** in a 3:1 basic (200 mM KOH) methanol/water mixture is added to a solution of trioctylphosphine oxide/oleylamine (TOPO/OAm) capped qdots (denoted as **1**-qdots) and vortexed for 1-5 min. Using this biphasic approach, the **2**-qdot immediately undergo phase transfer into buffer (10 mM borate buffer, pH = 8.3). This homogeneity and lack of precipitation greatly decreases the tendency for non-reversible aggregation, which is particularly useful, since the lack of aggregates allowed an immediate optically clear product that can be used without additional centrifugation, filtration, or sonication. If required, the **2**-qdot can then be purified free of excess **2** either by acetone precipitation, or dialysis.

Downloaded by NORTH CAROLINA STATE UNIV on November 27, 2012 | http://pubs.acs.org
Publication Date (Web): November 26, 2012 | doi: 10.1021/bk-2012-1112.ch003

Downloaded by NORTH CAROLINA STATE UNIV on November 27, 2012 | http://pubs.acs.org
Publication Date (Web): November 26, 2012 | doi: 10.1021/bk-2012-1112.ch003

This **2**-mediated phase transfer step was found to have a number of important qualities. First, the biphasic phase transfer and collection of the **2**-qdot is immediate, and does not require long incubation times, excessive concentrations, or elevated temperatures. Second, this process results in high phase transfer mass yields (75-90%). A third attribute of this approach is the modest preservation of optical properties and quantum yields (QY) of the qdots (*49*). The **1**-qdots had QY of ≈53% directly after synthesis, while the **2**-qdot showed a QY ≈30% after phase transfer. This QY loss was also influenced by core size, as well as ZnS-shell thickness and quality, thus batch to batch values varied.

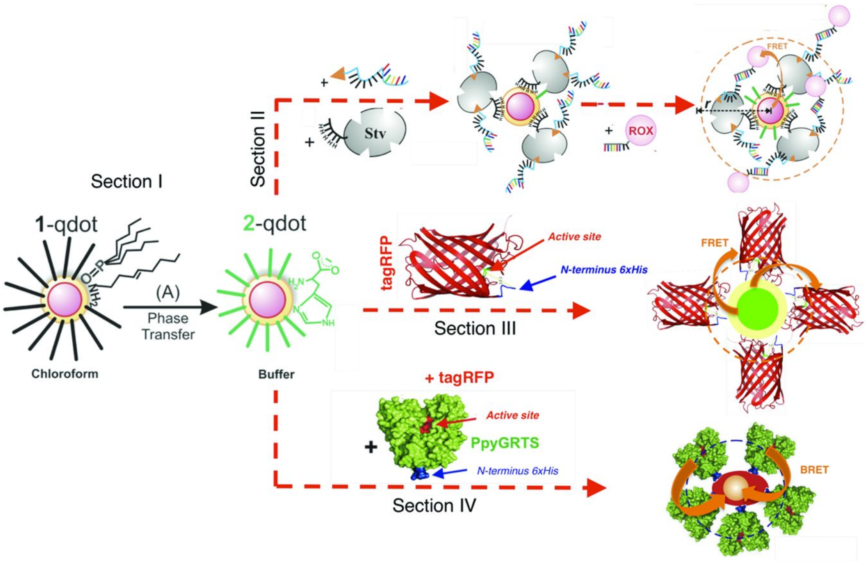

*Scheme 1. An idealized schematic illustrating the qdot functionalization steps reviewed. The OAm/TOPO-capped CdSe/ZnS (**1**-qdot) are first phase transferred (A) from chloroform to aqueous buffers using His (**2**), resulting in **2**-qdots. Next, the **2**-capping be further functionalized with hexahistidine-tagged Streptavidin, Red Flourescent Protein, and Firefly Luciferase*

The ability of **2** to induce such effective phase transfer while maintaining a large proportion of QY is notable, considering its small size, lack of alkyl chains for monolayer formation, and presumably weak coordination to the qdots ZnS shell. In biology, **2** is known to be key cation binding sites in metalloproteins, which coordinate via the N(2)-position at the imidazole ring (*125*). It is this binding to divalent cations, such as Ni^{2+}, that is the basis for polyhistidine based purification of engineered proteins (*126*). Moreover, in solution, **2** has been shown to form a bis(L-Histidinato-N,N′) complex with Zn^{2+} cations, which also chelate at the α-amino group and the N(2) of the imidazole ring, as shown by crystal structure analysis (*127*). Moreover, such histagged binding has also been shown by Mattoussi and co-workers to bind strongly to qdots dispersed in

Downloaded by NORTH CAROLINA STATE UNIV on November 27, 2012 | http://pubs.acs.org
Publication Date (Web): November 26, 2012 | doi: 10.1021/bk-2012-1112.ch003

aqueous media, presumably due to the coordination of the imidizole ring to free Zn^{2+} sites at the ZnS-lattice interface (*29*, *128*).

To investigate the binding mechanism, and probe the extent of ligand exchange, we turned to ^{1}H-NMR analysis. NMR analysis has emerged as a powerful analytical tool to investigate the organic-encapsulating shells of nanomaterials, particularly when studying the multiple surface chemistries, and ligand exchange dynamics at qdot interfaces (*129–133*). For instance, Hens and co-workers have utilized both 1D and 2D NMR techniques to characterize qdot interfaces, and to observe ligand exchange in-situ (*129–133*). Figure 1 shows a typical 1D ^{1}H-NMR spectra for purified solutions of **1**-qdot (i) and **2**-qdot (ii). The first observation is the significantly broadened ^{1}H resonances compared to the molecules themselves, which are a characteristic of surface bound molecules, particularly those at nanoparticle interfaces (*129–133*). The dense or close packing of the ligands at the surface leads to a molecularly crowded environment, leading to inter-ligand resonances, and more solid-state like characteristics, such as lacking free rotation, for instance. Added to this is the fact that the ligands themselves adopt the diffusion characteristics of the qdot, which have orders of magnitude slower diffusion constants ($<D>$) (*59–61*).

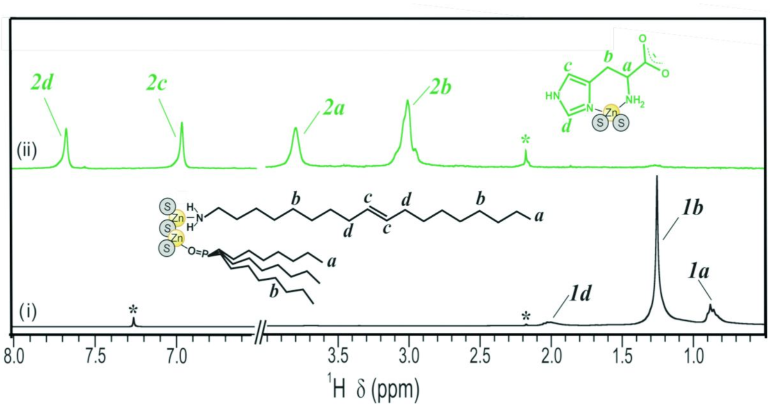

*Figure 1. The ^{1}H-NMR results for **1**-qdot (i) and **2**-qdot (ii) after purification and redispersion in $CDCl_3$ (i) and D_2O (ii) respectively. Insets: Illustration for **1** and **2** with labeled ^{1}H assignments. Modified from reference (49). Reprinted (adapted) with permission from Langmuir, 2011, 27, 4371-4379. Copyright 2011 American Chemical Society.*

Figure 1-i shows the **1**-qdot ^{1}H resonances at ≈0.88 and ≈1.26 ppm, which is consistent with the alkyl backbone of the **1**-capping, namely methyl (*1a*) and methylene (*1b*) protons respectively (see Fig. 1 inset). In addition, the 1*c* and *1d* resonance are observed at ≈ 5.4 (not shown) and ≈2 ppm respectively. Upon ligand exchange and phase transfer by **2,** the **2**-qdots show four new resonances; *2a, 2b*, *2c*, and *2d* that are characteristic of the **2**-capping (Fig. 1-ii). There is a considerable decrease (>98%) in resonance intensity at ≈1.28 ppm (*1b*), indicating the exchange of practically all the initial **1**-capping. Second, we

Downloaded by NORTH CAROLINA STATE UNIV on November 27, 2012 | http://pubs.acs.org
Publication Date (Web): November 26, 2012 | doi: 10.1021/bk-2012-1112.ch003

observe resonances at ≈3.00, and ≈3.80 corresponding to the 2*b*- and 2*a*-proton positions of **2**, and resonances at ≈6.97 (2*c*) and ≈7.67 ppm (2*d*) that correspond to the protons from the imidazole ring, which show broadened and decreased resonance intensities compared to the neat compound. Interestingly, the resonance signature for **2**-qdots is very similar to that observed for the **2**-coordination to Zn^{2+} cations in solution, indicating that both the amine and the imidazole ring to be participating in qdot coordination, whose increased sterical environment and crowding lead to resonance broadening.

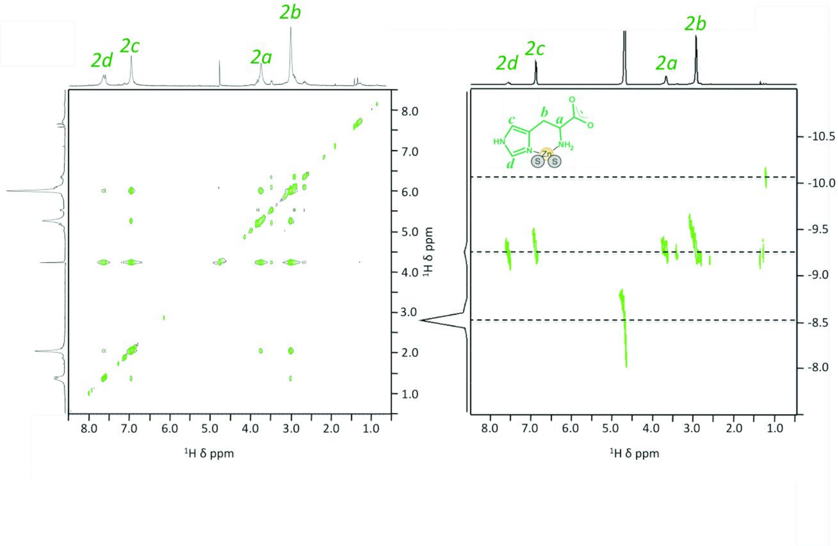

*Figure 2. The 2D NMR results for **2**-qdot after purification and redispersion in D_2O. A NOESY spectra (Left) and DOSY spectra (Right) Insets: Illustration for **2**, with labeled ^1H assignments.*

To further investigate the binding of the **2**-qdot, 2D NMR experiments were performed. Figure 2A shows the Nuclear Overhauser effect spectroscopy (NOESY) spectra for the **2**-qdots, which provides two important insights into the system, firstly that the histidine molecules are binding onto the qdot surface, which can be seen by the negative NOE cross peaks indicative of slow moving (bound) ligands. If there was no interaction the small **2** molecule would show fast motion (unbound) positive NOE crosspeaks (*131*). The second piece of information that can be gained from this spectra is that the 2*a* proton at 2.8ppm shows a NOE cross peak with the 2*c* proton at 6.97ppm, but not with the 2*d* proton at 7.67 ppm. Since the NOESY probes interactions through space this data support our hypothesis of how histidine binds to the qdot interface, namely that the distance between the 2*a* and 2*d* proton is greater then the distance between the 2*a* and 2*c* protons, (as shown by the NOE crosspeaks) consitant with the crystal structure (*127*). To further investigate this, 2D DOSY can provide information regarding whether or not the **2** is a static (high affinity) or dynamic (low affinity) interface. The diffusion ordered spectroscopy (DOSY) of the **2**-qdot is shown in Figure 2b, and reveals one main diffusion band with a diffusion constant of <*D*> = 0.54 x 10^{-9} m^2/s which strong evidence for a dynamic bond due to the similar diffusion coefficient (*127*), when compared to the 0.57 x 10^{-9} m^2/s diffusion coefficient of pure histidine in an aqueous solution (data not shown). Interestingly, some a small amount of residual organic capping ligand is still attached to the particle, with a <*D*> = 0.083 x 10^{-9}, which is consistent with the diffusion of a particle through solution (*129*).

Downloaded by NORTH CAROLINA STATE UNIV on November 27, 2012 | http://pubs.acs.org
Publication Date (Web): November 26, 2012 | doi: 10.1021/bk-2012-1112.ch003

II. Direct Biofunctionalization at Histidine-Capped Qdots

Having gained an understanding of the **2**-qdot system, we used this approach as a platform for the direct attachment of biomacromolecules to the qdot interface. As described above, the **2**-intermediate encapsulation is easily exchanged. Scheme 1 shows the general strategy employed. In this section we show the procedure followed for the functionalization of ***2***-qdots with histagged streptavidin (*Stv*). In this case, the hexahistidine at the *N*-terminus of the *Stv* binds to the Zn^{2+} terminated CdSe/ZnS qdot interface by displacing the bound ***2*** molecules. Similar binding has been shown for DHLA modified qdots (*110–114*, *134–136*). To a solution of purified ***2***-qdots, the histagged *Stv* is added at a molar ratio of [*Stv*]:[qdot] ≈ 4 in 10 mM borate buffer and let to incubate. Next, the *Stv*-qdots were incubated with *3′*-biotinylated ***A***-type (***A*** = *5′*-CAG TGT AGA GAA TTT TT-Biotin-*3′*) ssDNA at a molar ratio of [*A*]:[S*tv*] ≈ 4, and let to incubate in buffer, resulting in ***A***/*Stv*-qdots.

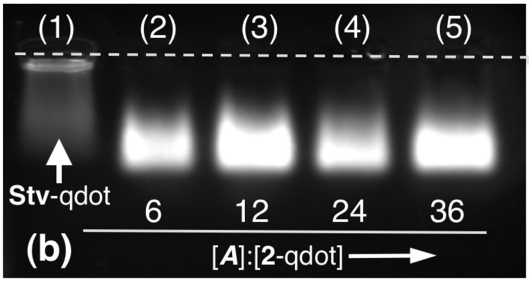

*Figure 3. Results for the Stv-qdots before (1) and after biotinylated **A**-type ssDNA functionalization to **A**/Stv-qdots (2-5) at increasing r = 6 – 36 (0.8 % agarose, 1x TBE, 25V, 60min). Modified from reference (41). Reprinted (adapted) with permission from Chem. Mater. **2011**, 23, 4975–4981. Copyright 2011 American Chemical Society.*

Figure 3 shows a representative agarose gel result for the *Stv*-qdots before and after functionalization by ***A***-type ssDNA at increasing [*A*]:[***2***-qdot] molar ratios. For instance lane 1 shows the initial minimal mobility due to similar instability and decrease in surface charge of *Stv*-qdot, and the improved mobility of the ***A***/*Stv*-qdots. Interestingly, the mobility remains similar despite increases in [*A*] (Lanes

Downloaded by NORTH CAROLINA STATE UNIV on November 27, 2012 | http://pubs.acs.org
Publication Date (Web): November 26, 2012 | doi: 10.1021/bk-2012-1112.ch003

2-5). This suggests ***A***-binding only to the accessible *Stv* recognition sites and not the qdot interface.

These gel results, as well as many other studies (not shown), are strong qualitative evidence for both histagged *Stv* absorption, and further direct ssDNA modification. We investigated this binding by taking advantage of the Förster Resonance Energy Transfer (FRET) between the DNA-qdots and complementary ssDNA modified with a fluorophore. A number of reports have used FRET to better understand biofunctionalized qdot interfaces (*110–114*, *138–141*). The qdot/dye FRET pair is analogous to classical FRET pairs, and the qdot itself has been well modeled as a single point dipole, due to the nature of the single exciton generation localized at the CdSe core (*142*). The ***A***/*Stv*-qdots prepared had a PL emission at 550 nm, and performed as FRET donors (D), whereas a complementary ssDNA of ***A′***-type modified with a fluorescent dye (ROX) with emission at 605 nm served as the FRET acceptor (A). The fluorophore ROX was chosen to sufficiently separate donor-acceptor emission spectra, while maintaining an acceptable overlap integral. The spectral properties and FRET efficiency plot is shown in Figure 4 (*41*).

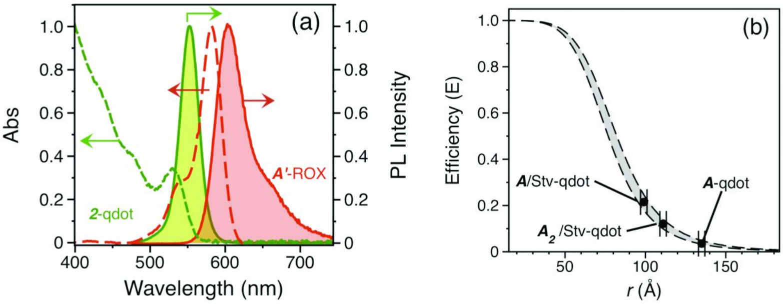

*Figure 4. (a) Normalized PL emission and absorption spectra for 550 nm emitting **2**-qdot donor and **A′**-ROX acceptor. (b) FRET efficiency curve calculated using equation 4, in ref. (41), at R_0 = 61.0 Å and n = 4, 5, and 6. Inserted experimental E results for the labeled assembly systems. Modified from reference (41). Reprinted (adapted) with permission from Chem. Mater. **2011**, 23, 4975–4981. Copyright 2011 American Chemical Society.*

Figure 5a shows a typical FRET response at $n = 0 \sim 40$. A FRET efficiency of $E \approx 21\%$ was measured. The ***A***/*Stv*-qdot was prepared at ratios in which a maximum of 5 (±1) ***A***-type ssDNA molecules were bound. As shown in the FRET efficiency plots (Fig. 4b), an *E* value of this magnitude correlates to a dipole-to-dipole distance of *r* ~10.0 (± 0.4) nm. Interestingly, this value is slightly less than the ideal estimate of ~ 12 nm, considering the size of the *Stv* macromolecule (~2 nm), the number of base pairs, as well as the ssDNA segments. We further probed the ***A***/*Stv*-qdot systems by using an analogue ssDNA sequence to ***A***-type that contained an increased number of bases (30b), $\boldsymbol{A_2}$-type ($\boldsymbol{A_2}$ = 5′-AGA CAG TGT AGA GAA (TTT)$_5$-Biotin-3′). The $\boldsymbol{A_2}$/*Stv*-qdot was prepared via the methods described above, again with a coverage of 5 (±1) ***A*₂** molecules/qdot. A typical FRET spectra is shown in Figure 5b. As one might expect from the longer ssDNA sequence, a lower $E \approx 12\%$ was calculated, which correlates with an r ~11.1 (± 0.4) nm. This value is also less than the ideal estimate of ~ 13 nm that takes into account the additional 15b poly-T spacer segments (*101–103*, *108*, *109*, *137*).

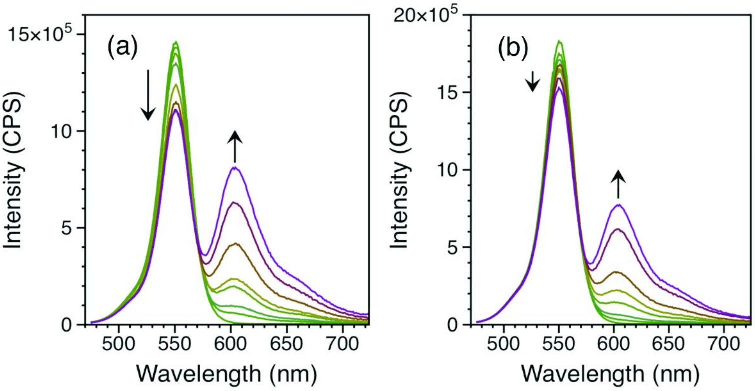

*Figure 5. Representative emission spectra during a typical FRET experiment between **A**/Stv-qdot (a), and **A₂**/Stv-qdot (b) donors with **A'**-ROX at n ≈ 2, 4, 7, 12, 21, 31, 42. (10 mM borate buffer, pH = 8.3, 50mM NaCl, [qdot] = 10.1 nM, λ_{Ex} = 400 nm). Modified from Reference (41). Reprinted (adapted) with permission from Chem. Mater.* ***2011****, 23, 4975–4981. Copyright 2011 American Chemical Society.*

The ***A***/*Stv*-qdots have higher than expected FRET efficiency, and subsequently *r*-values lower than estimates. This can be understood by considering that the initial *Stv* layer will extend the attachment point of the ssDNA by ~ 2nm. Since the number of ssDNA/qdot is maintained (as compared to a system with no *Stv* layer) (*41*), this results in sufficient free space near the qdot interface for close approach, resulting in, on average, increased FRET efficiency. Using the longer ssDNA ***A*₂**/*Stv*-qdot analogue that showed decreased efficiency substantiated this. Other factors may also play a role in the FRET efficiencies measured, such as a distribution of ZnS-shell thicknesses amongst the qdots used, as well the possibility of a distribution of ssDNA coverage across a qdot population. These factors, and further structural characterization are currently being investigated. Taken together, these results demonstrated an interesting finding in which the so-called direct attachment of ssDNA to a qdot interface by us did not necessarily result in optimum FRET. Other factors, such as surface coverage and surface accessibility are at play and also need to be engineered. Nevertheless, the histidine-mediated phase transfer method provided a suitable qdot interface for the direct functionalization with oligonucleotides and histagged proteins (*41*), opening up a new route for the integration of qdots into increasingly sophisticated self-assembly designs, one of which is described next.

Downloaded by NORTH CAROLINA STATE UNIV on November 27, 2012 | http://pubs.acs.org
Publication Date (Web): November 26, 2012 | doi: 10.1021/bk-2012-1112.ch003

Downloaded by NORTH CAROLINA STATE UNIV on November 27, 2012 | http://pubs.acs.org
Publication Date (Web): November 26, 2012 | doi: 10.1021/bk-2012-1112.ch003

III. Qdot Functionaliztion with Histagged Protiens

With the experience gained by the FRET method above, we next explored the direct attachment of a fluorescent protein tag Red Flourescent Protein (*tagRFP*) to a **2**-qdot interface. Similarly to above, the *tag*RFP was genetically expressed with a hexahistidine tag at the *N*-terminus which, as shown earlier, binds to the Zn^{2+} terminated CdSe/ZnS qdot interface by displacing the bound ***2*** molecules. A number of fluorescent proteins have been used as acceptors from qdots recently, including Yellow (*16*), mOrange (*143*), and mCherry (*144*), amongst others (*145*).

This particular FRET system consists of the **2**-qdot energy donors with PL emission at 534 nm and QY of 25.5% and *tagRFP* with emission at 584 nm serving as the FRET acceptor. The *TagRFP* was chosen to sufficiently separate donor-acceptor emission spectra, while maintaining an acceptable overlap integral. The spectral properties and FRET efficiency plot is shown in Figure 6.

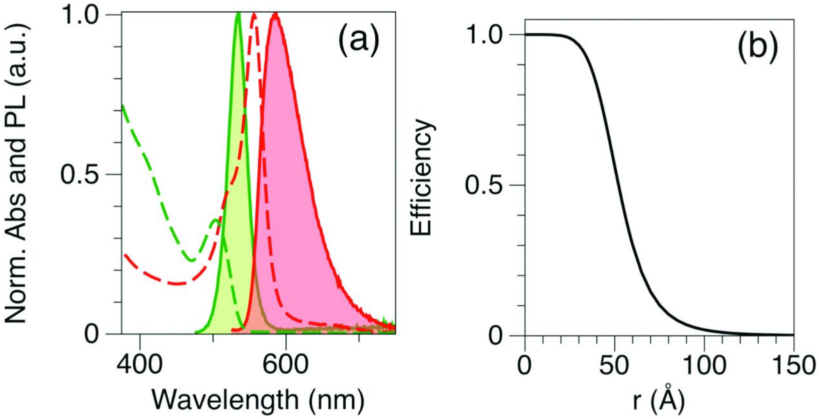

*Figure 6. Normalized PL emission and absorption spectra for 525 nm and 534 nm emitting **2**-qdot donor and tagRFP acceptor. The FRET efficiency curve was calculated with an R_0 of 52.5 Å at n = 1.*

A typical FRET profile between the **2**-qdot and *tagRFP* at acceptor/donor ratios (*n* = [*tagRFP*]/[qdot] of 0 ~ 5) is shown in Fig. 7a. The FRET efficiency (*E*) was calculated to be 72.6%. From this plot, along with the measured *E* value, and spectral overlap intergral (J_{tagRFP}= 4.26 x 10^{-13} M^{-1} cm^3) we estimate the qdot-to-RFP distance (*r*, center-to-center), of *r* ~ 4.4 nm. This estimate fits well with ideal models, since the radius of the qdot is 1.6 nm and the distance from the *N*-terminus to the active site of tagRFP is ~2.3 nm (*145*), giving a shortest acceptor to donor distage of ~3.9 nm, a value that is close to *r*. The additional distance can be attributed to *tagRFP* being expressed with an additional 15 amino acids on the *N*-terminus that consist of the hexahistidine tag and inserted thrombin cleavage site, resulting in a greater *r* value.

Downloaded by NORTH CAROLINA STATE UNIV on November 27, 2012 | http://pubs.acs.org
Publication Date (Web): November 26, 2012 | doi: 10.1021/bk-2012-1112.ch003

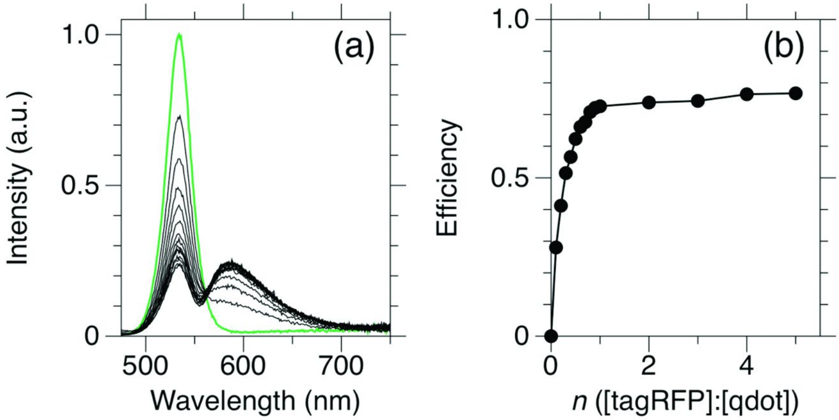

Figure 7. Representative emission spectra during a typical FRET experiment between qdot donor with tagRFP at n ≈ 0, 0.1, 0.2, 0.3, 0.4, 0.5, 0.6, 0.7, 0.8, 0.9, 1, 2, 3, 4, and 5. (10 mM borate buffer, pH = 8.3, [qdot] = 100 nM, λ_{Ex} = 400 nm).

These results further illustrate the ease at which biomaterials, such as histagged proteins, can bind to the newly developed **2**-qots. In these cases, optimum *r*-distances are possible because no long self-assembled monolayer is used, nor a thick polymer wrapping. With this in mind we began to address one resonance energy transfer system in which low efficiencies are often observed, that of bioluminescence resonance energy transfer (BRET), as described next.

IV. Qdot and Qrod Functionalization with Firefly Proteins

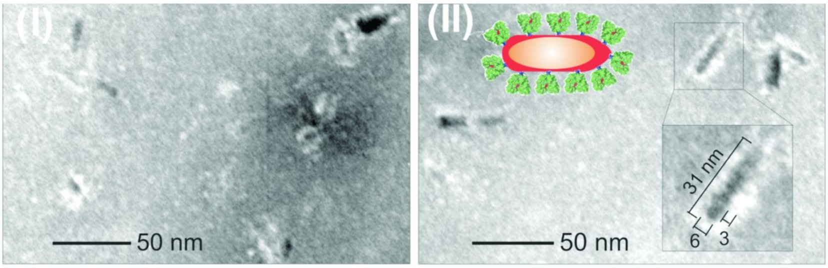

*Figure 8. A representative set of TEM micrographs (I-II) for PpyGRTS-QR(675) conjugates, in-which the PpyGRTS layer is visualized using negative staining. Figure modified from reference (50). Reprinted (adapted) with permission from Nano Lett. **2012**, 12, 3251-3256. Copyright 2011 American Chemical Society.*

Downloaded by NORTH CAROLINA STATE UNIV on November 27, 2012 | http://pubs.acs.org
Publication Date (Web): November 26, 2012 | doi: 10.1021/bk-2012-1112.ch003

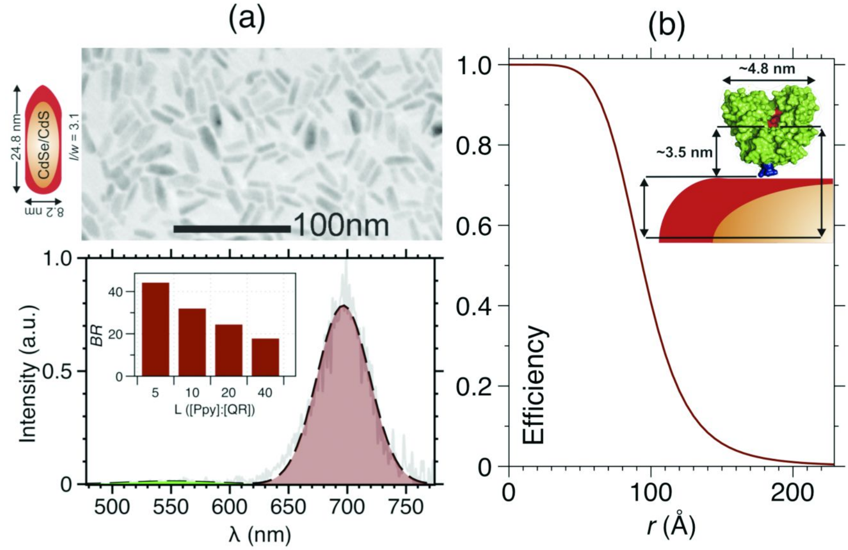

Figure 9. (a, Top Panel) TEM micrographs of CdSe/CdS QR(675) (l/w = 3.1 ± 0.5, l= 24.8 ± 3.6 nm, w= 8.2 ± 1.3 nm. (a, Botton Panel) The BRET emission profile for the respective QR(675) at L = [Ppy]:[QR] = 5. (b) Calculated BRET efficiency profile. Figure modified from reference (50). Reprinted (adapted) with permission from Nano Lett. ***2012****, 12, 3251-3256. Copyright 2011 American Chemical Society.*

The ***2***-qdot was also used as a nanosystem to facilitate the transfer of energy utilizing bioluminescence. We recently designed a qdot system for optimized bioluminescence resonance energy transfer (BRET) with firefly luciferase from *Photinus pyralis* (PPyGRTS). In particular, we chose the highly thermostable Ppy variant PpyGRTS (*146*). The PpyGRTS produced by Branchini and co-workers serves as the bioluminescence donor (λ = 546 nm) in the presence of LH_2 substrates (*146–148*). In addition to spherical qdots, we also utilized custom built semiconductive quantum rods (qrods). The native and recombinant Ppy luciferases are robust and emit yellow-green light (λ = 560 nm) at pH = 7.8 in the presence of the substrates firefly (beetle) luciferin (LH_2), Mg-ATP, and oxygen. The Ppy-LH_2 combination is one of the brightest systems in nature and has one of the highest known quantum yields for luciferases (41 ± 7.4 %) (*148*). A unique aspect to this system is that the PpyGRTS is the energy donor, whereas the qdot or qrod is the energy acceptor. We chose CdSe/CdS and CdSe/CdS/ZnS qrods as BRET acceptors due to long lifetimes (>20 ns), broad absorption, synthetic control of aspect ratio and microstructure, and increased surface area for higher acceptor/donor stoichiometry (*149*). The assembly design and main structural concerns in this biotic-abiotic BRET nanosystem is shown in Figure 8. For more information see reference (*50*). Similarly to those examples above, the PpyGRTS was directly attached to the ***2***-qrod interface by the *N*-terminus hexahistidine tag. The qrod acceptors are constructed from core/shell designs, where the inner CdSe core serves as the source for emission that is tailored by novel tuning of the QRs aspect ratios (*l/w*), which can be synthetically modified from 2 to ~7. Figure 8 shows a TEM micrograph of a typical PpyGRTS/QR sample that has been negatively stained to obserbe the PpyGRTS coating.

Figure 9 summarizes the BRET observed between the PpyGRTS donor, and CdSe/CdS qrod acceptor with λ_A = 675 nm. The TEM micrograph of the qrod reveals an aspect ratio (*l/w*) of 3.1 ± 0.5 (l = 24.8 ± 3.6 nm, w = 8.2 ± 1.3 nm). In addition, this particular qrod has a rod-in-rod morphology, which optimizes the core location in terms of FRET (or BRET). It was recently shown that CdSe rods, as well as CdSe/CdS rod-on-rod qrods posses improved energy transfer efficiencies (*150*), due in large part to a higher propability of closer *r* values, as well as the more linear like dipole moment. In our system, the BRET energy transfer efficiency, known as BRET ratio (*BR*), and this value was found to be highly susceptible to the molar loading ratio, L = [PpyGRTS]:[QR]. For example, Figure 9a shows typical BRET emission spectra at L = 5, the characteristic feature of which is the low PpyGRTS donor emission and the presence of a large emission from the qrod (QR). Unlike traditional QR photoluminescence spectra, no direct excitation is present in the system, which serves as an attractive internal control that demonstrates energy transfer from PpyGRTS. After spectral deconvolution, the *BR* of ≈ 44.2 at L = 5 was calculated based on integration of emission areas. Interestingly, a decrease in *BR* to 32.0, 24.4, and 17.8 was observed despite an increase in L = 10, 20, 40, respectively (Fig. 9a inset). These results suggest that an optimum L exists, possibly because some of the bound PpyGRTS is inactive or linked at distances too great for efficient Förster transfer (see below). These *BR* values are the highest achieved to date for a BRET nanosystem, and comparable to systems using molecular fluorophores with the highest quantum efficiency closest donor-acceptor distance (*117–121*, *147*).

A number of factors benefited this increased in energy transfer efficiency, which is unique to this system as the qrod is acting as the energy acceptor. One key is the calculation of a long Förster distance (R_0), which due to a high spectral overlap integral ($J_{QR(675)}$ = 1.19 x 10^{-11} M^{-1} cm^3), accounts a R_0 = 9.4 nm. By comparison, traditional FRET systems using molecular fluorophores have R_0 3-5 nm, and qdot systems can account for a rise in R_0 up to ~7-8. The second key factor is the fact that the PPyGRTS resides so close to the qrod interface, due to the initial ***2***-capping. For example, The LH_2 binding site at Ppy is located ~3.5 nm from the $(His)_6$ *N*-terminus of PPy (*151*), and since the radius of this particular qrod is ~4.1 nm, the shortest donor-to-acceptor distance can be approximated as r ~ 7.6 nm, well below the calculated R_0. Other factors, such as the length of the qrod, the interternal microstructure, as well as the collected average location of PPyGRTS was also considered. For these details, please see reference (*50*).

Taken together, these results show the importance of considering the surface chemistry of qdots for optimizing both biological functionalization and resonance energy transfer. By choosing a small molecule that effectively removes the initial hydrophobic monolayer of the as-synthesized qdots, and also is readily place exchanged, researchers can create a modular qdot interface that can serve as a

Downloaded by NORTH CAROLINA STATE UNIV on November 27, 2012 | http://pubs.acs.org
Publication Date (Web): November 26, 2012 | doi: 10.1021/bk-2012-1112.ch003

building block for increasingly complex surface energetics. In our ongoing work we are using these interfaces for biomimetic self-assembly of multifunctional qdot clusters that incorporate multiple energy transfer routes, that can serve as both biological sensors and fundamental platforms to study biotic-abiotic behavior.

Conclusions

In summary, we have use the small molecule histidine to induce phase transfer of qdots from as-synthesized organic solvents to aqueous buffers. The resulting histidine-capped qdots show remarkable stability, and probing of binding mechanism via 1D and 2D NMR showed that it effectively removes the organic layer, binds in a bidentate manner, while at the same showing dynamic on-off behavior. This behavior in particular was used to readily displace the histidine-capping with polyhistidine tagged proteins. In the first example, this was exploited for the DNA-functionalization of qdots, and this was substantiated via FRET analysis. In the second system, and anaologue qdot systems using qrods was used to serve as a binding site for the histagged firefly luciferase protein PPyGRTS. State of the art energy transfer (BRET) was observed for this system, owing in large part to the decreased qrod-to-PPyGRTS distances.

Acknowledgments

This work was supported by a Department of Defense PECASE award sponsored by the Air Force Office of Scientific Research (FA9550-10-1-0033). We thank Syracuse University and the Syracuse Biomaterials Institute (SBI) for generous start-up support. We thank Prof. Bruce Branchini of Connecticut College for the PPyGRTS enzymes, and Prof. James Hougland of Syracuse University for the tagRFP vector. Additional support was provided by the American Chemical Society Petroleoum Research Fund (ACS-PRF, 51303-DNI10), and photophysical work was performed by us as USERS of the Center for Functional Nanomaterials at Brookhaven National Laboratory (US-DOE DE-AC02-98CH10886).

References

1. Murray, C. B.; Norris, D. J.; Bawendi, M. G. *J. Am. Chem. Soc.* **1993**, *19*, 8706–8715.
2. Brennan, J. G.; Sigrist, T.; Carroll, P. J.; Stuczynski, S. M.; Brus, L. E.; Seigerwald, M. L. *J. Am. Chem. Soc.* **1989**, *11*, 4141–4143.
3. Alivisatos, A. P. *J. Phys. Chem.* **1996**, *100*, 13226–13239.
4. Mews, A.; Eychmüller, A.; Giersig, M.; Schooss, D.; Weller, H. *J. Phys. Chem.* **1994**, *98*, 934–941.
5. Fojtik, A.; Weller, H.; Henglein, A. *Chem. Phys. Lett.* **1985**, *120*, 552–554.
6. Schmid, G. *Nanoparticles*; Wiley-VCH: Weinheim, 2004.
7. Katz, E.; Willner, I. *Angew. Chem., Int. Ed.* **2004**, *43*, 6042–6108.
8. Bruchez, M.; Moronne, M.; Gin, P.; Weiss, S.; Alivisatos, A. P. *Science* **1998**, 2013–2016.

Downloaded by NORTH CAROLINA STATE UNIV on November 27, 2012 | http://pubs.acs.org
Publication Date (Web): November 26, 2012 | doi: 10.1021/bk-2012-1112.ch003

Downloaded by NORTH CAROLINA STATE UNIV on November 27, 2012 | http://pubs.acs.org
Publication Date (Web): November 26, 2012 | doi: 10.1021/bk-2012-1112.ch003

9. Chan, W. C. W.; Nie, S. *Science* **1998**, *281*, 2016–2018.
10. You, C. C.; De, M.; Rotello, V. M. *Curr. Opin. Chem. Biol.* **2005**, *9*, 639–646.
11. Rosi, N. L.; Mirkin, C. A. *Chem. Rev.* **2005**, *105*, 1547–1562.
12. Zhang, T.; Stilwell, J. L.; Gerion, D.; Ding, L.; Elboudwarej, O.; Cooke, P. A.; Gray, J. W.; Alivisatos, A. P.; Chen, F. F. *Nano Lett.* **2006**, *6*, 800–808.
13. Ruan, G.; Agrawal, A.; Marcus, A. I.; Nie, S. *J. Am. Chem. Soc.* **2007**, *129*, 14759–14766.
14. Medintz, I. L.; Uyeda, H. T.; Goldman, E. R.; Mattoussi, H. *Nat. Mater.* **2005**, *4*, 435–446.
15. Han, H.; Di Francesco, G.; Maye, M. M. *J. Phys. Chem. C* **2010**, *114*, 19270–19277.
16. Lu, H.; Schops, O.; Woggon, U.; Niemeyer, C. M. *J. Am. Chem. Soc.* **2008**, *130*, 4815–4827.
17. Wang, Q.; Liu, Y.; Ke, Y.; Yan, H. *Angew. Chem., Int. Ed.* **2008**, *47*, 316–319.
18. Zhang, C-Y.; Yeh, H-C.; Kuroki, M. T.; Wang, T-H. *Nat. Mater.* **2005**, *4*, 826–831.
19. Zhang, C-Y.; Johnson, L. W. *Anal. Chem.* **2009**, *81*, 3051–3055.
20. Cheng, A. K. H.; Su, H.; Wang, Y. A.; Yu, H-Z. *Anal. Chem.* **2009**, *81*, 6130–6139.
21. Ouyang, J.; Ratcliffe, C. I.; Kingston, D.; Wilkinson, B.; Kuijper, J.; Wu, X.; Ripmeester, J. A.; Yu, K. *J. Phys. Chem. C* **2008**, *112*, 4908–4919.
22. Crooker, S. A.; Hollingsworth, J. A.; Tretiak, S.; Klimov, V. I. *Phys. Rev. Lett.* **2002**, *89*, 186802.
23. Gao, J.; Chen, K.; Xie, R.; Xie, J.; Lee, S.; Cheng, Z.; Peng, X.; Chen, X. *Small* **2010**, *6*, 256–261.
24. Yang, M.; Tsang, M. W.; Wang, Y. A.; Peng, X.; Yu, H. *Langmuir* **2005**, *21*, 1858–1865.
25. Pellegrino, T.; Manna, L.; Kudera, S.; Liedl, T.; Koktysh, D.; Rogach, A. L.; Keller, S.; Radler, J.; Natile, G.; Parak, W. J. *Nano Lett.* **2004**, *4*, 703–707.
26. Yu, M.; Yang, Y.; Han, R.; Zheng, Q.; Wang, L.; Hong, Y.; Li, Z.; Sha, Y. *Langmuir* **2010**, *26*, 8534–8539.
27. Lesnyak, V.; Voitekhovich, S. V.; Gaponik, P. N.; Gaponik, N.; Eychmller, A. *ACS Nano* **2010**, *4*, 4090–4096.
28. Åkerman, M. E.; Chan, W. C. W.; Laakkonen, P.; Bhatia, S. N.; Ruoslahti, E. *Proc. Natl. Acad. Sci. U.S.A.* **2002**, *99* (20), 12617–12621.
29. Susumu, K; Uyeda, H. T; Medintz, I L.; Pons, T; Delehanty, J. B.; Mattoussi, H. *J. Am. Chem. Soc.* **2007**, *129*, 13987–13996.
30. Han, G.; Mokari, T.; Ajo-Franklin, C.; Cohen, B. E.; Helms, B. A. *J. Am. Chem. Soc.* **2008**, *130*, 15811–15813.
31. Bayles, A. R.; Chahal, H. S.; Chahal, D. S.; Goldbeck, C. P.; Cohen, B. E. *Nano Lett.* **2010**, *10*, 4086–4092.
32. Liu, W.; Howarth, M.; Greytak, A. B.; Zheng, Y.; Nocera, D. G.; Ting, A. Y.; Bawendi, M. G. *J. Am. Chem. Soc.* **2008**, *130*, 1274–1284.
33. Dubertret, B.; Skourides, P.; Norris, D. J.; Noireaux, V.; Brivanlou, A. H.; Libchaber, A. *Science* **2002**, *298*, 1759–1761.

34. Mitchell, G. P.; Mirkin, C. A.; Letsinger, R. L. *J. Am. Chem. Soc.* **1999**, *121*, 8122–8123.
35. Xu, Z.; Hine, C. R.; Maye, M. M.; Meng, Q.; Cotlet, M. *ACS Nano* **2012**, *6*, 4984–4992.
36. Zhou, D.; Piper, J. D.; Abell, C.; Klenerman, D.; Kang, D. J.; Ying, L. *Chem. Commun.* **2005**, 4807–4809.
37. Li, M.; Cushing, S. K.; Wang, Q.; Shi, X.; Hornak, L. A.; Hong, Z.; Wu, N. *J. Phys. Chem. Lett.* **2011**, *2*, 2125–2129.
38. Derfus, A. M.; Chan, W. C. W.; Bhatia, S. N. *Adv. Mater.* **2004**, *16*, 961–966.
39. Liu, W; Choi, H. S.; Zimmer, J. P.; Tanaka, E.; Frangioni, J. V.; Bawendi, M. *J. Am. Chem. Soc.* **2007**, *129*, 14530–14531.
40. Wang, Y. A.; Li, J. J.; Chen, H.; Peng, X. *J. Am. Chem. Soc.* **2002**, *124*, 2293–2298.
41. Han, H.; Zylstra, J.; Maye, M. M. *Chem. Mater.* **2011**, *23*, 4975–4981.
42. Zhou, D.; Ying, L.; Hong, X.; Hall, E. A.; Abell, C.; Klenerman, D. *Langmuir* **2008**, *24*, 1659–1664.
43. Boeneman, K.; Deschamps, J. R.; Buckhout-White, S.; Prasuhn, D. E.; Blanco-Canosa, J. B.; Dawson, P. E.; Stewart, M. H.; Susumu, K.; Goldman, E. R.; Ancona, M.; Medintz, I. L. *ACS Nano* **2010**, *4*, 7253–7266.
44. Lees, E. E.; Gunzburg, M. J.; Nguyen, T. L.; Howlett, G. J.; Rothacker, J.; Nice, E. C.; Clayton, A. H. A.; Mulvaney, P. *Nano Lett.* **2008**, *8*, 2883–2890.
45. Boeneman, K.; Prasuhn, D. E.; Blanco-Canosa, J. B.; Dawson, P. E.; Melinger, J. S.; Ancona, M.; Stewart, M. H.; Susumu, K.; Huston, A.; Medintz, I. L. *J. Am. Chem. Soc.* **2010**, *132*, 18177–18190.
46. Jin, T.; Fujii, F.; Komai, Y.; Seki, J.; Seiyama, A.; Yoshioka, Y. *Int. J. Mol. Sci.* **2008**, *9*, 2044–2061.
47. Freeman, R.; Finder, T.; Gill, R.; Willner, I. *Nano Lett.* **2010**, *10*, 2192–2196.
48. Sharon, E.; Freeman, R.; Willner, I. *Anal. Chem.* **2010**, *82*, 6130–6139.
49. Zylstra, J.; Amey, J.; Miska, N. J.; Pang, L.; Hine, C. R.; Langer, J.; Doyle, R. P.; Maye, M. M. *Langmuir* **2011**, *27*, 4371–4379.
50. Alam, R.; Fontaine, D. M.; Branchini, B. R.; Maye, M. M. *Nano Lett.* **2012**, *12*, 3251–3256.
51. Uyeda, H. T.; Medintz, I. L.; Jaiswal, J. K.; Simon, S. M.; Mattoussi, H. *J. Am. Chem. Soc.* **2005**, *127*, 3870–3878.
52. Mei, B. C.; Susumu, K.; Medintz, I. L.; Delehanty, J. B.; Mattoussi, H. *J. Mater. Chem.* **2008**, *18*, 4949–4958.
53. Susumu, K.; Mei, B. C.; Mattoussi, H. *Nat. Protoc.* **2009**, *4*, 424–436.
54. Wu, H.; Zhu, H.; Zhuang, J.; Yang, S.; Liu, C.; Cao, Y. C. *Angew. Chem., Int. Ed.* **2008**, *47*, 3730–3734.
55. Muro, E.; Pons, T.; Lequeux, N.; Fragola, A.; Sanson, N.; Lenkei, Z.; Dubertret, B. *J. Am. Chem. Soc.* **2010**, *132*, 4556–4557.
56. Duan, H.; Nie, S. *J. Am. Chem. Soc.* **2007**, *129*, 3333–3338.
57. Wang, M.; Felorzabihi, N.; Guerin, G.; Haley, J. C.; Scholes, G. D.; Winnik, M. A. *Macromolecules* **2007**, *40*, 6377–6384.
58. Nann, T. *Chem. Commun.* **2005**, 1735–1736.

Downloaded by NORTH CAROLINA STATE UNIV on November 27, 2012 | http://pubs.acs.org
Publication Date (Web): November 26, 2012 | doi: 10.1021/bk-2012-1112.ch003

Downloaded by NORTH CAROLINA STATE UNIV on November 27, 2012 | http://pubs.acs.org
Publication Date (Web): November 26, 2012 | doi: 10.1021/bk-2012-1112.ch003

59. Liu, W.; Greytak, A. B.; Lee, J.; Wong, C. R.; Park, J.; Marshall, L. F.; Jiang, W.; Curtin, P. N.; Ting, A. Y.; Nocera, D. G.; Fukumura, D.; Jain, R. K.; Bawendi, M. G. *J. Am. Chem. Soc.* **2010**, *132*, 472–483.
60. Allen, P. M.; Liu, W.; Chauhan, V. P.; Lee, J.; Ting, A. Y.; Fukumura, D.; Jain, R. K.; Bawendi, M. G. *J. Am. Chem. Soc.* **2010**, *132*, 470–471.
61. Wu, Y.; Chakrabortty, S.; Gropeanu, R. A.; Wilhelmi, J.; Xu, Y.; Shih, K.; Kuan, S. L.; Koynow, K.; Chan, Y.; Weil, T. *J. Am. Chem. Soc.* **2010**, *132*, 5012–5014.
62. Jana, N. R.; Erathodiyil, N.; Jiang, J.; Ying, J. Y. *Langmuir* **2010**, *26*, 6503–6507.
63. Yildiz, I.; McCaughan, B.; Cruickshank, S. F.; Callan, J. F.; Raymo, F. M. *Langmuir* **2009**, *25*, 7090–7096.
64. Yildiz, I.; Deniz, E.; McCaughan, B.; Cruickshank, S. F. *Langmuir* **2010**, *26*, 11503–11511.
65. Pinaud, F.; King, D.; Moore, H. P.; Weiss, S. *J. Am. Chem. Soc.* **2004**, *126*, 6115–6123.
66. Iyer, G.; Pinaud, F.; Tsay, J.; Weiss, S. *Small* **2007**, *3*, 793–798.
67. Clarke, S.; Pinaud, F.; Beutel, O.; You, C.; Piehler, J.; Dahan, M. *Nano Lett.* **2010**, *10*, 2147–2154.
68. Pathak, S.; Choi, S.; Arnheim, N.; Thompson, M. E. *J. Am. Chem. Soc.* **2001**, *123*, 4103–4104.
69. Wu, X.; Liu, H.; Liu, J.; Haley, K. N.; Treadway, J. A.; Larson, J. P.; Ge, N.; Peale, F.; Bruchez, M. P. *Nat. Biotechnol.* **2003**, *21*, 41–46.
70. Yu, W. W.; Chang, E.; Falkner, J. C.; Zhang, J.; Al-Somali, A. M.; Sayes, C. M.; Johns, J.; Drezek, R.; Colvin, V. L. *J. Am. Chem. Soc.* **2007**, *129*, 2871–2879.
71. Lees, E. E.; Nguyen, T. L.; Clayton, A. H. A.; Muir, B. W.; Mulvaney, P. *ACS Nano* **2009**, *3*, 1121–1128.
72. Sheng, W.; Kim, S.; Lee, J.; Kim, S. W.; Jensen, K.; Bawendi, M. G. *Langmuir* **2006**, *22*, 3782–3790.
73. Jin, T.; Fujii, F.; Yamada, E.; Nodasaka, Y.; Kinjo, M. *J. Am. Chem. Soc.* **2006**, *128*, 9288–9280.
74. Travert-Branger, N.; Dubois, F.; Carion, O.; Carrot, G.; Mahler, B.; Dubertret, B.; Doris, E.; Mioskowski, C. *Langmuir* **2008**, *24*, 3016–3019.
75. Dorokhin, D.; Tomczak, N.; Han, M.; Reinhoudt, D. N.; Velders, A. H.; Vansco, G. J. *ACS Nano* **2009**, *3*, 661–667.
76. Gerion, D.; Pinaud, F.; Williams, S. C.; Parak, W. J.; Zanchet, D.; Weiss, S.; Alivisatos, A. P. *J. Phys. Chem. B* **2001**, *105*, 8861–8871.
77. Selvan, S. T.; Patra, P. K.; Ang, C. Y.; Ying, J. Y. *Angew. Chem., Int. Ed.* **2007**, *46*, 2448–2452.
78. Chauhan, V. P.; Popovic, Z.; Chen, O.; Cui, J.; Fukumura, D.; Bawendi, M. G.; Jain, R. K. *Angew. Chem., Int. Ed.* **2011**, *50*, 11417–11420.
79. Mahtab, R.; Harden, H. H.; Murphy, C. J. *J. Am. Chem. Soc.* **2000**, *122*, 14–17.
80. Mahtab, R.; Rogers, J. P.; Murphy, C. J. *J. Am. Chem. Soc.* **1995**, *117*, 9099–9100.
81. Penn, S. G.; He, L.; Natan, M. J. *Curr. Opin. Chem. Biol.* **2003**, *7*, 609–615.

Downloaded by NORTH CAROLINA STATE UNIV on November 27, 2012 | http://pubs.acs.org
Publication Date (Web): November 26, 2012 | doi: 10.1021/bk-2012-1112.ch003

82. Alivisatos, A. P. *Nat. Biotechnol.* **2004**, *22*, 47–52.
83. Quach, A. D.; Crivat, G.; Tarr, M. A.; Rosenzweig, Z. *J. Am. Chem. Soc.* **2011**, *133*, 2028–2030.
84. Shi, L.; De Paoli, V.; Rosenzweig, N.; Rosenzweig, Z. *J. Am. Chem. Soc.* **2006**, *128*, 10378–10379.
85. Slocik, J. M.; Tam, F.; Halas, N. J.; Naik, R. R. *Nano Lett.* **2007**, *7*, 1054–1058.
86. Heinz, H.; Farmer, B. L.; Pandey, R. B.; Slocik, J. M.; Patnaik, S. S.; Pachter, R.; Naik, R. R. *J. Am. Chem. Soc.* **2009**, *131*, 9704–9714.
87. Coppage, R.; Slocik, J. M.; Briggs, B. D.; Frenkel, A. I.; Heinz, H.; Naik, R. R.; Knecht, M. R. *J. Am. Chem. Soc.* **2011**, *133*, 12346–12349.
88. Zhang, C. Y.; Johnson, L. W. *J. Am. Chem. Soc.* **2006**, *128*, 5324–5325.
89. Zhang, C. Y.; Johnson, L. W. *Anal. Chem.* **2006**, *78*, 5532–5537.
90. Zhang, Z. L.; Horsch, M. A.; Lamm, M. H.; Glotzer, S. C. *Nano Lett.* **2003**, *3*, 1341–1346.
91. Daniel, M. C.; Astruc, D. *Chem. Rev.* **2004**, *104*, 293–346.
92. Oh, E.; Hong, M. Y.; Lee, D.; Nam, S. H.; Yoon, H. C.; Kim, H. S. *J. Am. Chem. Soc.* **2005**, *127*, 3270–3271.
93. Cobbe, S.; Connolly, S.; Ryan, D.; Nagle, L.; Eritja, R.; Fitzmaurice, D. *J. Phys. Chem. B* **2003**, *107*, 470–477.
94. Maye, M. M.; Freimuth, P.; Gang, O. *Small* **2008**, *4*, 1941–1944.
95. Mirkin, C. A.; Letsinger, R. L.; Mucic, R. C.; Storhoff, J. J. *Nature* **1996**, *382*, 607–609.
96. Alivisatos, A. P.; Johnsson, K. P.; Peng, X.; Wilson, T. E.; Loweth, C. J.; Bruchez, M. P., Jr.; Schultz, P. G. *Nature* **1996**, *382*, 609–611.
97. Claridge, S. A.; Liang, H. W.; Basu, S. R.; Frechet, J. M.; Alivisatos, A. P. *Nano Lett.* **2008**, *8*, 1202–1206.
98. Lytton-Jean, A. K.; Mirkin, C. A. *J. Am. Chem. Soc.* **2005**, *127*, 12754–12755.
99. Demers, L. M.; Mirkin, C. A.; Mucic, R. C.; Reynolds, R. A.; Letsinger, R. L.; Elghanian, R.; Viswanadham, G. *Anal. Chem.* **2000**, *72*, 5535–5541.
100. Hurst, S. J.; Lytton-Jean, A. K.; Mirkin, C. A. *Anal. Chem.* **2006**, *78*, 8313–8318.
101. Hill, H. D.; Macfarlane, R. J.; Senesi, A. J.; Lee, B.; Park, S. Y.; Mirkin, C. A. *Nano Lett.* **2008**, *8*, 2341–2344.
102. Maye, M. M.; Nykypanchuk, D.; van der Lelie, D.; Gang, O. *J. Am. Chem. Soc.* **2006**, *128*, 14020–14021.
103. Maye, M. M.; Nykypanchuk, D.; van der Lelie, D.; Gang, O. *Small* **2007**, *3*, 1678–1682.
104. Prigodich, A. E.; Lee, O. S.; Daniel, W. L.; Seferos, D. S.; Schatz, G. C.; Mirkin, C. A. *J. Am. Chem. Soc.* **2010**, *132*, 10638–10641.
105. Jin, R.; Wu, G.; Li, Z.; Mirkin, C. A.; Schatz, G. C. *J. Am. Chem. Soc.* **2003**, *125*, 1643–1654.
106. Nykypanchuk, D.; Maye, M. M.; van der Lelie, D.; Gang, O. *Nature* **2008**, *451*, 549–552.
107. Park, S. Y.; Lytton-Jean, A. K.; Lee, B.; Weigand, S.; Schatz, G. C.; Mirkin, C. A. *Nature* **2008**, *451*, 553–556.

In Functional Nanoparticles for Bioanalysis, Nanomedicine, and Bioelectronic Devices Volume 1; Hepel, M., et al.;
ACS Symposium Series; American Chemical Society: Washington, DC, 2012.

108. Maye, M. M.; Kumara, M. T.; Nykypanchuk, D.; Sherman, W. B.; Gang, O. *Nat. Nanotechnol.* **2010**, *5*, 116–120.
109. Maye, M. M.; Nykypanchuk, D.; Cuisinier, M.; van der Lelie, D.; Gang, O. *Nat. Mater.* **2009**, *8*, 388–391.
110. Pons, T.; Medintz, I. L.; Sapsford, K. E.; Higashiya, S.; Grimes, A. F.; English, D. S.; Mattoussi, H. *Nano Lett.* **2007**, *7*, 3157–3164.
111. Algar, W. R.; Krull, U. J. *Langmuir* **2008**, *24*, 5514–5520.
112. Gill, R.; Willner, I.; Shweky, I.; Banin, U. *J. Phys. Chem. B* **2005**, *109*, 23715–23719.
113. Zhang, B.; Zhang, Y.; Mallapragada, S. K.; Clapp, A. R. *ACS Nano* **2011**, *5*, 129–138.
114. Robelek, R.; Niu, L.; Schmid, E. L.; Knoll, W. *Anal. Chem.* **2004**, *76*, 6160–6165.
115. Dhar, S.; Daniel, W. L.; Giljohann, D. A.; Mirkin, C. A.; Lippard, S. J. *J. Am. Chem. Soc.* **2009**, *131*, 14652–14653.
116. Sharon, E.; Freeman, R.; Willner, I. *Anal. Chem.* **2010**, *82*, 7073–7077.
117. So, M. K.; Xu, C.; Loening, A. M.; Gambhir, S. S.; Rao, J. *Nat. Biotechnol.* **2006**, *24*, 339–343.
118. So, M. K.; Loening, A. M.; Gambhir, S. S.; Rao, J. *Nat. Protoc.* **2006**, *1*, 1160–1164.
119. Zhang, Y.; So, M. K.; Loening, A. M.; Yao, H.; Gambhir, S. S.; Rao, J. *Angew. Chem.* **2006**, *45*, 4936–4940.
120. Xing, Y.; So, M. K.; Koh, A. L.; Sinclair, R.; Rao, J. *Biochem. Biophys. Res. Commun.* **2008**, *372*, 388–394.
121. Kim, Y. P.; Daniel, W. L.; Xia, Z.; Xie, H.; Mirkin, C. A.; Rao, J. *Chem. Commun.* **2010**, *46*, 76–78.
122. Qu, L.; Peng, X. *J. Am. Chem. Soc.* **2002**, *124*, 2049–2055.
123. Talapin, D.; Mekis, I.; Gotzinger, S.; Kornowski, A.; Benson, O.; Weller, H. *J. Phys. Chem. B* **2004**, *108*, 18826–18831.
124. Li, J.; Wang, Y.; Goy, W.; Keay, J.; Mishima, T.; Johnson, M.; Peng, X. *J. Am. Chem. Soc.* **2003**, *125*, 1257.
125. Dennis, A. M.; Bao, G. *Nano Lett.* **2008**, *8*, 1439–1445.
126. Loddenkötter, B.; Kammerer, B.; Fisher, K.; Flügge, U. *Proc. Natl. Acad. Sci. U.S.A.* **1993**, *90*, 2155–2159.
127. Kretsinger, H.; Cotton, F. A.; Bryan, R. F. *Acta Crystallogr.* **1963**, *16*, 651.
128. Sapsford, K. E.; Pons, T.; Medintz, I. L.; Higashiya, S.; Brunel, F. M.; Dawson, P. E.; Mattoussi, H. *J. Phys. Chem. C* **2007**, *111*, 11528–11538.
129. Hens, Z.; Moreels, I.; Martins, J. C. *ChemPhysChem* **2005**, *6*, 2578–2584.
130. Moreels, I.; Martins, J. C.; Hens, Z. *ChemPhysChem* **2006**, *7*, 1028.
131. Fritzinger, B.; Moreels, I.; Lommens, P.; Koole, R.; Hens, Z.; Marins, J. C. *J. Am. Chem. Soc.* **2009**, *131*, 3024–3032.
132. Terrill, R. H.; Postlethwaite, T. A.; Chen, C-H.; Poon, C-D.; Terzis, A.; Chen, A.; Hutchinson, J. E.; Clark, M. R.; Wignall, G.; Londono, J. D.; Superfine, R.; Falvo, M.; Johnson, C. S.; Samulski, E. T.; Murray, R. W. *J. Am. Chem. Soc.* **1995**, *117*, 12537–12548.
133. Owen, J. S.; Park, J.; Trudeau, P. E.; Alivisatos, A. P. *J. Am. Chem. Soc.* **2008**, *130*, 12279–12281.

Downloaded by NORTH CAROLINA STATE UNIV on November 27, 2012 | http://pubs.acs.org
Publication Date (Web): November 26, 2012 | doi: 10.1021/bk-2012-1112.ch003

134. Clapp, A. R.; Medintz, I. L.; Mattoussi, H. *Phys. Chem. Chem. Phys.* **2006**, *7*, 47–57.
135. Delehanty, J. B.; Mattoussi, H.; Medintz, I. L. *Anal. Bional. Chem.* **2009**, *393*, 1091–1105.
136. Medintz, I. L.; Mattoussi, H. *Phys. Chem. Chem. Phys.* **2009**, *11*, 17–45.
137. Brenner, H. *Int. J. Multiphase Flow* **1974**, *1*, 195–341.
138. Gueroui, Z.; Libchaber, A. *Phys. Rev. Lett.* **2004**, *93*, 166108–166111.
139. Singh, M. P.; Strouse, G. F. *J. Am. Chem. Soc.* **2010**, *132*, 9383–9391.
140. Jennings, T. L.; Singh, M. P.; Strouse, G. F. *J. Am. Chem. Soc.* **2006**, *128*, 5462–5467.
141. Yun, C. S.; Javier, A.; Jennings, T.; Fisher, M.; Hira, S.; Peterson, S.; Hopkins, B.; Reich, N. O.; Strouse, G. F. *J. Am. Chem. Soc.* **2005**, *127*, 3115–3119.
142. Medintz, I. L.; Mattoussi, H. *Phys. Chem. Chem. Phys.* **2009**, *11*, 17–45.
143. Dennis, A. M.; Rhee, W. J.; Sotto, D.; Dublin, S. N.; Boa, G. *ACS Nano* **2012**, *6*, 2917–2924.
144. Boeneman, K.; Mei, B. C.; Dennis, A. M.; Bao, G.; Deschamps, J. R.; Mattoussi, H.; Medintz, I. L. *J. Am. Chem. Soc.* **2009**, *131*, 3828–3829.
145. Subach, O. M.; Malashkevich, V. N.; Zencheck, W. D.; Morozova, K. S.; Piatkevich, K. D.; Almo, S. C.; Verkhusha, V. V. *Chem.Biol.* **2010**, *17*, 333.
146. Branchini, B. R.; Ablamsky, D. M.; Murtiashaw, M. H.; Uzasci, L.; Fraga, H.; Southworth, T. L. *Anal. Biochem.* **2007**, *3261*, 253–262.
147. Branchini, B. R.; Ablamsky, D. M.; Rosenberg, J. C. *Bioconjugate Chem.* **2010**, *21*, 2023–2030.
148. Ando, Y.; Niwa, K.; Yamada, N.; Enomot, T.; Irie, T.; Kubota, H.; Ohmiya, Y.; Akiyama, H. *Nat. Photonics* **2008**, *2*, 44.
149. Talapin, D. V.; Nelson, J. H.; Shevchenko, E. V.; Aloni, S.; Sadtler, B.; Alivisatos, A. P. *Nano Lett.* **2007**, *7*, 2951–2959.
150. Halivni, S.; Sitt, A.; Hadar, I.; Banin, U. *ACS Nano* **2012**, *6*, 2758–2765.
151. Conti, E.; Franks, N. P.; Brick, P. *Structure* **1996**, *4*, 287–298.

Downloaded by NORTH CAROLINA STATE UNIV on November 27, 2012 | http://pubs.acs.org
Publication Date (Web): November 26, 2012 | doi: 10.1021/bk-2012-1112.ch003

In Functional Nanoparticles for Bioanalysis, Nanomedicine, and Bioelectronic Devices Volume 1; Hepel, M., et al.;
ACS Symposium Series; American Chemical Society: Washington, DC, 2012.

Downloaded by UNIV DE SHERBROOKE on November 27, 2012 | http://pubs.acs.org
Publication Date (Web): November 26, 2012 | doi: 10.1021/bk-2012-1112.ch004

Chapter 4

Bioanalysis and Bioimaging with Fluorescent Conjugated Polymers and Conjugated Polymer Nanoparticles

Hui Xu,[†,‡] Lihua Wang,[§] and Chunhai Fan[*,§]

[†]School of Chemistry and Material Sciences, Ludong University,
Yantai 264025, China
[‡]Key Laboratory of Ecochemical Engineering, Ministry of Education,
College of Chemistry and Molecular Engineering, Qingdao University of
Science and Technology, Qingdao 266042, China
[§]Laboratory of Physical Biology, Shanghai Institute of Applied Physics,
Chinese Academy of Sciences, Shanghai 201800, China
[*]E-mail: fchh@sinap.ac.cn

Fluorescent conjugated polymers (CPs) and conjugated polymer nanoparticles (CPNs) have attracted great attention due to their wide applications in bioanalysis and bioimaging. CPs have been applied to detect DNA, protein, and other biological molecules with high sensitivity over the past decades. More recently, fluorescence imaging based on CPNs at the cellular level has been actively explored. Here, we summarize recent examples of applications of CPs and CPNs in biosensor and bioimaging.

Introduction

Conjugated polymers (CPs) are characterized by a backbone with a delocalized electronic structure, which have light-harvesting and molecular wires properties and allow electron or energy to move along conjugated backbones to amplify fluorescence sensing signals (*1*). Swager and coworker first designed a series of organic-phase chemosensors based on the superquenching principle, suggesting that the binding of a quencher to any site of the chain may efficiently block the electron or energy transfer in the polymer backbone (*2*). To meet the requirements of detecting biomolecules, water-soluble CPs were designed

In Functional Nanoparticles for Bioanalysis, Nanomedicine, and Bioelectronic Devices Volume 1; Hepel, M., et al.;
ACS Symposium Series; American Chemical Society: Washington, DC, 2012.

and synthesized through covalent binding of charged functionalities on the side chain. Of the various primary conjugated polymer backbones, poly(thiophene) (PT), poly(p-phenylenevinylene) (PPV), poly(p-phenyleneethynylene) (PPE) and poly(fluorene) (PF), have been widely used in fluorescent biological sensing platform. Scheme1 illustrates the chemical structure of some water-soluble CPs used in the references. Two main sensing mechanisms, the fluorescence resonance energy transfer (FRET) or electron transfer (ET) and the aggregation and conformational effects of CPs, are introduced to describe the principles of CPs-based biosensors. Sensitive detection of biomolecules (DNA, protein and biological-revelant molecules) has been designed and successfully accomplished due to different interaction of CPs with various kinds of biomolecular structures. Given that there have been several excellent reviews on optical detection of biomolecules with water-soluble CPs (*3–9*), and the optical principle including FRET, ET, and conformation-color effect have been described in detail. Here, we mainly focus on the application in the area of bioanalysis and bioimaging with fluorescent CPs and CPNs.

Downloaded by UNIV DE SHERBROOKE on November 27, 2012 | http://pubs.acs.org
Publication Date (Web): November 26, 2012 | doi: 10.1021/bk-2012-1112.ch004

Design of DNA Biosensor Based on Electron/Energy Transfer

FRET is a long-range excitation energy transfer from a donor chromophore to an acceptor chromophore through nonradiative dipole-dipole coupling. The energy transfer can occur efficiently from water-soluble CP to dye once they meet the requirement of FRET, which is the short separation distance between them (in proximity, typically less than 10 nm), the favorable dipole orientation and the efficient spectral overlap between the fluorescence spectrum of the water-soluble CP and the absorption spectrum of the dye. The high extinction coefficients and highly delocalized backbone make CPs excellent energy donor in FRET-based assays to amplify the acceptor signal. The Bazan and Heeger group firstly developed DNA biosensor using water-soluble cationic CPs and fluorescein labeled peptide nucleic acid (PNA) via FRET (*10*), in which the specific PNA-DNA recognition was introduced to design DNA sensors. The DNA probe was then widely used to detect DNA, protein, and other biomolecules through DNA hybridization and aptamer-target pair. In addition, other specific recognition pairs, including antigen-antibody, enzyme-substrate, and biotin-avidin etc have been used to fabricate biosensors with CPs. Here, we describe various kinds of biosensors based on different interaction of CPs with various kinds of probes.

FRET Principle-Based DNA Sensors with PNA or DNA Probe

As is known, DNA is the genetic material of almost all living organisms, and the genetic mutation, including deletion, insertion, transition, transversion and alteration etc, often lead to aging and disease. Thus, the detection of DNA attracted much interest, and various kinds of detection methods have been developed. In addition, DNA is a kind of polyelectrolyte that consists of negatively charged phosphate backbone and positively charged bases. Thus, the attraction or repulsion between charged CPs and DNA structures through electrostatic interaction contributes to the design of DNA sensors. Up to now, most biosensors were designed according to the FRET from CPs to dye-tagged DNA probes. Here, we summarized the DNA-based sensors according to the bio-recognition pairs, including PNA-DNA recognition, DNA-DNA hybridization, aptamer-target specific recognition pairs, and other biomolecule consisted designs etc.

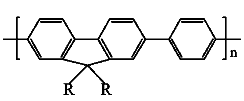

1 $R=(CH_2)_6N^+Me_3I^-$

2 $R=(CH_2)_6N^+Me_3Br^-$

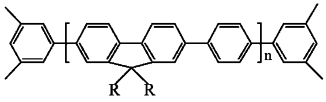

$R=(CH_2)_3N^+Me_3I^-$

3

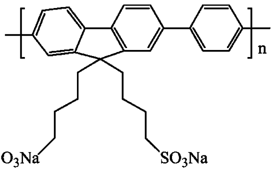
n
SO3Na
SO3Na

4

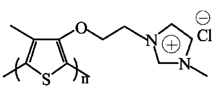

5

PMNT

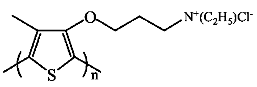
O
N+(C2H5)Cl-
S
n

6

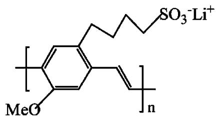

7

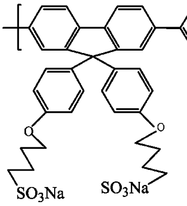
n
O
O
SO3Na
SO3Na

PFP-SO$_3^-$

8

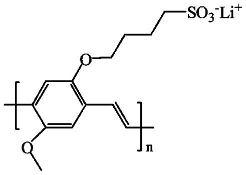

9

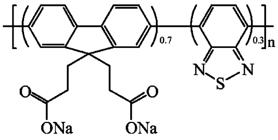
0.7
0.3
n
N
S
N
O
O
ONa
ONa

10

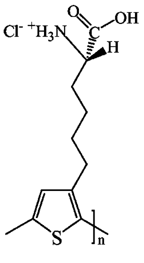
Cl- +H3N
O
C
OH
H
S
n

11

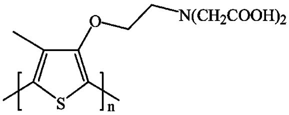
O
N(CH2COOH)2
S
n

12

Downloaded by UNIV DE SHERBROOKE on November 27, 2012 | http://pubs.acs.org
Publication Date (Web): November 26, 2012 | doi: 10.1021/bk-2012-1112.ch004

Downloaded by UNIV DE SHERBROOKE on November 27, 2012 | http://pubs.acs.org
Publication Date (Web): November 26, 2012 | doi: 10.1021/bk-2012-1112.ch004

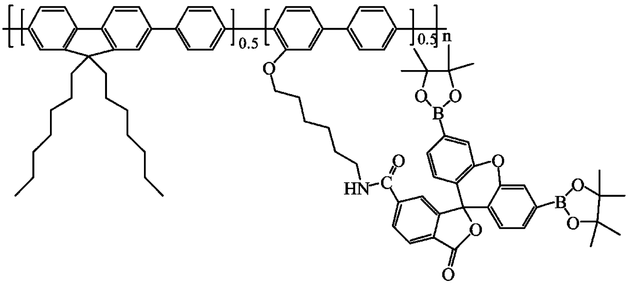

13

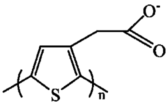

14

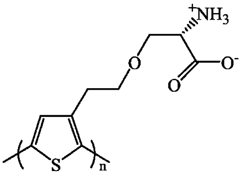

15

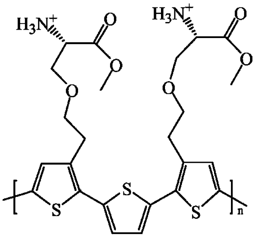

16

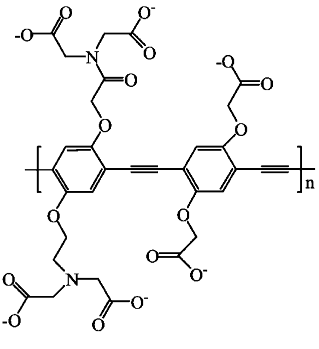

17

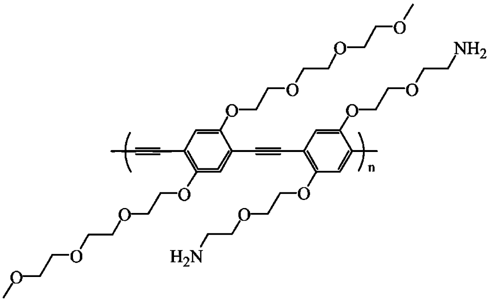

18

Downloaded by UNIV DE SHERBROOKE on November 27, 2012 | http://pubs.acs.org
Publication Date (Web): November 26, 2012 | doi: 10.1021/bk-2012-1112.ch004

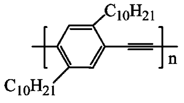
C10H21
C10H21
n

PPE

19

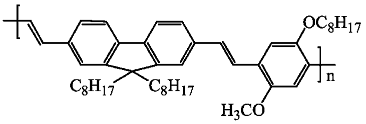
OC8H17
C8H17
C8H17
H3CO
n

PFPV

20

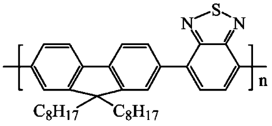
S
N
N
C8H17
C8H17
n

PFBT

21

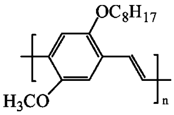
OC8H17
H3CO
n

MEHPPV

22

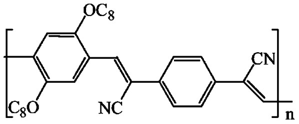
OC8
C8O
NC
CN
n

NIR-cvPD

23

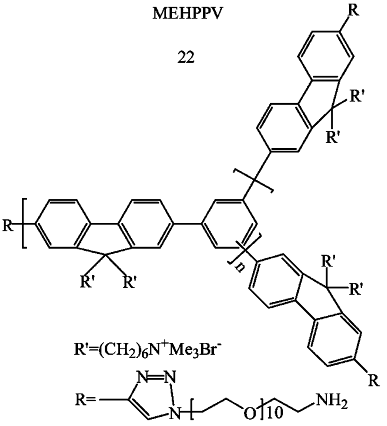
R
R'
R'
R
R'
R'
R'
R'
R
n
R'=(CH2)6N+Me3Br-
R=
N=N
N
O
10
NH2

24

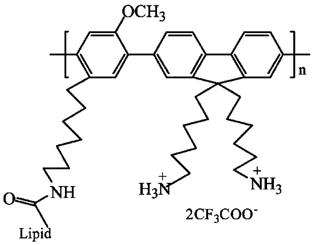
OCH3
n
O
NH
Lipid
H3N+
+NH3
2CF3COO-

25

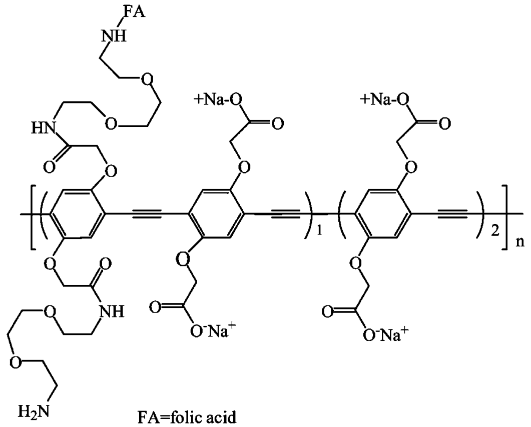
FA
NH
O
O
HN
O
O
+Na-O
O
O
+Na-O
O
O
1
2
n
O
O
NH
O
O
O-Na+
O
O
O-Na+
O
H2N

FA=folic acid

26

Downloaded by UNIV DE SHERBROOKE on November 27, 2012 | http://pubs.acs.org
Publication Date (Web): November 26, 2012 | doi: 10.1021/bk-2012-1112.ch004

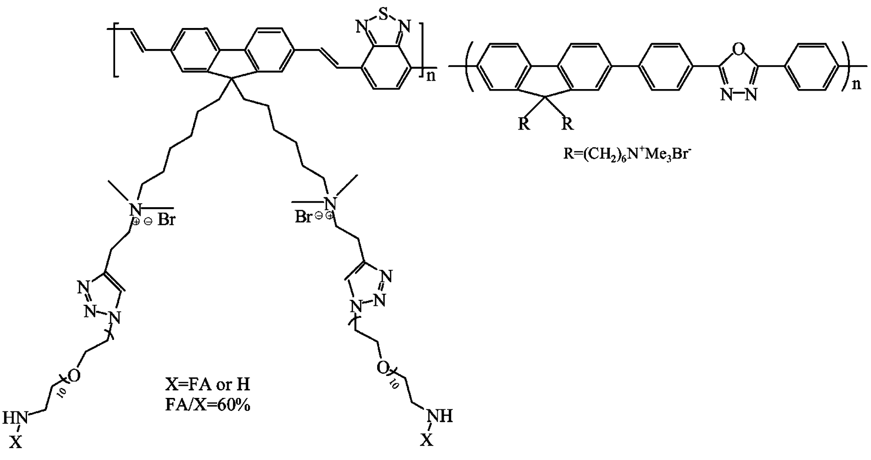

27

28

Scheme 1. Chemical structure of some water-soluble CPs, 1−28

For CPs-based sensors, PNA was first used for DNA detection due to the weak interaction of CPs with the neutral PNA molecule and the specific PNA-DNA recognition. The neutral PNA probe cannot bind charged CPs and lead to large donor-acceptor distance, which result in low FRET efficiency from CPs to dye-tagged PNA probe, while the charged PNA-DNA duplex can bind with CPs and lead to high FRET. As shown in Fig. 1, a PNA strand labeled with a chromophore (PNA-C*) was used as the probe and the optical properties of the cationic CP (CP 1, Scheme 1) and C* are chosen to favor FRET from CP (donor) to C* (acceptor). There is no FRET between positively charged CPs and neutral PNA-C* due to large CP-C* distance. Upon the addition of a target DNA that is complementary to the PNA probe, hybridization endows the C*-bearing macromolecule with multiple negative charges and electrostatic interaction brings the CPs close to the PNA-C*/single-stranded DNA (ssDNA) duplex, allowing for FRET from the polymer to fluorescein (Fig. 1). However, when non-complementary ssDNA is added, the PNA-C* is unable to form a duplex with negatively charged DNA and electrostatic complexation occurs only between CPs and DNA. The efficient FRET can not occur due to the large distance between CPs and fluorescein (Fig. 1). The resulting emission intensity of fluorescein by excitation of CPs is enhanced by more than 25 times higher than that obtained by exciting the dye, which can detect target DNA at concentrations of 10 pM. Moreover, they investigated the energy transfer processes in DNA sequence detection by using cationic CPs and PNA probes with ultrafast pump-dump-emission spectroscopy (*11*) and modify the strategy to detect single base mismatch by using S1 nuclease enzyme, fluorescein-labeled PNA and CP 2 (*12*). Additionally, Al Attar developed an improved single nucleotide polymorphism (SNP) detection using CP/surfactant system and PNA probes (*13*).

Multi-color detection is often required in order to detect a number of gene sequences simultaneously. In 2004, Bazan's group reported that multi-color detection can be realized via doping CPs backbones by using a chromophore labeled PNA strand (*14*).

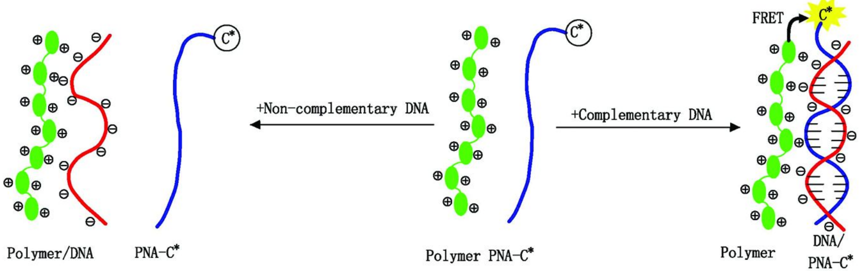

Figure 1. Schematic representation for complementary ssDNA detection using a water-soluble CP and a specific PNA-C optical reporter probe. Ref (4).*

A label-free method for DNA detection with PNA probes was developed by Liu's group, in which a DNA intercalator (thiazole orange, TO) was employed to accept the fluorescence from CPs (*15*) (Fig. 2). In comparison with labeled probe, this method is simple, cost-effective, and shows high performance. In combination with selective enzyme digestion of DNA sequences, Liu et al proposed a TO-based sequence specific assay through discrimination of PNA/DNA duplex and PNA/DNA triplex by employing TO intercalation and CPs' signal amplification. This method can discriminate perfectly complementary DNA (pcDNA) from a one-base mismatched sequence. As shown in Fig 2, the pcDNA sequence is sufficiently protected by the PNA probe, which ensures the intercalation of TO and addition of PFP (CP 2, Scheme 1) leads to enhanced TO emission due to FRET from the CP 2 to TO. Mismatched DNA can be efficiently digested by S1 nuclease to small fragments and addition of CCP does not induce any polymer fluorescence change. The assay shows a detection limit of 0.25 μM using a standard fluorometer (*15*).

PNA-DNA complexes form more quickly and are tighter and more specific than analogous DNA-DNA complexes, however, PNA is more expensive than DNA for practical use and DNA/DNA interactions are much more common in biology. Therefore, the dye-tagged DNA probe is required to fabricate sensor. The efficient FRET can occur from water-soluble CPs to dye tagged DNA because positively charged water-soluble CPs can interact with negatively charged DNA mainly through electrostatic attractions, leading to closer donor-acceptor distance. Moreover, the electrostatic interaction between a double-stranded DNA (dsDNA) and a cationic CP would be stronger than that of a ssDNA and the CP.

The difference of electrostatic interaction of CP-ssDNA complex and CP-dsDNA complex leads to different distance between CP and chromophore and following different FRET efficiency. Bazan's group developed a DNA hybridization detection using a traditional chromophore-labeled DNA as the optical probe (*16*). The authors observed a three-fold increase in fluorescence

Downloaded by UNIV DE SHERBROOKE on November 27, 2012 | http://pubs.acs.org
Publication Date (Web): November 26, 2012 | doi: 10.1021/bk-2012-1112.ch004

intensity from fluorescein when adding target complementary ssDNA relative to that of a noncomplementary strand although the fluorescein-labeled ssDNA probe have some electrostatic attractions to CP 1 (Scheme 1). When the ratio of polymer chains to DNA strands is approximately 1:1, the maximum energy transfer from CP 1 to the fluorescein can be observed. In 2008, Wang's group developed a selective and homogeneous fluorescent DNA detection by target-induced strand displacement using cationic conjugated polyelectrolytes (CPEs), which can detect single-nucleotide mismatches (*17*).

Downloaded by UNIV DE SHERBROOKE on November 27, 2012 | http://pubs.acs.org
Publication Date (Web): November 26, 2012 | doi: 10.1021/bk-2012-1112.ch004

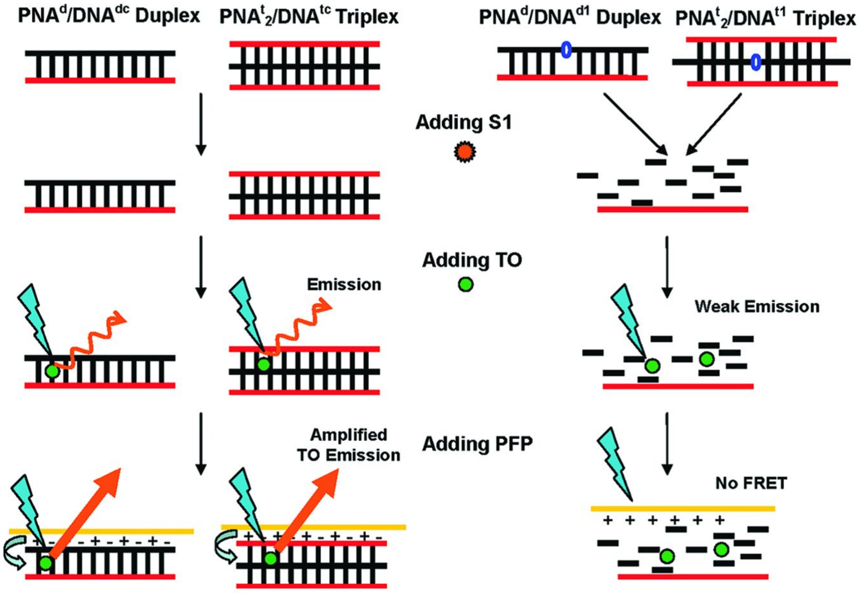
PNA^{d}/DNA^{dc} Duplex
PNA$^{t}_{2}$/DNA^{tc} Triplex
PNA^{d}/DNA^{d1} Duplex
PNA$^{t}_{2}$/DNA^{t1} Triplex
Adding S1
Adding TO
Emission
Weak Emission
Amplified TO Emission
Adding PFP
No FRET
+ + + + + +

Figure 2. Strategy for DNA detection using label free PNA, S1 nuclease, and PFP by excitation polymer amplified TO emission. Reprinted with permission from ref (9). Copyright (2009) American Chemical Society.

A label-free DNA detection method with DNA probes and DNA intercalator was developed, which was low cost and exhibited high performance due to the specific intercalation into dsDNA but not ssDNA. In 2009, Xu's group developed a label-free DNA sequence detection with enhanced sensitivity and selectivity using cationic CPs (CP 3, Scheme 1) and DNA intercalating dyes Picogreen (*18*). The absorption spectrum of PicoGreen has good overlap with the emission spectrum of PFP, ensuring efficient energy transfer from PFP to PicoGreen (Fig. 3). Recently, Wang's group developed a new strategy for nuclease assay based on FRET from the CP to the intercalating dye genefinder mediated by DNA (*19*).

Downloaded by UNIV DE SHERBROOKE on November 27, 2012 | http://pubs.acs.org
Publication Date (Web): November 26, 2012 | doi: 10.1021/bk-2012-1112.ch004

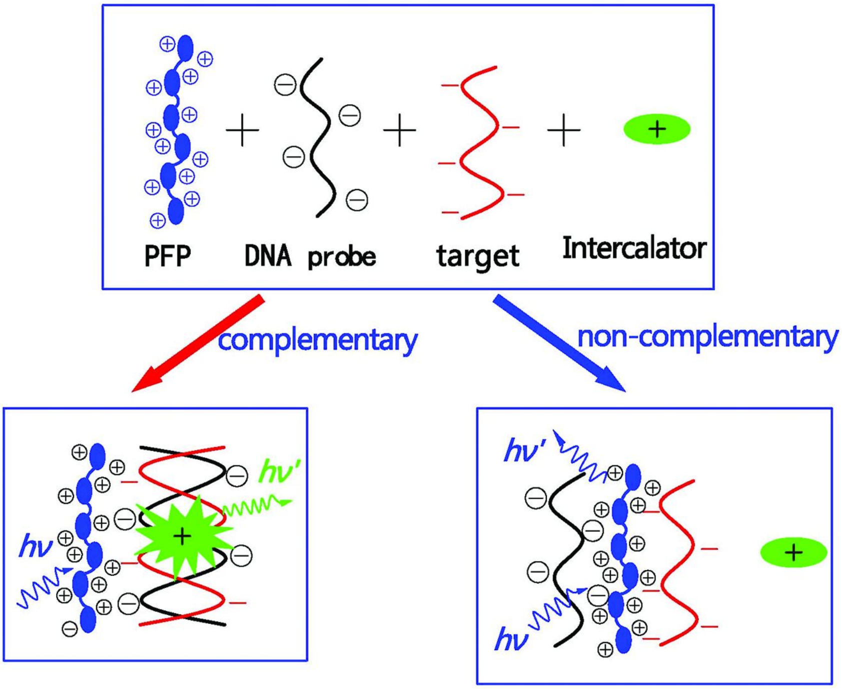
PFP
DNA probe
target
Intercalator
complementary
non-complementary
hν
hν'
hν'
hν

Figure 3. Schematic representation of a label-free DNA sensor using a combination of cationic CPs and DNA intercalators. Ref (12).

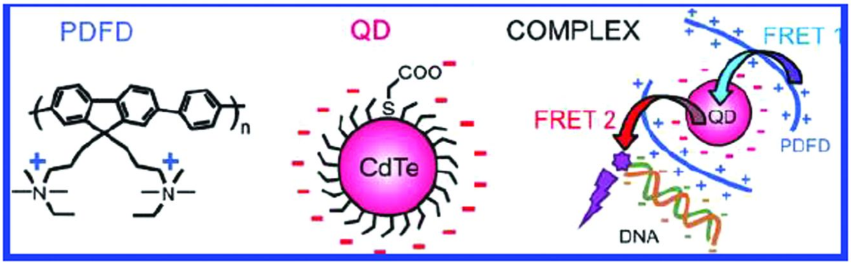
PDFD
QD
COMPLEX
COO
S
CdTe
n
N
N
FRET 1
FRET 2
QD
PDFD
DNA

Figure 4. Illustration of a cascade double FRET for DNA hybridization detection using PDFD/QD/dye-labeled complex. Reprinted with permission from ref (14). Copyright (2009) American Chemical Society.

In addition to organic dye as acceptor in FRET, other materials (e.g. QDs) can be used as acceptor. Jiang et al developed a DNA hybridization detection method based on cascaded FRET in CP/quantum dot/dye-labeled DNA complexes (*20*). A blue-emitting CP with positively charged side chains electrostatically self-assembles on the negatively charged surface of red-emitting CdTe QDs. The so-formed hybrid complex has a net positive charge and thus attracts negatively charged dye-labeled DNA molecules, which leads to a cascade double FRET from PDFD to QDs and FRET 2 from QDs to the dye on the DNA for DNA hybridization detection (Fig. 4).

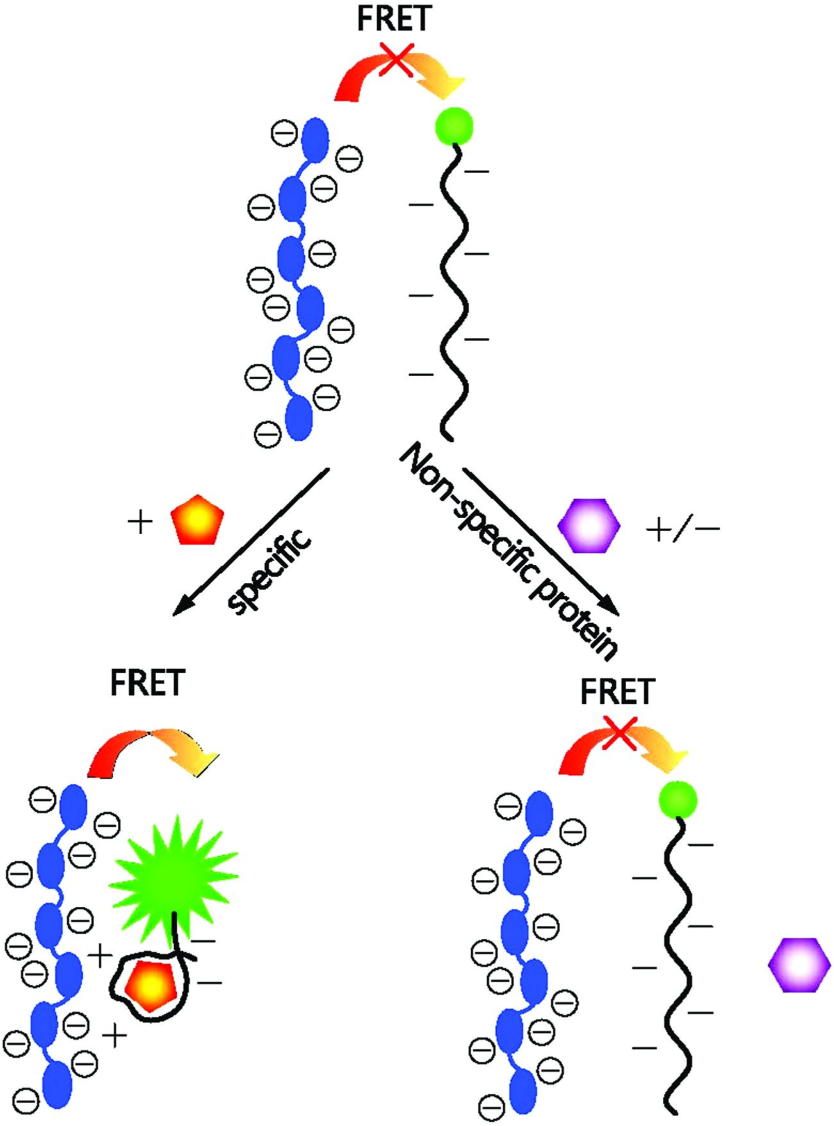

Figure 5. The detection mechanism of lysozyme. Ref (15).

Downloaded by UNIV DE SHERBROOKE on November 27, 2012 | http://pubs.acs.org
Publication Date (Web): November 26, 2012 | doi: 10.1021/bk-2012-1112.ch004

In addition to DNA hybridization, an aptamer-target pair was widely used in fabrication of biosensors. Aptamer is a kind of oligonucleic acid that binds to a specific target molecule. Since the specific binding with target often results in the conformational conversion of aptamer from random coiled ssDNA to rigid structure, CPs exhibit different interaction with these two structures. Several examples were listed as following.

In 2009, Liu's group developed a convenient detection method for lysozyme based on FRET between an anionic CP (CP 4, Scheme 1) and a 6-carboxyfluorescein (FAM) labeled lysozyme aptamer (*21*) (Fig. 5). In the absence of lysozyme, the negatively charged polymer and the aptamer repel each other and no energy transfer occurs in solution upon excitation of the polymer. In the presence of lysozyme, the FAM labeled aptamer binds to lysozyme and the surface charge is switched from negative to positive, which triggers FRET from CP 4 to FAM due to electrostatic association between the aptamer-lysozyme complex and the anionic polymer. This method presents high sensitivity and selectivity even in biological media.

A Guanine-rich oligonucleotide was used for K^+ detection, and the sequence is capable of forming four-stranded structures, known as G-quadruplexes that play an important role in inhibiting telomerase activity in most cancer cells. Wang's group developed methods to detect conformational change of DNA from G-rich ssDNA sequences to G-quadruplexes based on FRET from CPs (CP 2, Scheme 1) to chromophore-labeled DNA probes (*22*) and G-quadruplexes to duplex transition based on two-step FRET from CPs (CP 2, Scheme 1) to fluorescein and fluorescein to EB (*23*).

In addition to above three recognition modes, detection of certain kind of targets need to be designed carefully and some biomolecule progress should be employed. In which, enzyme-related process and the amplification-included progress (including PCR, RCA, and HCR etc) were widely used in the design of some bioassays. For example, SNP is the most common sequence variations in the DNA sequences of humans, which is highly related with diseases. The sensitive and selective detection of SNP is urgently needed in clinic and medicine application. By employing CPs and chromophore-labeled DNA probe, many SNP assays were developed with employment of enzyme-based process in Wang's group. For example, they developed a method for SNP detection by using cationic CP (PFP, Fig. 6), Taq DNA polymerase and dGTP labeled with a fluorescein (dGTP-Fl) at the guanine base based on FRET from CP to fluorescein (*24*). As shown in Fig. 6, the target DNA fragment as part of p53 exon8 contains a polymorphic site, in which the nucleotide G in a 32-mer wild target is replaced by A in a 32-mer mutant target. The 3′-terminal base of the 20-mer probe is T that is complementary to A in the mutant-type target and is not complementary to G in the wild-type target. Taq DNA polymerase and dGTP-Fl are used for probe extension reactions. Addition of Taq DNA polymerase, the dGTP-Fl is incorporated into the probe by extension reaction for mutant-type target. The presence of cationic CP brings the fluorescein close to PFP due to the strong electrostatic interaction between DNA and PFP and efficient FRET from PFP to fluorescein occurs. For wild-type target, the 3′-end of the probe is not complementary, blocking the base extension reaction. FRET from PFP to fluorescein is inefficient due to the much

Downloaded by UNIV DE SHERBROOKE on November 27, 2012 | http://pubs.acs.org
Publication Date (Web): November 26, 2012 | doi: 10.1021/bk-2012-1112.ch004

weaker electrostatic interactions between the dGTP-Fl and PFP. To identify three genotypes in one extension reaction, they realized multi-color and one-tube SNP genotyping assays, which interface with single-base extension, multi-step FRET and optical amplification properties of CPs (*25*). Later , they discriminated the SNP genotypes of 76 individuals of Chinese ancestry (*26*).

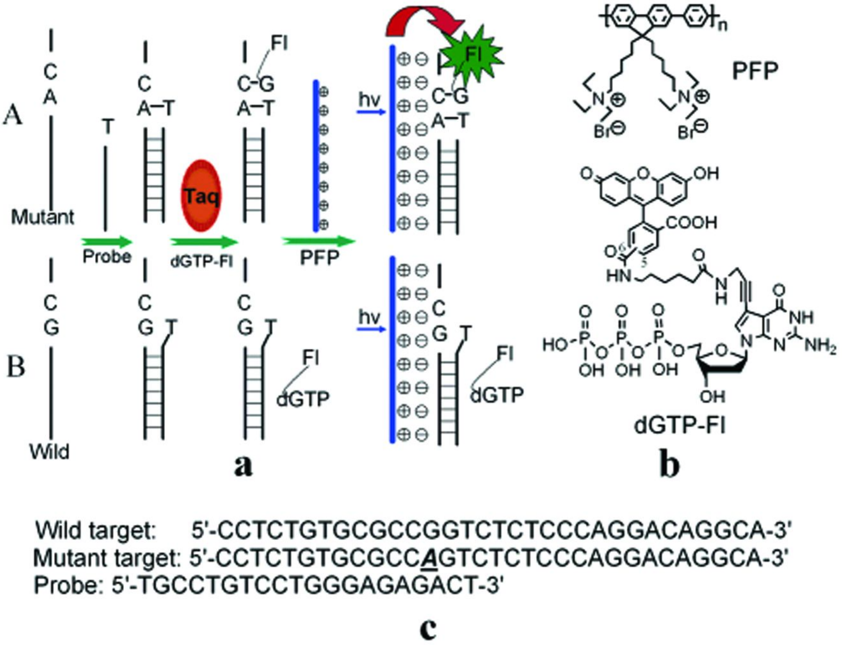

Wild target: 5'-CCTCTGTGCGCCGGTCTCTCCCAGGACAGGCA-3'
Mutant target: 5'-CCTCTGTGCGCCAGTCTCTCCCAGGACAGGCA-3'
Probe: 5'-TGCCTGTCCTGGGAGAGACT-3'

Figure 6. (a) Schematic Representation of the SNP Assay; (b) Chemical Structures of PFP and dGTP-Fl; (c) DNA Sequences Used in the Assay: The Mismatched Base in the Mutant Target is Underlined. Reprinted with permission from ref (18). Copyright (2007) American Chemical Society.

Similar principle was used for DNA methylation assay. DNA methylation is a biochemical process that is important for normal development in higher organisms, which occurs mainly at the C5 position of CpG dinucleotides. Hypermethylation of the CpG island in the promoter region of gene is highly related with various diseases and cancer. The detection of DNA methylation is imperative, which is useful for early cancer diagnosis and cancer type identification. In 2008, Wang's group developed a new method for DNA methylation detection based on highly selective single base extension reaction and significant optical amplification of cationic CPEs. For nonmethylated DNA, bisulfite treatment changes nonmetylated cytosine into uracil and is then substituted by thymine after PCR. The dGTP-Fl can not be incorporated into

Downloaded by UNIV DE SHERBROOKE on November 27, 2012 | http://pubs.acs.org
Publication Date (Web): November 26, 2012 | doi: 10.1021/bk-2012-1112.ch004

the probe and no efficient FRET from polymer to fluorescein occurs due to the large distance between polymer and fluorescein. While for methylated DNA, the cytosine of the CpG site remained unchanged upon bisulfite treatment and PCR amplification. The dGTP-Fl was incorporated into the probe by extension reaction and FRET from polymer to fluorescein can occur efficiently due to close distance between polymer and fluorescein (*27*). Later, they demonstrated the methylated statuses of the *p16*, *HPP1* and *GALR2* promoters of five cancer cell lines (HT29, HepG2, A498, HL60 and M17) by using this method. The method is simple, highly sensitive and cost-effective, which shows great potential for early cancer diagnosis (*28*).

It is worthy of noting that the molecule design of CPs was important to optimize the interaction between CPs and chromophore-labeled DNA for optical amplified fluorescence sensor. Liu's group (*29–32*), Huang's group (*33*) and Al Attar's group (*34*) reported many studies on synthesis and structural design of CPs, the effect of conjugated backbone and side chain properties, the effect of spectral overlap and stokes-shift. Here, we would not describe the molecular design detailed in this paper.

Downloaded by UNIV DE SHERBROOKE on November 27, 2012 | http://pubs.acs.org
Publication Date (Web): November 26, 2012 | doi: 10.1021/bk-2012-1112.ch004

DNA Biosensor Design Based on Conformational Effect of CP

Many CPs possess conformation-optical effects, i.e., diverse conformations respond to different spectra, which forms the basis of visible and fluorescence sensor. For example, cationic water-soluble PT derivatives present different conformation structures upon addition of ssDNA or dsDNA due to their flexible conjugated backbone and side chain, which can easily transduce hybridization events into measurable optical output. And we described this kind of biosensors according to the biorecognition progress.

The Leclerc group reported a rapid colorimetric and fluorometric detection method for DNA based on poly(3-alkoxy-4-methylthiophene) derivatives according to the DNA-DNA hybridization (*35*). The PT derivative CP 5 (Scheme 1) presents random-coil conformation in aqueous solution, which is highly fluorescent and has a less conjugated, nonplanar form with absorption maximum at a short wavelength (λmax = 397nm). Upon addition of ssDNA, the colour of the mixture changed from yellow to red (λmax = 527 nm) within 5 min because of the formation of a so-called duplex between the positively charged PT and the negatively charged oligonucleotide probe (Fig. 7). This duplex corresponds to a highly conjugated planar form and strongly quenched fluorescence. Upon addition of the complementary DNA, the color of mixture changed from red to yellow with fluorescence recovery at elevated temperature because of the formation of a new triplex complex between the polymer with the hybridized dsDNA (Fig. 7). There is a large difference between the duplexes and the triplexes. The duplexes are unstable at temperatures higher than 65°C, whereas triplexes do not form at temperatures lower than 45°C. The detection limit by measuring the fluorescence intensity at 530 nm for DNA was 20 fM. In a further step, they detect DNA at room temperature by using 20% formamide as denaturing agent to reduce reaction temperatures (*36*).

In Functional Nanoparticles for Bioanalysis, Nanomedicine, and Bioelectronic Devices Volume 1; Hepel, M., et al.;
ACS Symposium Series; American Chemical Society: Washington, DC, 2012.

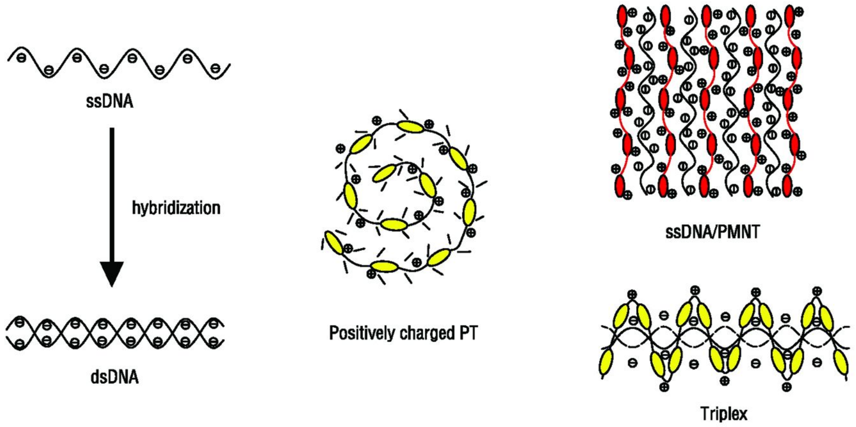

Figure 7. Illustration of the interaction between positively charged PT and ssDNA, dsDNA. Ref (26).

In addition, assay of cleavage of ssDNA by a single-strand-specific S1 nuclease and hydroxyl radicals (*37*) and SNP genotyping (*38*) have been reported based on the conformation change of cationic water-soluble PT derivatives.

By employment of aptamer-target recognition mode, the Leclerc's group developed a colorimetric or fluorometric method for thrombin detection based on conformational modifications of the conjugated backbone of a cationic poly-(3-alkoxy-4-methylthiophene) derivative (CP 5, Scheme 1) when mixed with ssDNA (Fig. 8 A) and a target protein (*39*)(Fig. 8 B). The aqueous solution of polymer CP 5 is yellow with an absorption maximum at 402 nm due to the random-coil conformation (Fig. 8A). In the presence of a nonspecific thrombin aptamer X2 or bovine serum albumin (BSA), the maximum absorption is red shifted (red-violet color) due to complex formation of unfolded anionic ssDNA and the polymer and the planar formation. When the specific aptamer (X1, 5′-GGTTGGTGTGGTTGG-3′) binds to human α-thrombin, α-thrombin promotes X1 to form quadruplex structure and allows polymer to wrap this folded structure (Fig. 8B). The folding of the conjugation chain leads to the decrease of the efficient conjugation length, which leads to the blue shift of the maximum absorption (λmax = 502 nm). The detection limit by this colorimetric method is about 1 × 10^{-7} M. At the same time, the yellow, random-coil form of polymer CP 5 is fluorescent with an emission maximum at 525 nm. When adding nonspecific thrombin aptamer or the absence of human thrombin, the fluorescence intensity is highly quenched and the maximum emission is red-shifted due to the highly conjugated form. When the 1:1:1 complex (human thrombin/specific thrombin DNA aptamer X1/polymer) is formed, the fluorescence is weaker than the yellow form but stronger than the red-violet form due to a partially planar conformation of the PT chain but with less aggregation of the chains. By using fluorescence method, a detection limit of 1 × 10^{-11} M in 200 μL for the human α-thrombin can

Downloaded by UNIV DE SHERBROOKE on November 27, 2012 | http://pubs.acs.org
Publication Date (Web): November 26, 2012 | doi: 10.1021/bk-2012-1112.ch004

be obtained. Later, they improved the method to detect thrombin on solid supports based on the PT optical transducer and a 3′-Cy3-labeled ssDNA aptamer (*40*).

Wang's and Fan's group developed a simple, highly sensitive, and highly selective protocol for mercury ion detection by using poly(3-(3′-*N*,*N*,*N*-triethylamino-1′-propyloxy)-4-methyl-2,5-thiophene hydrochloride) (PMNT, CP 6, Scheme 1) and a mercury-specific oligonucleotide (MSO) probe (*41*). The MSO probe, including several thymines (T), readily forms a stem-loop structure in the T-Hg^{2+}-T configuration (Fig. 8C). PMNT binds to the Hg^{2+}-free MSO and the Hg^{2+}-MSO complex in different ways, leading to distinguishable optical properties in response to the target-induced conformational change (Fig. 8C). By using the fluorometric method, the detection limit can reach nanomolar range (42 nM).

Recently, Fan's and Huang's group reported a colorimetric strategy for sensitive pH-driven conformation change of DNA i-motif structure based on the different interaction between cationic water-soluble PT derivatives CP 6 and i-motif, ssDNA structure (*42*) (Fig. 8A, D).

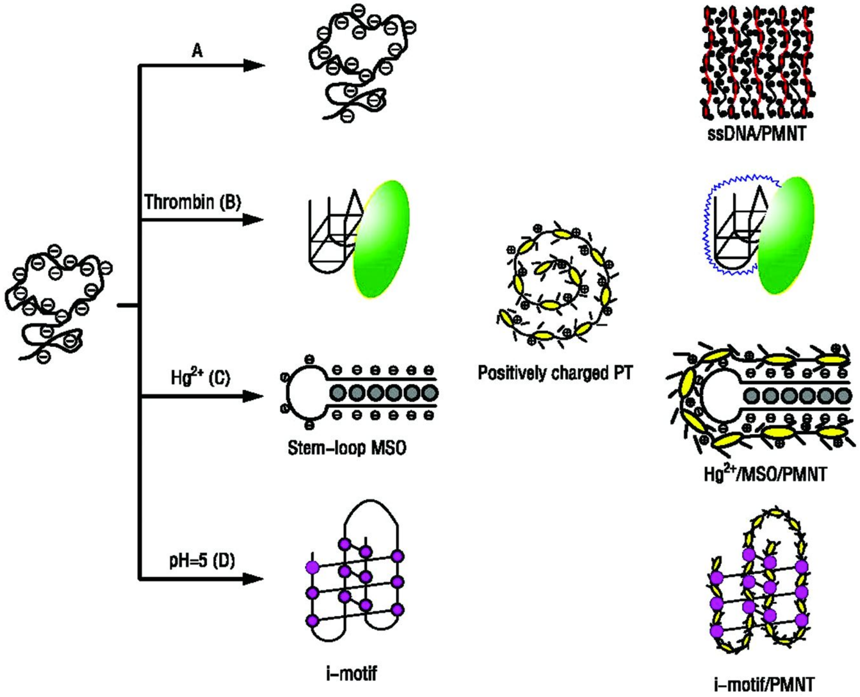

Figure 8. Schematic illustration of the specific detection of human α-thrombin, Hg^{2+} and i- motif structure based on specific ss-DNA and positively charged PT. Ref (30, 32, 33).

Downloaded by UNIV DE SHERBROOKE on November 27, 2012 | http://pubs.acs.org
Publication Date (Web): November 26, 2012 | doi: 10.1021/bk-2012-1112.ch004

Protein Sensors

Proteins are a kind of amphiphilic biomolecules consisting of polypeptide chains typically folded into a globular or fibrous form, and exhibit positive or negative charge in buffered solution. In comparison with linear DNA constructs, proteins exhibited diverse hydrophobic and different charged states, which facilitated the sensor's design according to CP-protein interaction. Here, we list several examples based on FRET and conformation effect.

Protein Sensor's Design Based on FRET Pair

Downloaded by UNIV DE SHERBROOKE on November 27, 2012 | http://pubs.acs.org
Publication Date (Web): November 26, 2012 | doi: 10.1021/bk-2012-1112.ch004

As described in DNA sensors, we can easily design various protein assays based on the application of CPs-dye FRET pair. For design of protein sensors, QTL (quencher tether ligand) strategy was developed firstly for detection of avidin. In addition, some proteins work as specific acceptors in FRET process and quench the fluorescence of CPs. Thus, various strategies have been used in detection of proteins, which were listed in following sections.

π-conjugated chains of water-soluble CP allow to quench the fluorescence of a whole chain by a single quencher (1:n), which is called superquenching and can provide strong signal amplification in CPs based biosensor by monitoring the fluorescence change of CPs in the absence and presence of analytes. Worthy of noting, fluorescence quenching refers to that the fluorescence (energy) of CPs was transferred to the acceptor and then exhausted in thermal energy. The efficiency of luminescence quenching is quantified by the Stern-Volmer constant, Ksv. It was calculated from the equation: $F_0/F = 1+Ksv[\mathrm{Q}]$, where F_0 is the fluorescence intensity in the absence of quencher, F is the fluorescence intensity in the presence of quencher.

Whitten's group observed that the fluorescence of a water-soluble PPV derivative MPS-PPV with sulfonic acid group (CP 7, Scheme 1), can be very efficiently quenched by an electron transfer acceptor, methyl viologen due to the electrostatic attraction between the anionic PPV and cationic viologen and collective molecular wire effect. The corresponding quenching constant (K_{SV}) value reaches 1.7×10^7, nearly four orders of magnitude greater than that for stilbene in micelles and six orders of magnitude greater than that for dilute stilbene solutions. Based on the superquenching observation, they developed a biosensor application for avidin detection. A biomolecular ligand biotin was tethered to viologen (QTL), and the tethered quencher can also efficiently quench the fluorescence of MPS-PPV. Upon addition of avidin, a specific target to biotin with high binding affinity, the target avidin binds to the ligand biotin and separates the PPV and viologen, which results in the recovery of the fluorescence (Fig. 9). They have demonstrated that nanomolar streptavidin can be detected using this principle (*43*). Later, they found that this kind of QTL sensor method for protein detection could be applied to solid state biosensor. In 2004, Whitten's group developed a method to detect protease using QTL method (*44*).

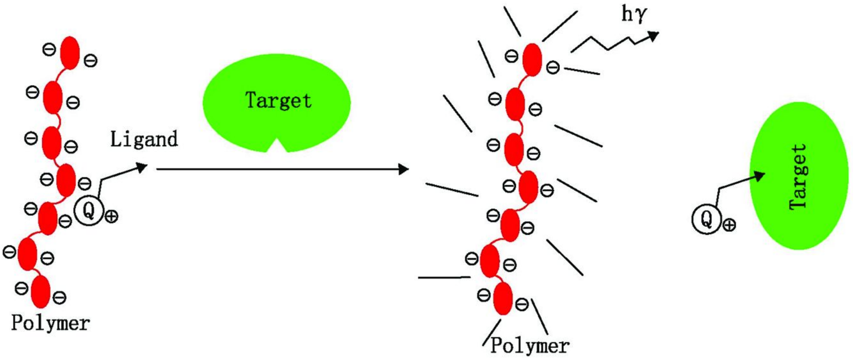

Target
Ligand
Q
Polymer
hγ
Polymer
Q
Target

Figure 9. Illustration of the QTL sensor mechanism based on water-soluble CP. Ref (34).

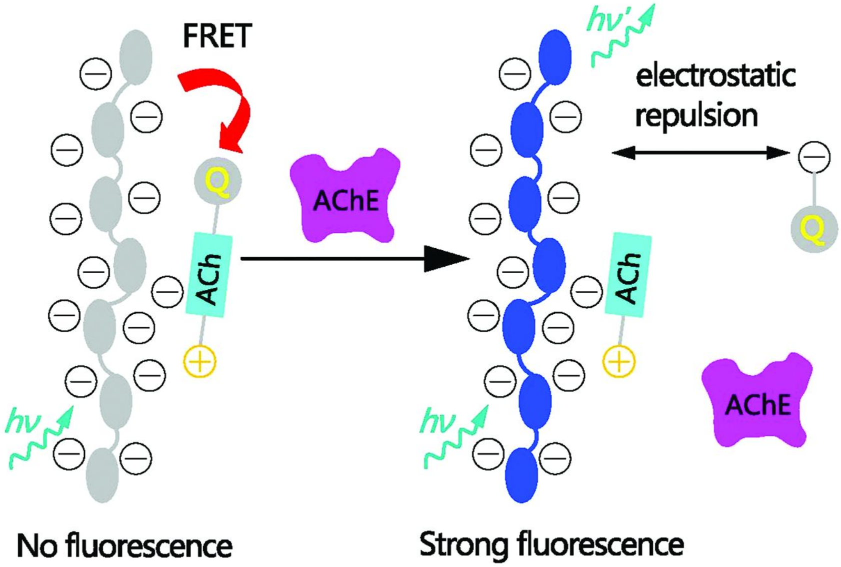

FRET
Q
ACh
AChE
hv
No fluorescence
hv'
electrostatic
repulsion
Q
ACh
AChE
hv
Strong fluorescence

Figure 10. Illustration of assays of AChE activity. Ref (36).

Replacement of biotin-avidin pair with substrate-enzyme pair, Wang's group modified the QTL strategy by using a "quencher-tether-substrate" to detect acetylcholinesterase (AChE) activity and inhibition rapidly and sensitively based on anionic CP PFP-SO_3^- (CP 8, Scheme 1). An acetylcholine (ACh) derivative labeled with quencher dabcyl was used as a substrate for AChE. The strong electrostatic interaction between positively charged Ach-dabcyl and negatively charged CP 8 can form a complex, which results in quenched fluorescence of CP 8 by the dabcyl moiety through the transfer of fluorescence resonance energy. Upon

Downloaded by UNIV DE SHERBROOKE on November 27, 2012 | http://pubs.acs.org
Publication Date (Web): November 26, 2012 | doi: 10.1021/bk-2012-1112.ch004

the addition of AChE, Ach-dabcyl undergoes catalytic hydrolysis to produce a negatively charged residue that contains the dabcyl moiety. The distance between dabcyl moiety and CP 8 increases due to the electrostatic repulsion, which results in the recovery of fluorescence of CP 8 (Fig. 10). The sensor is highly sensitive and the limit of detection (LOD) of this assay is 0.05 units mL^{-1}. Furthermore, the inhibition of AChE can also be analyzed with the CP 8/Ach-dabcyl complex, which provides a new method for screening Alzheimer's disease (AD) drugs (*45*).

Very recently, Fan's and Liu's group reported a graphene oxide (GO)-based bioassay for light-up detection of ConA and *Escherichia coli* (*E. coli*) based on a conjugated oligomer having a high density of α-mannose side chains. In this assay, mannose tether FBT was used as bioprobe and donor in FRET pair, while GO was acceptor (quencher). The fluorescence of (4,7-bis(9,9-bis(2-(2-(2-(2,3,4,5,6- pentahydroxyhexanal)-ethoxy)ethyl)fluorenyl)benzothiadiazole (FBT) is highly quenched by GO mainly attributed to strong π-π interaction between FBT and GO. Upon addition of ConA, the fluorescence of FBT increases due to specific binding between ConA to FBT (Fig. 11). This assay exhibits a linear range of 0-50 nM for ConA and the detection limit 0.5 nM with the GO/FBT probe. They also applied GO/FBT probe for bacterial detection and obtained better selectivity than using FBT probe only (*46*).

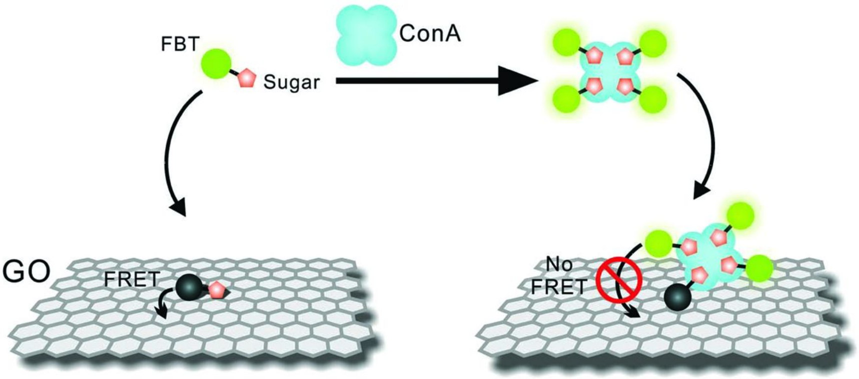

Figure 11. Illustration of ConA detection with the GO/FBT hybrid probe. Reprinted with permission from ref (37). Copyright (2011) WILEY-VCH Verlag GmbH & Co. KGaA.

Following the QTL strategy and replacing the quencher (MV) using a fluorescent dye (fluorescein), Wang's group developed a highly selective streptavidin detection method based on FRET with positively charged CP and negatively charged biotinylated fluorescein probe (Fl-B). The strong electrostatic interactions between CP 2 and fluorescein result in efficient FRET from CP

Downloaded by UNIV DE SHERBROOKE on November 27, 2012 | http://pubs.acs.org
Publication Date (Web): November 26, 2012 | doi: 10.1021/bk-2012-1112.ch004

2 to fluorescein. In the presence of streptavidin, the biotin moiety of Fl-B specifically binds to streptavidin and the fluorescein molecule is buried deeply in the neighboring vacant binding sites. The distance between fluorescein and CP 2 becomes larger, resulting in inefficient FRET from CP 2 to fluorescein (*47*).

Some proteins exhibit certain quenching ability of the fluorescence of CPs through their interaction, thus formed a simple protein detection method. Heeger's group found that a heme-containing protein cytochrome *c* (cyt *c*) can quench the fluorescence of CP poly[lithium 5-methoxy-2-(4-sulfobutoxy)-1,4-phenylenevinylene] (MBL-PPV, CP 9, Scheme 1) very efficiently and Ksv can reach 10^8 M^{-1} at pH 7.4. The high quenching efficiency is attributed to a combination of ultrafast photoinduced ET between cyt *c* and the luminescent CP and the formation of bound complexes (static quenching) between the cationic cyt *c* and anionic MBL-PPV. By controlling the protein's charge state the quenching efficiency can be "tuned" over more than 6 orders of magnitude. This study provides a new system for protein detection (*48*). They also applied the charge neutral complex to study the interaction between antibody and antigen for the first time (*49*).

A novel kind of CPs consisting of intrachain FRET pair was designed with high efficiency FRET and applied for visual detection of proteins. This kind of water-soluble CPs containing backbones with donor-acceptor architectures has been developed for direct visual detection. It is based on the fact that interchain FRET should be more efficient than intrachain FRET because interchain interactions have stronger electronic coupling and the increased dimensionality than intrachain interactions.

Based on the principle, Liu's group synthesized multicolor polymers containing fluorene segments and 2,1,3-benzothiadiazole (BT) units and demonstrated that they could be used for the naked-eye detection of proteins. The mechanism is based on aggregation-induced FRET from the fluorene segments to BT units. Addition of lysozyme, bovine serum albumin and cyt *c* to the blue emission polymer CP 10 (Scheme 1) solution results in a change of emission color from blue to yellow, green, and dark, respectively. The change in polymer fluorescent color in the presence of different proteins is due to the variation in hydrophobic nature, net charge, and the structure among proteins (*50*). Using a standard fluorometer, the detection limit for lysozyme is estimated to be 0.2 μM. Recently, they developed a fluorescent sensing method for concanavalin A (Con A) based on an α-mannose-bearing neutral polyfluorene derivative that contains 20 mol% BT. Upon addition of Con A, the polymer aggregates and facilitates energy transfer from the phenylene-fluorene segment and the BT due to the specific interaction between α-mannose and Con A. The method represents a linear range for Con A between 1 nM to 250 nM (*51*).

Wang's group developed a method to detect the enzyme activity based on BT-containing water-suluble CP by using the anionic adenosine triphosphate (ATP) and alkaline phosphatase (ALP) as the substrate and enzyme, respectively. The cationic polymer interacts with anionic substrate ATP upon addition of anionic ATP and induces polymer aggregation, which demonstrates intramolecular energy transfer from the fluorene units to the BT sites and a fluorescence color change from blue to green. When the substrates are cleaved into fragments by enzyme,

Downloaded by UNIV DE SHERBROOKE on November 27, 2012 | http://pubs.acs.org
Publication Date (Web): November 26, 2012 | doi: 10.1021/bk-2012-1112.ch004

the electrostatic attraction between the substrate fragment and the CP becomes weak and causes inefficient FRET from the fluorene units to the BT sites, leading to the recovery of the blue fluorescence (Fig. 12). The method presents a linear range from 0 to 1.0 × 10^{-3} unit μL^{-1} with a detection limit of 5.0 × 10^{-5} unit μL^{-1} for ALP detection with a standard commercial fluorometer (*52*).

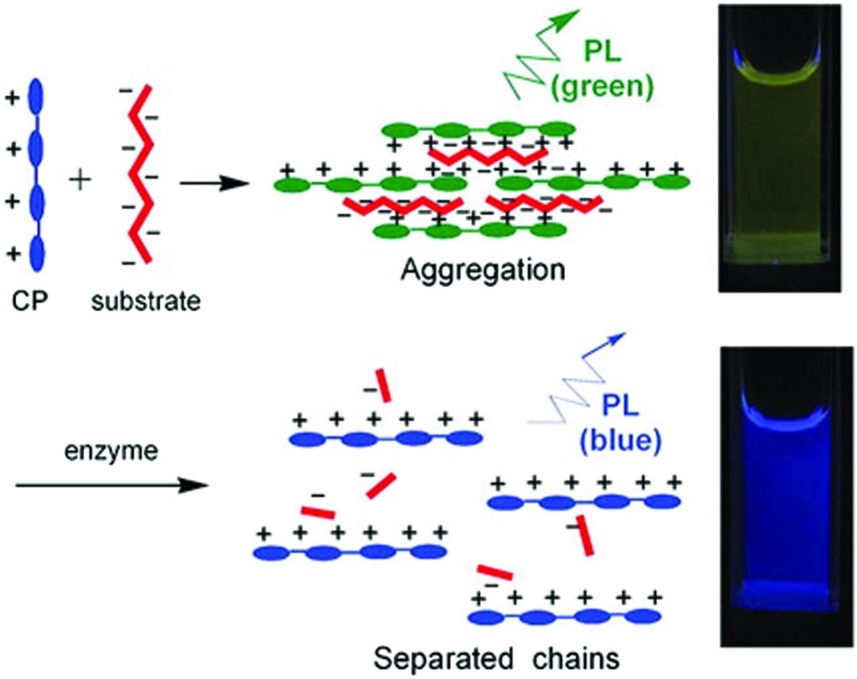

Figure 12. Schematic representation of the assay for enzyme (ALP) and the cleavage of charged substrates (ATP). Reprinted with permission from ref (43). Copyright (2007) The Royal Society of Chemistry.

In addition, Liu's group also realized the multicolor visual protein detection based on protein mediated distance-dependant FRET between a pair of donor-acceptor cationic CPEs (*53*). A pair of donor-acceptor cationic CPEs can not exhibit efficient FRET in the absence of proteins due to the large distance between donor and acceptor CPEs. Upon addition of proteins to the CPE blend solution, FRET efficiency changes in the presence of different proteins due to complex formation between the CPEs induced by proteins.

Protein Detection Based on Conformational Change of CPs

The Inganäs group synthesized PT derivatives carrying amino acid side chain and developed many methods to detect polypeptide and protein. Cationic fluorescent PTs can directly report conformational changes occurring in proteins or different forms of the same protein (*54–58*). Conformational changes of

Downloaded by UNIV DE SHERBROOKE on November 27, 2012 | http://pubs.acs.org
Publication Date (Web): November 26, 2012 | doi: 10.1021/bk-2012-1112.ch004

biomolecules are very important because many diseases are attributed to them. Conformational changes of biomolecules could lead to different conformations of the polymer backbone, which leads to the change of the absorption and emission properties from the polymer. For example, Polymer CP 11 (Scheme 1) has been utilized to fluorometric detection of calcium-induced conformational changes in calmodulin and calmodulin-calcineurin interactions (*55*). In a further step, they synthesize a regioregular, zwitterionic conjugated oligoelectrolyte to detect amyloid fibrils in chicken lysozyme using these novel conformation-sensitive optical methods (*54*).

Recently, Li's group developed a colorimetric method for AChE detection based on a complex between an anionic PT (PT-COO$^-$, CP 12, Scheme 1) and a cationic surfactant myristoylcholine. The addition of myristoylcholine makes aggregated PT-COO$^-$ disassemble and further addition of AchE into the above solution led to the reassembly of PT-COO$^-$ due to the catalyzed hydrolysis of myristoylcholine and the collapse of the complex (Fig. 13). The detection limit of the colorimetric method for AchE can reach 0.2 U/mL (*59*).

Downloaded by UNIV DE SHERBROOKE on November 27, 2012 | http://pubs.acs.org
Publication Date (Web): November 26, 2012 | doi: 10.1021/bk-2012-1112.ch004

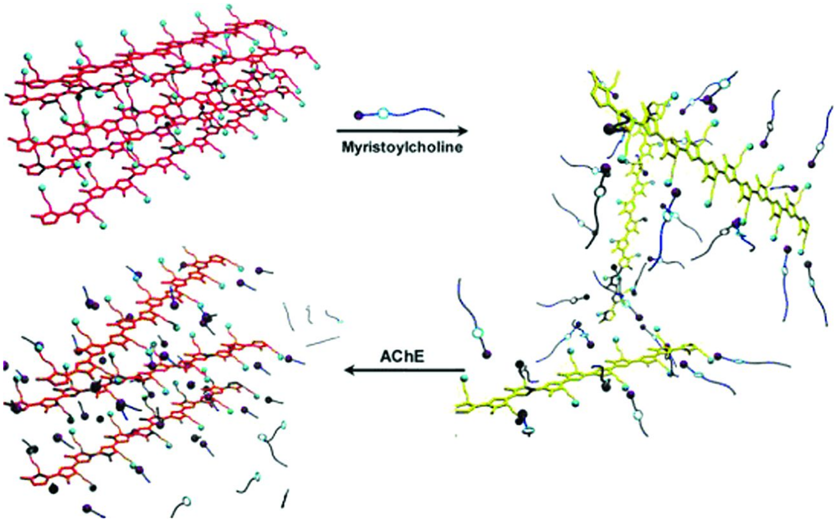

Figure 13. The disassembly reassembly process of PT-COO$^-$ in the presence of myristoylcholine and AChE. Reprinted with permission from ref (46). Copyright (2011) American Chemical Society.

Heterogeneous Assays

To satisfy the commercialized application of biosensor devices, CP-based biosensors can also be developed into solid-state biosensors. Polystyrene particles (*60*, *61*), magnetic microparticle (*62*), and silica nanoparticles (*63–66*) have been developed for heterogeneous biosensor assay. CP-based biosensor at chip surfaces have also been successfully demonstrated (*67*, *68*). As shown in Fig. 14, neutral PNA is first immobilized onto the surface, hybridization with complememtary ssDNA results in negatively charged surface, electrostatic forces cause the oppositely charged cationic CP to bind selectively to the "complementary" surfaces. The polymer fluorescence emission indicates that the ssDNA is complementary to the surface-bound PNA. A New light-harvesting CPE microgel has been developed to detect DNA and Enzyme. The microgel can realize solid phase detection, which shows great potential for biodetection in the real world (*69*).

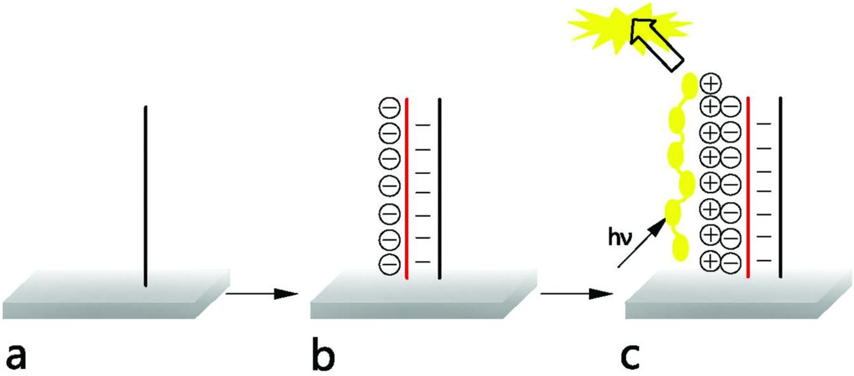

Figure 14. Hybridization of PNA (a) with ssDNA results in an increase of negative charge at the surface (b), and electrostatic interactions result in adsorption of the CCP (c).

Other Biological-Revelant Molecules

The design and construction of chemo- and biosensors for detecting biologically- relevant molecules have received considerable attention in recent years. In 2005, Shinkai's group developed a new selective biosensor for ATP based on a cationic water-soluble PT through electrostatic and hydrophobic cooperative interactions. The addition of ATP induces the conformation of PT to be more planar and leads to a pronounced red shift in the absorption maximum of PT. While other anions such as Cl^-, HPO_4^{2-}, and HCO_3^{2-}, ADP, adenosine monophosphate (AMP), or uridine triphosphate (UTP) all have a negligible effect. In addition, the addition of ATP can quench the fluorescence of PT. The detection limit for ATP based on fluorescence method was reported to be approximately 10^{-8} M (*70*). Wang's group developed a method for NO detection by using a cationic CP that contains imidazole moieties, Cu^{2+} ions, and the target nitric oxide. The fluorescence of polymer is quenched efficiently by Cu^{2+} due to the coordination of polymer with Cu^{2+} through weak N-Cu interactions. Upon addition of NO, The fluorescence of polymer recovers because of the transformation of the paramagnetic Cu^{2+} ion into a diamagnetic Cu^+ ion. The method not only shows

Downloaded by UNIV DE SHERBROOKE on November 27, 2012 | http://pubs.acs.org
Publication Date (Web): November 26, 2012 | doi: 10.1021/bk-2012-1112.ch004

high sensitivity but also exhibits good selectivity against other biologically relevant reactive nitrogen species, such as $NOBF_4$, $NaNO_2$, and $NaNO_3$ (*71*).

Liu's group developed a strategy for naked-eye detection and quantification of heparin in biological media. The addition of high negatively charged heparin interacts with positively charged PT, which induces the conformation and color of polymer to change. A linear calibration curve is observed in the 0-6.7 U/mL and 0-2.2 U/mL ranges for heparin quantification in pure water and in fetal bovine serum, respectively (*72*). The polymer can show distinguishable color difference between heparin and its analogues under optimized experimental conditions due to their lower charge density as compared to that of heparin. In addition, the selectivity can be improved further by increasing the detection temperature or adding some organic solvent to the aqueous media due to the decrease the polymer-polymer interchain π stacking.

Downloaded by UNIV DE SHERBROOKE on November 27, 2012 | http://pubs.acs.org
Publication Date (Web): November 26, 2012 | doi: 10.1021/bk-2012-1112.ch004

New Progress for CPs Properties

In order to improve sensing capabilities, researchers modified the side chain of CP by using fluorophores with biorecognition capabilities. In 2007, Wang's group reported a water-soluble CP substituted with a boronate-protected fluorescein (PF-FB, CP 13, Scheme 1) for the detection of hydrogen peroxide (H_2O_2) and glucose in serum. The FRET from fluorine units to peroxyfluor-1 is absent in the absence of H_2O_2 due to the lactone form of peroxyfluor-1. Efficient FRET from the fluorene units to the fluorescein can occur and generate green fluorescence in the presence of H_2O_2 because the peroxyfluor-1 can specifically react with H_2O_2 to deprotect the boronate protecting groups. The PF-FB probe can detect H_2O_2 in the range from 4.4 to 530 μM (*73*). At the same time, glucose detection is also realized with the PF-FB probe in serum because glucose oxidases can specifically catalyze the oxidation of β-D-(+)-glucose to generate H_2O_2. Liu's group also reported a CP substituted with an intercalating dye thiazole orange (TO) with improved DNA sensing capabilities (*74*).

Recently, new progress has appeared to increase the optical output from CPs, which is called metal-enhanced fluorescence (MEF). MEF is the use of Fluorophores metal near-field interactions. To date, MEF from plasmonic nanostructured materials are mainly silver and gold. Liu's group demonstrated MEF with water-soluble Poly[9,9-bis(9-N,N,Ntrimethylammoniumethoxyethoxyethyl)fluorene-alt-4,7-(2,1,3-benzothiadiazole) dibromide] (PFBT) by exploiting substrates with underlying Ag NP arrays. In addition, the Ag NP array amplified PFBT emission can be applied to detect ssDNA with higher selectivity and sensitivity by using PNA as probe (*75*). Later, Boudreau's group realized plasmon enhanced resonance energy transfer from a CP to fluorescent multilayer core-shell nanoparticles, which provides great potential for signal amplification schemes in polymer-based and FRET-based biosensors (*76*). MEF, as emerging tool in biotechnology, can improve the sensitivity of the detection. When using water-soluble CPs as signal probe, the cooperative signal amplification by CPs and nanoparticles can lower the detection limit further.

Downloaded by UNIV DE SHERBROOKE on November 27, 2012 | http://pubs.acs.org
Publication Date (Web): November 26, 2012 | doi: 10.1021/bk-2012-1112.ch004

Application of CPs in Bioimaging and Drug Delivery

It is well known that small fluorophores, fluorescent proteins, and quantum dots have been widely used in bioimaging. Some disadvantages, such as photobleaching, poor aqueous stability and high cytotoxicity, limit their application. The limitations provide motivation for designing new fluorescent nanoparticles for cellular imaging. Although CPs have been widely used for chemical and biological sensors, their exploitation in cell imaging is seldom reported, possibly due to the linear geometries of most CPs that affect cellular uptake process. However, recently, CPEs with hyperbranched structures or biocompatible long side chains were introduced to cellular imaging. At the same time, CPNs synthesized using the reprecipitation or miniemulsion method have established their application in bioimaging because of their unique optical and chemical features which exhibit small particle diameters, high fluorescence brightness, excellent photostability, high selectivity and lower toxicity. More importantly, CPs with hyperbranched structures and biocompatible long side chains are good carrier, and CPs could carry lots of bioprobe or drug molecules through covalent coupling and transport them into live cells with high efficiency, which made the diagnosis and treatment simultaneously possible.

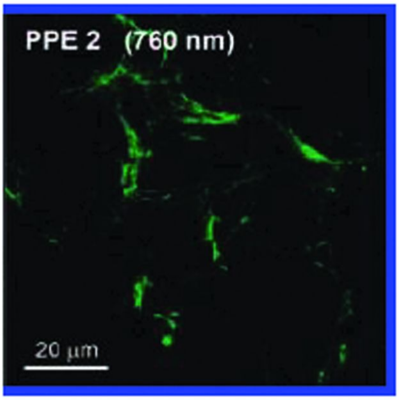

Figure 15. Two-photon excitation microscopy of CP 17 interacting with live mouse fibroblast cell. Reprinted with permission from ref (60). Copyright (2008) American Chemical Society.

The CPs have been demonstrated to selectively recognize certain components in the live cells, which is called passive target interaction. A series of CPs without specific bioprobe have been synthesized for bioimaging. Björk et al observed that CPE probes can be used for specific targeting of chromatin, nuclear and cytoplasmatic vesicles, and cytoskeletal components in a complex system of cultured cells (*77*). The PT derivatives including anionic, cationic, and zwitterionic form (CP 14-16) can target lysosome-related acidic vacuoles in

Downloaded by UNIV DE SHERBROOKE on November 27, 2012 | http://pubs.acs.org
Publication Date (Web): November 26, 2012 | doi: 10.1021/bk-2012-1112.ch004

cultured primary cells but can not target that in transformed cells. The mechanism and the detailed molecular state of the polymer in the cytoplasmatic vacuoles remains elusive and needs to investigate further (*77*). Bun's group found that a carboxylated-PPE (CP 17) could selectively bind and image the extracelluar matrix protein fibronectin of live fibroblast cells through multiple nonspecific interaction (polyvalent interactions) between CPs and cells (*78*), (Fig. 15) which explored a new way to specific bioimaging and contributed to the mechanism of uptake of CPs in live cells.

In order to improve the brightness and the cell uptake behavior of CPs, the CPs-based nanoparticles (CPNs) are designed and synthesized. Up to now, CPNs exhibited great potential in bioimaging, biosensing and nanomedicine due to their straightforward synthesis, tunable size and optics, excellent compatibility and low toxicity. More importantly, the CPs-based dots (<4nm) exhibit great excellent performance for biosensor and bioimaging since the dots possess the highest brightness/volume ratios of any nanoparticles tolerate through combining a number of favorable characteristics of CP molecules. Some papers reviewed the preparation and application of extremely bright CPdots (*79*, *80*). We list several examples of application of CPNs in bioimaging, and most of them were found to be internalized through endocytosis way and localized some component through passive target interaction. Moon et al designed an amine containing PPE CPNs (CP 18, Scheme 1) for live-cell imaging. The CPNs exhibit high resistance to photobleaching, which are cell permeable and accumulate exclusively in the cytosol without any measurable inhibition of cell viability (*81*). McNeill's group designed a variety of CPdots (PPE (CP19), PFPV (CP 20), PFBT (CP 21), and MEHPPV (CP 22)) which are promising for demanding fluorescence applications such as single molecule tracking in live cells and highly sensitive analysis because these nanoparticles exhibit extraordinary brightness, high emission rates and small particle diameters (*82*) (Fig. 16). These dots could be internalized by J774.A1 macrophages through pinocytosis way. And the selection of the cell system is based on the ability of macrophages to efficiently ingest cellular debris, pathogens, and small particles such as CPdots. Later, they reported energy-transfer-mediated phosphorescence from metalloporphyrin-doped polyfluorene nanoparticles and its application to biological oxygen sensing. The nanoparticles were characterized with high density of chromophores (about 700 phosphorescent chromophores per particle with 25 nm size). They observed the cellular uptake of these doped CPdots by incubating J774.A1 cells with CPdots. Extraordinary brightness and single-particle sensing and cellular uptake demonstrated that doped CPdots is promising for quantitative detection of molecular oxygen levels in living cells and tissue (*83*). Recently, Zumbusch and Mecking's group reported the preparation of aqueous nanoparticle dispersions by sonogashira coupling and their behavior and imaging in cells. The emission of the particles can be tuned, which allows for differentiation of the location of different particle species in cells (*84*). Fernando et al demonstrated the mechanism of cellular uptake and cytotoxicity of highly fluorescent CPNs poly[(9,9-dioctylfluorenyl-2,7-diyl)-co-(1,4-benzo-{2,1′,3}-thiadazole)] (PFBT) in J774A.1 cells. The nanoparticles can efficiently enter into the cell via endocytosis with no significant cytotoxic or inflammatory effects, making

PFBT nanoparticles attractive probes for live cell imaging (*80*). Kim et al have constructed cyanovinylene-backboned conjugated polymer dot nanoparticles (cvPDs) with near-IR (NIR) emission (CP 23, Scheme 1) as in vivo nanoprobes to real-time sentinel lymph node (SLN) mapping in a mouse model. The effective SLN mapping with NIR-cvPDs provides a possibility for real-time optical guidance, which may help surgeons during surgery (*85*). He's and Li's group applied self-assembly of CP-Ag@SiO_2 hybrid fluorescent nanoparticles to cellular imaging. Core-shell nanoparticles with silver nanoparticles core show MEF property compared with nanoparticles without silver cores. The nanocomposite exhibits good monodispersity and low cytotoxicity and can image A549 lung cancer cells (*86*). Very recently, Tan et al synthesized robust and bright fluorescent nanoparticles by encapsulating CPs in silica-shell cross-linked polymeric micelles (CP-SSCL) via a benign bioinspired silification process. The nanoparticles can image in cytoplasm region surrounding the nuclei of the MDA-MB-231 breast cancer cells via uptake of the CP-SSCL (*87*).

Downloaded by UNIV DE SHERBROOKE on November 27, 2012 | http://pubs.acs.org
Publication Date (Web): November 26, 2012 | doi: 10.1021/bk-2012-1112.ch004

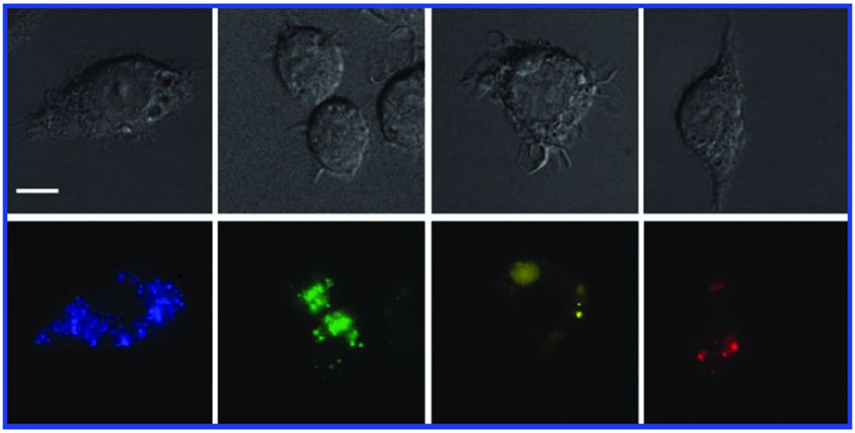

Figure 16. Differential interference contrast (DIC) images (top), and fluorescence images of macrophage cells labeled with PPE, PFPV, PFBT, and MEHPPV dots, respectively. Reprinted with permission from ref (64). Copyright (2008) American Chemical Society.

Similarly, a fluorescent single-molecular core-shell nanosphere of hyperbranched CPE (HCPE, CP 24) was designed for live-cell imaging, and this kind of nanospheres could be internalized by cells and accumulated in the cytoplasm of breast cancer cell MCF-7. The HCPE intrinsically forms single-molecular core-shell nanosphere with an average diamater about 11 nm, which possesses high quantum yield, good stability and low cytotoxicity (*88*).

Recently, Wang's group synthesized a new fluorescent nanoparticle based on lipid-modified cationic poly(fluorenylene phenylene) (PFPL, CP 25 in Fig. 1). The lipid was incorporated as a side chain due to its biocompatibility and entering ability into the cytoplasm, and the PFPL is amphiphilic, biocompatible and shows photostability and little cytotoxicity. It can easily enter the cytoplasm via endocytosis and is a good candidate for cell imaging. Furthermore, PFPL particles can work as a good carrier and successfully deliver plasmid (pCX-EGFP) into lung cancer cells (A549) for transcription and translation (Fig. 17) (*89*), which will be described in following section.

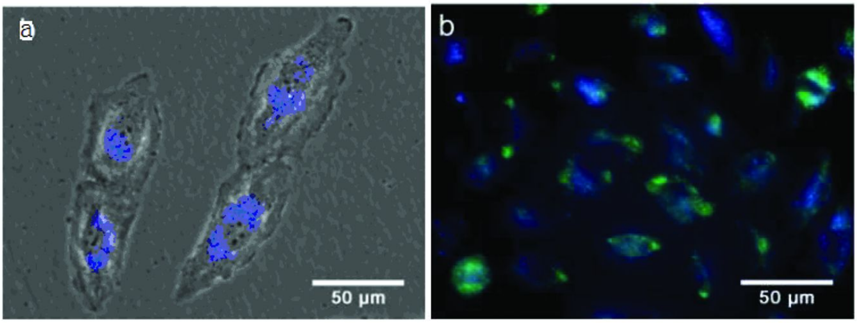

Figure 17. (a) The overlap image of phase contrast and fluorescence of A549 cells treated with (a) PFPL nanoparticles and (b) PFPL/pCX-EGFP complex. Reprinted with permission from ref (71). Copyright (2009) The Royal Society of Chemistry.

For multi-color imaging, Wang's group prepared multicolor CPN-encoded microparticles based on the self-assembly of a noninvasive bacteria (*E. coli*) and CPNs, and the biological membrane of an *E. coli* cell was used to construct particles due to it's composition (mainly lipid and protein). The amphiphilic CPs could bind to the outer surface membrane of *E. coli* cell through electrostatic attractions and hydrophobic interactions, which kept three polymers in close proximity to allow efficient intermolecular FRET. These particles exhibit low toxicity towards cells and have been successfully applied for cell imaging and optical barcoding. Their study open a new door in preparing multifunctional structures based on the self-assembly of living organism with functional materials (*90*). They also synthesized a new red-emissive CP (PBF) containing fluorene and boron-dipyrromethene repeat units in the backbones, which can form nanoparticles with negatively charged disodium salt 3,3′-dithiodipropionic acid (SDPA) via electrostatic interactions. In addition to the optical imaging capability, the nanoparticles can be used to kill bacterial and cancer cells through sensitizing the oxygen molecule to readily produce reactive oxygen species (*91*).

For above mentioned strategies, a lot of papers concerning design and application of CPNs have been published. However, the specific localization for certain target was urgently required in clinic diagnosis and treatment. Conjugation of CPs with bioprobes, including DNA, protein, peptide, small biomolecule, was a good solution for target imaging. Folic acid (FA) was the mostly used bioprobes

Downloaded by UNIV DE SHERBROOKE on November 27, 2012 | http://pubs.acs.org
Publication Date (Web): November 26, 2012 | doi: 10.1021/bk-2012-1112.ch004

for scientists, owing to the simple molecule structure, good stability and high specificity for FA-receptor over-expressed in malignant tumor cells. On the basis of well-designed CPs and CPNs, scientists developed target imaging using the CPs-FA complexes.

Bun's group modified the side chain of PPE using an anionic FA to realize targeted cellular imaging . The fluorescent polymer (CP 26) is photochemical stable and shows low cytotoxicity and can target and image KB cancer cells in vitro with high selectivity through receptor mediated uptake while its counterpart without FA groups did not stain KB cancer cells (*92*). The conjugation of FAs on the surface of CP-SSCL was investigated by Tan et al, and they observed that the cellular uptake and target imaging was improved significantly, which implied great potential for targeted imaging and early detection of cancer cells (*87*). Liu et al developed the far-red/near-infrared (FR/NIR) cellular imaging by using (FR/NIR) CPE backbone and poly(ethylene glycol) (PEG) side brushes with FA groups (CP 27, Scheme 1). This kind of polymer can self-assemble into a core–shell nanostructure in aqueous medium with an average size about 130 nm, which exhibits high quantum yield, high photostability, low cytotoxicity and reduced nonspecific interactions with biomolecules due to the shielding effect of PEG. It allows for effective visualization and discrimination of MCF-7 cancer cells from NIH-3T3 normal cells (*93*). They also reported conjugated oligoelectrolyte-polyhedral oligomeric silsesquioxane (COE-POSS) loaded and pH-triggered chitosan/poly(ethylene glycol) nanoparticles with FA functionalization for targeted imaging of cancer cell nucleus (*94*).

Chiu's group has done much work on bioimaging field using CPNs and bioprobes (chlorotoxin, streptavidin, and IgG etc). For example, they developed methods to form polymer dot bioconjugates based on entrapping heterogeneous polymer chains into a polymer dot particle. Streptavidin and IgG were used to localize the target component of cells, and these bioconjugates were identified as specific and effective in labelling cell surface receptors and subcellular structures in both live and fixed cells (*95*). More recently, they designed a polymer-blend nanodot (PBdot, a visible-light-harvesting polymer as the donor and an efficient deep-red emitting polymer as the acceptor) system that consists of donor-acceptor polymers for in vivo tumor targeting. They covalently conjugated the PBdot to a peptide ligand chlorotoxin (CTX, a tumor-targeting ligand), and demonstrated their specific targeting to malignant brain tumors by biophotonic imaging, biodistribution, and histological analyses. The PBdots have an average diameter of about 15 nm and exhibit high fluorescence quantum yield, which is the brightest nanoprobe at present among various fluorescent nanoparticles of similar size. This method provides a new nanoparticle-based diagnostic and therapeutic platform for clinical cancer diagnostics (*96*).

In addition to conjugation bioprobes, the CPs-based Nanoparticles were also excellent carriers for drug molecules and worked as a cargo to transfer the drug to target position. Thus, the CPs have been applied for efficient delivering high quantity of drug molecules (including DOX, cisplatin). Wang's group prepared a new CPN combining assembly of cationic CP PFO (CP 28, Scheme 1) and anionic poly (L-glutamic acid) conjugated with anticancer drug doxorubicin (PFO/PG-Dox) with the size of about 50 nm, which can be used for live-cell

Downloaded by UNIV DE SHERBROOKE on November 27, 2012 | http://pubs.acs.org
Publication Date (Web): November 26, 2012 | doi: 10.1021/bk-2012-1112.ch004

imaging (*97*). The fluorescence of the nanoparticle is highly quenched by Dox through electron transfer while recovers when the nanoparticles are exposed to carboxypeptidase or are taken up by cancer cells due to the hydrolysis of poly(L-glutamic acid). This multifunctional complex system can deliver Dox to targeted cells, detect the Dox release and image the cancer cells (Fig. 18). Their work shows good prospect for CP in simultaneous imaging and disease therapeutics. In 2011, they synthesized a new amphiphilic conjugated PT derivative (PT-Boc) to image human lung epithelial (A549) cells with good photostability and little toxicity. They linked the anticancer drug cisplatin to PT to obtain a conjugate PT-Pt and showed ability to monitor cellular distribution of cisplatin by fluorescence microscopy (*98*). Liu's group then reported a molecular brush based CPE-poly(ethylene glycol)-cisplatin nanoparticle (CPE-PEG-Pt) formulation as a FR/NIR fluorescent probe for in vivo imaging and cisplatin tracking in nude mice (*99*).

Downloaded by UNIV DE SHERBROOKE on November 27, 2012 | http://pubs.acs.org
Publication Date (Web): November 26, 2012 | doi: 10.1021/bk-2012-1112.ch004

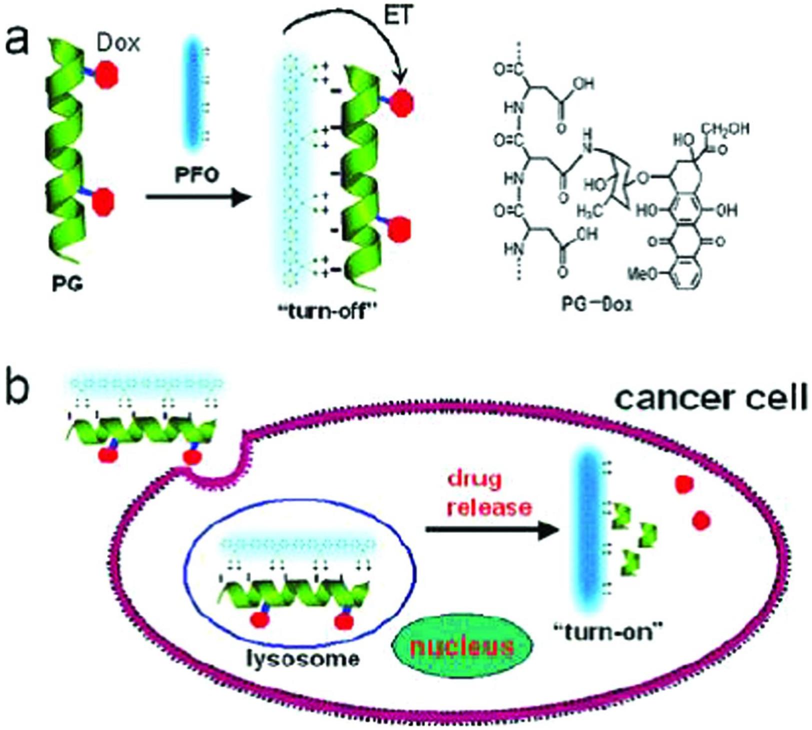

Figure 18. (a) Schematic illustration of PFO/PG-Dox complex system. (b) Schematic representation of uptake of the electrostatic complex nanoparticles into cancer cell, hydrolysis of poly(L-glutamic acid), release of Dox and recovery of the fluorescence of nanoparticle. Reprinted with permission from ref (79). Copyright (2010) American Chemical Society.

Conclusion

Water soluble fluorescent CPs and CPNs have been intensively studied for biosensor and bioimaging application due to their extraordinary signal amplification ability. Compared with other amplification technologies, the application of CPs and CPNs is simple and cost-effective. In this review, we discussed their applications on DNA, protein, other biological-revelant molecules detection and fluorescent imaging. As shown above, there has been tremendous progress in this field. Many detection methods with high sensitivity and selectivity based on water-suluble CPs have been established. Fluorescent imaging based on CPNs with high fluorescence brightness, excellent photostability, high selectivity and lower toxicity has been intensively explored. Nevertheless, there is much to be improved in this field. For example, the sensing mechanism based on the water-soluble polymer needs to be studied further. New efficient FRET or superquenching system needs to be explored. Increasing attention should be taken in the technology of protein array or chip with high selectivity, especially in detection of protein markers related with diseases. The synthesis of new fluorescent CPs that embodies multifunctional recognition side chain for new biological sensor and imaging application is also in high demand. Last but not least, how to improve their biocompatibility, decrease self-quenching and realize detection in situ is another major concern. For most applications of CPs in bioimaging and drug-delivery, most of them are focused on passive target through endocytosis way, while relatively less work explored active target and transportation by conjugation of bioprobe and drug molecules with CPs. It is still a long way to accurately localize target cells and act function of CPs-bioconjugates, as well as recognize their biodistribution and metabolism. It is envisaged that linkage of both bioprobes and drugs might be a nice way to simultaneous perform bioimaging and disease treatment for clinical theranostics (therapy and diagnostics).

Downloaded by UNIV DE SHERBROOKE on November 27, 2012 | http://pubs.acs.org
Publication Date (Web): November 26, 2012 | doi: 10.1021/bk-2012-1112.ch004

Acknowledgments

The authors would like to thank the Promotional Foundation for the Excellent Middle-Aged and Young Scientists of Shandong Province of China (BS2009SW040), the National Natural Science Foundation (20902096, 21104030), National Postdoctoral Science Foundation of China (No. 2012M510981) and a Project of Shandong Province Higher Educational Science and Technology Program (J11LB03).

References

1. Thomas, S. W., III; Joly, G. D.; Swager, T. M. Chemical Sensors Based on Amplifying Fluorescent Conjugated Polymers. *Chem. Rev.* **2007**, *107*, 1339–1386.
2. Swager, T. M. The Molecular Wire Approach to Sensory Signal Amplification. *Acc. Chem. Res.* **1998**, *31*, 201–207.

Downloaded by UNIV DE SHERBROOKE on November 27, 2012 | http://pubs.acs.org
Publication Date (Web): November 26, 2012 | doi: 10.1021/bk-2012-1112.ch004

3. Feng, F.; He, F.; An, L.; Wang, S.; Li, Y.; Zhu, D. Fluorescent Conjugated Polyelectrolytes for Biomacromolecule Detection. *Adv. Mater.* **2008**, *20*, 2959–2964.
4. Liu, B.; Bazan, G. C. Homogeneous Fluorescence-Based DNA Detection with Water-Soluble Conjugated Polymers. *Chem. Mater.* **2004**, *16*, 4467–4476.
5. Ho, H. A.; Najari, A.; Leclerc, M. Optical Detection of DNA and Proteins with Cationic Polythiophenes. *Acc. Chem. Res.* **2008**, *41*, 168–178.
6. Liu, X.; Fan, Q.; Huang, W. DNA Biosensors Based on Water-Soluble Conjugated Polymers. *Biosens. Bioelectron.* **2011**, *26*, 2154–64.
7. Liu, Y.; Ogawa, K.; Schanze, K. S. Conjugated Polyelectrolytes as Fluorescent Sensors. *J. Photochem. Photobiol., C* **2009**, *10*, 173–190.
8. Duarte, A.; Pu, K.-Y.; Liu, B.; Bazan, G. C. Recent Advances in Conjugated Polyelectrolytes for Emerging Optoelectronic Applications. *Chem. Mater.* **2011**, *23*, 501–515.
9. Li, K.; Liu, B. Water-Soluble Conjugated Polymers as the Platform for Protein Sensors. *Polym. Chem.* **2010**, *1*, 252–259.
10. Gaylord, B. S.; Heeger, A. J.; Bazan, G. C. DNA Detection Using Water-Soluble Conjugated Polymers and Peptide Nucleic Acid Probes. *Proc. Natl. Acad. Sci. U.S.A.* **2002**, *99*, 10954–7.
11. Xu, Q. H.; Gaylord, B. S.; Wang, S.; Bazan, G. C.; Moses, D.; Heeger, A. J. Time-Resolved Energy Transfer in DNA Sequence Detection Using Water-Soluble Conjugated Polymers: the Role of Electrostatic and Hydrophobic Interactions. *Proc. Natl. Acad. Sci. U.S.A.* **2004**, *101*, 11634–9.
12. Gaylord, B. S.; Massie, M. R.; Feinstein, S. C.; Bazan, G. C. SNP Detection Using Peptide Nucleic Acid Probes and Conjugated Polymers: Applications in Neurodegenerative Disease Identification. *Proc. Natl. Acad. Sci. U.S.A.* **2005**, *102*, 34–9.
13. Al Attar, H. A.; Norden, J.; O'Brien, S.; Monkman, A. P. Improved Single Nucleotide Polymorphisms Detection Using Conjugated Polymer/Surfactant System and Peptide Nucleic Acid. *Biosens. Bioelectron.* **2008**, *23*, 1466–72.
14. Liu, B.; Bazan, G. C. Interpolyelectrolyte Complexes of Conjugated Copolymers and DNA: Platforms for Multicolor Biosensors. *J. Am. Chem. Soc.* **2004**, *126*, 1942–1943.
15. Li, K.; Liu, B. Conjugated Polyelectrolyte Amplified Thiazole Orange Emission for Label Free Sequence Specific DNA Detection with Single Nucleotide Polymorphism Selectivity. *Anal. Chem.* **2009**, *81*, 4099–4105.
16. Gaylord, B. S.; Heeger, A. J.; Bazan, G. C. DNA Hybridization Detection with Water-Soluble Conjugated Polymers and Chromophore-Labeled Single-Stranded DNA. *J. Am. Chem. Soc.* **2003**, *125*, 896–900.
17. He, F.; Feng, F. D.; Duan, X. R.; Wang, S.; Li, Y. L.; Zhu, D. B. Selective and Homogeneous Fluorescent DNA Detection by Target-Induced Strand Displacement Using Cationic Conjugated Polyelectrolytes. *Anal. Chem.* **2008**, *80*, 2239–2243.
18. Ren, X. S.; Xu, Q. H. Label-Free DNA Sequence Detection with Enhanced Sensitivity and Selectivity Using Cationic Conjugated Polymers and PicoGreen. *Langmuir* **2009**, *25*, 43–47.

19. Pu, F.; Hu, D.; Ren, J.; Wang, S.; Qu, X. Universal Platform for Sensitive and Label-Free Nuclease Assay Based on Conjugated Polymer and DNA/Intercalating Dye Complex. *Langmuir* **2010**, *26*, 4540–5.
20. Jiang, G. X.; Susha, A. S.; Lutich, A. A.; Stefani, F. D.; Feldmann, J.; Rogach, A. L. Cascaded FRET in Conjugated Polymer/Quantum Dot/Dye-Labeled DNA Complexes for DNA Hybridization Detection. *ACS Nano* **2009**, *3*, 4127–4131.
21. Wang, J.; Liu, B. Fluorescence Resonance Energy Transfer Between an Anionic Conjugated Polymer and a Dye-Labeled Lysozyme Aptamer for Specific Lysozyme Detection. *Chem. Commun.* **2009**, 2284–6.
22. He, F.; Tang, Y.; Wang, S.; Li, Y.; Zhu, D. Fluorescent Amplifying Recognition for DNA G-Quadruplex Folding with a Cationic Conjugated Polymer: A Platform for Homogeneous Potassium Detection. *J. Am. Chem. Soc.* **2005**, *127*, 12343–12346.
23. He, F.; Tang, Y. L.; Yu, M. H.; Feng, F. D.; An, L. L.; Sun, H.; Wang, S.; Li, Y. L.; Zhu, D. B.; Bazan, G. C. Quadruplex-to-Duplex Transition of G-Rich Oligonucleotides Probed by Cationic Water-Soluble Conjugated Polyelectrolytes. *J. Am. Chem. Soc.* **2006**, *128*, 6764–6765.
24. Duan, X. R.; Li, Z. P.; He, F.; Wang, S. A Sensitive and Homogeneous SNP Detection Using Cationic Conjugated Polymers. *J. Am. Chem. Soc.* **2007**, *129*, 4154–4155.
25. Duan, X.; Wang, S.; Li, Z. Conjugated Polyelectrolyte-DNA Complexes for Multi-Color and One-Tube SNP Genotyping Assays. *Chem. Commun.* **2008**, 1302–4.
26. Duan, X.; Yue, W.; Liu, L.; Li, Z.; Li, Y.; He, F.; Zhu, D.; Zhou, G.; Wang, S. Single-Nucleotide Polymorphism (SNP) Genotyping Using Cationic Conjugated Polymers in Homogeneous Solution. *Nat. Protoc.* **2009**, *4*, 984–91.
27. Feng, F.; Wang, H.; Han, L.; Wang, S. Fluorescent Conjugated Polyelectrolyte as an Indicator for Convenient Detection of DNA Methylation. *J. Am. Chem. Soc.* **2008**, *130*, 11338–11343.
28. Feng, F.; Liu, L.; Wang, S. Fluorescent Conjugated Polymer-Based FRET Technique for Detection of DNA Methylation of Cancer Cells. *Nat. Protoc.* **2010**, *5*, 1255–64.
29. Liu, B.; Bazan, G. C. Tetrahydrofuran Activates Fluorescence Resonant Energy Transfer from a Cationic Conjugated Polyelectrolyte to Fluorescein-Labeled DNA in Aqueous Media. *Chem. Asian J.* **2007**, *2*, 499–504.
30. Pu, K.-Y.; Fang, Z.; Liu, B. Effect of Charge Density on Energy-Transfer Properties of Cationic Conjugated Polymers. *Adv. Funct. Mater.* **2008**, *18*, 1321–1328.
31. Pu, K. Y.; Liu, B. Optimizing the Cationic Conjugated Polymer-Sensitized Fluorescent Signal of Dye Labeled Oligonucleotide for Biosensor Applications. *Biosens. Bioelectron.* **2009**, *24*, 1067–73.
32. Liu, B.; Bazan, G. C. Optimization of the Molecular Orbital Energies of Conjugated Polymers for Optical Amplification of Fluorescent Sensors. *J. Am. Chem. Soc.* **2006**, *128*, 1188–1196.

Downloaded by UNIV DE SHERBROOKE on November 27, 2012 | http://pubs.acs.org
Publication Date (Web): November 26, 2012 | doi: 10.1021/bk-2012-1112.ch004

33. Huang, Y. Q.; Liu, X. F.; Fan, Q. L.; Wang, L.; Song, S.; Wang, L. H.; Fan, C.; Huang, W. Tuning Backbones and Side-Chains of Cationic Conjugated Polymers for Optical Signal Amplification of Fluorescent DNA Detection. *Biosens. Bioelectron.* **2009**, *24*, 2973–8.
34. Al Attar, H. A.; Monkman, A. P. FRET and Competing Processes between Conjugated Polymer and Dye Substituted DNA Strands: A Comparative Study of Probe Selection in DNA Detection. *Biomacromolecules* **2009**, *10*, 1077–1083.
35. Ho, H. A.; Boissinot, M.; Bergeron, M. G.; Corbeil, G.; Dore, K.; Boudreau, D.; Leclerc, M. Colorimetric and Fluorometric Detection of Nucleic Acids Using Cationic Polythiophene Derivatives. *Angew. Chem., Int. Ed.* **2002**, *41*, 1548–1551.
36. Béra-Abérem, M.; Ho, H.-A.; Leclerc, M. Functional polythiophenes as optical chemo- and biosensors. *Tetrahedron* **2004**, *60*, 11169–11173.
37. Tang, Y. L.; Feng, F. D.; He, F.; Wang, S.; Li, Y. L.; Zhu, D. B. Direct Visualization of Enzymatic Cleavage and Oxidative Damage by Hydroxyl Radicals of Single-Stranded DNA with a Cationic Polythiophene Derivative. *J. Am. Chem. Soc.* **2006**, *128*, 14972–14976.
38. Zhang, Y.; Li, Z.; Cheng, Y.; Wang, Y. Label-Free Genotyping of Single-Nucleotide Polymorphisms for DNA and RNA Targets Using a Cationic Polythiophene Derivate. *Talanta* **2009**, *79*, 27–31.
39. Ho, H. A.; Leclerc, M. Optical Sensors Based on Hybrid Aptamer/Conjugated Polymer Complexes. *J. Am. Chem. Soc.* **2004**, *126*, 1384–1387.
40. Béra Abérem, M.; Najari, A.; Ho, H. A.; Gravel, J. F.; Nobert, P.; Boudreau, D.; Leclerc, M. Protein Detecting Arrays Based on Cationic Polythiophene–DNA-Aptamer Complexes. *Adv. Mater.* **2006**, *18*, 2703–2707.
41. Liu, X.; Tang, Y.; Wang, L.; Zhang, J.; Song, S.; Fan, C.; Wang, S. Optical Detection of Mercury(II) in Aqueous Solutions by Using Conjugated Polymers and Label-Free Oligonucleotides. *Adv. Mater.* **2007**, *19*, 1471–1474.
42. Wang, L.; Liu, X.; Yang, Q.; Fan, Q.; Song, S.; Fan, C.; Huang, W. A Colorimetric Strategy Based on a Water-Soluble Conjugated Polymer for Sensing pH-Driven Conformational Conversion of DNA i-motif Structure. *Biosens. Bioelectron.* **2010**, *25*, 1838–42.
43. Chen, L. H.; McBranch, D. W.; Wang, H. L.; Helgeson, R.; Wudl, F.; Whitten, D. G. Highly Sensitive Biological and Chemical Sensors Based on Reversible Fluorescence Quenching in a Conjugated Polymer. *Proc. Natl. Acad. Sci. U.S.A.* **1999**, *96*, 12287–12292.
44. Kumaraswamy, S.; Bergstedt, T.; Shi, X.; Rininsland, F.; Kushon, S.; Xia, W.; Ley, K.; Achyuthan, K.; McBranch, D.; Whitten, D. Fluorescent-Conjugated Polymer Superquenching Facilitates Highly Sensitive Detection of Proteases. *Proc. Natl. Acad. Sci. U.S.A.* **2004**, *101*, 7511–5.
45. Feng, F.; Tang, Y.; Wang, S.; Li, Y.; Zhu, D. Continuous Fluorometric Assays for Acetylcholinesterase Activity and Inhibition with Conjugated Polyelectrolytes. *Angew. Chem.* **2007**, *119*, 8028–8032.

Downloaded by UNIV DE SHERBROOKE on November 27, 2012 | http://pubs.acs.org
Publication Date (Web): November 26, 2012 | doi: 10.1021/bk-2012-1112.ch004

46. Wang, L.; Pu, K. Y.; Li, J.; Qi, X.; Li, H.; Zhang, H.; Fan, C.; Liu, B. A Graphene-Conjugated Oligomer Hybrid Probe for Light-up Sensing of Lectin and Escherichia coli. *Adv. Mater.* **2011**, *23*, 4386–91.

47. An, L.; Tang, Y.; Wang, S.; Li, Y.; Zhu, D. A Fluorescence Ratiometric Protein Assay Using Light-Harvesting Conjugated Polymers. *Macromol. Rapid Commun.* **2006**, *27*, 993–997.

48. Fan, C. H.; Plaxco, K. W.; Heeger, A. J. High-Efficiency Fluorescence Quenching of Conjugated Polymers by Proteins. *J. Am. Chem. Soc.* **2002**, *124*, 5642–5643.

49. Wang, D.; Gong, X.; Heeger, P. S.; Rininsland, F.; Bazan, G. C.; Heeger, A. J. Biosensors from Conjugated Polyelectrolyte Complexes. *Proc. Natl. Acad. Sci. U.S.A.* **2002**, *99*, 49–53.

50. Yu, D.; Zhang, Y.; Liu, B. Interpolyelectrolyte Complexes of Anionic Water-Soluble Conjugated Polymers and Proteins as Platforms for Multicolor Protein Sensing and Quantification. *Macromolecules* **2008**, *41*, 4003–4011.

51. Shi, J.; Cai, L.; Pu, K. Y.; Liu, B. Synthesis and Characterization of Water-Soluble Conjugated Glycopolymer for Fluorescent Sensing of Concanavalin A. *Chem. Asian J.* **2010**, *5*, 301–8.

52. An, L.; Tang, Y.; Feng, F.; He, F.; Wang, S. Water-Soluble Conjugated Polymers for Continuous and Sensitive Fluorescence Assays for Phosphatase and Peptidase. *J. Mater. Chem.* **2007**, *17*, 4147–4152.

53. Pu, K. Y.; Zhan, R.; Liu, B. Conjugated Polyelectrolyte Blend as Perturbable Energy Donor-Acceptor Assembly with Multicolor Fluorescence Response to Proteins. *Chem. Commun.* **2010**, *46*, 1470–2.

54. Herland, A.; Nilsson, K. P. R.; Olsson, J. D. M.; Hammarstro¨m, P.; Konradsson, P.; Ingana¨s, O. Synthesis of a Regioregular Zwitterionic Conjugated Oligoelectrolyte, Usable as an Optical Probe for Detection of Amyloid Fibril Formation at Acidic pH. *J. Am. Chem. Soc.* **2005**, *127*, 2317–2323.

55. Nilsson, K. P. R.; Inganas, O. Optical Emission of a Conjugated Polyelectrolyte: Calcium-Induced Conformational Changes in Calmodulin and Calmodulin-Calcineurin Interactions. *Macromolecules* **2004**, *37*, 9109–9113.

56. Nilsson, K. P.; Rydberg, J.; Baltzer, L.; Inganas, O. Self-Assembly of Synthetic Peptides Control Conformation and Optical Properties of a Zwitterionic Polythiophene Derivative. *Proc. Natl. Acad. Sci. U.S.A.* **2003**, *100*, 10170–4.

57. Nilsson, K. P.; Hammarstrom, P.; Ahlgren, F.; Herland, A.; Schnell, E. A.; Lindgren, M.; Westermark, G. T.; Inganas, O. Conjugated Polyelectrolytes--Conformation-Sensitive Optical Probes for Staining and Characterization of Amyloid Deposits. *ChemBioChem* **2006**, *7*, 1096–104.

58. Herland, A.; Inganäs, O. Conjugated Polymers as Optical Probes for Protein Interactions and Protein Conformations. *Macromol. Rapid Commun.* **2007**, *28*, 1703–1713.

59. Li, Y.; Bai, H.; Li, C.; Shi, G. Colorimetric Assays for Acetylcholinesterase Activity and Inhibitor Screening Based on the Disassembly-Assembly of a

Downloaded by UNIV DE SHERBROOKE on November 27, 2012 | http://pubs.acs.org
Publication Date (Web): November 26, 2012 | doi: 10.1021/bk-2012-1112.ch004

Water-Soluble Polythiophene Derivative. *ACS Appl. Mater. Interfaces* **2011**, *3*, 1306–10.

60. Kushon, S. A.; Bradford, K.; Marin, V.; Suhrada, C.; Armitage, B. A.; McBranch, D.; Whitten, D. Detection of Single Nucleotide Mismatches via Fluorescent Polymer Superquenching. *Langmuir* **2003**, *19*, 6456–6464.
61. Kushon, S. A.; Ley, K. D.; Bradford, K.; Jones, R. M.; McBranch, D.; Whitten, D. Detection of DNA Hybridization via Fluorescent Polymer Superquenching. *Langmuir* **2002**, *18*, 7245–7249.
62. Xu, H.; Wu, H.; Huang, F.; Song, S.; Li, W.; Cao, Y.; Fan, C. Magnetically Assisted DNA Assays: High Selectivity Using Conjugated Polymers for Amplified Fluorescent Transduction. *Nucleic Acids Res.* **2005**, *33*, e83.
63. Wang, Y.; Liu, B. Amplified Fluorescence Turn-On Assay for Mercury(II) Detection and Quantification based on Conjugated Polymer and Silica Nanoparticles. *Macromol. Rapid Commun.* **2009**, *30*, 498–503.
64. Wang, Y.; Pu, K. Y.; Liu, B. Anionic Conjugated Polymer with Aptamer-Functionalized Silica Nanoparticle for Label-Free Naked-Eye Detection of Lysozyme in Protein Mixtures. *Langmuir* **2010**, *26*, 10025–30.
65. Wang, Y.; Liu, B. Conjugated Polymer as a Signal Amplifier for Novel Silica Nanoparticle-Based Fluoroimmunoassay. *Biosens. Bioelectron.* **2009**, *24*, 3293–8.
66. Wang, Y.; Liu, B. Silica Nanoparticle Assisted DNA Assays for Optical Signal Amplification of Conjugated Polymer Based Fluorescent Sensors. *Chem. Commun.* **2007**, 3553.
67. Nilsson, K. P.; Inganas, O. Chip and Solution Detection of DNA Hybridization Using a Luminescent Zwitterionic Polythiophene Derivative. *Nat. Mater.* **2003**, *2*, 419–24.
68. Liu, B.; Bazan, G. C. Methods for Strand-Specific DNA Detection with Cationic Conjugated Polymers Suitable for Incorporation into DNA Chips and Microarrays. *Proc. Natl. Acad. Sci. U.S.A.* **2005**, *102*, 589–93.
69. Feng, X.; Xu, Q.; Liu, L.; Wang, S. A New Light-Harvesting Conjugated Polyelectrolyte Microgel for DNA and Enzyme Detections. *Langmuir* **2009**, *25*, 13737–41.
70. Li, C.; Numata, M.; Takeuchi, M.; Shinkai, S. A Sensitive Colorimetric and Fluorescent Probe Based on a Polythiophene Derivative for the Detection of ATP. *Angew. Chem.* **2005**, *117*, 6529–6532.
71. Xing, C.; Yu, M.; Wang, S.; Shi, Z.; Li, Y.; Zhu, D. Fluorescence Turn-On Detection of Nitric Oxide in Aqueous Solution Using Cationic Conjugated Polyelectrolytes. *Macromol. Rapid Commun.* **2007**, *28*, 241–245.
72. Y., Z. R.; Fang, Z.; Liu, B. Naked-Eye Detection and Quantification of Heparin in Serum with a Cationic Polythiophene. *Anal. Chem.* **2010**, *82*, 1326–1333.
73. He, F.; Feng, F.; Wang, S.; Li, Y.; Zhu, D. Fluorescence Ratiometric Assays of Hydrogen Peroxide and Glucose in Serum Using Conjugated Polyelectrolytes. *J. Mater. Chem.* **2007**, *17*, 3702–2707.
74. Pu, K.-Y.; Liu, B. Intercalating Dye Harnessed Cationic Conjugated Polymer for Real-Time Naked-Eye Recognition of Double-Stranded DNA in Serum. *Adv. Funct. Mater.* **2009**, *19*, 1371–1378.

Downloaded by UNIV DE SHERBROOKE on November 27, 2012 | http://pubs.acs.org
Publication Date (Web): November 26, 2012 | doi: 10.1021/bk-2012-1112.ch004

75. Wang, Y.; Liu, B.; Mikhailovsky, A.; Bazan, G. C. Conjugated Polyelectrolyte-Metal Nanoparticle Platforms for Optically Amplified DNA detection. *Adv. Mater.* **2010**, *22*, 656–9.
76. L.-Viger, M.; Brouard, D.; Boudreau, D. Plasmon-Enhanced Resonance Energy Transfer from a Conjugated Polymer to Fluorescent Multilayer Core−Shell Nanoparticles: A Photophysical Study. *J. Phys. Chem. C* **2011**, *115*, 2974–2981.
77. Bjork, P.; Peter, R. N. K.; Lenner, L.; Kagedal, B.; Persson, B.; Inganas, O.; Jonasson, J. Conjugated Polythiophene Probes Target Lysosome-Related Acidic Vacuoles in Cultured Primary Cells. *Mol. Cell Probes* **2007**, *21*, 329–37.
78. McRae, R. L.; Phillips, R. L.; Kim, I. B.; Bunz, U. H. F.; Fahrni, C. J. Molecular Recognition Based on Low-Affinity Polyvalent Interactions: Selective Binding of a Carboxylated Polymer to Fibronectin Fibrils of Live Fibroblast Cells. *J. Am. Chem. Soc.* **2008**, *130*, 7851–7853.
79. Tuncel, D.; Demir, H. V. Conjugated Polymer Nanoparticles. *Nanoscale* **2010**, *2*, 484–94.
80. Fernando, L. P.; Kandel, P. K.; Yu, J.; McNeill, J.; Ackroyd, P. C.; Christensen, K. A. Mechanism of Cellular Uptake of Highly Fluorescent Conjugated Polymer Nanoparticles. *Biomacromolecules* **2010**, *11*, 2675–2682.
81. Moon, J. H.; McDaniel, W.; Maclean, P.; Hancock, L. F. Live-Cell-Permeable Poly(p-phenylene ethynylene). *Angew. Chem., Int. Ed.* **2007**, *46*, 8223–5.
82. Wu, C. F.; Bull, B.; Szymanski, C.; Christensen, K.; McNeill, J. Multicolor Conjugated Polymer Dots for Biological Fluorescence Imaging. *ACS Nano* **2008**, *2*, 2415–2423.
83. Wu, C.; Bull, B.; Christensen, K.; McNeill, J. Ratiometric Single-Nanoparticle Oxygen Sensors for Biological Imaging. *Angew. Chem., Int. Ed.* **2009**, *48*, 2741–5.
84. Pecher, J.; Huber, J.; Winterhalder, M.; Zumbusch, A.; Mecking, S. Tailor-Made Conjugated Polymer Nanoparticles for Multicolor and Multiphoton Cell Imaging. *Biomacromolecules* **2010**, *11*, 2776–2780.
85. Kim, S.; Lim, C. K.; Na, J.; Lee, Y. D.; Kim, K.; Choi, K.; Leary, J. F.; Kwon, I. C. Conjugated Polymer Nanoparticles for Biomedical in Vivo Imaging. *Chem. Commun.* **2010**, *46*, 1617–9.
86. Tang, F.; He, F.; Cheng, H.; Li, L. Self-Assembly of Conjugated Polymer-Ag@SiO2 Hybrid Fluorescent Nanoparticles for Application to Cellular Imaging. *Langmuir* **2010**, *26*, 11774–8.
87. Tan, H.; Zhang, Y.; Wang, M.; Zhang, Z.; Zhang, X.; Yong, A. M.; Wong, S. Y.; Chang, A. Y.; Chen, Z. K.; Li, X.; Choolani, M.; Wang, J. Silica-Shell Cross-Linked Micelles Encapsulating Fluorescent Conjugated Polymers for Targeted Cellular Imaging. *Biomaterials* **2012**, *33*, 237–46.
88. Pu, K.-Y.; Li, K.; Shi, J.; Liu, B. Fluorescent Single-Molecular Core−Shell Nanospheres of Hyperbranched Conjugated Polyelectrolyte for Live-Cell Imaging. *Chem. Mater.* **2009**, *21*, 3816–3822.

Downloaded by UNIV DE SHERBROOKE on November 27, 2012 | http://pubs.acs.org
Publication Date (Web): November 26, 2012 | doi: 10.1021/bk-2012-1112.ch004

89. Feng, X.; Tang, Y.; Duan, X.; Liu, L.; Wang, S. Lipid-Modified Conjugated Polymer Nanoparticles for Cell Imaging and Transfection. *J. Mater. Chem.* **2010**, *20*, 1312–1316.
90. Feng, X.; Yang, G.; Liu, L.; Lv, F.; Yang, Q.; Wang, S.; Zhu, D. A Convenient Preparation of Multi-Spectral Microparticles by Bacteria-Mediated Assemblies of Conjugated Polymer Nanoparticles for Cell Imaging and Barcoding. *Adv. Mater.* **2012**, *24*, 637–41.
91. Chong, H.; Nie, C.; Zhu, C.; Yang, Q.; Liu, L.; Lv, F.; Wang, S. Conjugated Polymer Nanoparticles for Light-Activated Anticancer and Antibacterial Activity with Imaging Capability. *Langmuir* **2012**, *28*, 2091–8.
92. Kim, I. B.; Shin, H.; Garcia, A. J.; Bunz, U. H. F. Use of a Folate-PPE Conjugate To Image Cancer Cells in Vitro. *Bioconjugate Chem.* **2007**, *18*, 815–820.
93. Pu, K.-Y.; Li, K.; Liu, B. A Molecular Brush Approach to Enhance Quantum Yield and Suppress Nonspecific Interactions of Conjugated Polyelectrolyte for Targeted Far-Red/Near-Infrared Fluorescence Cell Imaging. *Adv. Funct. Mater.* **2010**, *20*, 2770–2777.
94. Ding, D.; Pu, K. Y.; Li, K.; Liu, B. Conjugated Oligoelectrolyte-Polyhedral Oligomeric Silsesquioxane Loaded pH-Responsive Nanoparticles for Targeted Fluorescence Imaging of Cancer Cell Nucleus. *Chem. Commun.* **2011**, *47*, 9837–9.
95. Wu, C. F.; Schneider, T.; Zeigler, M.; B., Y. J.; Schiro, P. G.; Burnham, D. R.; D., M. J.; Chiu, D. T. Bioconjugation of Ultrabright Semiconducting Polymer Dots for Specific Cellular Targeting. *J. Am. Chem. Soc.* **2010**, *132*, 15410–15417.
96. Wu, C.; Hansen, S. J.; Hou, Q.; Yu, J.; Zeigler, M.; Jin, Y.; Burnham, D. R.; McNeill, J. D.; Olson, J. M.; Chiu, D. T. Design of Highly Emissive Polymer Dot Bioconjugates for in Vivo Tumor Targeting. *Angew. Chem., Int. Ed.* **2011**, *50*, 3430–4.
97. Feng, X.; Lv, F.; Liu, L.; Tang, H.; Xing, C.; Yang, Q.; Wang, S. Conjugated Polymer Nanoparticles for Drug Delivery and Imaging. *ACS Appl. Mater. Interfaces* **2010**, *2*, 2429–35.
98. Tang, H.; Xing, C.; Liu, L.; Yang, Q.; Wang, S. Synthesis of Amphiphilic Polythiophene for Cell Imaging and Monitoring the Cellular Distribution of a Cisplatin Anticancer Drug. *Small* **2011**, *7*, 1464–70.
99. Ding, D.; Li, K.; Zhu, Z.; Pu, K. Y.; Hu, Y.; Jiang, X.; Liu, B. Conjugated Polyelectrolyte-Cisplatin Complex Nanoparticles for Simultaneous in Vivo Imaging and Drug Tracking. *Nanoscale* **2011**, *3*, 1997–2002.

Downloaded by UNIV DE SHERBROOKE on November 27, 2012 | http://pubs.acs.org
Publication Date (Web): November 26, 2012 | doi: 10.1021/bk-2012-1112.ch004

Downloaded by NORTH CAROLINA STATE UNIV on November 27, 2012 | http://pubs.acs.org
Publication Date (Web): November 26, 2012 | doi: 10.1021/bk-2012-1112.ch005

Chapter 5

Biomolecular Recognition: Nanotransduction and Nanointervention

**Elizabeth Crew, Stephanie Lim, Hong Yan, Shiyao Shan,
Jun Yin, Liqin Lin, Rameshwori Loukrakpam, Lefu Yang,
Jin Luo, and Chuan-Jian Zhong***

**Department of Chemistry, State University of New York at Binghamton,
Binghamton, New York 13902, U.S.A.
*E-mail: cjzhong@binghamton.edu**

Detecting or intervening in biomolecular processes for medical diagnostics, drug delivery, and bacterial inactivation requires a functional probe which interfaces not only the targeted biomolecules but also provides an external stimulus. Metal nanoparticles serve as such functional probes. A key challenge is the ability to tailor the size, compositiosn, urface, and magnetic properties for a controllable biomolecular recognition, biocompatibility, toxicity, transduction, and intervention. Gold or silver based nanoparticles enable effective biomolecular recognition, biocompatibility and transduction, which, upon introducing a magnetic component as the core, impart intervention capability and reduced toxicity. This Chapter highlights a few examples in recent explorations of such biomolecular recognition. The nanoparticles are effective in probing DNA assembly for protein binding/cutting processes relevant to the DNA binding protein *p53*. The nanoprobes are also effective in delivering miRNAs to multiple myeloma cells for cell transfection and gene knockdown studies. For biologically relevant thiol-containing amino acids, the nanoprobes function not only as a detection platform, but also a driving force for chiral recognition. The magnetic core-shell nanoparticles enable an effective bio-separation function in

In Functional Nanoparticles for Bioanalysis, Nanomedicine, and Bioelectronic Devices Volume 1; Hepel, M., et al.;
ACS Symposium Series; American Chemical Society: Washington, DC, 2012.

protein recognition and bacterial inactivation. Each of the examples demonstrates the important role of the nanoprobe functionality in nano-transduction and nano-intervention of biomolecular recognition.

Introduction

The use of nanoparticles for the detection, manipulation, targeting or transport of biomolecules is a topic of broad interest having important applications in many different areas, including biosensing, medical diagnosis, and treatment of disease. Since the pioneering work by Mirkin and co-workers (*1–3*), there has been an explosion of research in explorations of gold based nanoparticles (Au NPs) coupled with DNA, RNA, and other biomolecules for drug delivery (*4–6*), disease detection and treatment (*4*, *6–9*), bio-sensing (*5*, *10–12*), materials synthesis (*13–15*), tissue engineering (*16*, *17*) and many other applications (*17–21*). The study of silver based nanoparticles (Ag NPs) have also attracted increasing interest in exploiting their antimicrobial properties, including wound dressings for antimicrobial action (*22*, *23*), mechanistic studies of biological responses (*24*), ecotoxicity on sea animals (*25*), and shape-dependent antibacterial activity (*26*).

The interests in exploiting nanoparticles and nanoparticle assemblies for recognition of various functional molecules and biomolecules largely stem from their unique electrical, optical, magnetic, catalytic properties, in addition to the inherent high surface area to volume ratio and the emergence of collective and nanoscale properties. The incorporation of macromolecules into metal or semiconductor nanoparticles have been demonstrated to produce interesting photo-induced charge transfer and separation properties (*27*, *28*). The tunable electrical properties of thin film assemblies of metal nanoparticles mediated by bifunctional mediators have been shown to function chemically sensitive materials for chemical sensors (*29–34*). Other functional materials make use of the optical properties of nanoparticles and assemblies such as light scattering and surface plasmon resonance (*35–38*). In addition, understanding how the functional properties correlate with the interparticle molecular interactions is very important for designing novel nanoparticle assemblies (*32*, *39*, *40*) mediated by thiol-containing amino acids (*41–43*), dyes (*44*) and fullerenes (*45*, *46*). These mediators provide well-defined structures or optical/spectroscopic signatures for manipulating the interparticle structural properties (*47*). For example, the study of how surface enhanced Raman scattering (SERS) effect of molecules on Au and Ag NPs is related to interparticle “hot spots” or enhanced plasmonic coupling field has captured growing interests in both experimental and theoretical investigations (*48–50*). There have been increasing examples focusing on labeling protein-functionalized gold and magnetic nanoparticles for detecting specific antibody/antigen binding events (*51*, *52*), and exploiting Au-coated magnetic core@shell nanoparticles (M@Au NPs) and assemblies (*53–55*) for spectroscopic bioassay coupled with magnetic bio-separation. Each of these studies involves the design of metal nanoparticles, which either interface directly with the targeted biomolecules to produce electrical, optical or

Downloaded by NORTH CAROLINA STATE UNIV on November 27, 2012 | http://pubs.acs.org
Publication Date (Web): November 26, 2012 | doi: 10.1021/bk-2012-1112.ch005

spectroscopic signals, or provide a magnetically or optically responsive platform to biomolecular interactions and reactivities. To achieve these functions, a key challenge is the ability to tailor the size, composition, surface, and magnetic properties for a controllable biomolecular recognition, biocompatibility, toxicity, transduction, and intervention, which has become one of the important focal areas of nanotechnological and biotechnological research activities in recent years.

In this Chapter, we highlight several areas of our recent studies aimed at addressing the challenges in biomolecular recognition using metal nanoparticles. First, some insights into the reactivity of a restriction enzyme on *p53*-recognition DNA-mediated assembly of Au NPs will be discussed, in relation to the development of nanoprobe strategies for detecting *p53* protein recogniton (*56*, *57*). Second, the exploitation of Au NPs as a vehicle for conjugating miRNAs will be discussed, which has implications for the development of controlled delivery in cell transfection studies (*58*). Third, assemblies of Au NPs mediated by thiol-containing amino acids, small peptides and proteins will be discussed, focusing on the control of interparticle molecular interactions for developing effective bioassay strategies (*42*, *43*, *51*, *52*, *59*, *60*). Last, the exploitation of silver coated magnetic nanoparticles as functional antibacterial agents will be discussed, which has implications for potential control or reduction of nanoparticle induced toxicity to human health (*61*).

Downloaded by NORTH CAROLINA STATE UNIV on November 27, 2012 | http://pubs.acs.org
Publication Date (Web): November 26, 2012 | doi: 10.1021/bk-2012-1112.ch005

Enzymatic Reactivity on *p53* Recognition DNA-Mediated Assembly

Extensive research efforts have been aimed at understanding the DNA-based nanoparticle assemblies (*62–86*), in which Au NPs are often used for detecting certain enzymes and proteins associated with diseases and pathogens through changes in the optical properties of the nanoparticles. One of the most widely studied DNA binding proteins, in relation to cancer, is the *p53* protein, mutations of which are found in more than 50% of all tumors (*87*). A scintillation proximity assay was recently used to analyze several known *p53* recognition sites, specifically the *mdm2*, *p21* and *cyclin G* genes, which provided important insights for understanding the role DNA transcription plays in diseases such as cancer (*88*).

The assembly of Au NPs by complimentary-strand binding of DNAs, designed using the *cyclin G* promoter sequence (*88*), has recently been demonstrated (*56*). As conceptually illustrated in Scheme 1, the top and bottom single-stranded DNA (ss-DNA) are conjugated to Au NPs. The interparticle complimentary binding of the top and bottom DNAs leads to the formation of a double strand in between Au NPs, which provides a *p53* recognition site.

One approach to probing the interactions and reactivities of the double-stranded DNAs (ds-DNAs) that are associated with the interparticle properties of the nanoparticle assembly is based on restriction enzyme cutting (*56*). For example, *MspI* is a restriction enzyme that cuts the ds-DNAs at a specific site. As illustrated in Scheme 2, the complementary bound DNAs in the assembly of DNA-Au NPs can be cut by an enzymatic reaction at a specific site. Upon assembly of the nanoparticles via complementary binding of DNAs, the restriction enzyme can be added to the assembly solution. If the cutting were achieved, disassembly would occur. A difference of the disassembled nanoparticles from the assembled nanoparticles would be detectable by spectroscopic techniques.

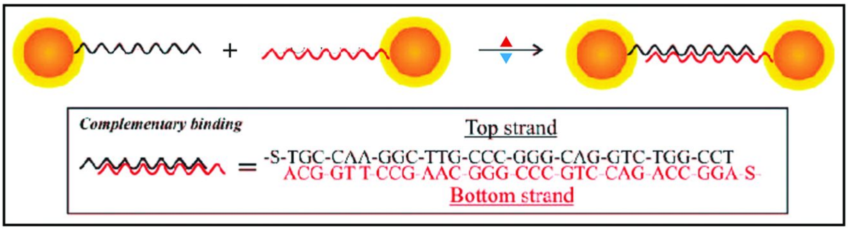
+
Complementary binding
Top strand
=
-S-TGC-CAA-GGC-TTG-CCC-GGG-CAG-GTC-TGG-CCT
ACG-GTT-CCG-AAC-GGG-CCC-GTC-CAG-ACC-GGA-S-
Bottom strand

Scheme 1. Illustration of the assembly of top strand (black) and bottom strand (red) through complementary strand binding of DNAs designed using the cyclin G promoter sequence for p53 recognition

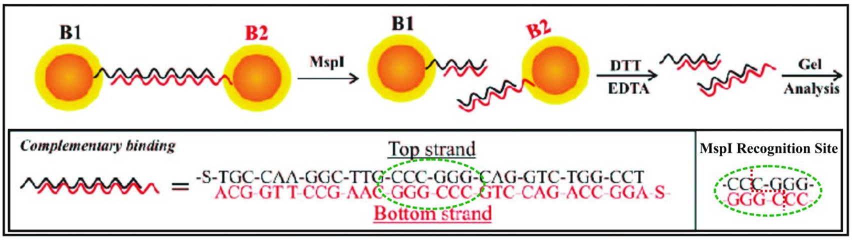
B1
B2
MspI
B1
B2
DTT
EDTA
Gel
Analysis
Complementary binding
Top strand
=
-S-TGC-CAA-GGC-TTG-CCC-GGG-CAG-GTC-TGG-CCT
ACG-GTT-CCG-AAC-GGG-CCC-GTC-CAG-ACC-GGA-S-
Bottom strand
MspI Recognition Site
-CCC-GGG-
GGG-CCC

Scheme 2. A schematic diagram (not to scale) illustrating the disassembly of the DNA-AuNPs assembly using MspI restriction enzyme and a subsequent detachment from Au NPs. Also included is the specific DNA sequence and a diagram showing the MspI cleavage site. (Adapted with permission from reference (56). Copyright 2008 American Chemical Society.)

One method to confirm the cutting is to analyze the cut DNA strands by gel electrophoresis. Typically, the addition of EDTA to the solution should inactivate the enzyme, and the addition of DTT should detach the nanoparticles from the DNAs (*80–83*). The released DNAs can then be analyzed using polyacrylamide gel electrophoresis separation. Indeed, the disassembly of the DNA-assembled Au NPs was demonstrated using a restriction enzyme, *MspI*, with a recognition site on the target DNA. The observed digestion is shown in Figure 1.

Downloaded by NORTH CAROLINA STATE UNIV on November 27, 2012 | http://pubs.acs.org
Publication Date (Web): November 26, 2012 | doi: 10.1021/bk-2012-1112.ch005

Downloaded by NORTH CAROLINA STATE UNIV on November 27, 2012 | http://pubs.acs.org
Publication Date (Web): November 26, 2012 | doi: 10.1021/bk-2012-1112.ch005

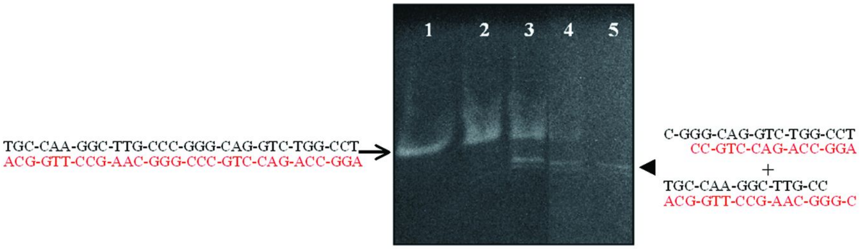

Figure 1. Gel electrophoresis of cut DNAs from the DNA-AuNPs assembly. Assembled DNA-AuNPs (51 µL) treated without (lane 1) and with 300 units of the MspI restriction enzyme for 0 (lane 2), 1 (lane 3), 5 (lane 4) and 7 hrs (lane 5). The arrow and arrowhead mark the positions of uncut and cut DNAs, respectively. (Adapted with permission from reference (56). Copyright 2008 American Chemical Society.)

As shown in Figure 1, in the presence of *MspI*, cutting of the ds-DNA assembled nanoparticles was observed in a time dependent manner. The smaller DNA bands that appear, in lanes 3-5, during enzyme digestion correspond to the fragments produced when the free oligonucleotides are cleaved. The *MspI* induced cutting of the assembled DNA-nanoparticles is similar to the observation reported previously for a DNA-nanoparticle assembly system using *EcoRI* and other restriction enzymes (*80–83*).

A similar study with a different approach to the cutting has also been demonstrated, which involved colorimetric detection of enzymatic cleaving and oxidative stress of DNA (*57*). The fact that DNAs adsorbed on AuNPs prevent salt induced aggregation of AuNPs; which was exploited for colorimetric detection. When the DNAs are subjected to enzymatic cleavage or oxidative damage fragmentation occurs, leading to a detectable colorimetric change (*57*).

In our latest work, we have demonstrated the ability of surface enhanced Raman scattering (SERS) detection of the DNA-mediated assembly and the enzymatic cleavage processes. In this approach, a Raman active molecule, mercaptobenzoic acid (MBA), is labeled on selected Au NPs (*47*, *51*, *52*). The formation of interparticle "hot spots" during the DNA-mediated assembly of Au NPs with the labeled Au NPs leads to an enhancement of the Raman signals at the characteristic wavenumbers. When an enzyme is used to cleave the assembly, the number of "hot spots" decreases, leading consequently to a decrease of the Raman signal, as shown in Figure 2, the detected diagnostic bands of MBA label (a) provides a measure of the assembly of AuNPs by the DNAs, whereas the reduced SERS intensity (b) serves as a gauge of the cleaving of double strand DNAs in the assembly by restriction enzyme.

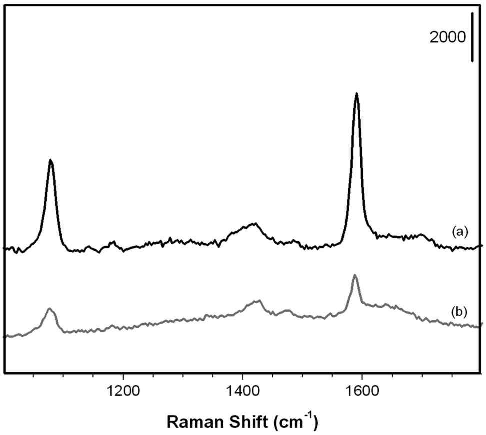

Figure 2. SERS spectra showing a solution sample of the DNA-AuNPs assembly before (a) and after restriction enzyme cutting (b). Some AuNPs are labeled with MBA as a Raman reporter molecule.

The oligonucleotide-complementary binding in the assembly processes is shown to be an effective strategy for the assembly of Au NPs. Cutting the DNA-assembled Au NPs using a restriction enzyme is shown to be a viable strategy for probing the interparticle properties. Further delineation of the quantitative aspects of the assembly and cutting processes, and the use of this strategy for bioassays of *p53* recognition is part of our on-going efforts.

MicroRNA-Conjugated Gold Nanoparticles for Cell Transfection

There has been increasing interest in delivering small strands of RNA, e.g., microRNA (miRNA), into cells for genetic manipulation or cellular marking (*89–107*). The association of miRNA with mRNA (messenger RNA) has been identified in relation to cancer treatments (*92*), such as the resistance of multiple myeloma (MM) to glucocorticoid treatment (*99*). Au NPs have been utilized for the delivery of siRNA (small interfering RNA) into cells for efficient knockdown of target genes without significant cytotoxicity (*98*, *108*). This type of delivery vehicle exploits the unique optical properties (*3*), low cytotoxicity (*108*, *109*), and enhanced lifespan in the blood stream (*110*) of Au NPs for cancer treatment or repression of certain genes (*111*). The importance of miRNA in the treatment of cancer and for the manipulation of genetic expression has been demonstrated recently (*99–101*). For instance, miR-130b was found to be expressed differently in glucocorticoid-sensitive versus glucocorticoid-resistant MM.1 cell lines. The over-expression of miR-130b in the MM.1S cell line decreases the expression of a glucocorticoid receptor protein (GR-α), inhibiting glucocorticoid-induced apoptosis of cells, which causes resistance to glucocorticoids (*99*).

Downloaded by NORTH CAROLINA STATE UNIV on November 27, 2012 | http://pubs.acs.org
Publication Date (Web): November 26, 2012 | doi: 10.1021/bk-2012-1112.ch005

Downloaded by NORTH CAROLINA STATE UNIV on November 27, 2012 | http://pubs.acs.org
Publication Date (Web): November 26, 2012 | doi: 10.1021/bk-2012-1112.ch005

While the delivery of miRNA into cells has used various NPs as carriers (*95*, *96*) and other systems (*97*, *98*), the immobilization of miRNAs on the nanoparticles followed by testing cell transfection had not been demonstrated. Similar to the protocol developed for immobilizing siRNA on Au NPs (*103*), Scheme 3 shows several steps for the conjugation of miRNAs (miR-130b) to Au NPs through their use in cell transfection that was demonstrated recently in our laboratory.

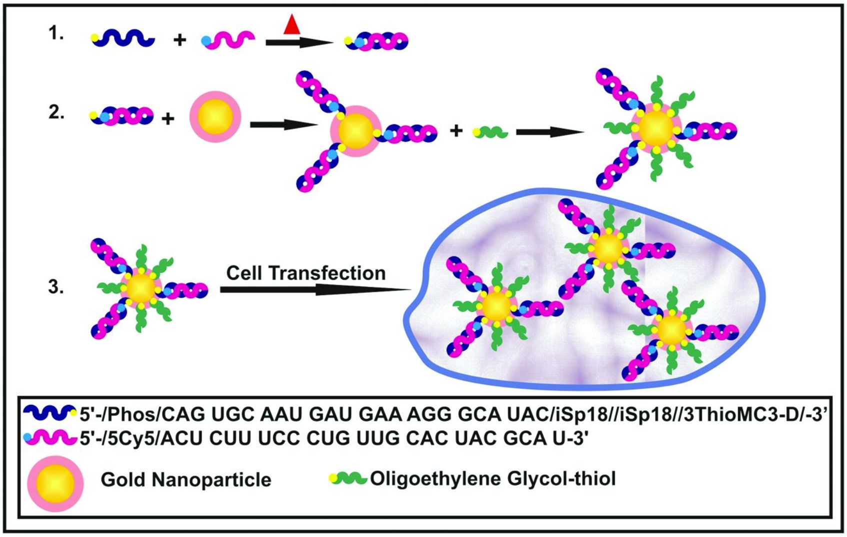
1.
+
2.
+
+
3.
Cell Transfection
5'-/Phos/CAG UGC AAU GAU GAA AGG GCA UAC/iSp18//iSp18//3ThioMC3-D/-3’
5'-/5Cy5/ACU CUU UCC CUG UUG CAC UAC GCA U-3'
Gold Nanoparticle
Oligoethylene Glycol-thiol

Scheme 3. Illustration (not to scale) of the preparation of miRNA-AuNP conjugates for delivering miRNAs to cells (miRNA is labeled with fluorescent dyes (e.g., Cy3 or Cy5)). (Reproduced with permission from reference (58). Copyright 2012 American Chemical Society.)

For the visualization of the cell transfection, the conjugation of miRNA to Au NPs involved immobilization of Cy5 (or Cy3) labeled miR-130b on the Au NPs (miRNA-AuNPs) (*58*). The conjugated dye label could also be detected using SERS (*50*, *52*, *112*). The assessment of the conjugation and stability of the nanoparticles was performed using agarose gel electrophoresis. This technique takes advantage of the highly charged nature of miRNAs for Au NP mobility. As an example of the gel electrophoresis analysis, Figure 3 shows a set of data comparing samples of unmodified AuNPs, miRNA-AuNPs and those treated with bis(p-sulfonatophenyl)phenylphosphine (BP). BP is a negatively charged surfactant often used for increasing the surface charge of NPs (*52*).

Downloaded by NORTH CAROLINA STATE UNIV on November 27, 2012 | http://pubs.acs.org
Publication Date (Web): November 26, 2012 | doi: 10.1021/bk-2012-1112.ch005

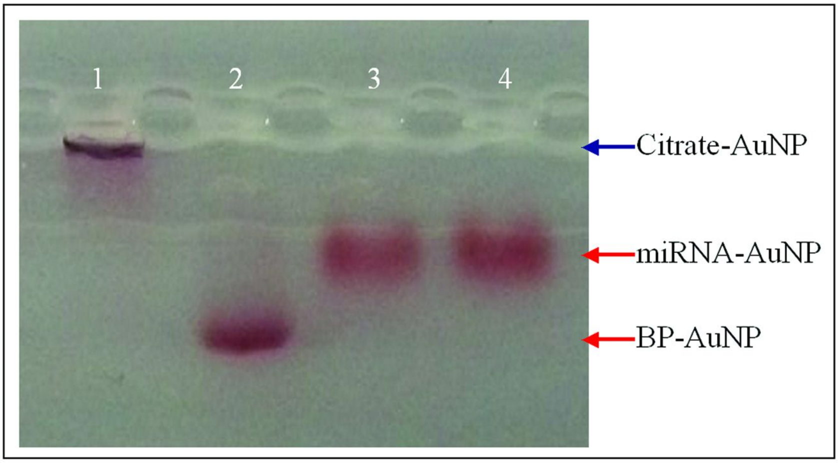

Figure 3. Photo showing the agarose gel electrophoresis: Lane 1: citrate-capped AuNPs; Lane 2: citrate-capped AuNPs after ligand exchange with BP; Lane 3: miRNA-conjugated AuNPs; and Lane 4: miRNA-conjugated AuNPs after ligand exchange with BP. (Reproduced with permission from reference (58). Copyright 2012 American Chemical Society.)

As shown in Figure 3, the mobility of Au NPs depends on their surface charges. For the citrate-capped Au NPs, the nanoparticle stayed in the well (lane 1), indicating the insufficient charges on the NPs. When the citrate-capped Au NPs are modified with BP, i.e., BP-AuNPs, via ligand-exchange reaction, a high mobility is evident (lane 2), which is consistent with the high surface negative charge of BP-AuNPs. When the Au NPs are capped with miRNAs, i.e., miRNA-AuNPs, a relatively high mobility is observed (lane 3), which is consistent with the high negative surface charge of miRNA-AuNPs. When surface ligand exchange reaction is performed with miRNAs-AuNPs and BPs in the solution, no effect on the mobility is observed (lane 4), indicating the absence of such surface exchange reactivity. This finding provides an important piece of evidence supporting the stability of the miRNA-conjugated Au NPs.

The miRNA-conjugated Au NPs were demonstrated to be viable for cell transfection. Samples of the miRNA-AuNPs were tested in cell transfection using a multiple myeloma cell line (MM.1S). The clear uptake of the conjugated nanoparticles was evidenced by the presence of Cy5-miRNA-AuNPs (Figure 4A) and Cy3-miRNA-AuNPs (Figure 4B) in the MM.1S cells. The clear contrast in the images is due to fluorescence from the entrance of the dye-labeled miRNA-AuNPs.

Downloaded by NORTH CAROLINA STATE UNIV on November 27, 2012 | http://pubs.acs.org
Publication Date (Web): November 26, 2012 | doi: 10.1021/bk-2012-1112.ch005

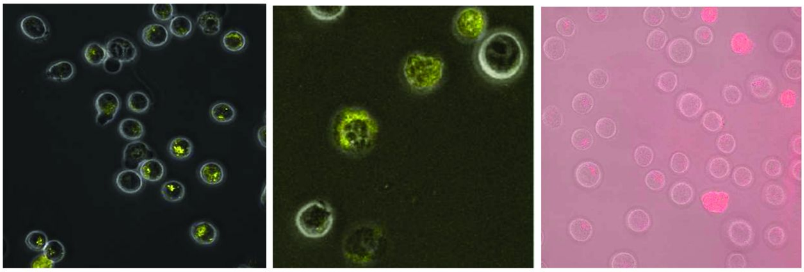

(A) (B)

Figure 4. Confocal/fluorescent composite microscopic images of the MM.1S cells 48 hours after transfection was initiated with Cy5-labeled miRNA-AuNPs (A, with two different magnifications), and Cy3-labeled miRNA-AuNPs (B). (Reproduced with permission from reference (58). Copyright 2012 American Chemical Society.)

Functional luciferase assays were performed to quantitatively determine if the miRNA delivered into the cells by the AuNPs was capable of reducing luciferase expression.

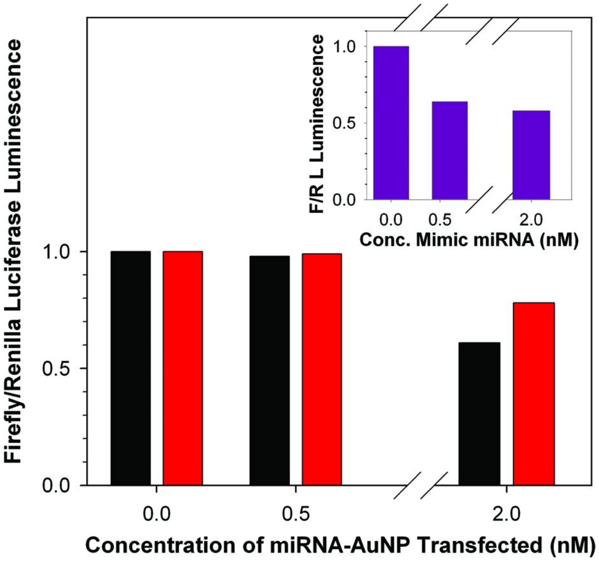

Figure 5. Plots showing the results of the functional luciferase assays for Cy5 labeled miRNA-AuNPs (right bars), Cy3 labeled miRNA-AuNPs (left bars), and a mimic system (insert chart). (Reproduced with permission from reference (58). Copyright 2012 American Chemical Society.)

Figure 5 shows the results of these assays. While little biological effect was observed at low concentrations, the increase of the concentration to 2 nM Cy5-miRNA-AuNPs led to an observable reduction in gene expression. The reduction in gene expression scales with the concentration of miRNAs.

The miRNA-AuNP solution contained ~15 miRNAs per nanoparticle in the luciferase knockdown. The surface coverage was apparently smaller than that reported for siRNA conjugated AuNPs (~33 siRNAs per particle (*103*)). Based on a comparison of the knockdown efficiencies between siRNA-AuNPs (~20% at 48 hours (*103*)) and miRNA-AuNPs (~40% at 48 hours), it appeared that the miRNA-AuNPs were somewhat more efficient at a much lower concentration (*103*).

Transfection of the miRNA-AuNPs in multiple myeloma cells is clearly demonstrated. However, to design the miRNA-conjugated Au NPs as effective biosensing and targeting probes, further studies using Au NPs of different sizes and with high miRNA surface coverages are needed to determine the concentrations needed for a high-efficiency knockdown.

Downloaded by NORTH CAROLINA STATE UNIV on November 27, 2012 | http://pubs.acs.org
Publication Date (Web): November 26, 2012 | doi: 10.1021/bk-2012-1112.ch005

Assemblies Mediated by Amino Acids, Small Peptides, and Proteins

The study of the interactions between biologically relevant molecules, such as amino acids, small peptides and proteins, and nanoparticles has attracted interest because of potential applications as nanoprobes for sensors, biosensors, and biomedical diagnostics (*2*, *51*, *77*, *113–118*). In this section, the assembly of Au NPs by thiol-containing amino acids and small peptides are first described as potential nanoprobes for their detection (*42*, *43*, *60*), highlighting the discovery of chiral recognition in these systems (*59*). This description is then followed by discussion of the assembly of M@Au nanocomposite particles as functional nanoprobes for protein recognition (*51*, *60*).

Assemblies Mediated by Thiol-Containing Amino Acids and Small Peptides

Thiol-Containinamino acids, such as cysteine (Cys) and homocysteine (Hcys), and small peptides, such as glutathione (GSH), are important biomolecules (*36*, *42*, *43*, *59–61*). A level of Hcys, in both reduced and oxidized forms, above the normal range in blood (5~15 μM) is used as an indication of cardiovascular disease and other medical disorders. Figure 6A-B show a set of surface plasmon resonance absorption and dynamic light scattering data demonstrating the Hcys- and Cys-mediated assembly of Au NPs (*42*, *58*). Interparticle, zwitterion-type, electrostatic interaction of the amino acids attached via thiol group on the surface of Au NPs has been proposed for the interparticle assembly, which can also be disassembled upon increasing pH or at elevated temperature. This type of interparticle interactions could be exploited for developing a colorimetric or fluorimetric nanoprobe in detecting the amino acids (e.g., homocysteine thiolactone (*119*)).

Downloaded by NORTH CAROLINA STATE UNIV on November 27, 2012 | http://pubs.acs.org
Publication Date (Web): November 26, 2012 | doi: 10.1021/bk-2012-1112.ch005

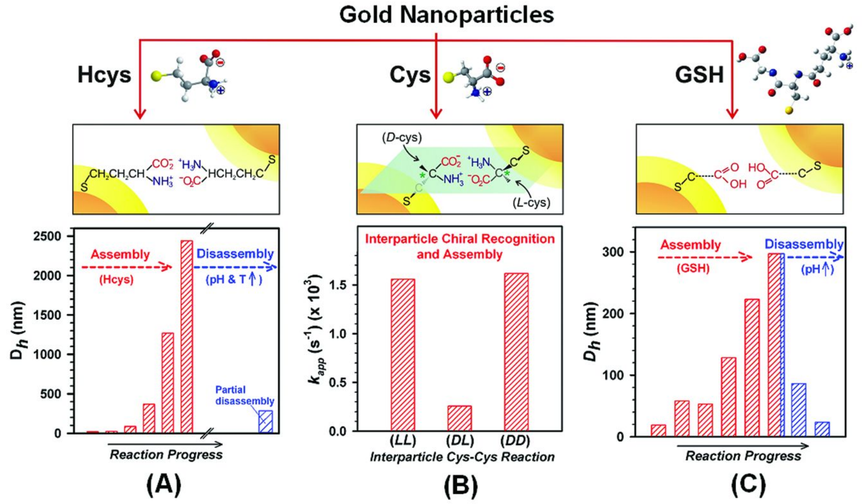

Figure 6. Assemblies of gold nanoparticles mediated by Hcys (A), Cys (B) and GSH (C). (A) Zwitterionic interaction and the change of D_h for Hcys-Au NP assembly/disassembly. (B) Interparticle chiral recognition and the apparent rate constants for assembly of D- and L-Cys enantiomers. (C) Hydrogen-bonding interaction and the change of D_h for GSH-Au NP assembly/disassembly. (Reproduced with permission from reference (60). Copyright 2009 American Chemical Society.)

In contrast to Hcys and Cys, the interparticle interactions in the assembly of Au NPs by glutathione (GSH), a tripeptide containing a cysteine, a glutamic acid and a glycine moiety with an SH group which acts as a reducing agent or antioxidant in biochemical processes, was found to involve primarily hydrogen-bonding. As such, the assembly and disassembly processes can be finely tuned by pH and monitored by the evolution of surface plasmon resonance bands and hydrodynamic sizes of the nanoparticle assemblies (Fig. 6C) (*43*).

One remarkable finding is the chiral recognition of cysteines driven by the Au NPs (Fig. 6B) (*59*). Understanding molecular chirality of basic amino acids has important implications in medicine for specific targeting. Cys is essential to the function of many proteins and enzymes. Scheme 4 shows a structural model to illustrate our nanoparticle-regulated pair-wise zwitterionic interactions using enantiomeric cysteines adsorbed on Au NPs as a model system. A hypothetical quasi-plane is drawn in Scheme 4 to illustrate the interparticle zwitterion interaction of different chiralities (*L* and *D*). Three possible interactions would include two homochiral (*LL* and *DD*) and one heterochiral (*DL*) modes. Both thermodynamic considerations and computational modeling results also suggest that there are differences between interparticle homochiral and heterochiral interactions. This type of interparticle chiral recognition serves as another intriguing example of nanoparticle-directed biomolecular recognition.

Downloaded by NORTH CAROLINA STATE UNIV on November 27, 2012 | http://pubs.acs.org
Publication Date (Web): November 26, 2012 | doi: 10.1021/bk-2012-1112.ch005

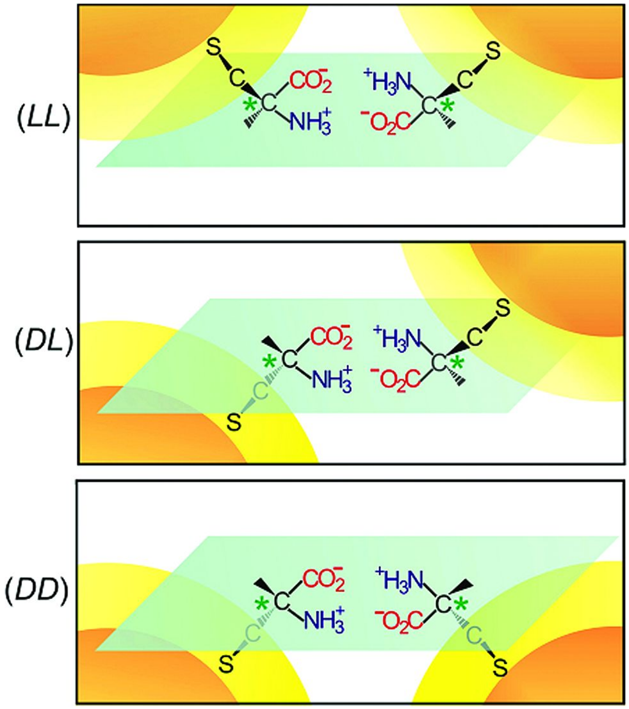

Scheme 4. A model for the interparticle pair-wise zwitterionic interactions (not to scale). A hypothetical quasi-plane is drawn for illustrating the relative positions of the amino acid groups. The particles are either on the same or opposite sides of the quasi-plane. (L-, D-cysteines: $HSCH_2C^*H(NH_3^+)CO_2^-$, C: chiral center). (Reproduced with permission from reference (59). Copyright 2009 American Chemical Society.)*

The interparticle pair-wise zwitterionic interaction of the cysteines adsorbed on Au NPs leads to the assembly of the nanoparticles via cysteine-cysteine linkages, which is characterized by the change of the surface plasmon (SP) resonance band of Au NPs in the visible region (*47*, *120–122*). Cysteines were introduced into a solution of Au NPs of 13 nm diameter (Au_{13nm}), and the SP band showed a decrease in absorbance at 520 nm and an increase in the ~630 nm region (Figure 7).

During this spectral evolution, the display of an isosbestic point at ~540 nm reflects the presence of two main species, the unlinked nanoparticles and the linked nanoparticles in the assembly. Based on a first-order reaction model, the apparent rate constants (k) obtained by curve fitting of the SP band evolution are found to show a significant difference between the interparticle homochiral and heterochiral assemblies. The k values for the *LL* and *DD* assemblies are found to be ~1 order of magnitude greater than that for the *DL* assembly (50% *L* and 50% *D*).

Downloaded by NORTH CAROLINA STATE UNIV on November 27, 2012 | http://pubs.acs.org
Publication Date (Web): November 26, 2012 | doi: 10.1021/bk-2012-1112.ch005

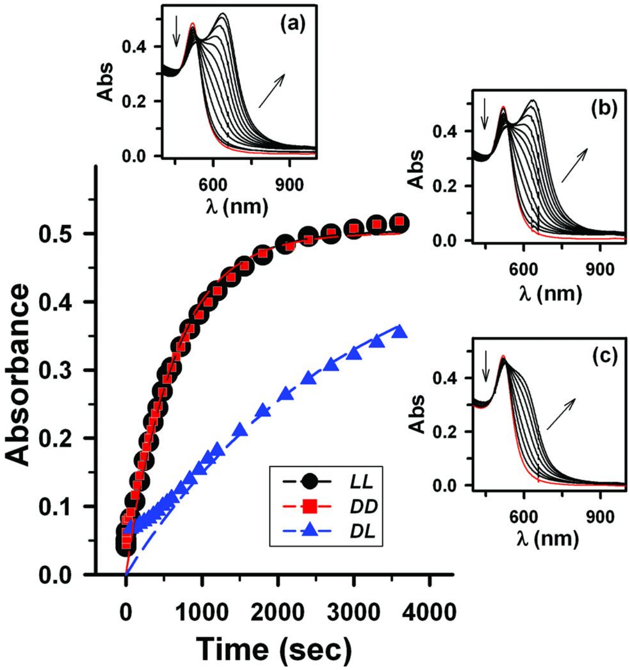

Figure 7. Plots of the SP band absorbance (at 630 nm) as a function time for assemblies of Au_{13nm} in the presence of LL- (•), DD- (▪), and DL- (▴) cysteines. The dotted lines represent curve fitting by a 1st order reaction model ($y = a(1-e^{-kt})$) which yields $k_{(LL)} = 1.6 \times 10^{-3}\ s^{-1}$, $k_{(DD)} = 1.6 \times 10^{-3}\ s^{-1}$, and $k_{(DL)} = 3.4 \times 10^{-4}\ s^{-1}$. Inserts: UV-Vis spectral evolution for the Au_{13nm} mediated assembly of LL- (a), DD- (b) and DL- (c) cysteines (pH = 6.2). The arrows indicate the direction of the spectral evolution. (Reproduced with permission from reference (59). Copyright 2009 American Chemical Society.)

The difference between the interparticle homochiral and heterochiral interactions is further substantiated by measurements of the spectral evolution of Au nanoparticles of different sizes in the presence of homochiral cysteines (*LL* or *DD*) or heterochiral cysteines (*DL*).

Based on analysis of the three possible combinations of the enatiomeric cysteines for the interparticle pair-wise dimerization using an idealized model, an excellent agreement between the experimental data and the theoretical modeling result is found for this type of interparticle chiral recognition phenomenon. If the heterochiral dimerization is less favorable than the homochiral dimerization (*123*), as supported by experimental data ($k_{(DL)} \ll k_{(LL)}$ (≈ $k_{(DD)}\ \chi_L$) of 50%.

Figure 8 shows the correlation between the apparent rate (*r*) or rate constant (*k*) of the interparticle reactivity and the relative concentration of the enantiomer in the solution (*L*%) for Au NPs of two different sizes. A characteristic "valley" feature is revealed, with the minimum appearing at 50%*L*:50%*D*. The assembly rate for nanoparticles in the presence of heterochiral *L*- and *D*-cysteines is much slower than those in the presence of homochiral *L*- or *D*-cysteines.

Downloaded by NORTH CAROLINA STATE UNIV on November 27, 2012 | http://pubs.acs.org
Publication Date (Web): November 26, 2012 | doi: 10.1021/bk-2012-1112.ch005

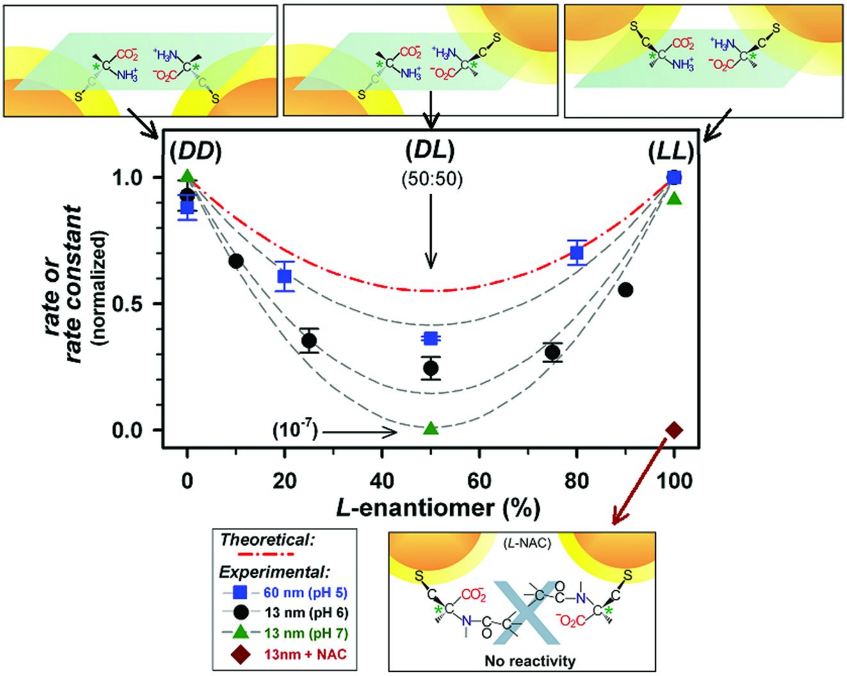

Figure 8. Correlation between the normalized rate or rate constant (k) and the enantiomeric percentage of cysteines (%) in the presence of gold nanoparticles of two different sizes Au_{60nm} (▪) (pH = 5), Au_{13nm} (•) (pH = 6) and Au_{13nm} (▴) (pH = 7). A data point for Au_{13nm} reacting with NAC (♦) is included to illustrate the inactivity. The red dot-dash line represents the theoretical rate derived from modeling LL, DD and DL dimerization kinetics, whereas the other dashed lines show the trends of the experimental data points (not fitting data). The schemes shown in the top and bottom panels are for the purpose of illustrating the different interparticle chiral interactions. (Reproduced with permission from reference (59). Copyright 2009 American Chemical Society.)

The inactivity observed for the assembly of Au NPs using N-acetyl-*L*-cysteine (NAC) as a mediator further confirms the important role of the interparticle pair-wise zwitterionic interaction of the amino acid groups in the interparticle chiral recognition and nanoparticle assembly. The interparticle homochiral (*LL* or *DD*) vs. heterochiral (*DL*) reactivity involve preferential interaction and differentiation of the different enantiomeric structures. There are important implications of the findings to the exploration of the nanoparticle-driven chiral recognition of cysteines in biomedical applications. One area stems from the linkage of elevated levels of cysteine to medical disorders (e.g., Parkinson's and Alzheimer's), where the potential use of nanoparticles to probe such elevated levels could lead to early diagnosis and identification. The importance of enantiomeric chirality in protein interactions is widely recognized in the broad interdisciplinary community of pharmaceutical science and technology (*124*, *125*). The nanoparticle-regulated chiral recognition strategy could potentially lead to the development of a highly effective route for controlling the enantiomeric specificity (*126*, *127*). For example, *L*-cysteine plays an important role in living systems and its deficiency is associated with a number of clinical situations (liver damage, skin lesions, AIDS, and certain neurodegenerative diseases). However, the role of *L*-cysteine in the central nervous system is not well understood (*126*). *D*-cysteine is believed to interfere with many targets inside the cell (*127*). The nanoparticle-regulated chiral recognition strategy exploits the interparticle chiral reactivity, which differs from chiralities with single-crystal surfaces (*128–130*) and chiral structures on metal NPs (*131–136*).

Downloaded by NORTH CAROLINA STATE UNIV on November 27, 2012 | http://pubs.acs.org
Publication Date (Web): November 26, 2012 | doi: 10.1021/bk-2012-1112.ch005

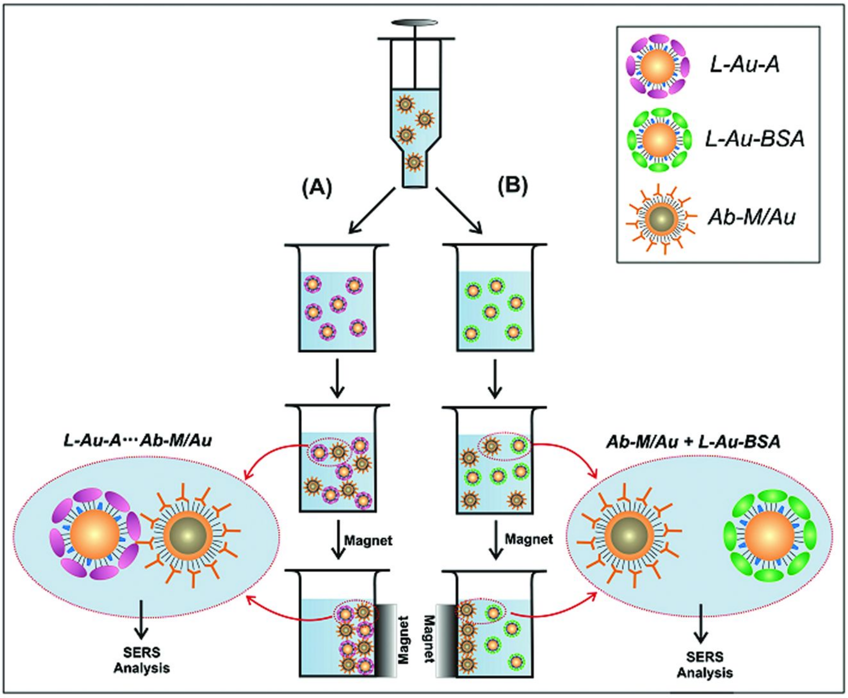

Scheme 5. Illustration of the use of surface functionalized Au and magnetic core (M)@shell (Au) nanoparticles in bio-separation and detection. (A) For the reactivity between protein A-labeled Au NPs: L-Au-A and antibody-labeled M@Au NPs: Ab-M@Au. (B) For the reactivity between BSA-labeled Au NPs L-Au–BSA with Ab-M@Au. This is an idealized scheme; the sizes of the NPs, MBA, DSP and antibody are not drawn to scale. (Reproduced with permission from I-I. S. Lim, P. N. Njoki, H.-Y. Park, X. Wang, L. Wang, D. Mott, C. J. Zhong, "Gold and Magnetic Oxide/Gold Core/Shell Nanoparticles as Bio-Functional Nanoprobes", Nanotechnology, ***2008****, 19, 305102. Copyright 2008 IOP Publishing Ltd.)*

Downloaded by NORTH CAROLINA STATE UNIV on November 27, 2012 | http://pubs.acs.org
Publication Date (Web): November 26, 2012 | doi: 10.1021/bk-2012-1112.ch005

Recognition by Proteins and Magnetic Separation (*51*, *52*).

The exploitation of the specific and selective binding activity between antibodies and antigens on NPs serves as important means of sandwich-type immunoassay. SERS readout of the assay has the capability of multiplexity (*50*). This type of protein recognition was recently expanded to the interparticle assembly between reporter-labeled Au NPs and magnetic core (M)@Au NPs for achieving both magnetic bio-separation and SERS-based bio-detection (*51*, *52*, *55*), as illustrated in Scheme 5.

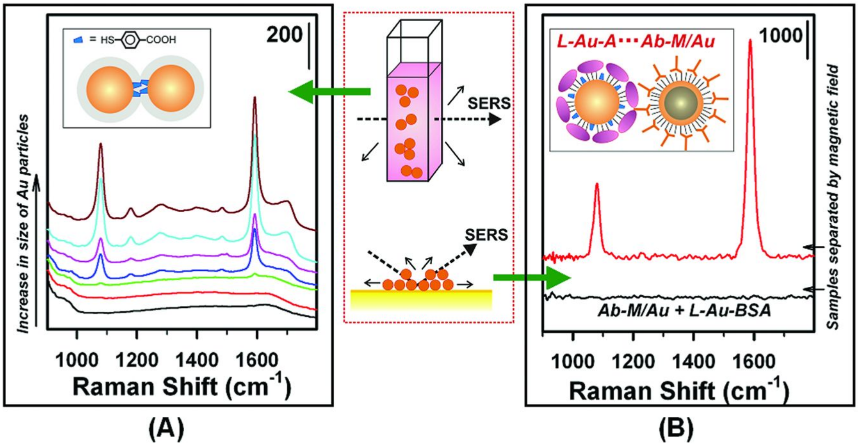

Figure 9. SERS spectra showing (A) particle size dependence for MBA-labeled Au NPs (30, 40, 50, 60, 70, 80 and 90 nm) in an aqueous solution as a result of interparticle interactions, and (B) the assembly of Au (80 nm) NPs labeled with Protein A or BSA and MBA and M@Au NPs (~8 nm) labeled with antibody (IgG). (Reproduced with permission from reference (60). Copyright 2009 American Chemical Society.)

While Au NPs have been demonstrated as effective nanoprobes for detection of DNAs or proteins via amplification of optical and SERS signals for medical diagnostics, the use of magnetic nanoparticles (M) coated with a biocompatible layer, e.g., M@Au, represents an advanced approach. This approach has many intriguing attributes, including a magnetic separation capability, an enhanced stabilization of the magnetic particles, a fine-tunable surface to impart biocompatibility, or other desired chemical and biological interfacial reactivities. There are increasing examples demonstrating the immobilization of biological recognition sites on Au or M@Au NPs that are spectroscopically labeled for recognition of the targeted proteins or as an effective means for the separation of biological molecules (*51*, *52*, *55*). For example, the size correlation of the surface plasmon resonance properties for Au NPs (*52*) exploits the plasmonic coupling of the localized fields between nanoparticles and substrates to produce an enhanced

Downloaded by NORTH CAROLINA STATE UNIV on November 27, 2012 | http://pubs.acs.org
Publication Date (Web): November 26, 2012 | doi: 10.1021/bk-2012-1112.ch005

SERS effect (*48–50*). Figure 9A shows a set of SERS spectra obtained for mercaptobenzoic acid (MBA)-labeled Au NPs of different sizes on Au thin film substrates and in aqueous solutions. The SERS intensity shows a gradual increase with particle size, which is attributed to the SERS effect from dimer/trimers in the solution formed via interparticle hydrogen-bonding of the adsorbed MBAs. In the solution the stable and small clusters of the nanoparticles (e.g., dimers or trimers) produces "hot spots" (*48*, *49*) that are believed to be responsible for the SERS effect (*52*, *112*).

Figure 9 B shows an example, which exploits the strong SERS effects (*52*, *112*) for developing SERS and magnetic nanoprobes for bio-separation and detection. This example involves the immobilization of Raman label (*L* =MBA), Protein A (*A*) and antibody (*Ab*) on Au and M@Au (or Ag) nanoparticle surfaces for SERS detection of the protein A-antibody binding activity (*51*, *52*, *55*). The application of a magnetic field to the solution containing the reaction product between Protein A capped Au NPs with a Raman label (*L-Au-A*) and the antibody-capped M@Au NPs (*Ab-M@Au*) should lead to its separation. The separated sample is then analyzed. The detection of the diagnostic signals of the MBA for the separated product ((*L-Au-A*)-(*Ab-M@Au*) pair) in the SERS spectra is in sharp contrast to the absence of such signals for the (*L-Au-BSA*)+(*Ab-M@Au*) pair derived in a control experiment using bovine serum albumin (BSA) to replace Protein A. This strategy is potentially viable for the development of magnetic SERS nanoprobes for bioassays. While the illustrated examples are limited (*42*, *43*, *51*, *52*, *59–61*), the basic principles are expected to be applicable to many other nanoparticle assemblies with biomolecules that are structurally defined for harnessing the nanoscale properties for developing effective immunoassay strategies.

Silver-Coated Magnetic Particles as Functional Antimicrobial Agent

The antimicrobial properties of silver and other metals have been known for a long time (*137*). There have been increasing reports showing that Ag NPs have enhanced antibacterial properties even at low concentrations, and such properties are size dependent (*137–139*). The higher surface to volume ratio provided by these NPs allow for a more efficient bacterial inactivation (*140–143*). Bacterial interaction with the nanoparticles starts from the surface layer of the nanoparticles. The antibacterial activity of Ag-based NPs involves releasing silver ions to the biological binding sites upon adhesion onto the surfaces of the target (*143–146*). This initial adhesion is important for achieving an effective targeting.

One area of interest involves the ability for Ag NPs to function as an antibacterial agent while being separable from the target biological fluids. Although pathogen contamination can occur in all blood products, it is the need to store platelets at room temperature that makes bacterial contamination of platelets a high risk of infection associated with transfusion. The antibacterial M@Ag NPs can be introduced into the platelets to inactivate the bacteria and be subsequently separated from the platelets prior to transfusion. The enhanced antibacterial properties of Ag NPs even at low concentrations (*141*, *142*, *147*) may provide a more efficient bacterial disinfection with minimized presence of Ag ions. The fabrication of metal-coated magnetic nanoparticles has been demonstrated using different methods (*51*, *53–55*, *148–156*), but the ability to control the nanoscale size, composition, magnetic and surface properties towards structurally-tailored nanomaterials for antibacterial applications remain challenging for specific applications. Scheme 6 illustrates one of our approaches that explores M@Ag NPs for bacterial inactivation of different samples of biological fluids, including blood platelets. The introduction of the magnetic cores into the Ag NPs enables the capabilities of effective separation, delivery and targeting of the antibacterial agents (*157–160*).

Downloaded by NORTH CAROLINA STATE UNIV on November 27, 2012 | http://pubs.acs.org
Publication Date (Web): November 26, 2012 | doi: 10.1021/bk-2012-1112.ch005

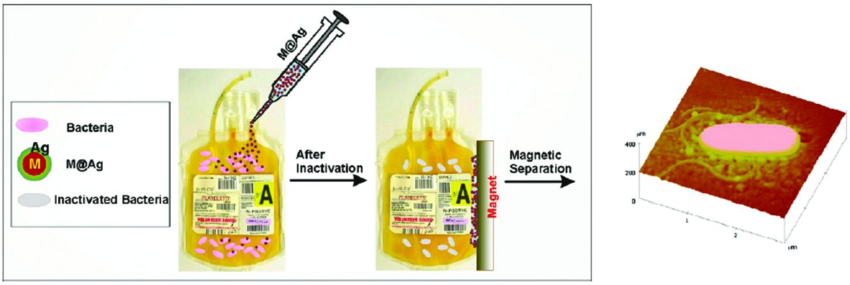

Scheme 6. Illustration of use of Ag-coated magnetic core@shell nanoparticles (M@Ag) as a functional antimicrobial agent in blood platelets and the magnetic separation to remove M@Ag from the platelets (not to scale). Image in right: an AFM image of Pseudomonas aeruginosa adsorbed on a mica surface. (Reproduced with permission from reference (61). Copyright 2011 American Chemical Society.)

Functional core-shell nanoparticles consisting of MnZn Ferrite as the magnetic cores and silver as the shells (MZF@Ag) were synthesized by a wet chemical method (*61*). The bacterial inactivation of the functional MZF@Ag nanoparticles was demonstrated in saline solution for several types of bacteria, including Gram-positive *Staphylococcus aureus* and *Bacillus cereus,* and Gram-negative *Pseudomonas aeruginosa*, *Enterobacter cloacae*, and *Escherichia coli*. The reduction in bacterial growth was determined in samples that contained either Ag NPs or MZF@Ag NPs. As shown in Figure 10(A) we monitored the growth of Gram-positive *Bacillus cereus* in saline solutions containing antimicrobial nanoparticles over a 24-hour period, and the bacterial concentration exhibits a clear reduction as a function of the incubation time. The MZF@Ag NPs seemed to be more efficient at killing *Bacillus cereus* when compared to the Ag NPs.

Downloaded by NORTH CAROLINA STATE UNIV on November 27, 2012 | http://pubs.acs.org
Publication Date (Web): November 26, 2012 | doi: 10.1021/bk-2012-1112.ch005

Figure 10(B) illustrates another set of results obtained from the Gram-negative bacteria, *Enterobacter cloacae*. The results were highly similar to those of the *Bacillus cereus* sample shown in Figure 10(A) with a slight difference with the silver nanoparticle sample. The nanoparticles seemed to work more rapidly on the *E. cloacae*, which could be attributed to it being Gram-negative.

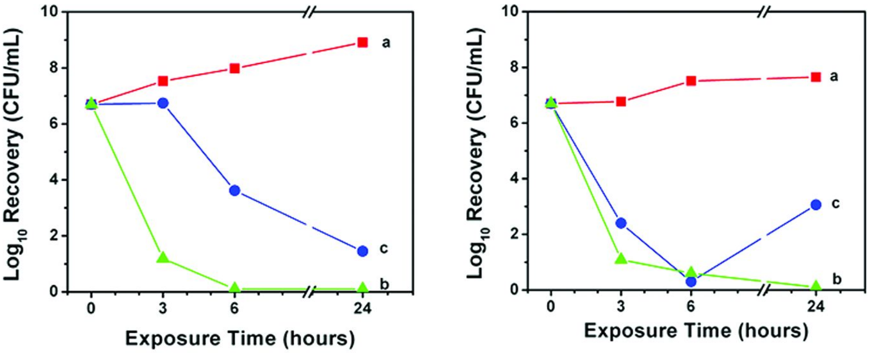

(A) **(B)**

Figure 10. The inactivation efficiency data for the inactivation of two different types of bacteria: (A) Bacillus cereus and (B) Enterobacter cloacae, in a PBS buffer solution (a), in a solution containing with MZF@Ag NPs (b), and in a solution containing with Ag NPs (c). (Reproduced with permission from reference (61). Copyright 2011 American Chemical Society.)

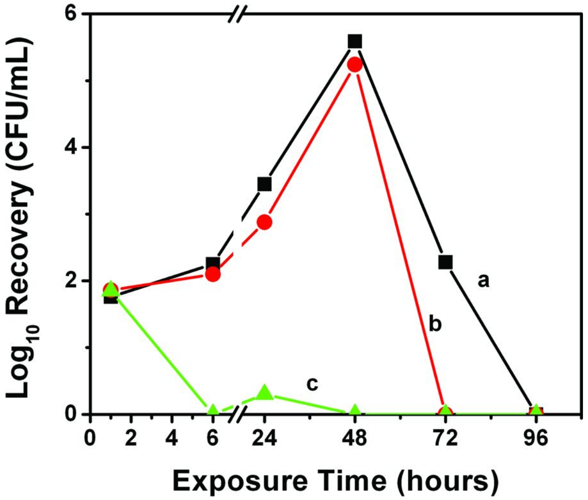

Figure 11. A comparison of the inactivation efficiency data for the inactivation of E. coli with water (a), MZF NPs (b), and MZF@Ag NPs (c) in blood platelets. (Reproduced with permission from reference (61). Copyright 2011 American Chemical Society.)

Based on the successful demonstration that the MZF@Ag NPs can inactivate bacterial growth with an effectiveness comparable to Ag NPs in saline solutions, the viability of the MZF@Ag NPs for inactivating bacteria in human blood platelet samples was tested. Figure 11 illustrates an example for the inactivation of *E. coli* using MZF@Ag NPs.

After only 6 hours of exposure, the bacterial concentration fell below a detectable level. This finding is in sharp contrast to the observation with MZF NPs in this experiment.

The total silver (ionic silver and suspended Ag NPs that could not be removed by a magnetic field) in the sample was analyzed, showing less than 1 ppm. Although the MZF@Ag treated samples showed slightly more silver found than in the controls, it provided significant bacterial inactivation. This finding is an important piece of evidence supporting that the inactivation is mainly caused by the direct contact of Ag on NPs rather than Ag ions leached into the liquid phase. This concentration is very low compared to other silver-based antimicrobial products such as those in medical bandages. The amount of silver found in the platelets was also less than the level that usually causes a reaction in the human body, suggesting that the idea of using MZF@Ag NPs to inactivate bacteria in blood products would be safe, when giving a transfusion after the removal of MZF@Ag NPs.

MZF@Ag NPs are shown to serve as a functional antibacterial agent for an effective inactivation of bacterial growth in both saline solution and blood platelets. Considering the increasing use of Ag NPs as antimicrobial agent in commercial products and increasing concern over the toxicity of Ag NPs (*161*), this strategy described in this section could offer the ability to recover the used silver nanoparticles and reduce the unwanted toxicity towards patients or the environment.

Downloaded by NORTH CAROLINA STATE UNIV on November 27, 2012 | http://pubs.acs.org
Publication Date (Web): November 26, 2012 | doi: 10.1021/bk-2012-1112.ch005

Summary

In summary, this chapter has highlighted selected examples in the explorations of gold and silver based nanoparticles as functional nanoprobes for biomolecular recognition. Gold nanoparticles have been demonstrated effective in probing DNA assembly for protein binding/cutting processes, which has the potential to be a diagnostic probe for *p53* mutation detection. Gold nanoprobes have also been demonstrated to serve as an effective vehicle for delivering miRNAs to multiple myeloma cells for cell transfection and gene knockdown studies, which, upon further understanding of their cellular uptake and mobility, has the potential for developing a useful technique for the genetic treatment of certain cancers. The nanoprobes have also been shown to function as not only a sensitive detection platform for biologically relevant thiol-containing amino acids or small peptides, but also a driving force for chiral recognition. This feature could prove useful in the detection of certain chronic diseases such as cardiovascular disease and Alzheimer’s disease, as well as in drug design. The magnetic core-shell nanoparticles have been demonstrated as functional nanoprobes to enable an effective bio-separation function in protein recognition and bacterial inactivation. These studies have the potential in establishing novel immunoassay probes and in reducing or eliminating nano toxicity associated with certain blood products. The ability to manipulate and separate the nanoprobes in the various biomolecular recognition processes also has important implications to developing effective strategies in administering nanomaterials in human and environmental applications while limiting toxicity.

Acknowledgments

We express our appreciation to former and current members of the Zhong Research Group and our collaborators who have made contributions to the work described in this article. The work is supported by grants from the National Science Foundation (CHE 0848701 and CMMI 1100736) and in part from NIH, AFOSR and DOE.

Downloaded by NORTH CAROLINA STATE UNIV on November 27, 2012 | http://pubs.acs.org
Publication Date (Web): November 26, 2012 | doi: 10.1021/bk-2012-1112.ch005

References

1. Mirkin, C. A.; Letsinger, R. L.; Mucic, R. C.; Storhoff, J. J. *Nature* **1996**, *382*, 607–609.
2. Elghanian, R.; Storhoff, J. J.; Mucic, R. C.; Letsinger, R. L.; Mirkin, C. A. *Science* **1997**, *277*, 1078–1081.
3. Storhoff, J. J.; Elghanian, R.; Mucic, R. C.; Mirkin, C. A.; Letsinger, R. L. *J. Am. Chem. Soc.* **1998**, *120*, 1959–1964.
4. Agasti, S. S.; Rana, S.; Park, M. H.; Kim, C. K.; You, C. C.; Rotello, V. M. *Adv. Drug Delivery Rev.* **2010**, *62*, 316–328.
5. Zhang, X. Q.; Xu, X. Y.; Lam, R.; Giljohann, D.; Ho, D.; Mirkin, C. A. *ACS Nano* **2011**, *5*, 6962–9670.
6. Al-Jamal, W. T.; Kostarelos, K. *Acc. Chem. Res.* **2011**, *44*, 1094–1104.
7. Lim, Z. Z. J.; Li, J. E. J.; Ng, C. T.; Yung, L. Y. L.; Bay, B. H. *Acta Pharmacol. Sin.* **2011**, *32*, 983–990.
8. Bhattacharyya, S.; Kudgus, R. A.; Bhattacharya, R.; Mukherjee, P. *Pharm. Res.* **2011**, *28*, 237–259.
9. Conde, J.; Rosa, J. R.; Lima, J. C.; Baptista, P. V. *Int. J. Photoenergy* **2012**, 619530 DOI: 10.1155/2012/619530.
10. Thiruppathiraja, C.; Kamatchiammal, S.; Adaikkappan, P.; Santhosh, D.; Alagar, M. *Anal. Biochem.* **2011**, *417*, 73–79.
11. Lee, J. B.; Campolongo, M. J.; Kahn, J. S.; Roh, Y. H.; Hartman, M. R.; Luo, D. *Nanoscale* **2010**, *2*, 188–197.
12. Hnilova, M.; Khatayevich, D.; Carlson, A.; Oren, E. E.; Gresswell, C.; Zheng, S.; Ohuchi, F.; Sarikaya, M.; Tamerler, C. *J. Colloid Interface Sci.* **2012**, *365*, 97–102.
13. Bassett, D. C.; Grover, L. M.; Mueller, F. A.; McKee, M. D.; Barralet, J. E. *Adv. Funct. Mater.* **2011**, *21*, 2968–2977.
14. Borteh, H. M.; Ferrell, N. J.; Butler, R. T.; Olesik, S. V.; Hansford, D. J. *Appl. Surf. Sci.* **2011**, *258*, 230–235.

Downloaded by NORTH CAROLINA STATE UNIV on November 27, 2012 | http://pubs.acs.org
Publication Date (Web): November 26, 2012 | doi: 10.1021/bk-2012-1112.ch005

15. Stadler, A.; Chi, C.; van der Lelie, D.; Gang, O. *Nanomedicine* **2010**, *5*, 319–334.
16. McKeon-Fischer, K. D.; Freeman, J. W. *J. Tissue Eng. Regener. Med.* **2011**, *5*, 560–568.
17. Sannomiya, T.; Voeroes, J. *Trends Biotechnol.* **2011**, *29*, 343–351.
18. Zeng, S. W.; Yong, K. T.; Roy, I.; Dinh, X. Q.; Yu, X.; Luan, F. *Plasmonics* **2011**, *6*, 491–506.
19. Sagle, L. B.; Ruvuna, L. K.; Ruemmele, J. A.; Van Duyne, R. P. *Nanomedicine* **2011**, *6*, 1447–1462.
20. Cao, X. D.; Ye, Y. K.; Liu, S. Q. *Anal. Biochem.* **2011**, *417*, 1–16.
21. Petryayeva, E.; Krull, U. J. *Anal. Chim. Acta* **2011**, *706*, 8–24.
22. Cerkez, I.; Kocer, H. B.; Worley, S. D.; Broughton, R. M.; Huang, T. S. *J. Appl. Polym. Sci.* **2012**, *124*, 4230–4238.
23. Zahedi, P.; Karami, Z.; Rezaeian, I.; Jafari, S. H.; Mahdaviani, P.; Abdolghaffari, A. H.; Abdollahi, M. *J. Appl. Polym. Sci.* **2012**, *124*, 4174–4183.
24. Koch, M.; Kiefer, S.; Cavelius, C.; Kraegeloh, A. *J. Nanopart. Res.* **2012**, *14*, 646.
25. Lapresta-Fernandez, A.; Fernandez, A.; Blasco, J. *TrAC, Trend. Anal. Chem.* **2012**, *32*, 40–59.
26. Sadeghi, B.; Garmaroudi, F. S.; Hashemi, M.; Nezhad, H. R.; Nasrollahi, A.; Ardalan, S.; Ardalan, S. *Adv. Powder Technol.* **2012**, *23*, 22–26.
27. Sudeep, P. K.; Ipe, B. I.; Thomas, K. G.; George, M. V.; Barazzouk, S.; Hotchandani, S.; Kamat, P. V. *Nano Lett.* **2002**, *2*, 29–35.
28. Guldi, D. M.; Zilbermann, I.; Anderson, G.; Kotov, N. A.; Tagmatarchis, N.; Prato, M. *J. Am. Chem. Soc.* **2004**, *126*, 14340–14341.
29. Leibowitz, F. L.; Zheng, W.; Maye, M. M.; Zhong, C. J. *Anal. Chem.* **1999**, *71*, 5076–5083.
30. Han, L.; Daniel, D. R.; Maye, M. M.; Zhong, C. J. *Anal. Chem.* **2001**, *73*, 4441–4449.
31. Han, L.; Luo, J.; Kariuki, N. N.; Maye, M. M.; Jones, V. W.; Zhong, C. J. *Chem. Mater.* **2003**, *15*, 29–37.
32. Wang, L.; Shi, X.; Kariuki, N. N.; Schadt, M.; Wang, G. R.; Rendeng, Q.; Choi, J.; Luo, J.; Lu, S.; Zhong, C. J. *J. Am. Chem. Soc.* **2007**, *129*, 2161–2170.
33. Wohltjen, H.; Snow, A. W. *Anal. Chem.* **1998**, *70*, 2856–2859.
34. Zamborini, F. P.; Leopold, M. C.; Hicks, J. F.; Kulesza, P. J.; Malik, M. A.; Murray, R. W. *J. Am. Chem. Soc.* **2002**, *124*, 8958–8964.
35. Murray, R. W. *Chem. Rev.* **2008**, *108*, 2688–2720.
36. Rosi, N. L.; Mirkin, C. A. *Chem. Rev.* **2005**, *105*, 1547–1562.
37. Ghosh, S. K.; Pal, T. *Chem. Rev.* **2007**, *107*, 4797–4862.
38. Daniel, M. C.; Astruc, D. *Chem. Rev.* **2004**, *104*, 293–346.
39. Wang, G. R.; Wang, L.; Rendeng, Q.; Wang, J.; Luo, J.; Zhong, C. J. *J. Mater. Chem.* **2007**, *17*, 457–462.
40. Wang, L.; Miller, D.; Fan, Q.; Luo, J.; Schadt, M.; Rendeng, Q.; Wang, G. R.; Wang, J.; Kowach, G. R.; Zhong, C. J. *J. Phys. Chem. C* **2008**, *112*, 2448–2455.

41. Zhang, F. X.; Han, L.; Israel, L. B.; Daras, J. G.; Maye, M. M.; Ly, N. K.; Zhong, C. J. *Analyst* **2002**, *127*, 462–465.
42. Lim, I-I. S.; Ip, W.; Crew, E.; Njoki, P. N.; Mott, D.; Zhong, C. J.; Pan, Y.; Zhou, S. *Langmuir* **2007**, *23*, 826–833.
43. Lim, I-I. S.; Mott, D.; Ip, W.; Njoki, P. N.; Pan, Y.; Zhou, S.; Zhong, C. J. *Langmuir* **2008**, *24*, 8857–8863.
44. Lim, I-I. S.; Goroleski, F.; Mott, D.; Kariuki, N. N.; Ip, W.; Luo, J.; Zhong, C. J. *J. Phys. Chem. B* **2006**, *110*, 6673–6682.
45. Lim, I-I. S.; Ouyang, J.; Luo, J.; Wang, L.; Zhou, S.; Zhong, C. J. *Chem. Mater.* **2005**, *17*, 6528–6531.
46. Lim, I-I. S.; Pan, Y.; Mott, D.; Ouyang, J.; Njoki, P. N.; Luo, J.; Zhou, S.; Zhong, C. J. *Langmuir* **2007**, *23*, 10715–10724.
47. Lim, I-I. S.; Zhong, C. J. *Gold Bull.* **2007**, *40*, 59–66.
48. Camden, J. P.; Dieringer, J. A.; Wang, Y.; Masiello, D. J.; Marks, L. D.; Schatz, G. C.; Van Duyne, R. P. *J. Am. Chem. Soc.* **2008**, *130*, 12616–12617.
49. Hao, E.; Schatz, G. C. *J. Chem. Phys.* **2004**, *120*, 357–366.
50. Driskell, J. D.; Lipert, R. J.; Porter, M. D. *J. Phys. Chem. B* **2006**, *110*, 17444–17451.
51. Park, H. Y.; Schadt, M. J.; Wang, L.; Lim, I-I. S.; Njoki, P. N.; Kim, S. H.; Jang, M. Y.; Luo, J.; Zhong, C. J. *Langmuir* **2007**, *23*, 9050–9056.
52. Lim, I-I. S.; Njoki, P. N.; Park, H. Y.; Wang, X.; Wang, L.; Mott, D.; Zhong, C. J. *Nanotechnology* **2008**, *19*, 305102.
53. Wang, L.; Luo, J.; Fan, Q.; Suzuki, M.; Suzuki, I. S.; Engelhard, M. H.; Lin, Y.; Kim, N.; Wang, J. Q.; Zhong, C. J. *J. Phys. Chem. B* **2005**, *109*, 21593–21601.
54. Wang, L.; Luo, J.; Maye, M. M.; Fan, Q.; Rendeng, Q.; Engelhard, M. H.; Wang, C.; Lin, Y.; Zhong, C. J. *J. Mater. Chem.* **2005**, *15*, 1821–1832.
55. Wang, L.; Park, H. Y.; Lim, I-I. S.; Schadt, M. J.; Mott, D.; Luo, J.; Wang, X.; Zhong, C. J. *J. Mater. Chem.* **2008**, *18*, 2629–2635.
56. Lim, I-I. S.; Chandrachud, U.; Wang, L.; Gal, S.; Zhong, C. J. *Anal. Chem.* **2008**, *80*, 6038–6044.
57. Shen, Q.; Nie, Z.; Guo, M.; Zhong, C. J.; Lin, B.; Li, W.; Yao, S. Z. *Chem. Commun.* **2009**, 929–931.
58. Crew, E.; Rahman, S.; Razzak-Jaffar, A.; Mott, D.; Kamundi, M.; Yu, G.; Tchah, N.; Lee, J.; Bellavia, M.; Zhong, C. J. *Anal. Chem.* **2012**, *84*, 26–29.
59. Lim, I-I. S.; Mott, D.; Engelhard, M.; Pan, Y.; Kamodia, S.; Luo, J.; Njoki, P. N.; Zhou, S.; Wang, L.; Zhong, C. J. *Anal. Chem.* **2009**, *81*, 689–698.
60. Lim, I-I. S.; Zhong, C. J. *Acc. Chem. Res.* **2009**, *42*, 798–808.
61. Wang, L.; Luo, J.; Shan, S.; Crew, E.; Yin, J.; Wallek; Wong, S.; Zhong, C. J. *Anal. Chem.* **2011**, *83*, 8688–8695.
62. Jin, R.; Wu, G.; Li, Z.; Mirkin, C. A.; Schatz, G. C. *J. Am. Chem. Soc.* **2003**, *125*, 1643–1654.
63. Reynolds, R. A., III; Mirkin, C. A.; Letsinger, R. L. *J. Am. Chem. Soc.* **2000**, *122*, 3795–3796.
64. Stoeva, S. I.; Huo, F.; Lee, J.; Mirkin, C. A. *J. Am. Chem. Soc.* **2005**, *127*, 15362–15363.

Downloaded by NORTH CAROLINA STATE UNIV on November 27, 2012 | http://pubs.acs.org
Publication Date (Web): November 26, 2012 | doi: 10.1021/bk-2012-1112.ch005

Downloaded by NORTH CAROLINA STATE UNIV on November 27, 2012 | http://pubs.acs.org
Publication Date (Web): November 26, 2012 | doi: 10.1021/bk-2012-1112.ch005

65. Demers, L. M.; Mirkin, C. A.; Mucic, R. C.; Reynolds, R. A., III; Letsinger, R. L.; Elghanian, R.; Viswanadham, G. *Anal. Chem.* **2000**, *72*, 5535–5541.
66. Storhoff, J. J.; Elghanian, R.; Mirkin, C. A.; Letsinger, R. L. *Langmuir* **2002**, *18*, 6666.
67. Lytton-Jean, A. K. R.; Han, M. S.; Mirkin, C. A. *Anal. Chem.* **2007**, *79*, 6037–6041.
68. Hurst, S. J.; Han, M. S.; Lytton-Jean, A. K. R.; Mirkin, C. A. *Anal. Chem.* **2007**, *79*, 7201–7205.
69. Xu, X.; Georganopoulou, D. G.; Hill, H. D.; Mirkin, C. A. *Anal. Chem.* **2007**, *79*, 6650–6654.
70. Li, H.; Rothberg, L. J. *J. Am. Chem. Soc.* **2004**, *126*, 10958–10961.
71. Li, H.; Rothberg, L. J. *Anal. Chem.* **2004**, *76*, 5414–5417.
72. Nicewarner-Pena, S. R.; Freeman, R. G.; Reiss, B. D.; He, L.; Pena, D. J.; Walton, I. D.; Cromer, R.; Keating, C. D.; Natan, M. J. *Science* **2001**, *294*, 137–141.
73. Keating, C. D.; Natan, M. J. *Adv. Mater.* **2003**, *15*, 451–454.
74. Mbindyo, J. K. N.; Reiss, B. D.; Martin, B. R.; Keating, C. D.; Natan, M. J.; Mallouk, T. E. *Adv. Mater.* **2001**, *13*, 249–254.
75. Braun, E.; Eichen, Y.; Sivan, U.; Ben-Yoseph, G. *Nature* **1998**, *391*, 775–778.
76. Maxwell, D. J.; Taylor, J. R.; Nie, S. *J. Am. Chem. Soc.* **2002**, *124*, 9606–9612.
77. Cao, C.; Jin, R.; Mirkin, C. A. *Science* **2002**, *297*, 1536–1540.
78. Sauthier, M. L.; Carroll, R. L.; Gorman, C. B.; Franzen, S. *Langmuir* **2002**, *18*, 1825–1830.
79. Zhou, X.; Zhou, J. *Anal. Chem.* **2004**, *76*, 5302–5312.
80. Kanaras, A. G.; Wang, Z.; Bates, A. D.; Cosstick, R.; Brust, M. *Angew. Chem., Int. Ed.* **2003**, *42*, 191–194.
81. Wang, Z.; Kanaras, A. G.; Bates, A. D.; Cosstick, R.; Brust, M. *J. Mater. Chem.* **2004**, *14*, 578–580.
82. Kanaras, A. G.; Wang, Z.; Brust, M.; Cosstick, R.; Bates, A. D. *Small* **2007**, *3*, 590–594.
83. Kanaras, A. G.; Wang, Z.; Hussain, I.; Brust, M.; Cosstick, R.; Bates, A. D. *Small* **2007**, *3*, 67–70.
84. Li, M.; Mann, S. *J. Mater. Chem.* **2004**, *14*, 2260–2263.
85. McIntosh, C. M.; Esposito, E. A., III; Boal, A. K.; Simard, J. M.; Martin, C. T.; Rotello, V. M. *J. Am. Chem. Soc.* **2001**, *123*, 7626–7629.
86. Vidal, B. C.; Deivaraj, T. C.; Yang, J.; Too, H.; Chow, G.; Gan, L. M.; Lee, J. Y. *New J. Chem.* **2005**, *29*, 812–816.
87. Joerger, A. C.; Fersht, A. R. *Oncogene* **2007**, *26*, 2226–2242.
88. Chandrachud, U.; Gal, S. *Technol. Cancer Res. Treat.* **2009**, *8*, 445–453.
89. Bartel, D. P. *Cell* **2004**, *116*, 281–287.
90. Reid, J. G.; Nagaraja, A. K.; Lynn, F. C.; Drabek, R. B.; Muzny, D. M.; Shaw, C. A.; Weiss, M. K.; Naghavi, A. O.; Khan, M.; Zhu, H. F.; Tennakoon, J.; Gunaratne, G. H.; Corry, D. B.; Miller, J.; German, M. S.; Gibbs, R. A.; Matzuk, M. M.; Gunaratne, P. H. *Genome Res.* **2008**, *18*, 1571–1581.

91. Shen, B.; Goodman, H. M. *Science* **2004**, *306*, 997.
92. Gu, P.; Reid, J. G.; Gao, X.; Shaw, C. A.; Creighton, C.; Tran, P. L.; Zhou, X.; Drabek, R. B.; Steffen, D. L.; Hoang, D. M.; Weiss, M. K.; Naghavi, A. O.; El-Daye, J.; Khan, M. F.; Legge, G. B.; Wheeler, D. A.; Gibbs, R. A.; Miller, J. N.; Cooney, A. J.; Gunaratne, P. H. *PLoS One* **2008**, *3*, e2548.
93. Marson, A.; Levine, S. S.; Cole, M. F.; Frampton, G. M.; Brambrink, T.; Johnstone, S.; Guenther, M. G.; Johnston, W. K.; Wernig, M.; Newman, J.; Calabrese, J. M.; Dennis, L. M.; Volkert, T. L.; Gupta, S.; Love, J.; Hannett, N.; Sharp, P. A.; Bartel, D. P.; Jaenisch, R.; Young, R. A. *Cell* **2008**, *134*, 521–533.
94. Swami, A.; Kurupati, R. K.; Pathak, A.; Singh, Y.; Kumar, P.; Gupta, K. C. *Biochem. Biophys. Res. Commun.* **2007**, *362*, 835–841.
95. Kim, J. H.; Yeom, J. H.; Ko, J. J; Han, M. S.; Lee, K.; Na, S. Y.; Bae, J. *J. Biotechnol.* **2011**, *155*, 287–292.
96. Thomsen, L. B.; Larsen, A. B.; Lichota, J.; Moos, T. *Curr. Med. Chem.* **2011**, *18*, 3330–3334.
97. Hwang, D. W.; Son, S.; Jang, J.; Youn, H.; Lee, S.; Lee, D.; Lee, Y. S.; Jeong, J. M.; Kim, W. J.; Lee, D. S. *Biomaterials* **2011**, *32*, 4968–4975.
98. Trang, P.; Wiggins, J. F.; Daige, C. L.; Cho, C.; Omotola, M.; Brown, D.; Weidhaas, J. B.; Bader, A. G.; Slack, F. J. *Mol. Ther.* **2011**, *19*, 1116–1122.
99. Tessel, M. A.; Benham, A. L.; Krett, N. L.; Rosen, S. T.; Gunaratne, P. H. *Horm. Cancer* **2011**, *2*, 182–189.
100. Tessel, M. A.; Krett, N. L.; Rosen, S. T. *Curr. Opin. Oncol.* **2010**, *22*, 592–597.
101. Gunaratne, P. H.; Tessel, M. A.; Creighton, C. J.; Krett, N. L.; Rosen, S. T. *Clin. Lymphoma Myeloma* **2009**, *9*, S129.
102. Nagaraja, A. K.; Creighton, C. J.; Yu, Z. F.; Zhu, H. F.; Gunaratne, P. H.; Reid, J. G.; Olokpa, E.; Itamochi, H.; Ueno, N. T.; Hawkins, S. M.; Anderson, M. L.; Matzuk, M. M. *Mol. Endocrinol.* **2010**, *24*, 447–463.
103. Giljohann, D. A.; Seferos, D. S.; Prigodich, A. E.; Patel, P. C.; Mirkin, C. A. *J. Am. Chem. Soc.* **2009**, *131*, 2072–2073.
104. Giljohann, D. A.; Seferos, D. S.; Daniel, W. L.; Massich, M. D.; Patel, P. C.; Mirkin, C. A. *Angew. Chem., Int. Ed.* **2010**, *49*, 3280–3294.
105. Mirkin, C. A. *MRS Bull.* **2010**, *35*, 532–539.
106. Massich, M. D.; Giljohann, D. A.; Schmucker, A. L.; Patel, P. C.; Mirkin, C. A. *ACS Nano* **2010**, *4*, 5641–5646.
107. Patel, P. C.; Hao, L. L.; Yeung, W. S. A.; Mirkin, C. A. *Mol. Pharmaceutics* **2011**, *8*, 1285–1291.
108. Lee, S. H.; Bae, K. H.; Kim, S. H.; Lee, K. R.; Park, T. G. *Int. J. Pharm.* **2008**, *364*, 94–101.
109. Lewinski, N.; Colvin, V.; Drezek, R. *Small* **2008**, *4*, 26–49.
110. Prencipe, G.; Tabakman, S. M.; Welsher, K.; Liu, Z.; Goodwin, A. P.; Zhang, L.; Henry, J.; Dai, H. J. *J. Am. Chem. Soc.* **2009**, *131*, 4783–4787.
111. Ghosh, P. S.; Kim, C. K.; Han, G.; Forbes, N. S.; Rotello, V. M. *ACS Nano* **2008**, *2*, 2213–2218.

Downloaded by NORTH CAROLINA STATE UNIV on November 27, 2012 | http://pubs.acs.org
Publication Date (Web): November 26, 2012 | doi: 10.1021/bk-2012-1112.ch005

112. Njoki, P. N.; Lim, I. S.; Mott, D.; Park, H. Y.; Khan, B.; Mishra, S.; Sujakumar, R.; Luo, J.; Zhong, C. J. *J. Phys. Chem. C* **2007**, *111*, 14664–14669.
113. Wang, W. H.; Rusin, O.; Xu, X. Y.; Kim, K. K.; Escobedo, J. O.; Fakayode, S. O.; Fletcher, K. A.; Lowry, M.; Schowalter, C. M.; Lawrence, C. M.; Fronczek, F. R.; Warner, I. M.; Strongin, R. M. *J. Am. Chem. Soc.* **2005**, *127*, 15949–15958.
114. Alivisatos, A. P.; Johnsson, K. P.; Peng, X.; Wilson, T. E.; Loweth, C. J.; Bruchez, M. P.; Schultz, P. G. *Nature* **1996**, *382*, 609–611.
115. Parak, W. J.; Gerion, D.; Pellegrino, T.; Zanchet, D.; Micheel, C.; Williams, S. C.; Boudreau, R.; Gros, M. A. L.; Larabell, C. A.; Alivisatos, A. P. *Nanotechnology* **2003**, *14*, R15–R27.
116. Ni, J.; Lipert, R. J.; Dawson, G. B.; Porter, M. D. *Anal. Chem.* **1999**, *71*, 4903–4908.
117. Grubisha, D. S.; Lipert, R. J.; Park, H. Y.; Driskell, J.; Porter, M. D. *Anal. Chem.* **2003**, *75*, 5936–5943.
118. Ghosh, P.; Han, G.; Erdogan, B.; Rosado, O.; Krovi, S. A.; Rotello, V. M. *Chem. Biol. Drug Des.* **2007**, *70*, 13–18.
119. Gates, A. T.; Fakayode, S. O.; Lowry, M.; Ganea, G. M.; Murugeshu, A.; Robinson, J. W.; Strongin, R. M.; Warner, I. M. *Langmuir* **2008**, *24*, 4107–4113.
120. Link, S.; El-Sayed, M. A. *Int. Rev. Phys. Chem.* **2000**, *19*, 409–453.
121. Ung, T.; Liz-Marzan, L.; Mulvaney, P. *J. Phys. Chem. B* **2001**, *105*, 3441–3452.
122. Maye, M. M.; Lim, I-I. S.; Luo, J.; Rab, Z.; Rabinovich, D.; Liu, T.; Zhong, C. J. *J. Am. Chem. Soc.* **2005**, *127*, 1519–1529.
123. Castronuovo, G.; Elia, V.; Niccoli, M.; Strollo, D.; Velleca, F. *Phys. Chem. Chem. Phys.* **1999**, *1*, 5653–5657.
124. Schaaff, T. G.; Whetten, R. L. *J. Phys. Chem. B* **2000**, *104*, 2630–2641.
125. Schaaff, T. G.; Knight, G.; Shafigullin, M. N.; Borkman, R. F.; Whetten, R. L. *J. Phys. Chem. B* **1998**, *102*, 10643–10646.
126. Janáky, R.; Varga, V.; Hermann, A.; Saransaari, P.; Oja, S. S. *Neurochem. Res.* **2000**, *25*, 1397–1405.
127. Soutourina, J.; Blanquet, S.; Plateau, P. *J. Biol. Chem.* **2001**, *276*, 40864–40872.
128. Kühnle, A.; Linderoth, T. R.; Hammer, B.; Besenbacher, F. *Nature* **2002**, *415*, 891–893.
129. Kühnle, A.; Linderoth, T. R.; Besenbacher, F. *J. Am. Chem. Soc.* **2006**, *128*, 1076–1077.
130. Kühnle, A.; Linderoth, T. R.; Hammer, B.; Besenbacher, F. *J. Am. Chem. Soc.* **2003**, *125*, 14680–14681.
131. Li, T.; Park, H. G.; Lee, H. S.; Choi, S. H. *Nanotechnology* **2004**, *15*, S660–S663.
132. Gautier, C.; Bürgi, T. *J. Am. Chem. Soc.* **2006**, *128*, 11079–11087.
133. Bieri, M.; Bürgi, T. *J. Phys. Chem. B* **2005**, *109*, 22476–22485.
134. Gautier, C.; Bürgi, T. *J. Am. Chem. Soc.* **2008**, *130*, 7077–84.

Downloaded by NORTH CAROLINA STATE UNIV on November 27, 2012 | http://pubs.acs.org
Publication Date (Web): November 26, 2012 | doi: 10.1021/bk-2012-1112.ch005

Downloaded by NORTH CAROLINA STATE UNIV on November 27, 2012 | http://pubs.acs.org
Publication Date (Web): November 26, 2012 | doi: 10.1021/bk-2012-1112.ch005

135. Yao, H.; Miki, K.; Nishida, N.; Sasaki, A.; Kimura, K. *J. Am. Chem. Soc.* **2005**, *127*, 15536–15543.
136. Nishida, N.; Yao, H.; Ueda, T.; Sasaki, A.; Kimura, K. *Chem. Mater.* **2007**, *19*, 2831–2841.
137. Lee, H. J.; Yeo, S. Y.; Jeong, S. H. *J. Mater. Science* **2003**, *38*, 2199–2204.
138. Morones, J. R.; Elechiguerra, J. L.; Camacho, A.; Holt, K.; Kouri, J. B.; Ramírez, J. T.; Yacaman, M. J. *Nanotechnology* **2005**, *16*, 2346–2353.
139. Baker, C.; Pradhan, A.; Pakstis, L.; Pochan, D. J.; Shah, S. I. *J. Nanosci. Nanotechnol.* **2005**, *5*, 244–249.
140. Tolaymat, T. M.; El Badawy, A. M.; Genaidy, A.; Scheckel, K. G.; Luxton, T. P.; Suidan, M. *Sci. Total Environ.* **2010**, *408*, 999–1006.
141. Lee, D.; Cohen, R. E.; Rubner, M. F. *Langmuir* **2005**, *21*, 9651–9659.
142. Yoon, K. Y.; Byeon, J. H.; Park, J. H.; Hwang, J. *Sci. Total Environ.* **2007**, *373*, 572–575.
143. Chopra, I. *J. Antimicrob. Chemother.* **2007**, *59*, 587–90.
144. Egger, S.; Lehmann, R. P.; Height, M. J.; Loessner, M. J.; Schuppler, M. *Appl. Environ. Microbiol.* **2009**, *75*, 2973–2976.
145. Panacek, A.; Kvıtek, L.; Prucek, R.; Kolar, M.; Vecerova, R.; Pizurova, N.; Sharma, V. K.; Nevecna, T.; Zboril, R. *J. Phys. Chem. B* **2006**, *110*, 16248–16253.
146. Sharma, V. K.; Yngard, R. A.; Lin, Y. *Adv. Colloid. Interface* **2009**, *145*, 83–96.
147. Hernández-Sierra, J. F.; Ruiz, F.; Cruz Pena, D. C.; Martínez-Gutiérrez, F.; Emilio Martinez, A.; Pozos Guillén, A. D. J.; Tapia-Perez, H.; Martinez-Castanon, G. A. *J. Nanomed. Nanotechnol.* **2008**, *4*, 237–240.
148. Wang, X.; Wang, L. Y.; Lim, S. I.; Bao, K.; Mott, D.; Park, H. Y.; Luo, J.; Hao, S. L.; Zhong, C. J. *J. Nanosci. Nanotechnol.* **2009**, *9*, 3005–3012.
149. Luo, J.; Wang, L. Y.; Mott, D.; Njoki, P.; Lin, Y.; He, T.; Xu, Z.; Wanjana, B. N; Lim, S. I.; Zhong, C. J. *Adv. Mater.* **2008**, *20*, 4342–4347.
150. Kinoshita, T.; Seino, S.; Mizukoshi, Y.; Otome, Y.; Nakagawa, T.; Okitsu, K.; Yamamoto, T. A. *J. Magn. Magn. Mater.* **2005**, *293*, 106–110.
151. Zhang, J.; Post, M.; Veres, T.; Jakubek, Z. J.; Guan, J.; Wang, D.; Normandin, F.; Deslandes, Y.; Simard, B. *J. Phys. Chem. B* **2006**, *110*, 7122–7128.
152. Caruntu, D.; Cushing, B. L.; Caruntu, G.; O'Connor, C. J. *Chem. Mater.* **2005**, *17*, 3398–3042.
153. Spasova, M.; Salgueirino-Maceira, V.; Schlachter, A.; Hilgendorff, M.; Giersig, M.; Liz-Marzan, L. M.; Farle, M. *J. Mater. Chem.* **2005**, *15*, 2095–2098.
154. Stoeva, S. I.; Huo, F.; Lee, J. S.; Mirkin, C. A. *J. Am. Chem. Soc.* **2005**, *127*, 15362–15363.
155. Lyon, J. L.; Fleming, D. A.; Stone, M. B.; Schiffer, P.; Williams, M. E. *Nano Lett.* **2004**, *4*, 719–723.
156. Mandal, M.; Kundu, S.; Ghosh, S. K.; Panigrahi, S.; Sau, T. K.; Yusuf, S. M.; Pal, T. *J. Colloid Interface Sci.* **2005**, *286*, 187–194.
157. Varshney, M.; Yang, L. J.; Su, X. L.; Li, Y. B. *J. Food Prot.* **2005**, *68*, 1804–1811.

158. Ito, A.; Shinkai, M.; Honda, H.; Kobayashi, T. *J. Biosci. Bioeng.* **2005**, *100*, 1–11.
159. Osaka, T.; Matsunaga, T.; Nakanishi, T.; Arakaki, A.; Niwa, D.; Iida, H. *Anal. Bioanal. Chem.* **2006**, *384*, 593–600.
160. Huang, W. C.; Tsai, P. J.; Chen, Y. C. *Small* **2009**, *5*, 51–56.
161. Johnston, H. J.; Hutchison, G.; Christensen, F. M.; Peters, S.; Hankin, S.; Stone, V. *Crit. Rev. Toxicol.* **2010**, *40*, 328–346.

Downloaded by NORTH CAROLINA STATE UNIV on November 27, 2012 | http://pubs.acs.org
Publication Date (Web): November 26, 2012 | doi: 10.1021/bk-2012-1112.ch005

Chapter 6

Functional Gold Nanoparticles for Biointerfaces

Maria Hepel[*]

Department of Chemistry, SUNY at Potsdam,
Potsdam, New York 13676, U.S.A.
[*]E-mail: hepelmr@potsdam.edu

Downloaded by UNIV DE SHERBROOKE on November 27, 2012 | http://pubs.acs.org
Publication Date (Web): November 26, 2012 | doi: 10.1021/bk-2012-1112.ch006

The state-of-the-art of the design of multi-functional nanoparticles for biomedical applications is presented and discussed with emphasis on nanoparticle drug carriers, gene delivery, photodynamic therapy, and image enhancers for diagnostic imaging, including MRI, CT scan, ultrasonic, photoacoustic, and surface-enhanced Raman scattering techniques. The multi-modality, as defined by theranostics, whereby the diagnostic enhancement capabilities are combined with therapeutic action, is the key feature of nanoparticle applications in nanomedicine. The important requirement in these applications is the high selectivity in cell targeting, especially as regards to the tumor cells, designated to be destroyed by highly cytotoxic drugs unloaded from the nanoparticle nanocarriers. The biocompatibility issues are discussed in view of the necessity of protecting healthy cells. For this purpose, the polyamine-coated gold nanoparticles have been reviewed and the adsorption hyper-Langmuirian model has been introduced. The formation of nanostructures from nanoparticle building blocks is also discussed.

Keywords: Au nanoparticles (AuNP); quantum dots (QD); carbon nanotubes (CNT); drug carriers; gene delivery; cancer cell targeting; theranostics

In Functional Nanoparticles for Bioanalysis, Nanomedicine, and Bioelectronic Devices Volume 1; Hepel, M., et al.;
ACS Symposium Series; American Chemical Society: Washington, DC, 2012.

Downloaded by UNIV DE SHERBROOKE on November 27, 2012 | http://pubs.acs.org
Publication Date (Web): November 26, 2012 | doi: 10.1021/bk-2012-1112.ch006

Introduction

Tremendous progress in understanding of nanoworld phenomena spawn by the explosive development of nanoimaging tools and investigative techniques has recently been achieved in divergent fields, from physics and chemistry to molecular biology and medicine. It is not only the possibility of visualizing the nanoworld that has led to this progress. Even more important is the fact that by employing these new imaging tools, scientists were able to create and control new nanoworld entities, sometimes called "building blocks", leading to the design of novel materials (the nanomaterials) with unique electronic, optical and magnetic properties and new devices for nanoelectronics and photonics. In particular, the design of nanoparticles with well-defined size and shape and derivatized by self-assembled monolayers (SAMs) of functional molecules has played a remarkable part in the discoveries of the nanoworld. In this Chapter, the design and new roles of functionalized nanoparticles in biomedical sciences are reviewed. The use of metal, semiconductor, and insulator nanoparticles as drug nanocarriers, in gene delivery, photodynamic therapy, and in medical diagnostics in image enhancement is discussed. The principles of theranostics, a new trend of combining medical diagnostics with therapy by designing multifunctional nanoparticles aiding in medical imaging, recognizing cancers, and delivering therapeutic drugs or participating in hyperthermic treatment, are presented. The review is further expanded onto the nanoparticles functionalized to target cancer cells and on designing biocompatible charged gold nanoparticle (AuNP) interfaces, with special emphasis on polyamine-capped AuNP nanocarriers and double-shell AuNPs coated with a bactericidal poly-L-lysine SAM. A theoretical treatment for molecules in protective monolayers in core-shell nanoparticles is then presented and an example of a hyper-Langmuirian linker-adsorption model is discussed. The final aspects of nanoparticle functionalization concerning the construction of larger nanoparticle cross-linked frameworks are then evaluated.

New Roles of Nanoparticles in Biomedical Sciences

Drug Carriers

Often drugs themselves are being prepared in the form of fine colloidal dispersions for better penetration to the target tissue and specially coated for controlled slow release (Loratadine and Danazol (*1*)). However, with the expansion of nanotechnology and the development of nanoparticle probes in medical diagnostics, a new field of nanoparticle-based nanocarriers for drug delivery has emerged. The basic concept of employing nanocarriers is justified by limiting the serious side effects of otherwise effective drugs by targeting specific locations of the disease and releasing the drug molecules from the carriers, and thereby activating them, only in the place or tissue where they are needed. The drug loading onto the nanocarriers is based on an electrostatic attachment, hydrophobic Van der Waals interactions, hydrogen bonding, or covalent bond

Downloaded by UNIV DE SHERBROOKE on November 27, 2012 | http://pubs.acs.org
Publication Date (Web): November 26, 2012 | doi: 10.1021/bk-2012-1112.ch006

formation. The release of drug molecules at the destination sites can be effected by a photoactivated bond breaking (*2*), ligand exchange interactions, electric field stimulation, thermodesorption, or medium change effects.

In Figure 1, the attachment and release of amines from a AuNP coated with a photocleavable succinimidyl ester are illustrated (*2*). Each AuNP was coated with a mixed SAM of two disulfides:

disulfide **1**: [bis(12-(4-(1-(succinimidyloxycarbonyloxy)ethyl)-2-methoxy-5-nitrophenoxy) dodecyl) disulfide] and

disulfide **2**: [a condensation reaction product of ω-methoxy-poly(ethylene glycol) (PEG) amine, (MW = 5000) and disuccinimidyl 11,11′-dithio-bisundecanoate].

Disulfide **1** was designed to react readily with amines via the succinimidyl ester. The adduct of **1** with amine can be photocleaved in the reaction of the 2-nitrobenzyl group upon near-UV irradiation releasing the amine in the form of a corresponding carbamate which decomposes rapidly to form the original amine. On the other hand, disulfide **2** containing PEG prevents the aggregation of AuNPs and nonspecific protein adsorption on AuNP surface.

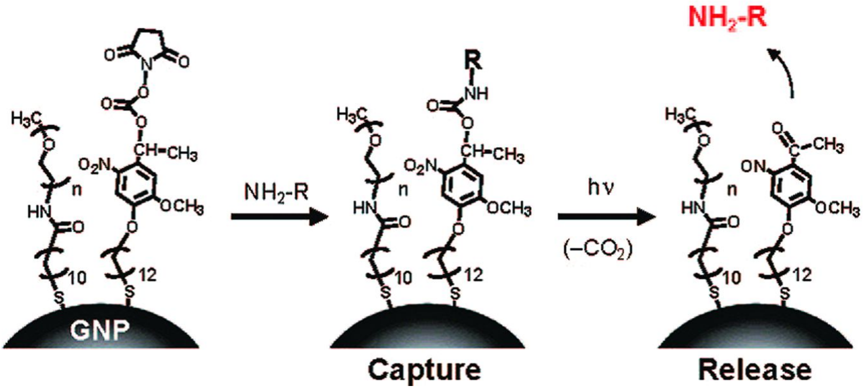

*Figure 1. Capture and release of amines from AuNP capped with a photocleavable succinimidyl ester disulfide **1** and disulfide **2** (both are shown in their thiol forms for clarity). (Reproduced with permission from (2). Copyright 2009 American Chemical Society.)*

Gene Delivery

As the human genome associated with various debilitating diseases and cancer is becoming readily available, the urgency of the development of a gene delivery technology becomes apparent. For many diseases, the gene replacement therapy appears to be the only therapeutic alternative giving a hope for survival. In this new approach in treating cancers, pieces of original non-mutated DNA or the entire genes are supplied to the cytoplasm by carrying them and transporting with the help of nanoparticle carriers. The nanocarriers may consist of inorganic or organic particles, or vesicles. In this Chapter, we will concentrate on gold nanoparticles (AuNPs) which are readily functionalized with self-assembling monolayers (SAMs) of organic molecules. The growing interest in applications of AuNP in nanomedicine and bioassays stems from the simplicity of their functionalization, high stability, biocompatibility, and the prospect of designing complex nanoarchitectures with precision recognition of DNA strands, antibody-antigen interactions, and other biorecognition systems (*3–10*). The principle of a gene delivery utilizing gold nanoparticles loaded with genetic material is illustrated in Figure 2.

Downloaded by UNIV DE SHERBROOKE on November 27, 2012 | http://pubs.acs.org
Publication Date (Web): November 26, 2012 | doi: 10.1021/bk-2012-1112.ch006

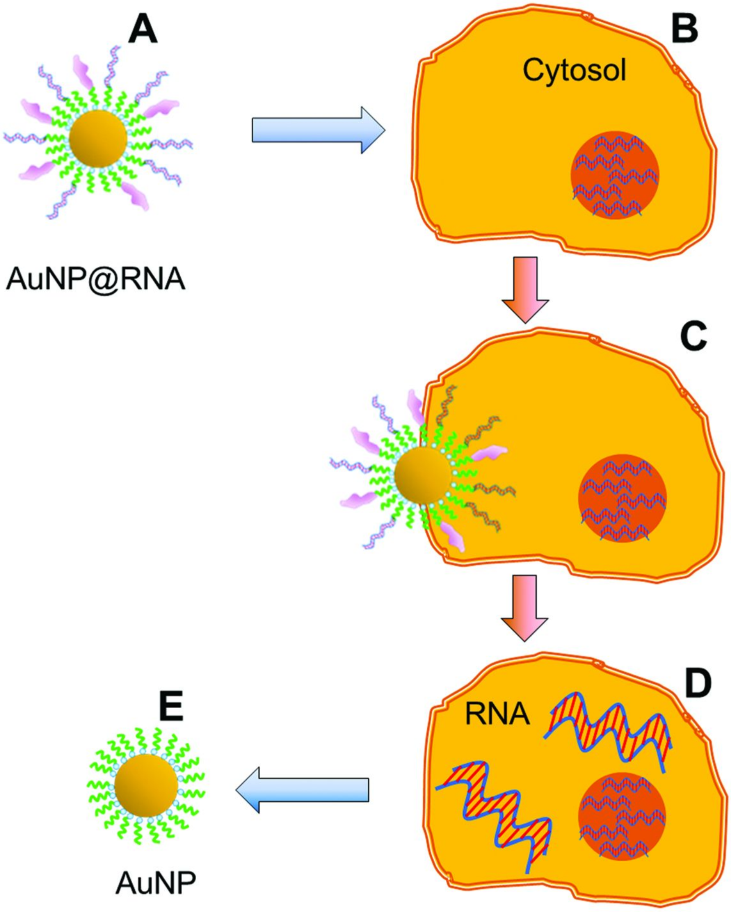

Figure 2. Illustration of a gene delivery by gold nanoparticles loaded with genetic material: AuNP@RNA (A) recognizes the target cell (B), enters the cytosol through the cell membrane (C), unloads the nucleic acid (D) through the ligand exchange with cell thiols, and leaves the cell (E).

The conditions for nanoparticles to be effective gene carriers include: (a) being able to pass through a cell membrane, (b) being able to hold a piece of DNA and to transport it through a membrane to cytoplasm, (c) being able to discharge the load in cytosol or nucleus, (d) exhibit no cytotoxicity and do not influence life processes taking place in cells, (e) they can be readily functionalized to target specific tissue and cells, (f) after unloading the gene, the nanocarriers are quickly excreted and do not accumulate in the body. Some of the promising candidates include AuNP functionalized with designer mercaptoamines, natural polyamines (eg. poly-L-lysine, PLL), phospholipid SAM with positively charged headgroups, and others. We have recently demonstrated that double-shell gold nanoparticles AuNP/Cit/PLL have a high affinity to dsDNA and can be utilized for the gene delivery (*11*).

Another mode of gene therapy consists of RNA interference (RNAi) designed to silence cancer-causing genes (*12–14*). In RNAi, to knockdown genes relevant to a given cancer, nanoparticle carriers loaded with small interfering RNA (siRNA), are utilized. The siRNA are short (*ca.* 21-25 base pair) pieces of double-stranded RNA able to inhibit gene expression by initiating an enzymatic degradation of mRNA that matches the siRNA (*15*). This is a natural process in which siRNA can control the gene expression. In recent work, DeSimone and coworkers (*16*) developed a lipid-coated poly(lactic acid-*co*-glycolic acid) nanoparticles carrying siRNA for prostate cancer treatment.

Downloaded by UNIV DE SHERBROOKE on November 27, 2012 | http://pubs.acs.org
Publication Date (Web): November 26, 2012 | doi: 10.1021/bk-2012-1112.ch006

Photodynamic Therapy

In photodynamic therapy (PDT), a drug called photosensitizing agent is injected into the bloodstream and is absorbed by the cells in a given tissue or in the whole body. After some period following the drug administration (typically about three days), a laser beam of light with specific wavelength is directed locally at the tumor. In a photochemical reaction, singlet oxygen and other reactive oxygen species (ROS) are generated that kill the tumor cells. The U.S. Food and Drug Administration has approved the photosensitizing agent called porfimer sodium (Photofrin®) for use in PDT to treat certain cancers. It can also be used to relieve the symptoms of other cancers, for instance in the case of gallbladder cancer, to clear the tumor blockage in the bile ducts. In addition to directly destroying cancer cells, PDT can cause shrinking of tumors in two other ways: (i) by damaging blood vessels in the tumor tissue, thereby preventing the cancer from getting necessary nutrient supply, and (ii) by activating the immune system response to begin attacking the tumor cells.

There are also several disadvantages of PDT, including shallow penetration of visible light, that is usually applied in PDT (the penetration depth is only on the order of 1 cm), limiting the use of this therapy to surface cancers and to cancers in organs where the irradiation can be applied through optical fibers (eg. non-small cell carcinoma of lungs). The second most important disadvantage of PDT is that the tissue oxygenation determines the therapeutic outcome after PDT treatment. It appears that the absence of molecular oxygen completely inhibits photosensitization. Since in practice, *ca.* 35–40% of cancer patients suffer from

Downloaded by UNIV DE SHERBROOKE on November 27, 2012 | http://pubs.acs.org
Publication Date (Web): November 26, 2012 | doi: 10.1021/bk-2012-1112.ch006

anemia (*17*) and 30% of carcinoma tumors show areas of a restricted oxygen supply (*18*), this seriously limits the therapeutic efficacy of PDT.

In order to enhance the photosensitization and diminish the two main disadvantages of PDT discussed above, a combined treatment by PDT and hyperthermia has been considered (*19*). Among other hyperthermic methods, a novel technology based on administration of light-scattering nanoparticles, for instance gold nanorods (AuNR), provides some clear advantages. By an appropriate functionalization, AuNR with propensity to target specifically the tumor tissue can be designed. Since the surface plasmon (SP) absorbance of AuNR can be tuned by properly selecting the nanorod length, the efficient scattering of light of any wavelength in targeted tissues can be achieved. For instance, UV-vis SP absorbance spectra for $AuNP_{5nm}$ as compared to AuNRs with aspect ratio 2:1 (10×20 nm) and 4:1 (10×40 nm) show that the SP absorbance maximum red-shifts considerably with the increasing nanorod length from 516 nm, to 660 nm, to 790 nm, respectively. This corresponds to the light absorbance by the longitudinal SP originating from the excitement of collective oscillation of conduction free-electrons on a surface of AuNR. The photothermal cancer cell destruction using nanosecond laser light pulses strongly absorbed by cancer-targeted metal nanoparticles is illustrated in Figure 3.

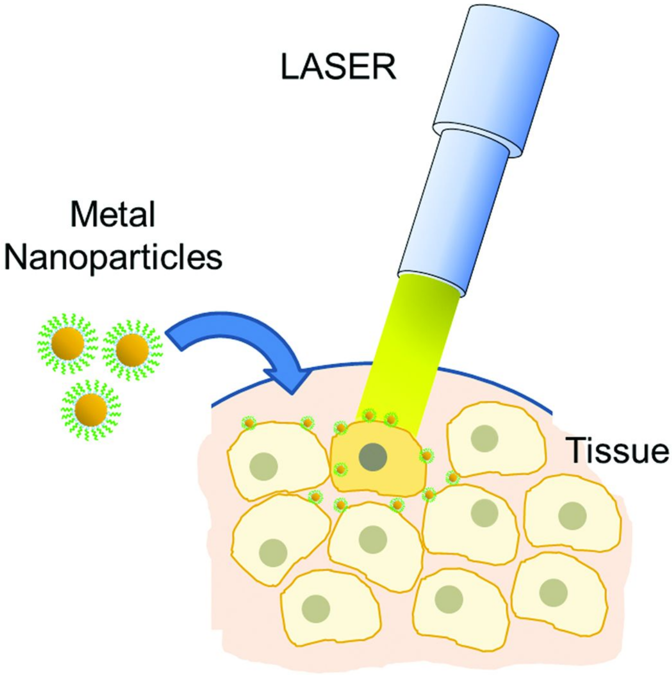

Figure 3. Photothermal cancer cell destruction using nanosecond laser light pulses strongly absorbed by cancer-targeted metal nanoparticles.

The cancer-cell targeting is achieved by two main ways. The first one is based on the specificity of cancer tissue enabling the enhanced permeation and retention (EPR) effects, owing to the increased porosity of the tumors as compared to the healthy tissue, thus aiding in an easy entrance of nanoparticle drug carriers which then concentrate in the areas of cancerous tissue. In addition to that, the drug nanocarriers can be targeted, i.e. functionalized with cancer-specific substrate biomolecules for which cancer cells overexpress receptors and present them in the external cell membrane, thus marking cancer-cells for nanocarrier attachment. The nanocarriers can also be equipped in the SAM shells with antibodies for proteins overexpressed in cancer cells making a biorecognition the principle of the tumor targeting.

Downloaded by UNIV DE SHERBROOKE on November 27, 2012 | http://pubs.acs.org
Publication Date (Web): November 26, 2012 | doi: 10.1021/bk-2012-1112.ch006

Image Enhancers

Functional nanoparticles have drawn considerable attention as image enhancers in ultrasonography, magnetic resonance imaging (MRI), and computed X-ray tomography (CT scan). The administration of nanoparticles not only improves the image contrast, but also shows the location of tumors by specific accumulation in targeted areas. This is achieved through the functionalization of nanoparticles with surface-conjugated antibodies for specific proteins overexpressed in targeted cells. The nanoparticles provide unique advantages due to their strong light-scattering propensity and excellent penetrability beyond the capillary vasculature due to the small size. Schematic view of a tissue-targeted imaging-enhancer nanoparticle probe with Raman marker, MRI imaging-enhancer (magnetic Fe_3O_4-core), tissue-targeting director antibody (Ab), and PEG-ylated SAM which prevents non-specific protein adsorption is depicted in Figure 4.

Liu et al. (*20*) have investigated *in vivo* the grey image enhancement in ultrasonography at 30 MHz center frequency, using SiO_2 nanoparticle suspensions in agar gel with different nanoparticle sizes, from 500 to 3000 nm. The increase in the image brightness with particle size has been found. In another contribution (*21*), they studied biodegradable polylactic acid (PLA) nanoparticles with surface functionalized to target specifically the breast-cancer cells. Thus, the PLA nanoparticles with 250 nm diameter have been functionalized with anti-Her2 antibodies, enabling them to biorecognize the breast cancer cells which overexpress Her2 receptors. The high-resolution ultrasound images have shown a 22% brightness enhancement in targeted cancer tissue.

AuNP-based SERS-probes have shown promise for disease detection and diagnostics. The Gambhir group (*22*, *23*) has utilized 60 nm dia. gold nanoparticles marked with a Raman probe, trans 1,2-bis(4-pyridyl)-ethylene, and coated with SiO_2 shell (or in short: gold-Raman nanoparticles, GRNP) for image enhancement of lung cancer (*24*), colorectal cancer (*22*), and aggressive brain-cancer, glioblastoma (*23*). The acute toxicity studies of polyethylene glycol (PEG) coated GRNP, administered intravenously to mice (*22*), have shown that GRNP have been removed from circulation by the reticuloendothelial system (macrophages in liver and spleen) and only a minor inflammatory reaction has been detected after 24 h following the GRNP injection. An increased oxidative stress has initially been observed in liver but it receded after two weeks. No toxicity of GRNP functionalized to bind specifically to the epidermal growth factor receptor has been found in studies of colorectal-cancer imaging enhancement (*22*). It has to be noted that the cytotoxicity of nanoparticle image-enhancers is considerably diminished by the fact that they are designed to accumulate primarily in the tumor tissue and they are virtually absent in a healthy tissue.

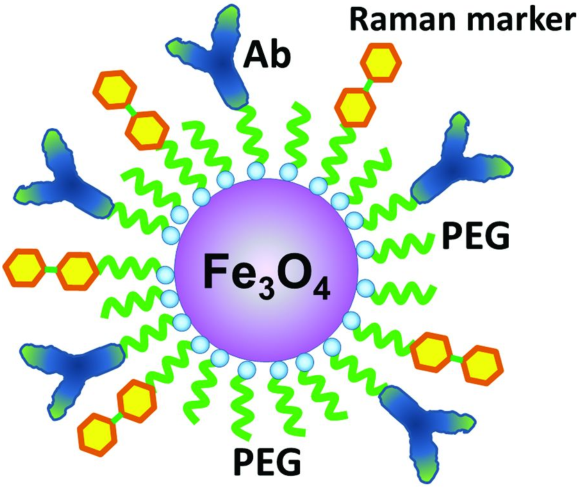

Figure 4. Schematic view of a tissue-targeted imaging-enhancer nanoparticle probe with Raman imaging-enhancer (Raman marker), MRI imaging-enhancer (Fe_3O_4-core), tissue-targeting director antibody (Ab), and PEG-ylated SAM which prevents non-specific protein adsorption.

The Raman-tagged nanoparticle image-enhancers have recently been shown to enable tri-modal brain-tumor imaging (*23*) and precise delineation of rough-surface edges of glioblastoma which is critical in patient survival prognosis. In these studies, Kircher et al. (*23*) performed MRI-photoacoustic-Raman imaging of the mouse human-glioblastoma and demonstrated the high sensitivity and precision of the Raman and photoacoustic techniques, surpassing the MRI. These techniques are also better suited to aid the surgeon in precision incision allowing sparing the parts of brain tissue that are healthy but are located in the close proximity to the cancer tissue. The current low survival rate of glioblastoma patients is due to the rough surface of the tumor and long finger-like projections (extrusions) into the healthy tissue. These extrusions are readily identified by the Raman imaging since they are well-populated by GRNP.

Downloaded by UNIV DE SHERBROOKE on November 27, 2012 | http://pubs.acs.org
Publication Date (Web): November 26, 2012 | doi: 10.1021/bk-2012-1112.ch006

Downloaded by UNIV DE SHERBROOKE on November 27, 2012 | http://pubs.acs.org
Publication Date (Web): November 26, 2012 | doi: 10.1021/bk-2012-1112.ch006

To improve structural and functional stability of SERS-tagged AuNP-probes for in vivo applications, a colloidal SERS gold nanoparticle that encapsulates Raman molecules adsorbed on a 60 nm AuNP with a nonthiol phospholipid coating has been synthesized (*25*). This novel lipid-based SERS probe provides a viable alternative to the strategies based on PEGylation and silica coating.

Quantum dot (QD) based image enhancers have been widely studied. In recent studies, Gao et al. (*26*) reported a novel, 5 nm diameter, InP/ZnS core-shell QD nanoparticles coated with dendrimer to reduce cytotoxicity. These nanoparticles have been shown to produce sharp fluorescence near infra-red (NIR) images of tumors, with emission wavelength λ_{em} = 710 nm. The tumor images are formed due to the enhanced permeability and retention (EPR) effect since the nanoparticles of this small size can readily penetrate the leaky blood vessel walls in tumors and are retained in the tumor tissue. In further investigations (*26*), the dendrimer-capped QDs have been conjugated with arginine-glycine-aspartic acid peptide dimers (RGD_2) in order to target more specifically the integrin $\alpha_v\beta_3$-positive tumors and angiogenesis.

The general guidelines for the validation of new image-enhancer nanoparticles have been proposed by Gambhir and coworkers (*27*). These authors also developed single-walled CNT-based imaging agents for photoacoustic and photothermal therapy, as well as cytometry and theranostics applications.

Theranostics

In 2002, Funkhouser (*28*) proposed to use a new term, theranostics, for rapidly emerging new field of therapy-specific diagnostics. This is especially significant in the case of nanomedicine, where the diagnostic capabilities of functionalized nanoparticles are utilized simultaneously with their therapeutic action. Thus, theranostic means here therapy + diagnostics and this combination well suits to the actual roles of nanoparticle carriers equipped with image enhancement tags (such as the Raman tag) and at the same time they carry a therapeutic load (e.g. a sensitizing agent for PDT or chemotherapeutic drugs). In fact, a multitude of combinations of diagnostic and therapeutic capabilities exists. Some of the most important can be listed as follows:

(a) diagnostic capabilities:

- electromagnetic scattering, e.g. X-ray CT scan image enhancing cores,
- MRI contrast agents, e.g. Gd^{3+} complexes conjugated to nanocarriers, or magnetic Fe_3O_4-core nanoparticles,
- Raman tags,
- fluorescent labels (quantum dots or organic dyes),
- nuclear imaging agents,
- photoacoustic enhancers,
- ultrasonography contrast enhancers (e.g. metal nanoparticle cores);

(b) therapeutic agents:

- chemotherapy drugs,
- photodynamic sensitizers,
- hyperthermia (photothermal ablation) agents,
- radiation therapy compounds,
- growth inhibitors, e.g. integrin inhibitors, preventing angiogenesis in tumors,
- gene silencers,
- gene replacement agents, e.g. piecies of RNA.

Downloaded by UNIV DE SHERBROOKE on November 27, 2012 | http://pubs.acs.org
Publication Date (Web): November 26, 2012 | doi: 10.1021/bk-2012-1112.ch006

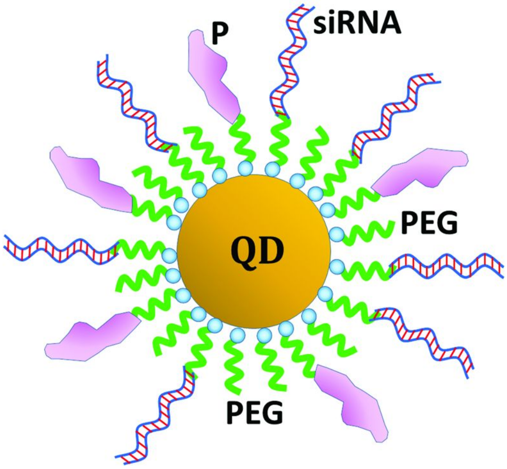

Figure 5. Schematic view of a theranostic nanoparticle nanocarrier with multifunctionality: QD-core fluorescent marker, P - homing peptide, siRNA - small interfering RNA fragment for gene replacement therapy, PEG - poly-ethylene glycol chains for diminishing nonspecific adsorption of proteins. (Adapted with permission from (29). Copyright 2007 American Chemical Society.)

The theranostic nanoparticle-based nanocarriers are also equipped with targeting functionalities, as discussed in previous sections, such as antibodies or peptides having sufficiently high affinity to receptors overexpressed in tumor cells. Such multimodal nanoparticle nanocarrier is depicted in Figure 5.

The broad applications of theranostic nanoparticle-based nanocarriers have been recently reviewed by Kelkar and Reineke (*30*). Pitsillides et al. (*31*) have discussed specific cell-targeting with light-absorbing nanoparticles for medical applications.

Downloaded by UNIV DE SHERBROOKE on November 27, 2012 | http://pubs.acs.org
Publication Date (Web): November 26, 2012 | doi: 10.1021/bk-2012-1112.ch006

Targeting Cancer Cells

In today's medicine, the major goal of nanoparticle administration is to aid in cancer therapy since the cancer survival rate is bleak in the case of many cancers and especially in the case of advanced tumor development stages. Targeting cancer cells is being pursued for several purposes:

(i) to accumulate highly toxic chemotherapeutic drugs in the tumor while saving the healthy tissue,
(ii) to provide means for thermotherapy to destroy tumor,
(iii) to deliver sensitizing agents for local photodynamic therapy,
(iv) to enhance the tumor imaging to aid the surgeon in removing the tumor out of the healthy tissue.

The methods of efficient targeting of cancer cells are based on functionalization of nanoparticles by attaching biorecognition molecules to nanoparticle shells that are able to interact with receptors and other targets overexpressed in cancer cells. For instance, single-walled CNT functionalized to target the integrin $\alpha_V\beta_3$ associated with tumor angiogenesis was proposed by Gambhir and coworkers (*27*). The integrin $\alpha_V\beta_3$-targeted gold nanobeacons have been applied in molecular photoacoustic tomography for a 3D-imaging of angiogenesis by Pan et al. (*32*). Since gold nanobeacons accumulate only on the newly forming blood vessels where the integrin is overexpressed, the photoacoustic signal is enhanced in the vessel growth areas over the mature blood vessels. This has a profound clinical significance since a wide range of prevalent diseases, especially cancer and cardiovascular diseases, are based on angiogenesis.

The targeted drug delivery is an attractive concept: it combines high local concentration of a drug and low systemic exposure minimizing the side-effects of the drug. Recent progress in the field has rekindled interest in the targeting approach. Since the tumor cells express many molecules on their surface that clearly distinguish them from normal cells, the nanocarrier targeting is directed to these molecules. For long time, these molecules were detected with appropriate antibodies but a widespread screening of peptides and aptamers has greatly extended the number of selective binders to tumor cells (*33*, *34*). A list of surface receptors overexpressed in tumor cells that can potentially be used for anticancer nanocarrier targeting is presented in Table I.

Those receptors which are only expressed in cancer cells or newly developing blood vessels are of particular importance, since they enable precise targeting of nanocarriers toward these receptors, focusing the therapeutic action of carried drugs right at the tumor sites. As an example may serve NG2, a chondroitin sulfate proteoglycan spanning the pericyte membrane and marking the angiogenesis (*35*). PDGF-B and PDGFRβ, platelet-derived growth factor receptors, are expressed in tumors and participate in vascular growth signaling pathways.

Table I. Tumor cell-membrane receptors and tumor blood-vessel receptors utilized for biorecognition and targeting of cancers

Receptor	Reference
aminopeptidaseN	(36)
annexin-1	(37)
endosialin	(38)
fibronectin	(39)
fibronectin-fibrin complex	(40)
integrin $\alpha_v\beta_3$	(32)
integrins $\alpha_v\beta_3$ and $\alpha_v\beta_5$	(33, 41)
interleukin-11 receptor α	(42)
NG2*	(35)
nuclealin	(43)
p32 receptor	(44)
PDGF-B and PDGFRβ**	(45)
plectin-1	(46)
protease-cleaved collagen IV	(47)
TEM	(48)

* NG2 - membrane spanning chondroitin sulfate proteoglycan is a biomarker of angiogenesis in pericytes and smooth muscle cells;

** PDGF-B and PDGFRβ - platelet-derived growth factor receptors.

Downloaded by UNIV DE SHERBROOKE on November 27, 2012 | http://pubs.acs.org
Publication Date (Web): November 26, 2012 | doi: 10.1021/bk-2012-1112.ch006

The PDGFRbeta+ perivascular progenitor cells regulate perivascular cell differentiation and vascular growth (*45*). The inhibition of PDGF-B and PDGFRβ signaling results in the disruption of blood vessel growth, microvascular leakage, and haemorrhage. These receptors can therefore be utilized in tumor targeting with nanocarriers as well as in the inhibition of the vascular growth, thereby cutting the supply of nutrients to the tumor. Note that both the endothelial cells (forming the inner lining of the blood vessels) and the perivascular cells (or: pericytes) that wrap around the vascular tubing forming a rigid scafold, are necessary for a growing blood vessel. However, the PDGF-B expressing endothelial cells are the first cells to move into the surrounding tissue to expand the blood vessel network (*49*, *50*).

The perspectives of targeting drugs and nanoparticle carriers to tumors have recently been discussed by Ruoslahti et al. (*51*), with particular emphasis on the tumor vascular growth targeting by functionalized nanoparticle carriers. Pitsillides et al. (*31*) have discussed cell-targeting with light-absorbing nanoparticles and the use of different biorecognition markers.

Designing Biocompatible Charged Functional AuNP Interfaces

Polyamine-Capped AuNP Nanocarriers

The exploration of non-toxic coatings plays a key role in the development of implants and tissue engineering (*52*). With the emergence of nanoparticle probes and nanocarriers in diagnostic imaging and therapy (*53*), the nanoparticle coating has become one of the most important fields of studies (*1*, *54–57*). Besides the nature-developed materials (e.g. phospholipids), the biomimetic coatings have been extensively investigated to achieve high degree of biocompatibility and reduced side-effects.

In living cells, different polyelectrolytes participate in life processes. A remarkable range of interactions has been observed for one polyelectrolyte, poly-L-lysine (PLL). PLL, which is positively charged due to the uncompensated protonated amine groups $-NH_3^+$, interacts with both DNA and phospholipids involved in various membranes in living organisms. The polycationic polyelectrolytes, such as PLL, induce the production of immunoglobulin and their presence in higher organisms is essential. For instance, PLL has been found to increase the production of interferon-beta while not acting on the cell proliferation (*58*). Moreover, PLL exhibits remarkable anti-proliferative properties (*59*) on many cancers, such as Ehrlich carcinoma, L1210 lymphoid leukemia, erythroleukemia, Lewis lung tumor, P388 tumors, and P38 macrophage derived tumor. On the other hand, the synthetic isomeric α-PLL boosts the astrocyte proliferation (*60*). The bioactivity of dendrimers composed of polylysine and peptides in the AC cyclase signaling system in rats myocardium and brain has recently been investigated (*61*). The PLL-derivative biopolymers present a high promise as the polycationic carriers for biologically relevant molecules. Both isomers, synthetic α-PLL and naturally occurring ε-PLL, have been proposed for use as virucidal agents for protecting eggplant family plants against tobacco mosaic virus, as well as against potato virus and cucumber mosaic virus (*62*).

It has been shown that direct interaction of lysine residues with gold metal surface stabilizes the AuNPs in solution (*63*). However, as pointed out by Guo et al. (*64*), there is virtually no interparticle interaction between PLL-coated AuNPs in the pH range 6.5-10.5, as evidenced by only a minute shift of SP absorbance band, from 522 to 526 nm. On the other hand, at pH > 11.5, a clear assembly of PLL-capped AuNPs has been detected together with the associated shift in the SP absorbance band to $\lambda_{max} = 538$ nm. The AuNP assembly has been ascribed to the interparticle Van der Waals attractive forces between β-sheets.

Joshi et al. (*65*) have shown that binding of lysine to AuNP at neutral pH is fairly weak, although it increases at pH > 11 simultaneously with deprotonation of $-NH_3^+$ groups (above the isoelectric point of lysine, $pI = 9.4$ (*65*)). By adding a condensing agent EDC (ethyl-3-(dimethylaminopropyl) carbodiimide), the assembly of 3D networks from lysine-capped $AuNP_{13nm}$ have been observed (*66*) and an efficient AuNP binding through a dipeptide cross-linker has been attained. Binding of amine groups directly to gold has also been achieved (*67–69*). The calculations of electronic structure of polylysine dendrimers has been carried out by Maiti et al. (*70*), Ouyang et al. (*71*), and Manisto et al. (*72*).

Downloaded by UNIV DE SHERBROOKE on November 27, 2012 | http://pubs.acs.org
Publication Date (Web): November 26, 2012 | doi: 10.1021/bk-2012-1112.ch006

Downloaded by UNIV DE SHERBROOKE on November 27, 2012 | http://pubs.acs.org
Publication Date (Web): November 26, 2012 | doi: 10.1021/bk-2012-1112.ch006

Various biomolecules interact with PLL, including DNA (*73*, *74*), lipids (*75*), cyclodextrin (*76*), etc. Varadan (*77*) has reported the immobilization of PLL onto a probe surface for endotoxin-detection. Interestingly, PLL has also been considered for applications as a biosorbent for removal of toxicants, such as Cr(VI) species causing oxidative DNA damage (*78*), from industrial waste water.

There are several important prospective applications of PLL-capped nanoparticles, including bactericidal and virucidal injections, carriers of stem cells, scaffolds in tissue repair, and as nanocarriers in gene delivery systems where DNA fragments can be attached electrostatically to the positively charged PLL shells (*11*). The key advantage of a PLL coating is its intrinsic non-toxicity to the eukaryotic cells.

In view of the much weaker direct interactions of PLL with a gold surface, we have investigated interactions of PLL with citrate-capped gold nanoparticles (*11*) for possible application of PLL-functionalized AuNP in gene delivery systems and anti-microbial injections.

The gene delivery concept has been pioneered by Rotello et al. (*53*, *79*, *80*) using AuNPs capped with amino acid-modified alkane thiols. The AuNPs with lysine residue-modified thiols have been found to interact with dsDNA and were able to penetrate eukaryotic membranes (*53*). The DNA unloading was induced by glutathione derivatives (*80*). However, the ligand exchange (thiol-for-thiol) is more difficult when thiolate AuNP coating is used. We have demonstrated this, for instance for the ligand exchange between homocysteine and glutathione (*81*)). On the other hand when a AuNP/Cit/PLL is used as the carrier, the gene cargo unloading becomes much easier.

To monitor the PLL-induced AuNP assembly, we have explored the utility of the resonance elastic light scattering (RELS) spectroscopy. The RELS technique is based on a momentary absorption of photons by molecules and nanoparticles in solution followed by an immediate re-emission of light in all directions without any energy loss (*82*). The re-emitted radiation is coherent. We have recently applied RELS to study nanoparticle assembly (*5*, *81–83*) and found it to be very sensitive to supramolecular ensemble formation. The high sensitivity of RELS to nanoparticle network assembly is due to the excitation of the local surface plasmon (SP) in gold nanoparticles and coupling of SP oscillations during the close approach of particles in the supramolecular structure formation. In this Chapter, we describe the interactions of AuNP with PLL and elucidate the mechanism of the PLL-linked citrate-capped AuNP assembly. The illustration of a network forming capabilities of PLL-linked AuNP/Cit nanoparticles is presented in Figure 6.

We have found that a hyper-Langmuirian electrosorption kinetics model best fits the experimental data. The interactions of PLL-coated AuNP with dsDNA have been tested to demonstrate the affinity of PLL amine functionalities in the nanoparticle shell environment to the model genes represented by short dsDNA fragments.

Hyper-Langmuirian Linker-Adsorption Model

The assembly of metal or semiconductor nanoparticle networks and their properties, including the interparticle distance, coordination number, optical density, electronic properties, and others, depend strongly on the linker functional groups' charge and the ability of nanoparticle shells to form hydrogen bonds and Van der Waals interactions.

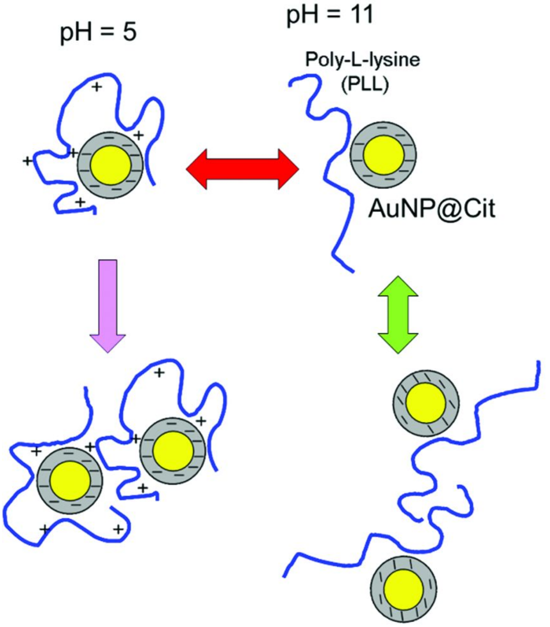

Figure 6. Scheme illustrating strong interactions of PLL with AuNP@Cit at pH 5 and weak β-sheet interactions at pH = 11. (Reproduced with permission from (11). Copyright 2011 Elsevier Publisher.)

Downloaded by UNIV DE SHERBROOKE on November 27, 2012 | http://pubs.acs.org
Publication Date (Web): November 26, 2012 | doi: 10.1021/bk-2012-1112.ch006

In the case of AuNP and a polyelectrolyte with a long chain, like PLL, the AuNP network formation depends on the linker chain length, nanoparticle size, number of charges on a nanoparticle and on a linker chain, as well as the structure and conformation of the linker. We describe here an attempt to evaluate the mean stoichiometry of a PLL-linker binding by AuNP. For this purpose, we analyze the PLL concentration dependence of the RELS intensity at a wavelength providing most sensitive RELS signal response to the nanoparticle framework assembly process.

Typical RELS spectra for citrate-capped $AuNP_{5nm}$ in solution are presented in Figure 7, for AuNP@Cit concentration of 3.8 nM.

Downloaded by UNIV DE SHERBROOKE on November 27, 2012 | http://pubs.acs.org
Publication Date (Web): November 26, 2012 | doi: 10.1021/bk-2012-1112.ch006

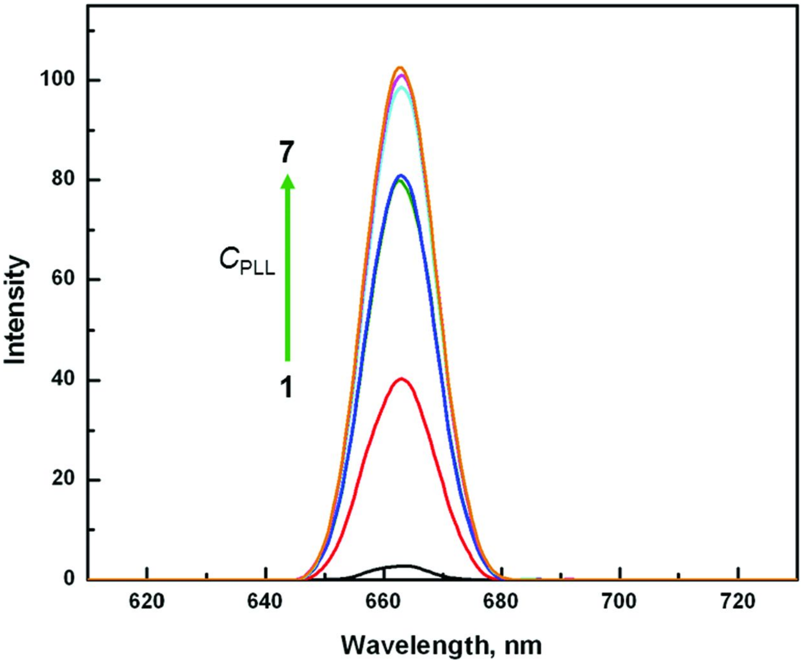

Figure 7. RELS spectra for 3.8 nM AuNP$_{5nm}$ solutions with varying concentration of PLL, C$_{PLL}$ [ppm]: (1) 0, (2) 0.33, (3) 0.83, (4) 1.17, (5) 1.5, (6) 1.83, (7) 2.17; λ_{ex} = 665 nm, pH = 5.20 ± 0.17. (Reproduced with permission from (11). Copyright 2011, Elsevier Publisher.)

The secondary emission spectra were obtained for constant excitation wavelength λ_{ex} = 665 nm (corresponding to photon energy of 1.86 eV) and the emission was recorded from λ_{em} = 610 to 730 nm. The high intensity of the resonance elastic light scattering from AuNP$_{5nm}$ nanoparticles in solution is due to the absorption of photons at 665 nm followed by secondary emission without any energy loss. Therefore, a coherent elastic Rayleigh scattering with Gaussian peak shape centered at λ_{em} = λ_{ex} = 665 nm is observed. The narrow bandwidth of $\Delta\lambda$ = 15 nm confirms that the radiation broadening, density fluctuation, and inelastic Raman scattering effects are negligible. Because of the low intensity of the background which is virtually zero, well defined RELS peaks are obtained.

Note that the RELS spectra can be obtained using a standard fluorescence spectrometer equipped with dual monochromators (for excitation and emission beams). For instance, the spectra presented in Figure 7, have been recorded on a Model LS55 Fluorescence Spectrometer (Perkin Elmer, Waltham, MA, U.S.A.) equipped with 20 kW Xenon light source operating in 8 μs pulsing mode. Pulse width at half height was less than 10 μs. The dual detector system consisted of a photomultiplier tube (PMT) and an avalanche photodiode. The RELS spectra were obtained at 90° angle from the incident (excitation) light beam. The excitation beam monochromator was either scanned simultaneously with the detector beam monochromator ($\Delta\lambda$ = 0) or set at a constant excitation wavelength.

The large increase in light scattering upon the addition of PLL indicates the nanoparticle assembly since I_{sc} increases strongly with increasing size of aggregates following relation (*1*) which we have recently derived (*5*):

$$I_{sc} = f(a_{rel}^3) \tag{1}$$

where $a_{rel} = a_2/a_1$ is the relative particle diameter and a_1, a_2 are the diameters of particles before and after the assembly, respectively. This is corroborated by the observed SP band absorbance shift toward longer wavelengths (*11*).

The dependence of RELS intensity maximum I_{sc} on C_{PLL} is shown in Figure 8, for λ_{ex} = 665 nm. The plot of I_{sc} on C_{PLL} shows a clear trend to level of at higher C_{PLL}. The value of λ_{ex} = 665 nm was selected since the absorbance change observed upon addition of PLL is the largest at this wavelength. The nonlinear dependence of I_{sc} on C_{PLL} is likely due to the limited surface sites' availability on Au nanoparticles for PLL molecules.

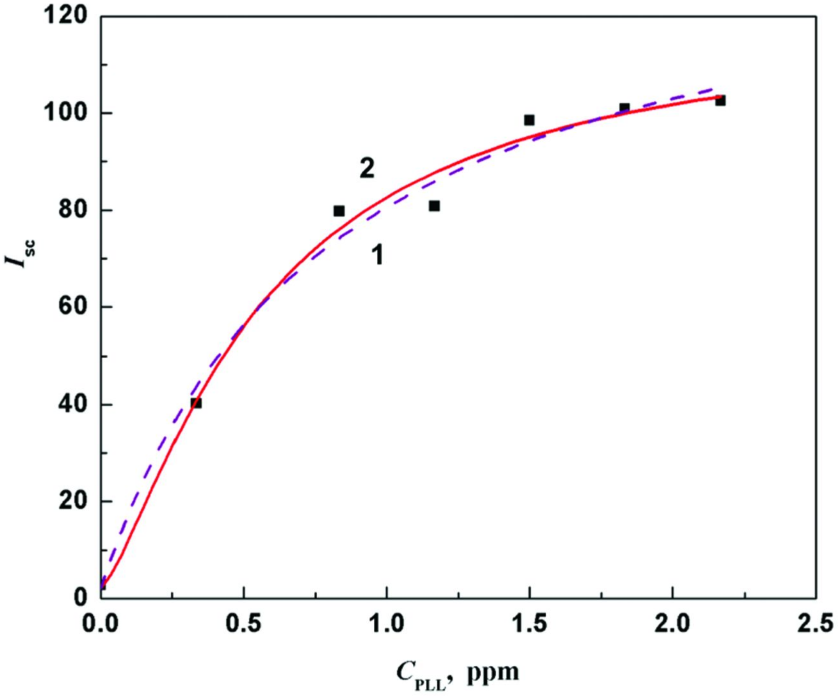

Figure 8. Dependence of RELS intensity I_{sc} on C_{PLL} for 3.8 nM AuNP$_{5nm}$ solutions recorded at λ_{ex} = 665 nm: (1) fit to Langmuir equation (dashed line), (2) fit to hyper-Langmuirian equation (3) with n = 1.35, K = 2.16 ppm^n, $I_{sc,sat}$ = 117, $I_{sc.bkgr}$ = 2.86 (solid line). (Reproduced with permission from (11). Copyright 2011, Elsevier Publisher.)

Downloaded by UNIV DE SHERBROOKE on November 27, 2012 | http://pubs.acs.org
Publication Date (Web): November 26, 2012 | doi: 10.1021/bk-2012-1112.ch006

This means that when most of the AuNP/Cit surface becomes coated with PLL molecules, further additions of PLL molecules would not result in the extension of the aggregation processes. Therefore, a Langmuir-type adsorption equation can be employed for the experimental data fitting:

$$I_{sc} = I_{sc,0} + \left(I_{sc,sat} - I_{sc,0}\right)\frac{KC_L}{\left(KC_L + 1\right)} \tag{2}$$

where C_L is the linker concentration (here: PLL), K – is the linking interaction equilibrium constant, $I_{sc,0}$ is the background scattering intensity, and $I_{sc,sat}$ is the maximum scattering intensity achieved at infinite linker concentration. By fitting this equation to the experimental data, one obtains the following values of constants: $K = 1.26$ ppm^{-1} and $I_{sc,sat} = 142$, with regression coefficient $R^2 = 0.988$. Further enhancement of the model has been attained by introducing the multi-site adsorption of a linker:

$$\begin{array}{ccccc} nL & + & S & = & S.L_n \\ C_L & & (1-\theta) & & \theta \end{array} \tag{3}$$

where L is the linker molecule, S – the surface of AuNP/Cit nanoparticles and θ is the surface coverage. This approach leads to the hyper-Langmuirian equilibrium equation:

$$I_{sc} = I_{sc,0} + \left(I_{sc,sat} - I_{sc,0}\right)\frac{KC_L^n}{\left(KC_L^n + 1\right)} \tag{4}$$

where the stoichiometric coefficient n can assume values higher than 1 or lower than 1. For $n>1$, several linker molecules can be accommodated on one equivalent site. The surface of a single AuNP/Cit particle can be assumed here as the equivalent unit site. For $n < 1$, equation (4) is still valid and in this case we have binding of more than one AuNP/Cit to a large linker molecule. It becomes clear that by fitting this three-parameter equation to the experimental data can provide good insights into the stoichiometry and geometry of the ensembles formed in the linker-induced AuNP assembly process. By applying simplex iterations in fitting a hyper-Langmuirian equation to the RELS data of Figure 7, the following parameters are obtained: $K = 2.17$ ppm^{-n}, $n = 1.35$, $I_{sc,sat} = 117.7$, $I_{sc,bkgr} = 2.86$, with regression $R^2 = 0.991$. The hyper-Langmuirian equation better evaluates the saturation level which is overestimated by the simple Langmuirian function. The obtained value of $n = 1.35$ indicates that, on average, more than one linker molecule binds to each gold nanoparticle. The illustration of a network of PLL-linked AuNP/Cit nanoparticles formed under such conditions is presented in Figure 6. Note that equation (4) neglects the lateral ligand self-interactions (corresponding to the cooperativity in Hill terms) which are assumed to be negligible in comparison to the high affinity of PLL to AuNP@Cit and, also, due to the small number of linker molecules present on each AuNP@Cit.

Downloaded by UNIV DE SHERBROOKE on November 27, 2012 | http://pubs.acs.org
Publication Date (Web): November 26, 2012 | doi: 10.1021/bk-2012-1112.ch006

The net charge carried on one AuNP@Cit/PLL nanoparticle can be evaluated on the basis of the experimental value of *n* ($n = 1.35$). For a AuNP with 5 nm diameter, the number of adsorbed Cit molecules and uncompensated PLL charge can be calculated as follows:

$$\Gamma_{Cit} = \frac{1}{S_{Cit}} \tag{5}$$

$$\gamma_{Cit} = \frac{\Gamma_{Cit}}{N_A} \tag{6}$$

$$q_{-} = z\Gamma_{Cit}S_{AuNP} \tag{7}$$

$$q_{+} = \frac{M_{PLL}}{M_{Lys}} \tag{8}$$

$$q = q_{-} + nq_{+} \tag{9}$$

where $S_{\text{Cit}} = 0.216$ nm^2 is the surface area per one adsorbed Cit molecule, $\Gamma_{\text{Cit}} = 4.63\text{x}10^{14}$ molec/cm^2, $\gamma_{\text{Cit}} = 0.768$ nmol/cm^2 is the surface excess of Cit, $z = -3$ is the number of charges per Cit molecule, $S_{\text{AuNP}} = 0.26$ nm^2 is the surface area of AuNP, $M_{\text{Lys}} = 146$ g/mol and $M_{\text{PLL}} = 150{,}000$ g/mol, are the molecular masses of lysine residue and PLL, respectively. Therefore, the total negative charge, generated by 363 Cit molecules in a AuNP shell, is: $q_{-} = -1{,}089$. This negative charge is overcompensated by the total positive charge of PLL, $q_{+} = 1{,}387$, generated by 1.35 PLL molecules, leading to the net uncompensated charge: $q = +297$. The superfluous positive charge, which is primarily due to the corrugation of PLL shell, is helpful in accommodating large negatively charged loads of DNA fragments and to engage in transmembrane crossing where the phospholipid heads of a bilayer membrane carry excess negative charge.

Molecular Dynamics Simulations of Core–Shell Nanoparticles

A molecular dynamics (MD) simulation of the electrostatic interactions and hydrogen bonding have been performed to gain further insights into the nature of interparticle Au/Cit/PLL interactions. The results of MD simulations for a citrate-capped $Au_9Cit_8^{8-}$ cluster with a model PLL, ε-$(Lys)_3$, in the form of ε-$(Lys)_3^{2+}$ dication are presented in Figure 9*ab* and for ε-$(Lys)_3^0$ neutral chain in Figure 9*c*. Figure 10 shows consecutive stages in the approach of a model deprotonated PLL chain, ε-$(Lys)_6$, to a citrate-capped gold cluster, $Au_9Cit_8^{8-}$. The frames 1 through 8 show a gradual formation of 9 hydrogen bonds, represented by broken lines.

Downloaded by UNIV DE SHERBROOKE on November 27, 2012 | http://pubs.acs.org
Publication Date (Web): November 26, 2012 | doi: 10.1021/bk-2012-1112.ch006

The interaction of citrate and PLL with gold surface has been confirmed using the electrochemical quartz crystal nanogravimetry (EQCN). The proof-of-concept of gene-carrying capability of a Au/Cit/PLL nanoparticle has been obtained by recording the binding characteristics of a calf thymus DNA (ctDNA). Figure 11 shows the apparent mass changes recorded upon the addition of Cit, PLL, and ctDNA to the solution with an immersed Au-coated quartz crystal resonator electrode. The effect of addition of ctDNA on RELS spectra of Au/Cit/PLL nanoparticles for excitation wavelength λ_{ex} = 520 nm, is illustrated in Figure 12.

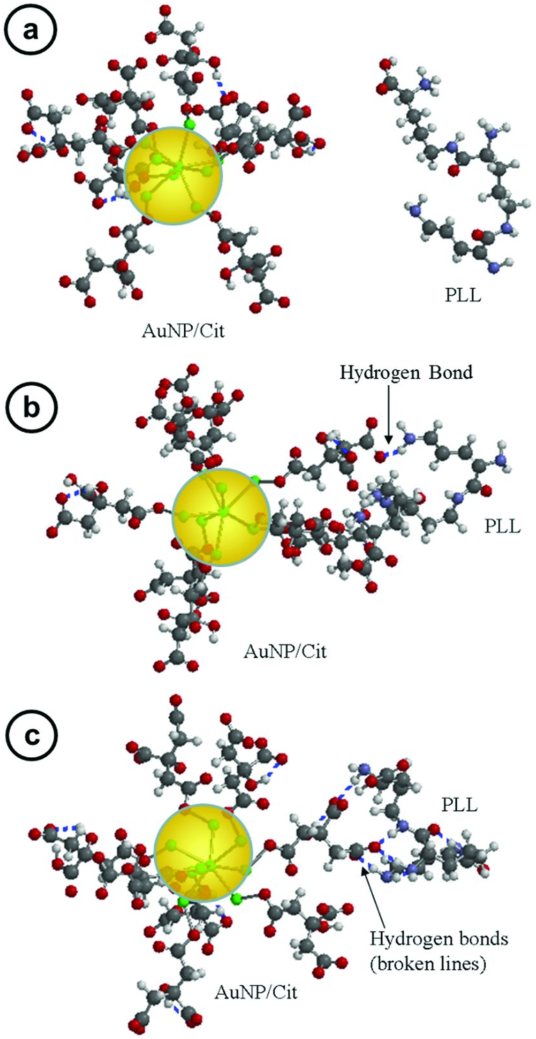

Figure 9. Molecular dynamics simulation of the electrostatic interactions and hydrogen bonding of a citrate-capped $Au_9Cit_8^{8-}$ cluster with a model PLL, ε-$(Lys)_3$, in the form of ε-$(Lys)_3^{2+}$ dication (a,b) and ε-$(Lys)_3^0$ neutral chain (c). (Reproduced with permission from (11). Copyright 2011, Elsevier Publisher.)

Downloaded by UNIV DE SHERBROOKE on November 27, 2012 | http://pubs.acs.org
Publication Date (Web): November 26, 2012 | doi: 10.1021/bk-2012-1112.ch006

Downloaded by UNIV DE SHERBROOKE on November 27, 2012 | http://pubs.acs.org
Publication Date (Web): November 26, 2012 | doi: 10.1021/bk-2012-1112.ch006

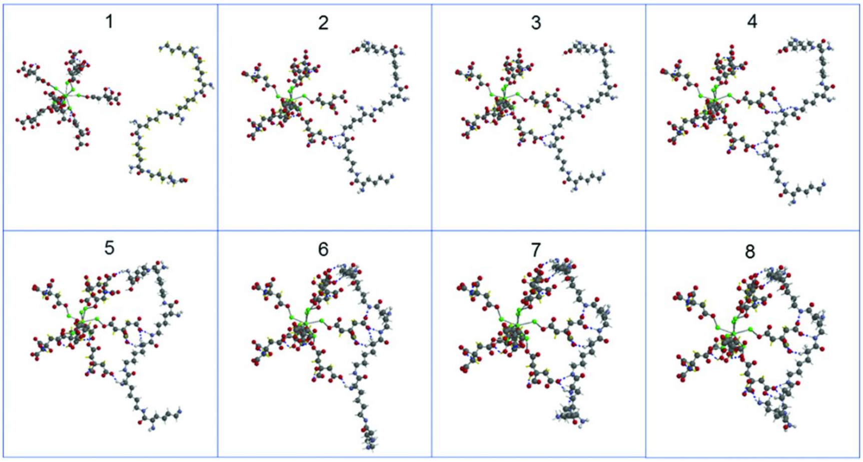

Figure 10. Molecular dynamics simulation of the interactions of a model deprotonated PLL chain, ε-(Lys)$_6$, with a citrate-capped $Au_9Cit_8^{8-}$ cluster; frames (1 to 8) show a gradual formation of 9 hydrogen bonds (broken lines). (Reproduced with permission from (11). Copyright 2011, Elsevier Publisher.)

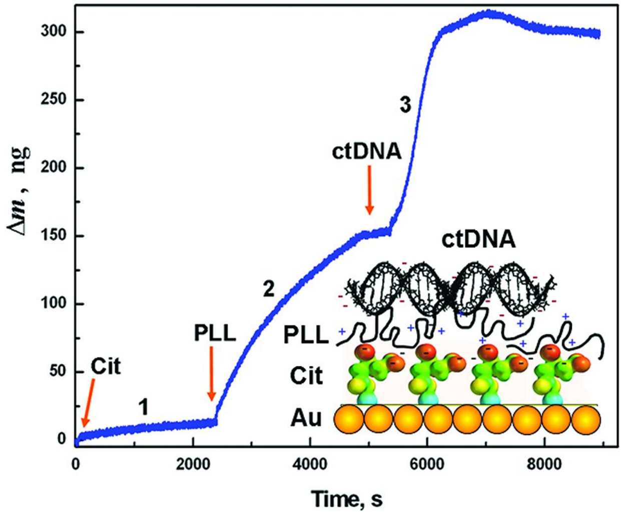

Figure 11. Transients of apparent mass Δm after injections of citrate (1), PLL (2), and ctDNA (3), recorded using EQCN on a QC/Au piezoresonator at open circuit; injections of reagent are marked with arrows; medium: 0.02 M PBS, pH = 7.45. C_{Cit} = 10 mM, C_{PLL} = 30 ppm, C_{ctDNA} = 45 μM bp (all final concentrations). Inset: schematic of an electrodic film with layers of Cit, PLL and ctDNA on a Au substrate. (Reproduced with permission from (11). Copyright 2011, Elsevier Publisher.)

Downloaded by UNIV DE SHERBROOKE on November 27, 2012 | http://pubs.acs.org
Publication Date (Web): November 26, 2012 | doi: 10.1021/bk-2012-1112.ch006

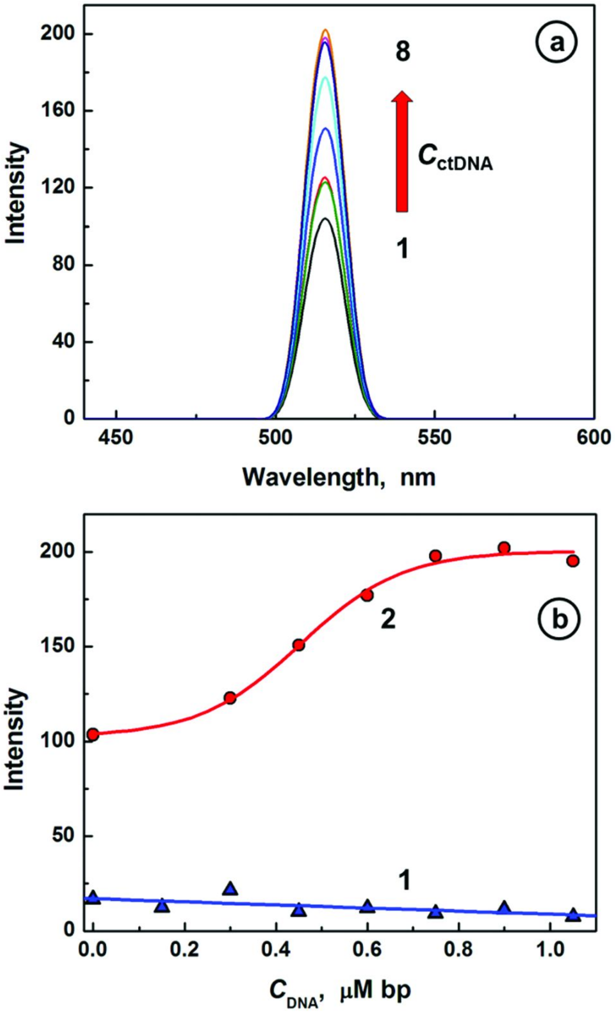

Figure 12. (a) RELS spectra for 3.8 nM AuNP/Cit/PLL core-shell nanoparticles recorded after addition of increasing concentrations of ctDNA [µM bp]: (1) 0, (2) 0.15, (3) 0.3, (4) 0.45, (5) 0.6, (6) 0.75. (7) 0.9, (8) 1.05. (b) Dependence of RELS intensity on ctDNA concentration for: (1) solutions without AuNP/Cit/PLL, and (2) 3.8 nM solutions of AuNP/Cit/PLL; λ_{ex} *= 520 nm,* λ_{em} *= 520 nm, pH = 7.3,* C_{PLL} *= 0.67 ppm (all concentrations are final concentrations). (Reproduced with permission from (11). Copyright 2011, Elsevier Publisher.)*

Polymeric Nanoparticles for Immunotherapy

Immunotherapy presents a serious challenge to medical treatment and is difficult to manage and control. Immunomodulatory therapy is required in such cases as the autoimmune disorders, trauma, non-biological implant-caused inflammations, and foreign-organ implantation and rejection control. For instance, in diabetes type I, which is a rapidly developing autoimmune disease, the islet β-cells in the pancreas are destroyed by own-body immune cells. To protect the insulin-producing islet β-cells against autoimmune destruction by leucocytes, the administration of anti-leucocyte drugs is necessary. However, the available drugs, such as the prednisone and cyclosporine A, are barred from use by FDA due to serious side effects that include kidney damage (*84*) and innate immune system damage (*85*). Recently, the group of Ingber (*86*) has developed a targeted nanoparticle nanocarrier able to deliver an anti-inflammatory drug to islet β-cells and prevent leucocytes from adhering to islet β-cells and destroying them. The polymeric compound developed is a PEG-ylated copolymer poly(D,L-lactide-*co*-glycolide) (PLGA) with amid-bonded peptide (Pep I) with sequence CHVLWSTRC, found to bind specifically to islet microvessels (*87*). This copolymer self-assembles spontaneously in aqueous solutions to form nanoparticles, 190 nm in diameter, with Pep I exposed on the surface. PLGA was also reported to be an efficient nanocarrier in gene knockdown using siRNA (*88*, *89*). For instance, the use of polymeric PLGA with nucleic acids and a polycation have been reported (*90*).

Downloaded by UNIV DE SHERBROOKE on November 27, 2012 | http://pubs.acs.org
Publication Date (Web): November 26, 2012 | doi: 10.1021/bk-2012-1112.ch006

Lipid-Coated Nanoparticles for Drug Delivery

An alternative to polycation coating is the lipid coating of nanoparticle nanocarriers. Lipids offer different charge options, including charge-neutral, biocompatibility, and low immunoresponse. Most research has been done with liposomes which are vesicles with lipid bilayer membranes. This means that in this case, the nanoparticle core is a liquid. However, polymer, metal, and semiconductor lipid-coated nanoparticles have also been investigated. Liposomes are highly efficient in carrying siRNA (*91*, *92*) and thus, they have been studied for gene knockdown applications. The electrostatic complexes of siRNA with peptides, cationic polymers, and membrane lipids in liposomes have also been investigated (*93–95*). They are called lipoplexes. The disadvantage of lipoplexes is that serum and extracellular matrix can induce lipoplex disassembly, thus limiting their applications in nanomedicine.

Recently, the DeSimone group (*16*) has developed a very successful PLGA-copolymer nanoparticle coated with lipids carrying multiple siRNA for prostate cancer gene knockdown.

Constructing Functional Nanostructures from Nanoparticle Building Blocks

The well-organized networks of metal nanoparticles are of special interest for biosensors, nanoelectronics and nanophotonics (*96*). One-dimensional AnNP structures have been built using DNA templates (*97–99*). The DNA scaffold has been used to construct 2D AuNP-structures (*100–104*). The discrete AuNP structures have been synthesized using circular viral genome (*105*) or by conjugating AuNP capped with short ssDNA helper-strands with origami

Downloaded by UNIV DE SHERBROOKE on November 27, 2012 | http://pubs.acs.org
Publication Date (Web): November 26, 2012 | doi: 10.1021/bk-2012-1112.ch006

DNA-scaffold assemblies (*106–111*). The origami DNA structures have been obtained, for instance, by utilizing a circular viral M13 DNA, folded by a group of some 200 short-sequence helper DNA strands with sequences designed to cause DNA folding and forming DNA-nanoarrays. The low efficiency of DNA immobilization on AuNP has been solved by adding a second sulfur atom bound to the gold nanoparticle. Thus, the monothiolate was replaced with a lipoic acid-terminated carbon chain of the target helper-DNA . The dithiol-modified DNA have shown to offer twice as high efficiency (*112–114*) of DNA binding to gold nanoparticles than a single thiol binding. The errors in DNA-directed AuNP assembly have been drastically improved with the dithiol technology. Previous efforts involved designing error-correction DNA tiles (*115*). Further improvement in DNA bonding capability to Au-biosensors with stronger and multiple bonding has been investigated (*116*).

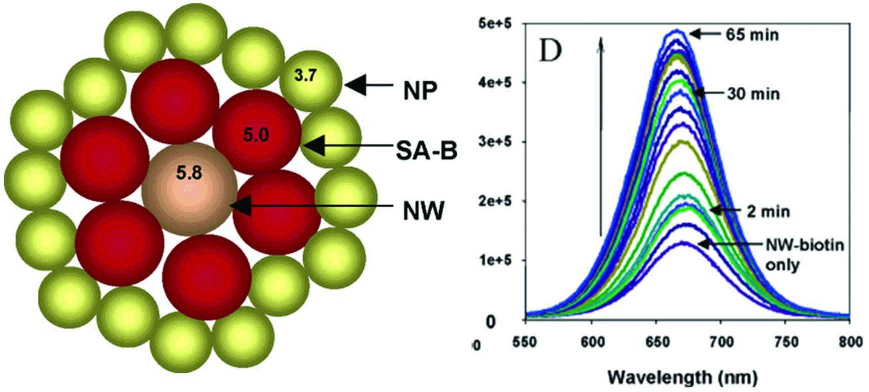

Figure 13. (Left) The Au nanoparticle (NP) nanostructure around CdTe nanowire (NW) self-assembled through a streptavidin- biotin (SA-B) bioconjugation. (Right) Temporal evolution of the fluorescence emission spectrum of NW during the assembly process. (Reproduced with permission from (117). Copyright 2004, American Chemical Society.)

Kotov and coworkers (*117*) described the formation of AuNP nanostructure surrounding a CdTe nanowire by bioinspired conjugation (Figure 13). They have found that the surface plasmon-exciton interaction result in five-fold luminescence increase of CdTe.

Conclusions

The broad range of functionalities the nanoparticles can be equipped with, including single-scope and theranostic multifunctional capabilities, expands the latitude of nanoparticles' biomedical applicability. Hence, extensive studies have been carried out to develop multi-modal nanoparticle nanocarriers specialized to target specific tissue, cells, and even organelles and aid in diagnostic imaging and/or in delivery of drugs. This trend is certainly growing and will develop in the near future into a new full-fledged field of nanomedicine. We have already seen tremendous successes of nanoparticle image enhancers in medical diagnostics, including MRI, CT scan, ultrasonic, photoacoustic, and Raman imaging. The greatest benefit of a nanoparticle drug delivery system is appreciated by the cancer therapy field since a precisely-targeted nanoparticle carrier, unloading a chemotherapeutic agent directly to a tumor tissue, reduces the effects of high cytotoxicity of these drugs to healthy cells. In the same way, the localization of the lethal photosensitizer decomposition in the tumor area in photodynamic therapy enables preservation of healthy tissue. Precision surgeries can now be performed on an aggressive brain tumor, glioblastoma, owing to targeted multi-modal nanoparticle image enhancers guiding the incision and removal of tumor together with outgrowths, without damaging healthy brain cells. Our knowledge about cytotoxicity of functionalized nanoparticles is still lacking. In many cases, there are serious biocompatibility issues and further investigations of all functionalized nanoparticles have to be carefully carried out to make sure that healthy cells remain protected and the nanoparticles do not accumulate in the body.

Downloaded by UNIV DE SHERBROOKE on November 27, 2012 | http://pubs.acs.org
Publication Date (Web): November 26, 2012 | doi: 10.1021/bk-2012-1112.ch006

Acknowledgments

This work was partially supported by National Science Foundation grant No. CCLI-0941364.

List of Abbreviations

AgNP - silver nanoparticles
AuNP - gold nanoparticles
Cit - citrate or citric acid
CNT - carbon nanotubes
CT scan - computed tomography scan
CV - cyclic voltammetry
DNA - deoxyribonucleic acid
dsDNA - double-stranded deoxyribonucleic acid
EPR - enhanced permeability and retention
EQCN - electrochemical quartz crystal nanogravimetry,
or: electrochemical quartz crystal nanobalance
GRNP - Raman probe-capped gold nanoparticles (gold-Raman nanoparticle
MRI - magnetic resonance imaging
PDGF - platelet-derived growth factor receptor
PDT - photodynamic therapy
PEG - poly(ethylene glycol)
PLA - poly(lactic acid)
PLL - poly-L-lysine
QC - quartz crystal piezoresonator wafer
QCN - quartz crystal nanogravimetry

QD - quantum dots
RELS - resonance elastic light scattering
RNA - ribonucleic acid
RNAi - RNA interference
SAM - self-assembled monolaye
ssDNA - single-stranded deoxyribonucleic acid

References

1. Škapin, S.; Matijević, E. *J. Colloid Interf. Sci.* **2004**, *272*, 90–98.
2. Nakanishi, J.; Nakayama, H.; Shimizu, T.; Ishida, H.; Kikuchi, Y.; Yamaguchi, K.; Horiike, Y. *J. Am. Chem. Soc.* **2009**, *131*, 3822–3823.
3. Stobiecka, M.; Deeb, J.; Hepel, M. *Electrochem. Soc. Trans.* **2009**, *19*, 15–32.
4. Boal, A. K.; Rotello, V. M. *J. Am. Chem. Soc.* **2000**, *122*, 734–735.
5. Stobiecka, M.; Deeb, J.; Hepel, M. *Biophys. Chem.* **2010**, *146*, 98–107.
6. Demers, L. M.; Mirkin, C. A.; Mucic, R. C.; Reynolds, R. A.; Letsinger, R. L.; Elghanian, R.; et al. *Anal. Chem.* **2000**, *72*, 5535–5541.
7. Alivisatos, A. P.; Johnsson, K. P.; Peng, X.; Wilson, T. E.; Loweth, C. J.; Bruchez, M. P.; Schultz, P. G. *Nature* **1996**, *382*, 610.
8. Elghanian, R.; Storhoff, J. J.; Mucic, R. C.; Letsinger, R. L.; Mirkin, C. A. *Science* **1997**, *277*, 1078–1081.
9. Park, S. J.; Taton, T. A.; Mirkin, C. A. *Science* **2002**, *295*, 1503–1505.
10. Taton, T. A.; Lu, G.; Mirkin, C. A. *J. Am. Chem. Soc.* **2001**, *123*, 5164–5165.
11. Stobiecka, M.; Hepel, M. *Biomaterials* **2011**, *32*, 3312–3321.
12. Soutschek, J.; Akinc, A.; Bramlage, B.; Charisse, R.; Donoghue, M.; Elbashir, S.; Geick, A.; Hadwiger, P.; Harborth, J.; John, M.; Venkitasamy, K.; Lavine, G.; Pandey, R. K.; Racei, T.; Rajeev, K. G.; Rohl, I.; Toudjarska, I.; Wang, G.; Wuschko, S.; Bumcrot, D.; Koteliansky, V.; Limmer, S.; Manoharan, M.; Hans-Peter, V. *Nature* **2004**, *432*, 173–178.
13. Fougerolles, A. d.; Vornlocher, H. P.; Maraganore, J.; Lieberman, J. *Nat. Rev. Drug Discovery* **2007**, *6*, 443–453.
14. Carthew, R. W.; Sontheimer, E. J. *Cell* **2009**, *136*, 642–655.
15. Barik, S. *J. Mol. Med.* **2005**, *83*, 764–773.
16. Hasan, W.; Chu, K.; Gullapalli, A.; Dunn, S. S.; Enlow, E. M.; Luft, J. C.; Tuan, S.; Napier, M. E.; Pohlhaus, P. D.; Rolland, J. P.; DeSimone, J. M. *Nano Lett.* **1212**, *12*, 287–292.
17. Luksiene, Z. *Medicina* **2003**, *39*, 1137–1150.
18. Vaupel, P.; Kelleher, D. K. *Tumor Hypoxia*; Wissenschafliche Verlagsgeselschaft mbH: Stuttgart, 1999.
19. Dickson, E. F. G.; Goyan, R. L.; Pottier, R. H. *Cell. Molec. Biol.* **2002**, *48*, 939–954.
20. Liu, J.; Levine, A. L.; Mattoon, J. S.; Yamaguchi, M.; Lee, R. J.; Pan, X.; Rosol, T. J. *Phys. Med. Biol.* **2006**, *51*, 2179.

Downloaded by UNIV DE SHERBROOKE on November 27, 2012 | http://pubs.acs.org
Publication Date (Web): November 26, 2012 | doi: 10.1021/bk-2012-1112.ch006

21. Liu, J.; Li, J.; Rosol, T. J.; Pan, X.; Voorhees, J. L. *Phys. Med. Biol.* **2007**, *52*, 4739.
22. Thakor, A. S.; Luong, R.; Paulmurugan, R.; Lin, F. I.; Kempen, P.; Zavaleta, C.; Chu, P.; Massoud, T. F.; Sinclair, R.; Gambhir, S. S. *Sci. Transl. Med.* **2011**, *3* (79), 79ra33.
23. Kircher, M. F.; de la Zerda, A.; Jokerst, J. V.; Zavaleta, C. L.; Kempen, P. J.; Mittra, E.; Pitter, K.; Huang, R.; Campos, C.; Habte, F.; Sinclair, R.; Brennan, C. W.; Mellinghoff, I. K.; Holland, E. C.; Gambhir, S. S. *Nature Med.* **2012**, advance online publication.
24. Arya, S. K.; Bhansali, S. *Chem. Rev.* **2011**, *111*, 6783–6809.
25. Tam, N. C.; Scott, B. M.; Voicu, D.; Wilson, B. C.; G., G. Z. *Bioconjugate Chem.* **2010**, *21*, 2178–2182.
26. Gao, J.; Chen, K.; Luong, R.; Bouley, D. M.; Mo, H.; Qiao, T.; Gambhir, S. S.; Cheng, Z. *Nano Lett.* **2012**, *12*, 281–286.
27. Zerda, A. d. l.; Kim, J. W.; Galanzha, E. I.; Gambhir, S. S.; Zharov, V. P. *Contrast Media Mol. Imaging* **2011**, *6*, 346–369.
28. Funkhouser, J. *Curr. Drug Discovery* **2002**, *2*, 17–19.
29. Derfus, A. M.; Chen, A. A.; Min, D. H.; Ruoslahti, E.; Bhatia, S. N. *Bioconjugate Chem.* **2007**, *18*, 1391–1396.
30. Kelkar, S. S.; Reineke, T. M. *Bioconjugate Chem.* **2011**, *22*, 1879–1903.
31. Pitsillides, C. M.; Joe, E. K.; Wei, X.; Anderson, R. R.; Lin, C. P. *Biophys. J.* **2003**, *84*, 4023–4032.
32. Pan, D.; Pramanik, M.; Senpan, A.; Allen, J. S.; Zhang, H.; Wickline, S. A.; Wang, L. V.; Lanza, G. M. *FASEB J.* **2011**, *25*, 875–882.
33. Ruoslahti, E. *Nat. Rev. Cancer* **2002**, *2*, 83–90.
34. Peer, D.; Karp, J. M.; Hong, S.; Farokhzad, O. C.; Margalit, R.; Langer, R. *Nat. Nanotechnol.* **2007**, *2*, 751–760.
35. Stallcup, W. B.; Huang, F. J. *Cell Adh. Migr.* **2008**, *2*, 192–201.
36. Pasqualini, R.; Koivunen, E.; Kain, R.; Lahdenranta, J.; Sakamoto, M.; Stryhn, A.; Ashmun, R. A.; Shapiro, L. H.; Arap, W.; Ruoslahti, E. *Cancer Res.* **2000**, *60*, 722–727.
37. Oh, P.; Li, Y.; Yu, J.; Durr, E.; Krasinska, K. M.; Carver, L. A.; Testa, J. E.; Schnitzer, J. E. *Nature* **2004**, *429*, 629–635.
38. Christian, S.; Ahorn, H.; Koehler, A.; Eisenhaber, F.; Rodi, H. P.; Garin-Chesa, P.; Park, J. E.; Rettig, W. J.; Lenter, M. C. *J. Biol. Chem.* **2001**, *276*, 7408–7414.
39. Nilsson, F.; Kosmehl, H.; Zardi, L.; Neri, D. *Cancer Res.* **2001**, *61*, 711–716.
40. Pilch, J.; Brown, D. M.; Komatsu, M.; Järvinen, T. A.; Yang, M.; Peters, D.; Hoffman, R. M.; Ruoslahti, E. *Proc. Natl. Acad. Sci. U.S.A.* **2006**, *103*, 2800–2804.
41. Desgrosellier, J. S.; Cheresh, D. A. *Nat. Rev. Cancer* **2010**, *10*, 9–22.
42. Lewis, V. O.; Ozawa, M. G.; Deavers, M. T.; Wang, G.; Shintani, T.; Arap, W.; Pasqualini, R. *Cancer Res.* **2009**, *69*, 1995–1999.
43. Christian, S.; Pilch, J.; Akerman, M. E.; Porkka, K.; Laakkonen, P.; Ruoslahti, E. *J. Cell Biol.* **2003**, *163*, 871–878.
44. Fogal, V.; Zhang, L.; Krajewski, S.; Ruoslahti, E. *Cancer Res.* **2008**, *68*, 7210–7218.

Downloaded by UNIV DE SHERBROOKE on November 27, 2012 | http://pubs.acs.org
Publication Date (Web): November 26, 2012 | doi: 10.1021/bk-2012-1112.ch006

45. Song, S.; Ewald, A. J.; Stallcup, W.; Werb, Z.; Bergers *Nat. Cell Biol.* **2005**, *7*, 870–879.
46. Kelly, K. A.; Bardeesy, N.; Anbazhagan, R.; Gurumurthy, S.; Berger, J.; Alencar, H.; Depinho, R. A.; Mahmood, U.; Weissleder, R. *PLoS Med.* **2008**, *5*, e85.
47. Xu, J.; Rodriguez, D.; Petitclerc, E.; Kim, J. J.; Hangai, M.; Moon, Y. S.; Davis, G. E.; Brooks, P. C.; Yuen, S. M. *J. Cell Biol.* **2001**, *154*, 1069–1079.
48. Carson-Walter, E. B.; Watkins, D. N.; Nanda, A.; Vogelstein, B.; Kinzler, K. W.; Croix, B. S. *Cancer Res.* **2001**, *61*, 6649–6655.
49. Bergers, G.; Benjamin, L. E. *Nat. Rev, Cancer* **2003**, *3*, 401–410.
50. Yankopoulos, G. D.; et al. *Nature* **2000**, *407*, 242–248.
51. Ruoslahti, E.; Bhatia, S. N.; Sailor, M. J. *J. Cell. Biol.* **2010**, *188*, 759–768.
52. Roe, D.; Karandikar, B.; Bonn-Savage, N.; Gibbins, B.; Roullet, J. B. *J. Antimicrob. Chemother.* **2008**, *61*, 869–876.
53. Ghosh, P. S.; Kim, C. K.; Han, G.; Forbes, N. S.; Rotello, V. M. *ACS Nano* **2008**, *2*, 2213–2218.
54. Matijevic, E. *Medical Applications of Colloids*; Springer Science: New York, 2008.
55. Lim, I. I. S.; Chandrachud, U.; Wang, L.; Gal, S.; Zhong, C. J. *Anal. Chem.* **2008**, *80* (15), 6038–6044.
56. Mirkin, C. A.; Letzinger, R. L.; Mucic, R. C.; Storhoff, J. J. *Nature* **1996**, *382*, 607–609.
57. Zhang, J.; Lao, R.; Song, S.; Yan, Z.; Fan, C. *Anal. Chem.* **2008**, *80*, 9029–9033.
58. Yamamoto, M. M.; Mori, Y.; Osada, K.; Murakami, H. *Biosci., Biotechnol., Biochem.* **1995**, *59*, 1842–1845.
59. Szende, B.; Szokan, G.; Tyiha, E.; Pal, K.; Gaborjanyi, R.; Almas, M.; Khiafulla, A. R. *Cancer Cell Int.* **2002**, *2*, 4.
60. Kozlova, M.; Kentroti, S.; Vernadakis, A. *Int. J. Dev. Neurosci.* **1993**, *11*, 513–519.
61. Shpakov, A. O.; Gurianov, I. A.; Baianova, N. V.; Vlasov, G. P. *Tsitologiia* **2008**, *50*, 1036–1043.
62. Fujii, M.; Morita, H.; Hiraki, J.; Hatakeyama, M. Agent for preventing plant virus diseases. U.S. Patent 4,867,974, 1989.
63. Xu, L.; Guo, Y.; Xie, R.; Zhuang, J.; Yang, W.; Li, T. *Nanotechnology* **2002**, *13*, 725–728.
64. Guo, Y.; Ma, Y.; Xu, L.; Li, J.; Yang, W. *J. Phys. Chem. C* **2007**, *111*, 9172–9176.
65. Joshi, H.; Shirude, P. S.; Bansal, V.; Ganesh, K. N.; Sastry, M. *J. Phys. Chem. B* **2004**, *108*, 11535–11540.
66. Xu, L.; Guo, Y.; Xie, R.; Zhuang, J.; Yang, W. *Nanotechology* **2002**, *13*, 725–728.
67. Kumar, A.; Mandal, S.; Selvakanna, P. R.; Pasricha, R.; Mandale, L. E.; Sastry, L. E. *Langmuir* **2003**, *19*, 6277.
68. Leff, D. V.; Brandt, L.; Heath, J. R. *Langmuir* **1996**, *12*, 4723–4730.
69. Wybourne, M. N.; Hutchison, J. E.; Clarke, L.; Brown, L. O.; Mooster, J. L. *Microelectron. Eng.* **1999**, *47*, 55–57.

Downloaded by UNIV DE SHERBROOKE on November 27, 2012 | http://pubs.acs.org
Publication Date (Web): November 26, 2012 | doi: 10.1021/bk-2012-1112.ch006

70. Maiti, P. K.; Bagchi, B. *Nano Lett.* **2006**, *6*, 2478–2485.
71. Gu, W.; Putral, L.; Hengst, K.; Minto, K.; Saunders, N. A.; Leggatt, G.; McMillan, N. A. J. *Cancer Gene Ther.* **2006**, *13*, 1023–1032.
72. Mannisto, M.; Vanderkerken, S.; Toncheva, V.; Elomaa, M.; Ruponen, M.; Schacht, E.; Urtti, A. *J. Controlled Release* **2002**, *83*, 169–182.
73. Niwa, M.; Morikawa, M. A.; Yagi, K.; Higashi, N. *Int. J. Biol. Macromol.* **2001**, *30*, 47–54.
74. Shapiro, J. T.; Leng, M.; G, F. *Biochemistry* **1969**, *8*, 3219–3232.
75. Fukushima, K.; Sakamoto, T.; Tsuji, J.; Kondo, K.; Shimozawa, R. *Biochim. Biophys. Acta* **1994**, *1191*, 133–140.
76. Huh, K. M.; Ooya, T.; Yui, N. *Polym. Prepr. Jpn.* **2000**, *49*, 4208–4209.
77. Varadan, V. K. *Proc. SPIE* **2007**, *6528*, 65281F.
78. Nowicka, A. M.; Kowalczyk, A.; Stojek, Z.; Hepel, M. *Biophys. Chem.* **2010**, *146*, 42–53.
79. Han, G.; Chari, N. S.; Verma, A.; Hong, R.; Martin, C. T.; Rotello, V. M. *Bioconjugate Chem.* **2005**, *16*, 1356–1359.
80. Hong, R.; Han, G.; Fernandez, J. M.; Kim, B. J.; Forbes, N. S.; Rotello, V. M. *J. Am. Chem. Soc.* **2006**, *128*, 1078–1079.
81. Stobiecka, M.; Hepel, M. *Sens. Actuators, B* **2010**, *149*, 373–380.
82. Stobiecka, M.; Coopersmith, K.; Hepel, M. *J. Colloid Interface Sci.* **2010**, *350*, 168–177.
83. Stobiecka, M.; Hepel, M. *Phys. Chem. Chem. Phys.* **2011**, *13*, 1131–1139.
84. Parving, H. H.; Tarnow, L.; Nielsen, F. S.; Rossing, P.; Mandrup-Poulsen, T.; Osterby, R.; Nerup, J. *J. Diabetes Care* **1999**, *22*, 478–483.
85. Berchtold, P.; Seitz, M. *Schwez. Med. Wochenschr.* **1996**, *126*, 1603–1609.
86. Ghosh, K.; Kanapathipillai, M.; Korin, N.; McCarthy, J. R.; Ingber, D. E. *Nano Lett.* **2012**, *12*, 203–208.
87. Yao, V. J.; Ozawa, M. G.; Trepel, M.; Arap, W.; McDonald, D. M.; Pasqualini, R. *Am. J. Pathol.* **2005**, *166*, 625–636.
88. Alshamsan, A.; Haddadi, A.; Hamdy, S.; Samuel, J.; El-Kadi, A. O. S.; Uludag, H.; Lavasanifar, A. *Mol. Pharmaceutics* **2010**, *7*, 1643–1654.
89. Lee, S. H.; Mok, H.; Lee, Y.; Park, T. G. *J. Controlled Release* **2011**, *152*, 152–158.
90. Basarkar, A.; Singh, J. *Int. J. Nanomed.* **2007**, *2*, 353–360.
91. Akinc, A.; Goldberg, M.; Qin, J.; Dorkin, J. R.; Gamba-Vitalo, C.; Maier, M.; Jayaprakash, K. N.; Jayaraman, M.; Kallanthottahil, G. R.; Manoharan, M.; Koteliansky, V.; Rohl, I.; Leshchiner, E. S.; Langer, R.; Anderson, D. G. *Mol. Ther.* **2009**, *17*, 872–879.
92. Moghimi, S. M.; Szebeni, J. *Prog. Lipid Res.* **2003**, *42*, 463–478.
93. Siegwart, D. J.; Whitehead, K. A.; Nuhn, N.; Sahay, G.; Cheng, H.; Jiang, S.; Ma, M.; Lyton-Jean, A.; Vegas, A.; Fenton, P.; Levins, C. G.; Love, K. T.; Lee, H.; Cortez, C.; Collins, S. P.; Li, Y. F.; Jang, J.; Querbes, W.; Zurenko, C.; Novabrantseva, T.; Langer, R.; Anderson, D. *Proc. Natl. Acad. Sci. U.S.A.* **2011**, *32*, 12996–13001.
94. Kwon, E. J.; Bergen, J. M.; Pun, S. H. *Bioconjugate Chem.* **2008**, *19*, 920–927.
95. Huang, L.; Li, S. *Nat. Biotechnol.* **1997**, *15*, 620.

Downloaded by UNIV DE SHERBROOKE on November 27, 2012 | http://pubs.acs.org
Publication Date (Web): November 26, 2012 | doi: 10.1021/bk-2012-1112.ch006

Downloaded by UNIV DE SHERBROOKE on November 27, 2012 | http://pubs.acs.org
Publication Date (Web): November 26, 2012 | doi: 10.1021/bk-2012-1112.ch006

96. Stewart, M. E.; Anderton, C. R.; Thompson, L. B.; Maria, J.; Gray, S. K.; Rogers, J. A.; Nuzzo, R. G. *Chem. Rev.* **2008**, *108*, 494–521.
97. Niemeyer, C. M.; Burger, W.; Peplies, J. *Angew. Chem., Int. Ed.* **1998**, *37*, 2265–2268.
98. Beyer, S.; Nickels, P.; Simmel, F. C. *Nano Lett.* **2005**, *5*, 719–722.
99. Pal, S.; Deng, Z.; Ding, B.; Yan, H.; Liu, Y. *Angew. Chem., Int. Ed.* **2010**, *49*, 2700–2704.
100. Le, J.; Pinto, Y.; Seeman, N. C.; Musier-Forsyth, K.; Taton, T. A.; Kiehl, R. A. *Nano Lett.* **2004**, *4*, 2343–2347.
101. Pinto, Y. Y.; Le, J. D.; Seeman, N. C.; Musier-Forsyth, K.; Taton, T. A.; Kiehl, R. A. *Nano Lett.* **2005**, *5*, 2399–2402.
102. Zhang, J.; Liu, Y.; Ke, Y.; Yan, H. *Nano Lett.* **2006**, *6*, 248–251.
103. Zheng, J.; Constantinou, P. E.; Mitcheel, C.; Alivisatos, A. P.; Kiehl, R. A.; Seeman, N. C. *Nano Lett.* **2006**, *6*, 1502–1504.
104. Stearns, L. A.; Chhabra, R.; Sharma, J.; Liu, Y.; Petuskey, W. T.; Yan, H.; Chaput, J. C. *Angew. Chem., Int. Ed.* **2009**, *48*, 8494–8496.
105. Sharma, J.; Chhabra, R.; Andersen, C. S.; Gothelf, K. V.; Yan, H.; Liu, Y. *J. Am. Chem. Soc.* **2008**, *130*, 7820–7821.
106. Loweth, C. J.; Caldwell, W. B.; Peng, X.; Alivisatos, A. P.; Schultz, P. G. *Angew. Chem., Int. Ed.* **1999**, *38*, 1808–1812.
107. Aldaye, F. A.; Palmer, A. L.; Sleiman, H. F. *Science* **2008**, *321* (5897), 1795–1799.
108. Zhao, W.; Gao, Y.; Kandadai, S. A.; Brook, M. A.; Li, Y. *Angew. Chem., Int. Ed.* **2006**, *45*, 2409–2413.
109. Aldaye, F. A.; Sleiman, H. F. *Angew. Chem., Int. Ed.* **2006**, *45*, 2204–2209.
110. Alivisatos, A. P.; Johnsson, K. P.; Peng, X.; Wilson, T. E.; Loweth, C. J.; Bruchez, J. M. P.; Schultz, P. G. *Nature* **1996**, *382*, 609–611.
111. Rothemund, P. W. K. *Nature* **2006**, *440*, 297–302.
112. Mattoussi, H.; Mauro, M. J.; Goldman, E. R.; Anderson, G. P.; Sundar, V. C.; Mikulec, F. V.; Bewendi, M. G. *J. Am. Chem. Soc.* **2000**, *122*, 12142–12150.
113. Li, Z.; Jin, R.; Mirkin, C. A.; Letsinger, R. L. *Nucleic Acid Res.* **2002**, *30*, 1558–1562.
114. Dougan, J. A.; Karlsson, C.; Smith, W. E.; Graham, D. *Nucleic Acid Res.* **2007**, *35*, 3668–3675.
115. Chen, H. L.; Schulman, R.; Goel, A.; Winfree, E. *Nano Lett.* **2007**, *7*, 2913–2919.
116. Mammen, M.; Choi, S. K.; Whitesides, G. M. *Angew. Chem., Int. Ed.* **1998**, *37*, 2754–2794.
117. Lee, J.; Govorov, A. O.; Dulka, J.; Kotov, N. A. *Nano Lett.* **2004**, *4*, 2323–2330.

Chapter 7

Biomarker Detections Using Functional Noble Metal Nanoparticles

Minghui Yang,[1] Jianxiu Wang,[1] and Feimeng Zhou*,[1,2]

[1]College of Chemistry and Chemical Engineering, Central South University, Changsha 410083, China
[2]Department of Chemistry and Biochemistry, California State University, Los Angeles, Los Angeles, California 90032
***E-mail: fzhou@calstatela.edu**

In this chapter, we detail recent advances in immunoassays for various cancer biomarkers and biomarkers of Alzheimer's disease (AD) using functional noble metal nanoparticles, such as gold nanoparticles (AuNPs) and silver nanoparticles (AgNPs). The fascinating properties of these nanomaterials, such as biocompatibility, large surface area, functional flexibility, and unique optical as well as electrical properties have been explored to enhance the sensitivity and selectivity of the proposed methods. The signal enhancement associated with the utilization of metal nanoparticles as amplifying labels as well as the construction of nanoparticle-protein assemblies provide the basis for ultrasensitive biomarker detection. Different immunoassay methods, including but are not limited to electrochemical, optical and surface-enhanced Raman scattering (SERS) techniques, are compared.

Introduction

Biomarker is generally a characteristic indicator of normal biological and pathogenic processes, or pharmacological responses to therapeutic treatment (*1–3*). The development of highly sensitive and selective methods for the detection of various biomarkers is of significant importance for clinical diagnosis as well as biomedical research (*4–8*). The most commonly used techniques include enzyme-linked immunosorbent assay (ELISA), immunoprecipitation, gel

In Functional Nanoparticles for Bioanalysis, Nanomedicine, and Bioelectronic Devices Volume 1; Hepel, M., et al.;
ACS Symposium Series; American Chemical Society: Washington, DC, 2012.

electrophoresis. Among them, ELISA utilizes an enzyme, such as horseradish peroxidase (HRP), as a catalytic label for signal amplification (*9–12*). In such an assay, a sandwich-type protocol is usually used (*13–16*). The capture antibody against a specific biomarker (antigen) is first immobilized in microtiter plates to bind the antigen, and the immobilized antigen is then recognized by the HRP-labeled detection antibody. The amount of antigen can be determined by monitoring the HRP-catalyzed reaction. Typically, the detection limit of ELISA is in the high ng/mL range. During the early stage of the diseases, the expression level of some biomarkers in human fluids is usually present in pg/mL range, so great interest has been paid to improve the sensitivity of the early clinical diagnostics.

The development of nanotechnology in recent decades has opened up new opportunities for the application of nanoparticles in bioassay (*17–21*). Different nanomaterials, such as carbon nanomaterials (*22*, *23*), metal nanoparticles (*24–26*), and magnetic nanoparticles (*27–29*), have been extensively used due to their fascinating physical and chemical properties. Among these nanomaterials, noble metal nanoparticles have attracted special interest because of their unique optical and electrical properties (*30*, *31*). The signal enhancement associated with the use of metal nanoparticle-protein assemblies provides the basis for ultrasensitive detection of various biomarkers (*32–35*). Gold nanoparticles (AuNPs), which possess good biocompatibility, functional flexibility as well as attractive optical, electronic, and catalytic properties, are arguably the most widely used nanomaterials in bioassay (*36–39*). Different molecules can either be directly adsorbed or covalently attached onto AuNPs through thiol-containing linkers. Great efforts have been made to increase the loading of the molecules onto AuNPs to enhance the sensitivity of the bioassay. Besides AuNPs, silver nanoparticles (AgNPs) are another widely used noble metal material with unique size-dependent optical and electrical properties (*40–43*).

In this chapter, we review the recent development on the detection of specific biomarkers using functional noble metal nanoparticles (mainly AuNPs and AgNPs), with emphasis on the assays of cancer and Alzheimer's disease (AD) biomarkers. The detection of these biomarkers is highly relevant to clinical diagnosis and drug discovery.

Detection of Biomarkers of AD—Amyloid-β Peptides

AD is a neurodegenerative disorder characterized by the presence of senile plaques formed via aggregation/fibrillization of amyloid-β (Aβ) peptides in brains of AD patients (*44–46*). Among the various Aβ aggregates, the oligomers (including insoluble and the soluble Aβ-derived diffusible ligands (ADDLs)) are toxic to neurons (*47*, *48*). Elevated ADDL levels have been found in cerebrospinal fluid (CSF) samples from AD patients (*49*, *50*). Two comprehensive reviews have demonstrated that the early stages of AD might be caused by the synaptic impact of ADDLs (*44*, *51*). The association of ADDLs with brain pathology suggests that a sensitive means to detect ADDLs in body fluids might provide an alternative early diagnosis of AD. The work performed by van Duyne's group is particularly noteworthy (*50*, *52*). Relying on the Ag nanotriangle arrays, for the first time they measured the binding constant between ADDL and anti-ADDL antibody with localized surface plasmon resonance (LSPR) (3.0×10^7 M^{-1}) (*52*). In general, LSPR-based biosensing utilizes a strong extinction band in the VIS-NIR range, originated from the collective oscillation of the conduction electrons in the metal nanoparticles (*53*, *54*). Based on the specific interaction, the LSPR biosensor has been successfully utilized for the quantification of ADDL with a detection limit below 1 fM (Figure 1) (*50*). The schematic protocol involves the passivation of the Ag nanoparticles with a mixed monolayer, covalent attachment of the first anti-ADDL antibody to the nanoparticles, capture of ADDLs with varying concentrations, and enhancement of the LSPR shift response by the second anti-ADDL antibody. The concentration levels of ADDLs in human brain extract and CSF samples from AD patients are much higher than those from controls. The LSPR nanosensor has been demonstrated to be attractive in enhancing the detection sensitivity of ADDLs, allowing for the analysis of biological species at ultra-low levels.

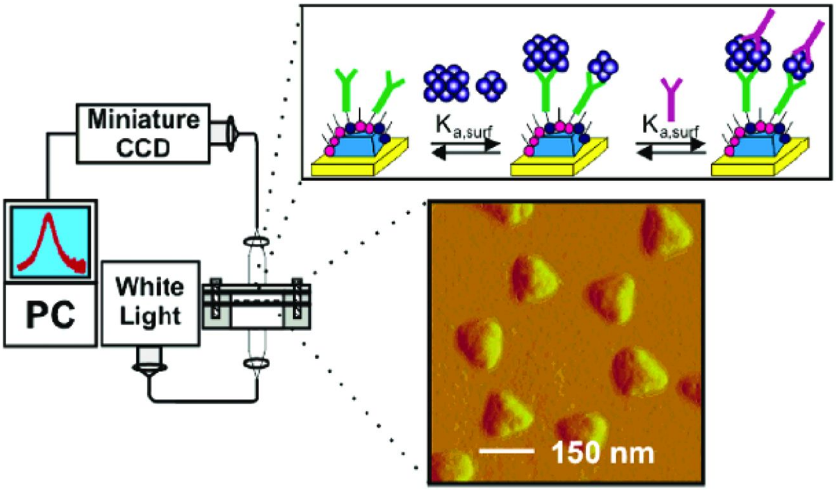

Figure 1. Design and experimental setup for the LSPR biosensor for the detection of ADDLs using a sandwich assay. (Adapted from ref. (50), with permission. Copyright © 2010 American Chemical Society.)

Mirkin and coworkers have reported an ultrasensitive bio-barcode assay of ADDLs in the CSF (*55*). A sandwich complex was formed via mixing synthetic ADDLs or CSF samples with magnetic microparticles (MMPs) and Au nanoparticles modified with double-stranded oligonucleotides (ds-ODNs), both functionalized with ADDL-specific antibodies. After magnetic separation of the sandwich complex, hundreds of barcode DNA strands were released via dehybridization of the ds-ODNs. The released barcode DNA strands, which correlated with the ADDL concentrations, were assayed by a scanometric method.

This work is more clinically relevant, as CSF samples analyzed are of a greater cohort (30 samples), with the AD patients showing a consistently higher ADDL level.

The abovementioned nanoparticle-based optical assays highly complement other optical or surface analyses with using only antibody or with antibody-based signal amplifications. For example, Homola and coworkers used antibody for SPR detection of Aβ in artificial CSF samples (*56*), though the detection level is not as high as those achieved with Ag or Au nanoparticles. We recently synthesized a conjugate of streptavidin-biotinylated Aβ antibody for simultaneous and amplified SPR detection of Aβ(1–40) and Aβ(1–42) in CSF samples of AD patients and healthy donors (*57*). With the signal amplification, the detection levels are highly comparable to those attainable by nanoparticle-based methods. Moreover, through the analysis multiple of CSF samples from age-matched AD patients, it was found that the ratio between the concentrations of Aβ(1–40) and Aβ(1–42) in AD CSF is consistently higher than that in CSF of healthy donors. This is conceivable since Aβ(1–42) is more prone to aggregation than Aβ(1–40). Consequently, the aggregation of Aβ(1–42) and the subsequent deposition in brain decreases the concentration of Aβ(1–42) in CSF of AD patients.

Tau Protein

The Tau protein is another AD biomarker with an important role in maintaining the integrity of neurons (*58*). Aggregation of hyperphosphorylated tau protein leads to the formation of insoluble neurofibrillary tangles in the brain tissue of AD patients (*58*). Ultrasensitive and selective detection of Alzheimer's tau protein using gold nanoparticle-based Rayleigh scattering assay has been demonstrated (*58*). After mixing tau protein with anti-tau antibody-coated gold nanoparticles, the Rayleigh scattering intensity increased by about 16 times (Figure 2). The detection level of 1 pg/mL is 2 orders of magnitude lower than the typical tau concentration in CSF. The gold nanoparticle-based Rayleigh scattering assay serves as a viable alternative for rapid, reliable diagnosis of AD biomarkers. Assay of Alzheimer's tau protein has also been reported using LSPR-based immunochip, enabling the detection of tau protein at 10 pg/mL (*59*).

Detection of Cancer Biomarkers

In general, cancer biomarkers are endogenous proteins or metabolites that can be used as possible diagnostic indicators of cancers (*60*, *61*). The expression profiles of these cancer biomarkers in tumor tissues or body fluids are indicative of tumorigenesis and progression, and may allow therapeutic treatments to be developed (*62–66*). Because there are numerous cancer biomarkers and it is impossible to cover all of them in this chapter, we focused mainly on three types of cancer biomarkers, transcription factors, cell surface receptors, and secreted proteins (*67*, *68*). These biomarkers are chosen because of their linkage to various cancers and the fact that they are widely studied. The cancer biomarkers selected herein are cell surface glycans, which are a type of cell surface receptor; interleukin-6 (IL-6) and tumor necrosis factor α (TNF-α), which are cell signaling molecules; prostate specific antigen (PSA), α-fetoprotein (AFP), carcinoembryonic antigen (CEA), all of which are secreted proteins; p53 and platelet-derived growth factor (PDGF), which are transcription factors, as well as some other biomarkers, such as mucin protein MUC4, carbohydrate antigens 15-3 (CA15-3), progastrin releasing-peptide (ProGRP) and Vascular endothelial growth factors (VEGF) (*69–71*).

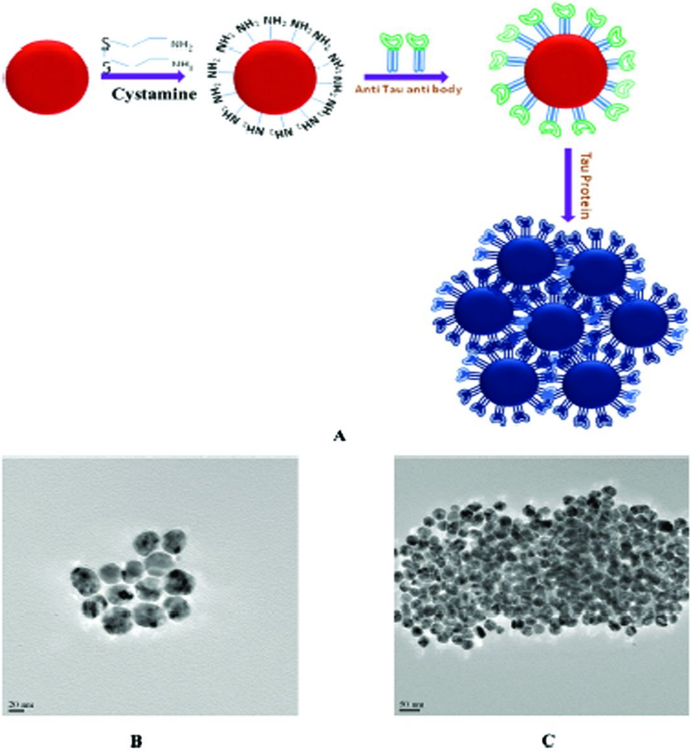

Figure 2. Schematic representation of the synthesis of monoclonal anti-tau antibody-conjugated gold nanoparticles and sensing of tau protein (A). TEM images of anti-tau antibody-conjugated gold nanoparticles before (B) and after addition of 20 ng/mL tau protein (C). (Adapted from ref. (58), with permission. Copyright © 2009 American Chemical Society.)

Cell Surface Receptors—Glycan Expression on Cell Surface

Cell surface glycans, a large group of biomolecules with diverse structures, play an important role in many cellular processes (*72–75*). The variation in cell surface glycans has been shown to be associated with many diseases, such as inflammation and cancers (*76*, *77*). For example, the overproduction of sialic acid groups (one kind of glycan) has been found on colorectal cancer cells (*78*). Tumor-associated alteration of cell surface glycans is crucial in metastasis of carcinoma cells since tumor cell adhesion or motility is changed (*79*, *80*). Recently, Zhang and co-workers measured the expression of mannose and sialic acid by normal and cancer cells (*81*). Lectin and thionine (Th) were co-immobilized onto AuNPs and the resulting bioconjugate was used as a label for signal amplification. Two lectins, concanavalin A (Con A) and *Sambucus nigra* agglutinin (SNA), were used to fabricate the Con A- and SNA-based bioconjugates that are specific to mannose and sialic acid, respectively. The lectins on the bioconjugates were then used for recognition of glycans on cell surface, while Th served as an electroactive probe. Enhanced sensitivity for the analysis of glycan expression has been achieved with the increased loading of Th molecules on AuNPs. The results demonstrate that mannose exhibits higher expression levels in both normal and cancer cells, while sialic acid is more abundant in cancer cells as compared to normal ones.

Ju's group studied glycan expression on living cells using multifunctional AuNP probes (*82*). The probe was fabricated by conjugating biotin-DNA and a large number of HRP molecules on AuNPs. The hydroxyl sites of sialyl and galactosyl groups on cell surfaces were selectively oxidized to aldehydes by periodate and galactose oxidase, respectively, followed by aniline-catalyzed hydrazone ligation with biotin-hydrazide for specific recognition to avidin. Through biotin-avidin complexation, the multifunctional AuNPs could be conveniently attached to the glycan sites on cell surface (Figure 3). The DNA chains on the AuNPs could obviate the steric effect, and horseradish peroxiase (HRP) could trigger the chemiluminescent (CL) emission of the luminal-H_2O_2 system. Thus the expression of both sialyl and galactosyl groups could be selectively detected by CL imaging.

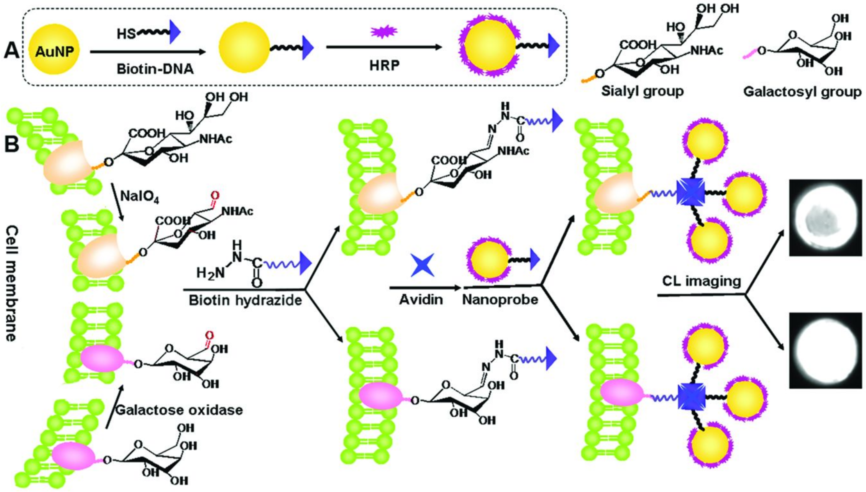

Figure 3. Schematic representation of (A) nanoprobe assembly and (B) CL imaging for analysis of cell surface glycan expression. (Adapted from ref. (82), with permission. Copyright © 2012 American Chemical Society.)

In another work by Ju's group, sensitive electrochemical monitoring of dynamic carbohydrate expression on living cells was reported using lectin (Con A)- and HRP-functionalized AuNP nanoprobes (*83*). The binding of the nanoprobes to cell surface results in the catalytic current by HRP. The method has been demonstrated to be highly sensitive with a detection limit down to 15 cells. The developed method is capable of monitoring the variation of carbohydrate expression on cancer cells in response to drugs, such as swainsonine (SW), which could increase the expression of terminal high-mannose type glycan on cell surface. The above mentioned papers are all based on co-immobilization of glycan-binding molecules and signaling (probe) species onto AuNPs. However, efforts should be made to prevent the aggregation of the functionalized AuNPs and to increase their stability.

Cell Signaling Molecules—Interleukin-6 (IL-6)

IL-6 is a cytokine that provokes a wide range of cellular and physiological responses, such as immune response, inflammation, hematopoiesis, and oncogenesis (*84–88*). It is also a biomarker of head and neck squamous cell carcinoma (HNSCC), which affects about 44 000 patients in the United States. The mean concentration of IL-6 exceeds 20 pg/mL in patients with HNSCC, while it is below 6 pg/mL in healthy controls (*89–91*). The ultralow levels of IL-6 in human sera present great challenges for its precise detection.

Wang et al. designed an electrochemical immunosensor for sensitive detection of IL-6 via a dual amplification strategy using AuNP-Poly-dopamine (PDOP) as the sensing platform and HRP-functionalized AuNP-PDOP@carbon nanotubes (CNTs) as a catalytic label (*92*). The AuNP-PDOP film was stable and exhibited high efficiency for the capture antibody immobilization. The AuNP-PDOP@CNTs, synthesized by electroless deposition of AuNPs on the PDOP-coated CNTs, is capable of loading a large number of HRP and the detection antibody molecules. Greatly enhanced sensitivity was achieved with a linear range from 4.0 to 800 pg/mL and a low detection limit of 1.0 pg/mL.

Liang and co-workers constructed a highly sensitive, fast and label-free conductometric immunosensor for determination of IL-6 via encapsulation of HRP-labeled anti-IL-6 antibody (HRP-anti-IL-6) in dendrimers- and AuNPs-modified nanocomposites (*93*). The incorporation of AuNPs and dendrimers provided a conductive microenvironment, leading to direct electron transfer between the immobilized HRP and the electrode. When exposed to IL-6-containing samples, the captured IL-6 molecules blocked the electron transfer process, resulting in a decreased catalytic current of HRP toward H_2O_2. However, due to the thick protein shell of the enzyme, direct electron transfer between HRP and the electrode is usually difficult, which leads to relatively low sensitivity.

The work by Rusling's group compared the performance of electrochemical immunosensors for IL-6 using single-wall carbon nanotube (SWNT) forests and glutathione-protected AuNPs (GSH-AuNPs) as sensing platforms (*94*). Both configurations were based on the sandwich structure using HRP as a label. The detection limit by GSH-AuNPs is lower than that by SWNT forests. Furthermore, a much wider linear range (20–4000 pg/mL) was obtained with GSH-AuNPs, in comparison with that achievable with SWNT forests (40–150 pg/mL). In another work by the same group, electrochemical detection of IL-6 by inkjet-printed AuNP array was performed (*95*). Such a configuration possesses a highly reproducible surface area and lowers the detection level of IL-6 to 20 pg/mL.

Recently, one of us reported the IL-6 detection based on AuNPs-mediated electron transfer across insulating self-assembled monolayers (SAMs) (*96*). Adsorption of metal nanoparticles onto insulating SAMs has been reported to be capable of mediating efficient electron transfer between the redox species and the electrode (*97*). To build the immunosensor, 11-mercaptoundecanoic acid (11-MUA) was self-assembled onto gold electrodes to insulate the electrode. Then the capture antibody, IL-6 of various concentrations and AuNPs-labeled detection antibody were sequentially attached onto the electrodes. The redox signal of $[Fe(CN)_6]^{3-}$ is proportional to the concentration of IL-6. The sensitivity was further enhanced by enlargement of the AuNPs and the subsequent modification with positively charged surfactant cetyltrimethylammonium bromide (CTAB). The enlarged AuNPs increases the electroactive surface area, resulting in a greater redox signal, while the electrostatic attraction between CTAB-modified AuNPs and $[Fe(CN)_6]^{3-}$ further facilitates the electron transfer reaction (Figure 4). A detection limit of 2.0 pg/mL was achieved.

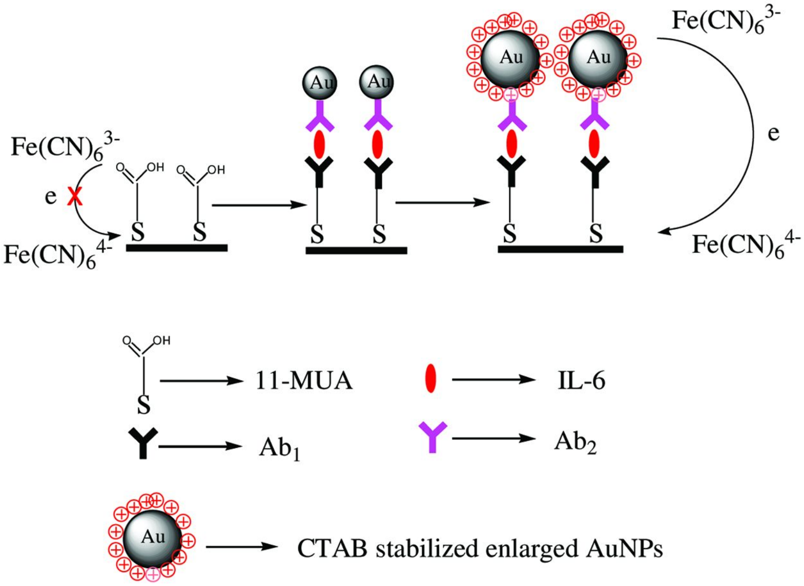

Figure 4. Schematic representation for construction of the immunosensor for detecting IL-6 with sequential attachments of IL-6 capture antibody, IL-6, and AuNPs coated with detection antibody. (Adapted from ref. (96), with permission. Copyright © 2011 Elsevier.)

Cell Signaling Molecules—Tumor Necrosis Factor α (TNF-Nα)

TNF-α is an inflammatory cytokine produced in response to infection or cancer (*98–100*). TNF-α is involved in a variety of pathological and physiological processes and linked to rheumatoid arthritis, psoriasis, and Crohn's disease (*101*, *102*). Usually, the concentration of TNF-α in healthy individuals is very low (2 pg/mL), thus sensitive and precise detection of TNF-α is much needed (*103*).

An electrochemical immunosensor for the detection of TNF-α using AuNPs-modified poly(styrene-acrylic acid) (PSAA) nanospheres has been reported by Zhu's group (*104*). Alkaline phosphatase (ALP) was conjugated to the nanospheres and used as a label for immunoassay. After the sandwich immunocomplex formation, the labeled ALP hydrolyzed α-naphthyl phosphate to the electroactive α-naphthol, which could be detected electrochemically. The proposed method can determine TNF-α with a concentration range of 0.02–200.00 ng/mL.

Lee and co-workers designed a gold nanoarray-based protein chip for the detection of TNF-α by total internal reflection fluorescence microscopy (TIRFM) (*105*). The gold nanoarray was fabricated on glass substrates using an electron beam evaporator. Dithiobis(succinimidyl propionate) was used as a protein linker and Protein A/G was selected to orient the immobilized antibody. Concentration range of 130 fM–13 aM of TNF-α was achieved with TIRFM. However, the method involves rather complicated instrumentation.

Secreted Proteins—Prostate Specific Antigen (PSA)

PSA is a protein generated by cells of the prostate gland (*106*). Typically, healthy men have a low level of PSA in their blood (below 4 ng/mL). However, prostate cancer or benign (not cancerous) conditions can result in an increased PSA level (*107–109*). The higher a man's PSA level, the more likely he will be susceptible to prostate cancer, though other possibilities also exist for an elevated PSA level (*110*). The PSA test has been approved by the U.S. Food and Drug Administration (FDA) to detect prostate cancers in men of 50 years or older.

Rusling's group developed an ultrasensitive electrochemical immunosensor for PSA via layer-by-layer assembly of poly(diallydimethylammonium chloride) (PDDA) and glutathione-protected AuNPs. Such a configuration renders a dense layer of AuNPs on the electrode, leading to an increased active area for antibody loading. Moreover, the good conductivity of AuNPs facilitates the electron transfer occurring at the electrode surface. Capture of anti-PSA antibody was then achieved via reaction between carboxylic acid groups on glutathione and amino groups on the antibody. HRP-conjugated magnetic beads were used as a catalytic label for PSA detection. The immunosensor exhibited high sensitivity and the detection limit was estimated to be 5.0 fg/mL (*111*).

Li and co-workers fabricated an immunosensing platform for the detection of PSA via monitoring the electrogenerated chemiluminescence (ECL) of luminal (*112*). ECL exhibits several advantages, such as high sensitivity, a wide linear range, low background and simple instrumentation (*113–117*). The sensing protocol involved a traditional sandwich immunoassay format in which gold nanorods (GNRs) served as a carrier to load the detection antibody and glucose oxidase (GOx) (Figure 5). The enzyme GOx on GNR could catalyze the luminal reaction in the presence of glucose and oxygen to generate ECL. GNR was not only used to increase the loading of GOx for an enhanced ECL intensity, but also catalyze the ECL reaction, further amplifying the detection signals. Under the optimized conditions, the immunosensor could determine PSA with a linear range from 10 pg mL^{-1} to 8 ng mL^{-1} and a detection limit down to 8 pg mL^{-1}.

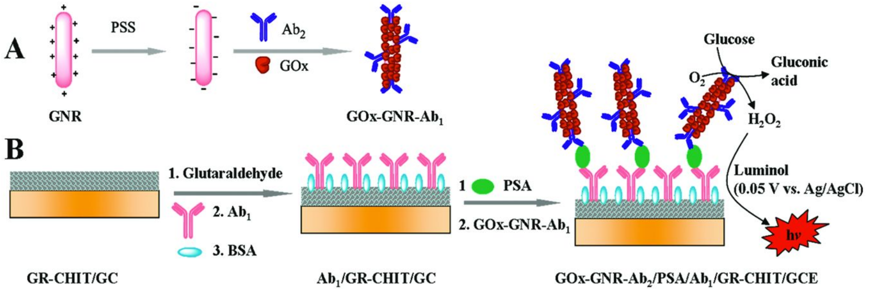

Figure 5. (A) Modification protocols of gold nanorods and (B) ECL immunoassay of PSA via multiple amplification strategy. (Adapted from ref. (112), with permission. Copyright © 2011 American Chemical Society.)

AuNPs exhibit unique and tunable optical properties, which have been utilized in bioassays. For example, a strong UV-vis absorption band was observed, which was absent in the spectra of bulk metals (*118*, *119*). The change in the size, aggregation status or surface properties of AuNPs could alter the UV-vis absorption (*120*, *121*). Huo et al. developed a homogeneous immunoassay for PSA using dynamic light scattering (DLS) (*122*). DLS has been commonly used to monitor the size distribution of proteins, polymers and nanoparticles (*123*, *124*). As shown in Figure 6, GNR was decorated with capture anti-PSA antibody and the detection antibody was conjugated to AuNPs. When the two modified nanoparticles were mixed in the presence of PSA, various immunocomplexes, such as dimers, oligomers, or aggregates were formed, depending on the concentration of PSA. Through DLS analysis, the relative ratio of dimers, oligomers, and aggregates versus individual nanoparticles could be determined. Such a ratio increased with the PSA concentration. The advantages of this method are obviation of any washing steps, high speed, and low sample volume requirement. The gold nanostructures serve as nanocarriers for proteins, and their size change could be utilized for quantification of PSA.

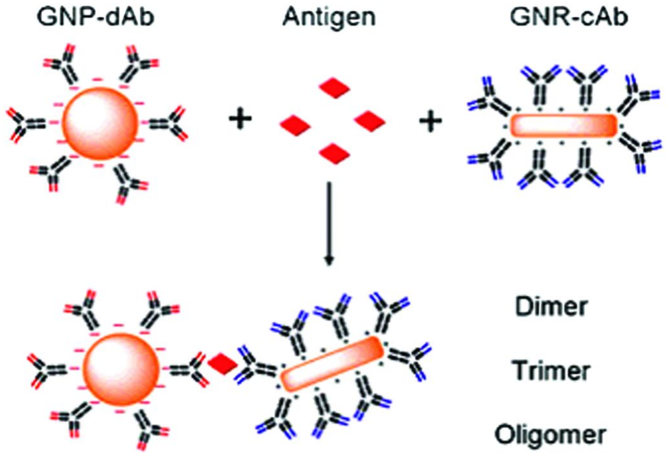
GNP-dAb
Antigen
GNR-cAb
+
+
Dimer
Trimer
Oligomer

Figure 6. Schematic illustration of the homogeneous immunoassay using antibody-conjugated nanoparticles and nanorods. (Adapted from ref. (122), with permission. Copyright © 2008 American Chemical Society.)

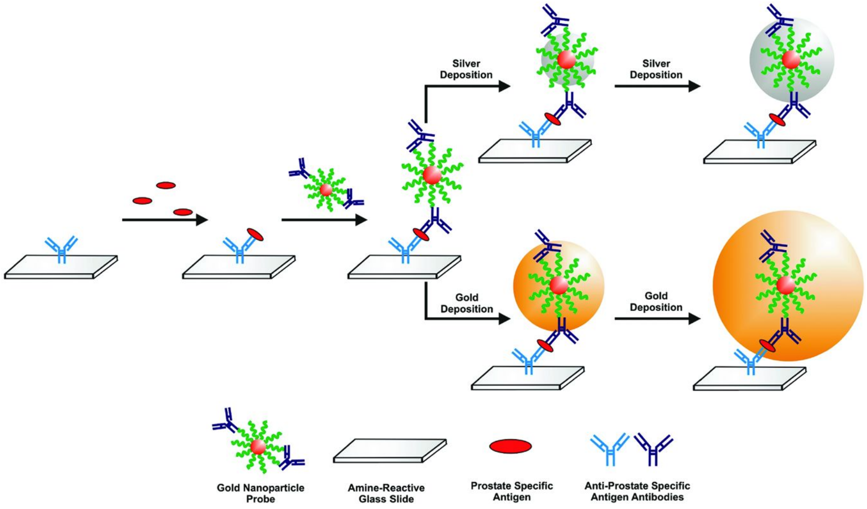
Silver Deposition
Silver Deposition
Gold Deposition
Gold Deposition
Gold Nanoparticle Probe
Amine-Reactive Glass Slide
Prostate Specific Antigen
Anti-Prostate Specific Antigen Antibodies

Figure 7. Schematic representation of the immunoassay procedures used for scanometric assay of PSA, hCG, and AFP. (Adapted from ref. (125), with permission. Copyright © 2009 American Chemical Society.)

Mirkin and co-workers reported a microarray-based multiplexed scanometric immunoassay using AuNPs as a detection antibody label (*125*). PSA was selected as a model biomarker and then the microarray was extended for the simultaneous detection of PSA, human chorionic gonadotropin (hCG), and α-fetoprotein (AFP). Electroless silver or gold deposition on AuNPs was performed for the following optical detection (Figure 7). Interestingly, they found that electroless Au deposition results in greater signal enhancement and lower detection limit than silver deposition. Such a difference could be ascribed to different growth mechanisms. After one round of Au deposition on AuNPs, the resultant nanoparticles could be used as nucleation sites for another round of deposition, which causes continuous nucleation of new AuNPs. While silver deposition usually caused autocatalytic reduction of silver on the AuNPs, the as-formed gold microstructures were much larger than those by silver. The proposed method has been demonstrated to be capable of determining PSA, hCG, and AFP at low picomolar levels in buffer and in 10% sera. The advantage of such method is the simple instrument used for the detection.

Surface-enhanced Raman scattering (SERS) is a surface-sensitive technique with enhanced Raman scattering caused by the adsorption of molecules onto rough metal surface (*126–128*). The enhancement factor could be as much as 10^{10} to 10^{11} with the use of AuNPs as the SERS substrate (*129*, *130*). Zhou et al. developed an immunoassay for PSA using SERS (*131*). Capture antibody was attached to the synthesized Fe_3O_4/Au nanoparticles, while SERS label malachite green isothiocyanate (MGITC) and the detection antibody were both conjugated to the 30-nm AuNPs. In the presence of PSA, immunocomplex of AuNP-PSA-Fe_3O_4/Au was formed. After magnetic separation, the MGITC was detected by SERS. The rough outer Au shells on the Fe_3O_4 surface act as an excellent substrate for antibody immobilization and for SERS detection.

Shin's group reported the use of elliptical Au nanodisk array as LSPR sensing substrate for immunodetection of PSA (*132*). Capture anti-PSA antibody, PSA and alkaline phosphatase-labeled detection antibody were immobilized sequentially onto the Au nanodisk to build the sandwich structure. The enzyme then catalyzed the reduction of 5-bromo-4-chloro-3-indolyl phosphate p-toluidine/nitro blue tetrazolium (BCIP/NBT) with the formation of the precipitates onto the Au nanodisk surface, which resulted in variations of local refractive index.

α-Fetoprotein (AFP)

AFP is an abundant protein normally found in the developing fetuses (*133*). Very low levels of AFP (below 10 ng/mL) are present in healthy children and adults, except for pregnant women (*134*, *135*). Elevated blood levels of AFP are associated with liver diseases, such as hepatocellular carcinoma (HCC), which is the sixth most common cancer worldwide with almost the lowest survival rates (*136*, *137*).

Many groups have fabricated AuNPs-based immunosensors for the detection of AFP. For example, immunosensors have been constructed by immobilization of capture anti-AFP antibodies onto AuNPs-decorated Nafion electrodes (*138*), by electrodeposition of AuNPs and Prussian Blue on ITO electrode (*139*), by using carbon paste electrodes prepared with ionic liquid and AuNPs (*140*), or by immobilization of AFP onto electrodes functionalized with AuNPs- and carbon nanotube (CNT)-doped chitosan film (*141*).

Yan and co-workers designed an inhibition assay for AFP based on fluorescence resonance energy transfer (FRET) in which functionalized AuNPs were used as a fluorescence quencher (*142*). Persistent-luminescence nanoparticles (PLNPs) of Eu^{2+}- and Dy^{3+}-doped $Ca_{1.86}Mg_{0.14}ZnSi_2O_7$ were prepared and modified with polyethyleneimine (PEI) to serve as a fluorescence acceptor (PEI-PLNPs). The electrostatic interaction between positively charged PEI-PLNPs and negatively charged antibody-modified AuNPs (Ab-AuNPs) resulted in quenching of the fluorescence. Addition of AFP to the PEI-PLNPs/Ab-AuNPs conjugates led to obvious recovery of the luminescence of PEI-PLNPs due to desorption of Ab-AuNPs from PEI-PLNPs caused by the competition of AFP with PEI-PLNPs for Ab-AuNPs. Furthermore, successful monitoring of AFP excretion by Bel-7402 cells (a kind of malignant HCC cell) and L-O2 cells (a kind of normal hepatic cell) has been demonstrated.

Wang's group described an amplified immunoassay for protein cancer biomarker AFP using DNAzyme-functionalized AuNPs as a catalytic label (*143*). The DNAzyme mimics the functions of peroxidase and can be used as a substitute of HRP. Enhanced sensitivity has been achieved via loading large number of DNAzyme units on each AuNP surface. The traditional immunoassay strategy was employed in which a sandwich complex MMPs-AFP-AuNPs was formed between the MMPs modified with capture anti-AFP antibody and the AuNPs functionalized with DNAzyme and the detection anti-AFP antibody in the presence of AFP. After magnetic collection of the complex, the DNAzyme unit on the AuNPs was released and then reacted with the substrate, resulting in color change of the substrate solution, which could be monitored by a UV-vis spectrometer. However, UV-visible absorption measurements usually results in relatively low sensitivity. To prevent nonspecific adsorption and to improve the selectivity of the assay, traditional blocking procedures should be attempted.

Tang and co-workers developed a multiplexed immunoassay protocol for simultaneous electrochemical determination of AFP and carcinoembryonic (CEA) using multifunctional nanogold hollow microspheres as a distinguishable signal label (*144*). HRP-ferrocene and HRP-thionine were incorporated into nanogold hollow microspheres (GSH), which were utilized as tags for the detection anti-AFP antibody and anti-CEA antibody, respectively. The assay was performed based on the catalytic reduction of H_2O_2 by the two GSH labels in the presence of the corresponding mediators. In another work by Tang's group, a sandwich electrochemical immunoassay for AFP using carbon nanotube-enriched gold nanoparticles (CNT-AuNPs) as a label has been demonstrated (*145*). In solutions containing p-nitrophenol (NP) and $NaBH_4$, NP was reduced to p-aminophenol (AP) by AuNPs on the CNT-AuNPs, and then the generated AP was electrochemically oxidized to p-quinoneimine (QI) by thionine on the electrode surface. The oxidized QI could be reduced back to AP by $NaBH_4$. The redox cycling of AP and QI could be continued, resulting in high sensitivity of the method. An extremely low detection limit of 0.8 fg/mL has been achieved, which is six orders of magnitude lower than that by commercially available ELISA.

Although the detection sensitivity was increased, the relatively complicated procedure associated with the signal amplification step somewhat hampers the reproducibility of the assay.

Carcinoembryonic Antigen (CEA)

CEA is a protein found in many different cells, being typically associated with certain tumors and the developing fetuses (*146*, *147*). The normal range of CEA is below 2.5 ng/mL in an adult. The most frequent cancer that exhibits an increased CEA level is colorectal cancer (*148*, *149*). Others include pancreatic cancer, stomach cancer, breast cancer, lung cancer, and certain types of thyroid and ovarian cancers (*150*, *151*).

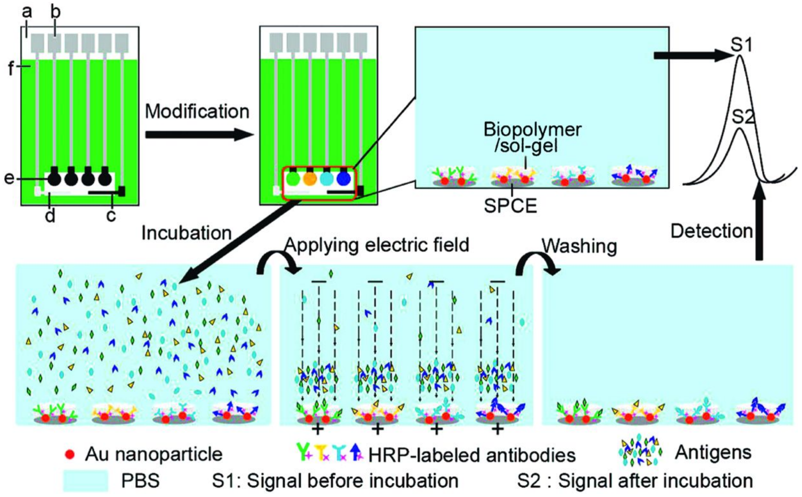
a
b
f
e
d
c
Modification
Biopolymer
/sol-gel
SPCE
S1
S2
Incubation
Applying electric field
Washing
Detection
Au nanoparticle
HRP-labeled antibodies
Antigens
PBS
S1: Signal before incubation
S2 : Signal after incubation

Figure 8. Schematic representation of the electrochemical immunosensor array and the electrochemical multiplexed immunoassay with an electric field-driven incubation process. (Adapted from ref. (152), with permission. Copyright © 2008 American Chemical Society.)

Ju's group reported the multiplexed detection of protein biomarkers carbohydrate antigens 153, 125, 199 (CA 153, CA 125, CA 199) and CEA using a disposable reagentless electrochemical immunosensor array (Figure 8) (*152*). AuNPs modified with HRP-labeled antibody were immobilized onto chitosan/sol-gel-modified electrodes to achieve enhanced direct electrochemical response of HRP. The HRP-labeled antibody could then capture the corresponding antigens in sample solution, resulting in decreased electrochemical signals of HRP due to increased spatial blocking and impedance caused by the nonconductive immunocomplex formation. An electric field-driven incubation strategy has been applied to shorten the antibody-antigen reaction time to 2 min. The multiplexed assay could find potential applications in high-throughput screening of tumor biomarkers. In another work by the same group, a triple signal amplification strategy for the detection of CEA has been reported (*153*). Graphene-modified electrode was used as a sensing platform for the immobilization of the capture antibody, and AuNPs-modified poly(styrene-co-acrylic acid) (PSAA) microbeads were designed as a label in which AuNPs could induce silver deposition for anodic stripping analysis. The high surface-to-volume ratio of PSAA microbeads leads to numerous AuNPs loaded onto the PSAA surface. CEA was determined by assay of silver on the PSAA surface.

Lv et al. reported an immunoassay for CEA based on gold-silver amplification by inductively coupled plasma-mass spectrometry (ICP-MS) (*154*). The sensing protocol is based on AuNPs-catalyzed silver deposition followed by the detection of the deposited silver using ICP-MS (Figure 9). But the detection based on ICP-MS increased the assay cost. Besides ICP-MS detection, after silver enhancement, visible black color appeared, which could enable detection of CEA as low as 10 ng/mL.

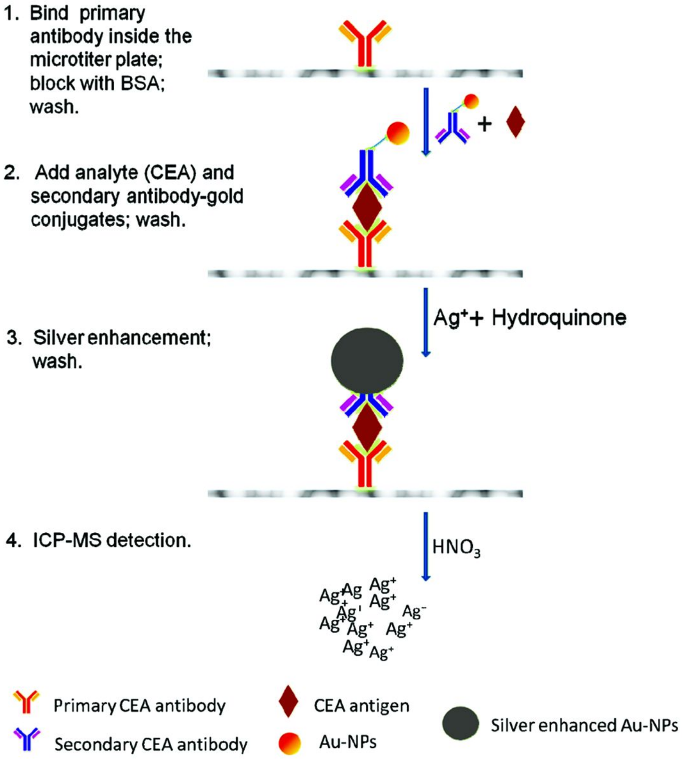
1. Bind primary antibody inside the microtiter plate; block with BSA; wash.
+
2. Add analyte (CEA) and secondary antibody-gold conjugates; wash.
Ag⁺+ Hydroquinone
3. Silver enhancement; wash.
4. ICP-MS detection.
HNO₃
Ag⁺ Ag⁺ Ag⁺ Ag⁺ Ag⁺ Ag⁺ Ag⁺ Ag⁺ Ag⁺ Ag⁺ Ag⁺
Primary CEA antibody
Secondary CEA antibody
CEA antigen
Au-NPs
Silver enhanced Au-NPs

Figure 9. Schematic diagram of the sandwich immunoassay for human CEA based on silver amplification. (Adapted from ref. (154), with permission. Copyright © 2011 American Chemical Society.)

Transcription Factors—P53

p53 is a transcription factor being capable of inhibiting the growth of tumor cells (*155–157*). The p53 tumor suppression pathway is deactivated in almost all human cancers (*158*) and about 50% of the cases are resulted from mutations in the p53 gene. The mutated p53 protein loses its ability to bind the consensus DNA fragments with specific sequences (*159*, *160*). We have designed a signal amplification strategy for the detection of p53 using ferrocene-capped gold nanoparticle/streptavidin conjugates (Figure 10) (*161*). The assay was performed with the capture of wild-type p53 protein by ds-ODNs containing the consensus DNA sequence and the subsequent derivatization of p53 for the attachment of the nanoconjugates. Because each AuNP was decorated with more than 100 ferrocene molecules, the electrochemical signals have been greatly amplified. The developed method can determine p53 concentration as low as 2.2 pM. Due to the specific binding of wild-type p53 to the consensus DNA sequence, the method is highly selective and sensitive for the wild-type p53 protein in normal and cancer cell lysates. However, such a protocol did not allow an accurate determination of the extent of p53 mutation. With a dual-channel surface plasmon resonance (SPR) instrument, simultaneous and label-free determination of wild-type and mutant p53 present in cancer cell lysates has been carried out (*162*). The dual-channel SPR affords a rapid route for determination of p53 mutation.

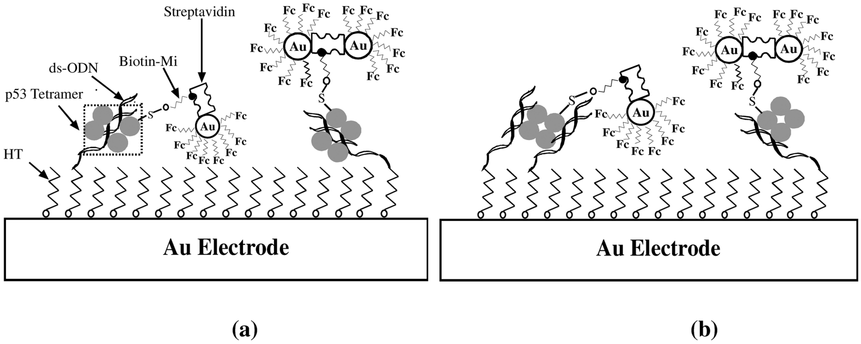

Figure 10. Schematic representations of the capture of p53 by ds-ODN-modified electrodes and the follow-up amplified voltammetric detection of p53 via oxidation of the ferrocene tags on the gold nanoparticle/streptavidin conjugates. Scheme (a) depicts the most stable p53 binding to ds-ODNs at the electrode, while scheme (b) shows two other possible surface binding configurations. (Adapted from ref. (161), with permission. Copyright © 2008 American Chemical Society.)

Lin and co-workers developed a multiplexed electrochemical immunoassay for fast and sensitive detection of phosphorylated and total p53 simultaneously (*163*). GNR was selected as a nanocarrier for HRP and the detection antibody to achieve multienzyme binding onto each GNR surface. Different capture anti-p53 antibodies were immobilized onto the working electrodes of the sensor array to enable simultaneous immunoassay without cross-talk between adjacent electrodes.

The whole sandwich immunoreaction processes were accelerated (less than 5 min) by applying a positive driving potential to accelerate the transport of negatively charged antigens and a low negative driving potential to accelerate the transport of positively charged GNR bioconjugates. Due to the greatly enhanced sensitivity and much shortened immunoreaction time, the method holds great promise for potential clinical applications.

Bizzarri et al. reported the detection of wild-type and mutant p53 proteins via SERS (*164*). The Raman reporter bifunctional linker 4-aminothiophenol (4-ATP) was used with a thiol group on one side binding to AuNPs, while the amino groups on the other side were functionalized to bind the lateral chains of p53. The resultant bioconjugates p53-4-ATP-AuNPs were then captured by the bacterial blue-copper protein azurin (Az)-covered self-assembled monolayers in which Az could strongly bind to both wild-type and mutant p53 proteins. Because one AuNP was covered with about 10^4 4-ATP molecules, the SERS signal was greatly enhanced. The method could determine both wild-type and mutant p53 proteins with high sensitivity and selectivity. The drawback of the method is that the p53 molecules need to be pre-labeled with 4-ATP-AuNPs.

Platelet-Derived Growth Factor (PDGF)

PDGF is a growth factor protein in human platelets, which regulates cell growth and division (*165*, *166*). PDGF is associated with a variety of disorders, cell transformation, tumor growth and progression (*167–170*). PDGF is composed of two A (PDGF-AA) or two B (PDGF-BB) chains or a combination of both (PDGF-AB).

Chang's group described the homogeneous photoluminescence quenching assay for PDGF-AA and PDGF α-receptor using Au nanoparticles of two different sizes, which acted separately as a donor and an acceptor (*171*). The construction of the donor and acceptor was realized via conjugation of PDGF-AA to 2.0-nm MUA-protected photoluminescent Au nanodots (AuNDs) and by attachment of thiol-derivative PDGF binding aptamer (Apt) to 13-nm AuNPs, respectively. The photoluminescence of PDGF-AA-AuNDs at 520 nm was quenched by the presence of Apt-AuNPs. However, in the presence of different concentrations of PDGFs, the competitive reaction between PDGF and Apt-AuNPs resulted in an increase in the photoluminescence intensity. The detection limit for PDGF-AA and PDGF α-receptor was estimated to be 80 pM and 0.25 nM, respectively. The feasibility of the method for real sample analysis has been demonstrated through assays of PDGF in serum-free conditioned cell media and urine samples. In another work by the same group, aptamer-modified AuNPs (Apt-AuNPs) were used as a molecular light switching sensor for PDGF detection (*172*). Due to the unique structure of the aptamer with triple-helix conformation, *N,N*-dimethyl-2,7-diazapyrenium dication (DMDAP) and PDGF could be both linked to the PDGF-binding aptamer. With intercalation of DMDAP into the aptamers, the fluorescence of DMDAP was almost completely quenched in the presence of the Apt-AuNPs complex. With the addition of PDGF of various concentrations, DMDAP and PDGF competed with the aptamer molecules on the AuNPs, restoring the fluorescence of DMDAP (Figure 11).

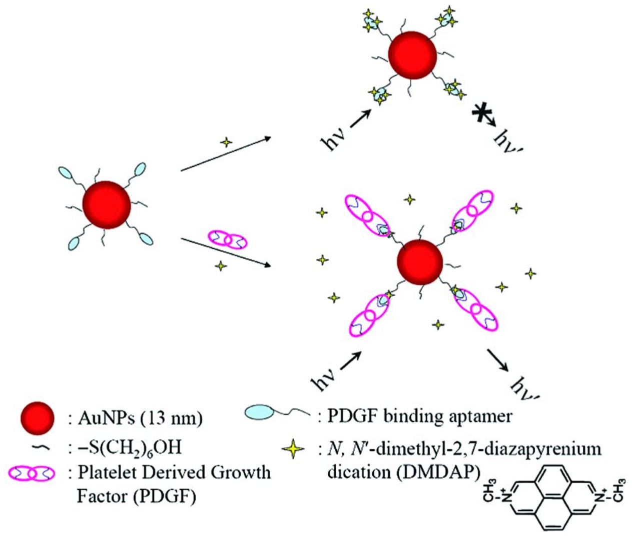
hν
hν'
hν
hν'
: AuNPs (13 nm)
: $-S(CH_2)_6OH$
: Platelet Derived Growth Factor (PDGF)
: PDGF binding aptamer
: *N, N'*-dimethyl-2,7-diazapyrenium dication (DMDAP)
CH_3
CH_3

Figure 11. Schematic representation of PDGF nanosensors based on modulation of the FRET between DMDAP and Apt-AuNPs. (Adapted from ref. (172), with permission. Copyright © 2007 American Chemical Society.)

Chang's group also developed a colorimetric assay for selective and sensitive detection of PDGF based on aptamer- and fibrinogen-modified AuNPs (Apt-AuNPs, and Fib-AuNPs, respectively) (*173*). PDGF-binding aptamer (Apt$_{\mathrm{PDGF}}$) and thrombin-binding aptamer (Apt$_{\mathrm{thr}}$) were both linked to AuNPs (Apt$_{\mathrm{PDGF}}$/Apt$_{\mathrm{thr}}$-AuNPs) for specific interaction with PDGF and thrombin, respectively. The cleavage of Fib on the Fib-AuNPs complex by thrombin induced fibrin assembly into fibrin-AuNPs aggregates, which caused the color change from light red-purple to dark blue. In the presence of Apt$_{\mathrm{PDGF}}$/Apt$_{\mathrm{thr}}$-AuNPs, the activity of thrombin was inhibited through its specific binding with Apt$_{\mathrm{thr}}$. However, due to the formation of PDGF-Apt$_{\mathrm{PDGF}}$/Apt$_{\mathrm{thr}}$-AuNPs, the addition of PDGF minimized the interaction between Apt$_{\mathrm{thr}}$ and thrombin as a result of steric effect. Such a decreased interaction restored the activity of thrombin toward Fib. As a result, the amount of fibrin-AuNP aggregates was increased, which could be easily monitored by UV-vis spectrometry. But compared to the two methods from the same group that we reviewed above, this is a more complex procedure.

Shen et al. designed a label-free self-locked bifunctional oligonucleotide probe for assay of PDGF-BB and p53 gene in parallel (*174*). Signal enhancement protocol of isothermal circular strand-displacement polymerization reaction has been employed to amplify the detection signals. In such a method, target/recognition probe interaction promoted the hybridization between the primers, which triggered the isothermal polymerization when using the linear recognition probe as the template. The polymerase then displaced the hybridized target during the primer extension, creating a primer-extended sequence/recognition probe hybrid. The displaced target in turn triggered the next polymerization reaction. The proposed method can determine PDGF-BB with a linear range of 8–5000 ng/mL and the detection limit was estimated to be 0.87 ng/mL. The sensing protocol could serve as an alternative for screening p53 gene. However, the sensing protocol is somewhat complex, reducing the reproducibility of the assay.

Detection of Other Cancer Biomarkers

In addition to the abovementioned biomarkers, attempts have also been made for sensitive detection of other biomarkers using functionalized metal nanoparticles. Pancreatic cancer (PC) is one of the most lethal tumors with a 5-year survival rate of only 6%. Mucin protein MUC4 was overexpressed in most PC, while it was undetectable in normal pancreas. Thus MUC4 is a potential diagnostic biomarker for PC (*175*). Lipert and co-workers reported an immunoassay for MUC4 using SERS (*176*). Raman reporter molecules and the detection antibody were both linked to AuNPs. Relying on the sandwich immunoassay protocol, MUC4 was quantified by the characteristic SERS spectrum of the immobilized Raman reporter molecules (Figure 12).

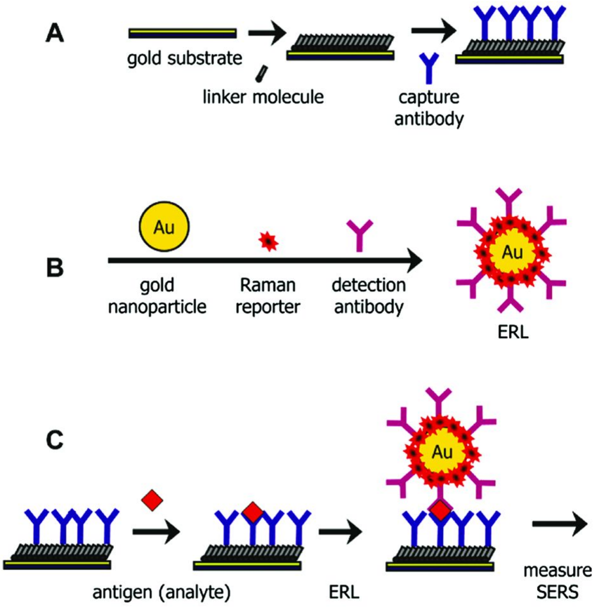

Figure 12. A SERS-based immunoassay chip design and the assay scheme: (A) a substrate was used to specifically extract and concentrate antigens from solution; (B) surface-functionalized AuNPs were allowed to bind to the captured antigens to generate intense SERS signals; and (C) the final sandwich immunoassay for the SERS readout. (Adapted from ref. (176), with permission. Copyright © 2011 American Chemical Society.)

Ambrosi et al. reported an optical immunoassay for CA15-3, an important biomarker of breast cancer (*177*). AuNPs were used as carriers for HRP-conjugated anti-CA15-3 antibody. The incorporation of AuNPs enables the attachment of multiple enzyme molecules, resulting in amplified optical signals and low background noise. Progastrin releasing-peptide (ProGRP) is a specific and reliable tumor biomarker of small-cell lung cancer (*178*). Yuan's group constructed an electrochemical immunosensor for ProGRP in which AuNPs were anchored onto TiO_2 nanoparticles (AuNP/TiO_2 nanocomposites) followed by the attachment of GOD and antibody (*179*). The large specific surface area of AuNP/TiO_2 increased the loading of GOD and the antibody, while the good biocompatibility of AuNPs retained the bioactivity of the biomolecules. Vascular endothelial growth factors (VEGF) is a signaling protein that stimulates vasculogenesis and angiogenesis, being overexpressed in many human solid tumors (*180*). Sung et al. reported the electrochemical immunoassay for VEGF using AuNPs-modified indium tin oxide (ITO) electrode as a sensing platform (*181*). VEGF antibodies were cleaved into two half fragments, which were immobilized onto the AuNPs-modified ITO surface through the thiol groups. In this way, oriented attachment of the antibodies with more available sites for VEGF has been achieved. Using ferrocene as a detection antibody tag, the immunosensor is capable of determining VEGF within a linear range from 100 to 600 pg/mL.

Conclusions and Outlook

We reviewed recent applications of noble metal nanoparticles to sensitive detection of trace levels of cancer biomarkers and biomarkers of Alzheimer's disease (AD) and commented on the novel aspects and limitations of many of the methods. The bioconjugated nanoparticles allow protein recognition events to be combined with different signal transduction processes, leading to the development of a variety of novel sensing protocols. Functional noble metal nanoparticles offer several attractive features, such as high sensitivity, simplicity, and direct visualization. It is well known that AuNPs displays good biocompatibility. AgNPs, similar to some heavy metal-based quantum dots, can be highly toxic to mammalian cells (*182–184*). Thus, more work needs be conducted to evaluate the toxicity of AgNPs to mammalian cells and caution should be exercised in future studies about the dosage and proper use of AgNPs for cell-based assays. From the select examples, it is evident that greater efforts need to be made to increase the stability, selectivity and reproducibility of the developed methods. Though appealing, the metal nanoparticles are prone to cause non-specific adsorption of the biomarkers. Therefore, care must be taken in devising effective surface modification schemes to prevent nonspecific adsorption to avoid false-positive readouts. Currently, many of the existing detection protocols are limited to mainly feasibility studies, and are still not regarded to be highly relevant to assays in clinical and point-of-care settings. Future efforts should be directed towards assessment of large quantities of clinical samples to demonstrate the applicability of given methods for reliable and high-throughput diagnostics. Undoubtedly, fully understanding the physical and chemical properties of the noble metal nanoparticles may expand their range of applications. With the development of nanotechnology and new detection methods, simple and cost-effective biomedical devices for point-of-care tests will continue to evolve.

Acknowledgments

Partial support of this work by the National Natural Science Foundation of China (No. 21105128 to M.Y. and Nos. 21175156, 20975114 to J.W.), Program for New Century Excellent Talents in University (NCET-10-0796 to J.W.), the NIH (SC1MS070155-01 to F.Z.), and an NSF Grant (No. 1112105 to F.Z.) is gratefully acknowledged.

Abbreviations

AD = Alzheimer's disease
AuNPs = gold nanoparticles
AgNPs = silver nanoparticles
SERS = surface-enhanced Raman scattering
ELISA = enzyme-linked immunosorbent assay
HRP = horseradish peroxidase
Aβ = amyloid-β
LSPR = localized surface plasmon resonance
ADDLs = Aβ-derived diffusible ligands
CSF = cerebrospinal fluid
MMPs = magnetic microparticles
ds-ODNs = double-stranded oligonucleotides
IL- 6 = interleukin-6
TNF-α = tumor necrosis factor α
PSA = prostate specific antigen
AFP = α-fetoprotein
CEA= carcinoembryonic antigen
PDGF = platelet-derived growth factor
ProGRP = Progastrin releasing-peptide (ProGRP)
CA15-3 = carbohydrate antigens 15-3
VEGF = vascular endothelial growth factor
Th = thionine
Con A = concanavalin A
SNA = *Sambucus nigra* agglutinin
CL = chemiluminescent
SW = swainsonine
HNSCC = head and neck squamous cell carcinoma
PDOP = Poly-dopamine
SWNT = single-wall carbon nanotube
GSH-AuNPs = glutathione-protected AuNPs
SAMs = self-assembled monolayers

11- MUA = 11-mercaptoundecanoic acid
CTAB = cetyltrimethylammonium bromide
ALP = Alkaline phosphatase
TIRFM = total internal reflection fluorescence microscopy
FDA = U.S. Food and Drug Administration
PDDA = poly(diallydimethylammonium chloride)
ECL = electrogenerated chemiluminescence
GNRs = gold nanorods
GOx = glucose oxidase
DLS = dynamic light scattering
hCG = human chorionic gonadotropin
MGITC = malachite green isothiocyanate
BCIP/NBT = 5-bromo-4-chloro-3-indolyl phosphate p-toluidine/nitro blue tetrazolium
HCC = hepatocellular carcinoma
FRET = fluorescence resonance energy transfer
PLNPs = Persistent-luminescence nanoparticles
PEI = polyethyleneimine
CNT = carbon nanotube
GSH = nanogold hollow microspheres
NP = p-nitrophenol
AP = p-aminophenol
QI = p-quinoneimine
PSAA = poly(styrene-co-acrylic acid)
ICP- MS = inductively coupled plasma-mass spectrometry
SPR = surface plasmon resonance
4-ATP = 4-aminothiophenol
Az = azurin
AuNDs = Au nanodots
DMDAP = *N,N*-dimethyl-2,7-diazapyrenium dication
PC = Pancreatic cancer
ITO = indium tin oxide

References

1. Sigdel, T. K.; Sarwal, M. M. *Expert Rev. Proteomics* **2011**, *8*, 705.
2. Miller, G. *Science* **2009**, *326*, 386.
3. Stastna, M.; Van Eyk, J. E. *Proteomics* **2012**, *12*, 722.
4. Huang, C.-S.; Chaudhery, V.; Pokhriyal, A.; George, S.; Polans, J.; Lu, M.; Tan, R.; Zangar, R. C.; Cunningham, B. T. *Anal. Chem.* **2012**, *84*, 1126.
5. Krisp, C.; McKay, M. J.; Wolters, D. A.; Molloy, M. P. *Anal. Chem.* **2012**, *84*, 1592.
6. Phuoc Long, T.; Kim, B. W.; Sim, S. J. *Lab Chip* **2012**, *12*, 1102.
7. Swierczewska, M.; Liu, G.; Lee, S.; Chen, X. *Chem. Soc. Rev.* **2012**, *41*, 2641.
8. Tang, C. K.; Vaze, A.; Rusling, J. F. *Lab Chip* **2012**, *12*, 281.

9. Zhou, F.; Wang, M.; Yuan, L.; Cheng, Z.; Wu, Z.; Chen, H. *Analyst* **2012**, *137*, 1779.
10. Wang, S.; Zhao, X.; Khimji, I.; Akbas, R.; Qiu, W.; Edwards, D.; Cramer, D. W.; Ye, B.; Demirci, U. *Lab Chip* **2011**, *11*, 3411.
11. Anborgh, P. H.; Wilson, S. M.; Tuck, A. B.; Winquist, E.; Schmidt, N.; Hart, R.; Kon, S.; Maeda, M.; Uede, T.; Stitt, L. W.; Chambers, A. F. *Clin. Chem.* **2009**, *55*, 895.
12. Zangar, R. C.; Daly, D. S.; White, A. M. *Expert Rev. Proteomics* **2006**, *3*, 37.
13. Liu, Q.; Han, M.; Bao, J.; Jiang, X.; Dai, Z. *Analyst* **2011**, *136*, 5197.
14. Kwon, M. J.; Lee, J.; Wark, A. W.; Lee, H. J. *Anal. Chem.* **2012**, *84*, 1702.
15. Wu, D.; Li, R.; Wang, H.; Liu, S.; Wang, H.; Wei, Q.; Du, B. *Analyst* **2012**, *137*, 608.
16. Zhang, J.-J.; Zheng, T.-T.; Cheng, F.-F.; Zhang, J.-R.; Zhu, J.-J. *Anal. Chem.* **2011**, *83*, 7902.
17. He, Y.; Zhang, X.; Zhang, S.; Kris, M. K. L.; Man, F. C.; Kawde, A.-N.; Liu, G. *Biosens. Bioelectron.* **2012**, *34*, 37.
18. Zhang, Y.; Ge, S.; Wang, S.; Yan, M.; Yu, J.; Song, X.; Liu, W. *The Analyst* **2012**, *137*, 2176.
19. Han, J.; Zhuo, Y.; Chai, Y.-Q.; Yuan, Y.-L.; Yuan, R. *Biosens. Bioelectron.* **2012**, *31*, 399.
20. Su, H.; Ma, Q.; Shang, K.; Liu, T.; Yin, H.; Ai, S. *Sens. Actuators, B* **2012**, *161*, 298.
21. Duan, N.; Wu, S.; Zhu, C.; Ma, X.; Wang, Z.; Yu, Y.; Jiang, Y. *Anal. Chim. Acta* **2012**, *723*, 1.
22. Chen, H.; Jiang, C.; Yu, C.; Zhang, S.; Liu, B.; Kong, J. *Biosens. Bioelectron.* **2009**, *24*, 3399.
23. Ray, S.; Reddy, P. J.; Choudhary, S.; Raghu, D.; Srivastava, S. *J. Proteomics* **2011**, *74*, 2660.
24. Jans, H.; Huo, Q. *Chem. Soc. Rev.* **2012**, *41*, 2849.
25. Porter, M. D.; Lipert, R. J.; Siperko, L. M.; Wang, G.; Narayanana, R. *Chem. Soc. Rev.* **2008**, *37*, 1001.
26. Siangproh, W.; Dungchai, W.; Rattanarat, P.; Chailapakul, O. *Anal. Chim. Acta* **2011**, *690*, 10.
27. Jain, K. K. *Expert. Rev. Mol. Diagn.* **2003**, *3*, 153.
28. Kuramitz, H. *Anal. Bioanal. Chem.* **2009**, *394*, 61.
29. Osaka, T.; Matsunaga, T.; Nakanishi, T.; Arakaki, A.; Niwa, D.; Iida, H. *Anal. Bioanal. Chem.* **2006**, *384*, 593.
30. Wang, J. *Electroanalysis* **2007**, *19*, 769.
31. Zhu, S.; Zhou, W. *J. Nanomater.* **2010**, 1–12.
32. Wang, G.; Jin, F.; Dai, N.; Zhong, Z.; Qing, Y.; Li, M.; Yuan, R.; Wang, D. *Anal. Biochem.* **2012**, *422*, 7.
33. Yuan, Y.; Zhang, J.; Zhang, H.; Yang, X. *Analyst* **2012**, *137*, 496.
34. Liu, X.; Zhao, R.; Mao, W.; Feng, H.; Liu, X.; Wong, D. K. Y. *Analyst* **2011**, *136*, 5204.
35. Zhu, J.; Zou, N.; Zhu, D.; Wang, J.; Jin, Q.; Zhao, J.; Mao, H. *Clin. Chem.* **2011**, *57*, 1732.

36. Baptista, P.; Pereira, E.; Eaton, P.; Doria, G.; Miranda, A.; Gomes, I.; Quaresma, P.; Franco, R. *Anal. Bioanal. Chem.* **2008**, *391*, 943.
37. Hu, W.; Li, C. M. *Wiley Interdiscip. Rev.: Nanomed. Nanobiotechnol.* **2011**, *3*, 119.
38. Yu, L.; Andriola, A. *Talanta* **2010**, *82*, 869.
39. Perfezou, M.; Turner, A.; Merkoci, A. *Chem. Soc. Rev.* **2012**, *41*, 2606.
40. Peng, J.; Feng, L.-N.; Ren, Z.-J.; Jiang, L.-P.; Zhu, J.-J. *Small* **2011**, *7*, 2921.
41. Chen, H.; Tang, D.; Zhang, B.; Liu, B.; Cui, Y.; Chen, G. *Talanta* **2012**, *91*, 95.
42. Aslan, K.; Grell, T. A. J. *Clin. Chem.* **2011**, *57*, 746.
43. Chikkaveeraiah, B. V.; Mani, V.; Patel, V.; Gutkind, J. S.; Rusling, J. F. *Biosens. Bioelectron.* **2011**, *26*, 4477.
44. Hardy, J.; Selkoe, D. J. *Science* **2002**, *297*, 353.
45. Masters, C. L.; Simms, G.; Weinman, N. A.; Multhaup, G.; McDonald, B. L.; Beyreuther, K. *Proc. Natl. Acad. Sci. U.S.A.* **1985**, *82*, 4245.
46. Thinakaran, G.; Koo, E. H. *Alzheimer's Disease*; Springer: New York, 2007.
47. Lambert, M. P.; Barlow, A. K.; Chromy, B. A.; Edwards, C.; Freed, R.; Liosatos, M.; Morgan, T. E.; Rozovsky, I.; Trommer, B.; Viola, K. L.; Wals, P.; Zhang, C.; Finch, C. E.; Krafft, G. A.; Klein, W. L. *Proc. Natl. Acad. Sci. U.S.A.* **1998**, *95*, 6448.
48. Walsh, D. M.; Klyubin, I.; Fadeeva, J. V.; Cullen, W. K.; Anwyl, R.; Wolfe, M. S.; Rowan, M. J.; Selkoe, D. J. *Nature* **2002**, *416*, 535.
49. Georganopoulou, D. G.; Chang, L.; Nam, J. M.; Thaxton, C. S.; Mufson, E. J.; Klein, W. L.; Mirkin, C. A. *Proc. Natl. Acad. Sci. U.S.A.* **2005**, *102*, 2273.
50. Haes, A. J.; Chang, L.; Klein, W. L.; Van Duyne, R. P. *J. Am. Chem. Soc.* **2005**, *127*, 2264.
51. Mattson, M. P. *Nature* **2004**, *430*, 631.
52. Haes, A. J.; Hall, W. P.; Chang, L.; Klein, W. L.; Van Duyne, R. P. *Nano Lett.* **2004**, *4*, 1029.
53. Li, C.; Wu, C.; Zheng, J.; Lai, J.; Zhang, C.; Zhao, Y. *Langmuir* **2010**, *26*, 9130.
54. Singh, M. P.; Strouse, G. F. *J. Am. Chem. Soc.* **2010**, *132*, 9383.
55. Georganopoulou, D. G.; Chang, L.; Nam, J.-M.; Thaxton, C. S.; Mufson, E. J.; Klein, W. L.; Mirkin, C. A. *Proc. Natl. Acad. Sci. U.S.A.* **2005**, *102*, 2273.
56. Sipova, H.; Zhang, S.; Dudley, A. M.; Galas, D.; Wang, K.; Homola, J. *Anal. Chem.* **2010**, *82*, 10110.
57. Xia, N.; Liu, L.; Harrington, M. G.; Wang, J.; Zhou, F. *Anal. Chem.* **2010**, *82*, 10151.
58. Neely, A.; Perry, C.; Varisli, B.; Singh Anant, K.; Arbneshi, T.; Senapati, D.; Kalluri Jhansi, R.; Ray Paresh, C. *ACS Nano* **2009**, *3*, 2834.
59. Vestergaard, M. d.; Kerman, K.; Kim, D.-K.; Hiep, H. M.; Tamiya, E. *Talanta* **2008**, *74*, 1038.
60. Sawyers, C. L. *Nature* **2008**, *452*, 548.
61. Topilow, A. A.; Davis, J. M.; Vernick, J. J.; Tang, D.; Corbett, S.; Veltman, T.; Wagner, S. J.; Gilvarg, C. *Cancer Biomarkers* **2012**, *10*, 27.

62. Laxman, B.; Morris, D. S.; Yu, J.; Siddiqui, J.; Cao, J.; Mehra, R.; Lonigro, R. J.; Tsodikov, A.; Wei, J. T.; Tomlins, S. A.; Chinnaiyan, A. M. *Cancer Res.* **2008**, *68*, 645.
63. Nesterova, M. V.; Johnson, N.; Cheadle, C.; Bates, S. E.; Mani, S.; Stratakis, C. A.; Kahn, I.; Gupta, R. K.; Cho-Chung, Y. S. *Cancer Res.* **2006**, *66*, 8971.
64. Schweigert, F. J.; Sehouli, J. *Cancer Res.* **2005**, *65*, 1114.
65. Arya, S. K.; Bhansali, S. *Chem. Rev.* **2011**, *111*, 6783.
66. Weber, G. F. *Cancer Genomics Proteomics* **2011**, *8*, 263.
67. Hannemann, J.; Pantel, K. *Onkologe* **2012**, *18*–260.
68. Lee, G.; Cheung, A. P.; Li, B.; Ge, B.; Chow, P.-M. *Immunol. Invest.* **2012**, *41*, 429.
69. Bakry, R.; Rainer, M.; Huck, C. W.; Bonn, G. K. *Anal. Chim. Acta* **2011**, *690*, 26.
70. Matarraz, S.; Gonzalez-Gonzalez, M.; Jara, M.; Orfao, A.; Fuentes, M. *Clin. Translat. Oncol.* **2011**, *13*, 156.
71. Oon, S. F.; Pennington, S. R.; Fitzpatrick, J. M.; Watson, R. W. G. *Nat. Rev. Urol.* **2011**, *8*, 131.
72. Rudd, P. M.; Elliott, T.; Cresswell, P.; Wilson, I. A.; Dwek, R. A. *Science* **2001**, *291*, 2370.
73. Ohtsubo, K.; Marth, J. D. *Cell* **2006**, *126*, 855.
74. Marth, J. D.; Grewal, P. K. *Nat. Rev. Immunol.* **2008**, *8*, 874.
75. Kinjo, Y.; Wu, D.; Kim, G. S.; Xing, G. W.; Poles, M. A.; Ho, D. D.; Tsuji, M.; Kawahara, K.; Wong, C. H.; Kronenberg, M. *Nature* **2005**, *434*, 520.
76. Bertozzi, C. R.; Kiessling, L. L. *Science* **2001**, *291*, 2357.
77. Dube, D. H.; Bertozzi, C. R. *Nat. Rev. Drug Discovery* **2005**, *4*, 477.
78. Qiu, Y.; Patwa, T. H.; Xu, L.; Shedden, K.; Misek, D. E.; Tuck, M.; Jin, G.; Ruffin, M. T.; Turgeon, D. K.; Synal, S.; Bresalier, R.; Marcon, N.; Brenner, D. E.; Lubman, D. M. *J. Proteome Res.* **2008**, *7*, 1693.
79. Lin, S. Q.; Kemmner, W.; Grigull, S.; Schlag, P. M. *Exp. Cell Res.* **2002**, *276*, 101.
80. Hakomori, S. *Cancer Res.* **1996**, *56*, 5309.
81. Zhang, X.; Teng, Y.; Fu, Y.; Xu, L.; Zhang, S.; He, B.; Wang, C.; Zhang, W. *Anal. Chem.* **2010**, *82*, 9455.
82. Han, E.; Ding, L.; Qian, R.; Bao, L.; Ju, H. *Anal. Chem.* **2012**, *84*, 1452.
83. Ding, L.; Ji, Q.; Qian, R.; Cheng, W.; Ju, H. *Anal. Chem.* **2010**, *82*, 1292.
84. Nibali, L.; Fedele, S.; D'Aiuto, F.; Donos, N. *Oral Dis.* **2012**, *18*, 236.
85. Jawa, R. S.; Anillo, S.; Huntoon, K.; Baumann, H.; Kulaylat, M. *J. Intensive Care Med.* **2011**, *26*, 3.
86. Suthaus, J.; Adam, N.; Groetzinger, J.; Scheller, J.; Rose-John, S. *Eur. J. Cell Biol.* **2011**, *90*, 495.
87. Edwards, C. J.; Williams, E. *Osteoporosis Int.* **2010**, *21*, 1287.
88. Le Goff, B.; Blanchard, F.; Berthelot, J.-M.; Heymann, D.; Maugars, Y. *Joint Bone Spine* **2010**, *77*, 201.
89. Duffy, S. A.; Taylor, J. M. G.; Terrell, J. E.; Islam, M.; Li, Y.; Fowler, K. E.; Wolf, G. T.; Teknos, T. N. *Cancer* **2008**, *113*, 750.

90. Poth, K. J.; Guminski, A. D.; Thomas, G. P.; Leo, P. J.; Jabbar, I. A.; Saunders, N. A. *Mol. Cancer Ther.* **2010**, *9*, 2430.
91. Van Tubergen, E.; Broek, R. V.; Lee, J.; Wolf, G.; Carey, T.; Bradford, C.; Prince, M.; Kirkwood, K. L.; D'Silva, N. J. *Cancer* **2011**, *117*, 2677.
92. Wang, G.; Huang, H.; Zhang, G.; Zhang, X.; Fang, B.; Wang, L. *Langmuir* **2011**, *27*, 1224.
93. Liang, K.; Mu, W.; Huang, M.; Yu, Z.; Lai, Q. *Electroanalysis* **2006**, *18*, 1505.
94. Munge, B. S.; Krause, C. E.; Malhotra, R.; Patel, V.; Gutkind, J. S.; Rusling, J. F. *Electrochem. Commun.* **2009**, *11*, 1009.
95. Jensen, G. C.; Krause, C. E.; Sotzing, G. A.; Rusling, J. F. *Phys. Chem. Chem. Phys.* **2011**, *13*, 4888.
96. Deng, C.; Qu, F.; Sun, H.; Yang, M. *Sens. Actuators, B* **2011**, *160*, 471.
97. Chazalviel, J.-N.; Allongue, P. *J. Am. Chem. Soc.* **2011**, *133*–762.
98. Postal, M.; Appenzeller, S. *Cytokine* **2011**, *56*, 537.
99. Jones, E. Y.; Stuart, D. I.; Walker, N. P. C. *Nature* **1989**, *338*, 225.
100. Old, L. J. *Nature* **1987**, *326*, 330.
101. Stuebgen, J.-P. *J. Neurol.* **2011**, *258*, 961.
102. Vinay, D. S.; Kwon, B. S. *Clin. Exp. Immunol.* **2011**, *164*, 145.
103. Urszula, T.-M.; Jerzy, L.; Bozena, K.; Ewa, F.; Agata, K.; Anna, N.; Tomasz, M. *Ginekol. Pol.* **2010**, *81*, 192.
104. Yin, Z.; Liu, Y.; Jiang, L.-P.; Zhu, J.-J. *Biosens. Bioelectron.* **2011**, *26*, 1890.
105. Kyuseo, L.; Seungah, L.; Hyunung, Y.; Seong Ho, K. *J. Nanosci. Nanotechnol.* **2010**, *10*, 3228.
106. Yeboa, D. N.; Guzzo, T.; Mitra, N.; Christodouleas, J. P.; Haas, N. B.; Vapiwala, N.; Armstrong, K.; Bekelman, J. E. *Urology* **2011**, *78*, 1107.
107. Orsted, D. D.; Nordestgaard, B. G.; Jensen, G. B.; Schnohr, P.; Bojesen, S. E. *Eur. Urol.* **2012**, *61*, 865.
108. Loeb, S. *Eur. Urol.* **2012**, *61*, 875.
109. Tang, P.; Sun, L.; Uhlman, M. A.; Robertson, C. N.; Polascik, T. J.; Albala, D. M.; Donatucci, C. F.; Moul, J. W. *Urology* **2010**, *76*, 1058.
110. Wallner, L. P.; Morgenstern, H.; McGree, M. E.; Jacobson, D. J.; St Sauver, J. L.; Jacobsen, S. J.; Sarma, A. V. *Urology* **2011**, *77*, 137.
111. Mani, V.; Chikkaveeraiah, B. V.; Patel, V.; Gutkind, J. S.; Rusling, J. F. *ACS Nano* **2009**, *3*, 585.
112. Xu, S.; Liu, Y.; Wang, T.; Li, J. *Anal. Chem.* **2011**, *83*, 3817.
113. Crespo, G. A.; Mistlberger, G.; Bakker, E. *J. Am. Chem. Soc.* **2012**, *134*, 205.
114. Ma, F.; Zhang, Y.; Qi, H.; Gao, Q.; Zhang, C.; Miao, W. *Biosens. Bioelectron.* **2012**, *32*, 37.
115. Fahnrich, K. A.; Pravda, M.; Guilbault, G. G. *Talanta* **2001**, *54*, 531.
116. Knight, A. W. *TrAC, Trends Anal. Chem.* **1999**, *18*, 47.
117. Miao, W. *Chem. Rev.* **2008**, *108*, 2506.
118. Cao, X.; Ye, Y.; Liu, S. *Anal. Biochem.* **2011**, *417*, 1.
119. Syed, M. A.; Bokhari, S. H. A. *J. Biomed. Nanotechnol.* **2011**, *7*, 229.
120. White, K. A.; Rosi, N. L. *Nanomedicine* **2008**, *3*, 543.
121. Zhao, W.; Brook, M. A.; Li, Y. *ChemBioChem* **2008**, *9*, 2363.

122. Liu, X.; Dai, Q.; Austin, L.; Coutts, J.; Knowles, G.; Zou, J.; Chen, H.; Huo, Q. *J. Am. Chem. Soc.* **2008**, *130*, 2780.
123. Xie, H.; Gill-Sharp, K. L.; O'Neal, P. *Nanomed. Nanotechnol.* **2007**, *3*, 89.
124. Schurr, J. M. *CRC Crit. Rev. Biochem.* **1977**, *4*, 371.
125. Kim, D.; Daniel, W. L.; Mirkin, C. A. *Anal. Chem.* **2009**, *81*, 9183.
126. Alvarez-Puebla, R. A.; Liz-Marzan, L. M. *Chem. Soc. Rev.* **2012**, *41*, 43.
127. Bantz, K. C.; Meyer, A. F.; Wittenberg, N. J.; Im, H.; Kurtulus, O.; Lee, S. H.; Lindquist, N. C.; Oh, S.-H.; Haynes, C. L. *Phys. Chem. Chem. Phys.* **2011**, *13*, 11551.
128. McNay, G.; Eustace, D.; Smith, W. E.; Faulds, K.; Graham, D. *Appl. Spectrosc.* **2011**, *65*, 825.
129. Ko, H.; Singamaneni, S.; Tsukruk, V. V. *Small* **2008**, *4*, 1576.
130. Tripp, R. A.; Dluhy, R. A.; Zhao, Y. *Nano Today* **2008**, *3*, 31.
131. Zhou, X.; Xu, W.; Wang, Y.; Kuang, Q.; Shi, Y.; Zhong, L.; Zhang, Q. *J. Phy. Chem. C* **2010**, *114*, 19607.
132. Lee, S.-W.; Lee, K.-S.; Ahn, J.; Lee, J.-J.; Kim, M.-G.; Shin, Y.-B. *ACS Nano* **2011**, *5*, 897.
133. Bei, R.; Mizejewski, G. J. *Curr. Mol. Med.* **2011**, *11*, 564.
134. Bader, D.; Riskin, A.; Vafsi, O.; Tamir, A.; Peskin, B.; Israel, N.; Merksamer, R.; Dar, H.; David, M. *Clin. Chim. Acta* **2004**, *349*, 15.
135. Mizejewski, G. J. *Exp. Biol. Med.* **2004**, *229*, 439.
136. Debruyne, E. N.; Delanghe, J. R. *Clin. Chim. Acta* **2008**, *395*, 19.
137. Evdokimova, V. N.; Butterfield, L. H. *Expert Opin. Biol. Ther.* **2008**, *8*, 325.
138. Shi, W. T.; Ma, Z. F. *Biosens. Bioelectron.* **2011**, *26*, 3068.
139. Li, Y.; Liang, W.-B.; Fang, L.-C.; Huang, H.; Deng, J.; Zheng, J.-S. *J. Chem. Sci.* **2009**, *121*, 1069.
140. Ding, C.; Zhao, F.; Ren, R.; Lin, J.-M. *Talanta* **2009**, *78*, 1148.
141. Lin, J.; He, C.; Zhang, L.; Zhang, S. *Anal. Biochem.* **2009**, *384*, 130.
142. Wu, B.-Y.; Wang, H.-F.; Chen, J.-T.; Yan, X.-P. *J. Am. Chem. Soc.* **2011**, *133*, 686.
143. Zhou, W.-H.; Zhu, C.-L.; Lu, C.-H.; Guo, X.; Chen, F.; Yang, H.-H.; Wang, X. *Chem. Commun.* **2009**, 6845.
144. Tang, J.; Tang, D.; Niessner, R.; Chen, G.; Knopp, D. *Anal. Chem.* **2011**, *83*, 5407.
145. Tang, J.; Tang, D.; Su, B.; Huang, J.; Qiu, B.; Chen, G. *Biosens. Bioelectron.* **2011**, *26*, 3219.
146. Goldstein, M. J.; Mitchell, E. P. *Cancer Invest.* **2005**, *23*, 338.
147. Duffy, M. J. *Clin. Chem.* **2001**, *47*, 624.
148. Mitchell, E. P. *Semin. Oncol.* **1998**, *25*, 12.
149. Mulcahy, M. F.; Benson, A. B., III *Curr. Oncol. Rep.* **1999**, *1*, 168.
150. Hodge, J. W. *Cancer Immunol. Immunother.* **1996**, *43*, 127.
151. Horie, Y.; Miura, K.; Matsui, K.; Yukimasa, A.; Ohi, S.; Hamamoto, T.; Kawasaki, H. *Cancer* **1996**, *77*, 1991.
152. Wu, J.; Yan, Y.; Yan, F.; Ju, H. *Anal. Chem.* **2008**, *80*, 6072.
153. Lin, D.; Wu, J.; Wang, M.; Yan, F.; Ju, H. *Anal. Chem.* **2012**, *84*, 3662.
154. Liu, R.; Liu, X.; Tang, Y.; Wu, L.; Hou, X.; Lv, Y. *Anal. Chem.* **2011**, *83*, 2330.

155. Knappskog, S.; Lonning, P. E. *Expert Opin. Ther. Targets* **2012**, *16*, S23.
156. Shen, L.; Sun, X.; Fu, Z.; Yang, G.; Li, J.; Yao, L. *Clin. Cancer. Res.* **2012**, *18*, 1561.
157. Wasserman, J. D.; Zambetti, G. P.; Malkin, D. *Mol. Cell. Endocrinol.* **2012**, *351*, 101.
158. Saldana-Meyer, R.; Recillas-Targa, F. *Epigenetics* **2011**, *6*, 1068.
159. Floquet, C.; Deforges, J.; Rousset, J.-P.; Bidou, L. *Nucleic Acids Res.* **2011**, *39*, 3350.
160. Li, J.; Zhang, Y.; Zhao, J.; Kong, F.; Chen, Y. *Mol. Cell. Biochem.* **2011**, *357*, 31.
161. Wang, J.; Zhu, X.; Tu, Q.; Guo, Q.; Zarui, C. S.; Momand, J.; Sun, X. Z.; Zhou, F. *Anal. Chem.* **2008**, *80*, 769.
162. Wang, Y.; Zhu, X.; Wu, M.; Xia, N.; Wang, J.; Zhou, F. *Anal. Chem.* **2009**, *81*, 8441.
163. Du, D.; Wang, J.; Lu, D.; Dohnalkova, A.; Lin, Y. *Anal. Chem.* **2011**, *83*, 6580.
164. Domenici, F.; Bizzarri, A. R.; Cannistraro, S. *Anal. Biochem.* **2012**, *421*, 9.
165. Kaigler, D.; Avila, G.; Wisner-Lynch, L.; Nevins, M. L.; Nevins, M.; Rasperini, G.; Lynch, S. E.; Giannobile, W. V. *Expert. Opin. Biol. Ther.* **2011**, *11*, 375.
166. Nakagawa, T.; Inoue, H.; Sasahara, M. *Curr. Opin. Nephrol. Hypertens.* **2012**, *21*, 80.
167. Alvarez, R. H.; Kantarjian, H. M.; Cortes, J. E. *Mayo Clin. Proc.* **2006**, *81*, 1241.
168. Heldin, C. H. *Cytokine Growth Factor Rev.* **2004**, *15*, 195.
169. Ruslinda, A. R.; Penmatsa, V.; Ishii, Y.; Tajima, S.; Kawarada, H. *Analyst* **2012**, *137*, 1692.
170. Vicens, M. C.; Sen, A.; Vanderlaan, A.; Drake, T. J.; Tan, W. H. *ChemBioChem* **2005**, *6*, 900.
171. Huang, C.-C.; Chiang, C.-K.; Lin, Z.-H.; Lee, K.-H.; Chang, H.-T. *Anal. Chem.* **2008**, *80*, 1497.
172. Huang, C.-C.; Chiu, S.-H.; Huang, Y.-F.; Chang, H.-T. *Anal. Chem.* **2007**, *79*, 4798.
173. Lin, T.-E.; Chen, W.-H.; Shiang, Y.-C.; Huang, C.-C.; Chang, H.-T. *Biosens. Bioelectron.* **2011**, *29*, 204.
174. Feng, K.; Qiu, L.-P.; Yang, Y.; Wu, Z.-S.; Shen, G.-L.; Yu, R.-Q. *Biosens. Bioelectron.* **2011**, *29*, 66.
175. Andrianifahanana, M.; Moniaux, N.; Schmied, B. M.; Ringel, J.; Friess, H.; Hollingsworth, M. A.; Buchler, M. W.; Aubert, J. P.; Batra, S. K. *Clin. Cancer. Res.* **2001**, *7*, 4033.
176. Wang, G.; Lipert, R. J.; Jain, M.; Kaur, S.; Chakraboty, S.; Torres, M. P.; Batra, S. K.; Brand, R. E.; Porter, M. D. *Anal. Chem.* **2011**, *83*, 2554.
177. Ambrosi, A.; Airo, F.; Merkoci, A. *Anal. Chem.* **2010**, *82*, 1151.
178. Yamaguchi, K.; Abe, K.; Kameya, T.; Adachi, I.; Taguchi, S.; Otsubo, K.; Yanaihara, N. *Cancer Res.* **1983**, *43*, 3932.
179. Zhuo, Y.; Chai, Y.-Q.; Yuan, R.; Mao, L.; Yuan, Y.-L.; Han, J. *Biosens. Bioelectron.* **2011**, *26*, 3838.

In Functional Nanoparticles for Bioanalysis, Nanomedicine, and Bioelectronic Devices Volume 1; Hepel, M., et al.;
ACS Symposium Series; American Chemical Society: Washington, DC, 2012.

180. Augustin, H. G.; Koh, G. Y.; Thurston, G.; Alitalo, K. *Nat. Rev. Mol. Cell Biol.* **2009**, *10*, 165.
181. Gang-Il, K.; Kyung-Woo, K.; Min-Kyu, O.; Yun-Mo, S. *Biosens. Bioelectron.* **2010**, *25*, 1717.
182. Lim, H. K.; Asharani, P. V.; Hande, M. P. *Front. Genet.* **2012**, *3*, 104.
183. Robinson, J. B.; Demmitt, B.; Collins, T.; Gorey, T.; Posgai, R.; Varma, R.; Hussain, S.; Rowe, J. *Abstracts of the Am. Chem. Soc.* **2011**, *241*.
184. Singh, R. P.; Ramarao, P. *Toxicol. Lett.* **2012**, *213*, 249.

Chapter 8

Assembly of Gold Nanoparticles Induced by Metal Ions

Maria Hepel,* Dustin Blake, Matthew McCabe, Magdalena Stobiecka,[1] and Kaitlin Coopersmith

Department of Chemistry, State University of New York at Potsdam, Potsdam, New York 13676, U.S.A.
[1]Permanent address: Department of Biophysics, Warsaw University of Life Sciences SGGW, Bldg. 34, 159 Nowoursynowska St., 02776 Warsaw, Poland
***E-mail: hepelmr@potsdam.edu**

The assembly of networks of mercaptopropionic acid-capped gold nanoparticles (AuNP/MPA) mediated by Cd^{2+} and Pb^{2+} ions has been investigated using surface plasmon (SP) absorbance, resonance elastic light scattering (RELS), laser-pulsed dynamic light scattering (DLS), and transmission electron microscopy (TEM). Two different kinds of assemblies have been observed depending on the preparation pathway: low-affinity assembly (LAA) and high-affinity assembly (HAA). In the nanoparticle networks formed in LAA pathway, single Au nanoparticles are linked by metal ions forming coordination bonds to partially deprotonated interface COOH groups of the nanoparticle shells. In the HAA pathway, the inter-core distance between single AuNP's is reduced due to the direct interparticle hydrogen bonding with side-line Cd^{2+} or Pb^{2+} crosslinking leading to the formation of more stable, larger, and denser AuNP networks, consistent with large bathochromic shift of SP band and higher RELS intensity. From the size analysis performed by DLS, the diameter of aggregates formed in LAA is $2r = 37.9 \pm 0.6$ nm and in HAA it is $2r = 82.5 \pm 0.9$ nm, with relatively low polydispersity $p = 0.239 \pm 0.016$ and 0.273 ± 0.006, respectively. The inter-core

In Functional Nanoparticles for Bioanalysis, Nanomedicine, and Bioelectronic Devices Volume 1; Hepel, M., et al.;
ACS Symposium Series; American Chemical Society: Washington, DC, 2012.

distances determined from molecular dynamics calculations for H-bonding and Cd^{2+}-linking are as follows: $d = 1.15$ and $d = 1.44$ nm, respectively, confirming the formation of denser AuNP networks in HAA pathway.

Keywords: Cd^{2+}-mediated AuNP assembly; Pb^{2+}-mediated AuNP assembly; RELS spectroscopy; surface plasmon resonance; resonance Rayleigh scattering; elastic light scattering

Introduction

The interactions of functional gold nanoparticles (AuNPs) with heavy metal ions have been extensively studied to gain understanding of the nanoparticle crosslinking and assembly processes and their effect on the local surface plasmon oscillations (*1–4*). Mirkin and coworkers (*3*) have demonstrated that functionalized AuNPs can provide a convenient and very sensitive means for trace analysis of Hg^{2+} ions by utilizing Hg^{2+}-induced assembly of DNA-modified AuNPs.

In this work, we have applied UV-Vis spectroscopy, resonance elastic light scattering (RELS) spectroscopy, and dynamic light scattering (DLS) to investigate pathways of AuNP assembly induced by heavy metal ions, Cd^{2+} and Pb^{2+}. We have found that AuNP assembly can follow a low-affinity or high-affinity pathway in forming aggregates which differ in density, size, and optical properties, despite the identical initial and final environmental conditions.

In general, the as-formed citrate-capped AuNPs exhibit a strong affinity to many multiply-charged metal cations (*2*, *5*), such as Cd^{2+}, Pb^{2+}, Ni^{2+}, Hg^{2+}, Cu^{2+}, Fe^{3+}, and others. An assay for a selective detection of Pb^{2+} has been developed by Thomas and coworkers (*1*) using gallic acid-capped AuNP and AgNP. Liu and Lu (*6–9*) reported successful development of a biosensor for Pb^{2+} based on DNA-zyme directed AuNP assembly. Guan et al. (*4*), exploiting amphoteric properties of Pb(II) in aqueous solutions, have proposed a simple and selective test for lead ions based on common citrate-capped AuNPs. Functionalization of AuNP with peptides (*10*) has provided further opportunities to study interactions of heavy metal ions with peptides with a convenient monitoring of the interactions with color change due to AuNP aggregate formation. The sensitivity of this method is higher in comparison with carboxylate-capped AuNP assembly based methods and enabled monitoring assembly processes in the nanomolar metal-ion concentration range. The following metal ions and complexes have been studied: Co^{2+}, Hg^{2+}, Pb^{2+}, $PdCl_6^{2-}$, and $PtCl_4^{2-}$. The particular peptide used in the study consisted of the sequence: Asp-Tyr-Lys-Asp-Asp-Asp-Asp-Lys-Pro-Ala-Tyr-Ser-Ser-Gly-Pro-Ala-Pro-Pro-Met-Pro-Pro-Phe. The net negative charge on this peptide in neutral solutions has provided the basis for efficient gold colloid stabilization ($pI = 3.9$). Several other colorimetric assays with excellent detection capabilities based on metal ion-induced AuNP assembly have been reported (*11–13*).

The color change observed during metal ion-induced AuNP assembly is due to the coupling of surface plasmon (SP) oscillations of individual nanoparticles upon decreasing interparticle distance occurring during the assembly process (*14–19*). As a result of this coupling, a red shift of the SP absorbance band is observed (*20–22*).

Hence, the UV-visible spectroscopy can be utilized in AuNP-assembly investigations. On the other hand, the RELS technique which is more sensitive than a UV-Vis spectroscopy because of low background light intensity, can provide more detailed information about the nanoparticle assembly process (*23–26*). RELS is inherently sensitive to the AuNP interparticle distance and the dielectric function of the medium surrounding the metal nanoparticles. The elastic light scattering is a fast process in which light is momentarily absorbed by a nanoparticle followed by immediate coherent re-emission of the absorbed energy in all directions. The RELS occurs when polarizable particles are subjected to the oscillating electric field of a beam of light which induces oscillating dipoles in the particles and these dipoles radiate light to the surroundings (*27*). RELS spectroscopy is becoming a very useful technique in bioanalysis for determinations of proteins, DNA, and various complexes (*24*, *28*). The light-scattering properties of gold and silver nanoparticles have been applied in biomedical imaging, in optical tomography (*29*, *30*), dark-field microscopy (*31*, *32*), and multi-photon phenomena-based techniques (*33*, *34*). The light scattering by targeted AuNP administered to a patient body has been employed in the thermal destruction of cancer cells (*35–37*) and as an enhancement in photoacoustic imaging (*38*, *39*).

Although the theoretical description of optical properties of AuNP based on the Mie theory (*17*) has been utilized to elucidate experimentally recorded spectra, further studies are needed to account for a wide variation of structural features which influence the SP coupling. Extensive studies have been performed to predict scattering from AuNP with different simple shapes and sizes using analytical solutions or discrete dipole approximation simulations (*40–50*). These phenomena are important for biomedical applications of metal nanoparticles.

In this work, the assembly and disassembly of networks of mercaptopropionic acid-capped spherical gold nanoparticles (AuNP/MPA) mediated by divalent metal ions (Cd^{2+}, Pb^{2+}) have been investigated. The UV-Vis spectroscopy, RELS, and DLS have been employed as highly sensitive methods for monitoring the nanoparticle assembly process and for detecting heavy metal ions.

Results and Discussion

Local Surface Plasmon Frequency Shifts for MPA-Capped AuNP in the Presence of Cd^{2+} and Pb^{2+} Ions

Typical local surface plasmon (SP) absorbance spectrum for as-synthesized citrate-capped AuNP is presented in Figure 1, curve 1. The SP band maximum at λ_{max} = 516 nm corresponds to the nanoparticle diameter of 5 nm which is also confirmed by TEM imaging (Fig. 1b). The injection of MPA into the solution of $AuNP_{5nm}$ results in gradual replacement of citrate ligand shell on AuNP with more strongly bound MPA due to the formation of thiolate bonds Au-S. This exchange reaction leads to a small bathochromic shift (Figure 1a, curve 2) and increase in polydispersity of the aggregates manifested by the increased SP absorbance peak width. In this reaction, the solution pH changed from the initial pH = 5.23 to the final pH = 3.1-3.5. At this pH value, some of the carboxylic functional groups of MPA shell are deprotonated but a majority of COOH moieties remain undissociated, since the $pK_a = 4.27$. Therefore, the protonated COOH groups can participate in interparticle hydrogen bonding. The assembly of AuNP on addition of MPA is attributed to this process. However, the growth of AuNP/MPA aggregates is strongly hindered by the presence of negative carboxylate charges at the shell-solution interface leading to the electrostatic interparticle repulsion forces. This is consistent with the observation of a relatively small bathochromic shift of the SP absorbance band ($\Delta\lambda = 7$ nm). The addition of Cd^{2+} ions to the MPA-capped AuNP solution results in the formation of larger assemblies, most likely due to the interparticle linkage attributed to doubly-charged Cd^{2+} ions. For different experimental pathways, different UV-Vis spectra have been obtained, although the same final Cd^{2+} concentration and the same final pH had been attained. Here, we present two pathways further called: low-affinity assembly (LAA) and high-affinity assembly (HAA).

The order of addition of reagents in LAA and HAA was as follows:

(1) for the LAA pathway:

  (a) MPA was added to the solution of as-synthesized citrate-capped AuNP,
  (b) with the addition of NaOH, the solution pH was adjusted to pH = 5.11,
  (c) Cd^{2+} ions were introduced.

(2) for the HAA pathway:

  (a) MPA was added to the solution of as-synthesized citrate-capped AuNP,
  (b) Cd^{2+} ions were introduced,
  (c) with the addition of NaOH, the solution pH was adjusted to pH = 5.69.

The obtained UV-Vis spectra are presented in Figure 1: curve 3 – for the LAA pathway, curve 4 – for the HAA pathway. Especially striking is the difference in the SP band shift. Whereas only a small bathochromic shift is encountered for the LAA pathway ($\Delta\lambda = 5$ nm), a large SP band shift is clearly seen for the HAA pathway ($\Delta\lambda = 62$ nm).

Similar effects were obtained after addition of Pb^{2+} ions to the MPA-capped AuNP solution. Only a small bathochromic shift is encountered for the LAA pathway (λ_{max} = 534 nm), while a large SP band shift is clearly seen for the HAA pathway (λ_{max} = 578 nm) (Figure 2).

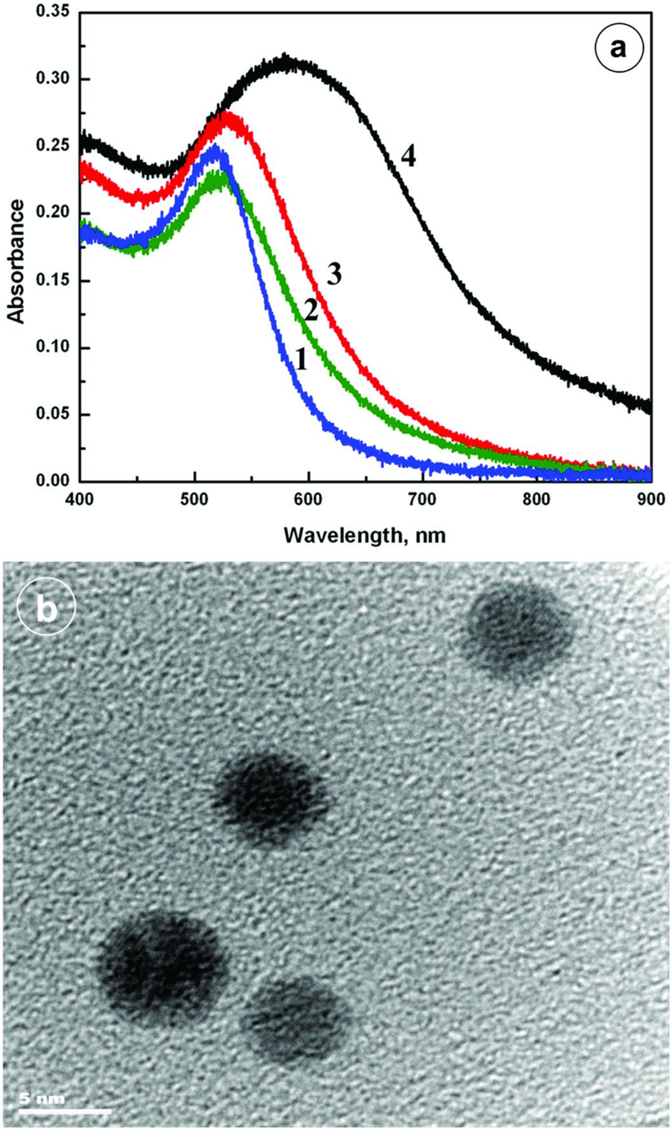

Figure 1. (a) SP absorbance spectra of: (1) original AuNP/Cit nanoparticles, (2) MPA-capped AuNP, pH = 5.1, (3) MPA-capped AuNP + NaOH + 222 μM Cd^{2+}, (4) MPA-capped AuNP + 222 μM Cd^{2+} + NaOH, pH 5.69; AuNP concentration: 2.53 nM, MPA added: 3.33 mM; (b) TEM images of AuNP.

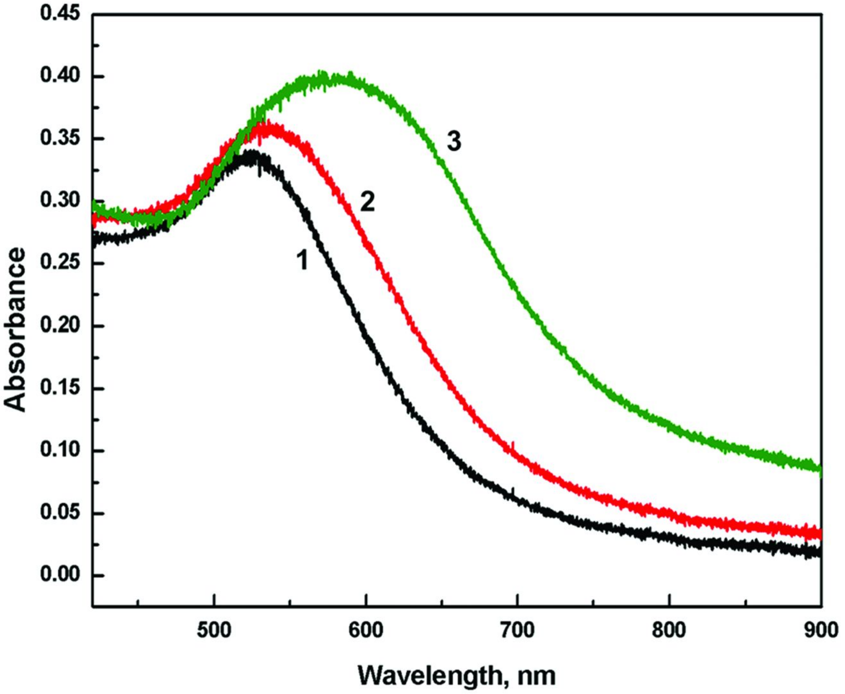

Figure 2. UV-Vis absorbance spectra of MPA-capped AuNP$_{5nm}$ solution: (1) without Pb(II) addition, (2) after pH adjustment to 5.7 followed by the addition of 125 µM Pb^{2+}, (3) after addition of 125 µM Pb^{2+} followed by pH adjustment to 5.7. AuNP$_{5nm}$ concentration: 1.875 nM; MPA added: 3.75 mM.

Low-Affinity Assembly of Cd^{2+}/ Pb^{2+}-Linked MPA-Capped AuNPs

The low-affinity assembly of MPA-capped AuNP has been investigated for Cd^{2+} concentration range from 0 to 500 µM. The obtained UV-Vis spectra of the SP band are presented in Figure 3. The absorbance maximum A_{max} increases from A_{max} = 0.226 in the absence of Cd^{2+} to A_{max} = 0.343 at C_{Cd} = 678 µM. The dependence of A_{max} on C_{Cd} is presented in Figure 3b. It is not linear and the experimental data can be fitted with Boltzmann function: $A_{max} = A_2 + (A_1 – A_2)/[1 + \exp((C_{Cd2+} - C_0)/s)]$, with the following parameters: A_1 = 2.013, A_2 = 0.341, C_0 = -0.379, s = 0.125.

The linear range of the dependence of A_{max} vs. C_{Cd2+} extends from C_{Cd} = 0 to C_{Cd} = 125 µM. The tendency to saturate at higher Cd^{2+} concentrations is most likely associated with attaining electrostatic balance between negatively charged AuNP$_{5nm}$@MPA nanoparticles and Cd^{2+} counterions which interact strongly with MPA ligands of the nanoparticle shell. The wavelength of the absorbance maximum increases slightly with increasing Cd^{2+} concentration from λ_{max} = 525 nm for the absence of Cd^{2+} to λ_{max} = 542 nm for C_{Cd} = 500 µM. The small bathochromic SP band shift is due to the interparticle interaction of AuNP. The dependence of λ_{max} vs. C_{Cd} is presented in Figure 3c.

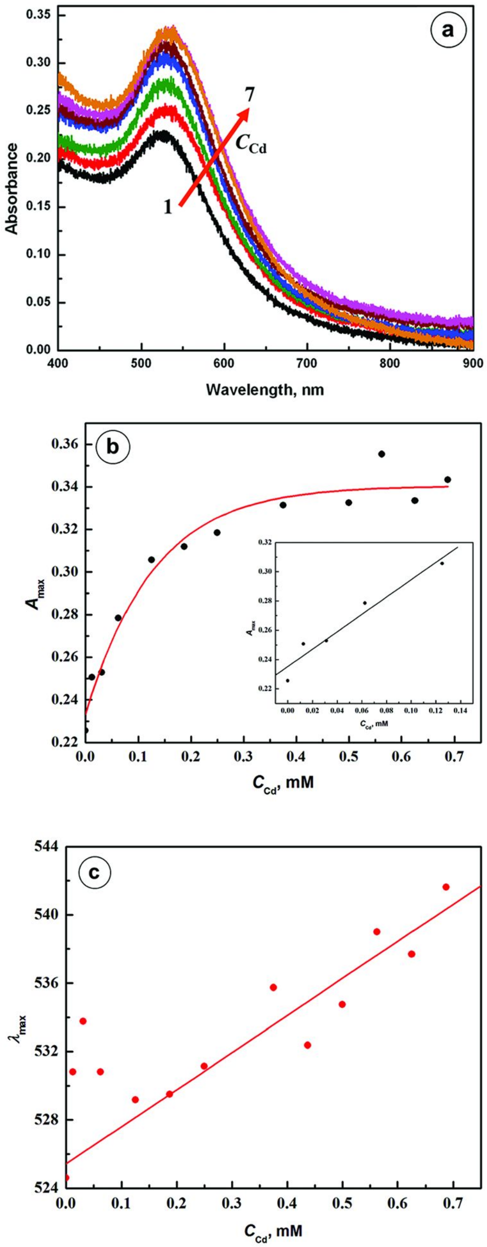

Figure 3. (a) UV-Vis absorbance spectra of MPA-capped AuNP$_{5nm}$ after the LAA assembly with Cd^{2+} [mM] : (1) 0, (2) 0.0125, (3) 0.0625, (4) 0.125, (5) 0.25, (6) 0.375, (7) 0.5. (b) Dependence of A_{max} vs. $C_{Cd.}$ (c) Dependence of λ_{max} vs. C_{Cd}. AuNP concentration: 2.85 nM; MPA added: 3.75 mM; pH 5.35-5.83.

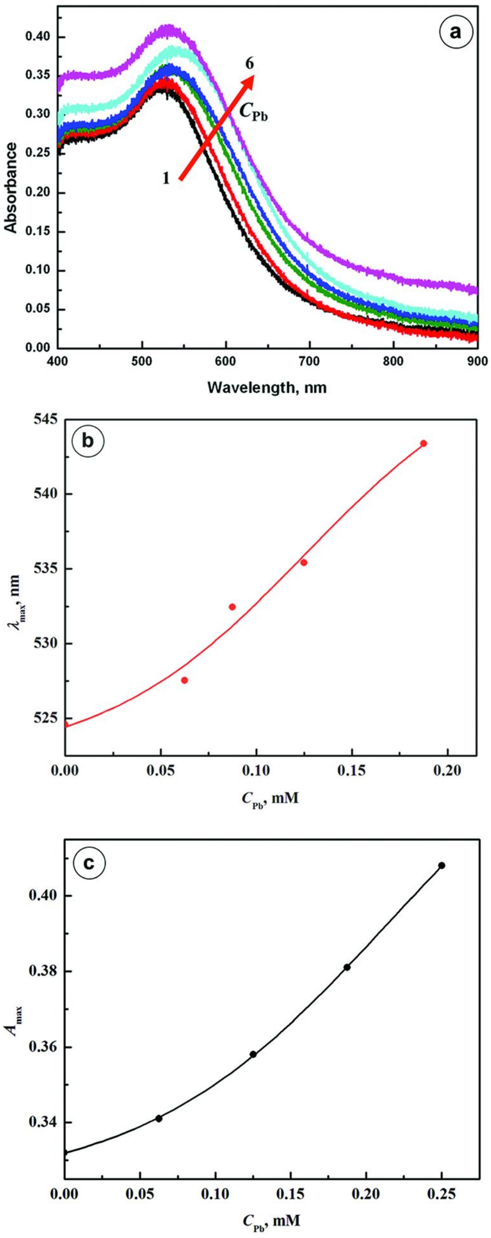

Figure 4. (a) UV-Vis absorbance spectra of MPA-capped AuNP$_{5nm}$ after LAA with Pb^{2+} [μM]: (1) 0, (2) 62.5, (3) 87.5, (4) 125. (5) 187.5, (6) 250. (b) Dependence of λ_{max} vs. C_{Pb}. (c) Dependence of A_{max} vs. $C_{Pb.}$ AuNP concentration: 1.875 nM; MPA added: 3.75 mM; pH 5.53-5.9.

In Figure 4, the UV-Vis absorbance spectra for the Pb^{2+}-linked MPA-capped $AuNP_{5nm}$ are presented. The absorbance maximum increases from $A_{max} = 0.332$ in the absence of Pb^{2+} to $A_{max} = 0.408$ at $C_{Pb2+} = 250$ μM. The dependence of A_{max} on C_{Pb2+} is presented in Figure 4c. It is not linear and the experimental data can be fitted with a sigmoidal Boltzmann function: $\lambda_{max} = A_2 + (A_1 - A_2)/[1 + \exp((C_{Pb2+} - C_0)/s)]$, with parameters: $A_1 = 0.32205$, $A_2 = 0.46637$, $C_0 = 0.21790$, $s = 0.083193$, $R^2 = 0.99992$. The wavelength of the absorbance maximum increases slightly with increasing Pb^{2+} concentration from $\lambda_{max} = 525$ nm for the absence of Pb^{2+} to $\lambda_{max} = 543$ nm for $C_{Pb2+} = 187$ μM. The small bathochromic SP band shift is due to the interparticle interaction of AuNP's leading to the coupling of local SP oscillations in individual AuNP's present in the assemblies. The dependence of λ_{max} vs. C_{Pb2+} is presented in Figure 4b. It can be fitted with a sigmoidal Boltzmann function with parameters: $A_1 = 521.96$, $A_2 = 550.13$, $C_0 = 0.12613$, $s = 0.0537$.

High-Affinity Assembly of Cd^{2+} and Pb^{2+}-Linked MPA-Capped AuNP

The strong bathochromic shifts were recorded in the high-affinity assembly of MPA-capped $AuNP_{5nm}$ upon addition of varying concentrations of Cd^{2+} ions (0- 687 μM), as shown in Figure 5a. The SP band maximum shifts toward longer wavelengths from $\lambda_{max} = 525$ nm to $\lambda_{max} = 591$ nm and the color changes from ruby red to violet. It indicates the assembly of gold nanoparticle networks mediated by Cd^{2+} ions and hydrogen bonds between undissociated carboxylic groups of mercaptopropionic acid capped gold nanoparticles. The experimental dependence $\lambda_{max} = f(C_{Cd\,2+})$ can be fitted with a sigmoidal Boltzmann function: $\lambda_{max} = A_2 + (A_1 - A_2)/[1 + \exp((C_{Cd\,2+} - C_0)/s)]$, with parameters: $A1 = -2991$, $A_2 = 641.5$, $C_0 = -2.87$, $s = 0.832$ (Figure 5b). The enhanced absorbance of the surface plasmon band was also observed. The maximum absorbance increased with increasing Cd^{2+} concentration as shown in Figure 5c from $A_{max} = 0.262$ in the absence of Cd^{2+} to $A_{max} = 0.437$ at $C_{Cd} = 678$ μM.

Strong bathochromic shifts were also observed upon addition of varying concentrations of Pb^{2+} ions (Figure 6). As the SP band maximum shifts toward longer wavelengths, from $\lambda_{max} = 534$ nm to $\lambda_{max} = 578$ nm, the color changes from ruby red to violet. The enhanced absorbance of the surface plasmon band was also observed. The maximum absorbance increased with increasing Pb^{2+} concentration from $A_{max} = 0.276$ in the absence of Pb^{2+} to $A_{max} = 0.399$ at $C_{Pb2+} = 125$ μM. It indicates the assembly of gold nanoparticle networks mediated by Pb^{2+} ions and hydrogen bonds between undissociated carboxylic groups of mercaptopropionic acid capped gold nanoparticles.

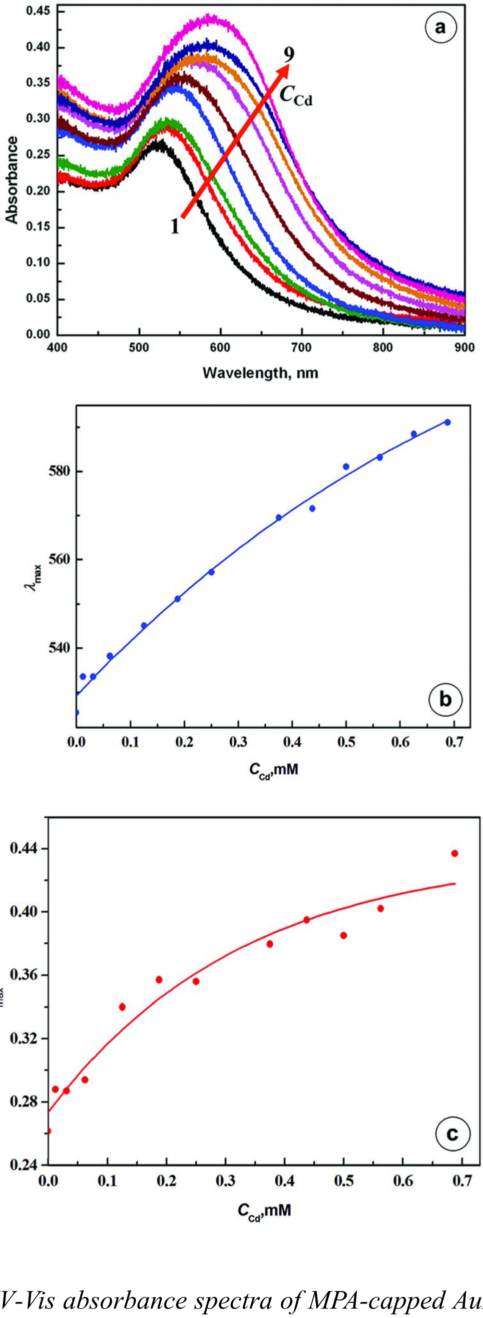

Figure 5. (a) UV-Vis absorbance spectra of MPA-capped AuNP$_{5nm}$ after the HAA assembly with Cd^{2+} [mM]: (1) 0, (2) 0.0125, (3) 0.0625, (4) 0.125, (5) 0.25, (6) 0.375, (7) 0.5, (8) 0.5625, (9) 0.6875. (b) Dependence of λ_{max} vs. C_{Cd}. (c) Dependence of A_{max} vs. C_{Cd}. AuNP concentration: 2.85 nM; MPA added: 3.75 mM; pH 5.41-5.78.

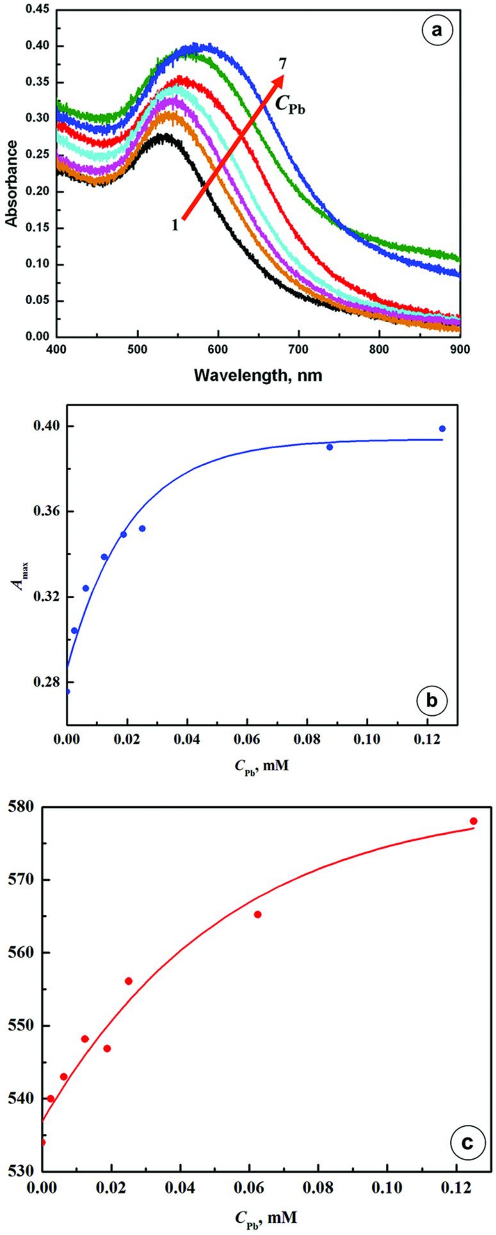

Figure 6. (a) UV-Vis absorbance spectra of MPA-capped AuNP$_{5nm}$ after HAA with Pb $_{2+}$ [μM]: (1) 0, (2) 2.5, (3) 6.25, (4) 12.5, (5) 25, (6) 87.5, (7) 125. (b) Dependence of A_{max} vs. C_{Pb}. (c) Dependence of λ_{max} vs. C_{Pb}. AuNP concentration: 2.85 nM; MPA added: 3.75 mM; pH 5.34 - 6.05.

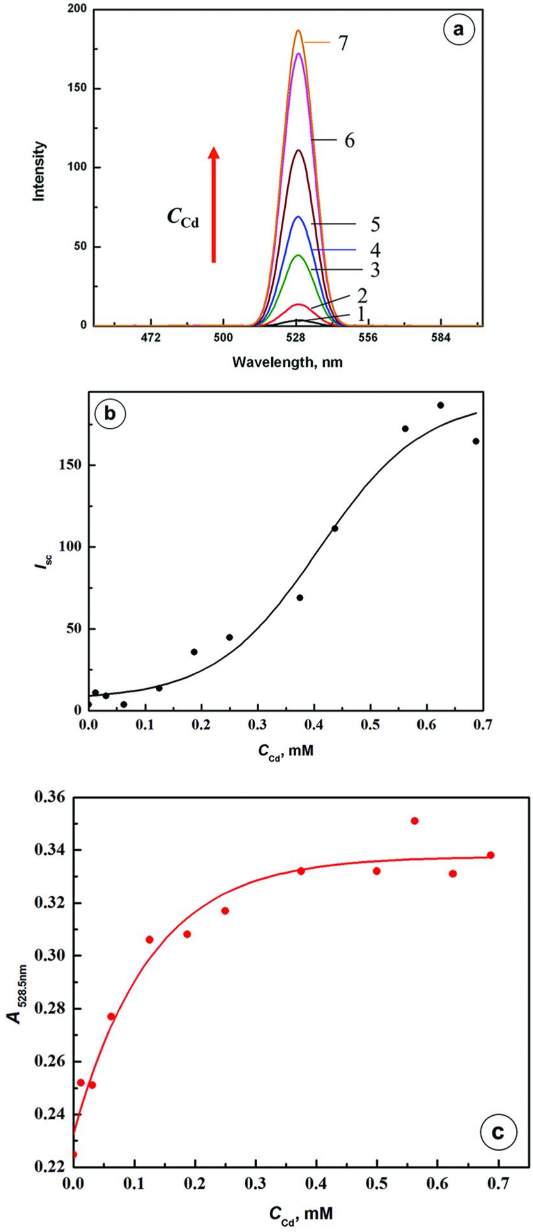

Figure 7. Dependence of resonance elastic light scattering spectra (a) for MPA-capped AuNP$_{5nm}$ nanoparticles assembled by LAA on concentration of Cd^{2+} [mM]: (1) 0, (2) 0.125, (3) 0.25, (4) 0.375, (5) 0.437, (6) 0.562, (7) 0.625. (b) dependence of scattering intensity maximum $I_{sc,max}$ vs. C_{Cd}. (c) Dependence of A_{528nm} vs. C_{Cd}. AuNP concentration: 2.85 nM; MPA added: 3.75 mM; λ_{ex} = 528 nm.

Monitoring of Cd^{2+} and Pb^{2+}-Linked AuNP Network Assembly by Resonance Elastic Light Scattering

The measurements of elastic light scattering from AuNP solutions show that considerable changes in the scattering intensity occur upon the injection of Cd^{2+} ions. Hence, we have investigated in detail the scattering intensity variation during the LAA and HAA pathways of Cd^{2+}-linked AuNP network assembly. The RELS spectra for a constant incident wavelength λ_{ex} recorded for the LAA and HAA pathways are presented in Figures 7 and 8, respectively. The incident light beam wavelengths were selected near the wavelength of absorbance maximum for the highest C_{Cd2+} concentration. Such a selection provides high sensitivity of RELS measurements under varying conditions and changing nanoparticle solution properties.

As illustrated in Figure 7, the RELS intensity increases dramatically with increasing Cd^{2+} concentration during the LAA pathway. The intensity increases from $I_{sc} = 3.6$ in the absence of Cd^{2+} ions to $I_{sc} = 186.6$ for $C_{Cd2+} = 625$ μM. The narrow bandwidth of RELS spectra ($\Delta\lambda = 14$ nm) indicates that any effects due to the inelastic (Raman) scattering and photoluminescence are negligible. The dependence of $I_{sc,max}$ vs. C_{Cd2+}, shown in Fig. 7b, is not linear. The experimental data are fitted well with Boltzmann function: $I_{sc,max} = A_2 + (A_1 - A_2)/[1 + \exp((C_{Cd2+} - C_0)/s\}]$, with: $A_1 = 6.812$, $A_2 = 190.6$, $C_0 = 0.407$, $s = 0.093$.

A quick comparison of the dependence of $I_{sc,max}$ vs. C_{Cd2+} with the dependence of absorbance A_{528} at $\lambda = 528$ nm vs. C_{Cd2+} shows significant differences in the form of these dependencies. Since the elastic light scattering consists of the absorbance followed by coherent secondary emission, the dependencies of I_{sc} and A_λ measurables on C_{Cd2+} concentration should be of similar nature provided that the secondary-emission efficiency is constant and high (possibly 100 %). Therefore, the appearance of the induction period on the $I_{sc} = f(C_{Cd2+})$ dependence, in the absence of such a period on the $A = f(C_{Cd2+})$ dependence, is likely to be due to the lower efficiency of secondary emission for lower Cd^{2+} concentrations where the extent of assembly is small. On the other hand, at higher Cd^{2+} concentrations when the number of Cd^{2+}-linked AuNP/MPA ensembles increases, the coupling of local surface plasmons between single gold nanoparticles in the same ensemble should result in more efficient secondary emission and thus higher intensity of light scattering. This stage corresponds to the intermediate Cd^{2+} concentration range (100 – 300 μM). Beyond $C_{Cd} = 300$ μM, both the $I_{sc} = f(C_{Cd})$ and $A = f(C_{Cd})$ characteristics show signs of a saturation which is evidently due to the hindrance of the growth of larger assemblies.

The RELS measurements similar to those described above for the LAA pathway have also been performed for the HAA pathway of AuNP assembly. The RELS spectra obtained for λ_{ex} = 585 nm are presented in Figure 8. The spectra show again that the scattering intensity increases with increasing Cd^{2+} concentration during the HAA pathway. The intensity increases from I_{sc} = 1.6 in the absence of Cd^{2+} ions to I_{sc} = 164.2 for C_{Cd2+} = 687 μM. The linewidth of RELS spectra is narrow ($\Delta\lambda$ = 15 nm). The dependence of $I_{sc,max}$ vs. C_{Cd2+}, shown in Fig. 7b, is fitted by the simplex routine with a Boltzmann function: $I_{sc,max} = A_2 + (A_1 - A_2)/[1 + \exp((C_{Cd\ 2+} - C_0)/s)]$, with: A_1 = -103.3, A_2 = 169.7, C_0 = 0.064, s = 0.143. In contrast to the LAA pathway, there is a clear linear region of the dependence of $I_{sc} = f(C_{Cd2+})$ in the low Cd^{2+} concentration range from 0 to 187 μM which can be utilized for a simple analytical determination of Cd^{2+} ions. The dependence of $A = f(C_{Cd2+})$ is of a similar shape as the dependence of $I_{sc} = f(C_{Cd2+})$. This means that the increase in absorbance of AuNP assemblies is paralleled with the increase in light scattering intensity. Hence, we can conclude that in the HAA pathway, there is a more uniform growth of AuNP assemblies and the increase in scattering intensity more closely reflects the increase in the SP absorbance.

The RELS spectra for a constant incident wavelength λ_{ex} recorded for the LAA and HAA pathways of Pb^{2+}-linked AuNP network assembly are presented in Figures 9 and 10, respectively. The wavelength λ_{ex} = 640 nm was selected for the LAA pathway as the incident light beam wavelength. For the HAA pathway, another wavelength ($\lambda_{ex,1}$ = 560 nm) near the absorbance maximum for the highest C_{Pb2+} concentration was chosen in addition to λ_{ex} = 640 nm. Such a selection provides a high sensitivity of RELS measurements under varying conditions and changing nanoparticle solution properties.

As illustrated in Figure 9, the RELS intensity increases with increasing Pb^{2+} concentration during the LAA pathway. The intensity increases from I_{sc} = 2.06 in the absence of Pb^{2+} ions to I_{sc} = 473.57 for C_{Pb2+} = 312.5 μM. The narrow bandwidth of RELS spectra ($\Delta\lambda$ = 15 nm) indicates that any effects due to the inelastic (Raman) scattering and photoluminescence are negligible. The dependence of $I_{sc,max}$ vs. C_{Pb2+}, shown in Fig. 9b, is not linear. The experimental data are fitted well with sigmoidal Boltzmann function: $I_{sc,max} = A_2 + (A_1 - A_2)/[1 + \exp((C_{Pb\ 2+} - C_0)/s)]$, with the following parametrs: A_1 = -14.98114, A_2 = 2464.01461, C_0 = 421.29434, s = 77.3719.

The RELS measurements described above for the LAA pathway have also been performed for the HAA pathway of AuNP assembly (Figure 10a). The spectra show that the scattering intensity increases with increasing Pb^{2+} concentration during the HAA pathway. The intensity increases from I_{sc} = 16.88 in the absence of Pb^{2+} ions to I_{sc} = 123.54 for C_{Pb2+} = 125 μM for the excitation lambda λ_{ex} = 560 nm and from I_{sc} = 8.23 to I_{sc} = 78.2 for the excitation lambda λ_{ex} = 640 nm. The dependence of $I_{sc,max}$ vs. C_{Pb+}, shown in Fig. 10b, is fitted by a sigmoidal Boltzmann function.

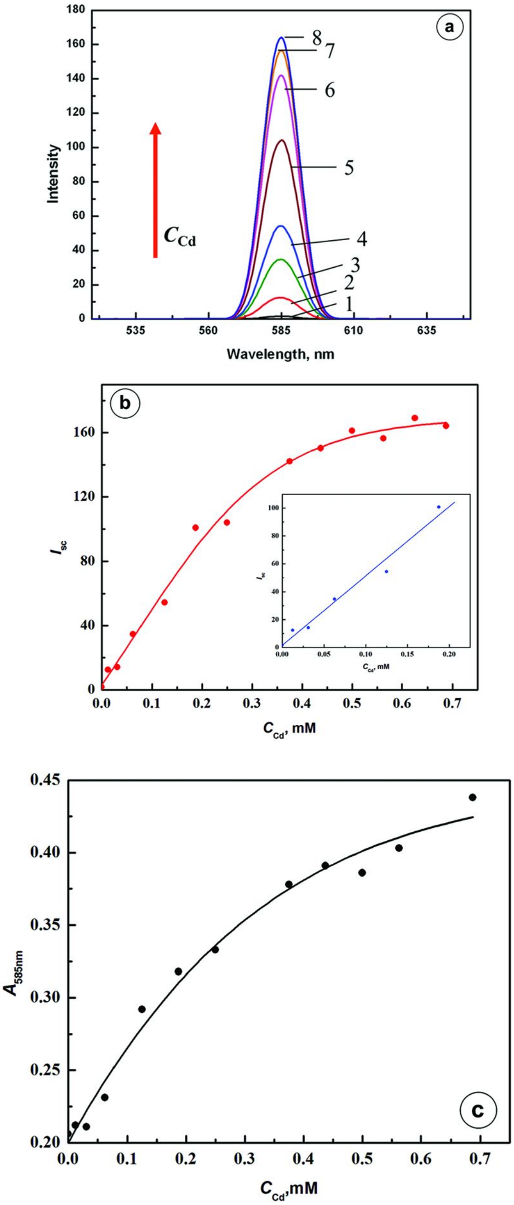

Figure 8. Dependence of resonance elastic light scattering spectra for MPA-capped AuNP$_{5\ nm}$ nanoparticles assembled by HAA on concentration of Cd(NO$_3$)$_2$ [mM]: (1) 0, (2) 0.0125, (3) 0.0625, (4) 0.125, (5) 0.25, (6) 0.375, (7) 0.562, (8) 0.687. (b) Dependence of RELS intensity maximum $I_{sc,max}$ on C_{Cd}. (c) Dependence of A_{585nm} on C_{Cd}. AuNP concentration: 2.85 nM; MPA added: 3.75 mM ; pH 5.5-5.9; λ_{ex} = 585 nm.

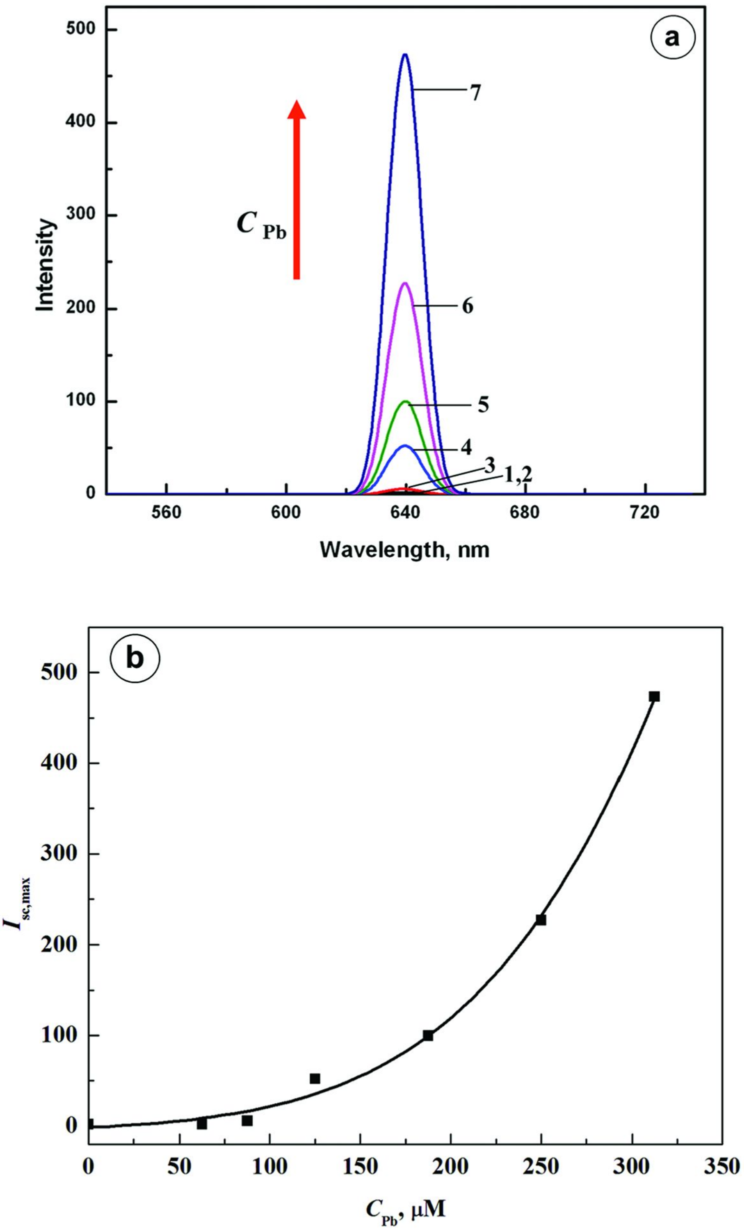

Figure 9. Dependence of elastic light scattering spectra for MPA-capped $AuNP_{5nm}$, assembled by LAA, on concentration of Pb^{+2} recorded after 1 min of $Pb(NO_3)_2$ injection. (b) Dependence of scattering intensity maximum $I_{sc,max}$ vs C_{Pb}. C_{Pb} [μM]: (1) 0, (2) 62.5, (3) 87.5, (4) 125, (5) 187.5, (6) 250, (7) 312.5. $AuNP_{5nm}$ concentration: 1.87 nM; MPA added: 3.75 mM; pH 5.53-5.9.

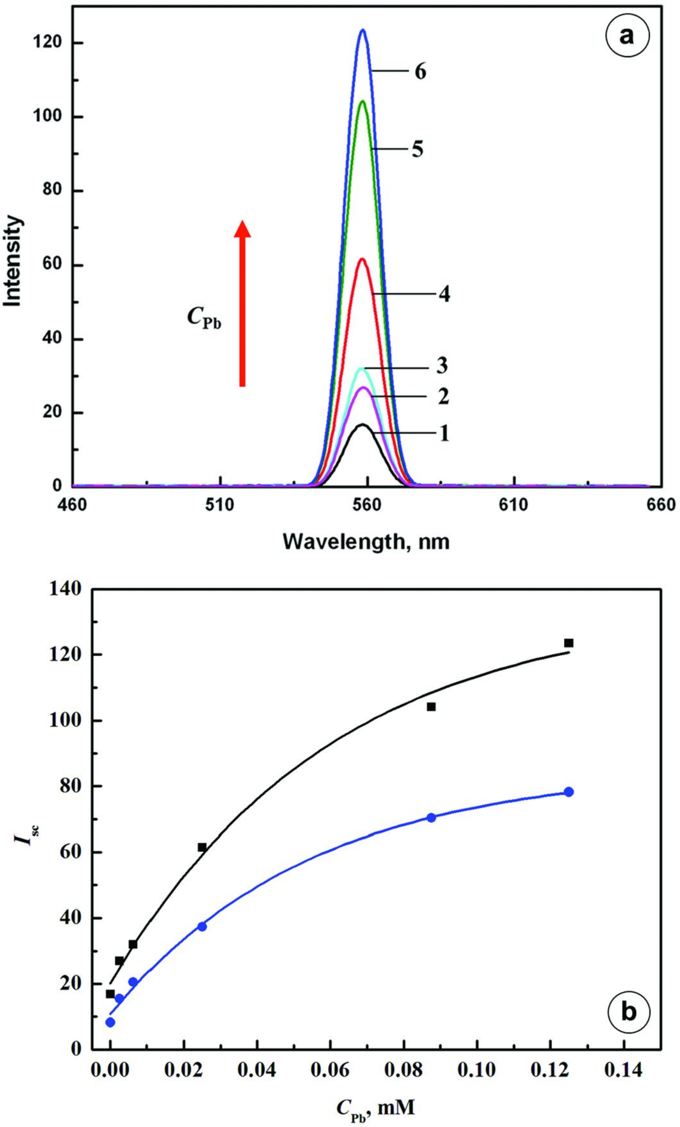

Figure 10. Dependence of resonance elastic light scattering spectra for MPA-capped $AuNP_{5nm}$ nanoparticles, assembled by HAA, on concentration of Pb^{2+} [μM]: (1) 0, (2) 2.5, (3) 6.25, (4) 25, (5) 87.5, (6) 125, excitation wavelength λ_{ex} = 560 nm. (b) Dependence of scattering intensity maximum $I_{sc,max}$ vs C_{Pb} for (1) λ_{ex} = 560 nm (squares), (2) λ_{ex} = 640 nm (circles). AuNP concentration: 2.85 nM; MPA added: 3.75 mM.

Temporal Evolution of Absorbance and Elastic Light Scattering Spectra of MPA-Capped Gold Nanoparticles after Addition of Pb^{+2} Ions

The dynamics of Pb^{2+}-induced assembly of MPA-capped AuNP$_{5nm}$ has been investigated by recording UV-Vis spectra following the injection of Pb^{+2} ions, as illustrated in Figure 11. The surface plasmon band for MPA-capped gold nanoparticles shows a bathochromic shift from λ_{max} = 520 nm before Pb(II) injection, to λ_{max} = 538 nm after the addition of 125 µM Pb(NO$_3$)$_2$. (t = 75 min). At the same time, the absorbance of the SP band maximum increased from A_{max} = 0.327 to A_{max} = 0.358, respectively. These spectral changes indicate that the gold nanoparticles assemble upon the addition of Pb^{2+} ions.

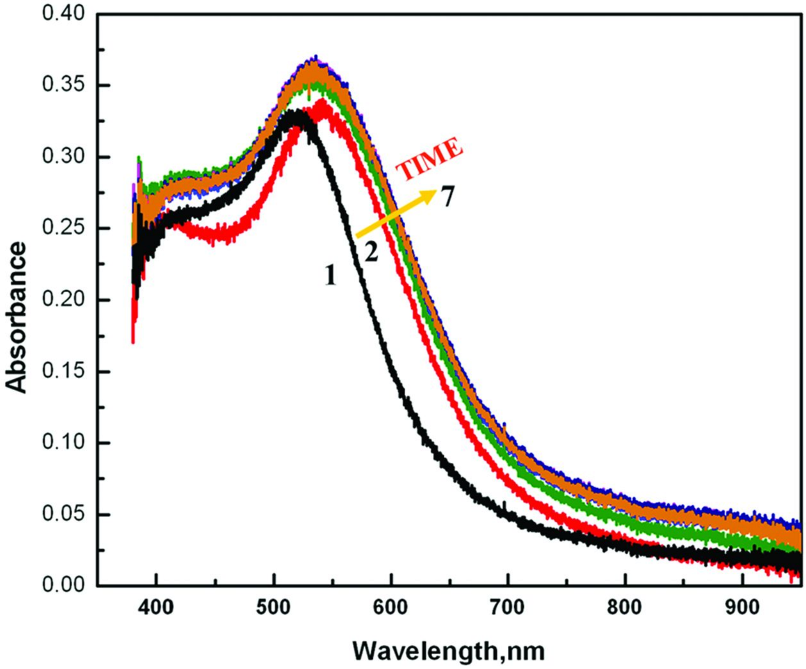

Figure 11. Temporal evolution of absorbance spectra of MPA-capped gold nanoparticles AuNP$_{5nm}$ after addition of 125 µM Pb(NO$_3$)$_2$ (1). Interaction time [min]: (2) 1, (3) 15, (4) 30, (5) 45, (6) 60 , (7) 75. AuNP concentration: 1.875 nM; MPA added: 3.75 mM; pH 5.5.

Typical temporal evolution of resonance elastic light scattering from MPA-capped AuNP$_{5nm}$ gold nanoparticles assembled by LAA after addition of 125 µM Pb(NO$_3$)$_2$ in solution is presented in Figure 12a. The concentration of AuNP$_{5nm}$ was 1.875 nM. The RELS spectra were obtained for λ_{ex} = 640 nm and the secondary emission spectrum was recorder from λ_{em} = 540 to 740 nm. The spectra show that the scattering intensity increased from I_{sc} = 8.4, after 1 min of 125 µM Pb(NO$_3$)$_2$

injection, to I_{sc} = 79.11 after 75 min. of injection. The dependence of scattering intensity maximum $I_{sc,\ max}$ vs time t shows a clear tendency to saturate after 30 min from injection of Pb^{+2} ions to MPA- capped gold nanoparticles $AuNP_{5nm}$ (Fig. 12b). The increase of scattering intensity upon addition of Pb^{+2} ions is indicative of nanoparticle assembly. This corroborates conclusions concerning the assembly of gold nanoparticles in the presence of Pb^{+2} on the basis of the SP band absorbance shift toward longer wavelengths.

Influence of Bonding on AuNP Aggregate Structure

To elucidate the mechanism of AuNP/MPA/Cd^{2+} and AuNP/MPA/Pb^{2+} assembly, further structural insights into the nature of interparticle bonding are needed. Therefore, the interactions of MPA-capped AuNP in the absence and presence of Cd^{2+}-linker were investigated using molecular dynamics simulations and quantum mechanical calculations of electronic structure. While the electrostatic repulsive interactions between negatively charged AuNP/MPA at higher pH (pH > 4.27) are well understood, the participation of hydrogen bonding at sufficiently low pH and the role of Cd^{2+}-linker are not. In particular, we wanted to evaluate the differences in bond lengths and angles for hydrogen bonding (O-H-O) and Cd^{2+}-linking (O-Cd^{2+}-O), as well as the overall distance between the nanoparticle cores in the case of hydrogen bonding and compare it with that for Cd^{2+}-linking.

The molecular arrangement of two undissociated MPA molecules interacting to form a hydrogen bond O-H-O between the COOH functional groups is presented in Figure 13a. The electronic structure calculated using the modified Hartree-Fock methods (SE PM3 method) is presented in Figure 13b. It is seen that the two MPA molecules are not in-line and form a zigzag conformation in order to satisfy the sp hybridization at the O atoms participating in the hydrogen bonding. The distance between O atoms in the O-H-O bond is 0.259 nm and the angle is 178.1 deg. The overall distance between H-atoms of the –SH groups, which may represent the distance between the cores of hydrogen bonded AuNP/MPA nanoparticles, is 1.149 nm.

The molecular arrangement in an ensemble of Cd^{2+}-linked MPA molecules is presented in Figure 14a and the electron density surface with electrostatic potential is presented in Figure 14b. The distance between O atoms in the O-Cd^{2+}-O bond is 0.345 nm and the angle is 110.1 deg. The overall distance between H-atoms of the –SH groups, representing the distance between the cores of Cd^{2+}-linked AuNP/MPA nanoparticles, is 1.437 nm.

It follows from these evaluations that hydrogen bonding provides much shorter inter-core distances in the AuNP assemblies as compared to Cd^{2+}-linking. Therefore, it is expected that the Cd^{2+}-linking, with its 25.1 % longer inter-core distance than in the corresponding H-bonding, should generate significantly less coupling between the local surface plasmon oscillations and lower SP band shift toward longer wavelengths, provided that the number of AuNP nanoparticles in the given ensemble is the same in case of the Cd^{2+}-linking and H-bonding.

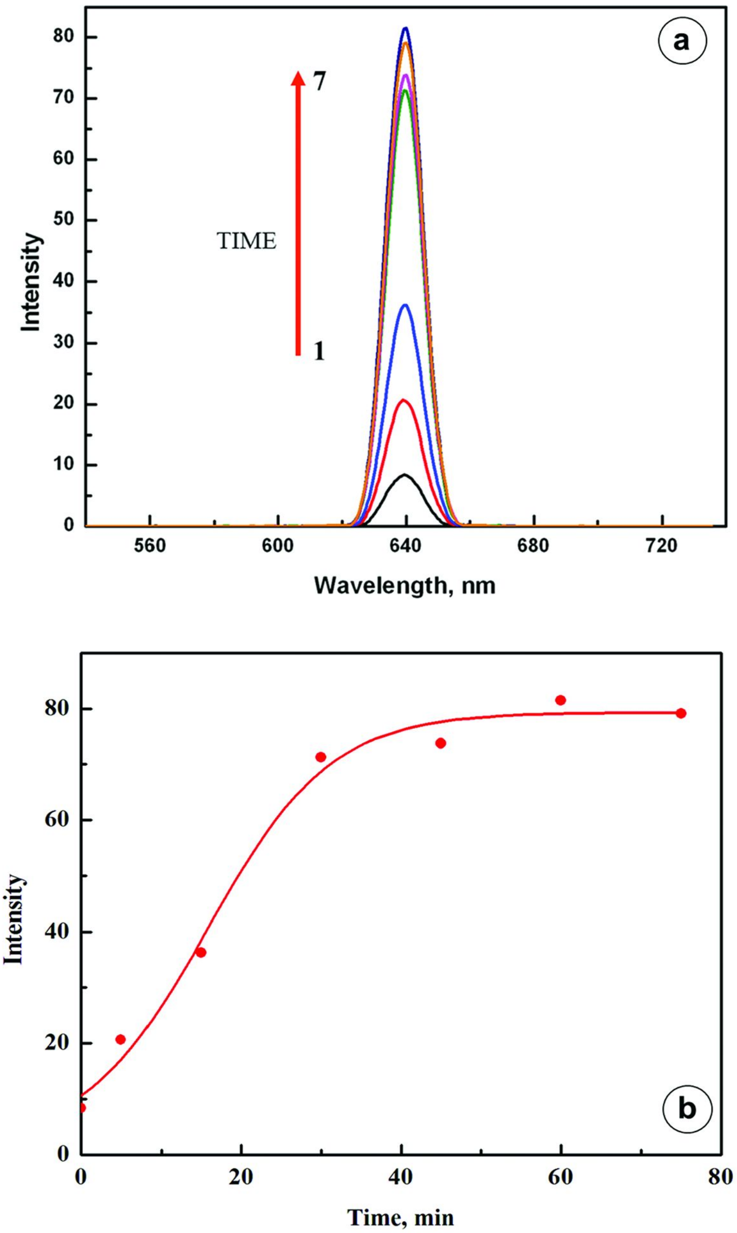

Figure 12. (a) Temporal evolution of resonance elastic light scattering spectra of MPA-capped gold nanoparticles $AuNP_{5nm}$ assembled by LAA after addition of 125 μM $Pb(NO_3)_2$ and (b) dependence of scattering intensity maximum $I_{sc,max}$ vs t. Interaction time [min]: (1) 1, (2) 5, (3) 15, (4) 30, (5) 45, (6) 60, (7) 75. AuNP concentration: 1.87 nM; MPA added: 3.75 mM; pH 5.5; λ_{ex} = 640 nm.

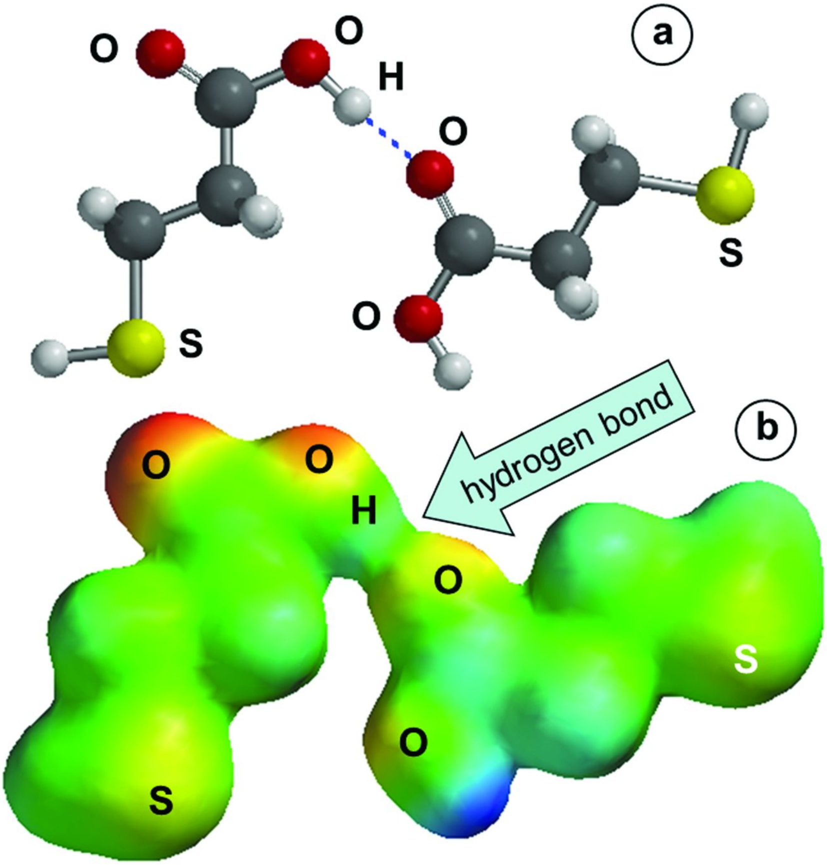

Figure 13. (a) Electronic structure of a H-bonding in a MPA-MPA ensemble as a model for interparticle H-bonding in MPA-capped AuNP assembly: (a) molecular dynamics atomic structure, (b) HF quantum mechanical electron density surface (ρ = 0.02) with mapped electrostatic potential (red to blue – negative to positive potential).

Disassembly of Metal Ion-Linked AuNP Networks by EDTA Chelating

The key element in both pathways of AuNP assembly is the linking provided by metal ions. These ions interact easily with carboxylate moieties of the AuNP/MPA shells. The proof that Cd^{2+} and Pb^{2+} ions are really essential in the assembly process has been obtained in experiments with the addition of EDTA to a solution of metal ion-linked AuNP assemblies, as illustrated in the set of UV-Vis spectra in Figures 15 and 16, for Cd^{2+} and Pb^{2+} ions, respectively. In these Figures, curve 1 represents the spectrum for the original MPA-capped AuNP and curve 2 the spectrum for the assembled Cd^{2+}/Pb^{2+}-linked AuNP/MPA networks.

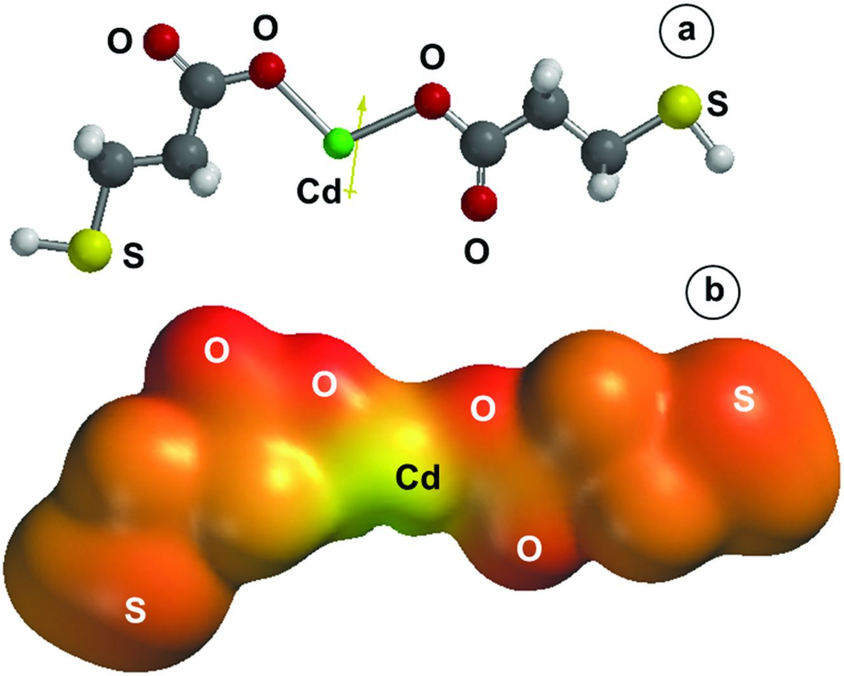

Figure 14. (a) Electronic structure of a Cd^{2+}-linkage in a MPA-Cd^{2+}-MPA ensemble as a model for Cd^{2+}-induced MPA-capped AuNP assembly: (a) molecular dynamics atomic structure, (b) HF quantum mechanical electron density surface (ρ = 0.002) with mapped electrostatic potential (red to blue – negative to positive potential).

A large bathochromic shift occurs during the assembly ($\Delta\lambda$ = 28 nm and $\Delta\lambda$ = 36 nm for Cd^{2+} and Pb^{2+} MPA@AuNP network, respectively), with the SP band maximum shifting toward longer wavelengths and with concomitant color change from ruby red to violet. The addition of EDTA (curve 3) results in a hypsochromic shift ($\Delta\lambda$ = -28 nm and $\Delta\lambda$ = - 45 nm, respectively) and a complete reversal of the color change from violet back to ruby red, signifying a full disassembly of AuNP aggregates.

In Figures 17 and Figure 18, a comparison of the RELS spectra is made for: (a) the original MPA-capped AuNP (curve 1), (b) the assembled Cd^{2+}/Pb^{2+}-linked AuNP/MPA networks (curve 2), and (c) same as (b) but after addition of EDTA (curve 3). As can be clearly seen, there is a dramatic increase in the light scattering from the assembled Cd^{2+}/Pb^{2+}-linked Au nanoparticles (curve 2) from $I_{sc,1}$ = 1.6 to $I_{sc,2}$ = 114.3 for Cd^{2+} and from $I_{sc,1}$ = 6.2 to $I_{sc,2}$ = 110.3 for Pb^{2+}. A complete diminution of scattering upon the addition of EDTA (curve

3) to $I_{sc,3}$ = 1.7 and 1.3 due to the complexation of Cd^{2+}/Pb^{2+} by EDTA ligands and neutralization of its positive charge, thereby rendering the Cd^{2+}/Pb^{2+}-linking ineffective. The formation constants for Cd-EDTA chelate CdL^{2-} and Pb-EDTA chelate PbL^{2-} (where L^{4-} is the deprotonated EDTA ligand) are: log K = 16.46 and log K = 18.04, respectively. Since the stability constants for Pb ions complexed by a ligand like MPA is much lower: log K = 4.1, the Pb^{2+} ions are completely removed from the AuNP assemblies and quantitatively bound by EDTA to form negatively charged chelates. The chelated lead ions become repelled from AuNP/MPA nanoparticles which are now even more separated than the original AuNP/MPA particles in the absence of Pb(II) and EDTA. That is the reason why the scattering intensity decreases below the level characteristic for the original AuNP/MPA (Figure 18, curve 3). For the same reason, the SP band on the UV-Vis spectrum shifts farther to the shorter wavelength (λ_{max} = 521 nm) than the original position of the band for AuNP/MPA (λ_{max} = 530 nm) (Figure 16, curve 3).

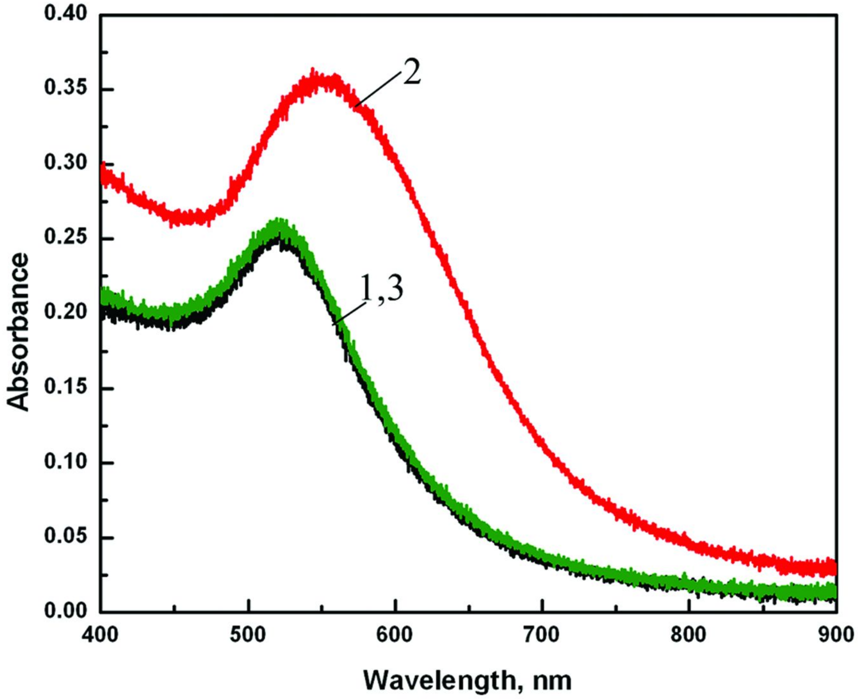

Figure 15. UV-Vis absorbance spectra for: (1) 3.75 mM MPA + 2.85 nM $AuNP_{5\,nm}$, (2) assembled Cd^{2+}-linked AuNP/MPA (0.875 mM Cd^{2+}) and (3) after addition of 1.875 mM EDTA.

In Functional Nanoparticles for Bioanalysis, Nanomedicine, and Bioelectronic Devices Volume 1; Hepel, M., et al.;
ACS Symposium Series; American Chemical Society: Washington, DC, 2012.

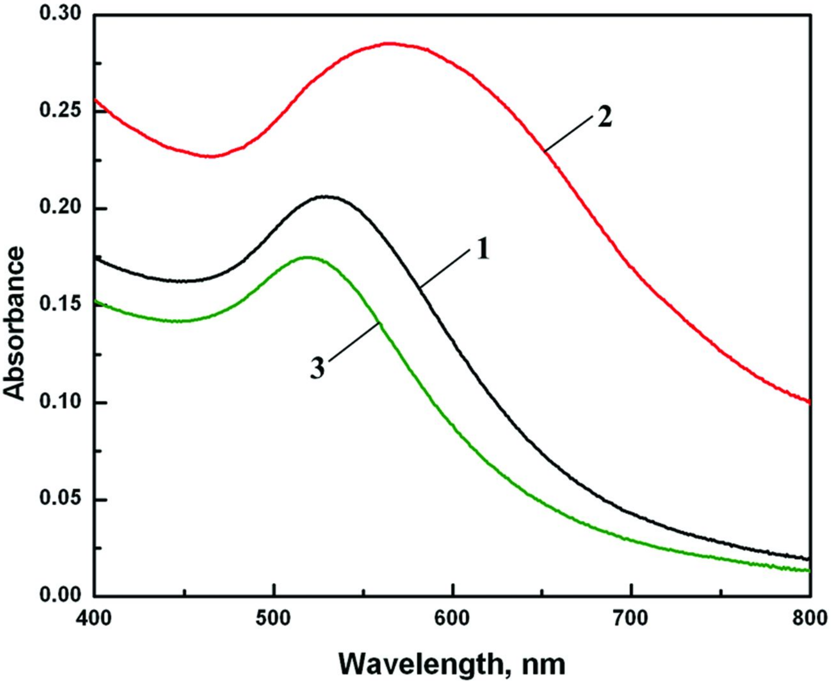

Figure 16. UV-Vis absorbance spectra for: (1) 3.75 mM MPA + 4.5 nM AuNP$_{5\ nm}$ (2) assembled Pb^{2+}-linked AuNP/MPA (125 μM Pb^{2+}) and (3) after addition of 750 μM EDTA.

Mechanistic Aspects of Low- and High-Affinity Assembly of AuNP Networks

The SP band absorbance measurements and the static RELS intensity experiments show the following main differences between the LAA and HAA pathways of AuNP assembly (Scheme 1):

(i) For LAA, the SP band shift associated with the addition of Cd^{2+} or Pb^{2+} ions is very low, although the absorbance maximum increases considerably. The RELS scattering increases dramatically with increasing Cd^{2+} or Pb^{2+} concentration.

(ii) For HAA, the SP band shift associated with the addition of Cd^{2+} or Pb^{2+} ions is large and the absorbance maximum increases considerably. A strong RELS scattering increase with increasing Cd^{2+} or Pb^{2+} concentration is also observed.

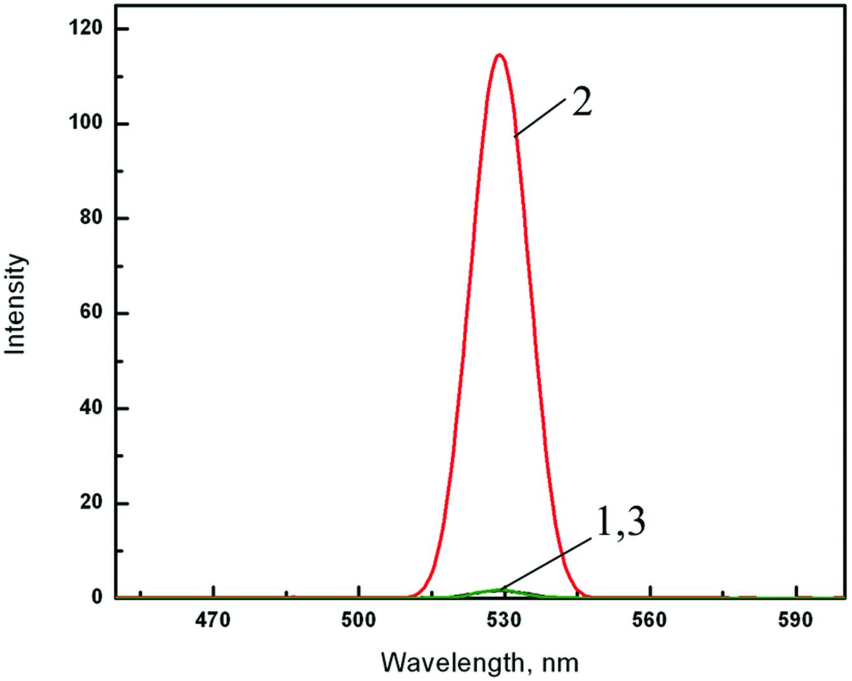

Figure 17. RELS spectra for: (1) 3.75 mM MPA + 2.85 nM AuNP$_{5\ nm}$, (2) assembled Cd^{2+}-linked AuNP/MPA (0.875 mM Cd^{2+}) and (3) after addition of 1.875 mM EDTA.

Whereas it is evident that the SP band shift produced in HAA is much larger than that observed in LAA, the maximum scattering intensity is more similar in both LAA and HAA pathways. This is however rather fortuitous since the incident beam wavelengths are different. From the Rayleigh equation for light scattering from small particles, we have:

$$I = I_0 \frac{\left(1+\cos^2\theta\right)}{2R^2}\left(\frac{2\pi}{\lambda}\right)^4 \frac{\left[\left(n_2-n_1\right)^2-1\right]}{\left[\left(n_2-n_1\right)^2+2\right]}\left(\frac{d}{2}\right)^6 \qquad (1)$$

where n_1 and n_2 are the refractive indices for the solution and particles, respectively, d is the particle diameter, and θ is the scattering angle. Since the scattering intensity I decreases with 4-th power of the wavelength λ, for unchanged other conditions, it is likely that the efficiency of secondary emission is considerably lower in the case of LAA because much larger scattering should be expected at lower incident beam wavelength. The higher SP band shift and relatively stronger scattering indicate that larger assemblies are formed in the HAA pathway. In Figure 19, HR-TEM images of Cd^{2+}- and Pb^{2+}- mediated MPA-capped gold nanoparticles are presented.

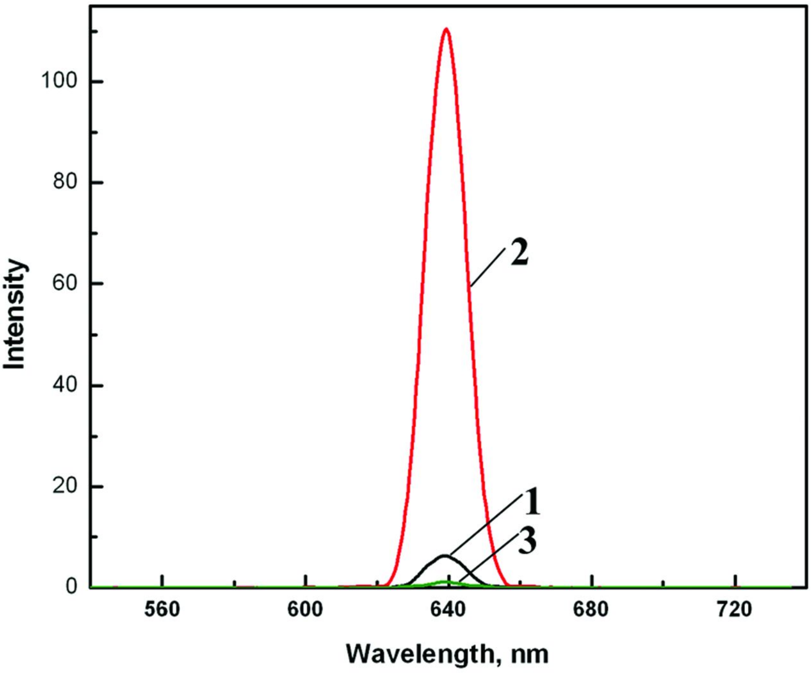

Figure 18. RELS spectra for: (1) 3.75 mM MPA + 4.5 nM AuNP$_{5nm}$ (2) assembled Pb^{2+}-linked AuNP/MPA (125 µM Pb^{2+}) and (3) after addition of 750 µM EDTA.

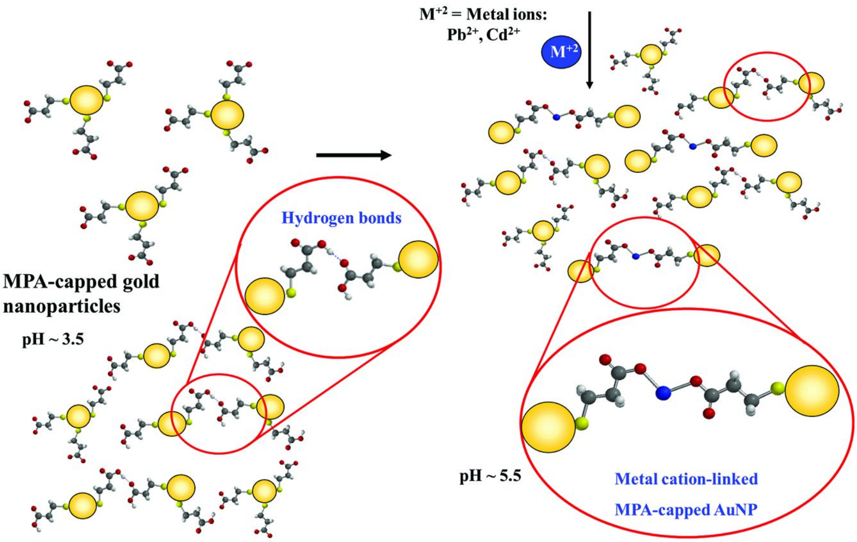
M^{+2} = Metal ions:
Pb^{2+}, Cd^{2+}
M^{+2}
Hydrogen bonds
MPA-capped gold nanoparticles
pH ~ 3.5
pH ~ 5.5
Metal cation-linked
MPA-capped AuNP

Scheme 1. Mechanistic aspects of heavy metal-induced assembly of gold nanoparticles

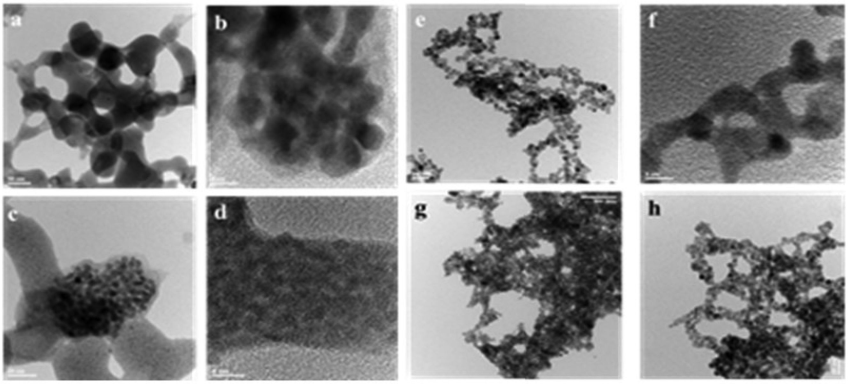

Figure 19. HR-TEM images of (a-d) Cd^{2+}- and (e-h) Pb^{2+}- mediated MPA-capped gold nanoparticles.

DLS Characteristics of Assembled Metal Ion-Linked MPA-Capped AuNP Nanoparticles

In order to determine the average size of AuNP aggregates formed in the LAA and HAA pathways, measurements of hydrodynamic diameters have been carried out using the dynamic light scattering (DLS) technique. The obtained correlation function $C(\tau)$, describing Brownian noise due to aggregates entering and leaving the laser beam spot pulsed onto the nanoparticle solution, for Cd^{2+}-linked AuNP/MPA networks LAA pathway is presented in Figure 20a. The function $C(\tau)$ correlates the frequency of the scattering intensity noise due to the Brownian diffusion with the particle-size dependent diffusion coefficient D. This enables one to determine the hydrodynamic diameter d_H of the particles from the Stokes-Einstein equation:

$$d_H = \frac{kT}{3\pi\eta D} \tag{2}$$

where k is the Boltzmann constant, T – absolute temperature, and η - dynamic viscosity of solution. The onset of the $C(\tau)$ decay at τ_A, marked with an A in Fig. 20a, relates to the size of assemblies (where a higher τ_A corresponds to a slower diffusion and larger assemblies) .

The inflection point on the correlation curve is found at $\tau = 235$ μs ($C(\tau) = 0.3088$). This corresponds to relatively small aggregates with hydrodynamic diameter of $d = 86.1 \pm 1.2$. The calculated lognormal particle distribution function shown in Figure 20b indicates that the assemblies formed are characterized with a relatively low polydispersity $p = 0.239 \pm 0.016$ with the particle-number distribution peak width of $w = 42.0$ nm. The true aggregate mean diameter obtained using the ZPALS routine is 37.9±0.6 nm.

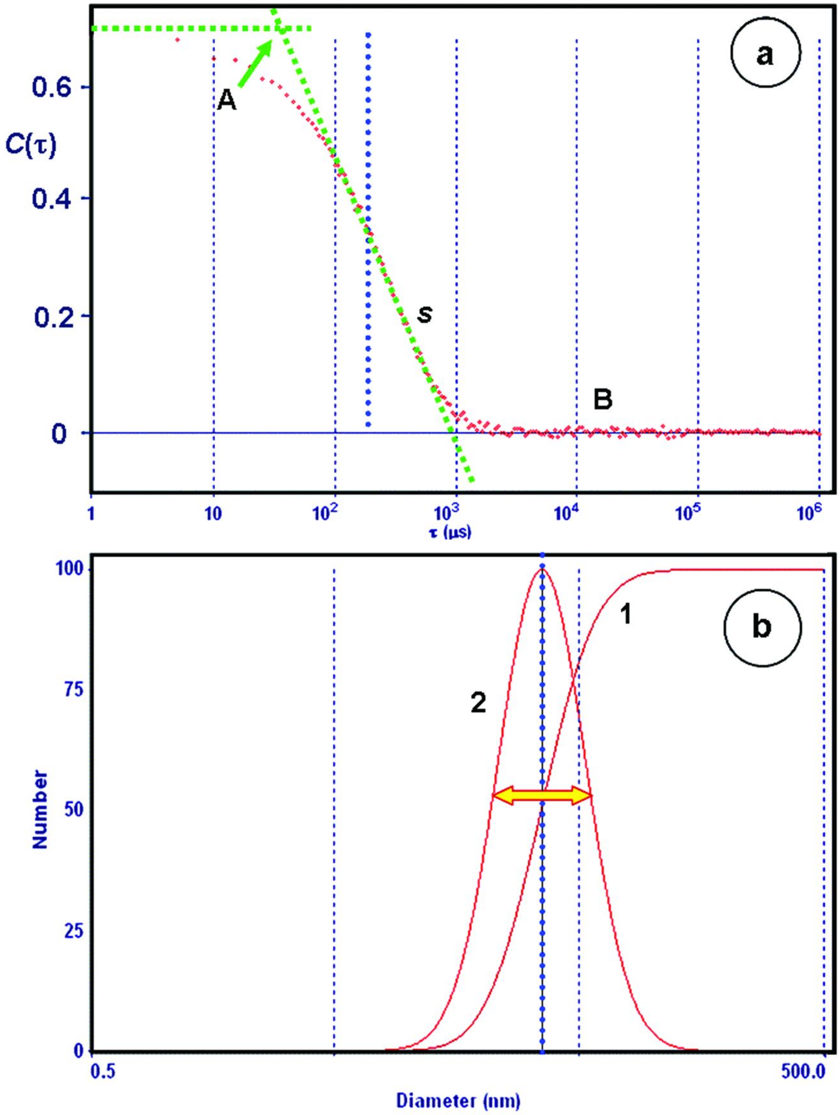

Figure 20. DLS characteristics of MPA-capped AuNP nanoparticles assembled by LAA: (a) correlation function C(τ) with decay onset at point A, decay slope s, and final branch B indicating absence of large particles; (b) lognormal particle number-distribution functions: (1) integral and (2) differential. Mean diameter of assemblies: 37.9±0.6 nm (n = 5), polydispersity: p = 0.239±0.016. AuNP concentration: 2.85 nM; MPA added: 3.75 mM; C_{Cd} = 0.687 mM.

Similar measurements performed for Cd^{2+}-linked AuNP/MPA networks in HAA pathway are presented in Figure 21a.

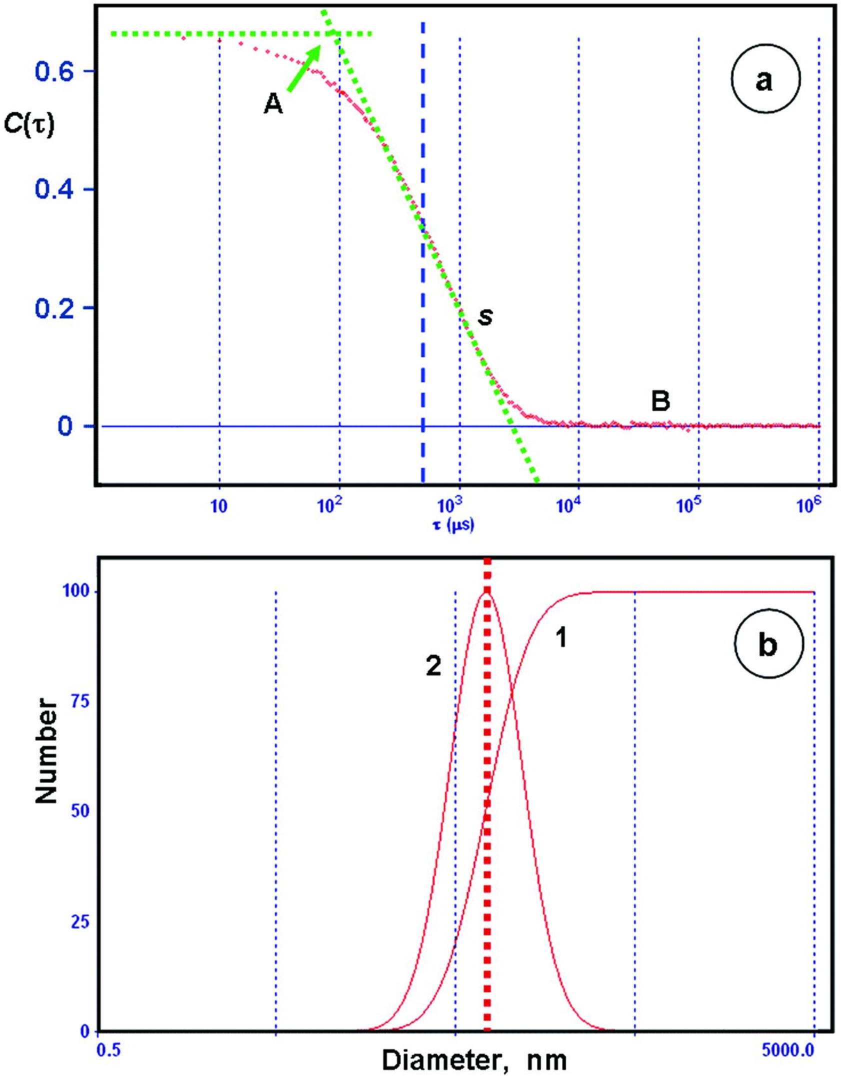

Figure 21. DLS characteristics of MPA-capped AuNP nanoparticles assembled by HAA: (a) correlation function C(τ) with decay onset A, decay slope s, and final branch B indicating absence of large particles; (b) lognormal particle number-distribution functions: (1) integral and (2) differential. Mean diameter of assemblies: 82.5±0.9 nm (n = 5), polydispersity: p = 0.273±0.006. AuNP concentration: 2.85 nM; MPA added: 3.75 mM; C_{Cd} *= 0.687 mM.*

The inflection point on the correlation curve is found at τ = 530 μs ($C(\tau)$ = 0.3539). This corresponds to larger aggregates than for LAA, with hydrodynamic diameter d = 236.1 ± 2.6. The calculated lognormal particle distribution function shown in Figure 21b indicates that the assemblies formed are characterized with a relatively low polydispersity p = 0.273 ± 0.006 with the particle-number distribution half-peak width w = 123.2 nm. The true aggregate mean diameter is 82.5±0.9 nm.

The DLS measurements corroborate conclusions from other methods concerning the size of assemblies formed in LAA and HAA pathways. The general question remains of how the assemblies grow larger in HAA path than in LAA path?

To answer this question, we have taken into account conclusions from all measurements performed in this work, as well as results obtained in molecular dynamics and quantum mechanical calculations presented in previous section. From the analysis of the steps in LAA path, one can see that the pH adjustment in step (b) leads to the partial deprotonation of carboxylic acid groups in the MPA shell in AuNP/MPA, rendering the interparticle cohesive forces ineffective in comparison to strong electrostatic repulsions. Therefore, the initial hydrogen-bonded AuNP/MPA aggregates have been disassembled in this step. Upon the injection of Cd^{2+}/Pb^{2+} ions in the next step (c) in LAA, the negatively charged AuNP/MPA nanoparticles attract the Cd^{2+} cations which become coordinatively bonded to carboxylate groups. Some of the Cd^{2+}/Pb^{2+} ions can form linkages between two AuNP/MPA nanoparticles and this process may progress to form larger assemblies. The distance between AuNP's in these assemblies is determined by the length of two MPA capping molecules and the length of cadmium linkage. As determined from molecular dynamics calculations, the distance equals to 1.4 nm.

In contrast to the LAA pathway, the second step in HAA involves injection of Cd^{2+}/Pb^{2+} ions before any pH adjustment. Hence, the initial hydrogen bonded small aggregates of AuNP/MPA are not disassembled due to the COOH group deprotonation. On the contrary, they are strengthened by Cd^{2+}/Pb^{2+} migration into the H-bonded aggregates, neutralizing any excess negative charge due to COO^- groups and providing additional side-line linking. The Cd^{2+}/Pb^{2+} cations can also bind to dissociated superficial carboxylate groups and thus provide means for aggregation of these assemblies. Therefore, we encounter here simultaneous H-bonding and Cd^{2+}/Pb^{2+} linkages that strengthen the aggregates and make inter-core distances shorter. Moreover, the cadmium or lead ions penetrating into the initial AuNP/MPA assemblies neutralize partial negative charge of carboxylate groups and form side-line linkages, thereby increasing the stability of these assemblies. This model is consistent with the growth of larger, more stable, and denser aggregates. This agrees with experimental evidence obtained with SP absorbance measurements, static RELS intensity measurements, DLS aggregate size analysis, and the theoretical evaluation of the length of H-bonding and Cd/Pb-linkages.

Conclusions

We have found two different kinds of aggregates formed in the assembly of MPA-capped AuNP (5 nm dia.) mediated by Cd^{2+} and Pb^{2+} ions, depending on the preparation pathway: low-affinity assembly (LAA) and high-affinity assembly (HAA). On the basis of the analysis of SP absorbance band shifts, static light scattering spectra (RELS), and dynamic light scattering (DLS), the differences appear to be due to the inter-core distances controlled by the length and conformation of molecules participating in the crosslinking. We have shown that the direct Cd^{2+}/Pb^{2+} linking through the formation of coordination bonds with superficial deprotonated COO^- group of MPA shells on neighboring AuNP/MPA nanoparticles results in longer inter-core distance (d = 1.437 nm), as compared to the hydrogen bonded AuNP/MPA for which d = 1.149 nm, as determined from the molecular dynamics calculations. In LAA, single Au nanoparticles are linked by Cd^{2+}/Pb^{2+} ions. In HAA, the H-bonding dominates with supporting side-line Cd^{2+}/Pb^{2+} crosslinking that strengthens the aggregates and enables them to grow larger. From the DLS size analysis, the diameter of aggregates formed in LAA is $2r = 37.9 \pm 0.6$ nm and in HAA it is $2r = 82.5 \pm 0.9$ nm, with low polydispersity p = 0.239 and 0.273, respectively. This model is consistent with large bathochromic shift of SP band and higher RELS intensity observed for HAA. The term *high-affinity assembly* used in this work is suitable since denser and larger aggregates are formed in this pathway and dual crosslinking (H-bonding, Cd-linking and Pb-linking) strengthens the interparticle interactions.

Materials and Methods

Chemicals

All chemicals used for investigations were of analytical grade purity. 3-mercaptopropionic acid (MPA) ($HSCH_2CH_2CO_2H$) and tetrachloroauric(III) acid trihydrate ($HAuCl_4 \cdot 3H_2O$, 99.9+%) were purchased from Sigma Aldrich Chemical Company and used as received. Sodium citrate dihydrate ($HOC(COONa)(CH_2COONa)_2 \cdot 2H_2O$) was obtained from J.T. Baker Chemical Co. Sodium borohydride ($NaBH_4$), disodium ethylenediamine tetraacetate (EDTA) ($Na_2C_{10}H_{14}O_8N_2 \cdot 2H_2O$), lead nitrate ($Pb(NO_3)_2$), cadmium nitrate ($Cd(NO_3)_2 \cdot 4H_2O$) and other reagents were obtained from Fisher Scientific Company. Solutions were prepared using Milli-Pore Milli-Q deionized water (conductivity σ = 55 nS/cm).

Apparatus

The transmission electron microscopy (TEM) images of Au nanoparticles were obtained using a Jeol Model JEM-2010 HR-TEM instrument (100 kV). The elastic light scattering spectra were recorded using LS55 Spectrometer (Perkin Elmer, Waltham, MA, USA) equipped with 20 kW Xenon light source operating at 8 µs pulsing mode allowing for the use of monochromatic radiation with wavelength from 200 nm to 800 nm with 1 nm resolution and sharp cut-off filters: 290, 350, 390, 430, 515 nm. The dual detector system consisted of a photomultiplier tube (PMT) and an avalanche photodiode. The pulse width at half height was less than 10 μs. The UV–Vis spectra were recorded using a model Varian Cary 50 Bio (Agilent Technologies, Santa Clara, CA, USA). Dynamic light scattering (DLS) measurements were performed using a Zeta Potential Analyzer Model ZetaPALS (Brookhaven Instruments Corp., Holtsville, NY, USA) to determine the hydrodynamic diameter, mean particle size and polydisperity index for AuNP assemblies.

Procedures

The Au nanoparticles were synthesized according to the published procedure (*25*, *51*). Briefly, 2.56 mL of 10 mM $HAuCl_4$ was mixed with 9.6 mL of 10 mM trisodium citrate solution (ratio 1:3.75) and poured into distilled water (88 mL). The obtained solution was vigorously stirred and fresh cold $NaBH_4$ solution (5 mM, 8.9 mL) was added dropwise. The solution slowly turned grey and then transparent ruby red. Stirring was maintained for 30 minutes. The obtained citrate-capped core-shell gold nanoparticles (AuNP/Cit) were stored at 4 °C. Their size was first estimated from UV–Vis surface plasmon absorption band shift and determined more precisely by HR-TEM imaging to be: 5.0 ± 0.9 nm (n = 85).

Molecular dynamics simulations of the arrangement of interacting MPA molecules and quantum mechanical calculations of electronic structure of hydrogen bonded and Cd^{2+}-linked MPA molecules, as the models for interparticle interactions of MPA-capped AuNP, were performed using modified Hartree-Fock methods with 6-31G* basis set and pseudopotentials, semi-empirical PM3 method, or density functional theory (DFT) with B3LYP functional and 6-31G* basis set, embedded in Wavefunction Spartan software (*52*). The electron density and density of states (LDOS) are expressed in atomic units, au^{-3}, where 1 au = 0.52916 Å and 1 au^{-3} = 6.74911 $Å^{-3}$.

Acknowledgments

This work was partially supported by the U.S. DoD Grant No. AS073218.

List of Abbreviations

AuNP - gold nanoparticles
AuNP/MPA - mercaptopropionic acid-capped gold nanoparticles
RELS - resonance elastic light scattering
DLS - laser-pulsed dynamic light scattering
TEM - transmission electron microscopy
SP - surface plasmon
LAA - low-affinity assembly
HAA - high-affinity assembly

References

1. Yoosaf, K.; Ipe, B. I.; Suresh, C. H.; Thomas, K. G. *Phys. Chem. Chem. Phys.* **2007**, *111*, 12839–12847.
2. Kim, Y.; Johnson, R. C.; Hupp, J. T. *Nano Lett.* **2001**, *1*, 165–167.
3. Lee, J.-S.; Han, M. S.; Mirkin, C. A. *Angew. Chem. Int. Ed.* **2007**, *46*, 4093–4096.
4. Guan, J.; Jiang, L.; Zhao, L.; Li, J.; Yang, W. *Colloids Surf. A: Physicochem. Eng. Aspects* **2008**, *325*, 194–197.
5. Israel, L. B.; Kariuki, N. N.; Han, L.; Maye, M. M.; Luo, J.; Zhong, C. J. *J. Electroanal. Chem.* **2001**, *517*, 69–76.
6. Liu, J.; Lu, Y. *J. Am. Chem. Soc.* **2003**, *125*, 6642–6643.
7. Liu, J.; Lu, Y. *Anal. Chem.* **2004**, *76*, 1627–1632.
8. Liu, J.; Lu, Y. *J. Am. Chem. Soc.* **2004**, *126*, 12298–12305.
9. Liu, J.; Lu, Y. *J. Am. Chem. Soc.* **2000**, *122*, 10466–10477.
10. Slocik, J. M.; Zabinski, J. S.; Phillips, D. M.; Naik, R. R. *Small* **2008**, *4*, 548–551.
11. Reynolds, A. J.; Haines, A. H.; Russell, D. A. *Langmuir* **2006**, *22*, 1156.
12. Huang, C. C.; Chang, H. T. *Chem. Commun.* **2007**, 1215.
13. Yang, W.; Gooding, J. J.; He, Z.; Li, Q.; Chen, G. *J. Nanosci. Nanotechnol.* **2007**, *7*, 712.
14. Kamat, P. V. *J. Phys. Chem. B* **2002**, *106*, 7729–2244.
15. Link, S.; El-Sayed, M. A. *J. Phys. Chem. B* **1999**, *103*, 8410–8426.
16. Link, S.; Mohamed, M. B.; El-Sayed, M. A. *J. Phys. Chem. B* **1999**, *103*, 3073–3077.
17. Mishchenko, M.; Travis, L.; Lacis, A., *Scattering, Absorption, and Emission of Light by Small Particles*. Cambridge University Press: Cambridge, 2002.
18. Storhoff, J. J.; Elghanian, R.; Mucic, R. C.; Mirkin, C. A.; Letsinger, R. L. *J. Am. CHem. Soc.* **1998**, *120*, 12674–12675.
19. Storhoff, J. J.; Lazarides, A. A.; Mucic, R. C.; Mirkin, C. A.; Letsinger, R. L.; Schatz, G. C. *J. Am. Chem. Soc.* **2000**, *122*, 4640–4650.
20. Lim, S.; Zhong, C. J. *Acc. Chem. Res.* **2009**, *42*, 798–808.
21. Maye, M. M.; Lim, I. I. S.; Luo, J.; Rab, Z.; Rabinovich, D.; Liu, T.; Zhong, C. J. *J. Am. Chem. Soc.* **2005**, *127*, 1519–1529.
22. Kariuki, N. N.; Luo, J.; Han, L.; Maye, M. M.; Moussa, L.; Patterson, M.; Lin, Y.; Engelhard, M. H.; Zhong, C. J. *Electroanal.* **2004**, *16*, 120–126.
23. Stobiecka, M.; Coopersmith, K.; Hepel, M. *J. Colloid. Interf. Sci.* **2010**, *350*, 168–177.
24. Stobiecka, M.; Hepel, M. *Sensors Actuators B* **2010**, *149*, 373–380.
25. Stobiecka, M.; Deeb, J.; Hepel, M. *Biophys. Chem.* **2010**, *146*, 98–107.
26. Stobiecka, M.; Hepel, M. *Biomaterials* **2011**, *32*, 3312–3321.
27. Stobiecka, M.; Hepel, M. *Phys. Chem. Chem. Phys.* **2011**, *13*, 1131–1139.
28. Pasternack, R. F.; Collings, P. J. *Science* **1995**, *269* (5226), 935–939.
29. Oldenburg, A. L.; Hansen, M. N.; Zweifel, D. A.; Wei, A.; Bopart, S. A. *Opt. Espress* **2006**, *14*, 6724.
30. Troutman, T. S.; Barton, J. K.; Romanowski, M. *Opt. Lett.* **2007**, *32*, 1438.
31. Jain, P. K.; El-Sayed, I. H.; El-Sayed, M. A. *Nano Today* **2007**, *2*, 18.

32. Ding, H.; Yong, K. T.; Roy, I.; Pudavar, H. E.; Law, W. C.; Bergey, E. J.; Prasad, P. N. *J. Phys. Chem. C* **2007**, *111*, 12552.
33. Wang, H.; Huff, B.; Zweifel, D. A.; He, W.; Low, P. S.; Wei, A.; Cheng, J. Z. *Proc. Natl. Acad. Sci. U.S.A.* **2005**, *102*, 15752.
34. Durr, N. J.; Larson, T.; Smith, D. K.; Korgel, B. A.; Sokolov, K.; Ben-Yakar, A. *Nano Lett.* **2007**, *7*, 941.
35. Chou, C. H.; Chen, D.; Wang, C. R. C. *J. Phys. Chem. B* **2005**, *109*, 11135.
36. Huff, T. B.; Tong, L.; Zhao, Y.; Hansen, M. N.; Cheng, J. X.; Wei, A. *Nanomedicine* **2007**, *2*, 125.
37. Tong, L.; Zhao, Y.; Huff, T. B.; Hansen, M. N.; Wei, A.; Cheng, J. X. *Adv. Mater. (Weinheim, Germany)* **2007**, *19*, 3136.
38. Kim, K.; Huang, S. W.; Ashkenazi, S.; O'Donnell, M.; Agarwal, A.; Kotov, N. A.; Denny, M. F.; Kaplan, M. J. *Appl. Phys. Lett.* **2007**, *90*, 223901.
39. Eghtedari, M.; Oraevsky, A. A.; Copland, J. A.; Kotov, N. A.; Conjusteau, A.; Motamedi, M. *Nano Lett.* **2007**, *7*, 1914.
40. Yang, W. H.; Schatz, G. C.; Duyne, R. R. v. *J. Chem. Phys.* **1995**, *103*, 869.
41. Draine, B. T.; Flatau, P. J. *J. Opt. Soc. Am. A* **1994**, *11*, 1491.
42. Lee, K. S.; El-Sayed, M. A. *J. Phys. Chem. B* **2005**, *109*, 20331.
43. Lee, K. S.; El-Sayed, M. A. *J. Phys. Chem. B* **2006**, *110*, 19220.
44. Ungureanu, C.; Rayavarapu, R. G.; Manohar, S.; Leeuwen, T. G. v. *J. Appl. Phys.* **2009**, *105*, 102032.
45. Jain, P. K.; Lee, K. S.; El-Sayed, I. H.; El-Sayed, M. A. *J. Phys. Chem. B* **2006**, *110*, 7238.
46. Brioude, A.; Jiang, X. C.; Pileni, M. P. *J. Phys. Chem. B* **2005**, *109*, 13138–13142.
47. Yin, G.; Wang, S. Y.; Xu, M.; Chen, L. Y. *J. Korean Phys. Soc.* **2006**, *49*, 2108.
48. Gonzales, A. L.; Noguez, C. *J. Comput. Theor. Nanosci.* **2007**, *4*, 231.
49. Prescott, S. W.; Mulvaney, P. *J. Appl. Phys.* **2006**, *99*, 123504.
50. Kooij, E. S.; Poelsema, B. *Phys. Chem. Chem. Phys.* **2006**, *8*, 3349.
51. Turkevich, J.; Stevenson, P. C.; Hiller, J. *Discuss. Faraday Soc.* **1951**, *11*, 55–75.
52. Hehre, W. J.; Radon, L.; Schleyer, P. R.; Pople, J. A. Wiley, New York 1985.

Chapter 9

Noble Metal Nanoparticles in Bioanalysis

Xiurong Yang,[*] Xiaolei Wang, Hui Zhu, and Xiaowen Xu

**State Key Laboratory of Electroanalytical Chemistry,
Changchun Institute of Applied Chemistry, Chinese Academy
of Sciences, Changchun, 130022 (P. R. China)
[*]E-mail: xryang@ciac.jl.cn**

Looking back upon the past decade, functionalized noble metal nanoparticles (NMNs) with controlled size, morphology, composition or structure have becoming a major motive force behind the development of modern bioanalytical chemistry. In this chapter, a brief introduction is given to the history and progress of NMNs based bioanalysis. Particular attention is devoted to some representive works in the area of biosensing and biorecognition applications. The article is mainly categorized into absorbance-based assay, electrochemical detection and fluorescent analysis.

Introduction

Bioanalysis is a fast growing subdiscipline covering the detection of a broad spectrum of biological analytes, such as inorganic ions, drugs, small organic molecules, proteins, nucleic acids and microorganisms. It is of great significance for human health because many physiological functions depend critically on maintaining the proper levels of inorganic ions and biological molecules. Besides, bioanalysis also plays a fundamental role in food security and environmental conservation. Therefore, numerous methods have been explored to detect biological targets. After years of investigation, researchers found that noble metal nanoparticles (NMNs) with attractive physicochemical properties can be of great value in biological analysis. Many NMNs, especially gold nanoparticles (AuNPs), can be synthesized, adjusted and functionalized in a facile and straightforward manner. The as-prepared products hold several important features, including excellent stability, unique optoelectronic activity and extremely high surface-to-volume ratio. Those benefits make NMNs promising

In Functional Nanoparticles for Bioanalysis, Nanomedicine, and Bioelectronic Devices Volume 1; Hepel, M., et al.;
ACS Symposium Series; American Chemical Society: Washington, DC, 2012.

candidates for preparing novel biological sensors. In at least three different ways, NMNs-based sensors can be utilized to improve the quality of bioanalysis. First, they can act as effective recognition units to provide selective binding with the target analytes. Second, they can be used as transducing components for signaling the binding process. Third, the S/N ratio can also be remarkably enhanced by using NMNs. Up to now, functionalized NMNs with controlled size, morphology, composition or structure have becoming a major motive force behind the development of modern bioanalytical chemistry.

In this chapter, a brief introduction is given to the history and progress of NMNs-based bioanalysis. Particular attention is devoted to some representative works in the area of biosensing and biorecognizing applications. The assay of biomolecules, and the detection of inorganic ions with biomolecules as recognition units by means of NMNs are emphasized. The article is mainly categorized into absorbance-based assay, electrochemical detection and fluorescent analysis, according to the measure techniques of the transduced signals. One thing should be mentioned is that the paper is not a comprehensive review but rather a quick guide to some aspects of NMNs in bioanalysis. Therefore, only a small part of the published papers were selected in this chapter, mainly on the basis of relevance, theoretical innovation and practical significance. We apologize to the authors of many excellent reports that could not be cited here because of our limitations.

Absorption Spectroscopic Analysis

Noble metal nanoparticles such as gold and silver nanoparticles (AuNPs and AgNPs) display intense colors, which results from the free electrons in metals, endowing them with plasmon resonances (*1*). The extinction coefficients of AuNPs or AgNPs are much higher than that of organic dyes, thus detectable absorbance can be obtained through the use of a low concentration of nanoparticles (usually at a nanomolar range). Moreover, the optical properties of AuNPs and AgNPs strongly depend on their inter-particle distances. Typically, 13 nm-diameter AuNPs display a red color with the maximum absorbance at 520 nm, whereas the aggregated ones display a purple or blue color with a new absorbance at the wavelength longer than 600 nm. The surface plasmon resonance peak and the extinction coefficients will change as the diameters of AuNPs vary (*2*). AgNPs likewise exhibit a distance-dependent color, usually from yellow to red or brown as AgNPs aggregate, and the extinction coefficient of AgNPs is higher than that of AuNPs of the same size. The visible color, high extinction coefficients and distance-dependent optical properties make AuNPs and AgNPs as ideal sensing elements in bioanalysis.

The most successful use of AuNPs and AgNPs in bioanalysis may be their combination with DNA oligonucleotides to perform the detection. In such sensing systems, DNA oligonucleotides serve as recognition units while noble metal nanoparticles serve as optical sensing elements. DNA can recognize not only their complementary sequences but a variety of targets such as small molecules, proteins, metal ions and even intact cells, known as functional nucleic acids (*3*). AuNPs and AgNPs can transduce the DNA recognition process into

In Functional Nanoparticles for Bioanalysis, Nanomedicine, and Bioelectronic Devices Volume 1; Hepel, M., et al.;
ACS Symposium Series; American Chemical Society: Washington, DC, 2012.

optical signals; since the color change in such a process is sensitive to the naked eye, the detection results can be visually observed, yielding the colorimetric detection. In 1996, the Mirkin group reported the use of DNA-modified AuNPs to achieve the reversible assembly of macroscopic AuNPs aggregates (*4*). When an oligonucleotide duplex contained “sticky ends” complementary to the two modified sequences on AuNPs, the nanoparticles self-assembled into large aggregates via DNA hybridization; when the temperature was higher than the melting temperature, the aggregates disassembled through duplex dehybridization. In the same year the Alivisatos group independently reported the organization of discrete numbers of DNA-attached gold nanocrystals into spatially defined structures by means of Watson-Crick base-pairing interactions (*5*). In the next year the Mirkin group applied their AuNPs-assembling method to the colorimetric detection of oligonucleotides, based on that DNA-modified AuNPs aggregated and underwent a color change from red to purple upon the introduction of single-stranded target sequences (*6*). This work pioneered the use of DNA and noble metal nanoparticles in the colorimetric assay. Based on such a prototype, an analyte can be extended to various types of targets, recurring to the recognition ability of DNA. Improvements were then adopted by the same group to substitute the tai-to-tail alignment for the head-to-tail alignment of AuNPs probes, obtaining an impressing selectivity (*7*). The Maeda group proposed AuNPs based DNA detection method through the non-cross-linking DNA hybridization (*8*); when the target DNA was perfectly complementary to the modified probe with equal length, the AuNPs would aggregate at considerably high salt concentration. Single-base mismatch at the terminus opposite to the modified site could be detected, which showed the same dispersed behavior as the single-stranded DNA-modified AuNPs. Recently, by taking advantage of a novel nicking endonuclease-assisted nanoparticle amplification (NEANA) process, the Liu group achieved the colorimetric detection of DNA with single-base mismatch selectivity and high sensitivity (ca. 10 pM) (Figure 1) (*9*). In such a detection system, the nicking endonuclease recognized specific nucleotide sequences in the target DNA / linker strand duplex and cleaves only the excess linker strand. The subsequent addition of two sets of different oligonucleotide-modified gold nanoparticles with sequences complementary to that of the linker strand would remain their dispersed state in the presence of the target DNA.

In 2003, the Lu group extended the prototype of AuNPs-based DNA colorimetric detection to the analysis of metal ion Pb^{2+} (*10*). The *in-vitro* selected DNAzymes were used with both the ends elongating to hybridize with the modified sequences on AuNPs to form nanoparticle aggregates, and the presence of Pb^{2+} would cleave the substrate strand and led to the AuNPs disassembly. The detection range could be tuned by varying the ratio between the active and inactive enzyme strands. This work not only extends the targets from oligonucleotides to metal ions in the DNA-modified AuNPs based colorimetric detection, but demonstrates that the attached DNA can still retain its ability as functional nucleic acids to perform recognition. The same group further optimized the experimental conditions, changed the nanoparticle alignment from a head-to-tail manner to a tail-to-tail manner and introduced invasive DNA, obtaining a fast color change in the presence of Pb^{2+} at room temperature

(*11*). Based on the same principle, adenosine (*12*) and UO_2^{2+} ion (*13*) were successfully detected by using aptazymes and DNAzymes, respectively; the presence of the analytes cleaved the ribonucleoside site in the substrate strand and induced the disassembly of aggregates. The Lu group further achieved adenosine and cocaine analysis using aptamers and DNA-modified AuNPs (Figure 2) (*14*). When the linker strand containing an aptamer domain was hybridized with the DNA-modified AuNPs to form nanoparticle aggregates, the target molecules would bind the aptamer and dehybridize the duplex strands, inducing the aggregates disassembly. The Chang group achieved the protein analysis using aptamer-modified AuNPs (*15*), in which case PDGF molecules acted as bridges to link aptamer-modified AuNPs together since one PDGF molecule had two binding sites to the aptamer. The Tan group achieved direct detection of cancerous cells using aptamer-conjugated AuNPs (*16*), based on that the assembly of aptamer-conjugated AuNPs around the cell surface caused a red shift in the absorption spectra. The Mirkin group developed the colorimetric screening of duplex DNA binding molecules (*17*) and triplex DNA binding molecules (*18*) with AuNPs probes. The presence of binding molecules would enhance the stability of duplex or triplex DNA and induce the nanoparticles aggregation, and their relative binding capabilities could be determined via the melting curves or with the naked eye. Also, the endonuclease activity and the efficiency of its inhibitors could be evaluated through the AuNPs-based colorimetric screening (*19*); the endonuclease degraded the DNA-duplex interconnects and dissembled nanoparticles while inhibitors decreased endonuclease activity and slowed down the disassembling process. Taking advantage of T-Hg^{2+}-T coordination chemistry (T represents thymine), the Mirkin group functionalized AuNPs with complementary oligonucleotides containing a single T-T mismatch and achieved Hg^{2+} assay through the melting temperature change of aggregates or the visual observation at elevated temperature (*20*). The Liu group then improved that method through sequences optimization by adding thymine mismatches to lower the melting temperature of DNA-AuNPs conjugates thus made the assay simply done at ambient temperature (*21*). By means of the strong interaction between cysteine and Hg^{2+}, DNA-modified AuNPs probes could be applied to distinguish cysteine from other amino acids (*22*). The Fan group modified AuNPs with a mixture of thymine oligonucleotides and incorporated the nanoparticles into a microfluidic device; the presence of Hg^{2+} would glue the adjacent probes on a single particle and alter the charge distribution on the surface, leading to the particle aggregation at high salt concentration with the concurrent formation of a visible deposition line in the microchannel (*23*). Based on the similar principle, the Dong group modified AuNPs with cytosine-rich sequences and achieved colorimetric detection of Ag^+ ions by means of C-Ag^+-C coordination chemistry (C represents cytosine) (*24*). Taking advantage of the specific interaction between adenine and coralyne, the Ren group achieved colorimetric detection of coralyne using homoadenine-modified AuNPs (*25*); AuNPs would aggregate through the linkages of homoadenine self-structures in the presence of coralyne.

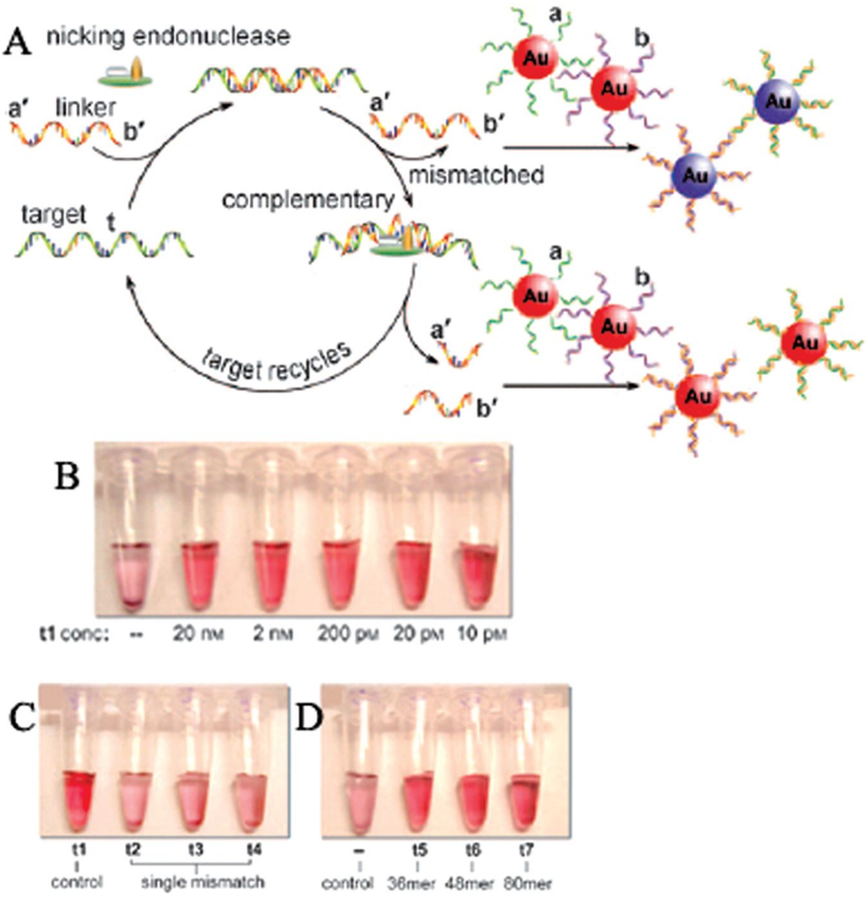
A
nicking endonuclease
a'
linker
b'
target
t
complementary
mismatched
target recycles
a
b
Au
B
t1 conc: -- 20 nM 2 nM 200 pM 20 pM 10 pM
C
t1
t2
t3
t4
control
single mismatch
D
–
t5
t6
t7
control
36mer
48mer
80mer

Figure 1. Nicking endonuclease assisted nanoparticle amplification (NEANA) for target DNA detection (A), colorimetric responses of the system in the presence of various concentrations of target DNA (B), the detection of oligonucleotides with a single mismatch (C) and the detection of target sequences of different length (D). Reproduced with permission from reference (9). Copyright 2009 WILEY-VCH Verlag GmbH & Co. KGaA.

The Li and Brook group used DNA-modified AuNPs to hybridize aptamer to detect adenosine (*26*); the aptamer would dissociate from AuNPs after the target binding, which reduced the negative charges and the steric effect on the surface of AuNPs, weakened the salt-resistant ability of the AuNPs and led to the nanoparticles aggregation at the same salt concentration. The same group further modified AuNPs with double-stranded DNA or *8-17* DNAzyme specific to Pb^{2+} and detected DNase I or Pb^{2+} (*27*); the removal of surface-bound DNA strands by enzymatic cleavage would lead to the rapid aggregation of AuNPs at the same salt concentration. When the surface-immobilized aptamer on AuNPs bound target and folded into target-stabilized structure, the nanoparticles were shown to be more stable toward salt-induced aggregation than those tethered to unfolded aptamers. Taking advantage of this mechanism, adenosine (*28*) and ATP (*29*) molecules could be detected, respectively. The mechanism in Ref. (*26*) to Ref. (*29*) can be considered as salt-induced non-cross-linking aggregation since the targets do not directly assemble or disassemble nanoparticles; instead, the presence of targets changed the charge density or the DNA conformation on the surface of AuNPs and subsequently influenced the stability of nanoparticles at high salt concentration.

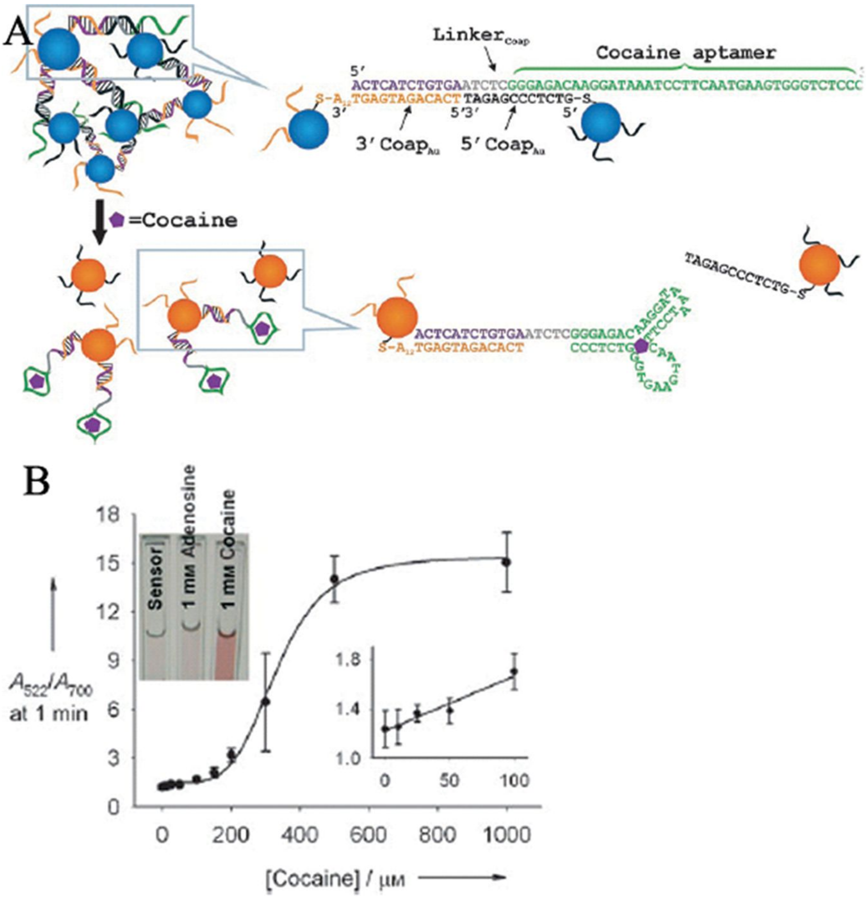

Figure 2. Colorimetric detection of cocaine based on cocaine-induced disassembly of nanoparticle aggregates linked by a cocaine aptamer (A) and the plots of absorption ratio versus cocaine concentration and the visual observation (B). Reproduced with permission from reference (14). Copyright 2006 WILEY-VCH Verlag GmbH & Co. KGaA.

In 2004, the Rothberg group proposed label-free colorimetric detection of DNA sequences using unmodified AuNPs (*30*, *31*). Random-coil single-stranded DNA could adsorb onto AuNPs and afford them a high negative charge density, protecting nanoparticles from salt-induced aggregation; whereas the double-stranded oligonucleotides could not effectively adsorb onto AuNPs thus nanoparticles aggregated at high salt concentration due to the screening of electrostatic repulsion. Utilizing the protecting ability of random-coil single-stranded DNA toward unmodified AuNPs and the target-induced DNA conformation change, various targets can be detected by means of the recognition ability of DNA based on the prototype proposed by the Rothberg group. The Fan group extended the principle to the analysis of K^+ using K^+ aptamer (*32*); the aptamer folded into the tetraplex structure in the presence of K^+ and the rigid structure lost the ability to protect AuNPs, leading to a color change after salt addition. The Dong group further extended the targets of the aptamer-based colorimetric detection using unmodified AuNPs to proteins by taking thrombin as an example (*33*). Based on the same principle, the Yang group reported the colorimetric detection of ochratoxin A (*34*) and dopamine (*35*) using unmodified AuNPs and the corresponding aptamers. The Fan group achieved the analysis of ATP using unmodified AuNPs and aptamer / complementary DNA duplexes (*36*); the binding of ATP to the aptamer induced the duplex dehybridization, releasing the complementary oligonucleotides to stabilize AuNPs at high salt concentration. Further, the Fan group demonstrated the detection of cocaine by using unmodified AuNPs and split aptamer fragments (*37*); the split fragments could protect AuNPs from salt-induced aggregation while the cocaine-induced association of the two fragments lost that ability. The Dong group (*38*) and the Lu group (*39*) independently reported the label-free colorimetric detection of Pb^{2+} using AuNPs and DNAzymes; the substrate strand / enzyme strand duplex could not stabilize AuNPs against salt-induced aggregation while the released single-stranded DNA upon cleavage by Pb^{2+} afforded protection. The Lu group further achieved the analysis of UO_2^{2+} based on the same principle (*13*). Taking advantage of the T-Hg^{2+}-T coordination chemistry, the Willner group developed the detection of Hg^{2+} using unmodified AuNPs and T-rich oligonucleotides, based on that the T-rich oligonucleotides would fold into hairpin structures in the presence of Hg^{2+} and lose protecting ability (*40*). The Chang group independently analyzed Hg^{2+} based on the similar principle, using T_{33} sequences as recognition units (*41*). The Yang group achieved the analysis of Hg^{2+} by means of AuNPs and dye-tagged single-stranded DNA containing T-T mismatches (*42*); the presence of Hg^{2+} induced the formation of duplexes which could not stabilize AuNPs against salt-induced aggregation, accompanied by a fluorescence restoration due to the poor adsorption of double-stranded DNA onto AuNPs. The Yang and Jiao group obtained a tunable detection range for Hg^{2+} using unmodified AuNPs and DNA oligonucleotides by varying the number of T-T mismatches in duplexes (*43*), and a common interference Pb^{2+} can be differentiated from Hg^{2+} by choosing the characteristic wavelength of aggregated AuNPs (*44*). Relying on the i-motif structure formation at acid pH, the Ren group designed a colorimetric pH meter using unmodified AuNPs (*45*). Based on that the intercalating molecule could increase the stability of duplex DNA, the Ling group achieved the colorimetric recognition of DNA intercalators (*46*). Relying on the different adsorption rates of long and short DNA sequences onto AuNPs, the Nie group achieved the colorimetric nuclease assay and measurement of oxidative DNA damage (*47*); the cleaved short single-stranded DNA by nuclease or hydroxyl radicals adsorbed more rapidly onto AuNPs and afforded better protection than long-strand DNA in the equal time. The Yang group further extended this principle to the colorimetric detection of Cu^{2+} by using the long sequence of Cu^{2+}-dependent DNAzyme (*48*). The Mao group achieved colorimetric detection of glucose in rat brain using unmodified AuNPs (*49*); the generated H_2O_2 from the oxidation of glucose would react with Fe^{2+} to produce hydroxyl radicals, which cleaved single-stranded DNA stabilizers into small fragments without protecting ability. The Heeger and Plaxco group achieved colorimetric detection of DNA, small molecules, proteins and ions using unmodified AuNPs and conjugated polyelectrolytes (Figure 3) (*50*). At low salt concentrations both single-stranded and double-stranded DNA could prevent the aggregation of AuNPs, while the conjugated polyelectrolyte specially inhibited that ability of single-stranded DNA instead of the double-stranded or folded DNA due to its stronger binding to random-coil single-stranded oligonucleotides, based on which the target-induced structure switch of DNA can be visualized by the dispersion of AuNPs.

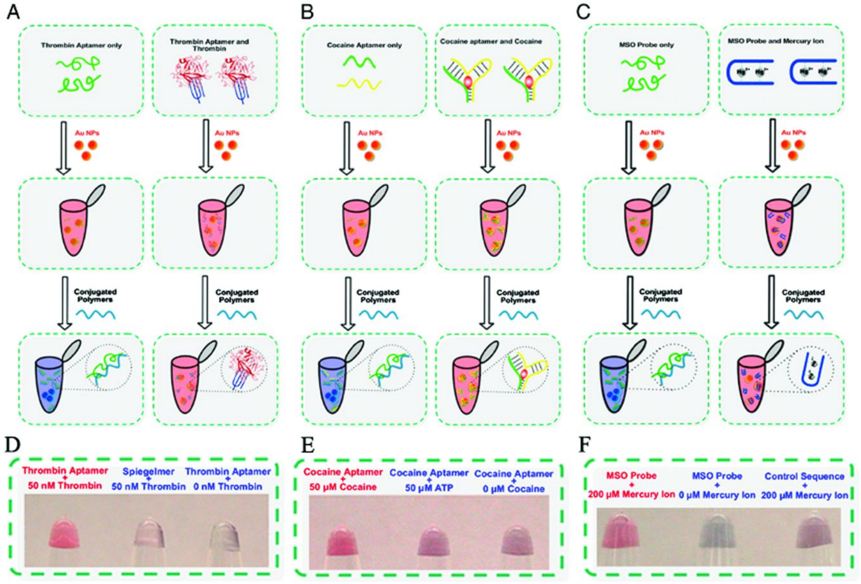
A
Thrombin Aptamer only
Thrombin Aptamer and Thrombin
B
Cocaine Aptamer only
Cocaine aptamer and Cocaine
C
MSO Probe only
MSO Probe and Mercury Ion
Au NPs
Conjugated Polymers
D
Thrombin Aptamer + 50 nM Thrombin
Spiegelmer + 50 nM Thrombin
Thrombin Aptamer + 0 nM Thrombin
E
Cocaine Aptamer + 50 μM Cocaine
Cocaine Aptamer + 50 μM ATP
Cocaine Aptamer + 0 μM Cocaine
F
MSO Probe + 200 μM Mercury Ion
MSO Probe + 0 μM Mercury Ion
Control Sequence + 200 μM Mercury Ion

Figure 3. Colorimetric detection of thrombin (A), cocaine (B) and Hg^{2+} ions (C) using unmodified AuNPs, conjugated polyelectrolytes and functional nucleic acids; (D), (E) and (F) correspond to the visual read in the presence of thrombin, cocaine and Hg^{2+} ions, respectively. Reproduced with permission from reference (50). Copyright 2010 National Academy of Sciences, U.S.A.

The combination of AuNPs and DNA can also be used to design the colorimetric logic gates, which has an indication of the presence or absence of the two targets, by regarding the two targets as two inputs. For example, for the "AND" logic gate, only in the presence of both targets can the system generate a true output value. With regard to the "OR" logic gate, only in the absence of both targets can the system generate a false output value. "INHIBIT" logic gate can be applicable to determine only the presence of target 1 but the absence of target 2. The Lu group designed smart "AND" and "OR" colorimetric logic gates using DNA-modified AuNPs and different linking DNA molecules (*51*). If AuNPs self-assembled to form aggregates through two different kinds of DNA linkers containing two types of aptamers, the nanoparticles would dissemble only in the presence of both targets which broke both kinds of linkers due to the formation of aptamer-target complexes, yielding an "AND" logic gate. If AuNPs self-assembled by one DNA linker flanked by two aptamers, the presence of either target could induce the aggregates disassembly via the linkage breaking, yielding an "OR" logic gate. The Zhang group reported the use of DNA-modified AuNPs for DNA computing and logic-based biomolecular detection (*52*); the coexistence of all three miRNA sequences resulted in the formation of complete linkages and induced the nanoparticles aggregation, which actually performed an "AND" logic. The Ogawa and Maeda group designed "OR" and "AND" logic gates using DNA-modified AuNPs and aptazymes, based on a non-cross-linking nanoparticles aggregation (*53*). In an "OR" logic gate, both the input molecules made each dependent aptazyme yield the same cleaved RNA which could hybridize to the probe DNA on AuNPs, and the full complementarity of the duplex terminus on DNA induced the nanoparticles aggregation at high salt concentration. In an "AND" logic gate, the sequences of cleaved RNA from two aptazymes hybridized with the probe DNA on AuNPs via a sandwich type to form the fully complementary duplexes without any dangling end, thus both inputs were required for AuNPs aggregation to occur. The Zhang group utilized DNA-modified AuNPs and supramolecular DNAzyme structures to develop a complete set of two-input logic gates (*54*); through various sequence designs in the supramolecular DNAzyme, the released DNA molecules would interconnect the DNA-modified AuNPs to form aggregates, obtaining the true output according to the logic. The Yang group demonstrated the colorimetric logic gates for small molecules using unmodified AuNPs and split / integrated aptamers (Figure 4) (*55*). The use of two integrated aptamers enabled the construction of the "OR" logic gate, since the two strands could reassemble to form target-stabilized structures in the presence of either input or both inputs, losing the ability to protect AuNPs. The use of two split aptamers and one integrated aptamer enabled the construction of "AND" logic gate, since only the presence of both inputs led to the formation of the DNA complex consisting of three strands, with no short strands releasing to stabilize AuNPs.

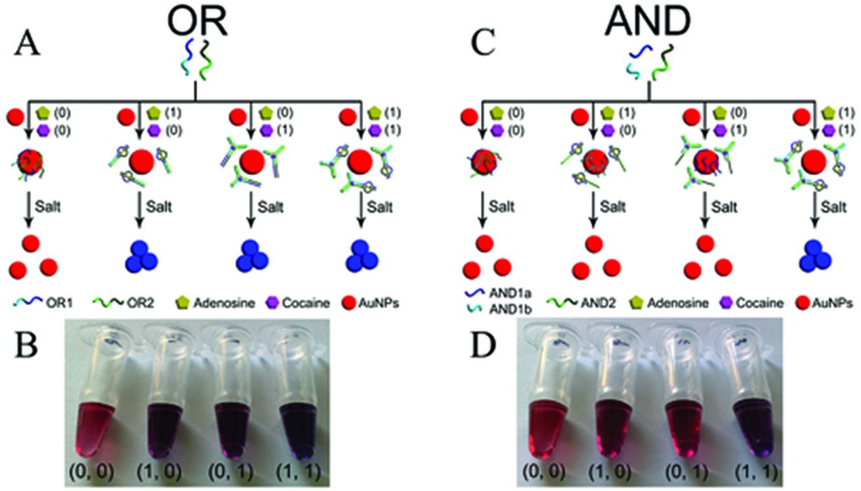

Figure 4. Schematic illustration of the "OR" logic gate using unmodified AuNPs and split / integrated aptamers (A) and the visually observed outputs (B), and schematic illustration of the "AND" logic gate using unmodified AuNPs and split / integrated aptamers (C) and the visually observed outputs (D). Reproduced with permission from reference (55). Copyright 2011 Royal Society of Chemistry.

The use of silver nanoparticles combined with DNA in the colorimetric assay is also exploited by the researchers, taking advantage of the recognition ability of DNA and the optical properties of AgNPs. The Mirkin group grew a thin Au shell on the Ag nanoparticle to make the DNA modification easy while retain the optical properties of AgNPs, achieving the analysis of oligonucleotides (*56*). The Han group coated AgNPs with a silica shell and modified DNA onto the nanoparticle to detect the target sequence (*57*). Target DNA interconnected Ag / Au (or SiO_2) core-shell nanoparticles via the sandwich hybridization with the modified DNA on the surface and induced the aggregates formation as well as the absorbance change. To make DNA attachment to AgNPs easier, the Wilson group loaded DNA on disulfide group-containing dextrans to form PDP-dextran-oligo conjugates, and target oligonucleotides could be detected through the hybridization with such conjugates (*58*). In those work efforts were made to fabricate either nanoparticles or oligonucleotides to enhance the affinity between them with the purpose of incorporating the two together. Besides, efforts were also made to modify AgNPs directly by employing DNA oligonucleotides with terminal functional groups. The Hutter group modified AgNPs with 12 mer-thiolated homo-oligonucleotides and performed the homoadenine recognition to homothymine, with the characteristic absorbance of AgNPs significantly decreasing upon hybridization (*59*). The Lee group functionalized thiolated random sequences onto AgNPs under acid conditions, and then readjust pH to neutral to perform assay; the absorbance of AgNPs would change in the presence of complementary conjugates (*60*). The Mirkin group prepared

AgNPs-oligonucleotide conjugates using DNA with cyclic disulfide-anchoring groups, and the complementary sequences would induce the formation of DNA-linked AgNPs aggregates and the concurrent color change from yellow to pale red (Figure 5) (*61*). The Graham group modified thoilated DNA probes onto AgNPs by introducing a spacer of adenine bases to improve the association, and achieved target sequences assay through the sandwich hybridization (*62*).

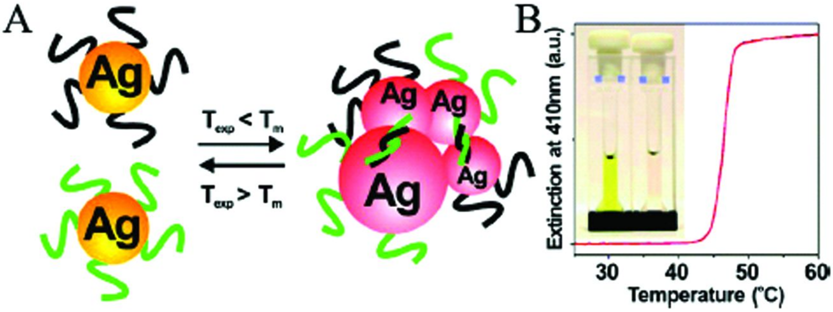
A
Ag
Ag
T_{exp} < T_m
T_{exp} > T_m
Ag
Ag
Ag
Ag
B
Extinction at 410nm (a.u.)
30
40
50
60
Temperature (°C)

Figure 5. (A) The assembly of DNA-conjugated AgNPs based on complementary oligonucleotides terminated with triple cyclic disulfide groups. (B) The melting transition curve monitored at 410 nm wavelength; the inset (B) shows the color change upon DNA hybridization. Reproduced with permission from reference (61). Copyright 2007 American Chemical Society.

Besides the use of DNA-modified AgNPs, unmodified AgNPs and DNA have also been utilized in the detection. The Su group achieved colorimetric detection of DNA using charge neutral peptide nucleic acids (PNA) and AgNPs, based on that the PNA oligomers induced the nanoparticles aggregation while the formed PNA-DNA complexes in the presence of target sequences afforded protection due to the negative charges of DNA strands (*63*, *64*). The Yang and Jiao group reported the label-free colorimetric detection of coralyne utilizing DNA oligonucleotides and AgNPs, extending the targets from oligonucleotides to small molecules (*65*). Homoadenine sequences were found to effectively stabilize AgNPs while the presence of ligands binding to homoadenine bound the adsorbed sequences and took them away from the surface of AgNPs, thus AgNPs were less well protected and aggregated after salt addition, accompanied by a color change from yellow to brown. By using unmodified AgNPs and the mercury-specific oligonucleotides, the Yang group further achieved the colorimetric detection of Hg^{2+}, based on that the random-coil oligonucleotides could protect AgNPs from salt-induced aggregation while the Hg^{2+}-induced stem-loop structure could not (*66*). The Luo group developed a label-free colorimetric detection method for biological thiols using AgNPs and DNA (*67*); the biological thiols such as homocysteine adsorbed onto AgNPs more easily than DNA due to their stronger binding affinity, which prevented the DNA adsorption and led to the nanoparticles aggregation after salt addition.

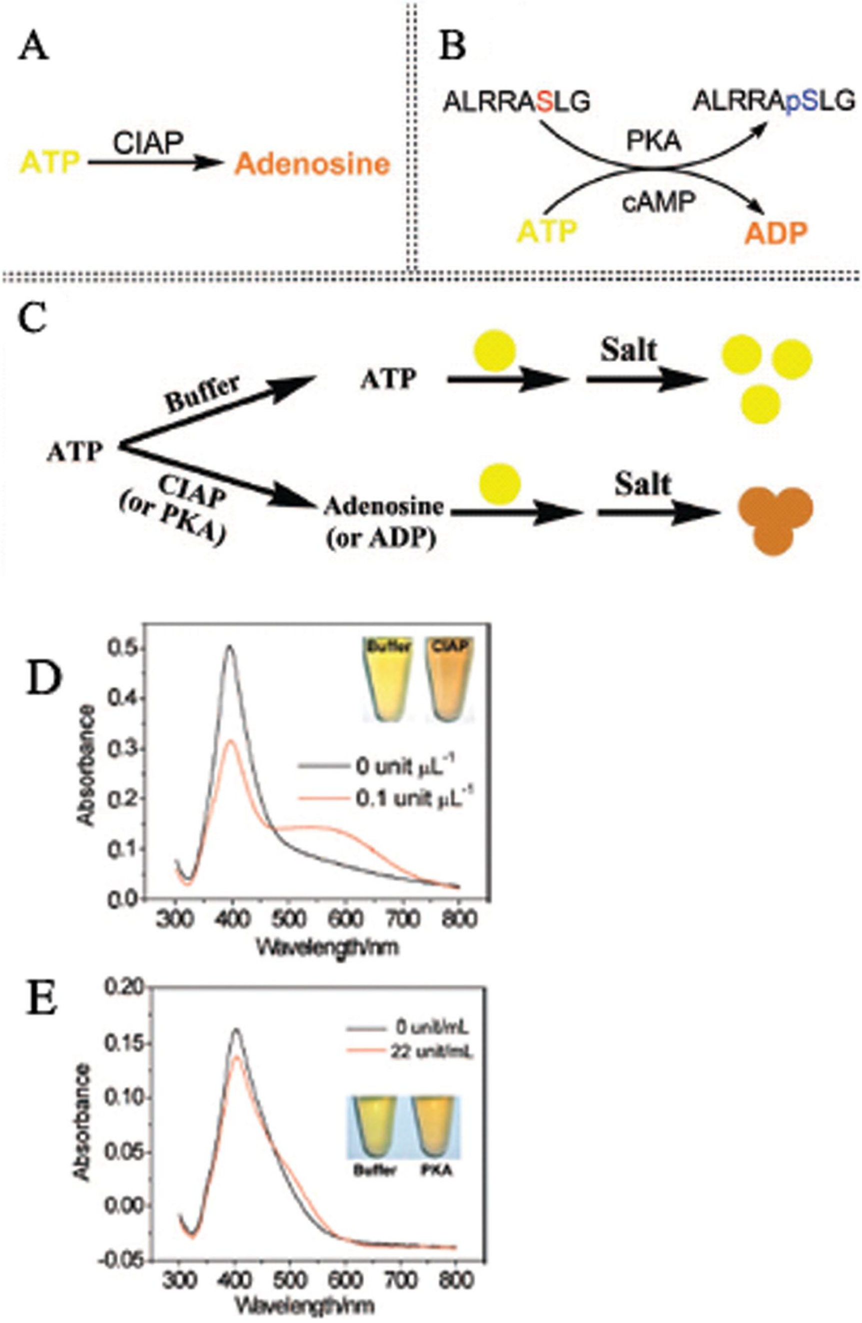

Figure 6. The enzymatic reactions with CIAP (A) and PKA (B), schematic illustration of AgNPs-based enzyme colorimetric assay (C), and colorimetric detection of CIAP (D) and PKA (E). Reproduced with permission from reference (69). Copyright 2008 American Chemical Society.

Without resorting to the recognition ability of DNA, AuNPs or AgNPs can also act as optical probes in the bioanalysis. The Li and Brook group reported the colorimetric enzyme sensing using unmodified AuNPs, based on that the highly charged nucleoside ATP could stabilize the AuNPs while the uncharged nucleoside adenosine could induce nanoparticles aggregation (*68*). Taking advantage of the enzymatic reaction to convert ATP into adenosine, the specific enzyme and its inhibitor could be analyzed. The Wang group achieved enzyme colorimetric assay using unmodified AgNPs, through the finding that ATP could protect AgNPs from salt-induced aggregation while the enzymatic reaction products adenosine or ADP could not; two enzymes corresponding to the products and one inhibitor could be detected (Figure 6) (*69*). The Xing group presented a colorimetric assay for *β*-lactamase and the screening for its inhibitors using unmodified AgNPs and AuNPs (*70*); the *β*-lactam ring opening in the presence of enzymes generated the fragment containing thiol and positively charged amino groups, which could replace citrate ions on nanoparticles and induce the aggregation. The Ren group reported the colorimetric detection of dopamine using unmodified AgNPs; dopamine could adsorb onto AgNPs via the Ag-catechol interaction, displacing the coated citrate ions and neutralizing the surface charge, eventually leading to the nanoparticles aggregation (*71*). The Li group synthesized positively charged AuNPs stabilized by cysteamine and achieved the visual detection of heparin, by means of the electrostatic attraction between the positively charged AuNPs and polyanionic heparin, which led to the nanoparticles aggregation due to charge neutralization (*72*). The same group further demonstrated the nuclease assay by using such positively charged AuNPs (*73*); the longer single-stranded DNA carrying more negative charge sites could induce the nanoparticles aggregation while the cleaved shorter fragments only produce insignificant aggregation. The Ye group synthesized UTP-stabilized AgNPs and utilized them to distinguish the chirality of cysteine (*74*); the aggregation of AgNPs induced by D-cysteine was much more sensitive than by L-cysteine by at least 2 orders of magnitude. The work from Ref. (*68*) to Ref. (*74*) can be considered as the direct use of the as-prepared AuNPs and AgNPs to perform assay. After the modification of nanoparticles with bio-recognition units, analytes interacting specially with the recognition unit can be detected through the optical probes. The Lu group functionalized 1-(2-mercaptoethyl)-1,3,5-triazinane-2,4,6-trione (MTT) onto AuNPs and achieved the analysis of melamine in raw milk and infant formula (*75*); the hydrogen-bonding between MTT and melamine would glue MTT-modified AuNPs together to form aggregates. The Yang and Zhang group reported the colorimetric detection of a peptide fragment from neurogenin3 using the anti-neurogenin3 antibody functionalized AuNPs (*76*); the binding of the positively charged peptide to the negatively charged AuNPs would neutralize the surface charge and induce the nanoparticles aggregation after salt-addition. The same group further demonstrated the analysis of a peptide fragment from neurogenin1 by using the anti-neurogenin1 antibody conjugated AgNPs (*77*); the binding of the negatively charged peptide to the likely charged AgNPs would increase the charge density of nanoparticles and enhance their stability to resist salt-induced aggregation. The Sreenivasan group immobilized glucose oxidase on AuNPs and achieved the colorimetric detection of glucose in urine (*78*);

glucose was oxidized to gluconic acid by the immobilized glucose oxidase, and the resulted H^+ ions brought down the net negative charge of nanoparticles, leading to their aggregation.

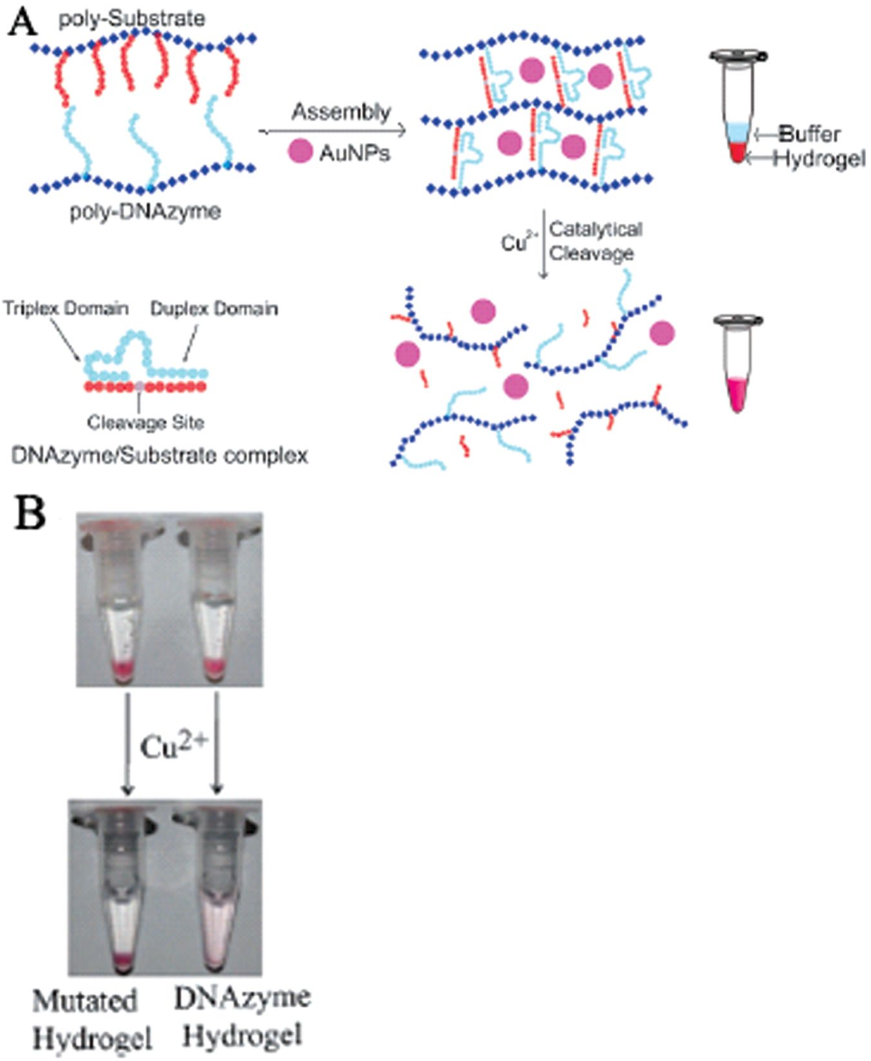
A
poly-Substrate
poly-DNAzyme
Assembly
AuNPs
Buffer
Hydrogel
Cu2+
Catalytical Cleavage
Triplex Domain
Duplex Domain
Cleavage Site
DNAzyme/Substrate complex
B
Cu2+
Mutated Hydrogel
DNAzyme Hydrogel

Figure 7. Schematic illustration of Cu^{2+} detection using AuNPs and Cu^{2+}-responsive DNAzyme crosslinked hydrogel (A) and the photographs of hydrogel dissolution to release the trapped AuNPs in the presence of Cu^{2+} and the Cu^{2+}-dependent DNAzyme (B). Reproduced with permission from reference (83). Copyright 2011 Royal Society of Chemistry.

Besides the utilization of the distinct color between the dispersed and aggregated AuNPs or AgNPs, two other properties of such noble metal nanoparticles can be used to generate the absorbance signal. The first one is to utilize nanoparticles' own intense color. As long as AuNPs or AgNPs are present, the corresponding color they display can be visualized or monitored. The Ioannou and Christopoulos group developed an AuNPs-based DNA assay in a dry-reagent strip (*79*). The biotinylated target would be attached to the AuNPs via an intermediate DNA hybridization and be captured through the loaded streptavidin in the test zone, giving a red line; the excess AuNPs would be captured in the control zone through DNA hybridization and gave a second red band to indicate that the strip-test worked properly. The Lu group designed a lateral flow device through immobilizing the adenosine or cocaine aptamer-linked AuNPs aggregates to achieve the "dipstick" test, via the observation of a red line in the membrane (*80*). The presence of targets would dissemble the aggregates due to the formation of aptamer-target complexes, and the dispersed nanoparticles could migrate along the membrane and be captured through the biotin-streptavidin interaction to form the red line; whereas the aggregated nanoparticles in the absence of targets could not migrate due to their large size and the red line could not be observed. The same group further detected Pb^{2+} ions by using the non-cross-linked AuNP-DNAzyme conjugates in the dipstick tests (*81*). The dispersed DNA-functionalized AuNPs could migrate both in the absence or presence of Pb^{2+}. The substrate strand would remain uncleaved in the absence of Pb^{2+} and AuNPs could be captured in the control zone through the interaction between the applied streptavidin and the biotin group terminated in the substrate strand, producing a red line in the control zone; while the substrate strand would be cleaved in the presence of Pb^{2+} and AuNPs would proceed to migrate and be captured in the test zone via the hybridization between the applied complementary sequences and the immobilized DNA on AuNPs, yielding a red line in the test zone. The Yang and Tan group achieved the detection of cocaine through the trapped AuNPs within the gel or released ones in the whole solution (*82*). Two pieces of DNA were grafted onto linear polyacrylamide polymers and the polymers would be cross-linked to transform into a gel after the addition of the linker DNA containing aptamer sequences, in which case AuNPs were trapped inside the gel with the upper solution layer appearing colorless; while the presence of cocaine would dehybridize the DNA duplex due to the formation of aptamer-target complex and induce the dissolution of the gel, in which case AuNPs were released and the whole solution became intense red. The same group further achieved the analysis of Cu^{2+} using AuNPs and DNAzyme crosslinked hydrogel (Figure 7) (*83*); the linear polyacrylamide would be cross-linked into a hydrogel through the hybridization between grafted enzyme strand and substrate strand. However, the addition of Cu^{2+} cleaved the substrate strand and dissociated the polymers, leading to the transformation of the gel into liquid form. AuNPs were used therein as colorimetric indicators to visually observe the gel formation or dissolution. The Liu group utilized AuNPs and DNA-functionalized monolithic hydrogels to perform the DNA detection (*84*); the probe DNA was covalently attached to the gel and the reporter DNA immobilized on AuNPs would be linked to the hydrogel surface in the presence of target DNA via the sandwich hybridization, producing a red color on the gel surface. The Ye and Tan group utilized AuNPs and aptamer-crosslinked hydrogels to develop logic gates, with the red color of the buffer solution defined as the true output (*85*). In the "AND" logic gate only the presence of both targets could dehybridize the Y-shaped DNA interconnects and led to the hydrogel dissolution, releasing AuNPs to the solution to display red; while in the "OR" logic gate the presence of either one target could break the sandwich type of linkages, disrupting the gel to release AuNPs. The Li group developed the direct detection of β-agonists using AuNPs-based colorimetric assay (*86*); β-agonists would directly reduce $HAuCl_4$ to atomic gold which formed AuNPs spontaneously, resulting in a red color and a strong absorbance at 528 nm.

The second one is to use the catalytic properties of noble metal nanoparticles to generate absorbance signal. The Higuchi and Chen group prepared DNA aptamers carrying Pt nanoparticles and exploited their use in the colorimetric sensing of thrombin and anti-thrombin antibodies (*87*). The DNA/Pt complexes possessed peroxidase enzymatic activity and retained the specific binding ability of the aptamers, and thrombin and anti-thrombin antibodies could be detected through the construction of the sandwich type and competitive type assay, respectively, by using the thrombin-binding aptamer/Pt complex to recognize thrombin and to react with 3,3',5,5'-tetramethylbenzidine (TMB) to generate absorbance. The Li group reported the hydrogen peroxide and glucose detection by taking positively-charged AuNPs as a peroxidase mimic (*88*); positively charged AuNPs possessed intrinsic peroxidase-like activity, catalyzing the oxidation TMB by H_2O_2 to produce a blue color, which could be used to sense H_2O_2 and glucose. The Fan and Li group demonstrated the nanoplasmonic detection of DNA hybridization using the catalytic activity of AuNPs (*89*). AuNPs were found to exhibit glucose oxidase-like activity and such an activity was extremely sensitive to surface properties; single-stranded DNA could adsorb strongly onto AuNPs and resulted in the suppressed enzyme-like activity, while the formed double-stranded duplex in the presence of target sequences bound weakly to AuNPs and had slight influence on the catalytic activity. The generated H_2O_2 through the AuNPs-catalyzed glucose oxidation was further evaluated by its cascade reaction with 2,2'-azino-bis(3-ethylbenzothiazoline-6-sulfonic acid) ($ABTS^{2-}$) in the presence of horseradish peroxidase, to obtain an absorbance dependent on target DNA.

Electrochemical Analysis

Recently, NMNs-based electrochemical detection for bioanalysis has drawn great attention, due to their merits of high surface area, high mechanical strength, rich electronic properties and excellent chemical and thermal stability (*90*, *91*). In addition, they also exhibit excellent biocatalytic activities and biocompatibility with biological components. Among them, AuNPs are the most attractive candidates for electrochemical systems due to the relatively low cost and ease of preparation (*92*). Hence, we will focus on the recent advances in AuNPs based biosensor systems, which include the enhanced detection in conventional electrochemical system and the promoted analysis in ECL system. The applications of other metal NPs will be excluded in this part.

The field of enzymatic biosensors has been expanding significantly with the evolution of nanostructures for electrode preparation with the utilization of several redox enzymes (*93*). Many efforts have been made to improve the electrochemical signal for the purpose of biosensing using nanostructured thin films (*94*). AuNPs can served as promoters to electron transfer from biological molecules to electrode surfaces, and NPs/protein conjugates are assembled on the electrode via simple self-assembly technology to fabricate the third generation NPs-based biosensors. Typically, Dong's group has developed a novel method to construct a third-generation horse radish peroxidase (HRP) biosensor by self-assembling AuNPs into three-dimensional sol–gel network, which exhibited the electrochemical behavior toward H_2O_2 detection (linear range of 0.005-10 mM) (*95*). Later, this procedure was extended by Raj et al (*96*).

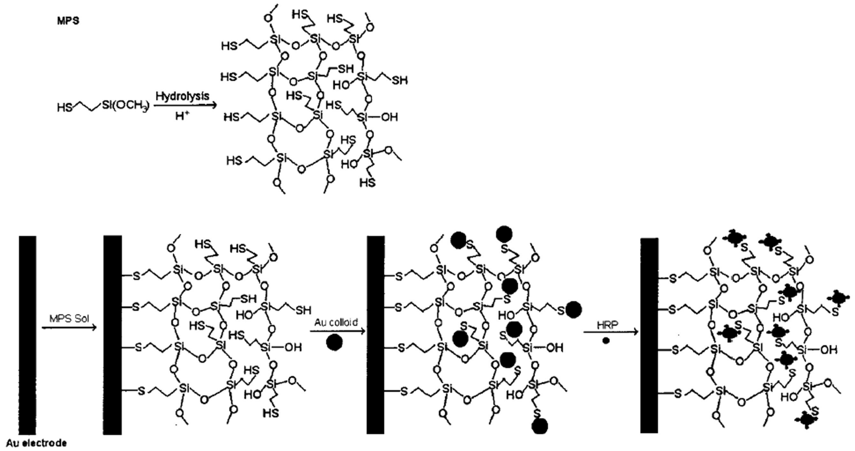

Figure 8. Hydrolysis of MPS and the Stepwise Biosensor Fabrication Process. Reproduced with permission from reference (95). Copyright 2002 American Chemical Society.

Figure 8 shows the preparation process of the biosensor (*95*). First, the gold electrode was modified with three-dimensional matrix by treatment with hydrolyzed (3-mercaptopropyl)-trimethoxysilane (MPS), then AuNPs were infiltrated into the matrix by forming Au-S covalent linkage. Finally, HRP was introduced into the electrode surface by electrostatic attraction between negatively charged AuNPs and positively charged HRP.

Besides this common used self-assembly method, the layer-by-layer (LBL) technique is also an efficient procedure to fabricate functional electrochemical sensing interfaces, in which redox proteins are used as the "glue molecules" (*97*). As a versatile route, many kinds of materials can be selected as building blocks (polyelectrolytes, conducting polymers, clays, carbon-based materials, biological molecules, et al.). For example, to develop more sensitive glucose sensors for medical application, Hu et al. described that dendrimer-protected AuNPs and Mb were alternately adsorbed on the surface of pyrolytic graphite (PG) electrodes (*98*). The prepared biosensors exhibited good electrochemical behavior and catalytic performances. Ju et al. reported a novel multilayer membrane with AuNPs, multi-walled carbon nanotubes (MWCNTs) and glucose oxidase (*99*). Excellent electrocatalytic character for glucose biosensing at a low potential was detected. The resultant sensor could detect glucose up to 9.0 mM with a LOD of 128 μM.

Another effective method for creating a favorable AuNPs modified biosensing interface is electrochemical deposition (*100*). Compared with above mentioned route, this process is simpler and quicker under moderate conditions. Typical instances include the direct electrodeposition of AuNPs on planar gold electrode and the direct electrodeposition of CHIT-oxidase-AuNPs hybrid (*101*, *102*).

In fact, with the advancement of material science, other components are also introduced to cooperate with AuNPs and bioactive enzymes to improve the sensitivity, stability and reproducibility. For example, an Au-$CaCO_3$ hybrid material was demonstrated as a promising template for enzyme immobilization which exhibited satisfactory biocompatibility and improved properties (*103*). The biosensor exhibited a fast amperometric response to H_2O_2 (linear range $4\text{-}8\times10^{-5}$ M with a LOD of 1×10^{-6} M at S/N=3). Several polyelectrolytes and conducting polymers were also used as a composite to facilitate enzyme immobilization (*104*). Most recently, with the development of carbon material, novel carbon-based materials (carbon nanotubes, carbon nanohorn and graphene) have been used to co-modify the electrode interface (*105–107*).

The other attractive approach is the nonenzymatic electrochemical approach, in which the electrocatalysts (Prussian blue (PB), metal oxide, Heteropoly Acid (HPA)) or some mimetic enzyme is responsible for its direct detection. Compared with the enzymatic route, several advantages are presented, for instance, the synthesis and storage of the sensors is simplified and the tolerance to environmental conditions is improved as no enzyme attachment/deactivation is involved. Several groups have demonstrated their successful work via this method. For example, our group has reported a PB@Pt NPs/CNT hybrid for efficient determination of H_2O_2 (*108*). With the synthetic effects of MnO_2 and AuNPs, another amperometric sensor for H_2O_2 was fabricated, which exhibited a wide linear range from 7.80×10^{-7} to 8.36×10^{-4}M with a detection limit of 4.68×10^{-8} M (*109*). In addition, its application in real samples (toothpastes) has obtained a satisfactory result.

Besides the biosensors mentioned above, AuNPs have been functionalized as sensors for the detection of dopamine (DA) (*110*), uric acid (UA), ascorbic acid (AA) (*111*), bilirubin (*112*), hemoglobin (Hb) (*113*), tryptophan (*114*), cytochrome c (*115*), et al. Compared to standard analytical techniques, these modified electrodes display desirable results, with a marked enhancement in response, fast response, long-term stability and reproducibility. However, this area is still on the horizon from the viewpoint of practical applications. There is still a great need to design and fabricate multi-functional nanosystems for effectively loading enzymes or electrocatalysts and to construct the corresponding electrochemical biosensors.

Great efforts have been paid to developing genosensors with many detection techniques. Compared with conventional methods (fluorescent, chemiluminescent and colorimetric signals), combining electrochemical techniques with NPs has proved to be an effective method for exploring DNA sensors with simple and cheap instruments. Despite the intensive reviews on the electrochemical DNA sensors using AuNPs by the groups of Wang and Merkoci (*116–118*), here we just make a brief summary of recent advances on it.

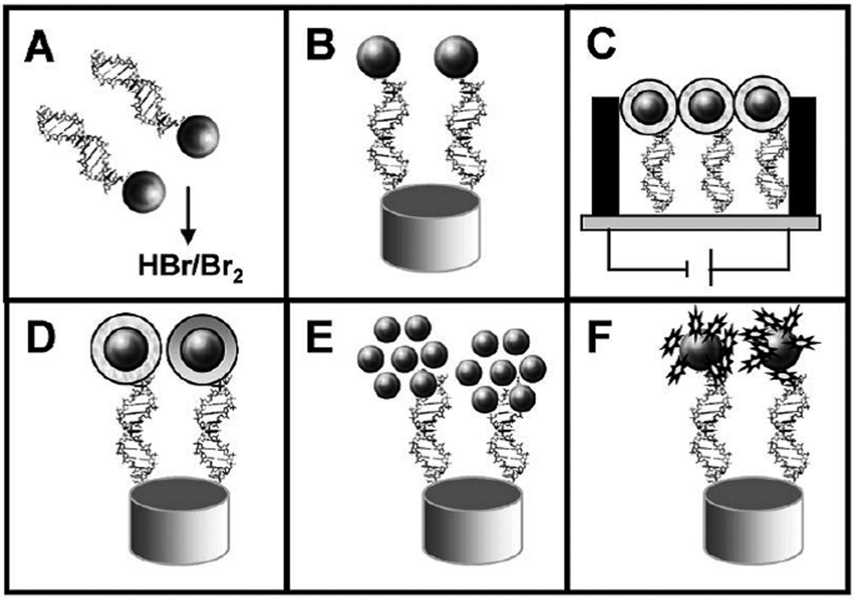

Figure 9. Schematic of the different strategies used for the integration of AuNPs into DNA sensing systems: (A) Previous dissolving of AuNP by using HBr/Br$_2$ mixture followed by Au(III) ions detection; (B) direct detection of AuNPs anchored onto the surface of the genosensor; (C) conductometric detection, (D) enhancement with silver or gold followed by detection; (E) AuNPs as carriers of other AuNPs; (F) AuNPs as carriers of other electroactive labels. Reproduced with permission from reference (116). Copyright 2007 WILEY-VCH Verlag GmbH & Co. KGaA.

As shown in Figure 9 (*116*), six important strategies have been introduced to integrate AuNPs in DNA sensing systems. In view of their functions, AuNPs acted as DNA attachment or signal amplifiers. Here we just focused on the direct detection of DNA that incorporated AuNPs as either signal amplifiers (transducer) or electroactive species. Recently, with the chemical adsporption of 1, 6-hexanedithiol, AuNPs were successfully modified on a gold electrode (*119*). When it was immerged into a mixture solution of DNA and daunomycin, it exhibited a DNA detection limit at the nanomolar level, proved to be one of the most sensitive and convenient approaches. Yang et al. and Zhang et al. described electrochemically entrapment of ssDNA molecules in a polymeric film, which enhanced the molecular loading and stability (*120*, *121*). Then AuNPs were introduced to promote the electron transfer reactions on electrode surfaces for DNA sensing. In addition, by using AuNPs as catalytic labels, a sandwich-type electrochemical sensor was fabricated to achieve ultrasensitive DNA detection, in which the high signal amplification and low background enabled the detection limit to 1 fM of target DNA (*122*). Furthermore, to enhance the sensitivity and the selectivity, MWCNTs were used to help AuNPs to immobilize DNA probes. The final sensor presented a detection limit in fM range, a good stability and reproducibility (*123*). Other inorganic materials were also integrated into the DNA sensing system besides the materials mentioned above. For example, CdS NPs modified AuNPs were applied to amplify the detection signal by an amidation reaction between bio-bar codes binding DNA on the surface of AuNPs and mercapto acetic acid on the surface of CdS NPs (*124*). The sensor exhibited excellent performance in concentration range from 1.01×10^{-14} to 1.0×10^{-13} M with a detection limit of 4.2×10^{-15} M of target DNA. In summary, to further improve the sensitivity and selectivity, greater efforts on preparing multifunctional hybrid materials and designing more sensitive strategies are needed.

Due to their practical applications in food industry, clinical diagnose and environmental protection, immunosensors have been paid much attention. Among the developed immunosensors, electrochemical biosensors provide simple, inexpensive and yet accurate platforms for selective targets detection. With the introduction of NPs, the high sensitivity in biological assays has been approved. Since several recent reviews have summarized the use of Metal-NP-based electrochemical detection for immunoassay applications (*125*, *126*), here we simply want to describe some recent advances in it.

With the concept of hybridation, enzyme-labeled immunosensors were well developed. For the sensitive detection of target antigen, HRP-labeled antibodies (HRP-Abs) were conjugated to AuNPs modified electrodes. For example, with the functionalization, the AuNPs/CNTs modified electrode exhibited a fast amperometric response to human Ig G (linear range 0.125-80 ng mL^{-1} with a LOD of 40 pg mL^{-1}) (*127*). With the aid of conducting polymer (poly-terthiophene carboxylic acid, poly-TTCA) and covalently bonded dendrimer, the modified AuNPs/GCE electrodes were used to diagnose lung cancer at the pg mL^{-1} level (*128*). In addition, using a sandwich-type format, the sensitivity of the electrochemical immunosensors can be enhanced by AuNPs labeled detection. Typically, after the immobilization of hepatitis B surface antibody (HBsAb) on AuNP/thionine/DNA-modified gold electrodes, a low detection limit of HBs Ag at pg mL^{-1} level was observed with the aid of AuNPs modified HRP-HBsAb (the secondary antibodies) (*129*).

Figure 10 demonstrates the scheme of the stepwise fabrication process. Similar enhancement was reported for alpha-fetoprotein (AFP) sensor, in which HRP polyclonal anti-human-AFP Ab were used as the secondary antibodies (*130*). Besides the sandwich-type sensors, a competitive strategy can be used for immunoassay. In this case, a detection limit of 0.6 ng mL^{-1} was found for AFP analysis with a CNT–AuNP-doped CS film (*131*).

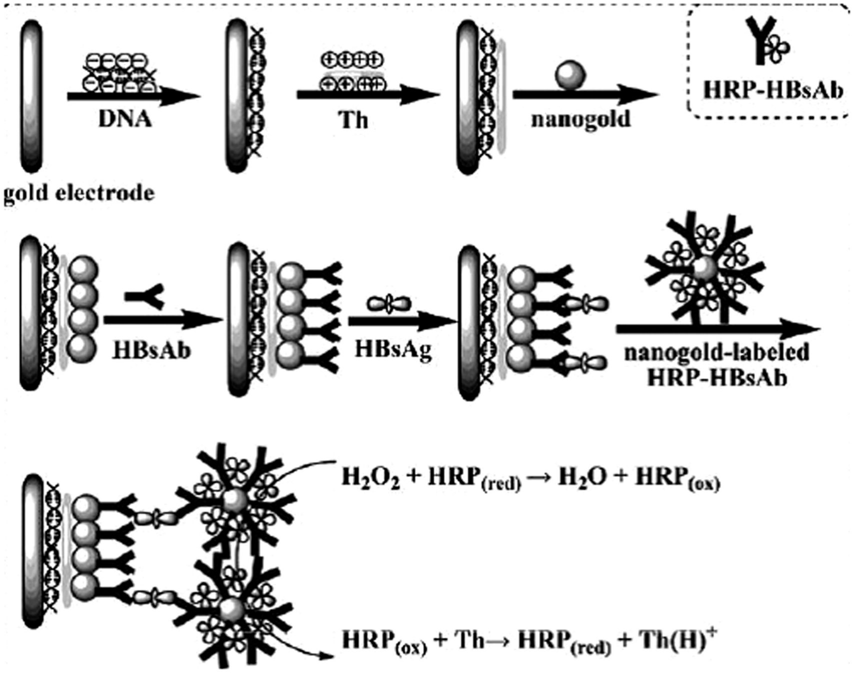
DNA
Th
nanogold
HRP-HBsAb
gold electrode
HBsAb
HBsAg
nanogold-labeled
HRP-HBsAb
$H_2O_2 + HRP_{(red)} \rightarrow H_2O + HRP_{(ox)}$
$HRP_{(ox)} + Th \rightarrow HRP_{(red)} + Th(H)^+$

Figure 10. Fabrication process of the electrochemical immunosensor and the pathway of electron transfer. Reproduced with permission from reference (129). Copyright 2009 Springer.

Alternatively, label-free electrochemical immunosensors have also been intensively researched because of their simplicity, speedy analysis and high sensitivity, in which AuNPs acted as amplifier for more sensitive sensor. Recently, using the amine-Au affinity, Shen group described a successful assembly between surface confined AuNPs and antibodies in a great amount (*132*). The high immunological activity was still preserved for this sensor. Additionally, the composited structure of antibody embedded AuNPs and SiO_2/thionine nanocomposition can be employed for the detection of carcinoembryonic antigen (CEA) at the ng mL^{-1} level (*133*). Furthermore, after the covalent attachment with Anti-CEA Abs, glutathione modified AuNPs were immobilization on Au electrodes by electro-copolymerization of o-aminophenol (*134*). The immuonsensor could detect the CEA with a detection limit of 0.1 ng mL^{-1} and a linear range of 0.5–20 ng mL^{-1}. Similarly, for the detection of AFP sensitively, AuNPs were functionalized with 1,1-bis-(2-mercapto)-4,4-bipyridinium dibromide, a kind of sulhydrylviologen (SV) (*135*). The fabricated immunosensors exhibited a broad linear range of 1.25–200 ng mL^{-1} and a LOD of 0.23 ng mL^{-1}.

Aptamers have exhibited potentials in recognizing and detecting various targets, which are produced though a process known as systematic evolution of ligands by exponential enrichment (SELEX) (*136*). They present some advantages over the traditional antibodies besides their comparable affinities and specificities,. For example, aptamers can be produced in mass due to their accurate chemical components. In addition, aptamers are more stable than antibodies, especially in extreme conditions. Furthermore, undergoing reversible denaturations, aptamers can be modified by attachment of new functional groups easily. Because of these predominant characters, they are widely used as recognition elements in biosensors, which have been named as aptasensors. Typically, since the first report in 2004 (*137*), electrochemical aptasensors have attracted a great attention, due to the merits of portability , low cost and easy operation. Considering the presence of several impressive reviews (*138–140*), we will introduce the roles of AuNPs in electrochemical aptasensors.

In 2007, He et al. reported an ultrasensitive label-free aptasensor for thrombin detection (*141*). After the capture by immobilized antibodies on micro-titer plates, thrombin were detected by aptamers modified AuNPs. Because the NP carried a large number of aptamers per thrombin binding event, the detection signals were amplified with a LOD of 0.1 ng mL^{-1}. In addition, Zhang et al. have demonstrated a “signal-on” aptasensor for cocaine, in which ferrrocene (Fc)-labeled thiolated aptamers were self-assembled on AuNPs (*142*). Upon cocaine binding, the conformation of the aptamers changed to hold the redox moieties in close proximity to the electrode. A detection limit of 0.5 mM and a wide linear range from 1 to 15 mM were obtained by SWV method. Regeneration can be achieved and good storage stability under a 15 day-period was also mentioned. Moreover, Wang et al reported an aptasensor for PDGF detection via sandwich frameworks, in which AuNPs were used to amplify the signal intensity and $Ru[(NH_3)_5Cl]^{2+}$ was selected as electrochemical probe (*143*). This approach obtained achieved an extraordinarily low detection limit of 1×10^{-14} M for purified samples, and 1×10^{-12} M for contaminated-ridden samples or undiluted blood serum. Similarly, a reusable “signal-off” aptasensor for adenosine detection has also been described (*144*). Thiolated capture DNA probes were self assembled on a gold NPs covered gold surface before partial hybridization with Fc-labeled aptamer probes. Upon adenosine binding, displacement of the Fc-labeled aptamers resulted in a decrease in signal current. This approach exhibited a detection limit of 20 nM and a linear range extended from 100 nM to 10 mM. Regeneration can be performed via a simple dehybridization in hot water.

Besides the amperometric aptasensors, detections based on electrochemical impedance spectroscopy (EIS) are the other attractive approach. For example, to improve the sensitivity for thrombin detection, several strategies have been proposed by different groups. Li et al. developed a simple and sensitive EIS aptasensor via the self assemble of thiolated apatamer on electrodeposited AuNPs on GCE (*145*). A linear range from 0.12 to 30 nM and a LOD of 0.03 nM was obtained for thrombin. Moreover, to improve the detection sensitivity, a sandwich sensing platform based on rhodamine 6G (R6G) functionalized AuNPs was described (*146*). The aptamers labeled AuNPs are negatively charged, which increase the interfacial electron transfer resistance in the presence of $Fe(CN)_6^{3-/4-}$.

The presence of R6G not only improved the signal but also allowed surface enhanced Raman Scattering (SERS) detection to be performed. To further improve the detection sensitivity, a three-level cascaded signal amplication was developed by Yu group, in which aptamers labeled AuNPs (Apt-AuNPs) was the first-level signal enhancement, the steric-hindrance between the enlarged Apt-AuNPs was the second-level signal amplification and the electrostatic repulsion between sodium dodecylsulfate and electrochemical probe acted as the third amplication (*147*). The prepared aptasensor presented a wide detection range from 100 fM to 100 nM for thrombin. This approach not only improved the detection sensitivity but also realized a simple and general model for signal application in EIS analysis.

Electrochemiluminescence (also called Electrogenerated chemiluminescence, ECL) is chemiluminescence triggered by electrochemical methods. ECL biosensors have attracted a great attention due to the characteristic advantages of ECL and the selectivity of the biological recognition elements. Since several critical reviews have been reported (*148*, *149*), we will give some typical examples to discover the roles of AuNPs in ECL biosensors.

Due to their excellent biocompatibility and good electron conductivity, AuNPs have been utilized to modify the electrodes. For example, Dong's group has proposed a self-assemble strategy to immobilize alcohol dehydrogenase (ADH) and ruthenium (II) tris(bipyridine) ($Ru(bpy)_3^{2+}$) to negatively charged AuNPs (*150*). Such biosensors exhibited high selectivity and sensitivity. In addition, AuNPs were used as tiny conduction centers to facilitate electron transfer. Wang et al. developed an ECL biosensor for biological substance (bovine serum albumin (BSA), and immunoglobulin (Ig G)). An AuNPs layer was first combined into the surface of the 2-mm-diameter gold electrode to increase the electrode area as well as the immobilized recognition elements (*151*). With AuNPs amplification, the ECL peak intensity was proportional to the concentration over the range 1-80 and 5-100 μg mL^{-1} for BSA and IgG consuming 50 μL of sample, respectively. A 10- and 6-fold sensitivity enhancements were obtained for BSA and IgG over their direct immobilization. Similar idea has been explored to DNA hybridization. With the enhancement in sensitivity, the detection limit of target ssDNA (6.7×10^{-12} M) is much lower than that on bare electrode (*152*).

Another important issue about AuNPs is their catalytic effects on ECL. Typically, Cui et al. have discovered that AuNPs modified electrode could generate strong luminol ECL signals, due to the catalytic effects (*153–155*). The biocompatibility of AuNPs and the enhanced ECL intensity entailed them with potential applications in biosensors. For example, they have developed a sandwich-type immunosensor for human Ig G with N-(aminobutyl)-N-ethylisoluminol (ABEI) labeling (*156*). This approach exhibited a linear range extending from 5.0 ng mL^1 to 100 ng mL^{-1} and a detection limit of 1.68 ng mL^{-1}. It has been successfully applied to the detection of hIgG in human serums. Homogeneous ECL immunoassay for human Ig G has also been developed using ABEI as labels at AuNPs modified paraffin-impregnated graphite electrode (PIGE) (*157*). Due to the formation of a rigid structure of the ABEI moiety, the detection limit for human IgG was 10 pg mL^{-1}. Recently, Xu et al. developed an ECL glucose biosensor, in which GOD was adsorbed onto silica sol-gel network with the aid of AuNPs (*158*). A linear range extending from 1 μM to 5 mM was obtained with a detection limit of 0.2 μM glucose. Alternatively AuNPs have been also used as both quencher and enhancer in quantum dot's ECL research. More recently, a simple ECL sensing platform has been fabricated to detect target DNA (*159*). In this case, CdS:Mn QDs has been selected as luminophores. The ECL signals were quenched by AuNPs as a result of fluorescence resonance energy transfer (FRET) phenomena. If the target hybridization took place, the ECL intensity would be enhanced by the surface plasmon resonances of AuNPs. In this proposal, a detection limit of 50 aM for target DNA was obtained.

AuNPs also can be used as ECL carriers for ECL probes. For example, $Ru(bpy)_3^{2+}$ -AuNPs aggregates have been synthesized via electrostatic interactions (*160*). The as-prepared aggregates were attached on ITO electrode for application in capillary electrophoresis or a CE microchip. Alternatively, Fang et al. described a controllable solid-state ECL film based on efficient quenching of ECL by oxidizing ferrocene labeled molecular beacon (*161*). The ECL intensity varied with the conformation change induced by the complementary DNA hybridization. More recently, the Yang group also introduced an assembly technique to immobile $Ru(bpy)_3^{2+}$, in which luminescent dyes was entrapped in silica and some functional NPs (Au, Fe_3O_4) were coated via electrostatic interaction (*162*). This approach provided a simple and effective method for electrode functionalization.

With the occurrence of aptamers, several ECL aptasensors have also been explored. For example, an ECL apatasensor has been developed for the detection of thrombin, in which a sandwich framework was fabricated with the AuNPs amplification (*163*). AuNPs labeled capture apatmers were immobilized onto thiolated ITO surfaces through Au-S bonds. After catching thrombin, the secondary signal apatamers labeled with luminescent $Ru(bpy)_3^{2+}$ were attached. With the presence of TPA, the detection limit was estimated to be 10 nM. Such aptasensor opened up a highly sensitive technique especially for application in microarray analysis. Beside this, combining with the signal amplification ability of AuNPs, a novel [$Ru(bpy)_2(dcbpy)NHS$] labeling/aptamer-based biosensor has been constructed for the determination of lysozyme (*164*). Another "signal off" aptasensor has also been fabricated on the basis of the displacement of ECL probe by Zhang et al (*165*). This approach exhibited a detection limit of 1.0 fM with high specificity.

Fluorescent Analysis

Fluorescence spectroscopy is a classical electromagnetic detection method which analyzes the spontaneous radiative decay of electronically excited molecules. It is widely applied in biochemical, medical and chemical research fields for analyzing various bimolecular compounds. Recently, the progress in the synthesis of NMNs with controlled morphologies or attractive properties has significantly impacted the development of fluorescence biomolecular analysis (*166–171*). NMNs, especially Au nanoparticles, can conjugated with biomolecules and retain their inherent biochemical activities, making NMNs ideal tools for several bio-analytical applications (*172*). Herein, we briefly introduce some related works concerning the preparation of fluorescent active NMNs and their applications in bio-analysis.

In 1994 , Brust & Schiffrin reported a method for the synthesis of thiol-derivatized gold nanoparticles in a two-phase liquid-liquid system (*173*). $AuCl^{4-}$ was transferred to toluene using tetraoctylammonium bromide as the phase-transfer reagent and reduced by $NaBH_4$ in the presence of dodecanethiol. This report has a profound impact on the future development of fluorescence based analysis. Because the as-prepared Au clusters provides impresive stability and monochromaticity, especially in comparison with the conventional organic dye molecular. Besides, thiol protected gold clusters, or other similar thiol-protected clusters, also provide well-defined excitation and emission spectra in contrast to larger semiconductor nanocrystals. The sample can be obtained in a relative facile manner which requires neither complicated high temperature syntheses with toxic precursors, nor tedious overcoating procedures (*174*). NMNs thus can serve as promising fluorescent probes in various biochemical fields (*175*). However, the fluorescence quantum efficiency of thiol-protected clusters is only around 10^{-4} at early stage. Such unfavorable factor severely limits their practical applications (*176*, *177*).

In 2003, Ag and Au nanodots with much higher fluorescence quantum yields were prepared by Dickson's group through biocompatible poly(amidoamine) dendrimer hosts. The strong size-dependent blue emission from these monodisperse Au nanodots was measured to be 41% ± 5%, in aqueous solution (*178*, *179*). After that, they prepared water-soluble Au quantum dots which behaved as multielectron artificial atoms with discrete, size-tunable electronic transitions throughout the visible and near IR (*180*). Recently, more high quality NMNs were manufactured by using DNA (*181*, *182*), oligonucleotide (*183*), cyclodextrin (*184*), peptide (*185*), protein (*186–188*) and polymer (*189*, *190*) as the templates .

Due to the excellent photo quenching (or photo enhancement) properties of noble nanoparticles, the sensitivity of fluorescence-based assays can be considerably increased (*191–197*). On the other hand, the selectivity of the fluorescence assessment can also be improved by utilizing the high selective binding affinity of different aptamer toward the target analyte (*198–201*). Based on these mechanisms, several noble metal NCs have been utilized as a new class of fluorescence detectors (*202*). For instance, Dong's group presented two sensitive cysteine assessment methods by using fluorescent conjugated polymer-stabilized gold nanoprobe (*203*) or water-soluble fluorescent Ag clusters (*204*), respectively. Later, they developed a near-infrared fluorescent dye (FR 730) protected AuNPs for sensitive detection of biological thiols. The entire detection process could be applied in a complex multicomponent mixture, such as human plasma, and had great potential for diagnostic purposes (*205*). Bai et al. described a fluorescence resonance energy transfer (FRET) system to identify molecules that stabilize G-quadruplexes. Unmodified Au nanoparticles was directly used here as a fluorescence quencher. This study provided a simple, sensitive, and reliable method to identify ligands with potential anticancer activity (*206*). Fan's group also has carried out a series of quantitative investigations on the detection of biomolecules (*207*). For instance, they prepared a multicolor fluorescent gold nanoprobe, which combines the specific binding abilities of aptamers with the excellent quenching ability of gold nanoparticles (AuNPs). The as-prepared multicolor fluorescent gold nanoprobe could simultaneously detect adenosine, potassium ion, and cocaine with high selectivity (*208*).

Semiconductor quantum dots (QDs) have also been utilized for FRET-based NMNs assays. QD–Au nanoparticle DNA conjugates have been widely applied as DNA fluorogenic probes, which was suitable for the detection of simple structured DNA in various aqueous environments. Malvin et al. reported a fluorescent competitive assay for DNA identification using QDs and AuNPs. The emission of quantum dots was efficiently quenched by contact with gold nanoparticles through a hybridisation event using specially prepared DNA conjugates (*209*). Afterwards, Kim's group developed an enzyme inhibition assay method based on the modulation in the FRET efficiency between streptavidin coated QDs and biotinylated AuNPs. The detection limit for avidin was around 10 nM (*210*). Then, they used the similar method to recognize glycoproteins (*211*). These works exert marked influence on various fields, including material science, medical technology and analytical chemistry (*212–217*).

Highly specific genetic analysis is extremely important in a variety of biomedical applications (*218*). One popular sensing approach is to create FRET-based systems by using modified oligonucleotide−AuNP conjugates (Figure 11). Nie et al. applied colloidal gold nanocrystals as a biosensor which is able to detect specific DNA sequences and single-base mutations in a homogeneous format (*219*). This work has profound implications for the fluorescent analysis of DNA. Later, Krauss's group proved that gold membrane supported fluorophore-tagged DNA hairpins can be used as immobilized "molecular beacons". This investigation indicated that DNA hairpins immobilized on a gold surface can remain their selectivity to bind complementary DNA sequences (*220*). Rothberg's group exploited a DNA sequence detection system based on its electrostatic properties (*221*). Gold nanoparticle could also be applied to monitor the cleavage of DNA by nucleases (*222*). Last year, a systematical research was carried out by Borghs's group, who investigated various sized fluorescence quenching and enhancement near Au nanoparticles. Different lengths of fluorescently labeled hairpin DNA probes were employed in this study (*223*). Mirkin's group has also developed several high quality AuNP fluorescent strategies to recognize and quantify intracellular mRNA. This year, they described their latest progress in the use of multiplexed nanoflare, a nanoparticle agent that is capable of simultaneously detecting two distinct mRNA targets inside a living cell. During the detection, one of the mRNA targets can be used as an internal control, allowing researchers to determine more precisely relative mRNA levels in individual cellular environment (*224*, *225*).

Apart from AuNP probe, Wang's group synthesized highly sequence-dependent silver nanoclusters, which could be applied to identify single nucleotide mutation (*226*). Recently, they demostrated that Pd nanowires (NWs) could also be used as a new biosensing platform for high-sensitivity nucleic acid detection.

The basic idea is based on the absorption of dye-labeled DNA onto nanosized Pd can substantially quench the fluorescence of dye while the specific hybridize with the complementary region of the target DNA sequence can restore the fluorescence (*227*).

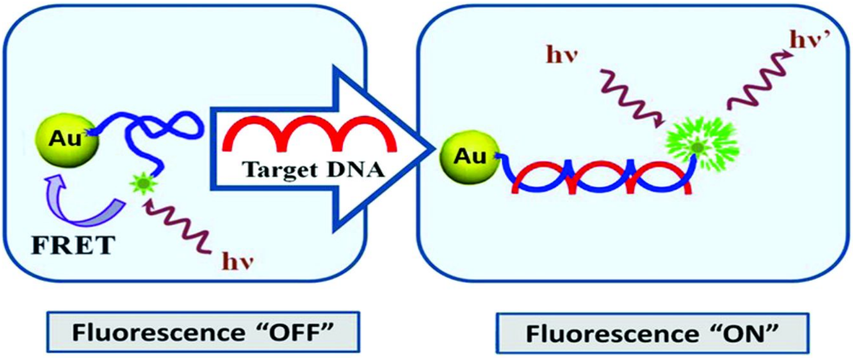

Figure 11. Schematic illustration of the DNA detection mechanism. The nucleic acid probe conjugated with the organic dye is self-complementary, forming a hairpin structured dye-oligonucleotide−AuNP conjugates with effective FRET fluorescence quenching. Such hairpin structure can be opened by the target DNA through complementary hybridization, coupled with a significant increase in fluorescence.

Mercapto biomolecules, such as cysteine, homocysteine and glutathione, are crucial factors for Alzheimer's disease and cardiovascular disease. Their selective detection is thus of interest in biomedical and bio-analytical research. On the basis of different aggregation kinetics, Tseng's group developed a fluorosurfactant (FSN)-capped gold nanoparticles for cysteine detection (*228*). In 2008, they used citrate-capped AuNPs modified with nonionic fluorosurfactant for selective detection of cysteine and homocysteine (*229*). One year later, they carried out a convenient method for the preparation of water-soluble fluorescent mannose-protected Au nanodots for the detection of Concanavalin A. Besides, the proposed Au nanodots system could be also used to detect *E. coli*. Incubation studies revealed that the Au nanodots could bind to the bacteria, resulting in brightly fluorescent cell clusters. Significant linear relationship (1.00×10^6 to 5.00×10^7) was observed between the fluorescence signal and the *E. coli* concentration (*230*). After that, they presented an upgraded detection system based on the combination of fluorosurfactant-capped gold nanoparticles and o-Phthaldialdehyde (*231*). By comparing the final fluorescent intensity, homocysteine could be detected with excellent sensitivity and selectivity. Although, the entire analytical process was a bit time-consuming and labor intensive, it was also true that their successive works have inspired a lot of papers in the task of fluorescent functional NMNs (*232–234*).

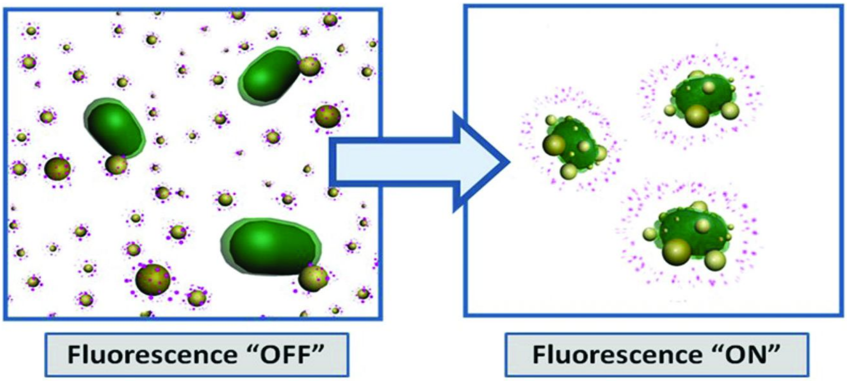

Figure 12. Schematic illustration of the fluorophore-displacement bacterial detection array. Cationic AuNPs (yellow particles) and anionic p-phenyleneethynylene (PPE, purplish red dots) polymer were used to generate the sensor. Presence of bacteria (Green Capsules) disrupts the initially quenched assemblies leading to fluorescence restoration of PPE. From the distinct fluorescence response patterns, the sensor array was capable of identifying different kinds of bacteria. Analogous AuNP-conjugated polymer systems can also be applied to detect and identify cells and proteins.

In the following, we would like to give a brief description of "chemical nose (tongue)", which is a new expanded concept of fluorescent recognition that employs several organized selective interactions to generate patterns, so as to monitor target analytes in complex mixtures (*235*, *236*). One good example of this idea is published by Rotello's group, who created a sensor array containing six non-covalent gold nanoparticle–fluorescent polymer conjugates to detect, identify and quantify protein targets. The presence of different proteins disrupts the nanoparticle–polymer interaction through competitive binding, resulting in distinct fluorescence response patterns. These patterns are highly repeatable and are characteristic for individual proteins at nanomolar concentrations. Those protein samples can even be quantitatively evaluated by linear discriminant analysis. Combined with ultraviolet measurements, the proposed approach has been successfully used to identify 52 unknown protein samples (seven different proteins) with an impressive accuracy (*237*). Analogous amino acid terminals functionalized water-soluble gold nanoparticles were fabricated to probe the effect of receptor surface on protein surface binding (*238*). Then, they manufactured a hybrid synthetic-biomolecule sensor that used arrays of green fluorescent protein and nanoparticles to detect proteins in human serum (*239*). Similar strategy can be also employed to detect bacteria (*240*) and mammalian cells (*241*) (Figure 12). In the future, the strategies of "chemical nose (tongue)" might be utilized as an upgraded alternative of gel electrophoresis that widely applied as a facile and powerful complement to the current biological and biomedical analysis (*242*).

In addition, AuNPs also have been widely used applied in biomedical imaging and diagnostic study, because of their ease of preparation, ready bioconjugation, high contrasts, flexible light absorption/scattering properties, and most importantly, excellent biocompatibilities (*243–246*). Several types of AuNPs, including nanoshells, nanorods and nanocages, have been prepared and applied as tracers and cellular trajectories (*247–250*).After appropriate surface modification, Au based nanostructures can also be used for subsequent treatment. For instance, Fe_3O_4@Au NPs have potential uses as a veratile contrast agent for MRI, CT, microwave-induced thermoacoustic, photoacoustic imaging and magnetomotive photoacoustic imaging (*251–254*). Apart from that, the excellent optical absorption properties of AuNPs making them attractive as photothermal agents for cancer therapy (*255*). In compared with the conventional cancer treatment, AuNPs based therapy is a promising noninvasive technique for target destruction of cancer cells with minimal physical sufurring. Along with the development of surface chemistry, more AuNPs based fluorescent agents with fascinating in-vivo properties will no doubt be explored in the near future, but meanwhile, the efficiency and long-term toxicity of these rising material must be systematically considered throughout the development process.

Conclusion and Outlook

In conclusion, NMNs based analytical method is definitely an attractive and promising approach for bio-analysis that has the advantages of rapidity, cheapness, sensitivity and selectivity. For absorption spectroscopic analysis, the distinct color between the dispersed and aggregated NMNs, their own intense color and their catalytic ability can all be used to generate a visual read-out as well as absorbance signals. The results can be determined with the naked eye thus reliance on complicated instruments can be minimized. However, unmodified NMNs are unstable in the presence of high ionic strength and tend to aggregate, which greatly limits their use in practical applications. Meanwhile, the sensitivity of the absorbance-based assay using NMNs still needs to be improved; since a high sensitivity can retain the system's response to the target while reduce the influence of interferences in the complex sample diluting process. Endeavors are still needed to achieve the accurate detection in real samples such as biological fluids by taking modified or unmodified NMNs as optical sensing elements.

The introduction of NMNs facilitated the immobilization of biomolecules or electrochemical probes, improved the interfacial electronic conductivity and enhanced electrocatalytic ability in electroanalysis. However, considering the practical biosensing, there is still a long way to go. For example, despite the improvement in sensitivity and selectivity, further enhancement in stability and recycle ability are still in progress. In addition, their application in miniaturized system with diverse functions is also in the infant stage. To circumvent the above issues, more efforts might be devoted to synthesizing innovative NMNs with high conductivity, high specific surface area and unique physicochemical properties for detection of specific target molecules, fabricating hybrid architectures with excellent biocompatibility, designing multifunctional nanodivices with enhanced detection efficiency.

There are also a number of challenges with regard to the practical applications of fluorescent detection. For instance, the fluorescence quantum efficiencies of bimolecular-protected NMNs are generally around 10^{-3}, which are much lower than most inorganic NCs or fluorescent molecules. When applied in complex biological environments, systematical studies are also demanded to optimize both the stability and the biocompatibility of the NMNs based fluorescent method. Furthermore, with respect to the "turn off" or "turn on" of the molecular fluorescence by using NMNs, a time consuming surface modification process is usually required. Therefore, although novel functionalized NMNs system with higher sensitivity and selectivity are still the primary research subjects, we believe that more efforts are also needed to improve the accessibility and reliability of the current NMNs based fluorescent assays.

Acknowledgments

This work was supported by the National Key Basic Research Development Project of China (No. 2010CB933602) and the National Natural Science Foundation of China (No. 21175124),

References

1. Liz-Marzán, L. M. *Mater. Today* **2004**, *7*, 26–31.
2. Haiss, W.; Thanh, N. T. K.; Aveyard, J.; Fernig, D. G. *Anal. Chem.* **2007**, *79*, 4215–4221.
3. Liu, J. W.; Cao, Z. H.; Lu, Y. *Chem. Rev.* **2009**, *109*, 1948–1998.
4. Mirkin, C. A.; Letsinger, R. L.; Mucic, R. C.; Storhoff, J. J. *Nature* **1996**, *382*, 607–609.
5. Alivisatos, A. P.; Johnsson, K. P.; Peng, X. G.; Wilson, T. E.; Loweth, C. J.; Bruchez, M. P.; Schultz, P. G. *Nature* **1996**, *382*, 609–611.
6. Elghanian, R.; Storhoff, J. J.; Mucic, R. C.; Letsinger, R. L.; Mirkin, C. A. *Science* **1997**, *277*, 1078–1081.
7. Storhoff, J. J.; Elghanian, R.; Mucic, R. C.; Mirkin, C. A.; Letsinger, R. L. *J. Am. Chem. Soc.* **1998**, *120*, 1959–1964.
8. Sato, K.; Hosokawa, K.; Maeda, M. *J. Am. Chem. Soc.* **2003**, *125*, 8102–8103.
9. Xu, W.; Xue, X. J.; Li, T. H.; Zeng, H. Q.; Liu, X. G. *Angew. Chem., Int. Ed.* **2009**, *48*, 6849–6852.
10. Liu, J. W.; Lu, Y. *J. Am. Chem. Soc.* **2003**, *125*, 6642–6643.
11. Liu, J. W.; Lu, Y. *J. Am. Chem. Soc.* **2005**, *127*, 12677–12683.
12. Liu, J. W.; Lu, Y. *Anal. Chem.* **2004**, *76*, 1627–1632.
13. Lee, J. H.; Wang, Z. D.; Liu, J. W.; Lu, Y. *J. Am. Chem. Soc.* **2008**, *130*, 14217–14226.
14. Liu, J. W.; Lu, Y. *Angew. Chem., Int. Ed.* **2006**, *45*, 90–94.

15. Huang, C. C.; Huang, Y. F.; Cao, Z. H.; Tan, W. H.; Chang, H. T. *Anal. Chem.* **2005**, *77*, 5735–5741.
16. Medley, C. D.; Smith, J. E.; Tang, Z. W.; Wu, Y. R.; Bamrungsap, S.; Tan, W. H. *Anal. Chem.* **2008**, *80*, 1067–1072.
17. Han, M. S.; Lytton-Jean, A. K. R.; Oh, B.-K.; Heo, J.; Mirkin, C. A. *Angew. Chem., Int. Ed.* **2006**, *45*, 1807–1810.
18. Han, M. S.; Lytton-Jean, A. K. R.; Mirkin, C. A. *J. Am. Chem. Soc.* **2006**, *128*, 4954–4955.
19. Xu, X. Y.; Han, M. S.; Mirkin, C. A. *Angew. Chem., Int. Ed.* **2007**, *46*, 3468–3470.
20. Lee, J. S.; Han, M. S.; Mirkin, C. A. *Angew. Chem., Int. Ed.* **2007**, *46*, 4093–4096.
21. Xue, X. J.; Wang, F.; Liu, X. G. *J. Am. Chem. Soc.* **2008**, *130*, 3244–3245.
22. Lee, J. S.; Ulmann, P. A.; Han, M. S.; Mirkin, C. A. *Nano Lett.* **2008**, *8*, 529–533.
23. He, S. J.; Li, D.; Zhu, C. F.; Song, S. P.; Wang, L. H.; Long, Y. T.; Fan, C. H. *Chem. Commun.* **2008**, 4885–4487.
24. Li, B. L.; Du, Y.; Dong, S. J. *Anal. Chim. Acta* **2009**, *644*, 78–82.
25. Song, G. T.; Chen, C. E.; Qu, X. G.; Miyoshi, D.; Ren, J. S.; Sugimoto, N. *Adv. Mater.* **2008**, *20*, 706–710.
26. Zhao, W. A.; Chiuman, W.; Brook, M. A.; Li, Y. F. *ChemBioChem* **2007**, *8*, 727–731.
27. Zhao, W. A.; Lam, J. C. F.; Chiuman, W.; Brook, M. A.; Li, Y. F. *Small* **2008**, *4*, 810–816.
28. Zhao, W. A.; Chiuman, W.; Lam, J. C. F.; McManus, S. A.; Chen, W.; Cui, Y. G.; Pelton, R.; Brook, M. A.; Li, Y. F. *J. Am. Chem. Soc.* **2008**, *130*, 3610–3618.
29. Chen, S. J.; Huang, Y. F.; Huang, C. C.; Lee, K. H.; Lin, Z. H.; Chang, H. T. *Biosens. Bioelectron.* **2008**, *23*, 1749–1753.
30. Li, H. X.; Rothberg, L. J. *J. Am. Chem. Soc.* **2004**, *126*, 10958–10961.
31. Li, H. X.; Rothberg, L. *Proc. Natl. Acad. Sci. U.S.A.* **2004**, *101*, 14036–14039.
32. Wang, L. H.; Liu, X. F.; Hu, X. F.; Song, S. P.; Fan, C. H. *Chem. Commun.* **2006**, 3780–3782.
33. Wei, H.; Li, B. L.; Li, J.; Wang, E. K.; Dong, S. J. *Chem. Commun.* **2007**, 3735–3737.
34. Yang, C.; Wang, Y.; Marty, J.-L.; Yang, X. R. *Biosens. Bioelectron.* **2011**, *26*, 2724–2727.
35. Zheng, Y.; Wang, Y.; Yang, X. R. *Sens. Actuators, B* **2011**, *156*, 95–99.
36. Wang, J.; Wang, L. H.; Liu, X. F.; Liang, Z. Q.; Song, S. P.; Li, W. X.; Li, G. X.; Fan, C. H. *Adv. Mater.* **2007**, *19*, 3943–3946.
37. Zhang, J.; Wang, L. H.; Pan, D.; Song, S. P.; Boey, F. Y. C.; Zhang, H.; Fan, C. H. *Small* **2008**, *4*, 1196–1200.
38. Wei, H.; Li, B. L.; Li, J.; Dong, S. J.; Wang, E. K. *Nanotechnology* **2008**, *19*, 095501.
39. Wang, Z. D.; Lee, J. H.; Lu, Y. *Adv. Mater.* **2008**, *20*, 3263–3267.

40. Li, D.; Wieckowska, A.; Willner, I. *Angew. Chem., Int. Ed.* **2008**, *47*, 3927–3931.
41. Liu, C. W.; Hsieh, Y. T.; Huang, C. C.; Lin, Z. H.; Chang, H. T. *Chem. Commun.* **2008**, 2242–2244.
42. Wang, H.; Wang, Y. X.; Jin, J. Y.; Yang, R. H. *Anal. Chem.* **2008**, *80*, 9021–9028.
43. Xu, X. W.; Wang, J.; Jiao, K.; Yang, X. R. *Biosens. Bioelectron.* **2009**, *24*, 3153–3158.
44. Wang, Y.; Yang, F.; Yang, X. R. *Biosens. Bioelectron.* **2010**, *25*, 1994–1998.
45. Chen, C. E.; Song, G. T.; Ren, J. S.; Qu, X. G. *Chem. Commun.* **2008**, 6149–6151.
46. Xin, A. P.; Dong, Q. P.; Xiong, C.; Ling, L. S. *Chem. Commun.* **2009**, 1658–1660.
47. Shen, Q. P.; Nie, Z.; Guo, M. L.; Zhong, C. J.; Lin, B.; Li, W.; Yao, S. Z. *Chem. Commun.* **2009**, 929–931.
48. Wang, Y.; Yang, F.; Yang, X. R. *Nanotechnology* **2010**, *21*, 205502.
49. Jiang, Y.; Zhao, H.; Lin, Y. Q.; Zhu, N. N.; Ma, Y. R.; Mao, L. Q. *Angew. Chem., Int. Ed.* **2010**, *49*, 4800–4804.
50. Xia, F.; Zuo, X. L.; Yang, R. Q.; Xiao, Y.; Kang, D.; Vallée-Bélisle, A.; Gong, X.; Yuen, J. D.; Hsu, B. B. Y.; Heeger, A. J.; Plaxco, K. W. *Proc. Natl. Acad. Sci. U.S.A.* **2010**, *107*, 10837–10841.
51. Liu, J. W.; Lu, Y. *Adv. Mater.* **2006**, *18*, 1667–1671.
52. Lee, I.-H.; Yang, K.-A.; Lee, J.-H.; Park, J.-Y.; Chai, Y. G.; Lee, J.-H.; Zhang, B.-T. *Nanotechnology* **2008**, *19*, 395103.
53. Ogawa, A.; Maeda, M. *Chem. Commun.* **2009**, 4666–4668.
54. Bi, S.; Yan, Y. M.; Hao, S. Y.; Zhang, S. S. *Angew. Chem., Int. Ed.* **2010**, *49*, 4438–4442.
55. Xu, X. W.; Zhang, J.; Yang, F.; Yang, X. R. *Chem. Commun.* **2011**, *47*, 9435–9437.
56. Cao, Y. W.; Jin, R. C.; Mirkin, C. A. *J. Am. Chem. Soc.* **2001**, *123*, 7961–7962.
57. Liu, S. H.; Zhang, Z. H.; Han, M. Y. *Anal. Chem.* **2005**, *77*, 2595–2600.
58. Chen, Y.; Aveyard, J.; Wilson, R. *Chem. Commun.* **2004**, 2804–2805.
59. Tokareva, I.; Hutter, E. *J. Am. Chem. Soc.* **2004**, *126*, 15784–15789.
60. Vidal, B. C.; Deivaraj, T. C.; Yang, J.; Too, H.-P.; Chow, G.-M.; Gan, L. M.; Lee, J. Y. *New J. Chem.* **2005**, *29*, 812–816.
61. Lee, J.-S.; Lytton-Jean, A. K. R.; Hurst, S. J.; Mirkin, C. A. *Nano Lett.* **2007**, *7*, 2112–2115.
62. Thompson, D. G.; Enright, A.; Faulds, K.; Smith, W. E.; Graham, D. *Anal. Chem.* **2008**, *80*, 2805–2810.
63. Kanjanawarut, R.; Su, X. D. *Anal. Chem.* **2009**, *81*, 6122–6129.
64. Su, X. D.; Kanjanawarut, R. *ACS Nano* **2009**, *3*, 2751–2759.
65. Xu, X. W.; Wang, J.; Yang, F.; Jiao, K.; Yang, X. R. *Small* **2009**, *5*, 2669–2672.
66. Wang, Y.; Yang, F.; Yang, X. R. *ACS Appl. Mater. Interfaces* **2010**, *2*, 339–342.

67. Chen, Z.; He, Y. J.; Luo, S. L.; Lin, H. L.; Chen, Y. F.; Sheng, P. T.; Li, J. X.; Chen, B. B.; Liu, C. B.; Cai, Q. Y. *Analyst* **2010**, *135*, 1066–1069.
68. Zhao, W. A.; Chiuman, W.; Lam, J. C. F.; Brook, M. A.; Li, Y. F. *Chem. Commun.* **2007**, 3729–3731.
69. Wei, H.; Chen, C. G.; Han, B. Y.; Wang, E. K. *Anal. Chem.* **2008**, *80*, 7051–7055.
70. Liu, R. R.; Teo, W. L.; Tan, S. Y.; Feng, H. J.; Padmanabhan, P.; Xing, B. G. *Analyst* **2010**, *135*, 1031–1036.
71. Lin, Y. H.; Chen, C. E.; Wang, C. Y.; Pu, F.; Ren, J. S.; Qu, X. G. *Chem. Commun.* **2011**, *47*, 1181–1183.
72. Cao, R.; Li, B. X. *Chem. Commun.* **2011**, *47*, 2865–2867.
73. Cao, R.; Li, B. X.; Zhang, Y. F.; Zhang, Z. N. *Chem. Commun.* **2011**, *47*, 12301–12303.
74. Zhang, M.; Ye, B. C. *Anal. Chem.* **2011**, *83*, 1504–1509.
75. Ai, K. L.; Liu, Y. L.; Lu, L. H. *J. Am. Chem. Soc.* **2009**, *131*, 9496–9479.
76. Yuan, Y.; Zhang, J.; Zhang, H. C.; Yang, X. R. *Biosens. Bioelectron.* **2011**, *26*, 4245–4248.
77. Yuan, Y.; Zhang, J.; Zhang, H. C.; Yang, X. R. *Analyst* **2012**, *137*, 496–501.
78. Radhakumary, C.; Sreenivasan, K. *Anal. Chem.* **2011**, *83*, 2829–2833.
79. Glynou, K.; Ioannou, P. C.; Christopoulos, T. K.; Syriopoulou, V. *Anal. Chem.* **2003**, *75*, 4155–4160.
80. Liu, J. W.; Mazumdar, D.; Lu, Y. *Angew. Chem., Int. Ed.* **2006**, *45*, 7955–7959.
81. Mazumdar, D.; Liu, J. W.; Lu, G.; Zhou, J. Z.; Lu, Y. *Chem. Commun.* **2010**, *46*, 1416–1418.
82. Zhu, Z.; Wu, C. C.; Liu, H. P.; Zou, Y.; Zhang, X. L.; Kang, H. Z.; Yang, C. J.; Tan, W. H. *Angew. Chem., Int. Ed.* **2010**, *49*, 1052–1056.
83. Lin, H. X.; Zou, Y.; Huang, Y. S.; Chen, J.; Zhang, W. Y.; Zhuang, Z. X.; Jenkins, G.; Yang, C. J. *Chem. Commun.* **2011**, *47*, 9312–9314.
84. Baeissa, A.; Dave, N.; Smith, B. D.; Liu, J. W. *ACS Appl. Mater. Interfaces* **2010**, *2*, 3594–3600.
85. Yin, B. C.; Ye, B. C.; Wang, H.; Zhu, Z.; Tan, W. H. *Chem. Commun.* **2012**, *48*, 1248–1250.
86. He, P. L.; Shen, L.; Liu, R. Y.; Luo, Z. P.; Li, Z. *Anal. Chem.* **2011**, *83*, 6988–6995.
87. Higuchi, A.; Siao, Y.-D.; Yang, S.-T.; Hsieh, P.-V.; Fukushima, H.; Chang, Y.; Ruaan, R.-C.; Chen, W.-Y. *Anal. Chem.* **2008**, *80*, 6580–6586.
88. Jv, Y.; Li, B. X.; Cao, R. *Chem. Commun.* **2010**, *46*, 8017–8019.
89. Zhang, X. X.; Liu, Q.; Jing, C.; Li, Y.; Li, D.; Luo, W. J.; Wen, Y. Q.; He, Y.; Huang, Q.; Long, Y. T.; Fan, C. H. *Angew. Chem., Int. Ed.* **2011**, *50*, 11994–11998.
90. Schmid, G. In *Nanoscale Materials in Chemistry*; Klabunde, K. J., Ed.; Wiley: New York, 2001.
91. Guo, S.; Wang, E. *Nano Today* **2011**, *6*, 240–264.
92. Guo, S.; Wang, E. *Anal. Chim. Acta.* **2007**, *598*, 181–192.
93. Sarma, A. K.; Vatsyayan, P.; Goswami, P.; Minteer, S. D. *Biosens. Bioelectron.* **2009**, *24*, 2313–2322.

94. Guindilis, A. L.; Atanasov, P.; Wilkins, E. *Electroanalysis* **1997**, *9*, 661–674.
95. Jia, J.; Wang, B.; Wu, A.; Cheng, G.; Li, Z.; Dong, S. *Anal. Chem.* **2002**, *74*, 2217–2223.
96. Jena, B. K.; Raj, C. R. *Anal. Chem.* **2006**, *78*, 6332–6339.
97. Iost, R. M.; Crespilho, F. N. *Biosens. Bioelectron.* **2012**, *31*, 1–10.
98. Zhang, H.; Hu, N. *Biosens. Bioelectron.* **2007**, *23*, 393–399.
99. Liu, Y.; Wu, S.; Ju, H.; Xu, L. *Electroanalysis* **2007**, *19*, 986–992.
100. Plowman, B. J.; Bhargava, S. K.; O'Mullane, A. P. *Analyst* **2011**, *136*, 5107–5119.
101. Shulga, O. J.; Kirchhoff, R. *Electrochem. Commun.* **2007**, *9*, 935–940.
102. Du, Y.; Luo, X.; Xu, J.; Chen, H. *Bioelectrochemistry* **2007**, *70*, 342–347.
103. Cai, W.; Xu, Q.; Zhao, X.; Zhu, J.; Chen, H. *Chem. Mater.* **2006**, *18*, 279–284.
104. Liu, Y.; Feng, X.; Shen, J.; Zhu, J.; Hou, W. *J. Phys. Chem. B* **2008**, *112*, 9237–9242.
105. Li, F.; Wang, Z.; Shan, C.; Song, J.; Han, D.; Niu, L. *Biosens. Bioelectron.* **2009**, *24*, 1765–1770.
106. Shi, L.; Liu, X.; Niu, W.; Li, H.; Han, S.; Chen, J.; Xu, G. *Biosens. Bioelectron.* **2009**, *24*, 1159–1163.
107. Shan, C.; Yang, H.; Han, D.; Zhang, Q.; Ivaska, A.; Niu, L. *Biosens. Bioelectron.* **2010**, *25*, 1070–1074.
108. Zhang, J.; Li, J.; Yang, F.; Zhang, B. L.; Yang, X. *Sens. Actuators, B* **2009**, *143*, 373–380.
109. Li, Y.; Zhang, J.; Zhu, H.; Yang, F.; Yang, X. *Electrochim. Acta* **2010**, *55*, 5123–5128.
110. Li, J.; Lin, X. Q. *Sens. Actuators, B* **2007**, *124*, 486–493.
111. Cui, Y.; Yang, C.; Pu, W.; Oyama, M.; Zhang, J. *Anal. Lett.* **2010**, *43*, 22–33.
112. Wang, C.; Wang, G.; Fang, B. *Microchim. Acta.* **2009**, *164*, 113–118.
113. Yang, J.; Pang, F.; Zhang, R.; Xu, Y.; He, P; Fang, Y. *Electroanalysis* **2008**, *20*, 2134–2140.
114. Guo, Y.; Guo, S.; Fang, Y.; Dong, S. *Electrochim. Acta.* **2010**, *55*, 3927–3931.
115. Zhao, J.; Zhu, X.; Li, T.; Li, G. *Analyst* **2008**, *133*, 1242–1245.
116. Castaneda, M. T.; Alegret, S.; Merkoci, A. *Electroanalysis* **2007**, *19*, 743–753.
117. Wang, J. *Anal. Chim. Acta* **2003**, *500*, 247–257.
118. Katz, E.; Willner, I. *Angew. Chem., Int. Ed.* **2004**, *43*, 6042–6108.
119. Zheng, H.; Hu, J.; Li, Q. *Acta Chim. Sin.* **2006**, *64*, 806–810.
120. Yang, J.; Yang, T.; Feng, Y.; Jiao, K. *Anal. Biochem.* **2007**, *365*, 24–30.
121. Zhang, Y.; Zhang, K.; Ma, H. *Am. J. Biomed. Sci.* **2009**, *1*, 115–125.
122. Selvaraju, T.; Das, J.; Jo, K.; Kwon, K.; Huh, C. H.; Kim, T. K.; Yang, H. *Langmuir* **2008**, *24*, 9883–9888.
123. Zhang, Y.; Wang, J.; Xu, M. *Colloids Surf. B.* **2009**, *75*, 179–185.
124. Du, P.; Li, H.; Mei, Z.; Liu, S. *Bioelectrochemistry* **2009**, *75*, 37–43.
125. Escosura-Muñiz, A.; Parolo, c.; Merkoçi, A. *Mater. Today* **2010**, *13*, 24–34.
126. Wang, J. *Electroanalysis* **2007**, *19*, 769–776.

127. Cui, R.; Huang, H.; Yin, Z.; Gao, D.; Zhu, J. *Biosens. Bioelectron.* **2008**, *23*, 1666–1673.
128. Kim, D.; Noh, H.; Park, D.; Ryu, S.; Koo, J.; Shim, Y. *Biosens. Bioelectron.* **2009**, *25*, 456–462.
129. Wu, S.; Zhong, Z.; Wang, D.; Li, M.; Qing, Y.; Dai, N.; Li, Z. *Microchim. Acta.* **2009**, *166*, 269–275.
130. Ding, C.; Zhao, F.; Ren, R.; Lin, J. *Talanta* **2009**, *78*, 1148–1154.
131. Lin, J.; He, C.; Zhang, L.; Zhang, S. *Anal. Biochem.* **2009**, *384*, 130–135.
132. Zhang, S.; Zheng, F.; Wu, Z.; Shen, G.; Yu, R. *Biosens. Bioelectron.* **2008**, *24*, 129–135.
133. Zhuo, Y.; Yu, R.; Yuan, R.; Chai, Y.; Hong, C. *J. Electroanal. Chem.* **2009**, *628*, 90–96.
134. Tang, H.; Chen, J.; Nie, L.; Kuang, Y.; Yao, S. *Biosens. Bioelectron.* **2007**, *22*, 1061–1067.
135. Liang, W.; Yi, W.; Li, S.; Yuan, R.; Chen, A.; Chen, S.; Xiang, G.; Hu, C. *Clin. Biochem.* **2009**, *42*, 1524–1530.
136. Http://en.wikipedia.org/wiki/Systematic_Evolution_of_Ligands_by_Exponential_Enrichment.
137. Hianik, T.; Wang, J. *Electroanalysis* **2009**, *21*, 1223–1235.
138. Sassolas, A.; Blum, L. J.; Leca-Bouvier, B. D. *Electroanalysis* **2009**, *21*, 1237–1250.
139. Xu, Y.; Cheng, G.; He, P.; Fang, Y. *Electroanalysis* **2009**, *21*, 1251–1259.
140. Ikebukuro, K.; Kiyohara, C.; Sode, K. *Anal. Lett.* **2004**, *37*, 2901–2909.
141. He, P.; Shen, L.; Cao, Y.; Li, D. *Anal. Chem.* **2007**, *79*, 8024–8029.
142. Li, X.; Qi, H.; Shen, L.; Gao, Q.; Zhang, C. *Electroanalysis* **2008**, *20*, 1475–1482.
143. Wang, J.; Meng, W.; Zheng, X.; Liu, S.; Li, G. *Biosens. Bioelectron.* **2009**, *24*, 1598–1602.
144. Wu, Z.; Guo, M.; Zhang, S.; Chen, C.; Jiang, J.; Shen, G.; Yu, R. *Anal. Chem.* **2007**, *79*, 2933–2939.
145. Li, X .; Shen, L.; Zhang, D.; Qi, H.; Gao, Q.; Ma, F.; Zhang, C. *Biosens. Bioelectron.* **2008**, *23*, 1624–1630.
146. Li, B.; Wang, Y.; Wei; Dong, S. *Biosens. Bioelectron.* **2008**, *23*, 965–970.
147. Deng, C.; Chen, J.; Nie, Z.; Wang, M.; Chu, X.; Chen, X.; Xiao, X.; Lei, C.; Yao, S. *Anal. Chem.* **2009**, *81*, 739–745.
148. Hu, L.; Xu, G. *Chem. Soc. Rev.* **2010**, *39*, 3275–3304.
149. Qi, H.; Peng, Y.; Gao, Q.; Zhang, C. *Sensors* **2009**, *9*, 674–695.
150. Zhang, L.; Xu, Z.; Sun, X.; Dong, S. *Biosens. Bioelectron.* **2007**, *22*, 1097–1100.
151. Yin, X.-B.; Qi, B.; Sun, X.; Yang, X.; Wang, E. *Anal. Chem.* **2005**, *77*, 3525–3530.
152. Li, Y.; Qi, H. L.; Yang, J.; Zhang, C. X. *Microchim. Acta.* **2008**, *164*, 69–76.
153. Cui, H.; Xu, Y.; Zhang, Z. *Anal. Chem.* **2004**, *76*, 4002–4010.
154. Dong, Y.; Cui, H.; Xu, Y. *Langmuir* **2007**, *23*, 523–529.
155. Wang, W.; Xiong, T.; Cui, H. *Langmuir* **2008**, *24*, 2826–2833.
156. Tian, D.; Duan, C.; Wang, W.; Li, N.; Zhang, H.; Cui, H.; Lu, Y. *Talanta* **2009**, *78*, 399–404.

157. Qi, H.; Zhang, Y.; Peng, Y.; Zhang, C. *Talanta* **2008**, *75*, 684–690.
158. Liu, X.; Niu, W.; Li, H.; Han, S.; Hu, L.; Xu, G. *Electrochem. Commun.* **2008**, *10*, 1250–1253.
159. Shan, Y.; Xu, J.; Chen, H. *Chem. Commun.* **2009**, 905–907.
160. Sun, X.; Du, Y.; Dong, S.; Wang, E. *Anal. Chem.* **2005**, *77*, 8166–8169.
161. Wang, X.; Yun, W.; Dong, P.; Zhou, J.; He, P.; Fang, Y. *Langmuir* **2008**, *24*, 2200–2205.
162. Qian, L.; Yang, X. *Adv. Funct. Mater.* **2007**, *17*, 1353–1358.
163. Fang, L.; Lv, Z.; Wei, H.; Wang, E. *Anal. Chim. Acta* **2008**, *628*, 80–86.
164. Bai, J.; Wei, H.; Li, B; Song, L.; Yang, L.; Lv, Z.; Zhou, W.; Wang, E. *Chem.–Asian J.* **2008**, *3*, 1935–1941.
165. Wang, X.; Zhou, J.; Yun, W.; Xiao, S.; Chang, Z.; He, P.; Fang, Y. *Anal. Chim. Acta* **2007**, *598*, 242–248.
166. Liu, D.; Wang, Z.; Jiang, X. *Nanoscale* **2011**, *3*, 1421–1433.
167. Swierczewska, M.; Lee, S.; Chen, X. *Phys. Chem. Chem. Phys.* **2011**, *13*, 9929–9941.
168. Guo, S.; Wang, E. *Acc. Chem. Res.* **2011**, *44*, 491–500.
169. Saha, K.; Agasti, S. S.; Kim, C.; Li, X.; Rotello, V. M. *Chem. Rev.* **2012**, *112*, 2739–2779.
170. Ling, J.; Huang, C. Z. *Anal. Methods* **2010**, *2*, 1439–1447.
171. Zhang, X.; Kong, R.; Lu, Y. *Ann. Rev. Anal. Chem.* **2011**, *4*, 105–128.
172. Cao, X.; Ye, Y.; Liu, S. *Anal. Biochem.* **2011**, *417*, 1–16.
173. Brust, M.; Walker, M.; Bethell, D.; Schiffrin, D. J.; Whyman, R. *Journal of The Chemical Society-Chemical Communications* **1994**, 801–802.
174. Demchenko, A. P. *Anal. Biochem.* **2005**, *343*, 1–22.
175. Zheng, J.; Nicovich, P. R.; Dickson, R. M. *Annu. Rev. Phys. Chem.* **2007**, *58*, 409–431.
176. Huang, T.; Murray, R. W. *J. Phys. Chem. B* **2001**, *105*, 12498–12502.
177. Link, S.; Beeby, A.; Fitzgerald, S.; El-Sayed, M. A.; Schaaff, T. G.; Whetten, R. L. *J. Phys. Chem. B* **2002**, *106*, 3410–3415.
178. Zheng, J.; Dickson, R. M. *J. Am. Chem. Soc.* **2002**, *124*, 13982–13983.
179. Zheng, J.; Petty, J. T.; Dickson, R. M. *J. Am. Chem. Soc.* **2003**, *125*, 7780–7781.
180. Zheng, J.; Zhang, C. W.; Dickson, R. M. *Phys. Rev. Lett.* **2004**, *93*, 077402.
181. Vosch, T.; Antoku, Y.; Hsiang, J.; Richards, C. I.; Gonzalez, J. I.; Dickson, R. M. *Proc. Natl. Acad. Sci. U.S.A.* **2007**, *104*, 12616–12621.
182. Lee, J. H.; Wang, Z.; Liu, J.; Lu, Y. *J. Am. Chem. Soc.* **2008**, *130*, 14217–14226.
183. Richards, C. I.; Choi, S.; Hsiang, J.; Antoku, Y.; Vosch, T.; Bongiorno, A.; Tzeng, Y.; Dickson, R. M. *J. Am. Chem. Soc.* **2008**, *130*, 5038–5039.
184. Zhang, N.; Liu, Y.; Tong, L.; Xu, K.; Zhuo, L.; Tang, B. *Analyst* **2008**, *133*, 1176–1181.
185. Yu, J.; Patel, S. A.; Dickson, R. M. *Angew. Chem., Int. Ed.* **2007**, *46*, 2028–2030.
186. Xie, J.; Zheng, Y.; Ying, J. Y. *J. Am. Chem. Soc.* **2009**, *131*, 888–889.
187. Hu, L.; Han, S.; Parveen, S.; Yuan, Y.; Zhang, L.; Xu, G. *Biosens. Bioelectron.* **2012**, *32*, 297–299.

188. Chaudhari, K.; Xavier, P. L.; Pradeep, T. *ACS Nano* **2011**, *5*, 8816–8827.
189. Lou, X.; Zhang, Y.; Qin, J.; Li, Z. *Chem.−Eur. J.* **2011**, *17*, 9691–9696.
190. Chandra, P.; Noh, H.; Won, M.; Shim, Y. *Biosens. Bioelectron.* **2011**, *26*, 4442–4449.
191. Kall, M.; Xu, H. X.; Johansson, P. *J. Raman Spectrosc.* **2005**, *36*, 510–514.
192. Kuehn, S.; Hakanson, U.; Rogobete, L.; Sandoghdar, V. *Phys. Rev. Lett.* **2006**, *97*, 017042.
193. Bek, A.; Jansen, R.; Ringler, M.; Mayilo, S.; Klar, T. A.; Feldmann, J. *Nano. Lett.* **2008**, *8*, 485–490.
194. Lakowicz, J. R.; Malicka, J.; Gryczynski, I.; Gryczynski, Z.; Geddes, C. D. *J. Phys. D: Appl. Phys.* **2003**, *36*, 240–249.
195. Dulkeith, E.; Morteani, A. C.; Niedereichholz, T.; Klar, T. A.; Feldmann, J.; Levi, S. A.; Van Veggel, F.; Reinhoudt, D. N.; M O Ller, M.; Gittins, D. I. *Phys. Rev. Lett.* **2002**, *89*, 203002.
196. Dulkeith, E.; Ringler, M.; Klar, T. A.; Feldmann, J.; Javier, A. M.; Parak, W. J. *Nano Lett.* **2005**, *5*, 585–589.
197. Huang, H.; Liu, X.; Hu, T.; Chu, P. K. *Biosens. Bioelectron.* **2010**, *25*, 2078–2083.
198. Chiu, T.; Huang, C. *Sensors* **2009**, *9*, 10356–10388.
199. Iliuk, A. B.; Hu, L.; Tao, W. A. *Anal. Chem.* **2011**, *83*, 4440–4452.
200. Fodey, T.; Leonard, P.; O'mahony, J.; O'kennedy, R.; Danaher, M. *TrAC, Trends Anal. Chem.* **2011**, *30*, 254–269.
201. Famulok, M.; Mayer, G. *Acc. Chem. Res.* **2011**, *44*, 1349–1358.
202. Shang, L.; Dong, S.; Nienhaus, G. U. *Nano Today* **2011**, *6*, 401–418.
203. Shang, L.; Qin, C.; Wang, T.; Wang, M.; Wang, L.; Dong, S. *J. Phys. Chem. C* **2007**, *111*, 13414–13417.
204. Shang, L.; Dong, S. *Biosens. Bioelectron.* **2009**, *24*, 1569–1573.
205. Shang, L.; Yin, J.; Li, J.; Jin, L.; Dong, S. *Biosens. Bioelectron.* **2009**, *25*, 269–274.
206. Jin, Y.; Li, H.; Bai, J. *Anal. Chem.* **2009**, *81*, 5709–5715.
207. Song, S.; Qin, Y.; He, Y.; Huang, Q.; Fan, C.; Chen, H. *Chem. Soc. Rev.* **2010**, *39*, 4234–4243.
208. Zhang, J.; Wang, L.; Zhang, H.; Boey, F.; Song, S.; Fan, C. *Small* **2010**, *6*, 201–204.
209. Dyadyusha, L.; Yin, H.; Jaiswal, S.; Brown, T.; Baumberg, J. J.; Booy, F. P.; Melvin, T. *Chem. Commun.* **2005**, 3201–3203.
210. Oh, E.; Hong, M. Y.; Lee, D.; Nam, S. H.; Yoon, H. C.; Kim, H. S. *J. Am. Chem. Soc.* **2005**, *127*, 3270–3271.
211. Oh, E.; Lee, D.; Kim, Y.; Cha, S. Y.; Oh, D.; Kang, H. A.; Kim, J.; Kim, H. *Angew. Chem. Int. Ed.* **2006**, *45*, 7959–7963.
212. Nie, Z.; Petukhova, A.; Kumacheva, E. *Nat. Nanotechnol.* **2010**, *5*, 15–25.
213. Mattoussi, H.; Palui, G.; Na, H. B. *Adv. Drug Delivery Rev.* **2012**, *64*, 138–166.
214. Gill, R.; Zayats, M.; Willner, I. *Angew. Chem., Int. Ed.* **2008**, *47*, 7602–7625.
215. Liu, J.; Cao, Z.; Lu, Y. *Chem. Rev.* **2009**, *109*, 1948–1998.
216. Sperling, R. A.; Rivera Gil, P.; Zhang, F.; Zanella, M.; Parak, W. J. *Chem. Soc. Rev.* **2008**, *37*, 1896–1908.

217. De, M.; Ghosh, P. S.; Rotello, V. M. *Adv. Mater.* **2008**, *20*, 4225–4241.
218. Maria Coto-Garcia, A.; Sotelo-Gonzalez, E.; Teresa Fernandez-Argueelles, M.; Pereiro, R.; Costa-Fernandez, J. M.; Sanz-Medel, A. *Anal. Bioanal. Chem.* **2011**, *399*, 29–42.
219. Maxwell, D. J.; Taylor, J. R.; Nie, S. M. *J. Am. Chem. Soc.* **2002**, *124*, 9606–9612.
220. Du, H.; Disney, M. D.; Miller, B. L.; Krauss, T. D. *J. Am. Chem. Soc.* **2003**, *125*, 4012–4013.
221. Li, H. X.; Rothberg, L. J. *Anal. Chem.* **2004**, *76*, 5414–5417.
222. Ray, P. C.; Fortner, A.; Darbha, G. K. *J. Phys. Chem. B* **2006**, *110*, 20745–20748.
223. Cheng, Y.; Stakenborg, T.; Van Dorpe, P.; Lagae, L.; Wang, M.; Chen, H.; Borghs, G. *Anal. Chem.* **2011**, *83*, 1307–1314.
224. Prigodich, A. E.; Randeria, P. S.; Briley, W. E.; Kim, N. J.; Daniel, W. L.; Giljohann, D. A.; Mirkin, C. A. *Anal. Chem.* **2012**, *84*, 2062–2066.
225. Prigodich, A. E.; Alhasan, A. H.; Mirkin, C. A. *J. Am. Chem. Soc.* **2011**, *133*, 2120–2123.
226. Guo, W.; Yuan, J.; Dong, Q.; Wang, E. *J. Am. Chem. Soc.* **2009**, *132*, 932–934.
227. Zhang, L.; Guo, S.; Dong, S.; Wang, E. *Anal. Chem.* **2012**, *84*, 3568–3573.
228. Wu, H.; Huang, C.; Cheng, T.; Tseng, W. *Talanta* **2008**, *76*, 347–352.
229. Huang, C.; Tseng, W. *Anal. Chem.* **2008**, *80*, 6345–6350.
230. Huang, C.; Chen, C.; Shiang, Y.; Lin, Z.; Chang, H. *Anal. Chem.* **2009**, *81*, 875–882.
231. Lin, J.; Chang, C.; Tseng, W. *Analyst* **2010**, *135*, 104–110.
232. Yu, P.; Wen, X.; Toh, Y.; Tang, J. *J. Phys. Chem. C* **2012**, *116*, 6567–6571.
233. Le Guével, X.; HöTzer, B.; Jung, G.; Hollemeyer, K.; Trouillet, V.; Schneider, M. *J. Phys. Chem. C* **2011**, *115*, 10955–10963.
234. Guo, C.; Irudayaraj, J. *Anal. Chem.* **2011**, *83*, 2883–2889.
235. Miranda, O. R.; Creran, B.; Rotello, V. M. *Curr. Opin. Chem. Biol.* **2010**, *14*, 728–736.
236. Swierczewska, M.; Liu, G.; Lee, S.; Chen, X. *Chem. Soc. Rev.* **2012**, *41*, 2641–2655.
237. You, C.; Miranda, O. R.; Gider, B.; Ghosh, P. S.; Kim, I.; Erdogan, B.; Krovi, S. A.; Bunz, U. H. F.; Rotello, V. M. *Nat. Nanotechnol.* **2007**, *2*, 318–323.
238. You, C. C.; De, M.; Han, G.; Rotello, V. M. *J. Am. Chem. Soc.* **2005**, *127*, 12873–12881.
239. De, M.; Rana, S.; Akpinar, H.; Miranda, O. R.; Arvizo, R. R.; Bunz, U. H. F.; Rotello, V. M. *Nature Chem.* **2009**, *1*, 461–465.
240. Phillips, R. L.; Miranda, O. R.; You, C.; Rotello, V. M.; Bunz, U. H. F. *Angew. Chem., Int. Ed.* **2008**, *47*, 2590–2594.
241. Bajaj, A.; Miranda, O. R.; Kim, I.; Phillips, R. L.; Jerry, D. J.; Bunz, U. H. F.; Rotello, V. M. *Proc. Natl. Acad. Sci. U.S.A.* **2009**, *106*, 10912–10916.
242. Bunz, U. H. F.; Rotello, V. M. *Angew. Chem., Int. Ed.* **2010**, *49*, 3268–3279.
243. Huang, X. H.; Neretina, S.; M. El-Sayed, A. *Adv. Mater.* **2009**, *21*, 4890–4910.

244. Connor, E. E.; Mwamuka, J.; Gole, A.; Murphy, C. J.; Wyatt, M. D. *Small* **2005**, *1*, 325–327.
245. Goodman, C. M.; Mccusker, C. D.; Yilmaz, T.; Rotello, V. M. *Bioconjugate Chem.* **2004**, *15*, 897–900.
246. Pernodet, N.; Fang, X.; Sun, Y.; Bakhtina, A.; Ramakrishnan, A.; Sokolov, J.; Ulman, A.; Rafailovich, M. *Small* **2006**, *2*, 766–773.
247. Hu, M.; Chen, J.; Li, Z. Y.; Au, L.; Hartland, G. V.; Li, X.; Marquez, M.; Xia, Y. *Chem. Soc. Rev.* **2006**, *35*, 1084–1094.
248. Au, Leslie; Zheng, D.; Zhou, F.; Li, Z.; Li, X.; Xia, Y. *ACS Nano* **2008**, *2*, 1645–1652.
249. Jain, P. K.; Huang, X.; El-Sayed, I.; El-Sayed, M. *Acc. Chem. Res.* **2008**, *41*, 1578–1586.
250. Pissuwan, D.; Valenzuela, S. M.; Cortie, M. B. *Trends Biotechnol.* **2006**, *24*, 62–67.
251. Zhou, T.; Wu, B.; Xing, D. *J. Mater. Chem.* **2012**, *22*, 470–477.
252. Jin, Y.; Jia, C.; Huang, S.; O'Donnell, M.; Gao, X. *Nat. Commun.* **2010**, *1*, 41.
253. Giljohann, D. A.; Seferos, D. S.; Daniel, W. L.; Massich, M. D.; Patel, P. C.; Mirkin, C. A. *Angew. Chem., Int. Ed.* **2010**, *49*, 3280–3294.
254. Popovtzer, R.; Agrawal, A.; Kotov, N. A.; Popovtzer, A.; Balter, J.; Carey, T. E.; Kopelman, R. *Nano Lett.* **2008**, *8*, 4593–4596.
255. Loo, C.; Lowery, A.; Halas, N.; West, J.; Drezek, R. *Nano Lett.* **2005**, *5*, 709–711.

Chapter 10

Nanoparticles of Different Shapes for Biosensor Applications

Radha Narayanan*

Department of Chemistry, University of Rhode Island, Kingston, RI 02881
***E-mail: rnarayanan@chm.uri.edu**

In this book chapter, we survey the use of different shapes of nanoparticles for biosensor applications. A wide variety of shapes have been studied such as spherical, rod, cube, triangular, hexagonal, and many others. Many different metals such as gold, zinc oxide, etc. have been used as the nanoparticles for the design of the biosensors. We focus on biosensor applications based on specific instrumental readout methods such as surface enhanced Raman spectroscopy (SERS), surface plasmon resonance (SPR), and electrochemical biosensors. We discuss several examples of different types of biomolecules that can be detected using each type of biosensor. We discuss the limits of detection and sensitivities of each of the different biosensor methods.

Introduction

A sensor is a material or device that can be used to detect a particular species of interest at trace levels. A biosensor is a type of sensor which is targeted for the detection of biological materials such as proteins, bacteria, viruses, and other such types of materials. There have been many different types of readout methods that have been used in biosensors such as SERS, SPR, electrochemical, and colorimetric methods. Many different types of biological materials have been detected using these different types of biosensors.

SERS based sensors are based on the greatly enhanced Raman signals that occur when the Raman scattering molecule is placed near or attached to the gold or silver nanoparticles or substrates. SPR based sensors come in two types: one involving the change in the refractive index and the other involving shifts

In Functional Nanoparticles for Bioanalysis, Nanomedicine, and Bioelectronic Devices Volume 1; Hepel, M., et al.;
ACS Symposium Series; American Chemical Society: Washington, DC, 2012.

in the surface plasmon bands. In electrochemical biosensors, different types of electrochemical techniques such as amperometry were used as readout methods. In colorimetry, changes in the color of the samples are used as a sensing platform to detect biological materials.

In this review, we focus on nanoparticles of different shapes for biosensing applications. Some examples of different shapes of nanoparticles include rod, cube, dogbone, trigonal pyramidal, and many others. One method for synthesizing different shapes of gold and silver nanoparticles is the seed-mediated growth method. The polyol growth method has also been used for synthesis of gold and silver nanoparticles of various shapes.

Types of Biosensor Readout

Surface-Enhanced Raman Spectroscopy

Cube-like gold nanoparticles have been used as extrinsic Raman labels for detection of human IgG proteins using a heterogeneous sandwich immunoassay format (*1*). Figure 1 illustrates the three step process involved in the heterogeneous sandwich immunoassay format. Extrinsic Raman labels (ERLs) are composed of DSNB, a Raman reporter molecule as well as an antibody that is bound to the DSNB through the amine group to form an amide bond. The capture substrate involves stamping the template strip gold substrate with octadecanethiol and exposing the unmodified central region with DSP. Then the antibody binds to the succinimidyl group of DSP via the amine group to form an amide bond. The actual sandwich immunoassay is conducted by first exposing the capture antibody substrate to different concentrations of antigen and finally applying the extrinsic Raman labels, completing the sandwich.

This heterogeneous sandwich immunoassay process was used for CTAB capped spherical and cube-like gold nanoparticles as ERLs (*1*). It was found that the CTAB-capped cube-like ERLs resulted in 336x lower limits of detection for human IgG protein compared to citrate capped spherical gold nanoparticle ERLs. In addition, the CTAB capped spherical gold nanoparticle ERLs showed 41x lower limits of detection compared to the citrate capped spherical gold nanoparticle ERLs. Overall, the cube-like gold nanoparticle ERLs resulted in low ng/mL detection of the human IgG protein, which corresponds to high pg/mL levels of detection of this protein.

A SERS based sandwich immunoassay conducted using antibody coated magnetic nanoparticles is used for the detection of low levels of E.coli (*2*). This methodology combines immunomagnetic separation with surface enhanced Raman spectroscopy. Figure 2 illustrates the sandwich immunoassay protocol using the spherical magnetic nanoparticles and the gold nanorods. The gold-coated spherical magnetic nanoparticles were prepared by immobilizing biotin-labeled anti-E. coli antibodies onto avidin-coated magnetic nanoparticles. These nanoparticles are used for the separation and enumeration of E. coli cells. The Raman labels used for the SERS studies are prepared using rod shaped gold nanoparticles coated with DTNB and subsequently with a molecular recognizer. The DTNB labeled gold nanorods are allowed to interact with the gold-coated spherical magnetic nanoparticles-antibody-E. coli complex. It was found that the linear dynamic range using SERS is 10^1 to 10^4 cfu/mL. Using SERS as the detection method resulted in the limit of detection to be 8 cfu/mL and the limit of quantitation to be 24 cfu/mL (*2*). It was also determined that this method can be used for detection of E. coli in real water samples and the results are similar to that obtained using plate-counting methods. The overall method is rapid and sensitive to target organisms with total analysis time of less than 70 minutes.

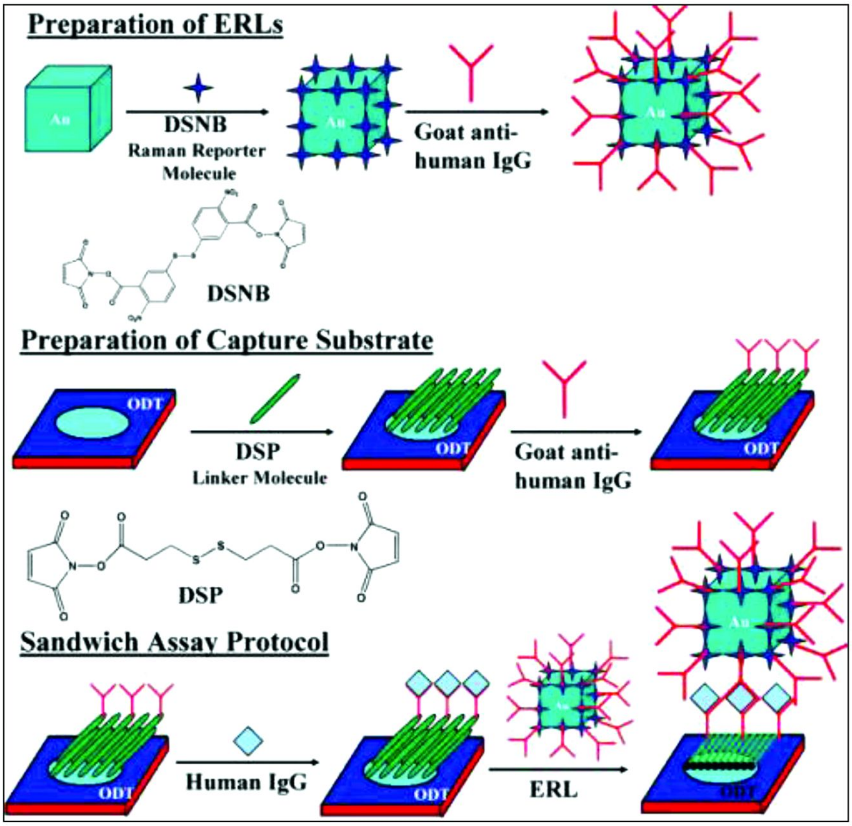
Preparation of ERLs
Au
DSNB
Raman Reporter Molecule
Au
Goat anti-human IgG
Au
DSNB
Preparation of Capture Substrate
ODT
DSP
Linker Molecule
ODT
Goat anti-human IgG
ODT
DSP
Sandwich Assay Protocol
ODT
Human IgG
ODT
ERL
Au
ODT

Figure 1. Three step process involved in a heterogeneous sandwich immunoassay for detection of proteins (1). Reproduced with permission from reference (1). Copyright (2008), (ACS).

Special shaped gold nanoparticles are used as SERS substrates due to its high sensitivity for this detection method and are especially advantageous for trace detection of biomolecules (*3*). Hexagon and boot shaped gold nanoparticles that are capped with starch are used as SERS substrates and it was found that the SERS properties varied for each gold nanoparticle shape. It was observed that using the boot-shaped gold nanoparticles resulted in 100 times higher SERS enhancements compared to spherical gold nanoparticles. Due to their very high

SERS enhancements, they have been applied for highly sensitive detection of avidin (*3*). It was found that concentrations as low as 0.01 unit/mL can be detected using the boot-shaped gold nanoparticles as SERS substrates. It is expected that these boot-shaped gold nanoparticles could find applications in other fields such as biolabeling, bioassays, biodiagnosis, and clinical diagnosis and therapy.

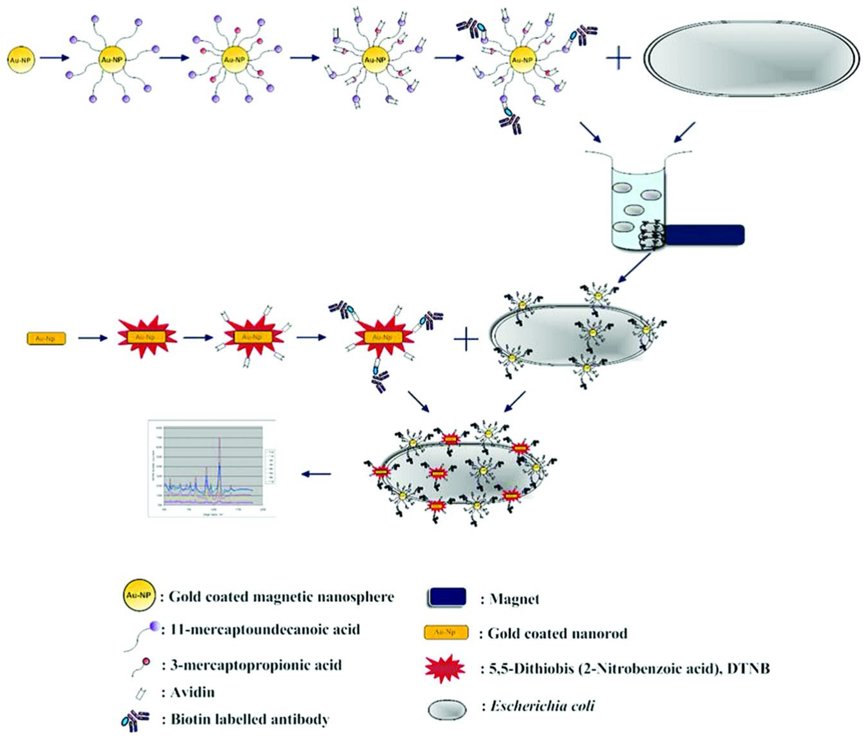
Au-NP
Au-Np
Au-NP : Gold coated magnetic nanosphere
: 11-mercaptoundecanoic acid
: 3-mercaptopropionic acid
: Avidin
: Biotin labelled antibody
: Magnet
Au-Np : Gold coated nanorod
: 5,5-Dithiobis (2-Nitrobenzoic acid), DTNB
: *Escherichia coli*

Figure 2. Schematic of sandwich immunoassay protocol using the spherical magnetic nanoparticles and the gold nanorods (2). Reproduced with permission from reference (2). Copyright (2011), (Royal Society of Chemistry).

Localized Surface Plasmon Resonance

Nanoparticle cluster arrays (NCAs) are a class of electromagnetic materials with chemically defined nanoparticles assembled into clusters of defined sizes and are fabricated via integration of chemically synthesized building blocks into predefined patterns (*4*). Figure 3 illustrates the method of formation of the NCAs and SEM images of the NCAs that have been formed using this method With NCAs, it is possible to sustain near-field interactions between nanoparticles within individual clusters as well as between entire neighboring clusters. The near-field interactions on multiple length scales coupled with the ability to further enhance the coupled plasmon modes through photonic modes in carefully designed array morphologies leads to a multi-scale cascade electromagnetic field enhancement throughout the array. The NCAs have potential applications in plasmon enhanced biosensing and surface enhanced Raman spectroscopy. The NCAs have been tested as potential biosensing substrates with two Gram-positive bacteria and one Gram-negative bacteria (*4*). The bacteria are grown to the log phase and washed with DI water prior to drop-coating onto the NCAs. There are stronger SERS signals for areas where the NCAs are coated with the bacteria compared to the uncoated areas. The NCAs showed consistently stronger SERS signals of the bacteria samples than the unpatterned Au NP film.

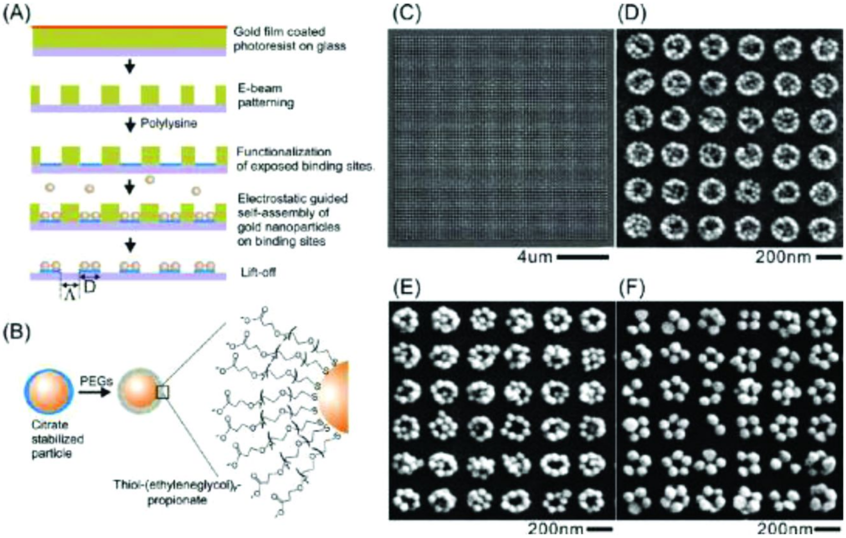
(A)
Gold film coated photoresist on glass
E-beam patterning
Polylysine
Functionalization of exposed binding sites
Electrostatic guided self-assembly of gold nanoparticles on binding sites
Lift-off
Λ
D
(B)
PEGs
Citrate stabilized particle
Thiol-(ethyleneglycol)$_n$-propionate
(C)
4um
(D)
200nm
(E)
200nm
(F)
200nm

Figure 3. Schematic showing the method of formation of the NCAs and SEM images of the NCAs that have been formed using this method (4). Reproduced with permission from reference (4). Copyright (2011), (ACS).

This paper discusses a single molecule biosensing scheme based on color differentiation of scattered light between single plasmonic NPs and DNA hybridization induced NP aggregates (*5*) . Figure 4 illustrates the concept of using the two different types of nanoparticles to conduct assay and detection via darkfield microscopy. By using a seed-mediated growth method and a fast DNA modification method, highly stable, spectrally uniform and monodisperse Au NPs and Au/Ag/Au composite NPs have been synthesized. The binding of a single-target molecule between two NP probes can be recognized without separation from the unbound NPs by using a darkfield microscope equipped with a conventional light source and a color charged coupled camera. This homogeneous assay has a limit of detection of 0.02 pM. It is also possible to do multiplexed sensing by using the two types of nanoparticles as different color probes(Xiao, Wei et al. 2010). This detection scheme can be applied to other areas such as multiplexed immunoassays, single cell analysis, and real time biomolecular interaction studies.

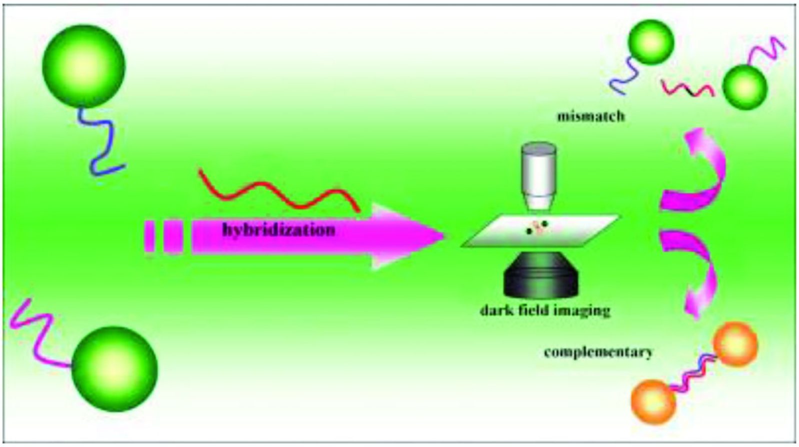
mismatch
hybridization
dark field imaging
complementary

Figure 4. Schematic illustrating the concept of using the two different types of nanoparticles to conduct assay and detection via darkfield microscopy (5). Reproduced with permission from reference (5). Copyright (2010), (ACS).

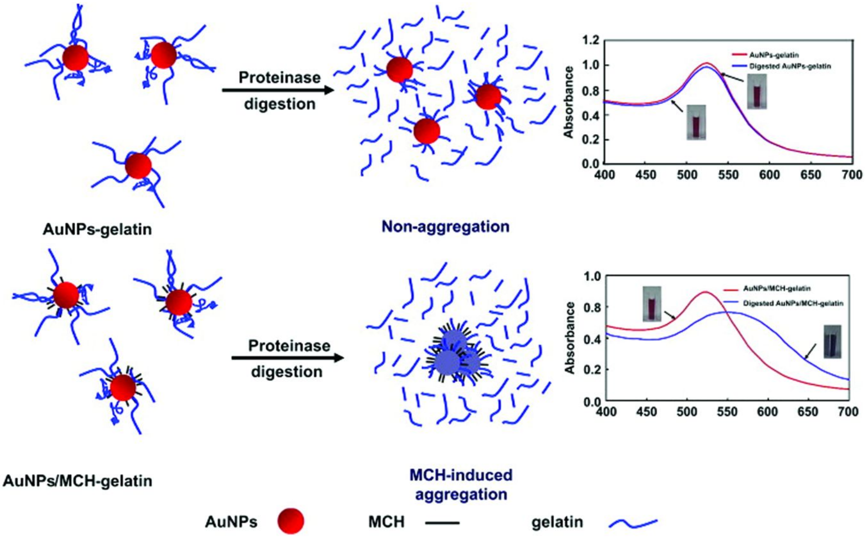
Proteinase
digestion
AuNPs-gelatin
Non-aggregation
Absorbance
1.2
1.0
0.8
0.6
0.4
0.2
0.0
400
450
500
550
600
650
700
AuNPs-gelatin
Digested AuNPs-gelatin
Proteinase
digestion
AuNPs/MCH-gelatin
MCH-induced
aggregation
Absorbance
1.0
0.8
0.6
0.4
0.2
0.0
400
450
500
550
600
650
700
AuNPs/MCH-gelatin
Digested AuNPs/MCH-gelatin
AuNPs
MCH
gelatin

Figure 5. Schematic of gold nanoparticle based optical biosensing platform used to assay proteinase activity (6). Reproduced with permission from reference (6). Copyright (2010), (Elsevier).

An optical biosensing platform for proteinase assay is established based on the SPR properties of the gold nanoparticles (*6*). Figure 5 illustrates gold nanoparticle based optical biosensing platform used to assay proteinase activity. The gold nanoparticles are modified with gelatin which serves as the proteinase substrate and then modified with 6-mercaptohexan-1-ol . After trypsin or gelatinous digestion, the gold nanoparticles lose shelter and the 6-mercaptohexan-1-ol increases the attractive forces between the modified gold nanoparticles. As a result of these increased attractive forces, the nanoparticles move closer to each other resulting in nanoparticle aggregation. There is a visible color change in the nanoparticles from red to blue and a shift in the surface plasmon band that occurs due to the aggregation. The proteinase activity can be quantitatively determined by looking at the ratio of the two absorption peaks. A linear correlation with the trypsin activity and the matrix metalloproteinase 2 has been established.

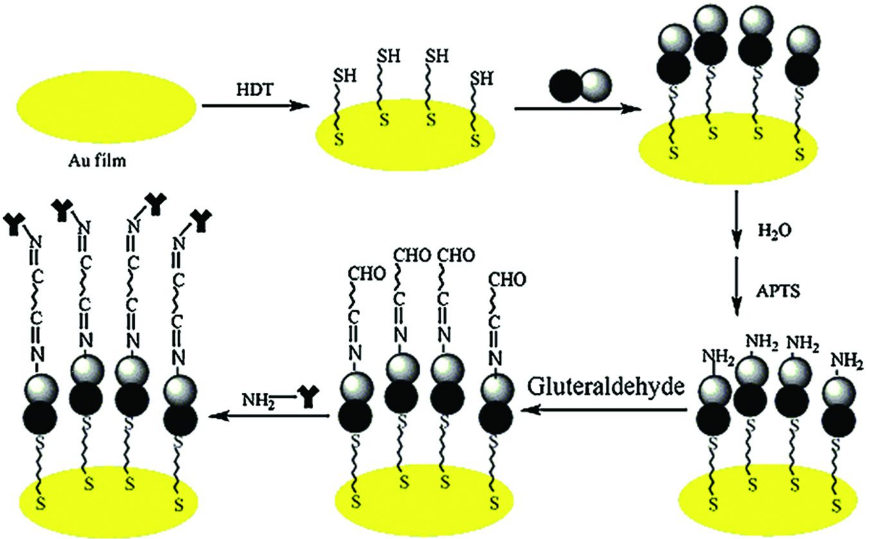

Figure 6. Schematic of the fabrication of the ZnO-Au nanocomposite based biosensor (7). Reproduced with permission from reference (7). Copyright (2009), (Elsevier).

A wavelength modulation surface plasmon resonance biosensor based on ZnO-Au nanocomposites was developed for the detection of human IgM (*7*). The self-assembly technique was applied to the building of the sensor as illustrated in Figure 6. The modified biosensor shows satisfactory response for human IgM in the concentration range from 0.3 – 20 µg/mL. This is better than the biosensor without the nanocomposites which exhibits a response of 1.25 – 20 µg/mL. The sensitivity for determination of concentration of human IgM is significantly enhanced when the biosensor based on the ZnO-Au nanocomposites was applied compared to the biosensor based on the Au film.

The use of biofunctionalized nanoparticles of different shapes and sizes have been used for the enhanced surface plasmon resonance detection of a protein biomarker at attomolar concentrations (*8*). The effect of different gold nanoparticle shapes were systematically compared. Each nanoparticle was functionalized with an antibody (anti-thrombin) and used as part of a sandwich assay in conjunction with an Au SPR chip modified with a specific DNA-aptamer probe specific to thrombin. The concentration of each nanoparticle-antibody conjugate solution was optimized first before establishing that quasi-spherical nanoparticles result in the greatest enhancement in sensitivity with the detection of thrombin at concentrations as low as 1 aM. When nanorod and nanocage nanoparticles are used, the minimum target concentrations that can be detected is 10 aM and 1 fM respectively. This is a significant improvement compared to previous studies and is attributed to functionalization of both the nanoparticle and chip surfaces resulting low nonspecific adsorption as well as a combination of density increases and plasmonic coupling inducing large shifts in the local refractive index at the chip surface upon nanoparticle adsorption.

Electrochemical

Cadmium sulfide nanoparticles have been synthesized using the solvothermal method (*9*). Rod and spherical shaped CdS nanoparticles have been formed using this method and the optical properties suggest quantum confinement by the nanoparticles. High photocatalytic activity towards the degradation of Rose Bengal has been achieved using the CdS nanoparticles. The CdS nanoparticles are also found to have peroxidase like activity that can catalyze the oxidation of the peroxidase substrate in the presence of hydrogen peroxide to produce a blue color reaction. The CdS nanoparticles have been anchored onto a glassy carbon electrode to study the electrochemical reduction of hydrogen peroxide in phosphate buffer solution. The modified electrode has also been used as amperometric biosensor for detection of hydrogen peroxide.

A highly sensitive electrochemical immunosensor based on combination of chitosan (CHT) and coral-shaped gold nanoparticles to form an immobilization matrix has been developed using human IgG as a model analyte (*10*). Figure 7 shows the design of the electrochemical immunosensor sensing device. The inorganic-organic hybrid film with abundant adsorbing sites and large surface area can reserve the biocompatibility of the biomaterials which can greatly increase the loading amounts of assembling and significantly improve the biosensing performance. The morphology is investigated by scanning electron microscopy (SEM). Under optimized conditions, the immunosensor exhibits excellent performance with detection limits of 5 pmol/L being achieved. Also the linear dynamic range is 3 orders of magnitude and there is also high specificity. This makes this electrochemical immunosensor an attractive platform for the direct immunoassay of human IgG or other biomolecules.

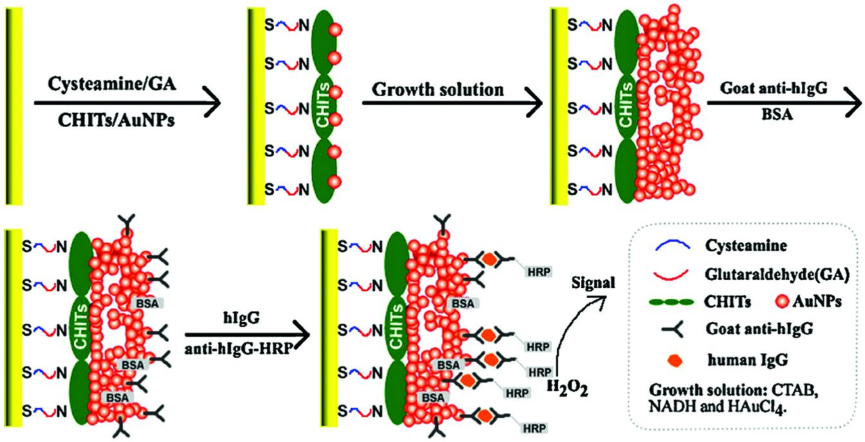

Figure 7. Schematic of the design of the electrochemical immunosensor sensing device (10). Reproduced with permission from reference (10). Copyright (2011), (Elsevier).

A tetragonal pyramid-shaped porous ZnO nanostructure is used for the immobilization, direct electrochemistry, and biosensing of proteins (*11*). The ZnO has a large surface area and good biocompatibility. Glucose oxidase is a model in which the shaped ZnO is tested for immobilization of proteins and the construction of electrochemical sensors with good electrochemical performances. The interaction between glucose oxidase and ZnO is examined by AFM, nitrogen adsorption isotherms, and electrochemical methods. The immobilized glucose oxidase on a zinc oxide modified glassy carbon electrode shows a good direct electrochemical behavior, which depends on the properties of the ZnO. The proposed biosensor exhibits a linear response to glucose concentrations ranging from 0.05 to 8.2 mM with detection limit of 0.01 mM at an applied potential of -0.5 V. As a result, these types of ZnO nanoparticles have better biosensing properties than other ZnO morphologies. This ZnO biosensor shows good stability, reproducibility, and low interferences. It can also diagnose diabetes very fast and sensitively.

A well-ordered nanosieve structure of silver nanoparticles was synthesized using a hydrothermal method (*12*). Figure 8 shows TEM images and electron diffraction pattern of the silver nanoparticles. The crystallinity of the silver nanoparticles was confirmed by X-ray diffraction. The silver nanoparticles have an average size of 35 nm and have a hexagonal shape with a nanosieve structure. Also, the SPR peak is at 410 based on the UV-Visible spectrum. The silver nanoparticle nanosieve modified electrode shows excellent catalytic activity towards the reduction of hydrogen peroxide at a low overpotential. The nanosieve may also be promising for electronics and photonics applications.

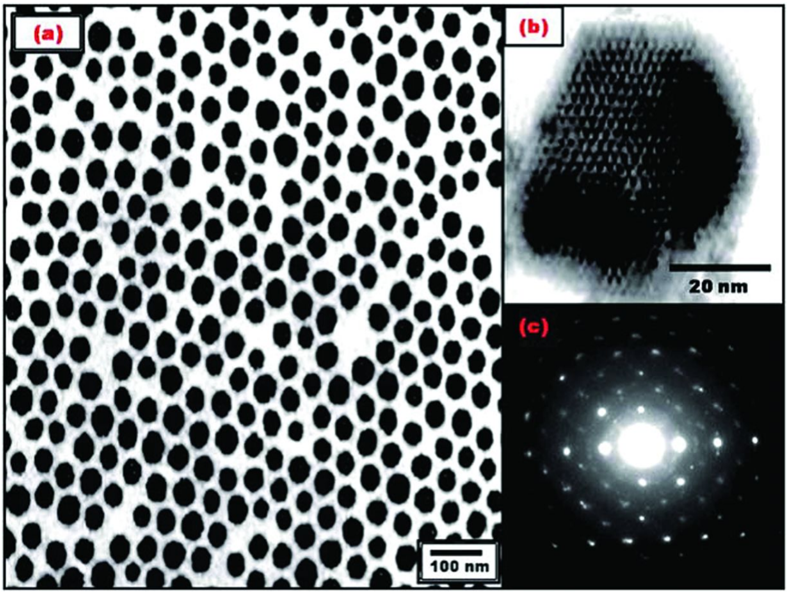

Figure 8. TEM images of the silver nanoparticles as well the electron diffraction pattern (12). Reproduced with permission from reference (12). Copyright (2011), (Royal Society of Chemistry).

A nano-sized tetragonal pyramid-shaped porous ZnO nanostructure was prepared in highly morphological yield by polyglycol assisted wet chemical method (*13*). The polyglycol has a significant effect on nucleation and pore formation in the ZnO nanostructure. The hydroxide concentration and the zinc counterion affected the morphology of the produced ZnO nanostructure. TPSP-ZnO can be used as an efficient matrix for immobilizing horseradish peroxidase and applied to sense hydrogen peroxide. These ZnO nanostructures have better biosensing properties then solid ZnO nanoparticles, which is due to the larger surface area of TPSP-ZnO, causing a higher HRP loading. Also, the tetragonal pyramid ZnO nanostructures have high fraction of surface atoms located on the corners and edges, resulting in an improved catalytic activity.

Colorimetric

The key to effective and successful treatment of diseases such as cancer is early and accurate diagnosis (*14*). A simple colorimetric and highly sensitive two-photon scattering assay as illustrated in Figure 9 for highly selective and sensitive detection of breast cancer SK-BR-3 cell lines at 100 cells/mL level is reported for the first time using a multifunctional (monoclonal anti-HER2/c-erb-2 antibody and S6 RNA aptamer-conjugated) oval-shaped gold-nanoparticle based nanoconjugate. When these oval-shaped gold nanoparticles are mixed with the breast cancer SK-BR-3 cell line, a distinct color change occurs and two-photon scattering intensity increases 13 times. Experimental data with the HaCaT noncancerous cell line, as well as with MDA-MB-231 breast cancer cell line, clearly demonstrated that this assay was highly sensitive to SK-BR-3 and it was able to distinguish from other breast cancer cell lines that express low levels of HER2. The mechanism of selectivity and the assay's response change has been discussed. These experimental results reported here open up a new possibility of rapid, easy, and reliable diagnosis of cancer cell lines by monitoring the colorimetric change and measuring TPS intensity from multifunctional gold nanosystems.

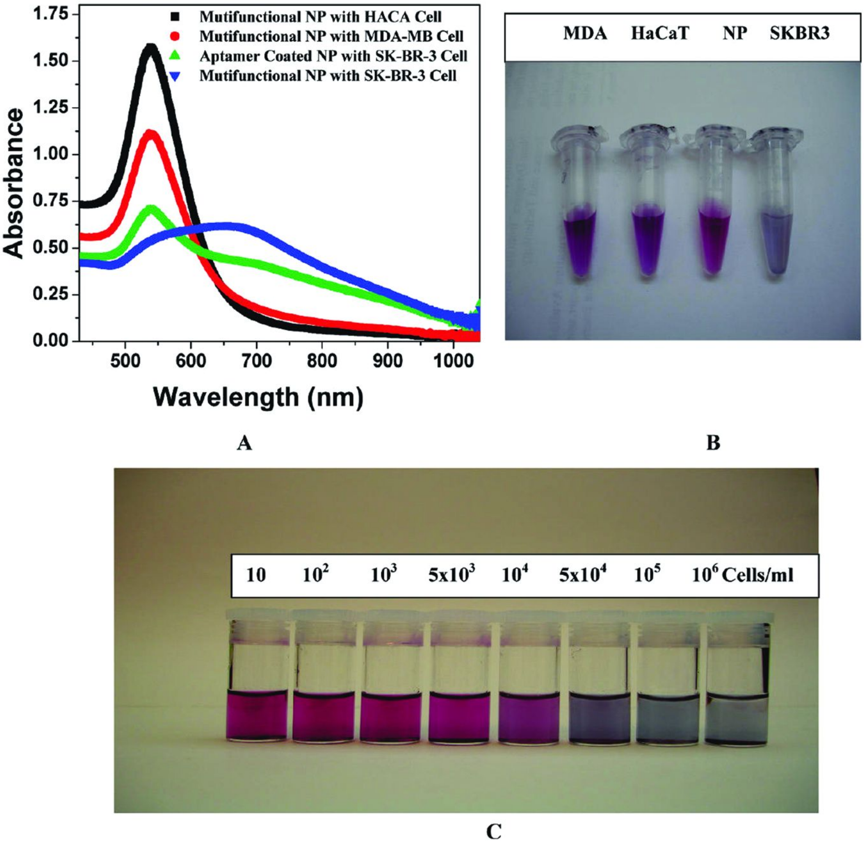

Figure 9. Results from the colorimetric experiments (14). Reproduced with permission from reference (14). Copyright (2010), (ACS).

References

1. Narayanan, R.; Lipert, R. L.; et al. Cetyltrimethylammonium Bromide-Modified Spherical and Cube-Like Gold Nanoparticles as Extrinsic Raman Labels in Surface-Enhanced Raman Spectroscopy Based Heterogeneous Immunoassays. *Anal. Chem.* **2008**, *80*, 2265–2271.
2. Guven, B.; Basaran-Akgul, N.; et al. SERS-based sandwich immunoassay using antibody coated magnetic nanoparticles for Escherichia coli enumeration. *Analyst* **2011**, *136*, 740–748.
3. Hu, J.; Wang, Z.; et al. Gold Nanoparticles With Special Shapes: Controlled Synthesis, Surface-enhanced Raman Scattering, and The Application in Biodetection. *Sensors* **2007**, *7*, 3299–3311.
4. Yan, B.; Boriskina, S. V.; et al. Design and Implementation of Noble Metal Nanoparticle Cluster Arrays for Plasmon Enhanced Biosensing. *J. Phys. Chem. C* **2011**, *115*, 24437–24453.
5. Xiao, L.; Wei, L.; et al. Single Molecule Biosensing Using Color Coded Plasmon Resonant Metal Nanoparticles. *Anal. Chem.* **2010**, *82*, 6308–6314.
6. Chuang, Y.-C.; Li, J.-C.; et al. An optical biosensing platform for proteinase activity using gold nanoparticles. *Biomaterials* **2010**, *31*, 6087–6095.
7. Wang, L.; wang, J.; et al. Surface plasmon resonance biosensor based on water-soluble ZnO–Au nanocomposites. *Anal. Chim. Acta* **2009**, *653*, 109–115.
8. Kwon, M. J.; Lee, J.; et al. Nanoparticle-Enhanced Surface Plasmon Resonance Detection of Proteins at Attomolar Concentrations: Comparing Different Nanoparticle Shapes and Sizes. *Anal. Chem.* **2012**, *84*, 1702–1707.
9. Maji, S. K.; Dutta, A. K.; et al. Peroxidase-like behavior, amperometric biosensing of hydrogen peroxide and photocatalytic activity by cadmium sulfide nanoparticles. *J. Mol. Catal. A: Chem.* **2012**, *358*, 1–9.
10. Tang, J.; Hu, R.; et al. A highly sensitive electrochemical immunosensor based on coral-shaped AuNPs with CHITs inorganic–organic hybrid film. *Talanta* **2011**, *85*, 117–122.
11. Dai, Z.; Shao, G.; et al. Immobilization and direct electrochemistry of glucose oxidase on a tetragonal pyramid-shaped porous ZnO nanostructure for a glucose biosensor. *Biosens. Bioelectron.* **2009**, *24*, 1286–1291.
12. Singh, R. P.; Pandey, A. C. Silver nanosieve using 1,2-benzenedicarboxylic acid: a sensor for detection of hydrogen peroxide. *Anal. Methods* **2011**, *3*, 586–592.
13. Dai, Z.; Liu, K.; et al. A novel tetragonal pyramid-shaped porous ZnO nanostructure and its application in the biosensing of horseradish peroxidase. *J. Mater. Chem.* **2008**, *18*, 1919–1926.
14. Lu, W.; Arumugam, S. R.; et al. Multifunctional Oval-Shaped Gold-Nanoparticle-Based Selective Detection of Breast Cancer Cells Using Simple Colorimetric and Highly Sensitive Two-Photon Scattering Assay. *ACS Nano* **2010**, *4*, 1739–1749.

Chapter 11

Electrochemical Sensors and Biosensors Based on Self-Assembled Monolayers: Application of Nanoparticles for Analytical Signals Amplification

Hanna Radecka,* Jerzy Radecki, Iwona Grabowska, and Katarzyna Kurzątkowska

Laboratory of Bioelectroanalysis, Department of Biosensors, Institute of Animal Reproduction and Food Research of Polish Academy of Sciences,
Tuwima 10, 10-748 Olsztyn, Poland
***E-mail: hanna.radecka@pan.olsztyn.pl. Phone: +48 89 523 46 36.**
Fax: +48 89 524 01 24

One of the most popular techniques to create well-defined functional surfaces is the formation of self-assembled monolayers (SAMs) based on the covalent interactions of thiols, disulphides, sulphides and other related molecules with the surfaces of noble metals, particularly gold, as well as platinum and mercury. This phenomenon is a base of sensors and biosensors presented. They can be divided into two main categories. The first type is based on ion-channel mimetic mode, where the analytical signals are governed by changing of accessibility of redox marker (present in the sample solution) to the electrode surface upon analyte recognition. This analytical approach was successfully applied for development of sensors and biosensors destined for determination of numerous analytes, relevant for medical diagnosis, such as: adenine nucleotides, ethene dicarboxylic acids, dopamine, viruses, His-tagged proteins and specific sequences of DNA.

Biosensors based on ion-channel mimetic mode were also suitable for screening of interactions between amyloid β-peptide and potential drugs.

In Functional Nanoparticles for Bioanalysis, Nanomedicine, and Bioelectronic Devices Volume 1; Hepel, M., et al.;
ACS Symposium Series; American Chemical Society: Washington, DC, 2012.

Another type of sensors and biosensors presented is based on redox active monolayers.The gold electrodes modified with (dipyrromenthene)$_2$-Cu(II) and porphyrine-Fe (III) were applied for amperometric determination of paracetamol and L-histidine, respectively.

The electrodes functionalized with dipyrromethe-Cu(II) SAM was suitable for oriented and stable immobilization of His-tagged proteins. This redox active monolayer was a base of biosensors destined for exploring the interactions between receptor protein and target species present in the aqueous solutions.

The analytical signal amplification obtained through application of the different kind of nanoparticles such as colloidal gold, nanorods and carbon nanotubes for sensor construction will be disused.

Keywords: Gold electrode; functionalization; self-assembling monolayers synthetic receptors; natural receptors; nanoparticles; voltammetry; electrochemical impedance spectroscopy

Introduction

Nowadays the main streams of analytical research are directed to improve the efficiency of medical diagnosis, safety food production and environment screening. The development of all of these branches is not possible without suitable analytical methods. Such situation is a drive force for continuous work on the new trends in analytical chemistry clearly visible in the numerous recent published scientific literatures (*1–8*).

The remarkable selectivity and sensitivity of molecular recognition processes occurring in the biological systems are going in water. This makes the inexhaustible source of inspiration for researchers dealing with supramolecular and analytical chemistry.

Generally, intermolecular recognition processes are relied on the formation of hydrogen bonds, electrostatic interactions, Van der Waals interactions, π electron interactions, and Lewis acid – acid base interactions.

The development of systems that can efficiently and selectively interact with target species in water is intrinsically difficult. Recent developments do however suggest that solutions can be found through a supramolecular approach which takes its inspiration from the natural world (*9–11*). Nature achieves high affinity and high selectivity towards targeted substrate in water through multiple weak, non covalent interactions between the functional groups on the binding partners.

Many of synthetic and natural receptors have lack of water solubility, which prevents binding studies in aqueous solution. One way of solution of this problem is immobilization of receptors at the surface of solid electrodes. Such system allows for observation of intermolecular recognition processes at the interface water / solid electrodes. Interface it is a place in which the most of biologically relevant recognition processes are going on.

Thus, intermolecular recognition processes occurring at the border between the surface of electrode and water sample solution are the base for development of new electrochemical sensors and biosensors suitable for medical diagnosis, food analysis and environmental screening.

Generally, sensor is a tool that integrates synthetic sensing element with physical transducer where the interactions between the sensing element and target molecules are directly converted into an electronic signal. Biosensors are sub-group of sensors that pose as a sensing element the biological molecules. Selectivity of sensors or biosensors is determined by selectivity of recognition process. On the other hands, sensitivity is governed by two parameters: sensitivity of intermolecular recognition and efficiency of transducer. In recent years, a continuous and fast increase of number of articles concerning the electrochemical sensors is clearly visible (*12–14*).

Here we described the of electrochemical sensors and biosensors based on modified electrodes consist of receptors and nanomaterials designated for medical diagnosis, food analysis and environmental screening.

According to mechanism of analytical signal generation, they can be divided into two general groups:

- Sensors and biosensors based on ion-channel mimetic mode
- Sensors and biosensors based on bi-functional redox active layers, which serve as a transducer and analytically active element at the same time.

Sensors and Biosensors Based on Ion-Channel Mimetic Mode

The ion-channel biomimetic sensor is one in which the kinetic of electron transfer reaction of the redox marker present in the sample solution is affected by analytes binding to the receptor. This system consist of two elements: electrode modified with receptor molecules and redox active marker in solution (Figure 1). This analytical approach was introduced by Umezawa and co – workers (*15*, *16*).

The mechanism of this sensing method relys on the control of the redox active marker accessibility to the electrode surface by the binding events between the analytes from solution and receptor molecules located on the surface of electrode.

There are two sub-groups of ion channel sensors:

- Intermolecular type in which the receptor monolayer and analyte as results of recognition formed the charged supramolecular complex and access of marker to surface of electrode is controlled by electrostatic interactions (Figure 1A).
- Intramolecular type in which the access of marker to the surface of electrode is controlled by steric hindrance which appear at the surface of electrode as a consequence of recognition process between the analytes an receptor molecules located at the surface of electrode (Figure 1B).

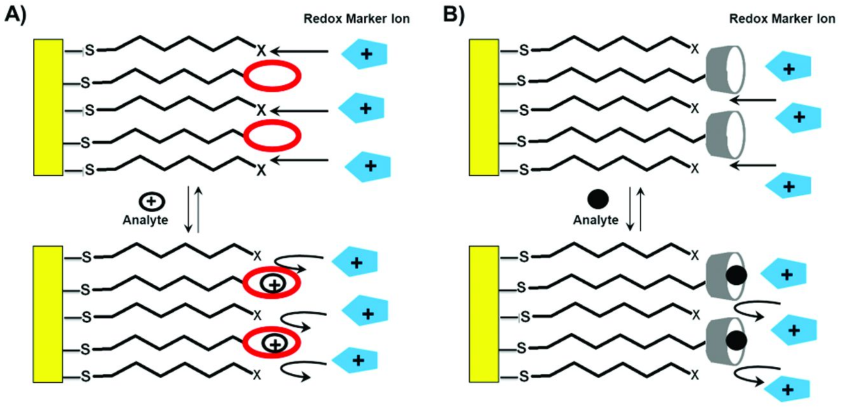

Figure 1. Working principle of ion-channel mimetic sensor: A - intermolecular type, B - intramolecular type. (see color insert)

The main advantage of ion-channel sensors is the possibility of determination with high sensitivity of the non electroactive analytes by using of amperometric techniques. Ion-channel sensors have the inherent possibility of signal amplification. The binding of only few numbers of analytes to the receptors monolayer can induce, or suppress oxidation and/or reduction of a greater numbers of markers (Figure 1A, B).

Generally in the literature there are not so many examples of intramolecular ion channels sensors. One of this approach is the detection of redox-inactive and electrically neutral analytes by a cyclodextrin derivative monolayer (*17*).

First examples *intramolecular ion channels sensors* developed in our laboratory are sensors based on gold electrodes modified with the macrocyclic polyamine as an analytically active element (*18*, *19*). In these cases for incorporation of host molecules on the electrode surface we have applied two methods. The first one uses macrocyclic polyamine host molecules containing six SH groups responsible for covalent bonding to the surface of gold electrode (Figure 2A). The second method of modification employ macrocyclic polyamine host incorporated into a 1-dodecanethiol SAM immobilized onto the Au surface via hydrophobic and van der Waals forces (embedment modification) (Figure 2B).

The electrodes modified in such manners were used for adenine nucleotides (*18*) and ethene dicarboxylic acids detection (*19*).

The sensing of adenine nucleotides was done using both type of electrodes with two techniques, CV and OSWV. The measurements have been performed in the presence of borate buffer, because components of this buffer showed no influence on the voltammetric behaviour of gold electrodes coated with macrocyclic polyamine films. Two redox markers: $[Ru(NH_3)_6]^{3+}$ and $[IrCl_6]^{2-}$ showed quasi-irreversible CV curves in the absence of anionic guests. The interactions of adenine nucleotides with the polyamine hosts were examined with the both of markers (*18*). In the case of positive $[Ru(NH_3)_6]^{3+}$ and negative $[IrCl_6]^{2-}$, the decrease of currents with increase of anionic guests concentration were observed. The highest response of both types of electrodes, modified via covalent and embedment method was observed in the presence of ATP^{4-}. The sensitivity sequence observed for both of redox markers was as follows:

$$HPO_4^{2-} < AMP^{2-} < ADP^{3-} < ATP^{4-}$$

The sensors prepared by the embedment method displayed two order of magnitude better detection limit (~1.0 × 10^{-7} M) for ATP^{4-} than the sensors modified by the covalent technique. This enhanced detection limit suggests that flexibility of the receptors, and decreasing of free energy of ion transfer across the interface may play a crucial role in recognition of target analytes. Both types of electrodes are characterized by good durability and sensor–to–sensor repeatability.

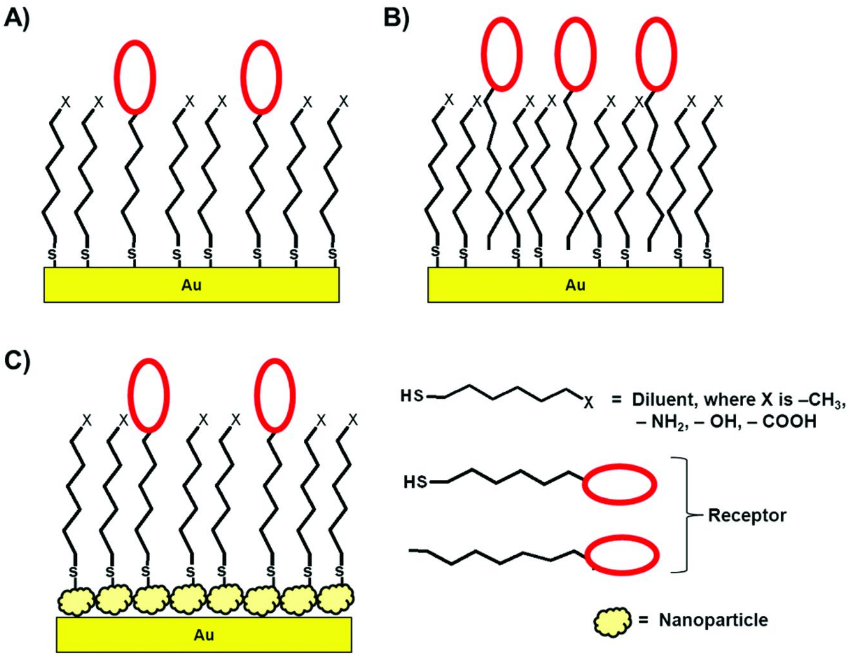

Figure 2. Schematic illustration of receptor immobilization on the surface of gold electrodes by: A - covalent bonds, B - embedment method, C - using nanoparticles. (see color insert)

As it was mentioned above we have observed that upon increasing concentration of anionic analytes, the current of redox reaction decreased, for both types of applied markers and macrocyclic polyamine modified gold electrodes.

A possible explanation of this phenomenon might be as follows. In this particular case, the molecular layer packing factor induced by host–guest complexation, which may cause a decrease in permeability of the cationic marker, seems to dominate over the effect of reduction of charge repulsion (*16*, *17*). The results obtained indicated that macrocyclic hexapolyamines incorporated into SAMs immobilized onto gold surfaces form rather intramolecular ion channel sensors. In such type of sensors, the interaction between host and guest control the permeation of marker ions through the intramolecular cavity of polyamines. With the increase of adenine nucleotides or ethene dicarboxylic acids concentration, the decrease of peak currents and their shifts to the negative potentials were observed. It appears that macrocyclic polyamines form on the surface of gold the intramolecular channel type sensors sensitive towards anionic guests (*18*, *19*).

The sensor for determination of dopamine is an example of *intermolecular ion channel* sensor developed in our laboratory (*20*). Dopamine (DA) is one of the most significant neurotransmitters because of its role in the functioning of the cardiovascular, renal, hormonal, and central nervous system. The majority of electrochemical sensors for dopamine determination exploit its ease of oxidation. However, the oxidative approaches suffer from interferences caused by other electroactive substances existing in the physiological samples. One of the main interferences is ascorbic acid (AA). The concentration of DA is extremely low (0.01-1 μM) while that of AA is as high as 0.1 mM in biological systems (*21*). Moreover, at almost all electrodes materials, DA and AA are oxidized at nearly the same potential, which results in overlapped voltammetric response. In order to solve this problem, we decided to apply the different approach for the detection of DA based on an intermolecular ion-channel mimetic sensor. In such type of sensor the binding of analytes to receptors immobilized on electrode surfaces facilitates or suppresses the access of an anionic (cationic) marker ion to the modified surface due to electrostatic attraction or repulsion of the marker and/or distortion of the modification layer arrangement. This leads to the changes of the electron transfer rate between the marker and electrode surface through the modification layer. This type of ion-channel sensor is a subject of numerous scientific literatures (*15*, *16*, *22–24*).

It has been already reported that corrole derivatives form complexes with dihydroxybenzene derivatives through a NH· · ·OH hydrogen bond (*25*). Thus, this compound has been selected as a suitable receptor for dopamine.

Figure 1A illustrates the working principle of the sensor proposed. The corrole host molecules have been covalently attached on the surface of gold electrodes through Au-S bonds. In the measuring condition (pH 7.0), corrole exists as an uncharged molecule (*25*). The monolayer created on the electrode surface is quasi permeable for a redox marker existing in the aqueous solution. Upon addition of dopamine, the corrole-DA complex is formed and the monolayer gained the positive charge, which repealed the positive charged redox marker. This leads to the decreasing of the electron transfer rate between the marker and electrode surface through the modification layer. The electroanalytical signals generated based on the corrole-DA complex formed at the electrode surface were explored using Osteryoung square-wave voltammetry (OSWV) and electrochemical impedance spectroscopy (EIS) in the presence of $[Ru(NH_3)_6\ ]^{+3}$

as an electroactive marker, which does not interfere with the oxidation of the DA or AA.

The proposed sensor is effective regarding the following parameters: very good sensitivity toward DA (detection limit in 10^{-12} M range by using both EIS and OSWV techniques), very good selectivity (human plasma components at 80-fold dilution have no influence on dopamine determination), simple, and quick procedure of electrode preparation. Therefore, the gold electrodes modified with mixed corrole-mercaptohexanol SAM work as intermolecular “ion-channel mimetic sensors” in the presence of $[Ru(NH_3)_6]Cl_3$ as the redox marker and could be applied for the determination of dopamine in clinical analysis (*20*).

The similar working manner was applied for the sensor designed for determination of acrylic acid in food samples based on gold electrode modified with tetralactam (*26*).

The recent example of ion-channel mimetic sensor electrochemically developed in our laboratories is genosensor with covalently attached HS-ss DNA probe destined to detection of specific DNA sequence of avian influenza virus H5N1 (*27*).The hybridization processes with target DNA was monitored with OSWV in the presence of $[Fe(CN)_6]^{3-/4-}$ redox probe. The genosensor displayed good sensitivity, namely detection limits of 2.2×10^{-11} M and 2.4×10^{-11} M for complementary 20-mer ssDNA and double stranded 181-bp DNA containing 20 nucleotides complementary to the probe. This genosensor was also able to discriminate different positions (at 3’-end, middle and 5’-end) of the complementary part in the PCR products.

Electrochemical Sensors and Biosensors Incorporating Nanoparticles

Nanotechnology has recently become one of the most exiting fields in analytical chemistry.

A wide variety of nanomaterials, especially gold nanoparticles have been applied in broad area (*28*). They allow increase in surface area of modified electrodes. This leads to increase of biomolecules numbers in analytically active layers and improving the sensitivity of analytical devices.

Nanoparticles (in the size range of 1-100 nm) exhibit unique chemical, physical and electronic properties that are different from those of bulk materials, and can be used to construct electrochemical sensors and biosensors with improving sensing properties (*28*).

The most popular metal nanoparticles are colloidal gold (*29–31*) and gold nanorods (*32–35*). The isotropic nature of spherical colloidal gold nanoparticles prevents the selective binding of molecules on surfaces. In contrast, the anisotropic features of Au nanorods allow their assembly in various orientations (*35*).

Both of them, having excellent conductivity and biocompatibility are widely used in electrochemical sensors for analytical signal amplification (*29*, *31*, *33*, *36–40*). The dynamic assembly and disassembly of double–strand DNA modified Au nanorods at different temperature was a base of plasmonic circular dichroism response towards ssDNA at nM level (*41*).

The type of nanoparticles suitable electrochemical sensor design are carbon nanotubes (*42–44*) and more recently graphene (*6–8*, *45*, *46*). The one of the crucial role of carbon nanotubes, graphene and gold nanoparticles in senor or biosensor construction is the enhancement of electron transfer from redox centers to the electrode surface (*8*, *28*).

The graphene is a flat monolayer of carbon atoms, tightly packed into a two–dimensional (2D) honeycomb lattice (*46*). Whereas, single-walled carbon nanotube (SWCNTs) can be interpreted as the graphene sheets rolled up to form hollow tubes with diameters ranging between 0.4 and 2 nm (1D structure) (*42*). The electronic properties of the tubes are strongly affected by both the rolling angle of the graphene sheets and their final diameter.

These carbon nanostructures are both one atom thick, and their electronic properties are extremely sensitive to adsorption of chemical species on their surface. The carbohydrate - functionalized carbon nanotubes as well as graphene could be employed for the rapid identification of bacteria in samples consisting of water systems, soils, or human specimens (*45*). Multilayered graphene – Al_2O_3 nanopore sensors showed high sensitivity for detection of DNA and DNA-protein complexes (*47*). Urea, clinically important analyte, was successfully detected with ITO electrode functionalized with multilayered graphene (*46*).

The self-assembly of gold nanoparticles on single–walled carbon nanotubes is the recent excellent example of complex nano-structure successfully applied for sensing of different gasses (*48*).

Taking into account the properties of the gold, as well as carbon nanostructures, we have applied them for fabrication of sensors and biosensors working in ion-channel bio-mimetic mode.

Two main strategies were employed for receptor immobilization on the nanoparticle surface: one is based on electrostatic interactions (Figure 3A) and another one is based on covalent bonds between Au–S atoms (Figure 3B).

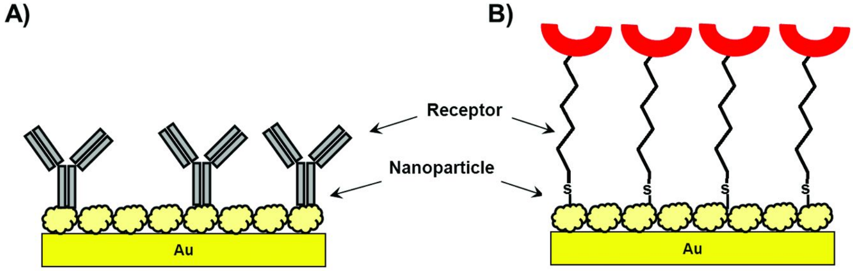

Figure 3. Schematic illustration of sensors based on nanoparticles. Receptor immobilization : A - via electrostatic interactions; B - via covalent bonds. (see color insert)

One of the example of the application of colloidal gold particles is ion-channel mimetic biosensor destined for the determination of association constant of β amyloid with selected alkaloids (*49*, *50*).

The main therapeutic strategy in Alzheimer's disease relays on use the inhibitors which should bind or stabilized the α-helical or early formed β-sheet structures (*51*, *52*).

The compounds used as the inhibitors of amyloidosis are: peptides (*53*), antibodies (*54*), isoflavones (*52*), nicotine and its metabolites (*51*, *55*), just to name a few.

Using the electrochemical biosensor based on impedance spectroscopy (EIS), the association constants of (−)cotinine and (−)nicotine ditartrate and selected alkaloids with Aβ (1–40) peptide were determined (*49*, *50*). Such attempt mimics well the physiological processes occurring at the interface. The crucial step of proposed method is the suitable immobilization of Aβ (1–40) peptide on the electrode surface. It is known that, adsorption of proteins onto bulk metal surfaces leads to their denaturation and loss of their bioactivity (*56*). The additional modification of gold electrodes with colloidal gold nanoparticles is one of the solution of the above problem. It has been recently reported that proteins adsorbed onto colloidal Au retain their bioactivity (*56*, *57*). In the work presented, the gold electrodes were modified with Au nano-particles by self-assembly with using 1,6-hexanedithiol as cross-linkers. So, the Aβ (1–40) peptide was adsorbed directly on the surface of colloidal Au (Figure 3A). The interactions between Aβ (1–40) peptide and with two potent drug molecules (−)nicotine ditartrate and (−)cotinine (*49*) and selected alkaloids (*50*) were monitored with using electrochemical impedance technique (EIS).

It might be concluded that the electrochemical impedance spectroscopy, together with electrode modified with self-assembled layer of colloidal Au is very suitable technique for screening the interactions between Aβ-peptides and compounds, which could be applied as the potential drugs. This measuring system is relatively simple in the comparison to other spectroscopic one and allows to determine not only thermodynamic of the interfacial interactions, but their kinetics as well (*57*).

The immunosensors incorporated antibodies as a sensitive element mainly work according to mechanism of intramolecular ion-channel.

This type of biosensors are promising tools for detection of pathogens since antibodies are natural receptors responsible for binding of antigens harmful for the organism. Thus their binding selectivity and efficiency are naturally high. The complex between antigen and specific antibody adsorbing on a surface of an electrode forms an insulating layer. This phenomenon can be monitored by electrochemical impedance spectroscopy (*58*).

In order to improve immunosensors sensitivity the colloidal gold and gold nanorods were applied for their fabrication (*59*, *60*) (Figure 3A). The successive electrode modification steps: (1) 1,6-hexanedithiol SAM formation on the Au electrode, (2) gold nanoparticles layer formation through Au-S covalent bonds, (3) deposition of antibody, (4) blocking the remaining spaces on gold layer with BSA, were controlled using CV and EIS.

Both type of gold nanoparticles facilitate the electron transfer between the redox marker and the electrode surface, and at the same time create the suitable environment for biomolecule deposition assuring keeping their biological activity (*49*, *50*, *59*, *60*). The immobilization of antibody on the gold nanoparticle layer, forming the insulating layer, decreased the accessibility of $[Fe(CN)_6\ ]^{-3/-4}$. Further decreasing of the faradaic current was observed upon immobilization of BSA onto the remaining space on the gold layer.

The electron interfacial resistance increased linearly with increasing concentration of specific antigen His_6-rSPI2 in the range between 10pg/ml and 1 ng/ml. Immunosensors using gold nanorods showed 40% better analytical response then this incorporating colloidal gold (*59*). Nanorods, unlike more symmetrically shape nanoparticles have the ability to assemble aligned configuration. This property make them suitable for electrochemical devices. The immunosensors for His-tagged proteins determination were very selective. The presence of culture medium has no influence on immunosensors performance (*59*, *60*).

The similar strategy was applied for the immunosensor fabrication destined for determination of *Plum pox virus* virus PPV (*61*). The formation of specific complex between antibody attached to the gold nanoparticles covalently attached to the electrode surface and viruses present in the sample solution caused the increase of interfacial electron transfer resistance dependent.

The quantitative assessment of sensitivity of PPV detection was performed using EIS with a series of dilutions of purified virions. The virus was suspended (and then diluted) either in 0.1 M PBS buffer pH 6.0, or in healthy plant (plum or tobacco) leaf extracts. The immunosensor proposed is not sensitive to the matrix of healthy leave extract. Only a very small increase of electron transfer resistance was observed between the value recorded for the pure PBS buffer and the value recorded for healthy plum leave extract (*61*). The immunosensor displayed very good analytical parameters: a very low detection limit (10 pg PPV) and very good dynamic range from 10 pg PPV/mL to 200 pg/mL.

The immunosensors based on electrochemical impedance spectroscopy incorporating gold nanaoparticles are promising devices for fast, reliable and simple PPV detection and His-tagged proteins control (*59–61*).

The determination of nucleic acid sequences humans, animals, bacteria and viruses constitute the starting point to solve different problems such as: food and water contamination caused by microorganisms, as well as detection of genetic disorders. The electrochemical genosensors could be very interesting analytical tools for solving these problems (*27*, *62*).

Among DNA sensors, two main groups can be distinguished according to the different protocols, based on labeling DNA target or using a label-free approach. Regarding the first approach, common label used for hybridization detection can be fluorescent dyes, redox active enzymes, magnetic particles or different kinds of nanoparticles.

An indirect labeling scheme consist of the use of redox couple indicators such as metal complexes in solution, which generate electrochemical analytical signal (*63*).

A polylysine/single-walled carbon nanotubes modified electrode was used for the impedimetric detection of transgenic plants gene fragment with an estimated detection limit around 0.1 pM (*64*). Bonanni et al. (*65*) employed screen-printed electrodes modified with carboxyl functionalized multi-walled carbon nanotubes as platforms for impedimetric genosensing of oligonucleotide sequences specific for transgenic insect resistant Bt maize. Amino-modified DNA probe was covalently immobilized by EDC-NHS chemistry. A similar platform, consisting of carboxylic acid functionalized single-walled carbon nanotubes modified graphite sensors was employed by Caliskan et al. (*66*) for electrochemical monitoring of DNA hybridization related to specific sequence of Hepatitis B virus. The presence of carbon nanotubes enhanced the electrochemical (voltammetric and impedimetric) signals in comparison to bare graphite. A novel biosensing platform was introduced by Nebel et al. (*67*) by combining a geometrically controlled DNA bonding using vertically aligned diamond nano-wires, a superior transducer material. Ultra-hard vertically aligned diamond nano-wires were electrochemically modified to bond phenyl linker molecules to their tips which provide mesospacing for DNA molecules on the transducer. Electro- and bio-chemical sensor properties were investigated using cyclic and differential pulse voltammetry as well as impedance spectroscopy with $Fe(CN)_6^{3-/4-}$ as redox markers, which provided sensitivities of 2 pM on 3 mm^2 sensor areas and superior DNA bonding stability over 30 hybridization/denaturation cycles. Yang et al. (*68*) deposited a poly-2,6-pyridinedicarboxylic acid film (PDC) on a glassy carbon electrode (GCE). Then gold nanoparticles (NG) were added to the platform to prepare NG/PDC/GCE. After that, the ssDNA probe was immobilized on the NG/PDC/GCE by the interaction of NG with DNA. The electron transfer resistance (R_{et}) of the electrode surface in $[Fe(CN)_6]^{3-/4-}$ solution increased after the immobilization of the DNA probe on the NG/PDC/GCE. The hybridization of the DNA probe with cDNA made R_{et} increase further. The NG modified on the PDC dramatically enhanced the immobilization amount of the DNA probe and greatly improved the sensitivity of the label-free detection of the sequence-specific DNA related to PAT gene in the transgenic plants with detection limit of 2.4×10^{-11} mol L^{-1}.

It might be concluded that the electrochemical sensors and biosensors working according to ion channel mimetic mechanism which are relatively simple measuring systems could be successfully applied as analytical devices with very high sensitivity as well as selectivity.

The main advantages of ion -channel mimetic sensors are as follow:

- Offering capability of signal amplification
- Suitability for detecting large, hydrophilic ionic species that have high charge number such as peptides, proteins, polysacharides, oligonucleotides as well as uncharged molecules
- Unique signal transduction - gating of the immobilized receptor membrane's permeability to redox marker ions in response to charged and uncharged analytes

- Signal transduction does not have to be changed or tailored for each analyte–receptor combination, in contrast with many conventional chemical or biosensors
- Permeability changes for redox markers are the only means for signal transduction for ion-channel sensors
- Incorporation of nanoparticles for ion-channel mimetic sensors improve their sensitivity

Electrochemical Sensors and Biosensors Based on Redox Active Monolayers

One of the most popular techniques to create well-defined functional surfaces of electrodes for their future application in electrochemical sensors and biosensors is formation of self-assembled monolayers (SAMs) based on the covalent interactions of thiols, disulfides, sulfides, and other related molecules with the surfaces of noble metals, particularly gold, as well as platinum and mercury (*69*, *70*). Electrodes with such way modified surface could be applied as a place of intermolecular recognition process in ion channel type sensors. Despite of the promising properties of SAMs, they also have some weak points. The most important is the presence of pinholes and defects, which effect on the faradaic response of blocking monolayers. In consequence, the ion channel type sensors based on such surfaces could loss their sensitivity and selectivity. Attaching a redox centers to SAMs is a possible solution of the above problem (*70*, *71*). Such prepared surface could play a double role as an analytically active element of sensor as well as transducer. The possible way of electrode functionalization with redox active receptors, via covalent Au-S bonds and via embedment strategy are illustrated in Figure 4 A,B,C.

In electroactive monolayers, all redox centres could be located on the outer surface of the SAM (Figure 4A, C) or could be buried into SAM (Figure 4B). The different locations of redox centre might have influence on their properties. Because of this, they display many advantages in comparison to monolayers without redox centres:

- Close packing prevents motion of the redox centres toward the electrode, toward a pinhole or a defect. Therefore, the faradaic current due to redox reaction at (or near) pinholes and defects becomes a negligible component of the total faradaic current.
- Because the electroactive centers are combined with the electrode surface, the diffusion does not have any influence on cyclic voltammetric responses. Thus, the double-layer correction for the surface concentration versus the bulk concentration is not necessary.

On the other hand, the new double-layer effect becomes important due to the changing oxidation state of the surface confined redox centres. Voltammetric waves frequently deviate from the ideal behavior, depending on such factors as the dielectric constants of film and solution, the concentration of electroactive species, supporting electrolyte composition and the film thickness (*70*, *71*).

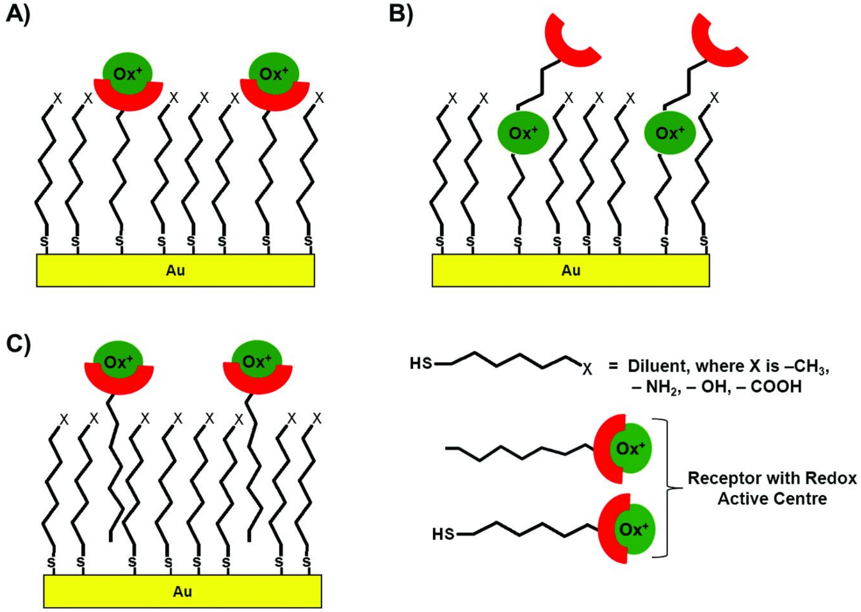

Figure 4. Schematic illustration of redox active centers location in SAM deposited on the electrode surface: A - outer, B - inner, C - using embedment method. (see color insert)

The distortions caused by double-layer effects are less significant when the distances between redox active units are greater and when the electrolyte concentration is high. Thus, the formation of mixed SAMs with a relatively low concentration of redox sites and working in concentrated electrolyte is highly recommended.

We have developed the method for creation of electroactive monolayers based on the two step complexation reaction of Cu(II) performing on the surface of a gold substrate, previously modified with dipyrromethene derivative (*72*, *73*).

As the example of transition metal ions, Cu(II) was selected. The obtained electroactive SAMs were characterized by wettability contact angle measurements, cyclic voltammetry, and atomic force microscopy.

The better reversibility of the redox processes proceeding on the electrode surface was observed for dipyrromentene SAMs with the Cu(II) redox centers located closer to the electrode surface. On the other hand, the electron transfer rate constants were very similar for both systems studied, 0.74 ± 0.21 and 0.44 ± 0.15 s^{-1} for dodecanethiol-dipyrromethene SAM and ethanethiol–dipyrromethene–Cu(II), respectively.

This indicates that the electron transfer rate constant depends not only on the distance of the redox centers from the electrode surface but also on the presence of hetero atoms such as nitrogen or oxygen. Their presence changed the dielectric properties of the system.

The proposed method of formation of electroactive SAMs might be useful for derivatization of gold surfaces with functional groups such as COOH, NH_2, or OH.

The possibility of the attachment of biomolecules to dipyrromethene−Cu(II) SAMs with controlled orientation offers an excellent framework for the study of interactions occurring in interfacial environments between biomolecules of the type protein−protein, protein−hormone, or ssDNA−drugs. Having surface confined Cu(II) centres, the system proposed might respond toward interfacial molecular recognition events without the redox markers in the solution. This is particularly beneficial, because some of them might cause the loss of biomolecule activity. By performing the transition metal coordination on the electrode surface by dipyrromethene derivatives, many electroactive monolayers could be designed and used to define paths of electron transfer into and out of the biomolecules. They could work also as the transducing layer of biosensors for exploring the interfacial molecular recognition processes. This research is currently in progress in our laboratory

One example of application of electroactive SAM with Cu(II)-dipyrromethene concerns the determination of paracetamol, a common analgesic and antipyretic drug. The Cu(II)-dipyrromethene molecules were immobilized on gold electrode surfaces, previously modified with a dodecanethiol monolayer via hydrophobic and van der Waals interactions (embedment technique) (Figure 4C) (*74*).

The dipyrromethene complex with Cu(II), selected as a host molecule for voltammetric sensor for paracetamol determination shows the reduction/oxidation peaks within the potential windows in which the paracetamol molecules remain electrochemically inactive. To our knowledge, this is the first report on paracetamol voltammetric sensors based on host–guest recognition and electroactive layer which plays a role of transducer.

The interaction between dipyrromethene-Cu(II) and paracetamol changed the redox properties of Cu(II) centers in quantitative relation with paracetamol concentration in human plasma.

Fe(III)-porphyrin was selected by us for determination of L-histidine (*75*). This host molecule, immobilized on the surface of Au electrode by the embedment method, (Figure 4C) played also transducer role.

Taking into account the simply way of preparation, low detection of 4.9×10^{-10} M limit and wide dynamic range, the sensor based on Fe(III)-porphyrin is superior to those already reported. The proposed mechanism of the recognition between the porphyrin host and L-histidine guest molecules might be associated to the Fe(III) centre coordination ability. It is well known that iron porphyrins display a selective affinity towards imidasol group in histidine due to strong coordination ability of Fe(III) centre to nitrogen atoms (*76*).

The idea working principle of sensors based on monolayers incorporated redox centres is illustrated in Figure 5. The mechanism of electrochemical signal generation by biosensor based on redox active SAM upon stimulation of specific analyte is not fully understood.

The recognition reaction might cause a change in microenvironment surrounding the receptor molecule, which influences the double layer structure (*77*). The model and potential distribution of the electroactive film was provided by Ohtani (*78*, *79*). In the algorithm to compute the voltammetric responses of quasi-reversible system for a surface-tethered redox species, the double layer effect on the electron transfer kinetics and ion-pair formation between surface confined redox species and electrolyte ions were considered. The effect of the position of the redox centres immobilized onto electrode surfaces, as well as the effect of the ions present in the electrolyte on the thermodynamics of redox active monolayers were reported by Rawe and Creager (*80*, *81*). They discovered that the distance of ferrocene units from the electrode surface as well as the presence of different anions in the basic electrolyte strongly influence the voltammetric response of redox active monolayer.

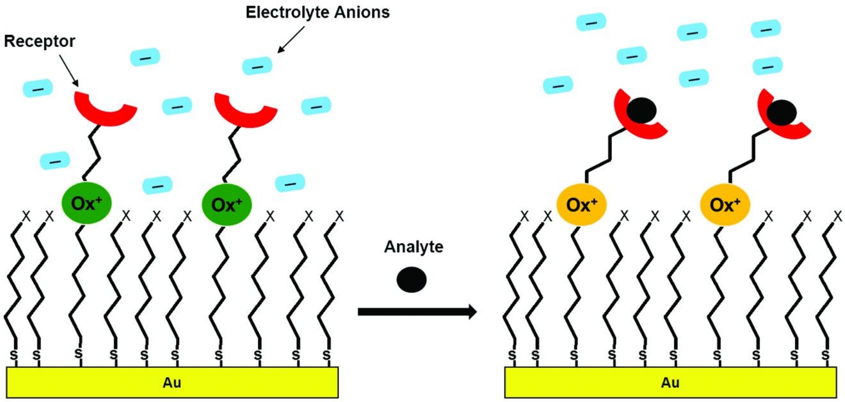

Figure 5. Working principle of sensor based on electroactive SAM. (see color insert)

A decrease in peak current of the Ni(II)-phenanthroline complex deposited onto glassy carbon electrode was observed after interactions with dsDNA (*82*). The authors concluded that binding of dsDNA to the redox active Ni(II)-phenantroline significantly blocked the electron transfer process. A similar phenomenon was observed for a system consisting of dipyrromethene-Cu(II) complex deposited on the surface of a gold electrode used for exploring the interactions between His-Tagged V domain of Receptor for Advanced Glycation End Products (RAGE) and Aβ peptide (*83*).

The main advantages of electrochemical sensors and biosensors based on redox active monolayers are as follow:

- No need of using redox marker in the sample solution.
- Lack of influence of pinholes in the monolayers carring the receptors on sensors performance
- Redox active centers can simultaneously act as host as well as a transducer of electrochemical signals generated upon analyte recognition

The incorporation of gold as well as carbon nanoparticles into fabrication of sensors and biosensors based on redox active monolayers might be very beneficial. Their presence facilitating the electron transfer from redox centers to the electrode surface might improve sensors performance (*1*, *8*, *84*, *85*). There is still much room for scientific research and application of nanostructures. This strategy is currently developing also in our laboratories.

The transition metals complexex with porphyrines, dipyromethenes, terpyrydines deposited onto gold nanoparticles as well as carbon nanostructures such as single-walled carbon nanorods and graphene, will be applied for proper receptor proteins and ssDNA probe immobilization. The biosensors prepared in such way will be tested for sensing of target analytes important for medical diagnosis as well as for environmental monitoring.

Conclusions

The two main types of electrochemical sensors: based on ion-channel mimetic mode and based on redox active layers were presented.

The main advantage of ion-channel mimetic sensors, apart from high sensitivity and selectivity, is the possibility for application in the investigations of recognition processes occurring at the water/solid interface. It is very important from biological as well as medical point of view. The main disadvantage of this type of sensors, in particularly from analytical point of view, is the necessity of using the redox markers in the solutions, which may have toxic effect on biomolecules tested.

The electrochemical sensors based on redox active layer are relatively new direction in sensing devices development. Their main advantage is the lack of the necessity of using the external redox marker. The application of redox centres in sensor giving very interesting possibilities. They can simultaneously act as host molecules and as well as transducers.

The incorporation of nanoparticles into ion-channel mimetic sensors and also in sensors based on redox active monolayers improve their analytical parameters, in particular sensitivity.

It might be concluded that they are relatively cheap analytical tools suitable from medical diagnosis and environment and food quality control.

References

1. Maneli, I.; Marco, M. P *Anal. Bioanal. Chem.* **2010**, *398*, 2451–2469.
2. Rapp, B. E.; Gruhl, F. J.; Länge, K. *Anal. Bioanal. Chem.* **2010**, *398*, 2403–2412.
3. Palchetti, I.; Mascini, M. *Anal. Bioanal. Chem.* **2008**, *391*, 455–471.
4. Viswanathan, S.; Radecka, H.; Radecki, J. *Monatsh. Chem.* **2009**, *140*, 891–899.
5. Viswanathan, S.; Radecki, J. *Pol. J. Food. Nutr. Sci.* **2008**, *58*, 157–164.
6. Pumera, M.; Ambrosi, A.; Bonanni, A.; Cheng, E. L. K.; Poh, H. L. *Trends Anal. Chem.* **2010**, *29*, 954–965.
7. Flower, J. D.; Allen, M. J.; Tung, V. C.; Yang, Y.; Kaner, R. B. *ACS Nano* **2009**, *3*, 301–306.
8. Shao, Y.; Wang, J.; Wu, H.; Liu, J.; Aksay, I. A.; Lin, Y. *Electroanalysis* **2010**, *22*, 1027–1036.
9. Gale, P. A. *Acc. Chem. Res.* **2011**, *44*, 216–226.
10. Gale, P. A. *Chem. Soc. Rev.* **2010**, *39*, 3746–3771.
11. Caltagirone, C.; Gale, P. A. *Chem. Soc. Rev.* **2009**, *38*, 520–563 3.
12. Ronkainen, N. J.; Halsall, H. B.; Heineman, W. R. *Chem. Soc. Rev.* **2010**, *39*, 1747–1763.
13. Pohanka, M.; Skládal, P. *J. Appl. Biomed.* **2008**, *6*, 57–64.
14. Vaddiraju, S.; Tomazos, I.; Burgess, D. J.; Jain, F. C.; Papadimitrakopoulos, F. *Biosens. Bioelectron.* **2010**, *25*, 1553–1565.
15. Sugawara, M.; Kojima, K.; Sazawa, H.; Umezawa, Y. *Anal Chem.* **1987**, *59*, 2842–2846.
16. Umezawa, Y.; Aoki, H. *Anal Chem.* **2004**, *76*, 320A–326A.
17. Nagase, S.; Kataoka, M.; Naganawa, R.; Komatsu, R.; Odashima, K.; Umezawa, Y. *Anal. Chem.* **1990**, *62*, 1252–1259.
18. Radecka, H.; Szymańska, I.; Pietraszkiewicz, M.; Pietraszkiewicz, O.; Aoki, H.; Umezawa, Y. *Chem. Anal. (Warsaw)* **2005**, *50*, 85–102.
19. Radecki, J.; Szymańska, I.; Bulgariu, L.; Pietraszkiewicz, M. *Electrochim. Acta* **2006**, *51*, 2289–2297.
20. Kurzątkowska, K.; Dolusic, E.; Dehaen, W.; Sieroń–Stołtny, K.; Sieroń, A.; Radecka, H. *Anal. Chem.* **2009**, *81*, 7397–7405.
21. Ali, S. R.; Ma, Y.; Parajuli, R. R.; Balogum, Y.; Lai, W. Y. C.; He, H. *Anal. Chem.* **2007**, *79*, 2583–2587.
22. Gadzekpo, V. P. Y.; Xiao, K. P.; Aoki, H.; Bühlmann, P.; Umezawa, Y. *Anal. Chem.* **1999**, *71*, 5109–5115.
23. Gadzekpo, V. P. Y.; Bühlmann, P.; Xiao, K. P.; Aoki, H.; Umezawa, Y *Anal. Chim. Acta* **2000**, *411*, 163–173.
24. Bühlmann, P.; Aoki, H.; Xiao, K. P.; Amemiya, S.; Tohda, K.; Umezawa, Y. *Electroanalysis* **1998**, *17*, 1149–1158.
25. Radecki, J.; Stenka, I.; Dolusic, E.; Dehaen, W.; Plavec, J. *Comb. Chem. High. Throughput Screening* **2004**, *7*, 375–381.
26. Krajewska, A.; Smet, M.; Dehaen, W.; Radecka, H. *Supramol. Chem.* **2009**, *21*, 520–531.

27. Malecka, K.; Grabowska, I.; Radecki, J.; Stachyra, A.; Góra-Sochacka, A.; Sirko, A.; Radecka, H. *Electroanalysis* **2012**, *24*, 439–446.
28. Schmid, G.; Talapin, D. V.; Shevchenko, E. V. In *Nanoparticles: From Theory to Application*, 2nd ed.; Schmid, G., Ed.; Wiley-VCH Verlag GmbH & Co. KGaA: Weinheim, 2010; pp 251−298.
29. Wang, M.; Wang, L.; Wang, G.; Ji, X.; Bai, Y.; Li, T.; Gong, S.; Li, J. *Biosens. Bioelectron.* **2004**, *19*, 575–582.
30. Lu, M.; Li, X. H.; Yu, B. Z.; Li, H. L. *J. Colloid Interface Sci.* **2002**, *248*, 376–382.
31. Wang, J.; Profitt, J. A.; Pugia, M. J.; Suni, I. I. *Anal. Chem.* **2006**, *78*, 1769–1773.
32. Busbee, B. D.; Obare, S. O.; Murphy, C. J. *Adv. Mater.* **2003**, *15*, 414–416.
33. Huang, X.; Neretina, S.; El-Sayed, M. A. *Adv. Mater.* **2009**, *21*, 4880–4910.
34. Ciszek, J. W.; Huang, L.; Tsonchev, S.; Wang, Y. H.; Shull, K. R.; Ratner, M. A.; Schatz, G. C.; Mirkin, C. A. *ACS Nano* **2010**, *4*, 259–266.
35. Shibu Joseph, S. T.; Ipe, B. I.; Pramod, P.; Thomas, K. G. *J. Phys. Chem. B* **2006**, *110*, 150–157.
36. Manneli, I.; Marco, M. P. *Anal. Bioanal. Chem.* **2010**, *398*, 2451–2469.
37. Stobiecka, M.; Hepel, M. *Biomaterials* **2011**, *32*, 3312–3321.
38. Stobiecka, M.; Hepel, M. *Biosens. Bioelectron.* **2011**, *26*, 3524–3530.
39. Stobiecka, M.; Hepel, M. *Phys. Chem. Chem. Phys.* **2011**, *13*, 1131–1139.
40. Nowicka, A. M.; Kowalczyk, A.; Donten, M.; Lech, D.; Hepel, M.; Stojek, Z. *Electroanalysis* **2010**, *22*, 2323–2329.
41. Li, Z.; Zhu, Z.; Liu, W.; Zhou, Y.; Han, B.; Gao, Y.; Tang, Z. *J. Am. Chem. Soc.* **2012**, *134*, 3322–3325.
42. Salina-Torres, D.; Huberta, F.; Montilla, F.; Morallón, E. *Electrochim. Acta* **2011**, *56*, 2464–2470.
43. Kuang, Z.; Kim, S. N.; Brookes-Goodson, W. J.; Farmer, B. L.; Naik, R. R. *ACS Nano* **2010**, *4*, 452–458.
44. Leong, S.; Shim, H. C.; Kim, S.; Han, C-S. *ACS Nano* **2010**, *4*, 324–330.
45. Chen, Y.; Dedala, H.; Kotchey, G. P.; Audfray, A.; Cecioni, S.; Imberty, A.; Vidal, S.; Star, A. *ACS Nano* **2012**, *6*, 760–770.
46. Srivastava, R. K.; Srivastava, S.; Narayanan, T. N.; Mahlotra, B. D.; Vajtai, R.; Ajayan, P. M.; Srivastava, A. *ACS Nano* **2012**, *6*, 168–175.
47. Venkatesan, B. M.; Estrada, D.; Banerjee, S.; Jin, X.; Dorgan, V. E.; Bae, M-H.; Aluru, N. R.; Pop, E.; Bashir, R. *ACS Nano* **2012**, *6*, 441–450.
48. Ding, M.; Sorescu, D. C.; Kotchey, G. P.; Star, A. *J. Am. Chem. Soc.* **2012**, *134*, 3472–3479.
49. Szymańska, I.; Radecka, H.; Radecki, J.; Kaliszan, R. *Biosens. Bioelectron.* **2007**, *22*, 1955–1960.
50. Grabowska, I.; Radecka, H.; Burza, A.; Radecki, J.; Kaliszan, M.; Kaliszan, R. *Curr. Alzheimer Res.* **2010**, *7*, 165–172.
51. Lahiri, D. K.; Farlow, M.; Greig, N. H.; Sambamurti, K. *Drug Dev. Res.* **2002**, *56*, 267–281.
52. Green, N. S.; Foss, T. R.; Kelly, J. W. *Proc. Natl. Acad. Sci. U.S.A.* **2005**, *102*, 14545–14550.
53. Reches, M.; Porat, Y.; Gazit, E. *J. Biol. Chem.* **2002**, *277*, 35475–35480.

54. Salomon, A. R.; Marcinkowski, K. J.; Friedland, R. P.; Zamorski, M. G. *Biochemistry* **1996**, *35*, 13568–13578.
55. Dickenson, T. J.; Janda, K. D. *Proc. Natl. Acad. Sci. U.S.A.* **2003**, *100*, 8182–8187.
56. Wang, L.; Wang, E. *Electrochem. Commun.* **2004**, *6*, 49–54.
57. Liu, Y.; Yin, F.; Long, Y.; Zhang, Z.; Yao, S. *J. Colloid Interface Sci.* **2003**, *258*, 75–81.
58. Lindholm-Sethson, B.; Nyström, J.; Malmsten, M.; Ringstad, L.; Nelson, A.; Geladi, P. *Anal. Bioanal. Chem.* **2010**, *398*, 2341–2349.
59. Wąsowicz, M.; Subramanian, V.; Dvornyk, A.; Grzelak, K.; Kłudkiewicz, B.; Radecka, H. *Biosens. Bioelectron.* **2008**, *24*, 284–289.
60. Wąsowicz, M.; Milner, M.; Radecka, D.; Grzelak, K.; Radecka, H. *Sensors* **2010**, *10*, 5409–5424.
61. Jarocka, U.; Wąsowicz, M.; Radecka, H.; Malinowski, T.; Michalczuk, L.; Radecki, J. *Electroanalysis* **2011**, *23*, 2197–2204.
62. Bonanni, A.; del Valle, M. *Anal. Chim. Acta* **2010**, *678*, 7–17.
63. Lisdat, F.; Schafer, D. *Anal. Chem.* **2008**, *391*, 1555–1567.
64. Jiang, C.; Yang, T.; Jiao, K.; Gao, H. W. *Electrochim. Acta* **2008**, *53*, 2917–2924.
65. Bonanni, A.; Esplandiu, M. J.; del Valle, M. *Biosens. Bioelectron.* **2009**, *24*, 2885–2891.
66. Caliksan, A.; Erdem, A.; Karadeniz, H. *Electroanalysis* **2009**, *21*, 2116–2124.
67. Nebel, C. E.; Yang, N.; Uetsuka, H.; Osawa, E.; Tokuda, N.; Wiliams, O. *Diamond Relat. Mater.* **2009**, *18*, 910–917.
68. Yang, J.; Yang, T.; Feng, Y.; Jiao, K. *Anal. Biochem.* **2007**, *365*, 24–30.
69. Bard, A. J.; Faulkner, L. R. In *Electrochemical Methods – Fundamental and Applications*, 2nd ed.; John Wiley & Sons Inc.: New York, 2001; pp 580−631.
70. Finklea, H. O. In *Electroanalytical Chemistry*; Bard, A. J., Rubinstein, I., Eds.; Marcel Dekker Inc.: New York, 1996; Vol. 19, pp 109−335.
71. Eckermann, A. L.; Feld, D. J.; Shaw, J. A.; Meade, T. J. *Coord. Chem. Rev.* **2010**, *254*, 1769–1802.
72. Szymańska, I.; Orlewska, Cz.; Janssen, D.; Dehaen, W.; Radecka, H. *Electrochim. Acta* **2008**, *53*, 7932–7940.
73. Szymańska, I.; Stobiecka, M.; Orlewska, Cz.; Rohand, T.; Janssen, D.; Dehaen, W.; Radecka, H. *Langmuir* **2008**, *24*, 11239–11245.
74. Saraswathyamma, B.; Grzybowska, I.; Orlewska, Cz.; Radecki, J.; Dehaen, W.; Kumar, K. G.; Radecka, H. *Electroanalysis* **2008**, *20*, 2317–2323.
75. Kurzątkowska, K.; Shpakovsky, D.; Radecki, J.; Radecka, H.; Jingwei, Z.; Milaeva, E. *Talanta* **2009**, *78*, 126–131.
76. Chen, Z.; Liu, J.; Han, Y.; Zhu, L. *Anal. Chim. Acta* **2006**, *570*, 109–115.
77. Shleev, S.; Tkac, J.; Christenson, A.; Ruzgas, T.; Yaropolov, A. I.; Whittaker, J. W.; Gorton, L. *Biosens. Bioelectron.* **2005**, *20*, 2517–2554.
78. Ohtani, M. *Electrochem. Commun.* **1999**, *1*, 448–492.
79. Ohtani, M.; Kuwabata, S.; Yoneyama, H. *Anal. Chem.* **1997**, *69*, 1045–1053.

80. Rowe, G. K.; Creager, S. E. *Langmuir* **1991**, *7*, 2307–2312.
81. Creager, S. E.; Rowe, G. K. *J. Electroanal. Chem.* **1997**, *420*, 291–299.
82. Qiu, B.; Guo, L.; Guo, Ch.; Guo, Z.; Lin, Z.; Chen, G. *Biosens. Bioelectron.* **2011**, *26*, 2270–2274.
83. Radecka, H.; Radecki, J.; Grabowska, I.; Dehaen, W.; Sirko, A.; Góra-Sochacka, A.; Wysłouch-Cieszyńsdka, A.; Dadlz, M. Polish Patent No WIPO ST 10/c PL 394798, 2011.
84. Nouira, W.; Maaref, A.; Vocanson, F.; Siadat, M.; Saulnier, J.; Lagarde, F.; Jaffrezic-Renault, N. *Electroanalysis* **2012**, *24*, 1088–1094.
85. Luo, X.; Morrin, A.; Killard, A. J.; Smyth, M. R. *Electroanalysis* **2006**, *18*, 319–326.

Chapter 12

Nanoparticles and Nanostructured Materials Used in Modification of Electrode Surfaces

Mikołaj Donten and Zbigniew Stojek*

**University of Warsaw, Faculty of Chemistry, 1 Pasteura Str.,
02-093 Warsaw, Poland**
***E-mail: stojek@chem.uw.edu.pl**

A variety of substances and materials either nanostructured or in the form of nanoparticles are used to modify electrode surfaces. These include metals, alloys, inorganic substances polymers and composites. Nanostructured materials speed up electrode processes and allow intelligent ingineering of the sensing layers on the surface of electrodes. As a result new possibilities appear in analysis, bioanalysis and bioelectrochemistry.

Introduction

Probably, nanoparticles were present on the surfaces of electrodes already in the early years of electrochemistry. Processes of precipitation, deposition and passivation could involve the formation of nanocrystals. For example the platinum electrodes were intentionally covered with platinum black what led to improved performance of the electrode towards the hydrogen ion reduction reaction. Their role could not be identified well and it was rather impossible to demonstrate their existence. The appearance of scanning and transmitting electron microscopies and scanning tunneling- and atomic force microscopies allowed the detection and characterization of nanoparticles. Regarding the electrodes, all substances that are placed, on purpose, on the surface of an electrode can be in the nano state, or have a nano size, and then can influence the electrode process, including the electron transfer rate.

In Functional Nanoparticles for Bioanalysis, Nanomedicine, and Bioelectronic Devices Volume 1; Hepel, M., et al.;
ACS Symposium Series; American Chemical Society: Washington, DC, 2012.

There are several reasons for placing nanoparticles and nanostructured materials on electrode surfaces. This type of electrode modification should result in some new properties of the surfaces. The first aim of introducing nanoparticles is just an expansion of the true electrode-surface area. This may result in an increase in the capacitive- and surface faradaic currents. Another aim behind the modification of electrode surface with nanoparticles is such decoration of the electrode that the proper attachment of macro-, supra- and biomolecules will be successful. Next goal may be related to a need of achieving an electrocatalytic effect. It is clear that nanoparticles will have the Fermi level different from that of the regular size crystals, and the energy bands will differ too. The electrode processes may become faster and this may lead to the enhancement of the current signal and better resolution in the case of several analytes. Finally, due to many possible shapes, sometimes unusual, of nanocrystallites and often many faces at a particular crystallite, the spatial freedom and orientation of the molecules attached to the nanocrystals is increased. It is also good to realize that for the modification of an electrode with nanoparticles of particular catalytical material a much less amount of the material is needed, which lowers the cost of the electrode. The nanoparticles used for the purpose of modification of electrodes can be assigned to several material groups: metals, metal alloys, carbon nanotubes and graphene, other inorganic compounds (including oxides, salts and core-shell objects) and composites including hybrid materials with biomolecules. Several review papers addressed the electrochemistry with nanoparticles (*1–4*).

Metallic Nanoparticles

Such nanoparticles are prepared just from noble metals and their salts. Gold, platinum, silver, iridium and palladium are most often used. Other metals, especially more active ones are rarely employed. Somewhat equivalent to the direct use of nanoparticles is the formation of various asperities on the surface. Often a bare metal electrode is modified with its nanoparticles, which leads to the systems like: Pt/Pt black, Pt/Pt nanoparticles, Au/Au nanoparticles, etc. Gold and platinum is mostly used for increasing the rate of many oxidation reactions e.g. oxidation of methanol and ethanol. However, the reduction processes are also affected by the presence of nanoparticles on the electrode surface, e.g. hydrogen evolution and reduction of oxygen.

A way of modification of electrode surfaces with metallic nanoparticles is either placing a drop of liquid containing nanoparticles on the electrode surface and evaporation of the solvent, or the electrodeposition of metals through the electroreduction of the metal ions. In the first case the nanoparticles used are usually already modified to avoid their possible agglomeration during the modification procedure. In the second way the nanoparticles with clean surfaces, without adsorbates on them, are obtained. Here are example publications on the use of electrodes modified with metallic nanoparticles (*5–19*).

A good example of how gold nanoparticles can be used for better distribution and ordering of probe DNA strands in the DNA sensor has been described in (*20*). In that paper a way of modification of crystalline gold surface with a high quality layer of gold nanoparticles (Au NPs) via self-assembled dithiol was presented. The addition of an Au NPs monolayer was tested with three types of biosensors differing in the construction and the detection method and described earlier in the literature. The modyfication of just one of the sensors is shown in Figure 1. An important finding was that that the necessary condition for a successful preparation of a perfect Au NPs monolayer is the preparation temperature of 4 °C. The preparations done at higher than 4 °C temperatures led to poor repeatability and therefore unsatisfactory precision of the results. It appeared that the addition of a perfect monolayer of Au NPs resulted in lowering of the detection limits (by circa 10 to 100 times) for all three examined DNA biosensors.

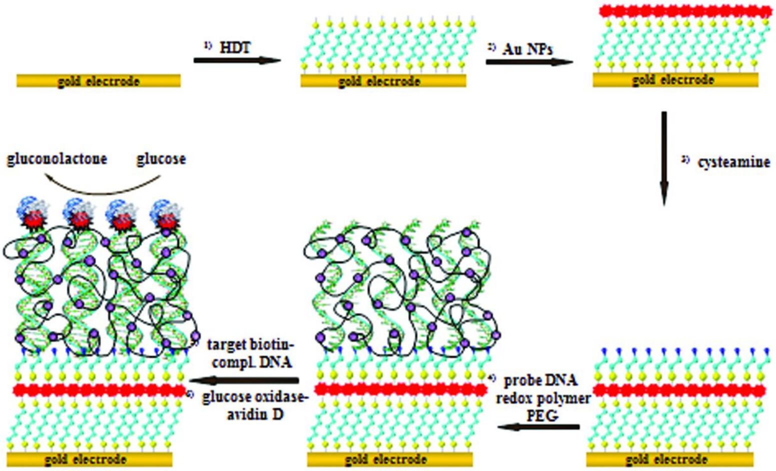

Figure 1. A scheme of the entire procedure of preparation of selected DNA sensor with added gold-nanoparticle layer (red spheres). HDT stands for hexane dithiol. (Reproduced with permission from reference (20). Copyright 2010 John Wiley & Sons.)

Another application of Au nanoparticles which allowed appropriate distribution of the active centers at the sensor surface for immobilization of hairpin DNA probes is illustrated in paper (*21*). The preparation of the electrode and the formation of graphene/AuNP nanocomposite on a screen-printed carbon electrode involved just one-step electrochemical reduction of a mixture of graphene oxide and $HAuCl_4$. Using the appropriate enzyme the target DNA strand was recycled and that allowed the amplification of the EIS detection signal. The amplification strategy for sensitive and label-free determination of DNA is illustrated in Figure 2. The hairpin DNA probes were self-assembled on the modified electrode, the unued surface was blocked with 6-mercapto-1-hexanol, and then the target DNA together with Exo III were added. The target DNA hybridized with the hairpin probe and a double stranded DNA was formed. The task of Exo III was to specifically cleave the open, hybridized hairpin DNA and to release the target DNA. Exo III was inactive to single stranded DNA. Finally, after the enzymatic cleavage of the probe DNA, the released target DNA could hybridize again with unused hairpin DNA strands. This action could be repeated till hairpin DNA existed on the surface. Finally, a small amount of target DNA could efficiently remove a substantial percentage of hairpin DNA probes. This resulted in a substantial change in the particular electrode property: the electron transfer resistance, which could be monitored by employing electrochemical impedance spectroscopy. The decrease in electron transfer resistance was well related to the quantity of the target DNA in the analysed samples.

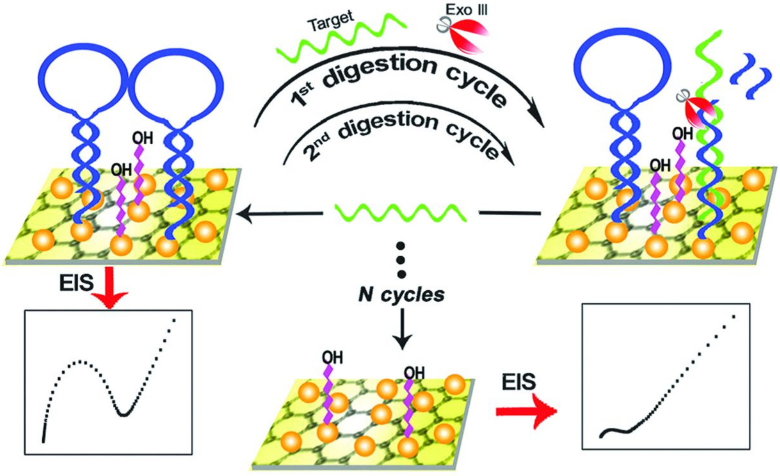

Figure 2. Illustration of the enzyme-assisted recycling of target (green strands) for amplified detection of DNA with a graphene/AuNP modified electrode using electrochemical impedance spectroscopy. (Reproduced with permission from reference (21). Copyright 2010 RSC.)

An interesting example of using Au nanocrystals in the detection of bioactive molecules was proposed by M. Maltez-da Costa et al. (*13*). Apparently, the formation of a modifying layer with nanoparticles on the electrode surface can lead to the detection of specific species present in the analyzed solution. The authors have shown how to detect and quantitatively determine human IgG by employing the effect of decreasing the overpotential of the hydrogen evolution in the presence of gold NPs. In this particular case, gold NPs were combined with the molecules that can recognize IgG, and after their immobilization on the surface of the electrode they produced an increased current of hydrogen evolution proportionally to the amount of gold (and lgG) in the modifying layer. The scheme of the modification process and its consequences are shown in Figure 3.

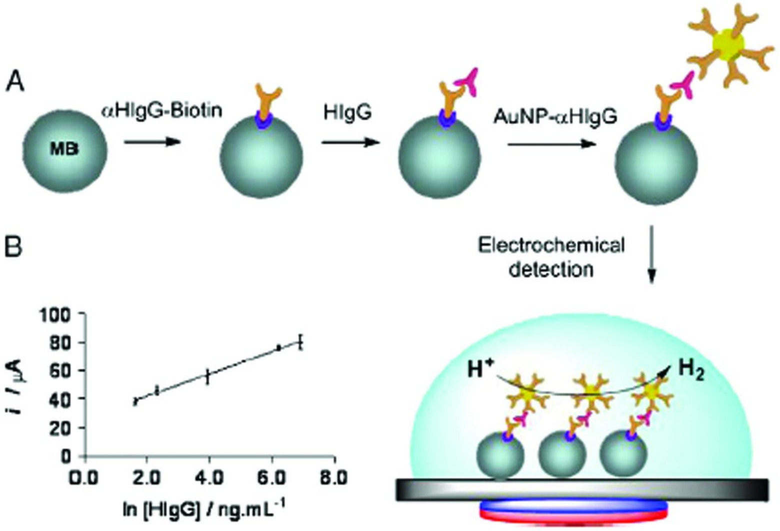

Figure 3. Modification of magnetic beads (MB) with specific antibodies modified with biotin (αHIgG-B), followed by immobilization of HIgG and of gold nanoparticles conjugated with secondary specific HIgG antibodies. The imposition of a magnetic field leads to accumulation of immunomagnetic sandwich on the electrode surface. (Reproduced with permission from reference (13). Copyright 2010 Elsevier.)

Carbon Nanostructured Materials

Carbon nanotubes were very extensively used as the material that increases substantially the electrochemical activity of the surfaces (*4*, *22*, *23*). Recently, graphene becomes more and more popular in decoration of electrode surfaces (*24–26*). The carbon nanostructures present alone in the modifying layer are already very active due to their developed surface and specific structure. The application of nanotubes led to a better resolution of the peaks and lower detection limits in the analytical methods based on voltammetry. Both nanotubes and graphene are very good platforms for immobilization of other nanoparticles and biomacromolecules such as enzymes, DNA and proteins. Extensive overviews on grapheme and carbon nanotubes are given in (*23*, *24*)

Metal-Compound- and Alloy Nanoparticles

Oxides of transition metals often exhibit semiconductor properties. These properties may be modified by decreasing the size of the crystals to that of nanoparticles. The nanocrystallites are usually anchored at bulk (often also nanostructured) inorganic materials or ordered layers, e.g. on nanotubes, nanorods and nanopore substances. The oxide nanoparticles are most often used to construct the electrodes for biocells, photogalvanic cells, fuel cells and supercapacitors (*27–30*).

For example, inorganic nanoparticles such as RuSe, PtSn and PtRu appeared to be good catalysts for the processes that proceed in fuel cells. A variety of materials, including tungsten and molybdenum oxides, were found useful as the support or matrix for these nanoparticles. (*31–35*).

Tungsten trioxide helped in raising the electroreduction of oxygen at RuSe nanoparticles; the quantity of unwanted hydrogen peroxide dropped by 50 %. The production of H_2O_2 in the process of electroreduction of oxygen is a very unwanted result. Also, the potential of oxygen electroreduction moved towards the thermodynamic potential, which gave a chance of limiting the quantity of platinum as the catalyst of that process. RuSe appeared to be able to reduce selectively oxygen in the presence of a fuel (methanol and etanol). PtSn and PtRh nanoparticles embedded in thin layers of WO_3 and MoO_3 were found suitable for the effective electrooxidation of ethanol in the fuel cell.

There is a hope that some enzymes, e.g. laccase, can be employed in the electroreducion of oxygen in the fuel cells. It has already been demonstrated that laccase can be embedded into carbon multiwalled nanotube layers, and in the presence of ABTS (2,2′-azino-bis(3-ethylbenzothiazoline-6-sulphonic acid), an effective mediator, can work as a good biocatalyst for the oxygen reduction, see for example (*36*). The composition of the modifying layer guaranteed good conductivity of the electrode and promising biocatalytic activity at pH 5.

Core−Shell Materials

The shell component may substantially change the properties of the pure material due to the influence of the core location and structure. As a result they may exhibit interesting catalytic properties. Also, the outer layer may be added to protect the core material. For example, iron nanoparticles with supermagnetic properties have been chemically protected by a carbon layer. In the paper (*37*) an effect of strong enhancement of the voltammetric peak height, at a glassy carbon electrode modified with iron nanoparticles, of paramagnetic ferrocene derivative was described. This effect was a result of cooperation of external magnetic field and iron nanoparticles. Iron was completely coated by carbon. No iron oxide was present in the nanoparticles. The coverage of the surface was stable in time. The carbon shells were believed to help in achieving a good adhesion of the nanoparticles to the GC surface. They also prevented the corrosion of the iron core. The use of Fe/C nanoparticles resulted in an increase in the voltammetric peak current of the paramagnetic ferroceneacetate anion by approximately 30 %. The additional use of an external magnetic field together with the electrode polarization apparently led to the reorganization of the nanoparticle layer, and the voltammetric current increased up to 165 % compared to that obtained with the bare electrode. This is illustrated in Figure 4. This experimental setup should be analytically useful in the detection and the determination of biomolecules with paramagnetic centers.

In Functional Nanoparticles for Bioanalysis, Nanomedicine, and Bioelectronic Devices Volume 1; Hepel, M., et al.;
ACS Symposium Series; American Chemical Society: Washington, DC, 2012.

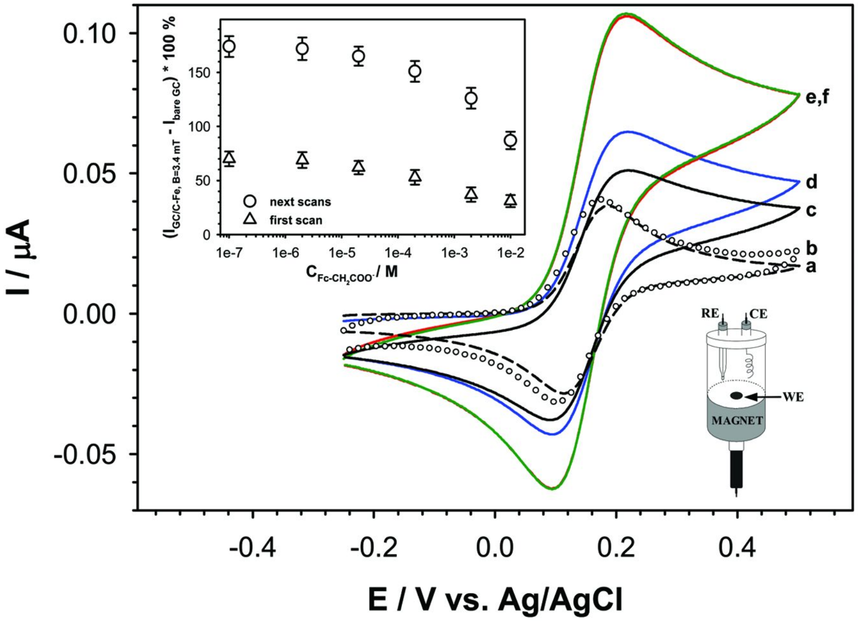

Figure 4. Effect of 3.4 mT (34 Gs) magnetic field on cyclic voltammograms of 0.02 mM Fc-CH$_2$COONa in 0.1 M aqueous NaClO$_4$ solutions at: (a) bare GC electrode, (b) bare GC electrode with magnetic field, (c) GC electrode modified with C-Fe Nps, (d) GC electrode modified with C-Fe Nps and with magnetic field (1st scan) and (e,f) GC electrode modified with C-Fe Nps and with magnetic field (next scans). Insets: dependence of increase in current caused by magnetic field vs. concentration of Fc-CH$_2$COONa (top); scheme of electrochemical cell with magnetic field (bottom). Experimental conditions: scan rate 100 mV/s, GC electrode modified by C-Fe Nps (θ = 3 mm), T = 22 °C. (Adapted with permission from reference (37). Copyright 2012 Elsevier.)

Composites

Mixtures of nanoparticles and various materials including polymers are more frequently suggested recently. The appropriate combination and composition of nanoparticles offers particularly good chances for improvement of the electrochemical processes. Under these conditions the nanoparticles used together can enhance their activities. Some nanostructured materials can be strongly adhered to the electrode surface and in this way make the entire composite layer more robust. They can also improve the electric conductivity and allow the preparation of relatively thicker layers. This is particularly important for the layers that work on the cell electrodes, where bigger currents flow and the time of work is expected to be as long as possible.

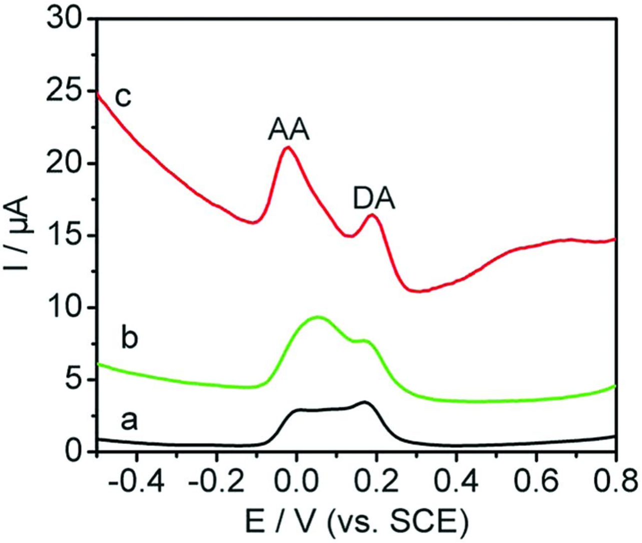

Figure 5. Differential pulse voltammograms (DPV) of mixture 50 μM DA + 1 mM AA in PBS of pH 6.0 obtained with: bare (a), graphene (b) and graphene–AuNPs (c) modified GC electrodes. Scan rate: 100 mV s-1. (Adapted with permission from reference (25). Copyright 2012 RSC.)

A number of biologically important compounds, including drugs as e,g, paracetamol, or acetaminophen, are electroactive and therefore can be monitored by an electrochemical method, however, when they are present in a mixture, which often happens, the problem with sufficiently good resolution of the signals appears. An enhancement of the electron transfer rate (the processes are usually not very fast) may correct the voltammetric peak potentials, decrease the peak width and finally improve the resolution. A good example of such application of nanoparticles is the modification of glassy carbon electrode with a graphene–Au nanoparticle composite film. Li et al. (*25*) proposed it to selectively detect dopamine (DA) in the presence of ascorbic acid (AA) by a voltammetric method. It appeared that compared to just bare- and graphene modified electrodes, the electrode modified with the nanocomposite not only significantly improved the difference between the electrochemical peak potentials of DA and AA, but also significantly increased the current response. While the increase in current may be partially caused by the increase in the electrode surface area by graphene, the better separation of the peaks must be a result of electrocatalytic action of gold nanoparticles. The constructed sensor gave a wide linear calibration range (5–1000 μM) and a low detection limit (1.86 μM). The improvement in the detection is shown in Figure 5.

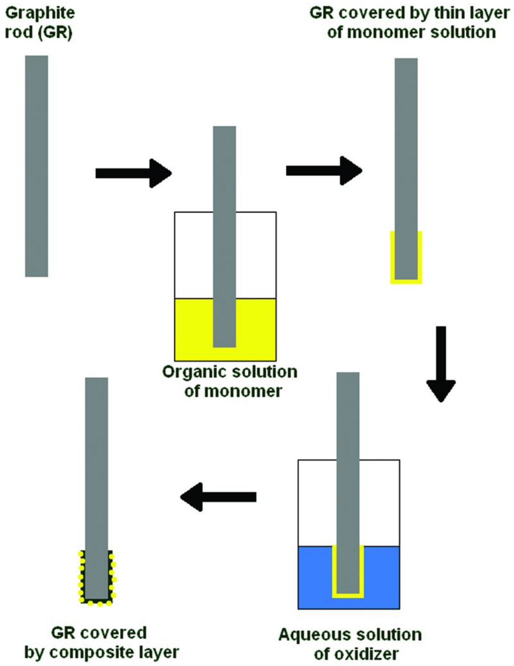
Graphite rod (GR)
GR covered by thin layer of monomer solution
Organic solution of monomer
GR covered by composite layer
Aqueous solution of oxidizer

Figure 6. Scheme of the dip-in polymerization method. Substrate: 0.5 mm in diameter graphite rod. Time of immersing in organic solution: 3 min. Time of immersing in aqueous solution of oxidant: 15 - 60 min. Reproduced with permission from reference (40). Copyright 2008 American Chemical Society.

The modification of the electrode surface with metal nanoparticles can be also done using a layer of composite consisting of a conductive polymer and metal nanocrystals. In this case the easiest way of formation of the modifying layer is the physical attachment of the conductive polymer-metal nanoparticle film (*38*, *39*). A more advanced method that guaranties a uniform, well attached coverage of the electrode surface is a method based on the interphase electroless deposition of a polymer film decorated with nanostructured gold, as was proposed by Gniadek et al (*40*). In this method the formation of thin layers of the composite material was done by using the interphase polymerization driven by a transport-controlled redox reaction. In the first step a graphite rod was covered by a thin layer of monomer solution. Then the monomer present in the layer was oxidized by the appropriate metal cation. This reaction led to the formation of the polymer and the metal nanoparticles. The modification procedure is illustrated in Figure 6.

The obtained films were 0.2-1 μm thick, consisted of gold nanoparticles distributed in polypyrrole (PPy) (up to 13.5 at. %), and were strongly adhered to the substrate surface. The layers were uniform. Different carbon and metallic materials and also nonconductive materials can be potentially used as the substrate for the working electrodes. The first step in the synthesis was deposition of an organic layer on the substrate. This was followed by dipping the substrate in an aqueous solution containing an oxidizer and finally by appropriate washing and drying the composite film.

Another way leading to the formation of compact and tightly covered electrode by a metal polymer composite film is based on the electroplating procedure described by Rapecki et al. (*41*). In that paper the authors described the formation of a PPy–Au nanoparticle composite on the graphite surface by using the pulse electrodeposition. A solution containing a gold salt and the monomer was prepared for that purpose. To determine the potential ranges of gold electrodeposition and PPy film electroformation the cyclic voltammetric technique was used. The voltammograms allowed also the optimization of the conditions of the composite electrosynthesis. Two peaks that were assigned to the reduction of the Au(I) cyanide complex and the oxidation of pyrrole appeared at -1.5 and 0.7 V, vs. Ag/AgCl, respectively. By changing the pulse-deposition time, the potential waveform and concentrations of the reagents the desired composition and uniformity of the composites at the graphite surface were obtained. The described method allowed the deposition of a layer of the PPy–Au composite of any percentage, including pure gold and pure polymer.

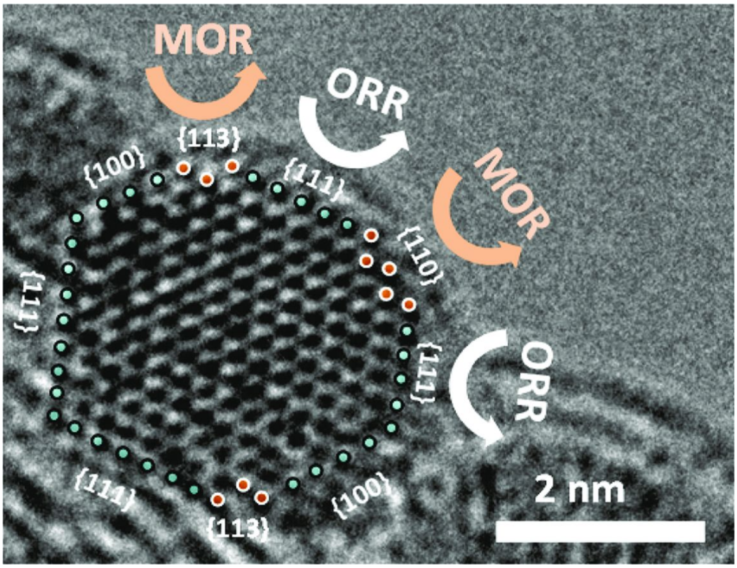

Figure 7. At nanoparticle terraces, oxygen reduction reaction (ORR) dominates, while at active sites involving surface steps MOR is enhanced. Reproduced with permission from reference (18). Copyright 2010 American Chemical Society.

Structure of Nanoparticles versus Their Activity

Nanostructured materials including metal nanoparticles exhibit enhanced chemical and electrochemical activity. This depends on the orientation of the atoms on the surface. For the surfaces with higher atom density (terraces 111) the reactions of smaller molecules is favored. Bigger molecules, including alcohols, require less dense packed planes. The extraordinary property of nanocrystals towards oxidation of bigger molecules is generated by the presence of centers of odd crystallographic structures on their surfaces. In particular, the increase in the electrocatalytic activity of metal nanocrystals, compared to bulk material, is believed to be a consequence of occurring odd crystallographic orientations typical for steps between terraces. This phenomenon was well discussed and illustrated for methanol oxidation reaction (MOR) by S.W.Lee et al. (*18*). In fact, these statements correlate well with the conclusions on the role of asperities present at the surface of polycrystalline metallic materials (*42*, *43*).

Generally when the ratio of the surface area of the material to its volume increases, what is typical for nanostructured materials, the electrocatalytic activity increases. Figure 7 illustrates the existence of places of different activity on a Pt nanoparticle.

In summary, this chapter briefly reports on the progress achieved recently in nanostructured materials applied in sensory films and points to the role of nanoparticles in improving biosensors' efficiency. The text includes several examples of metal, semiconductor and alloy nanoparticles and their influence on the electron transfer and general performance of various biosensors. Selected designs of nanoparticle-modified sensors are discussed in detail and their applications in bioanalysis and nanomedicine are emphasized.

References

1. Hu, M.; Chen, J.; Li, Z. Y.; Au, L.; Hartland, G. V.; Li, X.; Marquez, M.; Xia, Y. *Chem. Soc. Rev.* **2006**, *35*, 1084–1094.
2. Murray, R. W. *Chem. Rev.* **2008**, *108*, 2688–2720.
3. Luo, X.; Morrin, A.; Killard, A. J.; Smyth, M. R. *Electroanalysis* **2006**, *18*, 319–326.
4. Rivas, G. A.; Rubianes, M. D.; Rodríguez, M. C.; Ferreyra, N. F.; Luque, G. L.; Pedano, M. L.; Miscoria, S. A; Parrado, C. *Talanta.* **2007**, *74*, 291–307.
5. Feng, J. J.; Zhao, G.; Xu, J.-J.; Chen, H.-J. *Anal. Biochem.* **2005**, *342*, 280–286.
6. Ling, T. L.; Ahmad, M.; Heng, L. Y.; Seng, T. C. *J. Sens.* **2011** DOI:10.1155/2011/754171.
7. Alkasir, R. S. J.; Ganesana, M.; Won, Y. H.; Stanciu, L.; Andreescu, S. *Biosens. Bioelectron.* **2010**, *26*, 43–49.
8. Solla-Gullon, J.; Montiel, V.; Aldaz, A.; Clavilier, J. *J. Electroanal. Chem.* **2000**, *491*, 69–77.
9. Guo, S.; Wang, E. *Anal. Chim. Acta* **2007**, *598*, 181–192.
10. Minguzzi, A.; Lugaresi, O.; Aricci, G.; Rondinini, S.; Vertova, A. *Electrochem. Commun.* **2012**, *22*, 25–28.

In Functional Nanoparticles for Bioanalysis, Nanomedicine, and Bioelectronic Devices Volume 1; Hepel, M., et al.;
ACS Symposium Series; American Chemical Society: Washington, DC, 2012.

11. Li, W.; Su, B. *Electrochem. Commun.* **2012**, *22*, 8–11.
12. Zhou, Z. Y.; Shang, S. J.; Tian, N.; Wu, B. H.; Zheng, N. F.; Xu, B. B; Chen, C.; Wang, H. H.; Xiang, D. M.; Sun, S. G. *Electrochem. Commun.* **2012**, *22*, 61–64.
13. Maltez-da Costa, M.; Escosura-Muñiz, A.; Merkoçi, A. *Electrochem. Commun.* **2010**, *12*, 1501–1504.
14. Beyerlein, K. R.; Solla-Gullón, J.; Herrero, E.; Garnier, E.; Pailloux, F.; Leoni, M.; Scardi, P.; Snyder, R. L.; Aldaz, A.; Feliu, J. M. *Mater. Sci. Eng., A* **2010**, *528*, 83–90.
15. Chou, J.; Jayaraman, S.; Ranasinghe, A. D.; McFarland, E. W.; Buratto, S. K.; Metiu, H. *J. Chem. Phys. B* **2006**, *110*, 7119–7121.
16. Vidotti, M.; Gonçales, V. R.; Quartero, V. S.; Danc, B.; Córdoba de Torresi, S. I. *J. Solid State Electrochem.* **2010**, *14*, 675–679.
17. Kang, X.; Mai, Z.; Zou, X.; Cai, P.; Mo, J. *Anal. Biochem.* **2007**, *369*, 71–79.
18. Lee, S. W.; Chen, S.; Suntivich, J.; Sasaki, K.; Adzic, R. R.; Shao-Horn, Y. *J. Phys. Chem. Lett.* **2010**, *1*, 1316–1320.
19. Rahman, Md. A.; Noh, H. B.; Shim, Y. B. *Anal. Chem.* **2008**, *80*, 8020–8027.
20. Nowicka, A. M.; Kowalczyk, A.; Donten, M.; Leech, D.; Hepel, M.; Stojek, Z. *Electroanalysis* **2010**, *22*, 2323–2329.
21. Chen, Y.; Jiang, B.; Xiang, Y.; Chaia, Y.; Yuan, R. *Chem. Commun.* **2011**, *47*, 12798–12800.
22. Gooding, J. J. *Electrochim. Acta* **2005**, *50*, 3049–3060.
23. Lamberti, F.; Giomo, M.; Elvassore, N. In *Carbon Nanotubes – Growth and Applications*; Naraghi, M., Ed.; InTech: New York, 2011; pp 277–298.
24. Chen, D.; Tang, L.; Li, J. *Chem. Soc. Rev.* **2010**, *39*, 3157–3180.
25. Li, J.; Yang, J.; Yang, Z.; Li, Y.; Yu, S.; Xua, Q.; Hu, X. *Anal. Methods* **2012**, *4*, 1725–1728.
26. Zhou, X.; Wang, F.; Zhu, Y.; Liu, Z. *J. Mater. Chem.* **2011**, *21*, 3353–3358.
27. Salimia, A.; Sharifia, E.; Noorbakhsha, A.; Soltanian, S. *Biosens. Bioelectron.* **2007**, *22*, 3146–3153.
28. Jalani, N. H.; Dunn, K.; Datta, R. *Electrochim. Acta* **2005**, *51*, 553–560.
29. Hasobe, T.; Hattori, S.; Kamat, P. V.; Wada, Y.; Fukuzumi, S. *J. Mater. Chem.* **2005**, *15*, 372–380.
30. Chen, S.; Junwu Zhu, J.; Wu, X.; Han, Q.; Wang, X. *ACS Nano* **2010**, *4*, 2822–2830.
31. Kulesza, P. J.; Miecznikowski, K.; Baranowska, B.; Skunik, M.; Fiechter, S.; Bogdanoff, P.; Dorbandt, I. *Electrochem. Commun.* **2006**, *8*, 904–908.
32. Lewera, A.; Miecznikowski, K.; Hunger, R.; Kolary-Zurowska, A.; Wieckowski, A.; Kulesza, P. J. *Electrochim. Acta* **2010**, *55*, 7603–7609.
33. Ge, P. Y.; Scanlon, M. D.; Peljo, P.; Bian, X. J.; Vubrel, H.; O'Neill, A; Coleman, J. N.; Cantoni, M.; Hu, X. L.; Kontturi, K.; Liu, B. H.; Girault, H. H. *Chem. Commun.* **2012**, *48*, 6484–6486.
34. Miecznikowski, K.; Kulesza, P. J. *J. Power Sources* **2011**, *196*, 2595–2601.
35. Miecznikowski, K.; Kulesza, P. J.; Fiechter, S. *Appl. Surf. Sci.* **2011**, *257*, 8215–8222.

36. Karnicka, K.; Miecznikowski, K.; Kowalewska, B.; Skunik, M.; Opallo, M.; Rogalski, J.; Schuhmann, W.; Kulesza, P. J. *Anal. Chem.* **2008**, *80*, 7643–7648.
37. Nowicka, A. M.; Kowalczyk, A; Bystrzejewski, M.; Donten, M.; Stojek, Z. *Electrochem. Commun.* **2012**, *20*, 4–6.
38. Selvaraja, V.; Alagara, M.; Sathish Kumarb, K. *Appl. Catal., B* **2007**, *75*, 129–138.
39. Mokrane, S.; Makhloufi, L.; Alonso-Vante, N. *J. Solid State Electrochem.* **2008**, *12*, 569–574.
40. Gniadek, M.; Modzelewska, S.; Donten, M.; Stojek, Z. *Anal. Chem.* **2010**, *82*, 469–472.
41. Rapecki, T.; Donten, M.; Stojek, Z. *Electrochem. Commun.* **2010**, *12*, 624–627.
42. Nowicka, A. M.; Hasse, U.; Sievers, G.; Donten, M.; Stojek, Z.; Fletcher, S.; Scholz, F. *Angew. Chem., Int. Ed.* **2010**, *49*, 3006–3009.
43. Rapecki, T.; Donten, M.; Nowicka, A. M.; Stojek, Z. *J. Electroanal. Chem.* **2012**, *677-680*, 83–89.

Chapter 13

Manipulation of the Electronic Properties of Gold and Silver Core–Shell Nanoparticles

Derrick M. Mott* **and Shinya Maenosono**

Japan Advanced Institute of Science and Technology,
School of Materials Science, 1-1 Asahidai, Nomi,
Ishikawa 923-1292, Japan
***E-mail: derrickm@jaist.ac.jp**

Plasmonic nanoparticles, primarily composed of gold and silver are some of the most promising candidates for bio-molecular sensors and probes. The ability to extract the enhanced properties for these materials relies solely on the ability to control the particle size, shape, structure or composition. While much effort has gone into creating and understanding the resulting properties for gold and silver based nanoparticles, there is still a challenge to overcome in achieving optimized probes which are robust, have high plasmonic activity and possess a strong surface reactivity with a wide range of bio-molecules. The hybridization of particle properties in multi-component nanoparticles offers a powerful route towards achieving this goal. Core@shell nanoparticles composed of silver and gold display a wealth of enhanced sensing properties, yet suffer from two primary drawbacks. The sensitivity of silver to the galvanic replacement reaction and rapid oxidation in the presence of biological levels of salt effectively limits the ability to control the characteristics of these probes either through synthetic technique or in practical use. New studies however have emerged that reveal an enhanced stability for silver when it is coated as a shell onto gold particles. The enhanced resistance of the silver at an interfacial layer in the Au@Ag structure is revealed to arise as a result of a unique electronic transfer phenomenon, which ultimately causes the silver layer to become electron rich, leading to enhanced stability. The finding creates a new avenue for controlling the

In Functional Nanoparticles for Bioanalysis, Nanomedicine, and Bioelectronic Devices Volume 1; Hepel, M., et al.;
ACS Symposium Series; American Chemical Society: Washington, DC, 2012.

plasmonic and stability properties for not only gold and silver core@shell nanoparticles for bio-molecular diagnostics, but also for a host of other nanomaterials that can benefit through multicomponent designs.

Introduction

Nanotechnology is driven by the desire to discover materials with new, unique and technologically beneficial properties that can be used in advanced applications. Our knowledge in the field has come a long way in a short time, yet there is still much we don't understand about how to control the specific novel properties, which arise as a function of the particle characteristics such as size, shape, composition, structure, surface properties, etc. Gold (Au) and Silver (Ag) Nanoparticles (NPs) are some of the oldest known examples and have received the most attention in terms of synthetic refinement and elucidation of the resulting nanoscale properties. Yet there are still important discoveries being made that provide insight on how to more finely control these novel properties, which can be applied to a broad range of NP systems. Much of the knowledge being gained in this area today includes techniques for manipulating the NP structure or composition in multicomponent type NPs (*1*, *2*). Au and Ag core@shell NPs are a classic example that offers enhanced, synergistic or multi-functionality in a single particle probe (*3*, *4*). As a result, a wide range of core@shell structures with varying parameters have been synthesized with the target of controlling the optical, reactivity and stability properties (*5–7*).

This class of NP is considered very promising for use in molecular sensing and bio-diagnostics applications where the unique plasmonic properties of the particles serve as a sensitive route to detecting minute traces of analyte or target molecule (*8–19*). Ideally speaking, Ag@Au NPs are considered optimal for these applications because the Ag core would supply enhanced plasmonic properties (high extinction coefficient) while a Au shell would impart bio-molecular reactivity (*via* sulfur reactivity with the Au surface) as well as chemical stability against aggregation and oxidation (*5*, *8–12*, *20–24*). The ability to obtain this structure however, is elusive because of the relatively higher reduction potential for Au over Ag, resulting in the galvanic replacement reaction (*6*, *7*, *25–29*). The end result is typically quasi-core@shell particles that have imperfections such as gaps or holes in the Au shell, alloying, or even complete removal of the Ag core (*5–7*, *25–27*, *30–32*). The inverse structure (i.e. Au@Ag) is also interesting, but has traditionally not been considered feasible as a sensing probe because of the exposure of Ag to the outside environment, leading to surface oxidation and/or NP aggregation. However, it has recently been shown that careful control of the structure in Au@Ag NPs leads to the observation of enhanced properties for the Ag in terms of resisting oxidation and the galvanic replacement reaction (*28*, *33–35*). The observation is unexpected because many researchers have probed the properties for this NP structure without observing the enhanced stability (*36*). The key to the observation is to control the thickness of the Ag shell in a range where a unique electronic transfer from the Au core to the Ag shell can take place (*34*, *35*). Such a finding is of note not only because of the potential implications to the development of plasmonic sensors, but also because the phenomenon can be applied to other multicomponent NP systems, for example in catalysis, magnetics and thermoelectrics applications, among many others (*28*, *35*). The complete understanding of the recently discovered charge transfer phenomenon in Au@Ag NPs has the potential to lead to a new class of NPs with unique and novel properties and will provide the necessary insight to develop new and unique materials that are composed of abundant and non-toxic elements for future high technology applications.

This chapter discusses the recent findings and advancements in understanding and manipulating the plasmonic properties of the Au/Ag NP system towards highly sensitive bio-molecular probes. The discovery of the electronic transfer effect through analysis of both Ag@Au and Au@Ag type NPs reveals effective techniques to enhance the chemical stability as well as the plasmonic properties. First, a general background on the characteristics of Ag, Au, Ag@Au, Au@Ag and Au@Ag@Au NPs, which will be used as a basis for studying the electronic transfer and stability properties is presented. Next, Mie Theory is used to inspect the optical properties of the Ag@Au NPs, revealing subtle structural characteristics in these probes, which has implications to the plasmonic properties. This is followed by the inspection of the electronic properties of the Au@Ag NPs primarily through XPS and XANES techniques, revealing the origins of the electronic transfer phenomenon. The unique electronic properties are then revealed to result in improved particle stability in terms of susceptibility to oxidation. Finally, an assessment of the resulting enhanced plasmonic sensing properties is discussed. The results are presented in terms of particle characteristics, material characterization, understanding of the electronic properties and manipulation of those properties to create Au@Ag NPs with uniform structures and enhanced resistance to oxidation towards effective bio-molecular probes.

Gold and Silver Core@Shell Nanoparticles

Before delving into the in-depth enhanced properties displayed by Au and Ag core@shell NPs, the general morphology and optical properties of the NPs used throughout this discussion are presented. All of the NPs included in this work are prepared in aqueous phase from soluble metal salts using well established techniques (*5*, *27*, *28*, *33*, *35*). These approaches offer the ability to control the resulting NP properties such as particle size, shape, composition, or structure. While the specific techniques used to synthesize the NPs are not detailed here, the following section illustrates the typical particle qualities including the NP morphology, size, dispersity and general optical properties.

Characteristics of Ag NPs

Two types of Ag NPs suspended in water are used in this study. These particles were used to study the stability of monometallic Ag NPs, and were also used as core NPs for the further deposition of Au in later experiments to create Ag@Au NPs. The acrylate capped Ag NPs offer high NP size and shape uniformity, which has historically been challenging to achieve with an aqueous synthetic technique. The Ag NPs synthesized with citrate offers relatively larger sized NPs at the expense of particle size and shape uniformity.

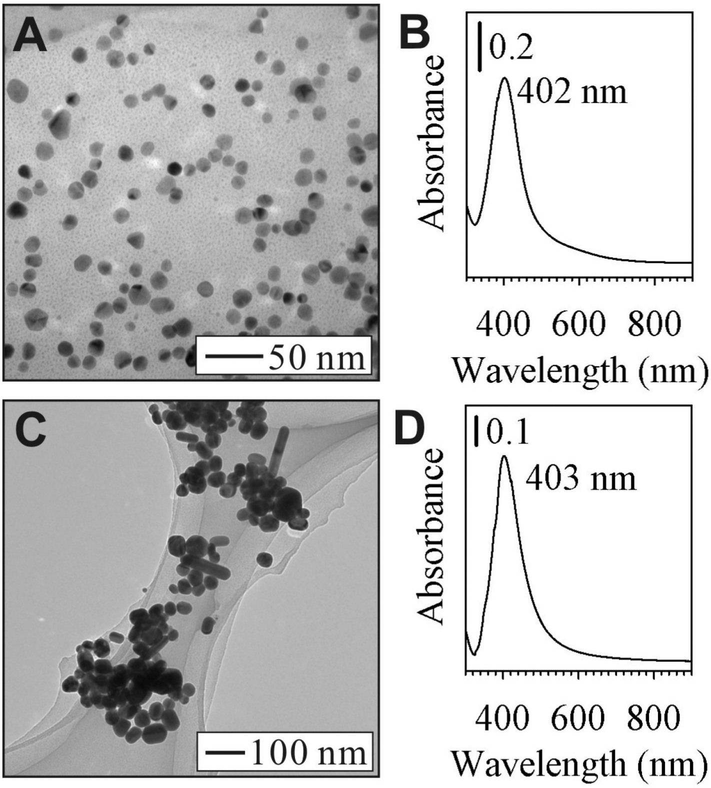

Figure 1. TEM images and UV-Vis spectra of as-synthesized Ag NPs capped with acrylate (A,B) and citrate (C,D). (Adapted with permission from references (33) and (35). Copyright 2012 IOP Publishing, Copyright 2011 American Institute of Physics.)

Acrylate-Capped Ag NPs

The ability to synthesize Ag NPs with controllable characteristics such as size, shape and surface properties is still elusive, especially for sensing and biodiagnostics applications which call for mono-dispersed hydrophilic NPs (*37*, *38*). These hydrophilic Ag NPs are noteworthy for enhanced mono-dispersity in the 20 nm size range (*5*). Figure 1A shows a TEM image of the Ag NPs capped by acrylate. The particle size distribution is 20.5 ± 3.3 nm. The UV-Vis spectrum in Figure 1B shows an SPR band maximum at 402 nm, consistent for Ag NPs (*5*).

Citrate-Capped Ag NPs

Ag NPs synthesized with citrate allows relatively larger sized NPs to be obtained (*33*). Figure 1C shows the TEM image of the NPs illustrating the general morphology. In general the particles have a spherical morphology with a minor fraction of nanorods incorporated, the particle size distribution is 39.4 ± 6.5 nm. Figure 1D shows the UV-Vis spectrum for the as-synthesized NPs with the SPR maximum occurring at 403 nm.

Characteristics of Au NPs

Two different sizes of Au NPs were prepared using the basic citrate reduction technique (*39–43*). These relatively small and large NPs were prepared for two different purposes, the small NPs (~13 nm diameter) are primarily used as cores for the further coating with Ag to create core@shell NPs while the larger Au NPs (~43 nm diameter) are used for comparison of the plasmonic properties of the larger Ag and core@shell NPs.

14 nm Au NPs

Au NPs were synthesized by the well-established citrate reduction method to be used as cores for the further formation of Au@Ag NPs (*39–43*). The Au NPs are a deep-red color with a SPR band at 518 nm. Figure 2 shows the representative TEM and UV-Vis spectrum for the particles. The particles have a uniform and spherical morphology with a mean diameter of 14.2 ± 0.7 nm (*35*).

43 nm Au NPs

For the synthesis of relatively larger Au NPs, a modified citrate reduction technique is followed where less capping/reducing agent is used (*33*). Figure 2 shows the TEM and UV-Vis spectrum collected for these Au NPs, illustrating the general morphology and optical properties. In general the particles have a spherical morphology with a particle size distribution of 43.1 ± 4.3 nm. The SPR maximum occurs at 525 nm, consistent for Au NPs (*33*).

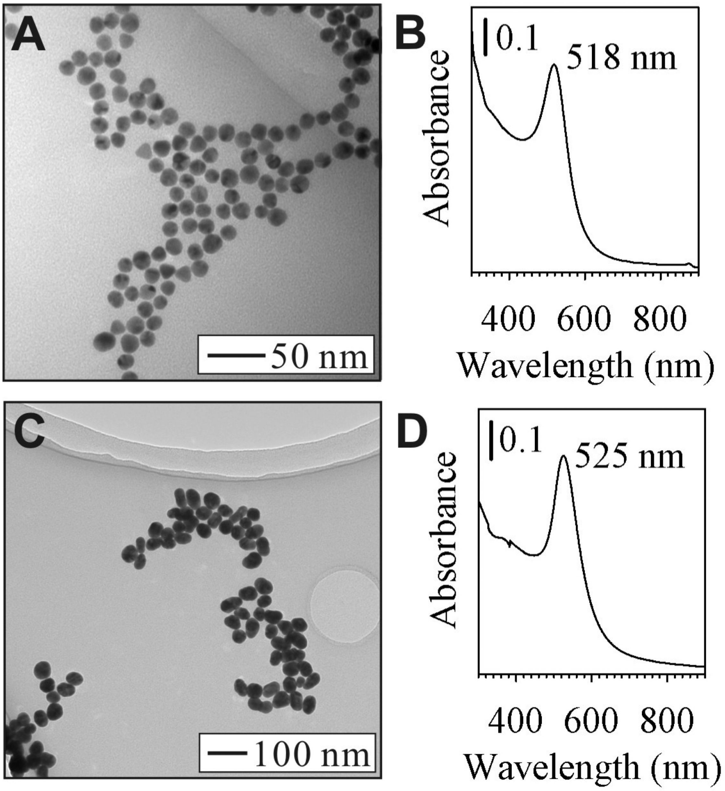

Figure 2. TEM images and UV-Vis spectra of both 14 nm (A,B) and 43 nm (C,D) Au NPs capped with citrate. (Adapted from references (33) and (35). Copyright 2012 IOP Publishing, Copyright 2011 American Institute of Physics.)

Characteristics of Ag@Au NPs

The effort to achieve the ideal Ag@Au NP structure has been highly elusive. Many studies have probed synthetic techniques including both organic and aqueous solvent based wet chemical methods, with mixed results. The galvanic replacement reaction causes a competition in the reduction of Au with the oxidation of the Ag core during typical deposition procedures. Careful control of the synthetic parameters in these reactions has led to the creation of quasi Ag@Au NPs with non-uniform structures such as NPs with partially hollow interiors, limited alloy formation, or non-continuous Au shells (*5*, *12*, *20*, *21*).

Acrylate-Capped Ag@Au NPs

The acrylate capped Ag@Au NPs are used as a platform to study the resulting plasmonic and structural properties for this class of nanomaterial (*5*). Table I lists the metallic feeding ratio, resulting NP size as determined by TEM and composition determined from EDS and XPS. The primary difference between the EDS and XPS techniques is that EDS reveals the composition individual NPs, while for XPS a relatively large irradiation area results in simultaneous analysis of many particles at the same time.

Table I. Metallic feeding ratio, TEM determined size and EDS/XPS determined compositions for Ag@Au NP samples. Source: Reproduced with permission from reference (*27*). Copyright 2011 The Japan Society of Applied Physics

Metallic Feeding Ratio	*TEM Size (nm)*	*EDS*	*XPS*
$Ag_{95}Au_5$	17.5 ± 3.7	$Ag_{93.0}Au_{7.0}$	$Ag_{94.8}Au_{5.2}$
$Ag_{85}Au_{15}$	16.3 ± 2.7	$Ag_{60.6}Au_{39.4}$	$Ag_{57.7}Au_{42.3}$
$Ag_{75}Au_{25}$	17.5 ± 5.1	$Ag_{50.8}Au_{49.2}$	$Ag_{60.6}Au_{39.4}$

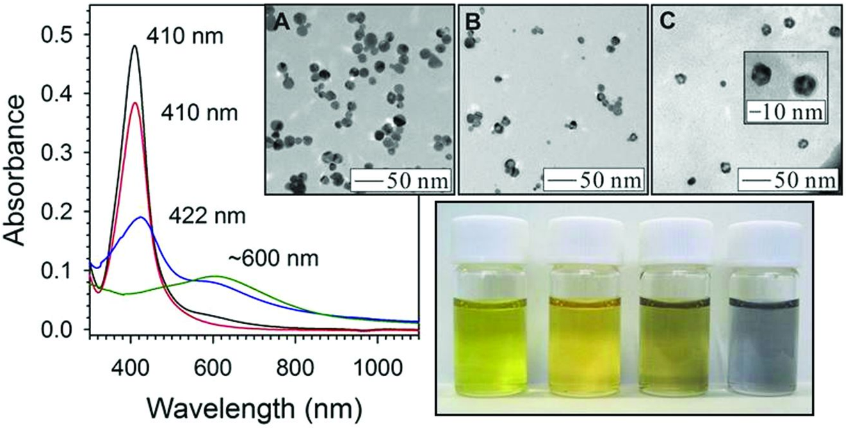

Figure 3. UV-Vis spectra for as-synthesized Ag NPs (black spectrum), 5% Au atomic feeding ratio (red), 15% Au atomic feeding ratio (blue) and 25% Au atomic feeding ratio (green). TEM images of Ag@Au NPs with atomic feeding ratio of 5% Au (A), 15% Au (B), and 25% Au (C). Photographs of the Ag and Ag@Au NPs with increasing shell thickness from left to right. (Adapted from reference (27). Copyright 2011 The Japan Society of Applied Physics.) (see color insert)

UV-Vis spectra, TEM images and photographs of the Ag@Au NP dispersions are shown in Figure 3. In general, all of the NP samples display uniform morphological properties with discrete particle size distributions. However, for the Ag@Au NPs synthesized with an atomic feeding ratio of 15% Au, many particles appear to have a light spot on the particle surface. These lighter colored spots arise from the formation of an incomplete Au shell on the Ag particle surface, a gap or hole in the Au shell occurring as a result of the galvanic replacement reaction (*6*, *7*). The NPs synthesized with 25% feeding ratio of Au have more highly accentuated light centers with darker outsides, likely representing partially hollow areas in the particle center. The UV-Vis spectra and particle photographs reveal an evolution in the plasmonic properties for the NPs as the amount of Au is increased in each sample. In general, the SPR band is slightly dampened in intensity for a feeding ratio of 5% Au. For a feeding ratio of 15% Au, the peak is significantly dampened and shifted to higher frequency with a new peak around 600 nm emerging for Au. Finally for a feeding ratio of 25% Au, the Ag component of the SPR is completely extinguished and only a broad peak is observed from the Au component.

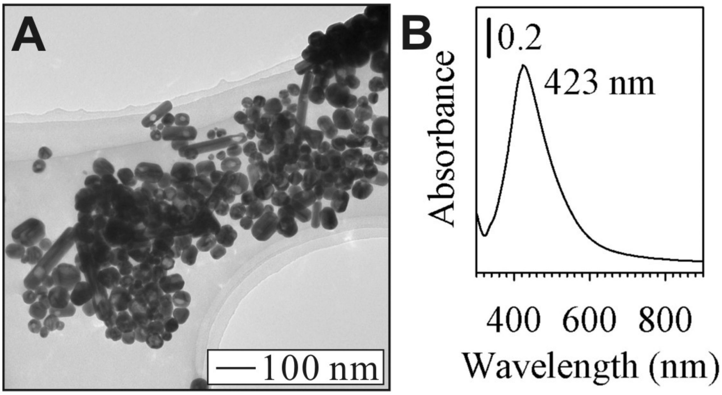

Figure 4. TEM image (A) and UV-Vis spectrum (B) of as-synthesized Ag@Au NPs capped in citrate with relatively larger size. (Adapted from reference (33). Copyright 2011 American Institute of Physics.)

Citrate-Capped Ag@Au NPs

The as-synthesized citrate-capped Ag NPs were used as core particles in the preparation of relatively larger sized Ag@Au NPs (*33*). Figure 4 shows the TEM image and UV-Vis absorption spectra of the as-synthesized Ag@Au NPs. The SPR peak wavelength occurs at 423 nm with a single non-symmetrical shape observed between that for Ag and Au indicating the coating of Au onto the Ag NPs. The TEM image shows that the NPs have a roughly spherical morphology (a minor fraction of nanorods forms in the Ag NP synthesis but the occurrence is too low to significantly impact the optical properties). In addition, slightly darker rings outside the lighter spherical centers are observed which likely indicates the operation of the galvanic replacement reaction (*5*). The mean size and size distribution is 43.9 ± 7.9 nm for these NPs.

Characteristics of Au@Ag NPs

The as-synthesized citrate-capped Au NPs were used as core particles (seeds) in the preparation of Au@Ag core@shell NPs (*28*, *35*). TEM images collected for five different Ag shell thicknesses obtained, including 0.4 ± 0.3, 1.0 ± 0.6, 2.2 ± 0.4, 3.1 ± 0.4 and 3.6 ± 0.4 nm are shown in Figure 5 along with the UV-Vis spectra and photographs of the NP dispersions. Table II shows the tabulated particle size parameters. The Ag shell thickness is expressed in the subscript hereafter ($Au@Ag_x$; x denotes the Ag shell thickness). These Au@Ag NPs are highly monodisperse in terms of size and shape in comparison to Ag NPs synthesized by comparable reduction methods, illustrating an important benefit of using Au NPs as seeds. In the UV-Vis spectra of the Au@Ag core@shell NPs, when x is increased, the SPR band gradually became blue-shifted, with the SPR peak of Ag eventually becoming dominant. The $Au@Ag_{3.6}$ NPs show a single LSPR band at 390 nm, which stems from the dominant plasmon resonance of the Ag shells. The appearance of a monomodal LSPR band corresponding to Ag indicates that the Au cores are uniformly covered by the Ag shell and the optical contribution from the Au cores becomes completely screened (*44*–*46*).

Characteristics of Au@Ag@Au Double Shell NPs

This section describes the general properties of Au@Ag@Au double shell NPs. These NPs display a well-defined heterostructure that consists of a Au core, Ag intermediate shell and an outer second shell of Au. The uniform particle morphologies and structures arise as a result of the suppression of galvanic replacement though electronic transfer in the Au-Ag system, which is discussed in later sections.

Characteristics of $Au@Ag_{3.6}@Au_{0.11}$ NPs

TEM, UV-Visible spectra, STEM-HAADF, and elemental mapping studies shown in Figure 6 illustrate the well-defined structure of these NPs. The TEM image shows that the $Au@Ag_{3.6}@Au_{0.11}$ double shell NPs are more uniform in size and shape when compared to typical Ag@Au NPs (*47*). Moreover, they have no observable gaps or defects in the particle structure. The UV-Visible spectra shown for Ag, $Au@Ag_{3.6}$ and the $Au@Ag_{3.6}@Au_{0.11}$ NPs demonstrate how the optical properties evolve as the NP structure becomes more complex. As Ag is coated onto the Au NPs, the LSPR band maxima shifts to lower wavenumbers than that for pure Ag NPs and also becomes broadened at higher wavenumber values. When these $Au@Ag_{3.6}$ NPs are further coated with the second Au shell, the peak again shifts towards higher wavenumbers and retains the broadened spectral shape.

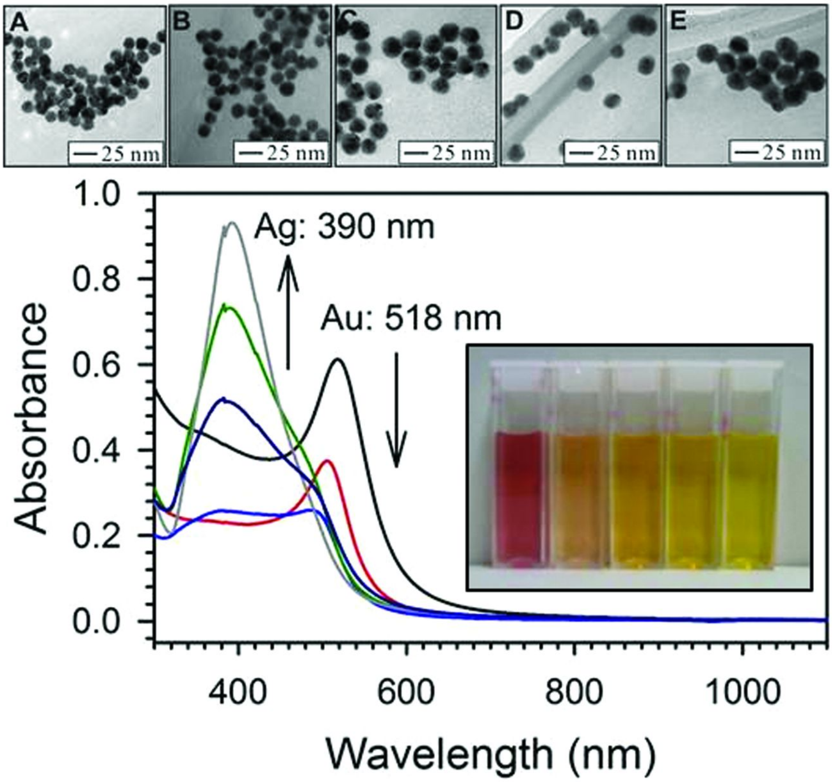

Figure 5. UV-Vis spectra for as-synthesized Au@Ag$_x$ NPs with varying Ag shell thickness, the arrows represent the dampening of the Au SPR band with a concurrent increase in the SPR band intensity for Ag as the Ag shell thickness is increased. TEM images for Au@Ag$_x$ NPs synthesized with increasing Ag shell thickness of 0.4 (A), 1.0 (B), 2.2 (C), 3.1 (D) and 3.6 (E) nm. The inset to the figure shows a photograph of the Au, and Au@Ag$_x$ NPs. (Adapted from reference (28). Copyright 2011 American Institute of Physics.) (see color insert)

One of the most frequent questions raised about such core@shell and heterostructured NPs is “how do you confirm the integrity of the structure?”. In general, the structural properties can be visualized by using STEM-HAADF and EDS elemental mapping techniques. The STEM-HAADF image of the Au@Ag$_{3.6}$@Au$_{0.11}$ double shell NPs displays high Z contrast, which allows elements with sufficiently different molecular weight to be differentiated in the image. Since the heavier Au atoms (atomic number, Z = 79) give rise to a brighter image than the lighter Ag atoms (Z = 47) in the dark field image, the Au core appears brighter than the Ag first shell. The visualization of a very thin and bright layer on the particle surface in the STEM-HAADF image indicates that a thin continuous Au second shell was successfully formed on the Au@$Ag_{3.6}$ NPs. The EDS mapping result also similarly indicates the positions of Au and Ag in the particle structure graphically. These two techniques give clear evidence that the resulting NPs have a discrete double shell structure.

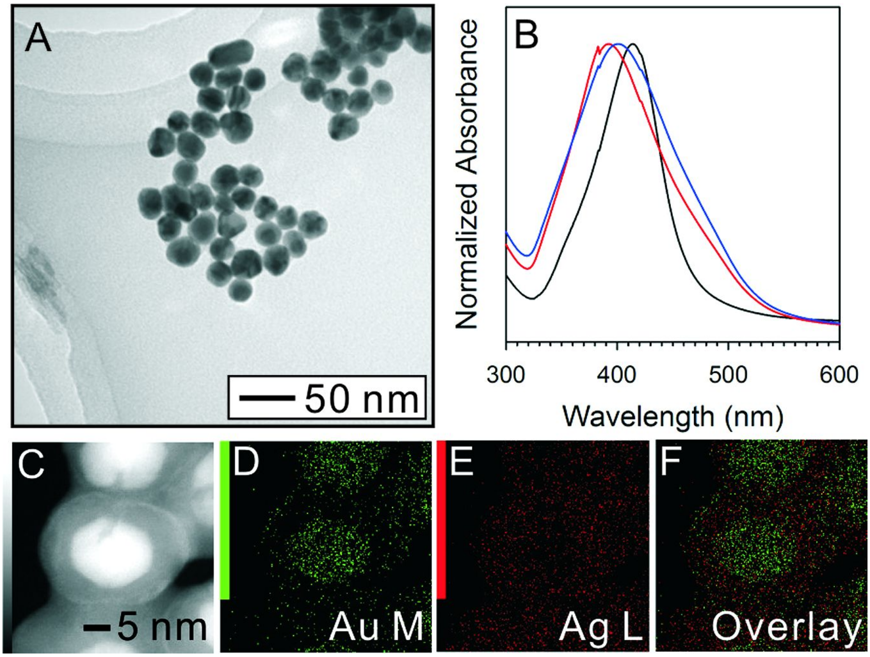

Figure 6. TEM image of Au@$Ag_{3.6}$@$Au_{0.11}$ (A), UV-Visible spectra for Ag (black curve), Au@$Ag_{3.6}$ (red curve) and Au@$Ag_{3.6}$@$Au_{0.11}$ (blue curve) (B), and STEM-HAADF (C) and EDS elemental mapping images for Au M map (D), Ag L map (E) and an overlay of the Au and Ag maps (F). (Adapted from reference (28). Copyright 2011 American Institute of Physics.) (see color insert)

Characteristics of Au@$Ag_{3.9}$@$Au_{1.2}$ NPs

Similar to the double shell NPs that have a thin Au second shell, these particles display a clearly defined thick Au second shell. Figure 7 shows the TEM, UV-Visible spectra, STEM-HAADF, and elemental mapping analysis, which illustrates the well-defined structure. The particles retain the uniform spherical morphology and structure, even though the second Au shell is now much thicker. UV-Visible spectra of Ag and the Au@$Ag_{3.9}$@$Au_{1.2}$ NPs show that the double shell NPs possess a LSPR band in nearly the same position as that for the Ag NPs with some peak broadening and asymmetry in the wavelength range for Au NPs. The STEM-HAADF and EDS elemental mapping studies also similarly confirm the well-defined heterostructured nature of the particles.

Table II. Mean diameter and shell thicknesses of Au@Ag$_x$ and double shell NPs. Source: Reproduced with permission from reference (*28*). Copyright 2011 American Institute of Physics

Type of NPs	*x (nm)*	*y (nm)*	*D (nm)*
Au	–	–	14.4 ± 0.7
Au@Ag$_{0.4}$	0.4 ± 0.3	–	15.2 ± 0.7
Au@Ag$_{1.0}$	1.0 ± 0.6	–	16.4 ± 1.2
Au@Ag$_{2.2}$	2.2 ± 0.4	–	18.8 ± 0.8
Au@Ag$_{3.1}$	3.1 ± 0.4	–	20.6 ± 1.2
Au@Ag$_{3.6}$	3.6 ± 0.4	–	21.6 ± 0.9
Au@Ag$_{3.6}$@Au$_{0.11}$	3.6 ± 0.4	0.11	21.8 ± 1.2
Au@Ag$_{3.9}$@Au$_{1.2}$	3.9 ± 0.7	1.2	23.0 ± 1.9

x: Ag first shell thickness, y: Au second shell thickness.

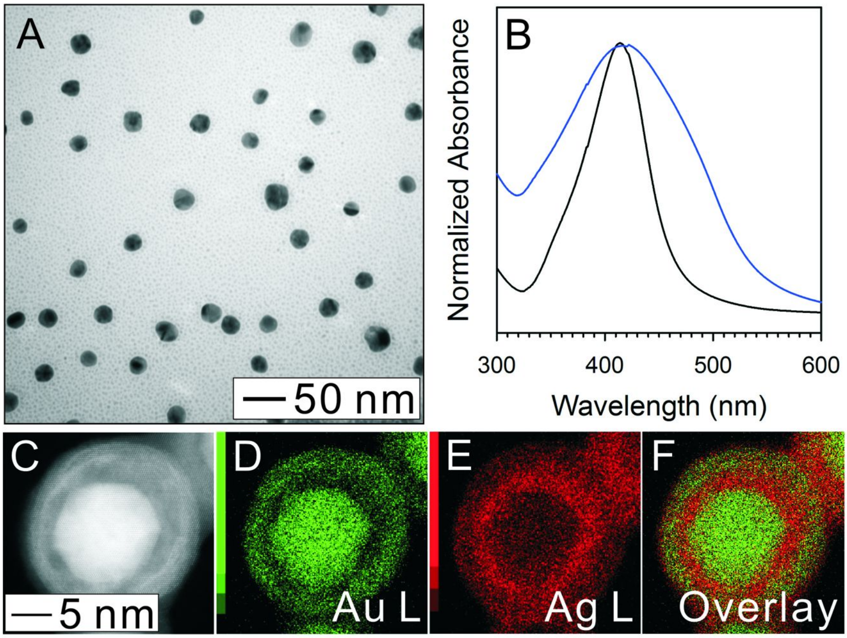

Figure 7. TEM image (A) of Au@Ag$_{3.9}$@Au$_{1.2}$ NPs, UV-Visible spectra for Ag (black curve) and Au@Ag$_{3.9}$@Au$_{1.2}$ NPs (blue curve) (B), and STEM-HAADF (C) and EDS elemental mapping images for Au L map (D), Ag L map (E) and an overlay of the Au and Ag maps (F). (Adapted from reference (28). Copyright 2011 American Institute of Physics.) (see color insert)

The Role of Galvanic Replacement Reaction in Ag@Au NP Synthesis

The galvanic replacement reaction is driven by the difference in the electrochemical potential between the two metals, with one serving as the cathode and the other as the anode. In terms of synthesizing Ag@Au NPs, the reduction potential of $AuCl_4^-/Au$ (0.99 V vs. SHE) is more positive than that of AgCl/Ag (0.22 V vs. SHE) (*48*). This causes the Ag NPs to serve as sacrificial templates and be oxidized by $HAuCl_4$ through Equation 1. The reaction typically occurs at a high-energy site (e.g., surface step, point defect, or hole in the capping layer) (*49*) rather than over the entire NP surface, causing the typical non-uniform structures that are observed. In the case that Au@Ag NPs are used as cores, however, the Ag shells have been demonstrated to have a higher electron density than pure Ag NPs due to electron transfer from the Au core to the Ag shell (*28*, *34*). The electron rich Ag shell results in a negative oxidation state, $Ag^{\delta-}$, leading to effective suppression of the galvanic replacement reaction. Many other researchers have studied multishell NP Au/Ag systems using aqueous preparation techniques (*36*). In these approaches however, the deposited intermediate Ag shell thickness is much too large to display the electronic transfer properties, which still leads to the formation of hollow structures with partial alloying when the second Au shell is deposited. In the studies presented here, the intermediate Ag shell thickness is limited to a range where the charge transfer phenomenon takes place, allowing the ability to create Au@Ag@Au NPs without significant alloying or defects in the structure (*28*).

$$3Ag(s) + HAuCl_4(aq) \longrightarrow Au(s) + 3AgCl(s) + HCl(aq) \qquad (1)$$

Mie Modeling of the Plasmonic Properties of Ag@Au NPs

Ag@Au core@shell NPs have been highly sought because of the expected enhanced plasmonic and reactivity properties, however, even for samples that seem to have a uniform structure, the optical properties do not always behave predictably. Mie Theory is a useful tool that can serve to clarify the resulting expected optical properties for this class of NP, enhancing the understanding of the particle structure and plasmonic properties relationship. An important factor that must be considered is the parameters used in the calculation, which can have a large impact in the modeled results. The calculations here are based on Mie Theory for nanosized metallic spheres placed in water (dielectric constant = 1.77) (*27*). In the theory, the metallic dielectric function $\varepsilon(\omega) = 1-\omega_p^2/\omega(\omega+i\gamma)$ for the sphere is incorporated, where ω_p is the plasmon frequency depending on the specific metal. This approach differs from other well established modeling efforts in that the dielectric constant of the materials is expressed by the Drude Model as opposed to calculated from bulk materials using Energy Electron Loss Spectroscopy (EELS) (*44–46*). The Drude Model offers an alternate approximation of the dielectric constants for nanoscale particles and provides an alternate expression of the optical properties for Ag@Au NPs (*27*). The Mie Model results give insight into how the complex structure of core@shell NPs affects the optical properties.

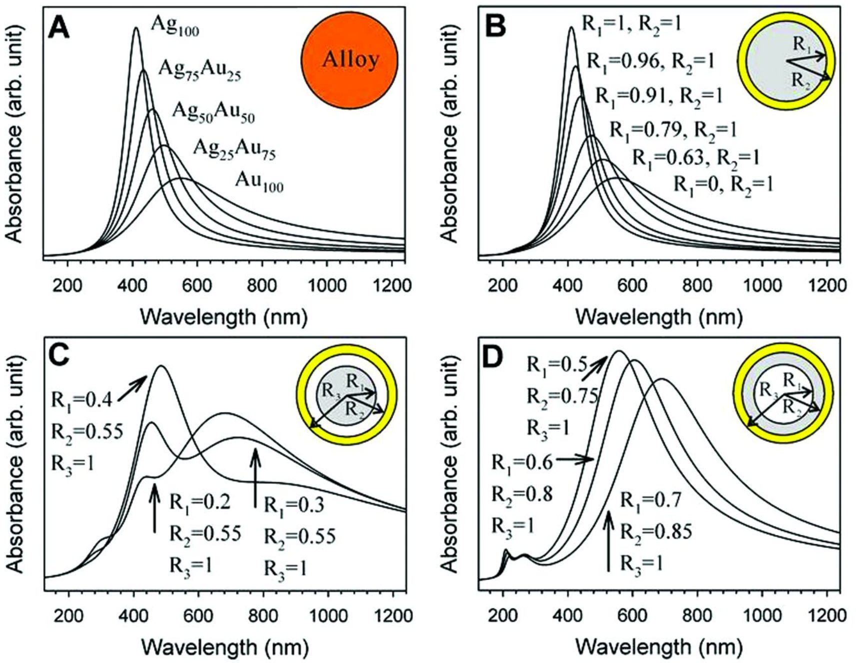

Figure 8. UV-Visible spectra calculated using Mie theory for alloy AuAg NPs (A), and Ag@Au NPs with the Model I (B) Model II (C), and Model III (D) structures. The insets to the figure represent the NP model used in the calculation where the grey color represents Ag, yellow indicates Au and white indicates a void space. (Adapted with permission from reference (27). Copyright 2011 The Japan Society of Applied Physics.) (see color insert)

Mie Study of Ag@Au NP Optical Properties

Four fundamentally different types of NP structure were studied with Mie. Figure 8 shows the Models as well as the particle structural parameters used in the calculation. In general, the optical properties of a AuAg alloy, a perfect Ag@Au structure (Model 1), Ag@Au with a void space between Ag and Au (Model 2), and a Ag@Au structure with a void space in the center of the NP (Model 3) were studied. When comparing the modeled results of the alloy to the perfect Ag@Au structure (Figure 8A and B), the LSPR spectral shape is nearly identical. A single asymmetric peak is observed that shifts in position as a function of the composition (*27*). This demonstrates how challenging it can be to differentiate between alloys and core@shell structures based solely on the optical properties. For the imperfect core@shell structures however, the optical properties are vastly different. Now the Model 2 spectra in Figure 8C show two primary peaks with the feature in the range of ~400-500 nm attributed to the Ag core while the component at ~650-900 nm is attributed to the Au shell. The Model 3 spectra in Figure 8D show a single broad feature in the range of ~500-700 nm, depending on the NP composition. The low intensity peaks observed at ~200-300 nm arise in the calculation due to the inner surface resonances of Au, or the interface resonance of Au and Ag, but are not practically observable in the real particle structure, so are not diagnostic.

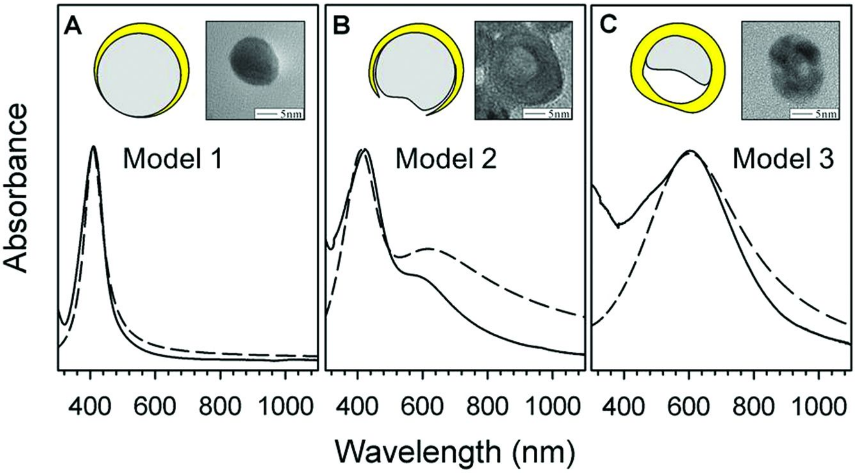

Figure 9. UV-Visible spectra for the three different types of Ag@Au NPs synthesized along with the corresponding best fit spectra calculated using Mie theory for atomic feeding ratio of 5% Au and Model I (A), atomic feeding ratio of 15% Au and Model II (B), and atomic feeding ratio of 25% Au and Model III (C), respectively. Solid lines represent experimentally collected data while dashed lines are for Mie Modeling. (Adapted with permission from reference (27). Copyright 2011 The Japan Society of Applied Physics.) (see color insert)

Correlation of Mie Study to Acrylate-Capped Ag@Au NP Optical Properties

The variation in the spectral shape allows a diagnostic comparison between experimentally collected spectra for acrylate capped Ag@Au NPs and the Mie theory calculated spectra. By qualitatively matching the two types of spectra, fine structural details in the NPs can be identified. Figure 9 shows the UV-Vis spectra for three different compositions of acrylate capped Ag@Au NPs along with the closest matching UV-Vis spectrum calculated using Mie theory. The insets to the figure show the corresponding practical particle structure as well as a TEM image for an individual Ag@Au NP exhibiting the structure. For the Ag@Au NPs synthesized with atomic feeding ratio of 5% Au (Figure 9A), Model 1 with parameters of R_1=0.7 and R_2=1 shows the best fit, which reflects a very thin and perhaps non-continuous Au shell. For the Ag@Au NPs with atomic feeding ratio of 15% Au (Figure 9B), Model 2 with parameters of R_1=0.3, R_2=0.45, and R_3=1 provides the best fit. This reflects the fact that some particles display gaps in the Au coating, exposing the inner Ag, causing two peaks to be observed in the UV-Vis spectrum. Finally for the Ag@Au NPs with atomic feeding ratio of 25% Au in Figure 9C, Model 3 with parameters of R_1=0.6, R_2=0.8, and R_3=1 shows the best fit. This reflects the action of Au etching away some of the Ag core leaving a void space within the particle, with Au eventually forming a continuous shell over the remaining core material. Note that while the spectra do show significant deviation, it is the spectral features that the qualitative fitting is based on.

The results of the Mie study illustrate the challenges associated with trying to achieve Ag@Au NPs by coating aqueous Au onto metallic Ag cores. Namely, the galvanic replacement reaction consistently causes NPs that have structural imperfections, such as gaps in the Au shell, or void spaces within the particle interior. These particles may still be core@shell in nature, but the structural imperfections negatively impact the particle properties such as LSPR peak shape, or, as will be discussed later, susceptibility to oxidation. Understanding the optical properties for these structurally imperfect NPs allows the ability to distinguish between perfect core@shell structures and those with imperfections.

Electronic Properties of Au@Ag NPs

In essence, the charge compensation mechanism in core@shell NPs is based on the Au-Ag alloy system where a depletion of d electrons at the Au site accompanied by an increase in d electrons at the Ag site is observed (*50*, *51*). In addition, a study on the Ag-Pt system where Ag adatoms were vapor-deposited onto a Pt(111) surface was found to increase d electron populations (*52*). These early studies served as a basis for probing the electronic properties in the Au@Ag NP system where the small size regime of the particle components allows the charge transfer phenomenon to be operable. The electronic and chemical properties of the Ag component in Au@Ag NPs could be tuned by taking advantage of this charge compensation mechanism. By increasing the electron density within the Ag shell, a negative Ag oxidation state would be achieved which could suppress the galvanic replacement reaction at the Ag shell surface and increase stability against oxidation. In order to probe the theory, the electronic properties of Au@Ag NPs were studied using both XPS and XANES analysis techniques. The results of these studies provide insight into the electronic structure of the Au@Ag NP system.

XPS Analysis of the Electronic Properties for Au@Ag NPs

The electronic properties for the citrate capped Au@Ag_x and Au@$Ag_{3.6}$@$Au_{0.11}$ NPs was studied using XPS. Figure 10 shows the XPS spectra taken in both the Ag3d and Au4f areas along with expanded views of the $Ag3d_{5/2}$ and $Au4f_{7/2}$ peaks. The Ag component of the spectra gives a sensitive assessment of the electronic properties for the NPs. The Ag3d$_{5/2}$ peak displayed multiple components that were isolated by deconvolution using two Gaussian functions as shown in Figure 10B. For the monometallic Ag NPs, both a monometallic component (blue line) as well as a significant oxide peak (red dashed line) were identified. However, for the Au@Ag$_x$ NPs, no oxide peak is observed. Instead, a minor alloy component (indicated by the red lines) is observed. This alloy component forms at the interface of Au and Ag in the NP structure and can never be completely eliminated (*28*). These observations provide indirect evidence of the electronic transfer effect because no oxide is seen for the Au@Ag$_x$ NPs. The electronic transfer effect is essentially protecting these NPs from oxidation. In addition, the deconvoluted pure Ag component of the peak is shifted towards lower binding energy when compared to monometallic Ag, which is discussed in the next section. While the spectra of the Au4f component shown in Figure 10C is not as diagnostic as the Ag3d peak, an expanded view of the Au4f$_{7/2}$ component reveals a subtle peak shift to higher binding energy as more Ag is added to the NP surface. This peak shift is more easily visualized by the addition of the vertical line in Figure 10D.

The direct impact of the NP structure on the electronic properties can be observed in a plot of the Ag^0 3d$_{5/2}$ peak energy as a function of Ag shell thickness, x as shown in Figure 11. All Au@Ag$_x$ NPs exhibit a negative shift in the Ag^0 3d$_{5/2}$ BE compared to that of pure Ag NPs (368.26 eV). Moreover, the Ag^0 3d$_{5/2}$ BE increases toward the value of pure Ag NPs with increasing x when $x \geq 1.0$ supporting the idea that the charge transfer is an interfacial phenomenon. The deposition of the second Au shell onto the Ag surface again causes the reduction of Ag^0 3d$_{5/2}$ BE indicating that further electron transfer between the Au second shell and the Ag first shell occurs.

The XPS analysis on Au@Ag$_x$ and Au@Ag$_{3.6}$@Au$_{0.11}$ NPs demonstrates that the general electronic properties of the two metals are modified in the core@shell structure and gives a basis for enhanced properties such has resistance to oxidation, or the ability to deposit a second shell of Au. The XPS study provides a good assessment of the electronic properties of Ag, but is less diagnostic for assessing the properties of the Au component. In order to gain a more full understanding of the properties of the Au in the core@shell structure, XANES analysis was used, offering a more rigorous understanding of the electronic transfer phenomenon.

XANES Study on the Electronic Structure of Au@Ag and Au@Ag@Au NPs

XANES has been increasingly used to study the electronic properties for a wide range of materials including NPs (*53–60*). The technique has been employed to study the relationship between oxidation state and catalytic activity in catalysts (*61–63*), redox behavior (*64–66*), and for following the formation mechanism of metal NPs (*67–69*). In this section of the study on the electronic properties for core@shell NPs, the L-edge XANES analysis provides critical information on the charge transfer effect. In particular, the Au@Ag and Au@Ag@Au NPs are revealed to possess a unique electronic configuration in the Au L$_{2,3}$-edge XANES spectra.

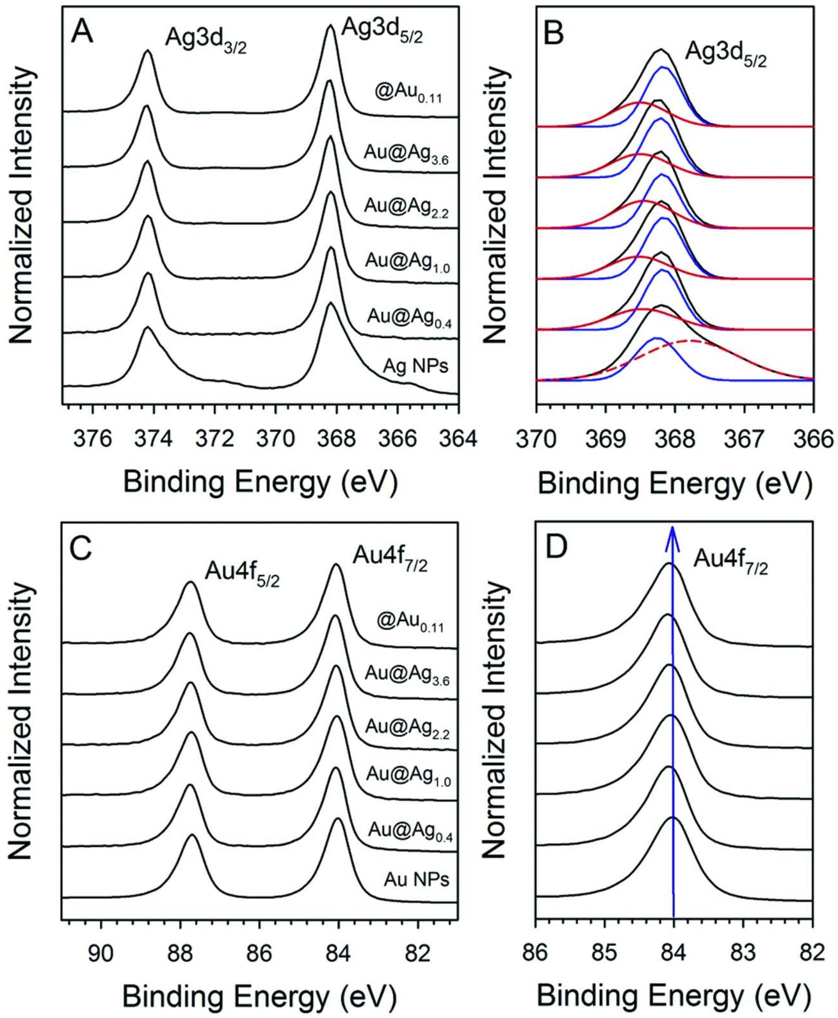

Figure 10. XPS spectra of Ag, Au@Ag$_x$ (x = 0.4, 1.0, 2.2 and 3.6), and Au@Ag$_{3.6}$@Au$_{0.11}$ double shell NPs in the Ag3d (A) area with an expanded view of the Ag3d$_{5/2}$ component (B). XPS spectra in the Au4f area are shown in (C) with an expanded view of the Au4f$_{7/2}$ area (D). The deconvolution shown for the Ag3d$_{5/2}$ area corresponds to Ag^0 (blue curves) and Ag−Au alloy (red curves) [or Ag oxide (red dashed curve)] components. The blue line in (D) aids in visualizing the subtle peak shift. (Adapted with permission from reference (28). Copyright 2011 American Institute of Physics.) (see color insert)

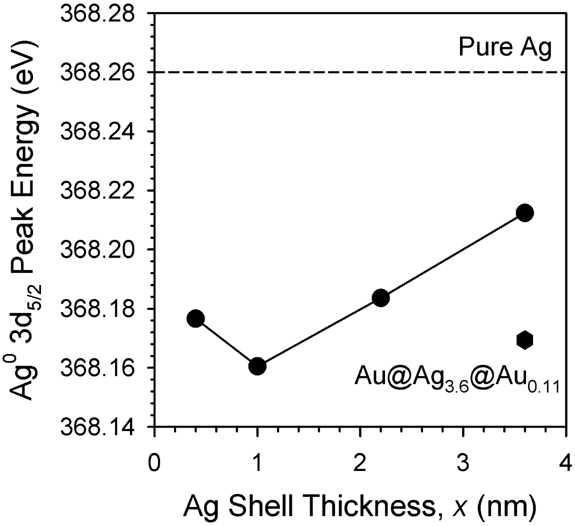

Figure 11. Plot of the Ag3d$_{5/2}$ Peak Energy for the Au@Ag$_x$ and Au@Ag$_{3.6}$@Au$_{0.11}$ double shell NPs. (Adapted with permission from reference (28). Copyright 2011 American Institute of Physics.)

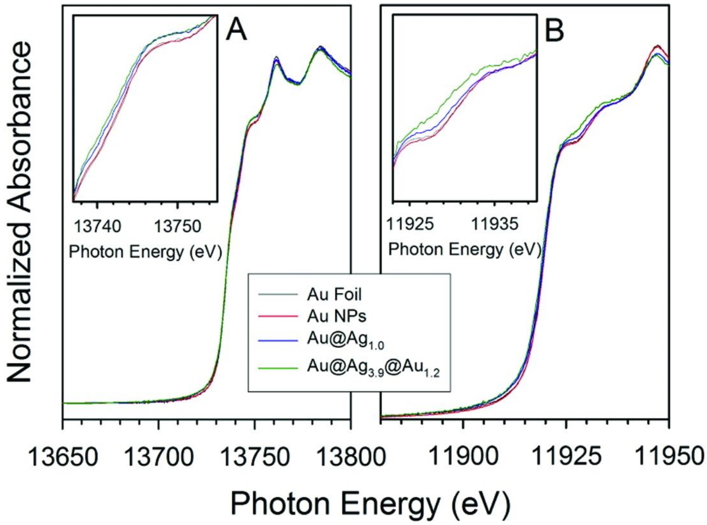

Figure 12. (A) Au L$_2$-edge and (B) Au L$_3$-edge XANES spectra of Au foil, Au NPs, Au@Ag$_{1.0}$ NPs and Au@Ag$_{3.9}$@Au$_{1.2}$ NPs. The insets show an expanded view. (Adapted from reference (34). Copyright 2012 American Chemical Society.) (see color insert)

Table III. Derived parameters for the unoccupied *d* states. Source: Reproduced from reference (*34*). Copyright 2012 American Chemical Society

Samples	ΔA_2 ($eV \cdot cm^{-1}$)	ΔA_3 ($eV \cdot cm^{-1}$)	$\Delta h_{3/2}$	$h_{3/2}$	$\Delta h_{5/2}$	$h_{5/2}$	$\Delta h_{3/2}+\Delta h_{5/2}$
Au foil	0	0	0	0.118	0	0.283	0
Au NPs	157.1	−148.5	6.3×10^{-3}	0.124	-5.5×10^{-3}	0.278	7.8×10^{-4}
$Au@Ag_{1.0}$ NPs	383.0	617.2	1.5×10^{-2}	0.133	1.6×10^{-2}	0.299	3.1×10^{-2}
$Au@Ag_{3.9}@Au_{1.2}$ NPs	516.0	1340.6	2.1×10^{-2}	0.139	3.7×10^{-2}	0.320	5.7×10^{-2}

The citrate capped Au (13 nm), Au@Ag$_{1.0}$ and Au@Ag$_{3.9}$@Au$_{1.2}$ NPs were analyzed using the XANES technique. Figure 12 shows the XANES spectra in the Au L$_2$- and L$_3$-edges for Au foil, Au, Au@Ag$_{1.0}$ and Au@Ag$_{3.9}$@Au$_{1.2}$ NPs. All spectra showed the same resonance patterns as that of Au metal. The Au foil and Au NPs showed almost identical XANES spectra both in L$_2$- and L$_3$-edges, but a gradual increase of the threshold resonance at the shoulder peak occurs in the order Au NPs < Au@Ag$_{1.0}$ < Au@Ag$_{3.9}$@Au$_{1.2}$ NPs in both L$_2$- and L$_3$-edges. The increase in the White Line (WL) area in the L$_2$- and L$_3$- edge XANES spectra can be attributed to a decrease in 5d electronic occupancy for Au (*70*).

The relevant parameters used to investigate the unoccupied d states are listed in Table III (*34*). Small differences can be detected in the hole densities between Au NPs and foil, but these are too small to be diagnostic. There is relatively no electronic difference between them primarily because the Au NPs have a diameter (14.4 nm) which is too large to exhibit size-dependent effects (*71–74*). However, the values of both $\Delta h_{3/2}$ and $\Delta h_{5/2}$ (*d*-orbital vacancy) increased in the Au@Ag core-shell NPs when compared to the Au NPs. From Au@Ag$_{1.0}$ core-shell NPs to the Au@Ag$_{3.9}$@Au$_{1.2}$ double-shell NPs, a further increase in both $\Delta h_{3/2}$ and $\Delta h_{5/2}$ was observed. This trend is a clear indication that the electron transfer from Au to Ag takes place in the heterostructured NPs.

A visual representation of the change in both *d*-orbital vacancy ($\Delta h_{3/2} + \Delta h_{5/2}$) and energy shift of the Au 4f$_{7/2}$ XPS peak is shown in Figure 13. In the cases of Au@Ag$_{1.0}$ and Au@Ag$_{3.9}$@Au$_{1.2}$ NPs, an increase in the total *d*-orbital vacancies and a positive energy shift in the 4f$_{7/2}$ peak are simultaneously observed. Both of these values increase with increasing Ag-Au interfacial area. This observation, in conjunction with the observation in the XPS analysis that a negative shift in the Ag3d peak energy occurs for both Au@Ag$_{1.0}$ and the Au@Ag$_{3.9}$@Au$_{1.2}$ NPs when compared to bare Ag NPs (*28*) creates strong evidence for the electronic transfer phenomenon. The collective results of XANES for Au and XPS for Au and Ag demonstrate that a unique charge transfer from Au to Ag occurs through the formation of the Au@Ag core-shell structure, which is further enhanced by Au outer-shell formation. This phenomenon provides an avenue to tune the resulting plasmonic and stability properties for Au/Ag structures through manipulation of the electron density within the Ag shell (*28*). With the elucidation of the mechanism to the electronic transfer, we next discuss the general qualities of the enhanced plasmonic and stability properties.

Assessment of the NP Stability

In this section, the relative stability of the various NPs are studied when exposed to a range of chloride containing electrolytes. The stability properties of these NPs is discussed primarily in terms of oxidation because this plays a key role in affecting the sensing properties. For example, the detection of many biomolecules requires a salt concentration approaching that of biological levels, which typically causes oxidation and/or aggregation of Ag containing NP sensing probes. The relative stability of Ag@Au NPs is breifly appraised, followed by a more in-depth look at the stability for the Au@Ag type NPs.

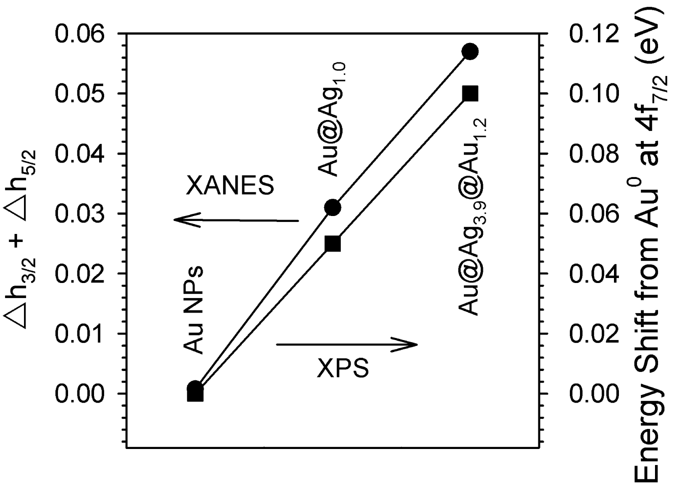

Figure 13. Differences of the d-orbital vacancies from bulk Au and XPS energy shift in the $4f_{7/2}$ peak from bulk Au. (Adapted from reference (34). Copyright 2012 American Chemical Society.)

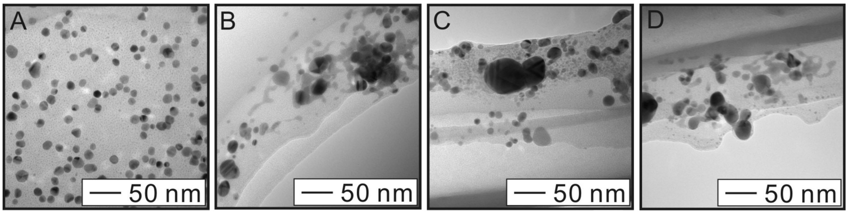

Figure 14. TEM images for Ag NPs (A) exposed to NaCl (B), $CaCl_2$ (C) and HCl (D) after 24 hours when the Cl^-/NP concentration ratio is 2.1×10^6. (Adapted with permission from reference (35). Copyright 2012 IOP Publishing.)

Stability of Ag and Ag@Au NPs Exposed to Chloride Electrolytes

One of the expectations for core@shell NPs is an enhanced chemical stability over pure Ag NPs. In demonstration of the severe susceptibility of Ag NPs to oxidation, the acrylate capped Ag NPs were exposed to three different types of chloride containing electrolytes. Figure 14 shows representative TEM images obtained after 24 hours for adding NaCl (Figure 14A), $CaCl_2$ (Figure 14B) and HCl (Figure 14C) to the acrylate capped Ag NPs. The Cl^-/NP concentration ratio is fixed at 2.1×10^6 for each sample to standardize the relative amount of Cl^- ions available to react with Ag in each system. Each sample experienced oxidation as evidenced by the appearance of large aggregates, larger particle sizes and overall a loss of particle dispersity. In these cases, the Ag has been completely oxidized and converted to AgCl through the oxidative etching process (*35*).

The oxidative etching process for Ag NPs consists of three steps. First, metallic Ag becomes oxidized in the presence of oxygen as illustrated in Equation 2 (*36*, *44–46*). Next, the Ag oxide reaches an equilibrium state with the surrounding aqueous medium creating Ag and hydroxide ions as shown in Equation 3 (*44–46*, *75*). Finally, the Cl^- ions in the system react with the Ag ions to form insoluble AgCl, shown in Equation 4 (*76*). In this way, as long as there is a sufficient supply of oxygen and Cl^- ions, a sample of Ag NPs can be completely oxidized, leading to AgCl.

$$2Ag^{\circ} + \tfrac{1}{2}O_2 \longrightarrow Ag_2O(s) \tag{2}$$

$$Ag_2O(s) + H_2O \longleftrightarrow 2Ag^+ + 2OH^- \tag{3}$$

$$Ag^+ + Cl^- \longrightarrow AgCl(s) \tag{4}$$

Even though the Ag@Au NPs display imperfections in the structure, after formation these NPs display features of the electron transfer phenomenon, providing some protection from oxidation of the remaining Ag component. Figure 15 shows TEM images of Ag@Au NPs taken before and 1 hour after adding NaCl. The Ag@Au NPs retain the original morphology and structure without severe aggregation or particle destruction (*33*). The Au@Ag NPs further display this feature as discussed in the following section.

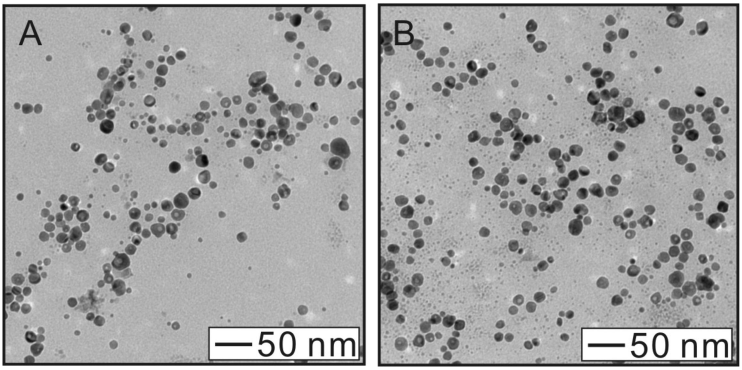

Figure 15. TEM images of Ag@Au NPs before (A) and 1 hour after (B) adding NaCl. (Adapted with permission from reference (33). Copyright 2011 American Institute of Physics.)

Stability of Au@Ag NPs Exposed to Chloride Electrolytes

The relative stability of the $Au@Ag_{3.1}$ NPs was more rigorously tested by exposing them to various chloride containing electrolytes, including NaCl, $CaCl_2$ and HCl. TEM images for the $Au@Ag_{3.1}$ NPs were taken for these three conditions as shown in Figure 16. In each case the Cl^-/NP concentration ratio is fixed at

2.1×10^6. For all samples the NPs maintained a spherical morphology. For NaCl the NPs remain well despersed while for $CaCl_2$ or HCl, the particles appear to be partly aggregated, oftentimes forming chainlike structures. While the particle morphology remained spherical, the mean particle size decreased for each sample. For NaCl, the NP size decreased to 18.8 ± 1.6 nm (remaining Ag shell thickness of 2.3 nm), $CaCl_2$ showed a size of 16.1 ± 1.2 nm (remaining Ag shell thickness of 1.0 nm) while for HCl the particle size is about 15.6 ± 0.6 nm (remaining Ag shell thickness of 0.7 nm). While a sufficient amount of chloride was used to completely convert all of the Ag in the samples to AgCl (an order of magnitude more Cl^- than Ag), the particles retain a size greater than that of the Au core. The fact that the NP size could not be reduced to approach that of the Au core suggests that oxidative etching is increasingly inhibited as the Ag layer becomes thinner. One question though is "what is the composition of the remaining surface layer of the Au@Ag NPs?". To address this, EDS elemental mapping is a useful tool, and was used to study the relationship between NP composition and structure after exposure to the electrolytes.

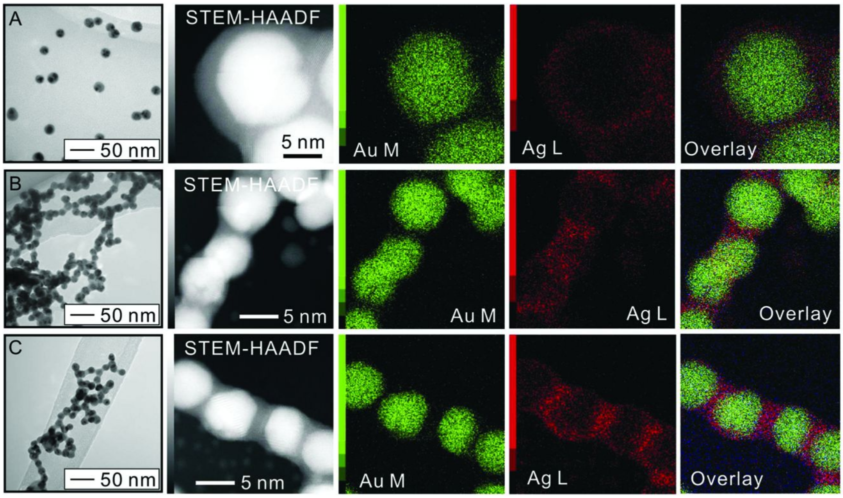

Figure 16. TEM images of Au@Ag NPs exposed to NaCl (A), $CaCl_2$ (B) and HCl (C) after 24 hours when the Cl^-/NP concentration ratio is 2.1×10^6. The TEM images are accompanied by STEM-HAADF images and EDS elemental maps for Au M area, Ag L area, and an overlay of the Au and Ag maps for each sample. (Adapted with permission from reference (35). Copyright 2012 IOP Publishing.) (see color insert)

For each condition of exposing the $Au@Ag_{3.1}$ NPs to the electrolytes (NaCl, $CaCl_2$ and HCl) STEM-HAADF and EDS elemental mapping were performed. The corresponding images in this study are shown alongside the TEM images in Figure 16. From left to right, the STEM-HAADF image, map of Au M area, Ag L area, and an overlay of the Au and Ag maps is shown. These images demonstrate that in all three cases, the core@shell structure is retained after treatment with the electrolyte as visualized by Au remaining at the NP center with a layer of Ag observed at the NP surface. The maps did not reveal any significant presence of chloride or oxygen at the NP surfaces (*35*). While each sample retains the Au@Ag structure, there are subtle differences in the action of the electrolyte on the NPs. In general, the Au@Ag NPs showed enhanced stability against oxidation, primarily because the first step in the oxidative etching process (Equation 2) is suppressed due to the electron transfer from the Au core to the Ag shell leading to a negative oxidation state for Ag. For the case of NaCl, the NPs resisted both aggregation and oxidative etching. For $CaCl_2$ and HCl cases, the particles displayed aggregation due to the de-protection of Au@Ag NP surfaces owing to the different effects of cations, but still resisted oxidative etching of the Ag shell (*35*). In all cases the Ag shell thickness was reduced after exposure to the different electrolytes, but a critical shell thickness exists where further etching appears to be suppressed, supporting the fact that the electron transfer effect is an interfacial phenomenon.

Stability of Au@$Ag_{3.6}$@$Au_{0.11}$ Double Shell NPs

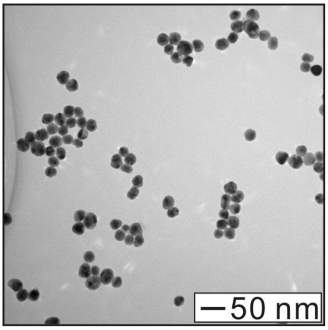

Figure 17. TEM image of Au@$Ag_{3.6}$@$Au_{0.11}$ NPs after exposure to NaCl. (Adapted with permission from reference (28). Copyright 2011 American Institute of Physics.)

The stability of Au@$Ag_{3.6}$@$Au_{0.11}$ double shell NPs was assessed in the presence of NaCl (0.5 M). In this case, the morphology was completely preserved (Figure 17) as a result of both the more negative Ag oxidation state and the fact that the Au second shell effectively protects the Ag first shell from contact with Cl^- ions. This suggests that the chemical stability of the Au@$Ag_{3.6}$@$Au_{0.11}$ NPs is extremely high even under severe conditions. The mean size of Au@$Ag_{3.6}$@$Au_{0.11}$ NPs before exposure to NaCl was 21.9 ± 1.2 nm as compared to 21.7 ± 1.6 nm 3 hours after exposure, indicating that the NPs are highly stable in the presence of even very high levels of salt.

Assessment of the Molecular Sensing Properties

In this section of the discussion, the basic sensing properties for the various core@shell NPs is studied. These sensing properties are probed primarily using the Raman analysis technique to identify well known reporter molecules, which allows an indirect assessment of the plasmonic properties for these NPs. While the NPs used in these studies have not been optimized in terms of particle size, shape or structure for the analysis, they nevertheless illustrate the ability to manipulate the particle parameters to achieve enhanced Raman activity (*33*).

The analysis relies on the assembly of the various NPs using two kinds of Raman active molecular linker systems with different chemical properties. For the first linker system, rhodamine 6G dye (R6G) is used, relying on electrostatic interactions in the adsorption of the molecule to the NP surface. The second linker system used is the thiol containing 3-amino-1,2,4-triazole-5-thiol (ATT), which adsorbs to the NP surface *via* the sulfur functionality. Figure 18 shows the structure of these two Raman active linker molecules. Both molecules lead to spontaneous assembly of the different NP systems, which can be manipulated by controlling the concentration of ionic electrolytes in the assembly solution. The resulting aggregates exhibit Raman activity which is used to assess the general sensing properties of the various NP probes.

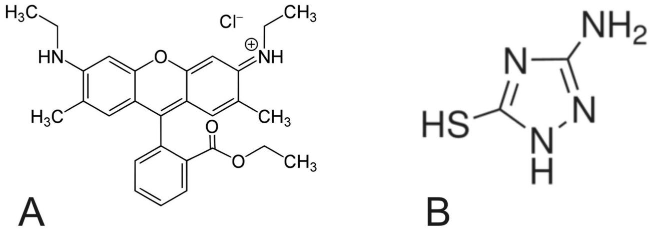

Figure 18. Chemical structures of (A) R6G and (B) ATT.

Molecular Sensing Properties of 43 nm Citrate-Capped Ag@Au NPs

The 43 nm citrate capped Ag@Au NPs were assembled using both R6G and ATT molecules. The processed samples were then analyzed using Raman spectroscopy (*33*). Figure 19A shows the spectra collected when R6G is used to assemble the NPs. Relatively strong peaks are observed at 1650 and 1357 cm^{-1} corresponding to the C-C stretching vibration of the benzene ring, along with several other weaker bands. In this case the pure Ag NPs show the highest SERS intensity by a large margin. However, when ATT is used to assemble the NPs, the relative activity of the probes is different. Figure 19B shows the Raman spectra collected when ATT is used to assemble the NPs. These SERS spectra show an intense band at 1340 cm^{-1} along with weak bands occurring at 1080, 1257 and 1417 cm^{-1}. In this case, the Ag and Ag@Au NPs show nearly identical Raman activity (*33*). A more quantitative assessment of the Raman activity is achieved by calculating the enhancement factors for the various samples. In the case of R6G, the enhancement factor for Ag NPs (4957) is almost 5 times higher than that of Ag@Au NPs (1157). In the case of ATT the calculated enhancement factors for Ag and Ag@Au NPs are 23.5 and 19.5, respectively. The results can be explained based on the nature of the ligand interaction with the NP surfaces. R6G interacts with the negatively charged NP surface primarily through electrostatic interaction while for ATT the thiol component interacts directly with the NP metal surface while simultaneously interacting with a neighboring NP electrostatically to achieve the aggregation of NPs. Because of the beneficial strong interaction of the thiol component in ATT with the Au surface, the Ag@Au NPs show a relatively higher Raman activity as compared to when an electrostatic based assembly molecule is used (*33*).

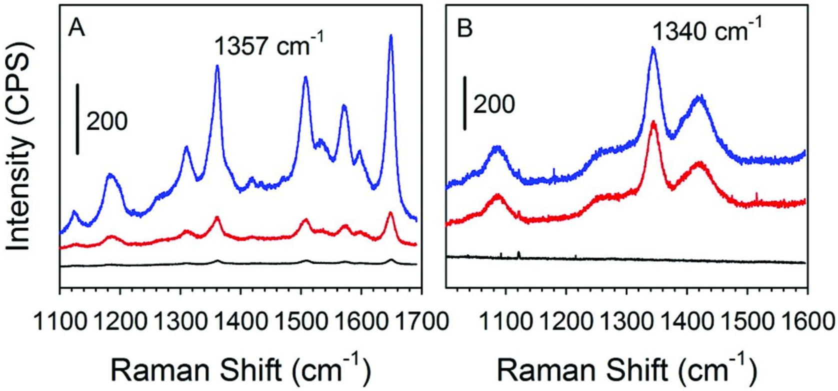

Figure 19. Raman spectra of NP assemblies created by using (A) R6G and (B) ATT Raman active molecules. Black, blue and red curves represent the spectra of Ag, Au and Ag@Au NP assemblies, respectively. (Adapted with permission from reference (33). Copyright 2011 American Institute of Physics.) (see color insert)

Molecular Sensing Properties of Ag, Au@Ag$_x$ and Au@Ag$_{3.6}$@Au$_{0.11}$ NPs

The enhanced electronic properties observed for the Au@Ag NP structure make them intriguing as plasmonic probes for biomolecular sensing applications. The sensing properties of these NP probes was tested in an experiment where Ag and Au@Ag$_{3.1}$ NPs are exposed to NaCl (a Cl$^-$/NP concentration ratio of 2.1×10^7) and ATT (0.005 mM total ATT concentration, a large excess) (*31*). After 24 hours of exposure the samples were analyzed using Raman spectroscopy (*31*). Five different sample areas were inspected for the various assemblies. Figure 20 shows the resulting Raman spectra collected for each sample. For the Ag NPs, a single broad peak with varying intensity is observed centered at 1345 cm^{-1} while for the Au@Ag$_{3.1}$ NPs three distinct peaks with relatively uniform intensity are observed at 1270, 1355 and 1420 cm^{-1}. The Raman spectra collected for the Au@Ag$_{3.1}$ NPs is characteristic for ATT laying flat on a metal surface through bidentate bonding arising from the triazole ring vibrations (*77*, *78*). Because of the tendency for Ag NPs to be oxidized towards AgCl, the band observed at about 1345 cm^{-1} for the Ag NP sample likely originates from ATT molecules weakly adsorbed onto AgCl surfaces. If it is assumed that the bands observed at 1345 and 1355 cm^{-1} for Ag and Au@Ag NPs respectively are characteristic for ATT, the standard deviation associated with the intensity at the maxima of the peaks in each sample can be assessed. For the Ag NP case the average intensity is 93 ± 38 counts/sec while for the Au@Ag NPs the intensity is 207 ± 20 counts/sec. The Ag NPs show an intensity deviation of about 41% while the Au@Ag NPs have a deviation of only 10%. These results demonstrate that the Au@Ag NPs possess a reliable and reproducible sensing capability in the presence of salt.

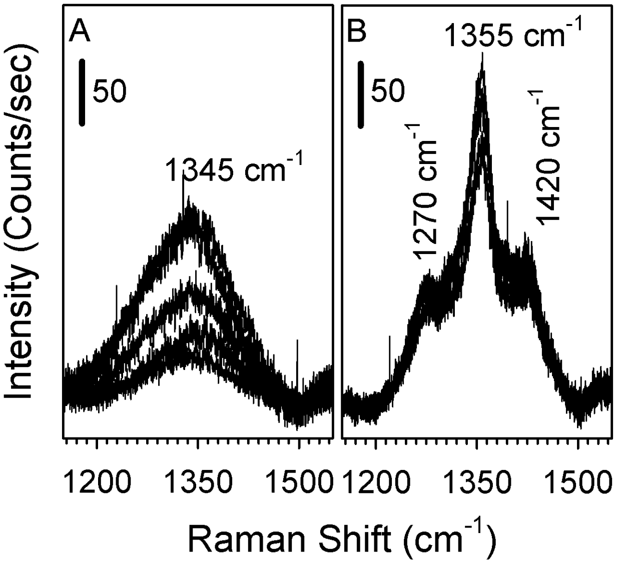

Figure 20. Raman spectra taken for Ag NPs (A) and Au@Ag NPs (B) exposed to ATT and NaCl with a Cl^-/NP concentration ratio of 2.1 × 10^7. (Reproduced with permission from reference (35). Copyright 2012 IOP Publishing.)

The Raman activity of the Au@Ag$_x$ and Au@Ag$_{3.6}$@Au$_{0.11}$ NPs was also investigated using ATT (*33*). It was found that the SERS activity dramatically increases with increasing *x* in the case of the Au@Ag$_x$ NPs. Figure 21 shows the increasing Raman activity of the Au@Ag$_x$ NPs as well as the comparatively high activity of the Au@Ag$_{3.6}$@Au$_{0.11}$ NPs. The results illustrate the effect of increasing the Ag content in the particles which possess a high extinction coefficient and extremely high field enhancement. Moreover, the Au@Ag$_{3.6}$@Au$_{0.11}$ NPs exhibited a SERS activity as high as that for Au@Ag$_{3.6}$ NPs, indicating that the Au shell is operable in creating a strong reaction with the reporter molecule through the thiol functionality.

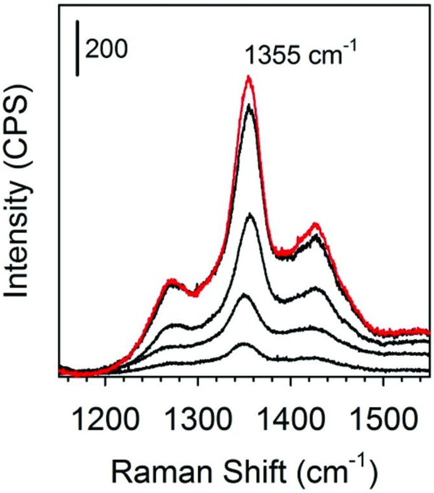

Figure 21. Raman spectra of Au@Ag$_x$ (from bottom to top, x = 0.4, 1, 2.2, and 3.6 nm) and Au@Ag$_{3.6}$@Au$_{0.11}$ (red curve) NP assemblies created by using ATT. (Adapted with permission from reference (28). Copyright 2011 American Institute of Physics.) (see color insert)

Conclusions

Manipulation of the electronic structure in the Au and Ag NP system has been revealed to offer an effective route to more precisely control the resulting plasmonic and stability properties for this class of NP. Specifically, the identification and utilization of the charge transfer phenomenon has allowed the ability to create structurally flawless Au@Ag@Au NPs, impart enhanced tolerance for oxidation and accentuate the Raman sensitivity in Au@Ag NPs, which is remarkable because of exposure of the Ag component to the outside reactive medium. These abilities are an essential step in more fully integrating plasmonic NPs to widespread practical use, for example to detect malady or disease, which will greatly benefit from the use of NP probes that are more sensitive and robust. The electronic transfer effect also has the potential to impact other NP systems. The observation of the electronic transfer phenomenon in Au and Ag core@shell NPs is an important step in enhancing our ability to manipulate the novel properties of NPs with a wide range of composition for a wealth of different applications. As our understanding of the electronic transfer nanoscale phenomena deepens, the ability to tailor or control individual and specific NP properties will emerge. The electronic transfer phenomenon will be one important tool for the future materials scientist in achieving that goal.

References

1. Mott, D.; Luo, J.; Smith, A.; Wang, L. Y.; Njoki, P. N.; Zhong, C. J. *Nanoscale Res. Lett.* **2007**, *2*, 12.
2. Mott, D.; Luo, J.; Njoki, P. N.; Lin, Y.; Wang, L. Y.; Zhong, C. J. *Catalysis Tod.* **2007**, *122*, 378.
3. Cortie, M. B.; McDonagh, A. M. *Chem. Rev.* **2011**, *111*, 3713.
4. Lauhon, L. J.; Gudiksen, M. S.; Wang, D.; Lieber, C. M. *Nature* **2002**, *420*, 57.
5. Mott, D.; Nguyen, T. B. T.; Aoki, Y.; Maenosono, S. *Philos. Trans. R. Soc. London, Ser. A* **2010**, *368*, 4275.
6. Sun, Y.; Xia, Y. *Anal. Chem.* **2002**, *74*, 5297.
7. Sun, Y.; Xia, Y. *J. Am. Chem. Soc.* **2004**, *126*, 3892.
8. Cao, Y. -W.; Jin, R.; Mirkin, C. A. *J. Am. Chem. Soc.* **2001**, *123*, 7961.
9. Rosi, N. L.; Mirkin, C. A. *Chem. Rev.* **2005**, *105*, 1547.
10. Mirkin, C. A.; Letsinger, R. L.; Mucic, R. C.; Storhoff, J. J. *Nature* **1996**, *382*, 607.
11. Taton, T. A.; Mirkin, C. A.; Letsinger, R. L. *Science* **2000**, *289*, 1757.
12. Cui, Y.; Ren, B.; Yao, J. -L.; Gu, R. -A.; Tian, Z. -Q. *J. Phys. Chem. B* **2006**, *110*, 4002.
13. Lee, K. J.; Nallathamby, P. D.; Browning, L. M.; Osgood, C. J.; Xu, X. H. N. *ACS Nano* **2007**, *1*, 133.
14. Skrabalak, S. E.; Chen, J.; Au, L.; Lu, X.; Li, X.; Xia, Y. *Adv. Mater.* **2007**, *19*, 3177.
15. Zhang, Z.; Jia, J.; Lai, Y.; Weng, J.; Sun, L. *Bioorg. Med. Chem.* **2010**, *18*, 5528.
16. Malinsky, M. D.; Kelly, K. L.; Schatz, G. C.; Van Duyne, R. P. *J. Am. Chem. Soc.* **2001**, *123*, 1471.
17. Haes, A. J.; Van Duyne, R. P. *J. Am. Chem. Soc.* **2002**, *124*, 10596.
18. Riboh, J. C.; Haes, A. J.; McFarland, A. D.; Yonzon, C. R.; Van Duyne, R. P. *J. Phys. Chem. B* **2003**, *107*, 1772.
19. McFarland, A. D.; Van Duyne, R. P. *Nano Lett.* **2003**, *3*, 1057.
20. Šloufová, I. S.; Vlčková, B.; Bastl, Z.; Hasslett, T. L. *Langmuir* **2004**, *20*, 3407.
21. Šloufová, I. S.; Lednicky, F.; Gemperle, A.; Gemperlova, J. *Langmuir* **2000**, *16*, 9928.
22. Yang, Y.; Shi, J.; Kawamura, G.; Nogami, M. *Scr. Mater.* **2008**, *58*, 862.
23. Lu, L.; Kobayashi, A.; Tawa, K.; Ozaki, Y. *Chem. Mater.* **2006**, *18*, 4894.
24. Pillai, Z. S.; Kamat, P. V. *J. Phys. Chem. B* **2004**, *108*, 945.
25. Sun, Y.; Mayers, B. T.; Xia, Y. *Nano Lett.* **2002**, *2*, 481.
26. Sun, Y.; Xia, Y. *Science* **2002**, *298*, 2176.
27. Mott, D.; Lee, J. D.; Thuy, N. T. B.; Aoki, Y.; Singh, P.; Maenosono, S. *Jpn. J. Appl. Phys.* **2011**, *50*, 065004–1.
28. Anh, D. T. N.; Singh, P.; Shankar, C.; Mott, D.; Maenosono, S. *Appl. Phys. Lett.* **2011**, *99*, 073107.
29. Wiley, B.; Sun, Y.; Xia, Y. *Acc. Chem. Res.* **2007**, *40*, 1067.
30. Bi, Y.; Hu, H.; Lu, G. *Chem. Commun.* **2010**, *46*, 598.

In Functional Nanoparticles for Bioanalysis, Nanomedicine, and Bioelectronic Devices Volume 1; Hepel, M., et al.;
ACS Symposium Series; American Chemical Society: Washington, DC, 2012.

31. Pearson, A.; O'Mullane, A. P.; Bansal, V.; Bhargava, S. K. *Chem. Commun.* **2010**, *46*, 731.
32. Gong, X.; Yang, Y.; Huang, S. *J. Phys. Chem. C* **2010**, *114*, 18073.
33. Singh, P.; Thuy, N. T. B.; Aoki, Y.; Mott, D.; Maenosono, S. *J. Appl. Phys.* **2011**, *109*, 094301.
34. Nishimura, S.; Anh, D. T. N.; Mott, D.; Ebitani, K.; Maenosono, S. *J. Phys. Chem. C* **2012**, *116* (7), 4511.
35. Shankar, C.; Anh, D. T. N.; Singh, P.; Higashimine, K.; Mott, D. M.; Maenosono, S. *Nanotechnology* **2012**, *23*, 245704.
36. González, B. R.; Burrows, A.; Watanabe, M.; Kiely, C. J.; Marzán, L. M. L. *J. Mater. Chem.* **2005**, *15*, 1755.
37. Yin, Y. D.; Li, Z. Y.; Zhong, Z. Y.; Gates, B.; Xia, Y. N.; Venkateswaran, S. *J. Mater. Chem.* **2002**, *12*, 522.
38. Chen, M.; Wang, L. Y.; Han, J. T.; Zhang, J. Y.; Li, Z. Y.; Qian, D. J. *J. Phys. Chem. B* **2006**, *110*, 11224.
39. Lim, I.-I. S.; Ip, W.; Crew, E.; Njoki, P. N.; Mott, D.; Zhong, C. J. *Langmuir* **2007**, *23*, 826.
40. Lim, I.-I. S.; Mott, D.; Ip, W.; Njoki, P. N.; Pan, Y.; Zhou, S.; Zhong, C. J. *Langmuir* **2008**, *24*, 8857.
41. Lim, I.-I. S.; Mott, D.; Engelhard, M. H.; Pan, Y.; Kamodia, S.; Luo, J.; Njoki, P. N.; Zhou, S.; Wang, L.; Zhong, C. J. *Anal. Chem.* **2009**, *81*, 689.
42. Lim, I-I. S.; Goroleski, F.; Mott, D.; Kariuki, N. N.; Ip, W.; Luo, J.; Zhong, C. J. *J. Phys. Chem. B* **2006**, *110*, 6673.
43. Grabar, K. C.; Freeman, R. G.; Hommer, M. B.; Natan, M. J. *Anal. Chem.* **1995**, *67*, 735.
44. Mulvaney, P.; Linnert, T.; Henglein, A. *J. Phys. Chem.* **1991**, *95*, 7843.
45. Henglein, A. *Chem. Mater.* **1998**, *10*, 444.
46. Henglein, A.; Linnert, T.; Mulvaney, P. *Ber. Bunsen-Ges. Phys. Chem.* **1990**, *94*, 1449.
47. Quian, L.; Yang, X. *Colloids Surf. A* **2005**, *260*, 79.
48. Skrabalak, S. E.; Chen, J.; Sun, Y.; Lu, X.; Au, L.; Cobley, C. M.; Xia, Y. *Acc. Chem. Res.* **2008**, *41*, 1587.
49. Wang, Z. L. *J. Phys. Chem. B* **2000**, *104*, 1153.
50. Tyson, C. C.; Bzowski, A.; Kristof, P.; Kuhn, M.; Sammynaiken, R.; Sham, T. K. *Phys. Rev. B* **1992**, *45*, 8924.
51. Roy, R. K.; Mandal, S. K.; Pal, A. K. *Eur. Phys. J. B* **2003**, *33*, 109.
52. Rodriguez, J. A.; Kuhn, M. *J. Phys. Chem.* **1994**, *98*, 11251.
53. Endo, T.; Yamamura, S.; Nagatani, N.; Morita, Y.; Takamura, Y.; Tamiya, E. *Sci. Technol. Adv. Mater.* **2005**, *6*, 491.
54. Mansour, A. N.; Cook, J. W.; Sayers, D. E. *J. Phys. Chem.* **1984**, *88*, 2330.
55. Mott, N. F. *Proc. Phys. Soc., London, Sect. A* **1949**, *62*, 416.
56. Sham, T. K. *Phys. Rev. B* **1985**, *31*, 1888.
57. Muller, J. E.; Jepsen, O.; Wilkins, J. W. *Solid State Commun.* **1982**, *42*, 365.
58. Mattheiss, L. F.; Dietz, R. E. *Phys. Rev. B* **1980**, *22*, 1663.
59. Nemoshkalenko, V. V.; Antonov, V. N.; John, W.; Wonn, H.; Ziesche, P. *Phys. Status Solidi B* **1982**, *111*, 11.
60. Horsley, J. A. *J. Chem. Phys.* **1982**, *76*, 1451.

61. Lytle, F. W. *J. Catal.* **1976**, *43*, 376.
62. Tsuji, A.; Rao, K. T. V.; Nishimura, S.; Takagaki, A.; Ebitani, K. *ChemSusChem* **2011**, *4*, 542.
63. Ebitani, K.; Tanaka, T.; Hattori, H. *Appl. Catal., A* **1993**, *102*, 79.
64. Yamamoto, T.; Suzuki, A.; Nagai, Y.; Tanabe, T.; Dong, F.; Inada, Y.; Nomura, M.; Tada, M.; Iwasawa, Y. *Angew. Chem., Int. Ed.* **2007**, *46*, 9253.
65. Nagai, Y.; Dohmae, K.; Teramura, K.; Tanaka, T.; Guilera, G.; Kato, K.; Nomura, M.; Shinjoh, H.; Matsumoto, S. *Catal. Today* **2009**, *145*, 279.
66. Shishido, T.; Asakura, H.; Amano, F.; Sone, T.; Yamazoe, S.; Kato, K.; Teramura, K.; Tanaka, T. *Catal. Lett.* **2009**, *131*, 413.
67. Polte, J.; Ahner, T. T.; Delissen, F.; Sokolov, S.; Emmerling, F.; Thunemann, A. F.; Kraehnert, R. *J. Am. Chem. Soc.* **2010**, *132*, 1296.
68. Abecassis, B.; Testard, F.; Kong, Q.; Francois, B.; Spalla, O. *Langmuir* **2010**, *26*, 13847.
69. Ohyama, J.; Teramura, K.; Higuchi, Y.; Shishido, T.; Hitomi, Y.; Kato, K.; Tanida, H.; Uruga, R.; Tanaka, T. *ChemPhysChem* **2011**, *12*, 127.
70. Qi, B.; Perez, I.; Ansari, P. H.; Lu, F.; Croft, M. *Phys. Rev. B* **1987**, *36*, 2972.
71. Haruta, M.; Kobayashi, T.; Sano, H.; Yamada, N. *Chem. Lett.* **1987**, 405.
72. Tsunoyama, H.; Sakurai, H.; Negishi, Y.; Tsukuda, T. *J. Am. Chem. Soc.* **2005**, *127*, 9374.
73. Comotti, M.; Pina, C. D.; Matarrese, R.; Rossi, M. *Angew. Chem,. Int. Ed.* **2004**, *43*, 5812.
74. Jin, R. C. *Nanoscale* **2010**, *2*, 343.
75. Kapoor, S. *Langmuir* **1998**, *14*, 1021.
76. Shon, Y. -S.; Cutler, E. *Langmuir* **2004**, *20*, 6626.
77. Wrzosek, B.; Bukowska, J. *J. Phys. Chem. C* **2007**, *111*, 17397.
78. Kudelski, A. *J. Phys. Chem. B* **2010**, *114*, 5180.

Chapter 14

Silver Nanostructures: Properties, Synthesis, and Biosensor Applications

Raghda El-Dessouky, Mariam Georges, and Hassan M. E. Azzazy*

Department of Chemistry and Yousef Jameel Science &
Technology Research Center, The American University in Cairo,
New Cairo, Egypt 11835
***E-mail: hazzazy@aucegypt.edu**

Biosensor technology has recently been witnessing momentous progress, thanks to the advent of nanoscience and especially with the realization of the great role that noble metal nanostructures can play as basic platforms. Nanosilver exhibits superior optical properties as compared to other noble metals and thus has attracted a great deal of interest in the sensors arena. Remarkable results were reported which correlate properties such as size, morphology, and composition of silver nanostructures and their biosensing performance. This chapter presents a comprehensive overview on silver nanostructures, their optical properties, synthesis and utilization in biosensor applications.

Introduction

Biosensor research aims at developing miniaturized, integrated systems that can rapidly and inexpensively detect trace amounts of analyte(s) in minute volumes with high sensitivity and specificity (*1*). Early detection of pathogens and disease markers is essential for improving treatment efficiency and the chances of full recovery, especially in cases of cancer or vicious infections such as viral hepatitis and HIV. Therefore, the need for highly sensitive, specific and efficient diagnostic systems is indispensable. The field of biosensors has been revolutionized by the use of nanomaterials, which were proved to offer unique properties and the potential of producing cheap and easy-to-handle biosensing platforms. Such platforms can be used for multiplexing and point-of-care

In Functional Nanoparticles for Bioanalysis, Nanomedicine, and Bioelectronic Devices Volume 1; Hepel, M., et al.;
ACS Symposium Series; American Chemical Society: Washington, DC, 2012.

testing with remarkable diagnostic performance and short turn-around times. Silver is a relatively inexpensive noble metal; on the nanoscale, it was found to exhibit superior properties (mainly of optical nature) over gold, which is the most widely used noble metal in nanobioapplications (*2*). The utilization of nanosliver-based platforms –either naked or conjugated with recognition probes- as signal transduction elements for analyte detection in biosensors was shown to improve the detection limits of existing biosensors and enhance their diagnostic performance. In this chapter, a theoretical background on the main optical properties of noble metal nanoparticles is presented, through which the superiority of silver nanoparticles (AgNPs) as optical signal transducers is justified, followed by an overview of their main synthetic methods and applications as remarkable biosensor platforms.

Optical Properties of Silver Nanostructures

Surface Plasmon Resonance

A metal can be viewed as a pool of electrons (plasma) surrounding a lattice of positive ions. The electrons of a metal occupy its valence band while the conduction band is rather empty. As the interface between a metal nanostructure and a dielectric (insulator) is irradiated with electromagnetic radiation, the electrical field component of the radiation causes the quantized coherent oscillation of the conduction band electrons (referred to as surface plasmons). The charge separation associated with the displacement of the electronic cloud from the heavier ionic core results in restoring forces that create an oscillating dipole; the electrons are polarized in such a way so as to exclude the electric field from the metal's interior. When the frequency of the oscillating dipole matches that of the incident radiation, 'resonance' occurs and the oscillating dipole absorbs maximum energy. For a metal nanoparticle (MNP) that is smaller than the wavelength of the incident radiation, this phenomenon is referred to as localized surface plasmon resonance (LSPR) (*3–8*). An illustration of LSPR is shown in Figure 1. The system of displaced electrons along with the restoring field of the MNP can be qualitatively viewed as a simple harmonic oscillator. Such representation means that the energy of the oscillating dipole is eventually 'damped' either by re-radiation (scattering) or by the formation of electron-hole pairs, therefore limiting the amplitude of the LSPR and defining its spectral bandwidth: the higher the damping, the broader the bandwidth (*9*).

LSPR is the cornerstone of the exquisite optical properties observed with metals at the nanoscale. LSPR is associated with a great enhancement in the metal's optical cross-section, which explains the superior extinction properties (absorption and scattering) of MNPs. Moreover, LSPR intensifies the local electric field creating 'hot spots' where spectroscopic signals such as Raman scattering and luminescence signals are amplified (*6*, *10*).

The LSPR spectral properties such as the main absorption peak (λ_{max}), number of peaks and bandwidth are functions of the nanoparticle's size, morphology, composition, the dielectric constant of its environment and interparticle separation (*3*, *4*, *10–12*).

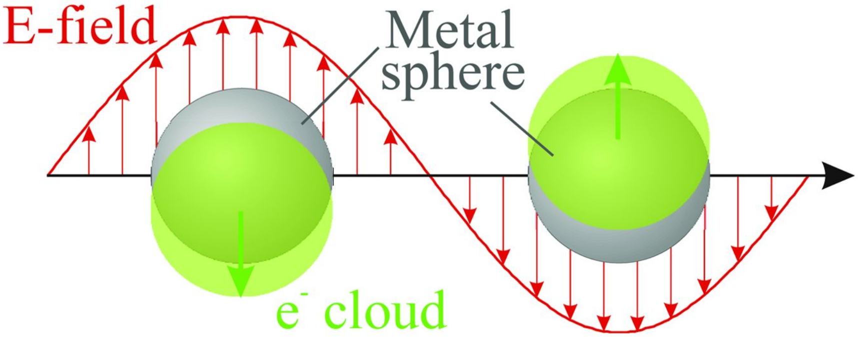

Figure 1. Schematic of the plasmon oscillation for a spherical nanoparticle, the electronic cloud is displaced away from the core nuclei at particular frequency. Reproduced from reference (10). Copyright 2003 American Chemical Society.

Size Effects

For spherical metallic nanoparticles of dimensions much smaller than the wavelength of the incident light (< 20 nm.), the electromagnetic field is capable of homogeneously polarizing the whole nanoparticle: all the surface electrons can 'sense' the same phase of the incident electromagnetic wave and are polarized simultaneously resulting in a pure dipole oscillator, which appears a single sharp peak in the extinction spectrum. For nanoparticles of this size nature, the extinction properties (the sum of absorption and scattering properties) can be described accurately by the Mie formula:

$$\sigma_{ext}(\omega) = 9\frac{\omega}{c}\varepsilon_m^{3/2}.V.N\frac{\varepsilon_2(\omega)}{[\varepsilon_1(\omega)+2\varepsilon_m]^2+\varepsilon_2(\omega)^2} \tag{1}$$

According to Mie, the extinction coefficient σ_{ext} is a function of the angular frequency of the incident radiation ω, the wavelength-independent dielectric constant of the surrounding medium ε_m, the speed of light c, the volume and the number density of the nanoparticles: V and N respectively; and finally the wavelength-dependent dielectric constant of the metal $\varepsilon(\omega)$ which reflects how its electrons interact with light and its ability to support strong surface plasmons. The metal dielectric constant $\varepsilon(\omega)$ is a complex function expressed in terms of $\varepsilon_1(\omega)$ and $\varepsilon_2(\omega)$, which represent the real and the imaginary components of the function respectively. It can be deduced from equation 1 that for the resonance condition to be fulfilled (maximal extinction coefficient at the given wavelength), the expression $[\varepsilon_1(\omega)+2\varepsilon_m]^2+\varepsilon_2(\omega)^2$ should approach zero; a condition that can be made possible if $\varepsilon_1(\omega) = -2\varepsilon_m$ and if $\varepsilon_2(\omega)$ has a value close to zero. Only few metals can achieve such criteria: mainly nanoparticles of gold and silver whose resonance conditions are fulfilled at the visible portion of the electromagnetic spectrum; gold nanoparticles of 20 nm in diameter appear red at a maximum extinction of ~530 nm while silver nanoparticles of the same size appear yellow at ~400 nm (*2–5*). It is worth mentioning here, that the superiority of the optical properties of silver over gold stems from the fact that its imaginary component of the dielectric constant $\varepsilon_2(\omega)$ is relatively small at the resonance wavelength as compared to gold, rendering its LSPR particularly strong. The LSPR damping can be described by a physical parameter called the quality factor (*Q*), which is expressed by the following equation:

$$Q = \frac{w\left({}^{d\varepsilon_1}\!\big/_{dw} \right)}{2(\varepsilon_2)^2} \qquad (2)$$

w represents the resonance frequency of the exciting radiation. *Q* defines the sharpness of the resonance peak and is directly related to the LSPR strength (high *Q* means strong LSPR). Silver has the highest *Q* value across the electromagnetic spectrum from 300-1200 nm, which explains why it exhibits the strongest and sharpest extinction bands (*2*).

For metallic nanoparticles of bigger sizes (d ≥/20) the dipole approximation becomes inapplicable, because the electromagnetic field cannot homogeneously polarize the surface electrons simultaneously and retardation effects arise culminating in higher-order oscillation modes (e.g. quadrupolar and octupolar modes). Large MNPs have absorption spectra with multiple peaks, the dipolar LSPR peak undergoes significant broadening due to radiation damping, and is red-shifted by the LSPR peaks of multipolar modes (*3*, *5*, *7*)

It must be noted that for nanoparticles of sizes less than 40 nm in diameter, the main contribution to the extinction coefficient is radiation absorption (radiative processes are negligible); however for larger particles of more than 100 nm in diameter, scattering becomes more significant and it dominates the optical response (*7*).

Morphology Effects

The LSPR spectral response is a matter of whether the exciting electromagnetic field induces a homogeneous polarization all over the MNP or not. The polarization homogeneity depends on geometrical aspects of the MNP such as symmetry, number and sharpness of vertices and number of facets; all these factors – and more- reflect in the spectral features observed such as number of LSPR peaks, their frequencies and widths. For a small spherical MNP, as mentioned above, the electromagnetic field polarizes the MNP homogeneously and the absorption spectrum comprises a single and sharp LSPR peak corresponding to a single homogenous dipolar oscillation mode. As the MNP deviates from symmetry, the number of peaks increases both of dipolar and multipolar oscillatory modes as shown in Figure 2. Multipolar modes do not only appear at higher frequencies than those of dipolar modes but they also generate an electric field, which shifts the dipolar mode to lower frequency values (*3*, *7*, *12*). It was observed that the truncation of the AgNPs edges causes a blue-shift in the main LSPR peak while the increase in the sharpness of vertices such as for cubic and star decahedral AgNPs is associated with an increase in the number of resonances, in addition to the broadening and red-shifting of the LSPR peak. This red-shift is significant and is attributable to the high degree of charge separation at the sharp corners of the nanostructure, which decreases the energy of the oscillation. As a consequence of the concentration of charges at the sharp tips, the dipolar electric fields are highly enhanced at these regions and asymmetric MNPs of sharp edges are associated with a more pronounced local enhancement of spectroscopic signals than symmetric MNPs, an effect called the ‘lightning rod’ effect. Such effect can be harnessed to create highly efficient ‘hot spot’ regions in sensing applications (*7*, *12*, *15*). The useful aspect of using anisotropic MNPs lies in the fact that LSPR can be fine-tuned by changing the geometry without sacrificing the bandwidth features by size changes. Anisotropic nanoparticles can have their LSPR tuned to the near infrared region (NIR) where biomolecules can be spectroscopically studied in their native environment with minimal background noise from the biological components of the sample (at this window of wavelengths, biological tissues have maximal transparency) (*3*, *16*).

Composition Effects

The fine-tuning of the LSPR is also made possible by the use of composite metallic nanostructures. Silver can be mixed with another metal during synthesis to produce either core/shell or alloy bimetallic nanostructures. Silver/gold (Ag/Au) composite nanostructures have been of particular interest because of their sharp and intense resonance peaks, and the compatibility of their lattice constants (*16*, *17*). Ag/Au alloy nanostructures are produced by the simultaneous reduction of Au and Ag ions in a refluxed aqueous solution. While the mixture of pure Au and Ag nanoparticles exhibits two separate LSPR peaks, alloy nanoparticles exhibit one LSPR peak that falls in between both λ_{max} values and shifted to longer wavelengths on increasing the mole fraction of Au in the reaction mixture. The LSPR position was shown to change linearly with the mole fraction of Au, and it is tunable between the absorption maxima of pure silver and gold (*4*, *17*). Core-shell nanostructures are associated with very high absorption and scattering coefficients; the contribution of each to the optical extinction in addition to the tuning of the LSPR peak can be modulated by changing the core diameter (D) and the thickness of the nanoshell (H). Theoretical studies show that composite nanostructures with Ag nanoshells exhibit superior optical properties as compared to ones with Au nanoshells and pure Au nanostructures in general; however the challenge is to synthesize high quality Ag nanoshells (*16*). Sometimes multiple metallic nanoshells are deposited upon the core metal by the successive reduction of Ag and Au salts, and such multi-shell nanoparticles were shown to exhibit very interesting and tunable optical properties (*18*).

Interparticle Separation Effects

At a low-concentration of MNPs, the nanoparticles do not interact and the LSPR-induced electric field of each nanoparticle is not 'sensed' by the surrounding ones. As the interparticle separation decreases to distances smaller than the excitation light's wavelength, the MNPs' transient dipoles couple to one another and their electromagnetic fields interfere coherently causing the LSPR absorption peak to red-shift and broaden. As MNPs aggregate, a second absorption band appears at lower energy; the optical properties of such aggregates are dependent on the number of MNPs involved, their shapes, interparticle distance within the aggregate and their orientation with respect to the polarized light (*1*, *4*, *12*).

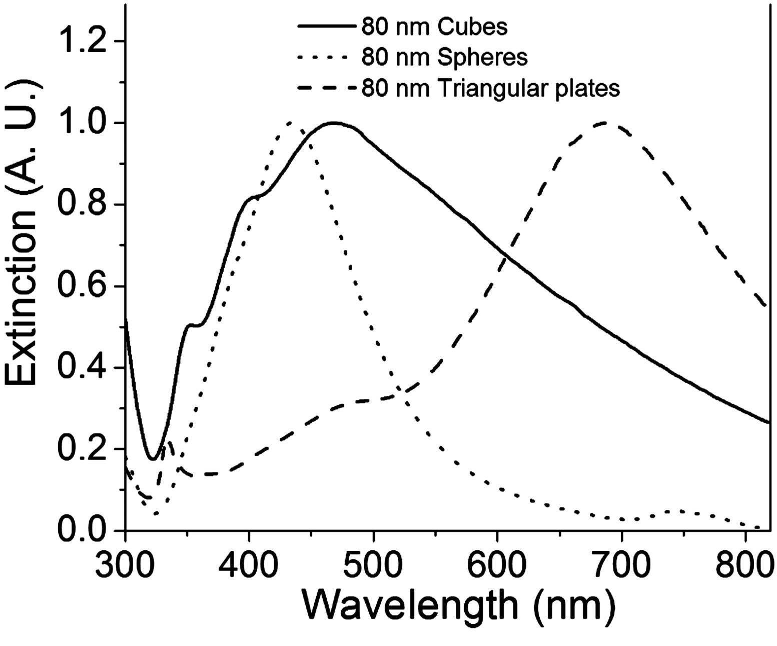

Figure 2. Schematic representations of the UV-Vis extinction spectra of an aqueous dispersion of AgNPs of approximately the same lateral dimensions (~ 80 nm). The symmetric spherical nanoparticles exhibit a strong LSPR band around 430 nm; the cubic nanoparticles exhibit three peaks (located at 350, 400, and 470 nm). The triangular nanoplates exhibit three peaks (at 335, 470, and 690 nm), which correspond to the out-of-plane quadrupole, in-plane quadrupole, and in- plane dipole plasmon resonance modes, respectively. Reproduced with permission from reference (14). Copyright 2007 Wiley & Sons.

Refractive Index-Sensitivity of LSPR

The LSPR of MNP is sensitive to changes in the refractive index (optical density) of its immediate environment. The refractive index changes and the corresponding LSPR spectral shift are related through the following formula:

$$\Delta\lambda \approx m(n_{adsorbate} - n_{medium})(1 - e^{-2d/l_d}) \qquad (3)$$

It shows from this relationship that the spectral shift (Δλ nm) is a function of the sensitivity factor *m* (Δλ nm per unit change in the refractive index in RIU), the refractive indices of both the medium and the adsorbed species (n_{medium} and $n_{adsorbate}$ respectively), the effective adsorbate layer thickness in nm (d) and the decay length of the electromagnetic field (l_d) in nm (l_d describes the dependence of the LSPR response on the separation distance between the nanoparticle's surface and the adsorbate, which defines the 'sensing volume' of the nanoparticles). Equation 3 shows that the LSPR sensitivity to the local refractive index is controlled through nanoparticle-related parameters such as *m* and l_d, which can be controlled by the nanoparticle's shape, size and composition; for example increasing the aspect ratio of the nanoparticles (width/height) results in larger *m* values and longer l_d (*8*, *11*, *12*). According to theoretical investigations for nanoparticles of equi-volume diameter (d_{eq}) in the range of 15-60 nm, it was demonstrated that maximum sensitivity factor values were associated with nanoparticles of silver; it was also shown that the sensitivity factor increases directly with equi-volume diameter. Zamkovets and coworkers studied refractive index-sensitivity in monolayers of silver nanoparticles and it was shown that increasing the AgNP concentration (close-packing) was associated with particle-particle electrodynamic interactions resulting in LSPR red-shift which substantially improved the nanostructure's sensitivity to the refractive index of its environment. It was proposed that the superiority of AgNPs' sensitivity factor to the other metals is due to the fact that its LSPR absorption band does not overlap with the edge of its interband absorption peak (*19*). The response of the AgNPs' LSPR to changes in the medium's refractive index was also investigated. As the refractive index of the medium increases (such as in presence of organic molecular adsorbates), the spectrum undergoes a red-shift and the LSPR band becomes wider; however the number of resonances is preserved (*7*).

Further theoretical and experimental investigations on the optical properties of both isolated and embedded silver nanoparticles and their relationship to size, morphology and environmental factors have been reported (*3*, *7*, *10*, *20*, *21*).

Local Field Enhancement of Spectroscopic Signals

Surface-Enhanced Raman Scattering (SERS)

On the incidence of electromagnetic radiation upon a molecular sample, its energy momentarily perturbs the electrical field of the sample molecules inducing their polarization; the molecules relax by releasing the energy of this polarization as scattered photons. The Raman effect refers to the inelastic scattering of incident photons; where they are detected at different wavelengths from that of the incident light. The incident photons exchange energy with the molecular sample corresponding to quantized transitions in the molecular vibrational modes; the scattered photons either lose energy and are detected at a longer wavelength (Stokes shift) or gain energy and are detected at a shorter wavelength (anti-Stokes shift). The Stokes shift signal is more intense than the anti-Stokes signal and it is more valuable in analytical applications (*22*, *23*). Probing the Raman effect yields specific information on the identity, molecular structure and interfacial properties of the investigated sample in the form of fine spectral features, which makes Raman spectroscopy a valuable spectroscopic tool in chemical and biological analyses. Raman spectroscopy is challenged, though, with the inefficiency of the Raman scattering process; molecular Raman scattering cross-sections are in the range of 10^{-30} – 10^{-25} cm^2/molecule, which are extremely small as compared to high quantum yield fluorophores of cross-sections of around 10^{-16} cm^2/molecule (*3*, *23*).

Raman scattering from molecules in the vicinity of plasmonic nanostructures (metallic nanoparticles or rough –nanotextured- metal surfaces) is greatly enhanced; the enhancement factor could reach up to 10^6 – 10^8 for an aggregate of molecules and 10^{14}-10^{15} for single molecules (*11*). Such phenomenon is called surface-enhanced Raman scattering (SERS). The enhancement of the Raman signal is attributed to two simultaneous enhancement effects: a long-range electromagnetic enhancement effect which is thought to contribute the most to the enhancement factor (~10^4 – 10^7) and a short-range chemical enhancement effect of less contribution to the enhancement factor (~10 – 10^2) (*24*).

The intensity of the Stokes Raman signal depends on a number of factors that are represented as follows:

$$I_{SERS}(\upsilon_s) = N.I(\upsilon_L).\,|\,f(\upsilon_L)\,|^2\,.\,|\,f(\upsilon_s)\,|^2\,.\sigma_{ads} \tag{4}$$

σ_{ads} is the enhanced Raman scattering cross section of the adsorbed molecule, $f(\upsilon_L)$ and $f(\upsilon_s)$ refer to the field enhancement factors at the excitation radiation (usually laser) frequency and the Stokes frequency respectively, I(υ_L) refers to the intensity of the excitation radiation, and finally N which represents the number of molecules involved (*3*, *25*).

The electromagnetic enhancement contribution to SERS results from the coupling of the nanoparticle's surface plasmons with both the Raman excitation and emission fields causing their amplification at resonance conditions; such effect is most pronounced when LSPR λ_{max} is located between the excitation and emission photons' wavelengths. When both the excitation laser frequency and the Stokes frequency are close in value to the LSPR frequency, the Raman signal is observed to be proportional to the fourth power of the local field enhancement factor, which means that the smallest structural variations that affect the local field enhancement factor have substantial influence on the SERS response (*3*, *11*, *12*). Even though both individual and aggregated nanoparticles contribute to SERS;

the scale of enhancement is dramatically higher for aggregated nanoparticles: around 3 to 6 orders of magnitude for individual nanoparticles versus 10 to 15 orders of magnitude for aggregates (*5*). This is explained by the fact that at sub-wavelength separation distances, the coupling of the nanoparticles' induced dipoles and the coherent interference of their electromagnetic fields culminate in regions –hot zones- where the signal enhancement is highly pronounced (*5*, *12*). Exploitation of such hot spots is made possible by fabrication of intricately designed nanoparticle arrays as SERS substrates for biosensing (*26*). It is worth mentioning that anisotropic MNPs were shown to exhibit superior local field enhancement effects when compared to spherical MNPs due to the fact that the enhanced field localizes at regions of high-curvature (tips or vertex-like regions) which is only possible with non-spherical MNPs (the 'lightening rod' effect). The chemical enhancement factor of SERS simply results from the electronic interactions between the analyte and the nanoparticle's surface; the effect is highly dependent on the analyte-nanoparticle separation distance: an effect called the 'first layer effect' where the analyte molecules in the first layer in vicinity to the plasmonic surface experience greater enhancement than the other layers. The adsorption of the analyte molecule to the nanoparticle's surface is associated with electronic resonance-charge transfer interactions, which ultimately perturb the electronic structure of the analyte molecule with subsequent induction of polarizability. The increase of the molecular polarizability effectively increases the Raman scattering cross section and thus the SERS signal (*12*, *13*, *27*). The chemical enhancement is mainly a function of the analyte properties and its adsorption settings such as the adsorption site, bonding geometry and molecular energy levels (*23*).

Both the electromagnetic and chemical enhancement effects can be controlled by changes in the nanoparticle's morphology, size, surface properties, assembly configuration and the analyte-nanoparticle bonding characteristics (*3*); studies on such relationships have been recently reported and discussed in the context of fabricating nanostructures for the tuning and optimization of the required SERS response (*27–31*).

Metal-Enhanced Fluorescence (MEF) and Fluorescence Quenching

Fluorescence serves as an important signal transduction tool in analytical applications like detection of trace amounts of analytes, cellular imaging and genetic studies, just to name a few (*3*). The excitation of the molecular species is a result of the absorption of photons corresponding to transitions in electronic energy levels. Depending on the molecular structure and chemical surroundings, relaxation of an electron in an excited state to the ground state results from the combined effect of the emission of radiation and through radiationless processes. The dominance of either deactivation route is a matter of which route minimizes the lifetime of the excited state at the given conditions more quickly. A fluorophore is characterized by its quantum yield (Q), which describes the ratio of the emitted photons to the absorbed ones, and its fluorescence lifetime (τ). The depopulation of the excited state is a function of both the radiative decay rate of the fluorophore species (Γ) and the rate of non-radiative decay to the ground state (k_{nr}). Such parameters relate to *Q* through the following relationship:

$$Q = \frac{\Gamma}{\Gamma + k_{nr}} \tag{5}$$

and to the fluorescence lifetime through the following relationship:

$$\tau = \frac{1}{\Gamma + k_{nr}} \tag{6}$$

High intensity fluorescence is observed with fluorophores of high quantum yield and short lifetime (such fluorophores, when in their excited state, have less time to interact with their surroundings and are thus more photostable) (*22*, *32*). The excited molecular species may have its fluorescence quenched due to collisions with molecules in solution, forming non-fluorescent complexes (self-quenching), attenuation of the exciting field by a nearby absorbing species, or by resonance energy transfer (RET), also commonly called Förster resonance energy transfer (FRET). RET occurs when the emission spectrum of the fluorophore (donor) overlaps with the absorption spectrum of the quencher (acceptor), and the excitation energy of the donor fluorophore is transferred in a non-radiative manner to the acceptor via dipole-dipole interactions (*3*, *32*). How efficient the energy transfer process is depends on the extent to which both spectra overlap, which is reflected in the Förster radius (R_0): the distance at which there is a 50% energy transfer efficiency, in addition to the donor-acceptor separation distance r as shown in equation 7 (*32*, *33*).

$$E = \frac{R_0^6}{R_0^6 + r^6} \tag{7}$$

Conventional fluorophores are challenged by a number of limitations that compromise their efficiency as transduction tools, such as the prolonged lifetime of the molecular excited states leading to their poor photostability, photoblinking (fluorescence interrupted by non-fluorescent states), and low signal-to-noise (S/N) ratios (*13*, *34*). The presence of plasmonic nanoparticles in the vicinity of a fluorescent species was found to either dramatically enhance the fluorescence intensity or quench it depending on the separation distance between them. From equations 5 and 6, it is shown that the fluorescence intensity is a direct function of both the radiative and non-radiative decay rates; and it is upon these that the plasmonic nanostructure has its influence.

The enhancement of a fluorophore's emission due to proximity to a metallic nanostructure as compared to a fluorophore in 'free space' (the apparent quantum yield, Y) can be described by the following relationship:

$$Y = |L(\omega_{exc})|^2 \, Z(\omega_{em}) \tag{8}$$

$L(\omega_{exc})$ is the intensity of the exciting radiation, and $Z(\omega_{em})$ is the relative radiation yield: the ratio of the quantum yield of the fluorophore in the presence of the metal Φ^M to its intrinsic quantum yield Φ^0 unperturbed (in free space) (*35*). The increase in the quantum yield of a metal-enhanced fluorophore is directly dependent on the excitation field intensity and radiative processes. The local field enhancement around metallic nanostructures due to the coupling of LSPR with the excitation field concentrates the field near the fluorophore and increases its rate of excitation (*3*, *36*). Due to the fact that the apparent quantum yield is proportional to the square of the excitation field intensity (equation 8), the effect of LSPR can result in 10^4-fold increase or more in the excitation intensity. The maximum enhancement of quantum yield by a metal due to increasing radiative rates is $1/\Phi^0$ which means that only fluorophores of poor intrinsic quantum yield values experience pronounced metal-enhanced-fluorescence effects (*35*, *37*). To increase the relative radiation rate $Z(\omega_{em})$, Φ^M must increase. As shown from equation 5, the quantum yield can be increased by increasing the radiative decay rate (Γ); this the metal nanoparticle makes possible by amplifying the photonic mode density around the fluorophore (*12*) by adding new radiative decay paths to the fluorophore; these are represented by adding Γ_m to equations 5 and 6:

$$Q_m = \frac{\Gamma + \Gamma_m}{\Gamma + \Gamma_m + k_{nr}} \quad (9)$$

$$\tau_m = \frac{1}{\Gamma + \Gamma_m + k_{nr}} \quad (10)$$

Increasing Γ_m culminates in increasing the quantum yield and reducing the fluorescence lifetime (*3*, *35*, *38*). Such increase is attributed to the fact that now more fluorophores can decay radiatively before non-radiative processes are initiated. Metal-enhanced fluorescence is observed at metal-fluorophore distances of around 100 Å (*39*).

At fluorophore-metal separations of less than λ/4, distance-dependent fluorescence quenching is observed (*40*). The metal nanoparticles, being too close to the fluorophore, contribute non-radiative decay channels; and RET comes into play where the excited state fluorophore interacts with surface plasmons of the metal and the excitation energy is transferred to the metal. The donor-acceptor Förster distances observed between a fluorophore and MNPs reached up to almost 10 times bigger than typical Förster distances (*3*, *12*, *34*, *36*). Whether fluorescence enhancement or quenching takes place is a matter of how the metal influences the radiative and non-radiative decay rates of the fluorophore. Factors to be considered encompass the spatial location of the fluorophore with respect to the metal, the distance between them, anisotropy of the metallic nanostructure, orientation of the fluorophore's transition dipole moment with respect to the metal and the illumination geometry (*3*, *12*, *34*, *36*, *38*, *41*).

In Functional Nanoparticles for Bioanalysis, Nanomedicine, and Bioelectronic Devices Volume 1; Hepel, M., et al.;
ACS Symposium Series; American Chemical Society: Washington, DC, 2012.

In developing biosensors, the aim is to employ the useful effects of metal enhanced fluorescence such as increased photostability, high quantum yields and increased resonance energy transfer distances for highly sensitive detection and enhanced S/N ratios. The critical issue here is the ability to 'engineer' substrates that can efficiently harness the fluorescence enhancement/quenching effect of MNPs in favor of the detection process. It was reported that superior fluorescence enhancement was observed with MNPs of higher scattering cross-sections, which amplifies the fluorophore emission intensity; this justifies the superiority of AgNPs relative to AuNPs of the same size in fluorescence enhancement and thus their common use in MEF-based sensing. Anisotropic silver nanoparticles were shown to exhibit higher fluorescence enhancement factors than isotropic ones: the presence of multiple LSPR modes increases the probability of their coupling to the excited fluorophore (*12*). Silver has a characteristic plasmon absorption peak in the range of 300-450 nm, which makes it the metal of choice to be used with fluorophore dyes that emit in the Vis-NIR region (*39*).

Synthesis, Characterization, and Functionalization of Silver Nanostructures

The photophysical properties of silver nanostructures can be tailored and fine-tuned by the careful selection of the synthetic method and the optimization of its parameters; the aim is to efficiently and reproducibly control the size, shape, crystallinity, structure and composition of the resultant nanoparticles so as to serve the sensing application desired (*14*). AgNPs utilized in most biosensing applications are either in the form of colloidal dispersions or immobilized upon solid substrates. Several methods have been investigated and established for the fabrication of such nanostructures (*2*, *16*). This section presents a brief overview on the main synthetic methods employed in the synthesis of silver nanostructures (with emphasis on the chemical approaches), the techniques used for their characterization and their functionalization for biosensor applications.

Synthesis of Colloidal Dispersions of Silver Nanoparticles

The general approach to the synthesis of AgNPs is based on the controlled reduction of Ag^+ ions from a silver precursor species into elemental Ag; clusters of Ag atoms serve as nuclei, which support subsequent growth into nanoparticles. Generally speaking, nanoparticles are thermodynamically unstable due to their high surface energy, and thus have a tendency to grow in size or agglomerate which poses a challenge during their synthesis. To overcome such a challenge, in addition to the precursor species and the reducing agent, a stabilizing (capping) agent is employed during synthesis; these stabilizers are divided based on their stabilizing mechanism into: electrostatic and steric stabilizers. Electrostatic stabilization relies on the mutual repulsion of like charges associated with the formed nanoparticles to prevent their agglomeration. On the other hand, steric stabilization is based on limiting the diffusion of the growth species to the nanoparticle's surface through the use of an adsorbed polymeric layer that acts

In Functional Nanoparticles for Bioanalysis, Nanomedicine, and Bioelectronic Devices Volume 1; Hepel, M., et al.;
ACS Symposium Series; American Chemical Society: Washington, DC, 2012.

as a physical barrier to further growth. Diffusion-limited growth allows for the synthesis of highly monodisperse nanoparticles, and in case of their coalescence, the particles are always re-dispersible, which is in contrast to electrostatically stabilized dispersions (*43*, *44*).

The final nanoparticles' size, morphology and monodispersity are controlled by manipulating the reduction conditions, the rates of the initial nucleation and the subsequent growth; these factors were shown to be influenced by various synthetic parameters such as the strength of the reducing agent, the concentration of the reactants, pH, reaction temperature and the choice of the capping agent (*44*). The strength of the reducing agent was shown to affect the size of the nanoparticles by affecting the rate of reduction; strong reducing agents enhance the rate of reduction and consequently produce smaller AgNPs than with weak reducing agents (*43*, *44*). The concentration of reactants and the reaction pH were also found to affect the nanoparticle's size through affecting the rate of reduction (*44–46*). The choice of the capping agent is critical not only for stabilizing the colloid against aggregation, but also because it plays an important role in determining the size, shape (as will be discussed later in this section) and other properties of the nanoparticles such as their solubility, reactivity and biocompatibility. In particular cases, the capping agent acts as a reducing agent itself enabling one-pot synthesis of AgNPs. Examples of capping agents include thiol derivatives, aniline, surfactants, polymers such as polyvinylpyrrolidone (PVP), polyacrylate, polyacrylonitrile and polyacrylamide (PAM) (*47*).

The methods for producing colloidal dispersions of AgNPs can be grouped according to the type of reductant into wet chemical, physical, and biological methods.

Wet Chemistry

Wet chemistry is the most popular and investigated route for the synthesis of silver nanostructures. Reduction of the silver precursor species is done chemically either using strong reducing agents such as sodium borohydride and hydrazine, or weak ones such as glucose, sodium citrate, dimethylformamide, ascorbic acid, alcohols and polyols (*47*).

The citrate reduction method is a simple and a rapid approach to the synthesis of Ag colloids with minimal laboratory skills. In addition to its role as a reducing agent, citrate acts as a capping agent as well. AgNPs can be produced by the addition of a certain amount of sodium citrate to a boiling aqueous solution of $AgNO_3$. Such a simple method, however, produces AgNPs of a broad distribution in their sizes (20 – 600 nm) and shapes (polyhedrons and nanoplates) (*2*). Citrate has a pH-dependent reduction activity, and thus changes in the reaction pH allow for shape- and size-controlled synthesis of AgNPs. The effect of pH changes in the range of 5.7-11.1 on the shape of the produced nanoparticles was investigated; it was shown that at high pH spherical and rod-like AgNPs dominated the reaction product, whereas at low pH triangular and polygonal AgNPs were produced. Purely spherical AgNPs were produced by the step-wise citrate reduction of $AgNO_3$ where the nucleation and growth processes were carried out at high and low pH respectively (*48*). The addition of NaOH was shown to direct the synthesis of Ag nanowires, and the concentration of hydroxide ions was found to be the key to the control over the nanowires yield (*49*). Even though the citrate reduction method eliminates the need for capping agents, sometimes certain capping agents are added to the reaction so as to direct the nanoparticles' growth into certain shapes. Zhou et al. reported a surfactant-assisted approach to the synthesis of Ag nanorods and nanowires in aqueous solution; $AgNO_3$ was reduced by tri-sodium citrate in the presence of the anionic surfactant dodecyl benzene sulfonic acid sodium (DBS) as a capping agent. The concentrations of tri-sodium citrate and DBS in particular were shown to play a crucial role in determining the final size and morphology of the nanoparticles formed. A tri-sodium citrate concentration of 2.4 mM and DBS concentration of 1 mM produced nanowires and nanorods of lengths in the range of 2-8 μm and 150 nm-2.5 μm respectively. Deviations from these optimum concentrations resulted in the absence of nanorod and nanowire morphologies, heterogeneity in size and morphology distribution and/or the appearance of other nanostructures at the expense of nanorods and nanowires (*50*). The effect of citrate concentration as a capping agent was investigated by Henglein et al.; an optimum concentration in the range of 1×10^{-4} - 5×10^{-4} M. was found to generate rather spherical AgNPs of narrow size distribution and minimal imperfections (*51*). Ascorbic acid reduction of Ag^+ ions was also established for the synthesis of silver nanostructures of various sizes and shapes; examples include quasi-spheres, nanoplates and complex branched structures in presence of stabilizing agents such as PVP and sodium citrate (*52–55*).

One of the most versatile and robust approaches to the synthesis of a diversity of silver nanostructures is the polyol chemical process. Polyols, such as ethylene glycol, act as both reducing agents and as solvents in the chemical reaction; their reducing power is temperature-dependent which means that the tuning of the reaction temperature enables precise control over the nucleation and growth processes and thus the final morphological properties of the nanostructures (*14*). A typical reaction comprises a polyol, which is heated with a silver precursor along with a polymeric capping agent. At the initial phase of the reaction, Ag atomic clusters form on the reduction of Ag^+ ions; these clusters assemble into crystal nuclei (also called "seeds"), which fluctuate in structure and eventually acquire a certain morphology depending on the balance between the available thermal energy and the energetic cost of the structural change. The nuclei emerge into a Boltzmann-like distribution of multiply twinned, singly twinned, and single-crystalline structures. The most abundant morphology is the five-fold twinned decahedron since it possesses the least free energy (*2*, *56*, *57*). Cubic, right bipyramidal and pentagonal wire silver nanostructures are the most commonly observed morphologies associated with polyol syntheses; further manipulation of the reaction conditions, though, can force the seeds to grow into other morphologies (*2*, *57–60*). The final size and shape are determined by how the reaction conditions selectively direct the addition of the silver atoms to particular faces of the nuclei as they grow, which can be influenced by the choice of the capping agent, the ratio of the reagents, the rate of their addition, the reaction's temperature and the presence of certain ions/impurities in the reaction solution (*16*). PVP was demonstrated to allow for the production of silver nanostructures with excellent stability, quality and size/shape monodispersity, it preferentially adsorbs to certain crystallographic facets and thus enables anisotropic growth of the silver nanostructure (*2*, *14*). Chemical etchants were also found to play an important role in shape-controlled synthesis; they can selectively activate growth at certain crystallographic facets, truncate sharp edges or vertices and generate hollow structures. High-quality, size-controllable and monodisperse Ag nanospheres were prepared by the wet etching of uniform Ag nanocubes; rapid mixing and the selection of a strong chemical etchant, in addition to the uniformity of the precursor Ag nanocubes were the main determinants of the final quality of the nanospheres (*61*). In another study, the synthesis of Ag nanowires using HNO_3 as a chemical etchant was investigated and it was found that adjusting the HNO_3 concentration allows for the transformation of the morphology from nanowires to triangular nanoplates (*62*). A novel polyol reaction for the synthesis of high-quality silver nanocubes was reported by Zhang et al. The reaction comprised a new silver precursor, CF_3COOAg, which was shown to be more advantageous than $AgNO_3$, along with trace amounts of NaSH and HCl; such protocol generated Ag nanocubes of edge length in the range of 30-70 nm with high quality and on a relatively large scale (*63*).

Shape-controlled synthesis has also been possible by using seed-mediated growth, where the separation of nucleation and growth steps is what exerts control over the final nanoparticle's morphology; in addition to soft-templating where amphiphilic surfactant molecules are used to form micelles and reverse-micelles that serve as 'nanoreactors' in solution. These nanoreactors incorporate the nanostructure being formed and confine its growth into controllable sizes and morphologies, which depend on the template structure and the various synthetic conditions such as the type and concentration of the precursor, the reducing agent used, reduction time and temperature. Various shapes were produced via soft template-directed growth such as nanoplates, dendrites, hollow spheres, nanowires and nanorods (*2*). Examples of soft templates include CTAB (cetyl trimethylammonium bromide), the reverse micellar system AOT (di(2-ethyl-hexyl)sulfosuccinate)/isooctane/water system and the octylamine/water bilayer system, which were reported to produce silver nanorods, nanodisks and nanoplatelets respectively (*64–66*).

An interesting approach to shape-modulation of chemically produced nanostructures relies on the unique interaction of silver with light allowing for different silver nanostructures to be synthesized photo-chemically. Subjecting a silver colloid to certain types of radiation was found to induce the reshaping of the existent morphologies into new ones (*2*, *17*, *44*).

A number of 'green' approaches utilizing environment-friendly reagents such as β-D-glucose, starch, Tollen's reagent and others were used for synthesis of AgNPs to minimize the use of environmentally toxic chemicals (*67*, *68*). Eid and Azzazy reported a novel fast, inexpensive and safe method for the synthesis of anisotropic silver nanostructures. Three-dimensional hollow flower-like silver nanostructures with sizes in the range of 0.2 - 5.0 µm and surface area between 25–240 m^2/g were prepared by the use of $AgNO_3$ as a precursor, dextrose as a reducing agent, tri-sodium acetate as a capping agent and NaOH. Optimizing the concentrations of the reactants enabled shape and size tunability (*69*).

Physical Methods

The reduction of the silver precursor species can be done by the physical irradiation of the reaction solution by γ-rays, UV, visible light, microwave or ultrasound irradiation (*47*). The use of radiation-induced reduction is quite useful as it allows precise control over the driving forces of Ag^+ ions reduction, nucleation and subsequent growth away from thermodynamic considerations; in addition to the production of nanostructures of higher purity than with chemical methods (*42*). Yoksan and Chirachanchai reported the synthesis of chitosan-stabilized Ag nanospheres with an average diameter of 7-30 nm by γ -radiolytic reduction; the final size was found to be dependent on the dose of γ-radiation, the starting $AgNO_3$ content and chitosan concentration (*70*). Jurasekova et al. performed another high-energy-radiation-based synthesis, where electron beam irradiation (EBI) was used for the reduction of Ag^+ ions in solution; nanoparticles of long-term stability and different sizes and shapes (nanospheres, nanocubes and nanostars) were produced (*71*). Silver nanoclusters (discussed later in the chapter) have been proved to possess excellent optophysical properties and have recently gained great interest as fluorescent labels. Being even smaller than AgNPs (~100 atoms), the solution-phase synthesis of such ultra-small clusters is extremely challenging, as they tend to grow in size and aggregate to minimize their surface energy. Xu et al. reported the preparation of highly fluorescent water-soluble silver nanoclusters of high stability via a sonochemical approach. The reduction of Ag^+ ions was promoted by the ultrasonic irradiation of an aqueous solution of $AgNO_3$ in presence of polymethylacrylic acid (PMAA) as a capping agent. Controlling reaction conditions such as the sonication time, carboxylate-to-silver ion stoichiometry and the polymer molecular weight were found to tune the optical response and the strength of fluorescence (*72*).

Biological Methods

Living organisms and/or their extracts were found to offer the appropriate conditions for the synthesis of metallic nanostructures of well-defined sizes and morphologies. A number of microorganisms were reported to allow for the production of AgNPs; the microorganisms-induced reduction of silver ions into silver nanostructures can take place both extracellularly and intracellularly. The photoautotrophic cyanobacterium *Plectonema boryanum* was used for the synthesis of AgNPs in presence of aqueous $AgNO_3$ at temperatures between 25-100 °C. Spherical, octahedral and platelet-shaped AgNPs were produced both intracellularly (<10 nm) and extracellularly (~1−200 nm) (*73*). The use of eukaryotic organisms, such as fungi, in AgNPs' biosynthesis was also investigated. Mukherjee et al. reported the intracellular production of AgNPs in the *Verticillium* fungus on exposure to aqueous silver ions; nanoparticles of 25 ± 12 nm in diameter were formed below the cell wall surface; this observation lead to the proposal that the reduction of silver ions was done by enzymes in the cell wall (*74*). Extracellular biosynthesis on the other hand was performed with fungal cells of *Fusarium oxysporum* in a study by Ahamed et al., where AgNPs of 5-15 nm in diameter were synthesized extracellularly through an enzymatic process and stabilized by proteins secreted by the fungus (*75*). Biological extracts from microorganisms and plants contain biomolecules such as proteins, enzymes, polysaccharides, vitamins and others; these were found to serve as reducing and capping agents and thus also used for the synthesis of AgNPs. Such biosynthetic methods offer more economic and environment-friendly alternatives to chemical and physical methods (*67*).

Synthesis of Substrate-Immobilized Silver Nanostructures

Unlike solution-phase syntheses, fabrication of nanostructures on solid substrates using techniques such as lithography allow for more precise control over the structural aspects, such as the nanoparticle's size, shape and interparticle spacing. Electron beam lithography (EBL) is considered the most versatile and well-established fabrication technique used for the synthesis of substrate-immobilized nanostructures. A focused electron beam scans across a polymeric resist (most commonly polymethyl methacrylate, PMMA) according to a pre-programmed pattern; regions subjected to the electron beam become labile to being etched away on solvent treatment. As these regions dissolve away, they leave behind a solid mask, which serves as a substrate upon which silver is deposited by physical vapor deposition. After removing the PMMA mask, a high-resolution ordered array of Ag nanoparticles is produced. A variety of morphologies have been fabricated with EBL such as cylinders, ellipsoids, rectangles and triangles. Another commonly used lithographic technique is focused ion beam lithography (FIB), which is similar to EBL except for the use of an ionic beam of Gallium ions (Ga^+) instead of electrons. FIB can also be used for direct patterning (without the need for a mask) through chemical vapor deposition (FIB-CVD). EBL and FIB are limited by their complexity, high-cost, high time-consumption and their need of highly specialized facilities (*2*, *76*, *77*). A range of unconventional lithographic techniques have been developed to overcome such limitations; one of the most popular and inexpensive techniques is nanosphere lithography (NSL). In NSL, a colloidal suspension of monodisperse nanospheres (usually made of polystyrene) self-assembles upon a solid substrate in a close-packed arrangement of hexagonal symmetry. This self-assembled monolayer serves as a physical mask upon which silver is vapor-deposited; it fills the voids in between the nanospheres in the monolayer lattice forming a regularly arrayed thin film of pyramidal AgNPs, which shows upon the mask removal. The lateral dimensions of the AgNPs and their interparticle spacing is dictated by the size of the nanospheres, whereas the vertical dimensions depend on the deposition time and rate. If the mask comprises a double-layer of nanospheres, hexagonal dots emerge instead of the pyramidal morphology. Further modulation of size and shape is also possible by varying the deposition angle, thermal annealing of the AgNPs array or ion etching of the nanospheres. NSL was demonstrated to produce size tunable MNPs in the range of 20-1000 nm (*11*, *76*, *78*, *79*).

Characterization of Silver Nanostructures

Structural aspects of silver nanostructures such as size, shape and composition can be investigated and characterized by various techniques (*2*); these include atomic force microscopy (AFM), scanning tunneling microscopy (STM), transmission electron microscopy (TEM), high resolution TEM (HRTEM), UV/Visible spectroscopy, energy dispersive spectroscopy (EDS/EDX), selected area electron diffraction (SAED), fast Fourier transform (FFT), X-ray diffraction (XRD) and X-ray photoelectron spectroscopy (XPS), in addition to many other techniques which are employed where appropriate (*42*, *80*).

Functionalization of Silver Nanostructures

MNPs used in biosensors need to be associated with recognition molecules that can selectively detect and capture the analyte of interest; such functionalities include oligonucleotides (DNA or RNA), antibodies, carbohydrates and many others. The functionalization of MNPs can be achieved either during synthesis, where the functional groups are the stabilizing agents themselves (direct functionalization) or the MNPs are first stabilized by labile capping agents and functionalization takes place post-synthesis by replacing the capping agents (*81*). The functionalization of AgNPs is a challenging process. They are less stable in aqueous dispersions than AuNPs as they are susceptible to oxidation and etching by chloride ions; the efficiency of their thiol-conjugation is low and all thiol-functionalized AgNPs exhibit poor stability in saline buffer and do not show cooperative binding properties (as is the case with thiol-functionalized AuNPs). Producing thiol-functionalized AgNPs is a lengthy process, which could last for over 2 days; it requires delicate balancing of the levels of the added NaCl and the thiolated functional groups (*82–85*). To overcome such challenges a number of approaches have been used to ease the functionalization of AgNPs; one way is to coat the AgNPs with stabilizing self-assembled monolayer (SAM) of alkanethiols such as mercaptoundecanoic acid, which is functionalized in a subsequent step with the required recognition molecules. Another approach is to coat the AgNPs with a layer of another material such as gold or silica; these support the AgNPs stability while allowing for easy functionalization (*12*, *13*, *83*). Amendola et al. reported a synthetic method, which produces stable chemical-free AgNPs in organic solvents; these AgNPs are surrounded by carbon shells/matrices, which allow for their direct functionalization during synthesis (*86*). Lee et al. recently reported the functionalization of AgNPs by oligonucleotides terminated by a triple cyclic disulfide moiety as the anchoring group; which was found to increase the binding affinity of the oligonucleotides to the AgNP's surface and enhance their stability. This functionalization strategy produces DNA-AgNP conjugates in less than 30 min, the conjugates show high-salt stability and exhibit high cooperativity of binding, which is demonstrated by their sharp melting profiles, as shown in Figure 3 (*83*).

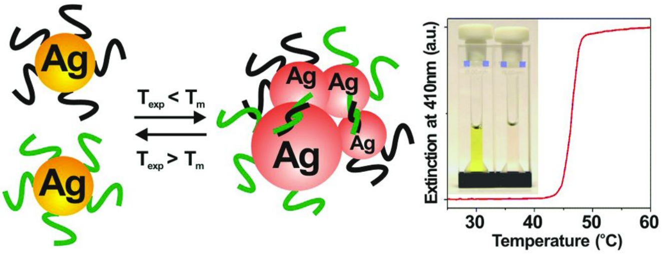

Figure 3. An illustration of the cooperative binding properties of AgNP−oligonucleotide conjugates based on DNA terminated with triple cyclic disulfide moieties in hybridization assays. Two sets of AgNPs are functionalized with complementary DNA sequences, on hybridization-based aggregation of AgNPs the solution color changes from yellow to pale red; the color change is reversible on heating the solution above the melting point (T_m) which shows the sharp melting temperature transition. Reproduced from reference (83). Copyright 2007 American Chemical Society.

Silver Nanostructures-Based Biosensors

The sensitivity of LSPR to changes in the MNPs’ environment means that such structures can be used as effective signal transducers in sensing applications. The dependence of LSPR on the geometrical aspects of the MNPs and their interparticle distances means that the synthetic protocols and fabrication strategies employed to produce MNP-based sensing platforms can be optimized to tune such spectral properties so as to serve the purpose of the sensing application and yield the most efficient settings for maximum sensor performance. Silver nanostructures were demonstrated to exhibit superior optical properties as compared with other noble metal nanostructures. AgNPs have a resonance absorption cross-section that is four times bigger than that of AuNPs (*16*). It was shown that a spherical AgNP of ~80 nm in diameter can scatter blue light (λ=445 nm) with a scattering cross section of $3x10^{-2}$ μm^2 which is a million fold greater than the scattering cross-section of a fluorescein molecule. Unlike fluorophores, they do not blink or bleach and thus provide unlimited photon budget for long-interval investigations (*11*, *12*). The optical profile of nanosilver exhibits the sharpest and most intense bands amongst all metals (*12*). Moreover, AgNPs are associated with exceptionally enhanced local electromagnetic fields and thus can amplify local spectroscopic signals remarkably: an effect that can be usefully harnessed for signal transduction in biosensing applications (*13*).

Optical detection methods in AgNPs-based biosensors can be broadly divided into two main types: detection methods based on analyte-induced LSPR spectral shifts and those based on enhanced spectroscopic signals; of most applications are surface enhanced Raman scattering (SERS) and fluorescence-based spectroscopies.

LSPR Shift-Based Biosensors

Colorimetric Detection

Colorimetric assays are highly popular because of their simplicity, low cost and convenience. The LSPR shift-induced colorimetric signal depends on the presence/absence of the target biomolecule, which affects the separation distance between the nanoparticles and thus their plasmonic coupling by changing the MNPs' aggregation/dispersion status. Such colorimetric strategies were reported to achieve femto-molar detection concentrations of oligonucleotides by Mirkin and coworkers (*1*, *87–89*).

There are two main approaches to the utilization of AgNPs in colorimetric detection assays: a cross-linking approach and a non-cross-linking approach. In the cross-linking method the aggregation is induced by the use of functionalized AgNPs, which cross-link on target binding to form a network of closely-spaced plasmonic centers. On the other hand, in the non-cross-linking method the aggregation status is dependent on the ionic strength of the AgNPs' medium (*82*).

Oligonucleotide-functionalized AgNP probes have been used in a number of colorimetric biosensors for detecting hybridization events, detecting single-nucleotide polymorphisms (SNPs), and detection of nucleic-acid binders (small molecules, metal ions or drugs for example). Thompson et al. reported a cross-linking approach where two sets of AgNPs were used; each functionalized with complementary probes to one half of the target DNA. In the presence of the target DNA, the AgNPs cross-link in a sandwich format on hybridization to the target accompanied by a visual color change of the solution. Conjugating oligonucleotides with MNPs is associated with highly sharp melting profiles which are much more sensitive to the transition from dsDNA to ssDNA than with unmodified nucleic acids. Since the melting profile of DNA duplexes depends on the efficiency of hybridization (the degree of base-complementarity between the two strands), such sharp melting transitions can be used to identify single-base mismatches. Due to the superior extinction coefficient of AgNPs, the minimum detectable target oligonucleotide concentration was demonstrated to be 50 times lower than that of AuNPs (*90*). An interesting colorimetric sequence-specific DNA-protein binding assay was reported by Tan et al. using AgNP-dsDNA conjugates. This assay is a 'light off' colorimetric assay i.e. the presence of the target analyte stabilizes the nanoparticles against aggregation. Two sets of AgNPs were used; each set was functionalized with a dsDNA segment corresponding to half of the protein-binding sequence, both terminated with complementary sticky-ends. The complementarity of the dsDNA overhangs along with optimum salt concentration drives the aggregation of a mixture of both sets of AgNPs through the formation of a transient DNA duplex and the solution color changes from yellow to pale brown. In the presence of the target protein, it binds to this transient duplex introducing steric hindrance and stabilizing the AgNPs against aggregation. This sensing platform was used to detect estrogen receptor α and its response elements; the sensitivity of the assay was demonstrated to be more superior to that using AuNPs, with a detection limit of 25 nM and assay time of 1 minute. The fact that the analyte detection is based on stabilizing the nanoparticles against aggregation avoids the risks of false positive results. This sensing platform was proven to be a valuable and a convenient tool that can be extended to other transcription factors (*91*).

Cao et al. reported the use of Au/Ag composite nanoparticles in a dual-color detection strategy for SNP discrimination. AuNPs and Ag/Au core-shell NPs of the same size and melting profiles were synthesized and functionalized with two sets of probes. AuNPs were functionalized with oligonucleotide probes of perfect complementarity to the wild-type sequence of the beta-globin gene; while the Ag/Au core-shell NPs were functionalized with ones complementary to the mutant beta-globin gene sequence (which contains a SNP) that is responsible for sickle-cell anemia. The wild type and the mutant targets were added to both types of nanoparticles, each on its own. Both AuNPs and Ag/Au nanoparticles aggregate in the presence of either of the two targets; however, on heating the aggregates, probe-target binding of perfect complementarity has the higher melting profile as compared to the one with mismatched hybridization. The results can be easily distinguished using a TLC spot test, as shown in Figure 4. This strategy was shown to be highly accurate in SNP discrimination (*92*).

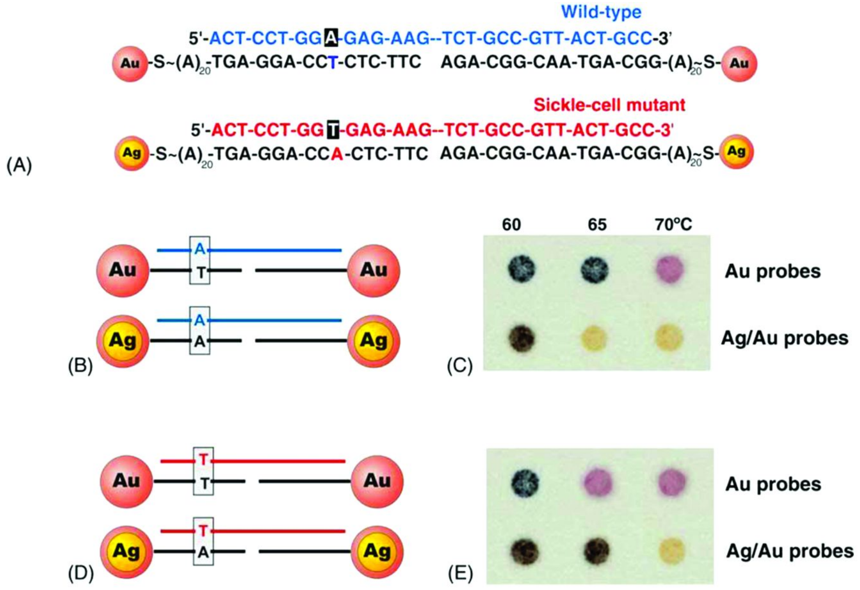
Wild-type
5'-ACT-CCT-GGA-GAG-AAG--TCT-GCC-GTT-ACT-GCC-3'
Au -S~(A)20-TGA-GGA-CCT-CTC-TTC AGA-CGG-CAA-TGA-CGG-(A)20-S- Au
Sickle-cell mutant
5'-ACT-CCT-GGT-GAG-AAG--TCT-GCC-GTT-ACT-GCC-3'
Ag -S~(A)20-TGA-GGA-CCA-CTC-TTC AGA-CGG-CAA-TGA-CGG-(A)20-S- Ag
(A)
Au
A
T
Au
Ag
A
A
Ag
(B)
60
65
70°C
Au probes
Ag/Au probes
(C)
Au
T
T
Au
Ag
T
A
Ag
(D)
Au probes
Ag/Au probes
(E)

Figure 4. (A) Oligonucleotide-functionalized Ag/Au core-shell and pure Au nanoprobes and their complementary targets. (B) Addition of the wild-type targets to both nanoprobes. (C) Spot-test result showing the higher melting temperature for the Au nanoprobes. (D) Addition of the mutant targets to both nanoprobes. (E) Spot-test result showing the higher melting temperature for the Ag/Au core-shell nanoprobes. Reproduced with permission from reference (92). Copyright 2005 Elsevier.

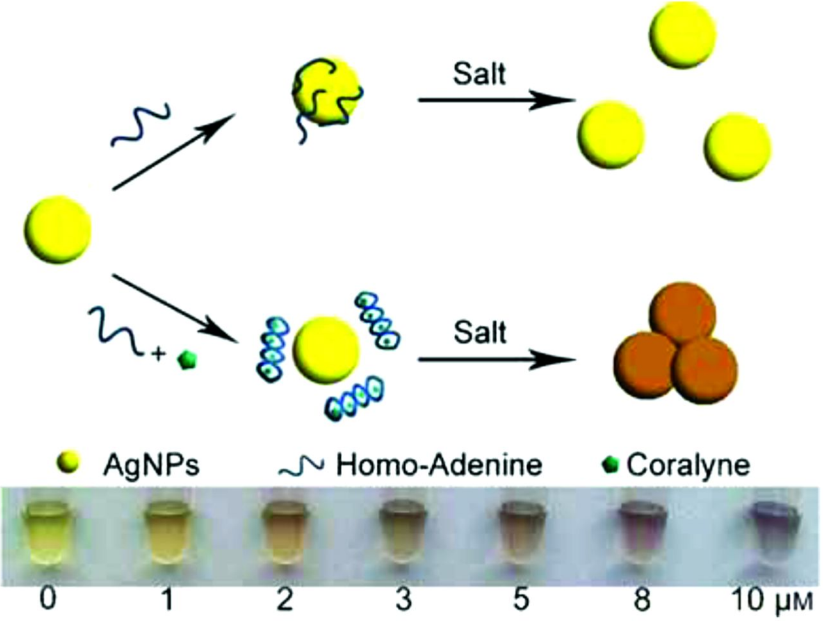

Figure 5. An illustration of the non-cross-linking colorimetric detection of coralyne using non-functionalized AgNPs. Reproduced with permission from reference (93). Copyright 2009 John Wiley & Sons.

A number of colorimetric assays utilizing non-functionalized AgNPs have been also reported in attempt to avoid the challenges associated with functionalizing AgNPs. The stability of unmodified AgNPs against aggregation depends on the ionic strength of their medium. Electrostatic repulsion between the negatively charged capping agents (such as citrate) on the AgNPs' surface stabilizes them against aggregation; on increasing the ionic strength of the colloidal solution, the repulsive charges are screened from one another and aggregation takes place (*13*, *82*, *93*). The use of unmodified MNPs for colorimetric detection acknowledges the difference in electrostatic properties of ssDNA from dsDNA. dsDNA has a highly stable geometry, which displays the negative charge of its phosphate backbone and thus would not adsorb onto the negatively charged surfaces of MNPs. On the other hand, ssDNA has sufficient flexibility to uncoil and expose its bases to the MNPs maintaining distance from the negatively charged backbone and allowing for van der Waals attraction forces to dominate. These attractive forces promote the adsorption of ssDNA upon the MNPs surface, which increases the charge density and stabilizes them against salt-induced aggregation (*94*). Xu et al. reported a non-cross-linking colorimetric assay based on unmodified AgNPs to detect homoadenine sequences-binding small molecules. The assay exploited the high affinity of adenine deoxynucleosides to adsorb onto AgNPs and stabilize them against aggregation to detect the poly (A)-binding ligand coralyne. In the presence of coralyne, the poly (A) sequence desorbs from the AgNPs and binds to coralyne forming a homoadenine duplex;

the AgNPs are destabilized and they aggregate on salt addition, changing the color of the solution from yellow to pale brown (Figure 5). Concentrations as low as 1 μM were shown to cause a visual color change; the assay was selective to coralyne and had higher sensitivity than when using AuNPs; the assay had a limit of detection (LOD) of 0.3 μM (*93*). Table I lists a few more examples of AgNP-based colorimetric biosensors.

Table I. Summarizes a few more examples on AgNP-based colorimetric biosensors

Method	*Platform/Target*	*Performance*	*Reference*
Cross-linking method	Mannose protected AgNPs. Detection of concanavalin A (Con A) lectin protein	LOD: 0.1 μM	(*95*)
	Unmodified AgNPs. Detection of Homocysteine in human plasma samples.	LOD: 0.5 μM. Good linear detection was established in the range of 2–12 μM.	(*96*)
Non-cross-linking method	Unmodified AgNPs and cationic peptide probe (p1). Detection of cyclin A_2 (cancer marker protein).	LOD: 30 nM.	(*97*)
	Unmodified AgNPs and charge neutral peptide nucleic acids (PNA) as coagulants and hybridization probes. DNA detection.	A specific DNA can be detected in an environment of at least 10 times of interference DNA. LOD: at a DNA/PNA ratio of 0.05. SNP discrimination.	(*98*)
	Antibody-functionalized AgNPs (negatively charged). Detection of the specific peptide fragment of Neurogenin 1 (ngn1)	LOD: 30 ng/mL	(*99*)

LSPR Sensors

LSPR sensors – also referred to as refractive index sensors- are based on the sensitivity of the MNP's LSPR and corresponding spectral shift ($\Delta\lambda_{max}$) to local refractive index changes induced by the adsorption of analyte molecules to the MNP's surface; such sensing strategy has been used for detecting molecular recognition events and measuring conformational changes and binding processes' kinetics in real time. LSPR sensors are label-free, accurate and exhibit high sensitivity and selectivity (*8*, *13*, *100*, *101*). AgNPs have been utilized as LSPR sensing platforms either in the form of nanoparticle arrays or as single-nanoparticle sensors. In the array format, AgNPs (mostly of anisotropic morphologies which have superior refractive-index sensitivity) of tailored size, shape and interparticle separation are adhered to optically transparent solid substrates. Shifts in λ_{max} are probed by UV/Vis extinction spectroscopy; the dependence of the spectral shifts upon surface concentration of adsorbed species provides for the possibility of quantitative measurements. The solid substrate platform is easily fabricated and its chip-based design allows for multiplex analyses. Another format for LSPR sensing is to probe the $\Delta\lambda_{max}$ for single nanoparticles. Single-nanoparticle sensors are highly advantageous because of their improved LOD values (which could reach single-molecule detection limit), high spatial resolution in multiplex analyses and their applicability for measurements in solution and within cells and tissues unlike nanoparticle arrays. Monitoring single-nanoparticle LSPR is done by resonant Rayleigh scattering spectroscopy rather than UV/Vis absorption spectroscopy, which is impractical for this purpose; the technique involves the evanescent illumination of the nanoparticles, scattered light is collected with a high-magnification microscope objective and analyzed by a spectrometer. Using the microscope, the AgNP of sharpest spectral features can be selected from the field of view to guarantee a high S/N ratio (*11*, *13*, *101*, *102*). The selectivity of both types of LSPR sensors is conferred by the surface functionalization of AgNPs with the required recognition probes. The LSPR is measured before and after analyte binding, a spectral red-shift is usually observed due to the increase in the medium's refractive index, and the magnitude of the shift is correlated with the analyte concentration (*24*).

A number of LSPR sensors based on NSL-fabricated arrays of triangular AgNPs were investigated. These platforms were demonstrated to have great selectivity and sensitivity, with detection limits in the low picomolar to high femtomolar range (*103*). Haes et al. developed – for the first time- an ultrasensitive LSPR sensor-based sandwich immunoassay for the diagnosis of Alzheimer's disease. The assay is based on the detection of amyloid β derived diffusible ligands (ADDLs), which were recently proposed as sensitive biomarkers for Alzheimer's disease. The LSPR sensor comprises triangular AgNPs (width = 90 nm and height = 25 nm, with an effective sensing distance of ~35 nm) upon which a mixed SAM of 1-octanethiol and 11-mercaptoundecanoic acid molecules are immobilized activating the AgNPs surface for further functionalization by the anti-ADDL antibodies. Incubation of the sensing platform with ADDL is associated with a $\Delta\lambda_{max}$ value which is further amplified by exposure of the sample to secondary anti-ADDL antibodies that form the sandwich immunoglobulin-antigen complex. The assay was shown to be specific to ADDL, allowing for analyte quantitation (concentrations down to 100 fM were detected) and was applicable to clinical samples from brain extracts and cerebrospinal fluid to differentiate Alzheimer's patients from controls (*104*, *105*). Yonzon et al. developed an LSPR sensor for investigating protein-carbohydrate interactions. Mannose-functionalized AgNPs arrays were used to detect the lectin Concanavalin A (Con A) in solution; the real-time binding kinetics and the selectivity of this biosensor were established. The group also fabricated a multiplex LSPR carbohydrate-sensing chip where the simultaneous binding of Con A to mannose and galactose functionalized SAMs were probed (*106*). An interesting approach for enzyme-based glucose detection using an LSPR biosensor was reported by Endo and co-workers where the sensing platform comprised a stimuli-responsive hydrogel–AgNPs composite immobilized upon a glass substrate. Hydrogels undergo reversible changes in their volume in response to certain stimuli. The glucose oxidase enzyme (GOx) molecules were incorporated into the composite hydrogel; in presence of glucose, GOx catalyzes glucose turnover forming reduced flavin adenine dinucleotide (FAD) and gluconic acid, such recognition event increases the osmotic pressure within the hydrogel and it swells increasing the mean interparticle separation. The LSPR spectral shifts are probed by UV/Vis spectroscopy; the limit of detection associated with this biosensor is 10 pM (*107*).

LSPR shifts can be maximized via a number of strategies that affect the m, l_d and Δn parameters of equation 2. Examples of such strategies include the use of rhombic AgNPs arrays sensing platforms which were demonstrated to offer superior refractive index sensitivity than triangular AgNPs (*108*, *109*) and using AuNP-labeled antibodies for detecting AgNP surface-bound analytes which was shown to provide for a 400% amplification in LSPR shift (*110*). A few more examples on AgNP-based LSPR biosensors are listed in table II.

Surface-Enhanced Raman Scattering-Based Biosensors

A number of approaches for utilizing SERS in biosensing have been established. These approaches can be classified into label-free approaches, and approaches that employ Raman labels (*12*). Label-free approaches involve the direct interaction of the Raman-active analyte with the MNP surface; specificity can be conferred by conjugating the MNP with target-specific functionalities. The target analyte is detected via analyzing the Raman spectrum before and after its capture (*12*, *24*).

SERS label-based approaches on the other hand detect the analyte with the aid of Raman labels – mostly aromatic nitrogen or sulfur-containing compounds with strong Raman scattering properties. These molecular labels are coated onto the nanoparticle's surface via the affinity of their N and S containing moieties to the metal element. The coating strategy enables the control over the number and density of Raman labels and thus the enhancement factor and sensitivity of detection. The Raman labels are enclosed by a shell of a dielectric material like silica, titania or a polymeric material which stabilizes the core/shell structure, retains the Raman labels preventing their desorption and increases analyte specificity (*12*, *24*).

Silver nanostructures were demonstrated to exhibit superior enhancement of SERS signals as compared to gold, copper and other plasmonic materials (up to 10^{14} -10^{15} enhancement factors) thus silver nanostructures have been thoroughly studied as substrates in SERS experiments for ultrasensitive biosensor applications (*23*, *115–119*).

Table II. Summarizes a few more examples of AgNP-based LSPR biosensors

Sensor configuration	*Platform/Target*	*Performance*	*References*
AgNPs arrays on solid substrates	Triangular AgNPs array, functionalized with monoclonal mouse anti-p53 antibodies. Detection of serum p53 protein which is involved in head and neck squamous cell carcinoma (HNSCC).	Significant diagnostic value in differentiating HNSCC patients from healthy volunteers	(*111*)
	NSL-fabricated AgNPs array functionalized with anti-human albumin antibody. Used for the detection of microalbuminuria	LOD: 1 ng/ml, The biosensor can detect albumin concentrations in a wide dynamic range from 1 ng/ml up to 1 μg/ml.	(*112*)
	Triangular Au/Ag hybrid nanoparticles array; functionalized with monoclonal mouse anti-SEB (*Staphylococcus aureus* enterotoxin B) IgG antibodies. Used for the detection of SEB.	SEB detection at a concentration of 1 ng/ml in 1 minute was achieved. The detection system costs 1/30th of the commercialized SPR instruments.	(*113*)
Single-nanoparticle sensors	Ag nanodots of ~2.6 nm in diameter conjugated to monoclonal antibodies (MABs) Used for sensing and imaging of tumor necrosis factor (TNFα); and probing its binding kinetics to the MABs in real time.	Single TNFα molecules were detected with an unprecedentedly high sensitivity and selectivity, with a wide dynamic range (0-200 ng/mL). The Ag nanodot sensors resist photodecomposition and blinking with remarkable photostability for hours.	(*114*)

Label-Free SERS Biosensors

Metal film-over-nanospheres (MFON) substrates constitute remarkably robust and stable SERS-based detection platforms. These substrates are fabricated by nanosphere lithography (NSL) and optimized for maximizing their SERS response by controlling the nanospheres core diameter, the metal film thickness and the interparticle separations, which collectively reflect on the distribution of the roughness features and consequently the emergence of 'hot spot' regions (*120*). The development and optimization of silver film over nanospheres (AgFON) SERS substrates were reported and demonstrated to be used in two applications: the detection of the anthrax (*Bacillus anthracis*) biomarker calcium dipicolinate (CaDPA) (*121*) and glucose (*122*) in bovine plasma. In an attempt to maximize the SERS signal enhancement, for both experiments the AgFON was optimized so as the LSPR extinction maximum falls in between the excitation and Stokes wavelengths. Near Infrared (NIR) laser excitation radiation was used in both experiments to reduce noise from the biological background. The adjustment of LSPR in accordance with the excitation laser wavelength was done by changing the diameter of the nanospheres; and the LSPR of nearest wavelength to the NIR excitation wavelength dictated the choice of the optimum nanospheres diameter. The detection dielectric media must be considered in this optimization procedure because the LSPR depends on it. CaDPA detection is conducted in air while glucose detection is conducted in an aqueous medium. The AgFON substrate in CaDPA sensor comprises nanospheres of diameter of 600 nm and Ag thickness of 200 nm, while the glucose sensor comprises nanospheres that are 390 nm in diameter. The SERS-based detection is dependent on the affinity of the analyte in either case to the AgFON substrate. CaDPA of the anthrax spores exhibits such affinity, however, glucose does not. In the glucose sensor, the AgFON is surface-modified with a mixed self-assembled monolayer (SAM) of decanethiol (DT) and mercaptohexanol (MH). This mixed SAM exhibits both hydrophilic and hydrophobic properties allowing the glucose to partition within it and reach the substrate surface. The CaDPA sensor was demonstrated to achieve superb limits of detection of the anthrax spores, where sub-infectious dose levels (around 2.6×10^3 spores) were detected in 11 minutes. Such results provide a rapid, real-time, on-site sensing strategy that is 200 times more sensitive than previous CaDPA SERS detection assays (*121*, *123*). In another study, the detection limit was improved (up to 1.4×10^3 spores) by functionalizing the AgFON surface with a layer of alumina, which happened to improve the stability and the binding affinity to CaPDA (*124*). As for the glucose sensor, it was demonstrated that the DT/MH-modified AgFON SERS substrate for sensing glucose yields accurate measurements even in presence of interfering analytes. It was tested in bovine plasma to simulate the in-vivo conditions similar to the case where the sensor is implanted under the skin in the interstitial fluid (*123*).

Raman Label-Based Biosensors

Despite its superior optical properties, colloidal silver in solution suffers from lack of monodispersity and low stability against aggregation that may compromise the efficiency of its assays (*3*, *125*, *126*). On the other hand, AuNps form colloidal solutions with narrow size distribution and long-term stability, but exhibit relatively modest optical properties. In order to overcome the limitations of both nanoparticles and to synergistically benefit from their combined properties, there is a trend toward synthesizing composite Au/Ag nanostructures and tuning their structural parameters in order to upgrade their analytical performance such as in SERS-based detection experiments (*82*).

Ji et al. presented one of the earliest reports on the use of Au/Ag core-shell Raman probe-labeled nanoparticles in a sandwich-type immunoassay for the detection of Hepatitis B Virus surface antigen (HBsAg) by SERS spectroscopy. Monodisperse 28 nm-sized Au/Ag core-shell nanoparticles were prepared and then functionalized with anti-HBsAg monoclonal antibodies along with p-mercaptobenzoic acid (MBA) as the Raman label; these particles comprise the SERS tags in solution. Polyclonal HBsAg capture antibodies are immobilized on a silicon support that is modified with (3-amino-propyl) trimethoxysilane SAM. Applying the HBsAg-containing sample to the silicon chip along with the Au/Ag core-shell nanoparticle Raman tags is followed by chip rinsing and SERS measurement. As shown in Figure 6, using the Au/Ag nanostructure was demonstrated to exhibit superior Raman enhancement factor as compared to pure nanogold and thus is considered as a promising SERS substrate for conducting high-sensitivity immunoassays (*125*).

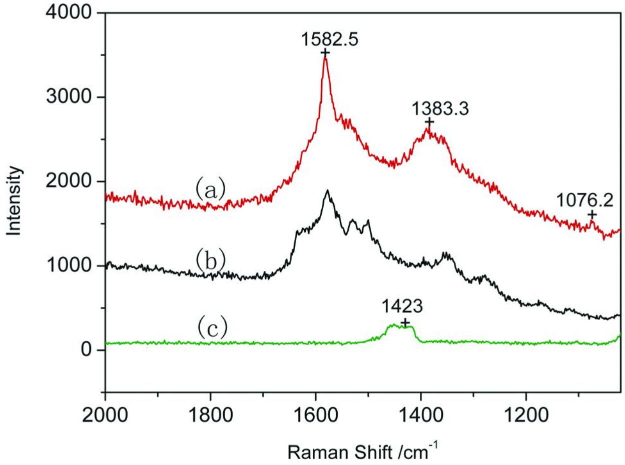

Figure 6. The SERS spectra of Raman tags based on (a) immuno-Au/Ag core-shell NPs, (b) immuno-AuNPs with silver enhancement, and (c) pure immuno-AuNPs. Reproduced with permission from reference (125). Copyright 2005 Elsevier.

A similar study was conducted by Lu et al.; however unlike Ji et al.'s approach where the Raman label is directly functionalized to the NP, the Raman label in this case (the p-aminothiophenol, pATP) was incorporated into the core-shell structure in an intermediate step between the AuNPs synthesis and the Ag shell deposition producing what was called p-aminothiophenol embedded Au/Ag core-shell nanoparticles. The enhancement of the SERS signal from the Raman tag was demonstrated to be superior to AuNP-pATP; moreover the enhancement factor was correlated to the thickness of the Ag shell and maximum SERS signal was attained at a 10 nm thickness of the Ag nanoshell. As the Ag shell thickness increased, the SERS signal enhancement increased up to a certain thickness value and then declined. This was explained by the fact that the intensity of the SERS signal is a function of the presence of 'hot spots' of local electromagnetic field enhancement; in the Ag shell these 'hot spot' regions existed at pinholes and cervices developed on the deposition of the Ag shell. The existence of such nano-features in the Ag shell is most pronounced at the beginning of Ag deposition and increases with the Ag nanoshell formation up until a certain point where such features start to disappear as the nano-shell smoothens. This pATP-Au/Ag core-shell SERS tag was used in a sandwich immunoassay of the same principle as the one reported by Ji et al. for the detection of Muramidase Released Protein (MRP) which is a significant biomarker for *Streptococcus suis type 2* (SS2) –an infectious bacteria of humans and swine. The high SERS activity of the developed SERS tag enabled the highly sensitive detection of MRP with a detection limit as low as 1 pg/ml (*126*). Ag core-Au shell SERS tags have also been developed and optimized for SERS-based biosensing (*127*, *128*).

SERS-based hybridization assays employing AgNPs have also been investigated. Possible approaches for the use of MNPs in SERS-based nucleic acid detection are illustrated in Figure 7.

Zhang and coworkers reported the development of a SERS-based DNA detection assay that allows for multiplexing. The detection strategy is based on the emergence of SERS signals on the aggregated assembly of oligonucleotide-functionalized AgNPs in solution when the target sequence is present, resulting in multiple 'hot spots' of pronounced local electromagnetic field enhancement (*129*). In order to guarantee the stability of the AgNP-SERS probes, they were functionalized with triple cyclic disulfide-capped DNA molecules which were demonstrated to form DNA-AgNP conjugates of superior stability as compared to those functionalized with mono-thiol capped DNA (*83*). Two sets of functionalized AgNPs are used: the first set comprises AgNPs conjugated to a layer of mixed DNA probes that are complementary to multiple targets, but only to half of each sequence. The second set of AgNPs is conjugated to thiolated Raman labels (4-aminothiophenol, 6-mercaptonicotinic acid and 2-mercaptopyrimidine), and probe DNA molecules complementary to the other half of the target sequences under investigation (each AgNP of this set has just one type of Raman label and probe). In absence of the target sequence, the two sets of AgNPs are at distance from each other; the SERS signals corresponding to individual AgNPs is rather weak and appear as insignificant background SERS signals: the 'off-state'. If the target sequence is present, hybridization of the complementary probes of both sets to their respective target sequences takes place bringing the nanoparticles into an aggregated state associated with a dramatic enhancement of the SERS signals: the 'on-state'. The assay displayed sufficient resolution to discriminate and distinguish the SERS peaks of the different target sequences present in the sample thus proving its capability to serve as a rapid, efficient, and reproducible multiplex assay that could simplify DNA detection processes, reduce the amount of sample and reagents needed and consequently the assay cost. An illustration of the principle of this assay is shown in Figures 8 and 9 (*129*).

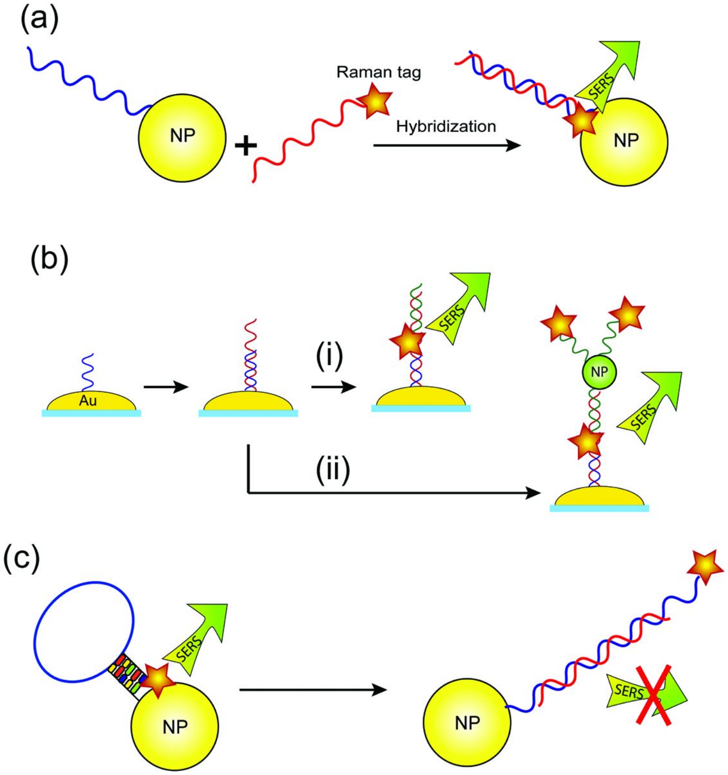

Figure 7. SERS-based nucleic acid detection approaches: (a) Target is Raman tag-labeled and directly detected on hybridization to the complementary NP probe (b)NP array substrate is used for SERS-based detection either (i) directly with Raman tag-labeled target or (ii) with the aid of a secondary conjugated NP to enhance detection sensitivity (c) Molecular beacon design detecting hybridization to target by reduction in SERS signal. Adapted with permission from reference (12). Copyright 2011 Elsevier.

Vo Dinh and co-workers reported a novel SERS probe based on a molecular beacon design that measures the decrease in SERS signal; this novel probe was termed Molecular Sentinel probe (MS). An MS probe is based on a nucleic acid that is conjugated with a Raman label at one end, and thiol-linked to the AgNP at the other. The MS probe exists in a hairpin configuration where the SERS signal is at maximum due to the proximity of the AgNP to the Raman label. In the presence of the target nucleic acid, hybridization takes place and the MS probe opens separating the AgNP and the Raman label from one another and diminishing the SERS signal. The principle of the MS probe is depicted in Figure 10. The MS probe was demonstrated to exhibit high specificity, selectivity and capability of multiplexing; such probes were used to detect the gag gene sequence of the human immunodeficiency virus type 1 (HIV-1) and BRCA-1 gene of breast cancer (*131*). A few more examples of AgNP-based SERS biosensors are listed in table III.

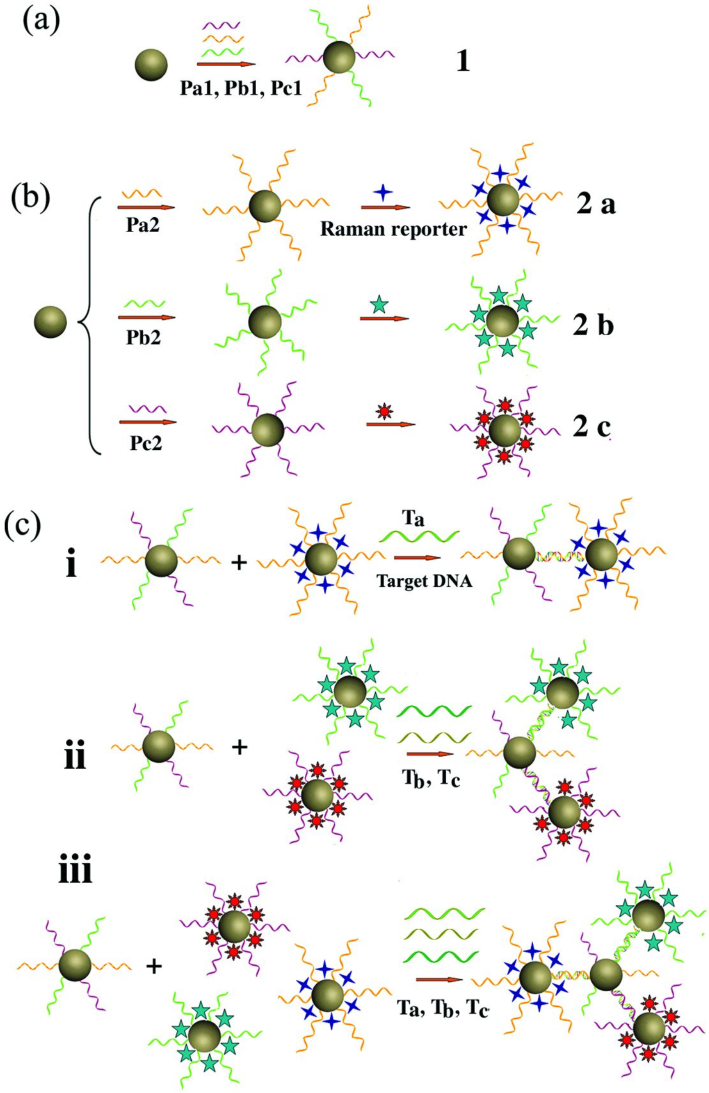

Figure 8. An illustration of the multiplex SERS detection system. (a) Functionalization of one set of AgNPs with mixed DNA probes, (b) conjugating the other set of AgNPs with the Raman labels and the rest of the DNA probes, (c) the sandwich hybridization assay system for the detection of one (i), two (ii) and three (iii) DNA targets. Reproduced with permission from reference (129). Copyright 2011 The Royal Society of Chemistry.

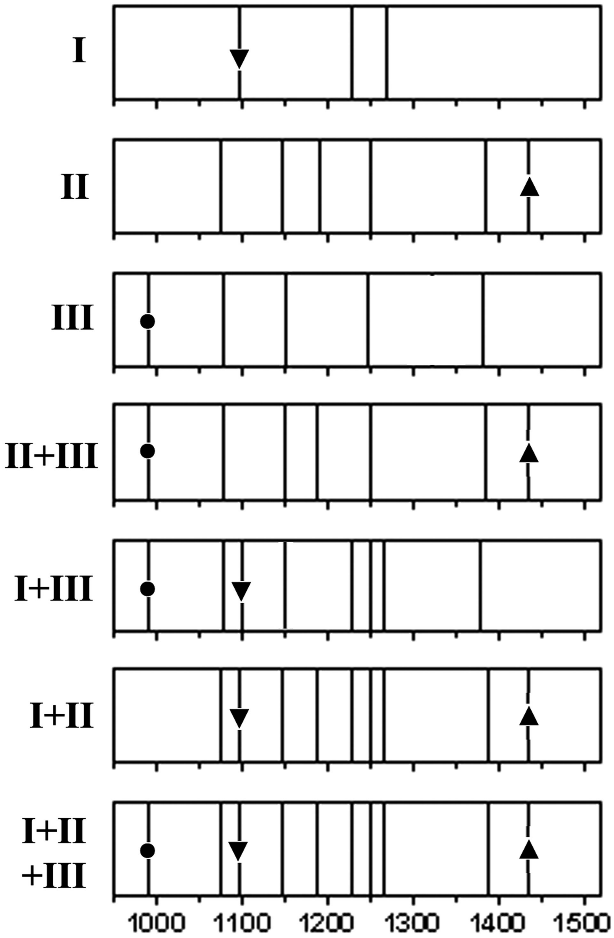

Figure 9. A bar-code representation of the SERS spectra for the different hybridization scenarios: I, II and III represent single-target detection. (II + III), (I + III) and (I+II) represent two-target detection. (I + II + III) represent three-target detection. Reproduced with permission from reference (129). Copyright 2011 The Royal Society of Chemistry.

Fluorescence Modulation-Based Biosensors

Several silver-based nanostructures have been observed to exhibit remarkable enhancement in fluorescence intensity and resonance energy transfer and therefore were utilized in MEF and RET-based biosensors.

A number of silver nanostructures have been synthesized and investigated for their MEF performance by Lakowicz and coworkers; one example is silver island films (SIFs), which comprise AgNPs of sub-wavelength dimensions and heterogeneous morphologies deposited on a glass substrate (*136*). A SIF nanostructure was developed by Sabanayagam et al. to increase the sensitivity of DNA hybridization fluorescence-based detection on microarrays. SIF is grown by the deposition of silver ions on a slide coated with MPTS (3-mercaptopropyltrimethoxysilane), which imparts affinity to silver. Heterogeneous Ag islands (in size and shape –mostly elongated) form upon the substrate with diameters in the range of 50-100 nm and an average diameter of ~80 nm. The SIF substrate is then biotinylated and functionalized with avidin. Single-stranded biotinylated capture probes were immobilized on the SIF substrate via binding to avidin and then exposed to dye-labeled complementary targets; the dyes employed in this experiment are Cy3 and Cy5. Surface hybridization brings the fluorophore in proximity to the SIF and fluorescence enhancements of ~10 fold for Cy5 and ~3 fold for Cy3 were observed (Φ^0 is smaller for Cy5). The MEF effect was found to depend on the probe density and hence the surface dye concentration; MEF increases up till a certain concentration beyond which hybridization of more dye-labeled strands becomes sterically and electrostatically hindered. On the other hand, enhancements of up to ~28 fold for Cy5 and ~4 fold for Cy3 were observed when the probe-target hybridization occurred before immobilization upon the SIF substrate, which concentrated the labeled DNA bound to the surface (*39*). Using fluorophore-conjugated dendrimers as secondary probes was shown by Stears et al. to exhibit a 16-fold detection sensitivity as compared to linear probes; which could significantly improve the sensitivity of microarray DNA detection (*137*). Such system is suggested for use in APEX (arrayed primer extension) assays for genotyping purposes, encouraged by the fact that the SIF can withstand highly stringent conditions such as elevated temperatures and high salt buffers. It was proven in this investigation that SIF substrates are superior to glass-substrate assays guaranteeing spotting uniformity and thus simpler analysis, high detection sensitivity and robustness (*39*). An illustration of solid-phase MEF assays is shown in Figure 11.

SIF-based enhancement of fluorescence was not only applied to extrinsic fluorescent dyes, but also to biomolecules of intrinsic fluorescence such as DNA. Each DNA nucleotide residue has a UV absorbing base that could fluoresce; however when it does, the fluorescence is extremely weak due to the dominance of the non-radiative decay paths. The use of MEF for DNA fluorophores has been reported and used in applications such as DNA single-strand sequencing (*35*, *37*, *138*).

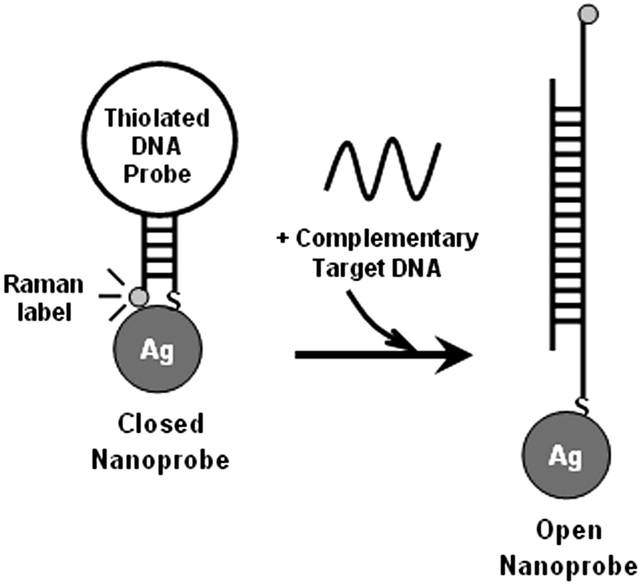
Thiolated DNA Probe
Raman label
S
Ag
Closed Nanoprobe
+ Complementary Target DNA
S
Ag
Open Nanoprobe

Figure 10. SERS-based molecular sentinel (MS) nanoprobes. Left: closed-state, right: open-state. Reproduced with permission from reference (130). Copyright 2009 IOP science.

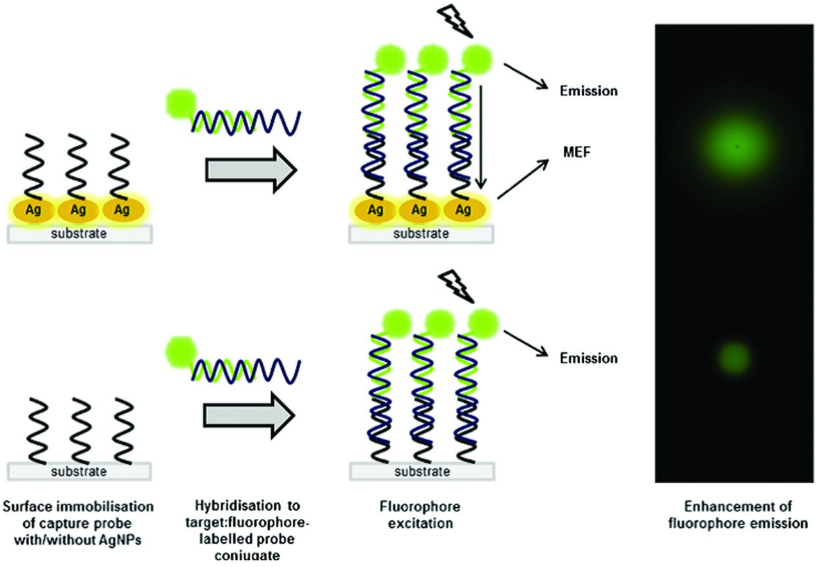
Ag
Ag
Ag
substrate
Ag
Ag
Ag
substrate
Emission
MEF
substrate
substrate
Emission
Surface immobilisation of capture probe with/without AgNPs
Hybridisation to target:fluorophore-labelled probe conjugate
Fluorophore excitation
Enhancement of fluorophore emission

Figure 11. A schematic representation of solid-phase silver-enhanced-fluorescence assays for nucleic acid detection. Reproduced with permission from reference (82). Copyright 2011 Elsevier.

Table III. Summarizes a few more examples on AgNPs-based SERS biosensors

Type of SERS biosensor	*Platform/Target*	*Performance*	*Reference*
Label-free	Ag nanoclusters on anodic aluminum oxide (AAO) template Detection of Bovine serum albumin, cardiac troponin T and IgG.	LOD: 3 ng/ml	(*132*)
	AgNPs distributed upon an anatase (TiO_2) film. DNA detection.	Reliable detection of hybridization based on specific changes of the DNA Raman line intensities that differentiate ssDNA from dsDNA. Spatially addressed DNA detection was possible.	(*133*)
Raman label-based	Ag/SiO_2 core-shell nanoparticles embedded with rhodamine B isothiocyanate dye molecules and functionalized with α-fetoprotein (AFP) polyclonal antibodies. Detection of AFP for the diagnosis of hepatocellular carcinoma via a sandwich immunoassay.	LOD: 11.5 pg/ml and concentrations of human AFP up to 0.12 μg /ml were detected.	(*134*)
	Composite Organic-Inorganic Nanoparticles (COINs) based on Ag nanoclusters encapsulated in a layer of BSA and glutaraldehyde; the Raman label is Basic Fushin. The COINs are functionalized with Prostate specific antigen (PSA) antibodies.	The COIN-antibody conjugates showed high Raman intensity and offered the capability for multiplexing and tissue-imaging applications without enzyme amplification.	(*135*)

Continued on next page.

Table III. (Continued). Summarizes a few more examples on AgNPs-based SERS biosensors

Type of SERS biosensor	*Platform/Target*	*Performance*	*Reference*
	Mapping of PSA in tissue samples.		

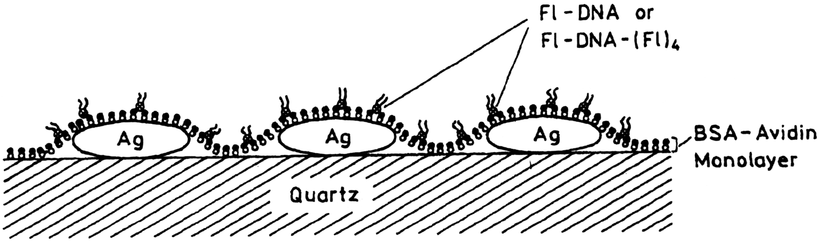

Figure 12. An illustration of the SIF substrate upon which the BSA-avidin monolayer is deposited. Fl-DNA or Fl-DNA(Fl)$_4$ were captured to avidin using the complementary oligonucleotides. Reproduced from reference (139). Copyright 2003 American Chemical Society.

In addition to improving the intrinsic quantum yield from fluorophores, SIF substrates are also employed to overcome problems encountered with some fluorophores such as photoblinking and self-quenching. Self-quenching is observed with some dyes such as fluorescein and rhodamine when used in multiple labeling of probes to amplify their signals. Despite their high extinction coefficients and quantum yields, the excited state of these fluorophores relax non-radiatively by RET to another residue of the same type (homo RET), a consequence attributed to the small Stokes-shift of the dye's emission spectrum from its absorption profile which leads to their overlap. Self-quenching compromises the sensitivity of the assay and it needs to be overcome. Proximity to SIF at an optimal distance was shown to avoid self-quenching of multiply labeled DNA oligomers and increase their fluorescence intensity. Two sets of fluorescein labeled oligomers (23 basepairs) were hybridized to biotinylated complementary probes immobilized on an avidin-BSA (bovine serum albumin)-coated SIF substrate (Figure 12): one set was labeled with one fluorescein residue (F1-DNA) and the other set was labeled with 5 fluorescein residues (Fl-DNA (Fl)$_4$ – one residue is conjugated to the 3'end and the rest are distributed along the oligomer's length) (*139*). The BSA-avidin coat provides the optimal separation distance of ~90 Å between the fluorescein and the metal surface that maximizes the fluorescence enhancement (*140*). When compared to immobilization on a quartz substrate without silver, the enhancement of fluorescence for fluorescein was found to be 7-fold for F1-DNA and 19-fold for Fl-DNA $(Fl)_4$. The more dramatic enhancement for the Fl-DNA $(Fl)_4$ is attributed to its lower quantum yield in solution. The release of self-quenching is due to the increase in radiative decay rate Γ_m contributed by the silver metal. Moreover, dye photostability was increased on SIF substrates due to decreased lifetimes; and high S/N ratios were obtained. The high sensitivity and cost-efficiency of this detection method encourage its wide use in DNA microarrays (*139*). The problem of photoblinking of fluorophores such as quantum dots (QDs) was greatly suppressed by immobilization near SIFs, which increased their 'on' time and their fluorescence intensity (*141*).

SIF substrates were also used to improve the sensitivity of immunoassays by either enhancing fluorescence from the labeled antibody or the labeled protein. A sandwich immunoassay for the detection of the cardiac biomarker myoglobin was investigated by utilizing fluorophore labeled antibodies and a SIF substrate. Anti-myoglobin antibodies were immobilized upon the silver particles of SIF and the myoglobin in the sample was captured. Incubation in fluorophore labeled anti-myoglobin antibodies was followed by the detection of fluorescence signals that were 10-15 times larger than those observed upon a glass substrate alone. The format of this immunoassay allowed for detection limits below 50 ng/mL; which corresponds to half the clinical cut-off level of myoglobin in healthy individuals (*142*). Ultrabright signals from highly labeled proteins such as fluorescein isothiocyanate labeled Human Serum Albumin (FITC-HSA) were obtained due to release of self-quenching at optimized proximity to a SIF substrate. The emission from this configuration was found to be 17 times larger than in absence of SIF (*143*).

Recent studies have demonstrated that silicon wafers could also support MEF (*144*); which suggested that the use of SIF on silicon chips as substrates for hybridization assays and immunoassays should maximize the assay sensitivity and S/N ratio. Li et al. investigated the fluorescence enhancement of four dyes: green fluorescent protein (GFP), Alexa Fluor 555 (AF555), phycoerythrin (PE) and Cy3, upon AgNPs-coated silicon-based electronic chips (p-Chips) in improving the detection sensitivity in interleukin-6 (IL-6) immunoassay and in a hybridization assay. The four fluorophores exhibited from 5-50 fold enhancements in fluorescence which means that the performance of the platform is not dye-specific and could therefore be extended for different systems. For the immunoassay, a sensitivity of 4.3 pg/ml was established which is 25 times larger than in the absence of SIF and within the healthy range of IL-6 in the human body. For the hybridization assay, the sensitivity was 0.05 nM which is 38 times larger than in the absence of SIF. The SIF-p-Chip substrate can support highly sensitive hybridization assays and immunoassays in addition to its multiplexing potential (*145*). Silver colloids (monodisperse spherical silver nanoparticles) immobilized on substrates have also been used for similar purposes and fluorescence enhancements of some visible dyes up to 17 fold were reported which were superior to SIFs in the same settings (*146*).

In contrast to the difficult control over the fabrication of a solid-state MEF substrate such as SIF, preparation of colloidal silver suspensions is relatively simple and easily controllable yielding rather monodisperse and spherical particles in suspension. One would resort to colloidal suspensions instead of solid-phase structures when aiming at in-vivo imaging applications where injection of the AgNPs is needed; such as in retinal angiography for example, where the AgNPs enhance the quantum yield and photostability of the associated dyes (*138*, *142*). Aslan and coworkers were the first to report that solution phase SiO_2-coated silver nanoballs (Ag@SiO2) achieved a 3-5 fold enhancement of fluorescence signals from Cy3 on their aggregation as compared to unaggregated/unlabeled systems. The aggregation was based on the binding of the biotinylated nanoballs with streptavidin-conjugated Cy3 in solution. The silica shell protects the surface plasmon absorption of silver, alleviates quenching of fluorescence by nearby metal nanoparticles, controls the metal-fluorophore distance for maximum enhancement and serves the purpose of surface functionalization with biomolecules by adjusting the surface chemistry of the nanoballs (*147*, *148*).

Such Ag@SiO_2 nanoballs have been extended for use in sensing applications but with a slight amendment in the architecture where the fluorophore is embedded within the silica shell: MEF nanoballs. For developing high sensitivity solution-phase bioassays and cellular imaging, Aslan et al. investigated MEF nanoballs comprising silver nanospheres of ~ 130 nm in diameter and silica shells of up to 35 nm in thickness for fluorescence enhancement of Rhodamine 800 (Rh800). The hydrophobic Rh800 residues were embedded within the pockets of the silica shell. A 20-fold enhancement in fluorescence intensity and 10-fold decrease in fluorescence lifetime were observed with the MEF nanoballs of ~ 11 nm thick silica shell as compared with the silver-etched control nanoballs. Such results suggest the potential of a 200-fold enhancement in particle-detectability and thus sensitivity (*148*).

Low-power microwave heating has been employed in MEF assays (microwave-assisted MEF, MAMEF) in order to accelerate the kinetics of molecular recognition events. MAMEF has been employed for the detection of cardiac biomarkers like Troponin 1 in whole blood samples at a LOD of 0.05 μg/L in 1 minute (*149*, *150*) and in a number of DNA-detection bioassays with LODs below 50 nM and ultra-rapid performance (*151*).

Metal-Enhanced RET-Based Detection

Resonance energy transfer between donor fluorophores and acceptor molecules is utilized for biosensing applications such as hybridization-detection assays, DNA amplicons detection, DNA sequencing and molecular rulers. In the presence of a SIF substrate, the rate of resonance energy transfer can be increased along with an increase Förster distances which enables the use of RET in assays employing large biomolecules such as immunoglobulins in immunoassays. For a double-stranded calf thymus DNA labeled with a donor fluorophore and an acceptor, the enhancement of Donor-Acceptor (D-A) RET by SIF substrates was demonstrated to increase the Förster distance from 35 Å to 166 Å (*152*). Recently, silver nanoparticles have been utilized as super nanoquenchers themselves and were shown to yield very high sensitivity and S/N ratios in the detection of biothiols in urine. (*153*).

Nanoclusters are made of a few up to a hundred atoms, with a size comparable to the Fermi wavelength of electrons and diameters below 2 nm. Silver nanoclusters (Ag NCs) show special characteristics falling between atomic and nanoparticle behavior. The small size of the nanoclusters results in the loss of the continuity of the density of states and the discretization of electronic energy levels making the emission of radiation possible and rendering them fluorescent on photoexcitation. Besides their ultra-small size, allowing a high surface area-to-volume ratio, Ag NCs have many advantages such as their good biocompatibility and excellent photostability, allowing their use as fluorescent labels in biological applications, especially with their facile surface tailorability and color tunability (*154*). Fluorescent Ag NCs have been used to detect various types of analytes, including metal ions, small biomolecules, proteins and nucleic acids. Their synthesis is quite challenging due to their instability in aqueous solutions toward further growth, and thus the use of templates and/or capping agents is indispensible. Examples include DNA scaffolds, polymers, dendrimers, polymer capsules and microgels (*72*). DNA-templated Ag NCs (DNA/Ag NCs) represent an emerging class of fluorophores that is demonstrated to manifest exceptional fluorescence properties as compared to conventional fluorophores. DNA-templated nanostructures can be produced due to the interactions of metal cations with DNA. Silver ions in particular have a high affinity to cytosine bases on single stranded DNA, making DNA oligonucleotides good stabilizers for preparing Ag NCs. Oligonucleotide-encapsulated Ag NCs can be produced using $NaBH_4$ as a reducing agent. $NaBH_4$ allows 1-4 atom-NCs to bind to 12-base oligo. Red and blue/green emitting Ag NCs can be prepared with 12-mer cytosine as templates. The nitrogeneous bases have a great influence on cluster formation and both base complication and cluster stability contribute to the type of DNA encapsulated Ag NCs (*155–158*). Fluorescent Ag NCs based on DNA hairpins can have their stability and fluorescence tuned by the number of cytosines in the loop. Also, mismatched double-stranded DNA templates can be used for site-specific growth of fluorescent Ag NCs (*159*).

Besides the advantages of DNA/AgNCs such as the great photostability and brightness, an exceptional and not-well-understood property of DNA/Ag NCs has been observed where their fluorescence color changes under certain surrounding conditions; such a property has been exploited as a signal transduction mechanism in biosensor applications. Yeh et al. reported that the red fluorescence of DNA/Ag NCs can be enhanced up to 500-fold when nearby guanine-rich sequences, and accordingly designed a DNA detection nanoprobe (NanoCluster Beacon, NCB) that relies on the reversible conversion of the nanocluster from dark species to bright red on target binding. The NCB strategy is simple, inexpensive and can achieve extraordinarily high signal-to-background ratios (*160*). In contrast to this 'light–on' assay, DNA/Ag NCs probes were also used for microRNA detection but the principle is different where target binding is associated with the diminishing of the red fluorescence (*161*).

Future Perspective

Theoretical and experimental investigations of the properties and fabrication strategies of different silver nanostructures have gained a substantial momentum over the past few years. The use of silver nanostructures in the biomedical field is not limited to biosensors; silver nanostructures exhibit remarkable performance as drug delivery platforms, therapeutic and antimicrobial agents. The trend is to develop multifunctional, integrated and controllable systems that can perform multiple tasks with high efficiency and reproducibility. Diagnosis and therapy can be combined in the same theranostic platform; for example the drug-bearing nanoparticle can be used in-vivo to target the diseased site, deliver/release the drug and its opto-physical properties can be used to image it. AgNPs are being studied as proliferation and survival enhancers in stem-cell research, as wound healers and as anti-inflammatory, antiviral and anti-platelet agents (*162*). AgNPs were found to be environmentally safe; their biological safety, though, is of major concern especially for in-vivo applications and detailed toxicological investigations of AgNPs are needed before their in-vivo applications can be commercialized.

References

1. Nath, N.; Chilkoti, A. *J. Fluoresc.* **2004**, *14*, 377–389.
2. Rycenga, M.; Cobley, C. M.; Zeng, J.; Li, W.; Moran, C. H.; Zhang, Q.; Qin, D.; Xia, Y. *Chem Rev* **2011**, *111*, 3669–3712.
3. Sau, T. K.; Rogach, A. L.; Jäckel, F.; Klar, T. A.; Feldmann, J. *Adv. Mater.* **2010**, *22*, 1805–1825.
4. Link, S.; El-Sayed, M. A. *Annu. Rev. Phys. Chem.* **2003**, *54*, 331–366.
5. Nath, N.; Chilkoti, A. Radiative Decay Engineering; Lakowicz, J., Geddes, C. D., Eds.; In *Topics in Fluorescence Spectroscopy*; Springer Science+Business Media, Inc.: New York, 2005; Vol. 8, pp 353−380.
6. Lindsay, S. M. *Introduction to Nanoscience*; Oxford University Press Inc.: New York, 2010; pp 329−331.
7. González, A. L.; Noguez, C. *Phys. Status Solidi C* **2007**, *4*, 4118–4126.
8. Zhao, J.; Sherry, L. J.; Schatz, G. C.; Duyne, R. P. V. *IEEE J. Sel. Top. Quantum Electron.* **2008**, *14*, 1418–1429.
9. Hohenau, A.; Leitner, A.; Aussenegg, F. R. Surface Plasmon Nanophotonics; Brongersma, M. L.. Kik, P. G., Eds.; In *Optical Sciences*; Springer: Dordrecht, Netherlands, 2007; pp 11−25.
10. Kelly, K. L.; Coronado, E.; Zhao, L. L.; Schatz, G. C. *J. Phys. Chem. B* **2003**, *107*, 668–677.
11. Anker, J. N.; Hall, W. P.; Lyandres, O.; Shah, N. C.; Zhao, J.; Duyne, R. P. *Nat. Mater.* **2008**, *7*, 442–453.
12. Petryayeva, E.; Krull, U. J. *Anal. Chim. Acta* **2011**, *706*, 8–24.
13. Caro, C.; Castillo, P. M.; Klippstein, R.; Pozo, D.; Zaderenko, A. P. In *Silver Nanoparticles*; Perez, D. P., Ed.; In-Tech: Vukovar, Croatia, 2010; pp 201−223.
14. Wiley, B.; Sun, Y.; Mayers, B.; Xia, Y. *Chem. Eur. J.* **2005**, *11*, 454–463.

15. Cobley, C. M.; Skrabalak, S. E.; Campbell, D. J.; Xia, Y. *Plasmonics* **2009**, *4*, 171–179.
16. Dement'eva, O. V.; Rudoy, V. M. *Colloid J.* **2011**, *73*, 724–742.
17. Sun, Y.; Xia, Y. *Analyst* **2003**, *128*, 686–691.
18. Rodríguez-González, B.; Burrows, A.; Watanabe, M.; Kiely, C. J.; Marzán, L. *J. Mater. Chem.* **2005**, *15*, 1755–1759.
19. Zamkovets, A. D.; Kachan, S. M.; Ponyavina, A. N. *J. Appl. Spectrosc.* **2008**, *75*, 588–592.
20. Chen, S.; Webster, S.; Czerw, R.; Xu, J.; Carroll, D. L. *J. Nanosci. Nanotechnol.* **2004**, *4*, 254–259.
21. Lee, K.; El-Sayed, M. A. *J. Phys. Chem. B* **2006**, *110*, 19220–19225.
22. Skoog, D.; West, D. *Principles of Instrumental Analysis*, 2nd ed.; Saunders College: Philadelphia, PA, 1980; p 262.
23. Vo-Dinh, T.; Yan, F. In *Optical Chemical Sensors*; Baldini, F., Chester, A. N., Homola, J., Martellucci, S., Eds.; Springer: Dordrecht, Netherlands, 2006; pp 239−259.
24. Zhao, W.; Tripp, R. A. In *Metallic Nanomaterials*; Kumar, C. S. S. R., Ed.; Wiley-VCH Verlag GmbH & Co. KGaA: Weinheim, Germany, 2009; pp 173−224.
25. Kneipp, K.; Kneipp, H.; Itzkan, I.; Dasari, R. R.; Feld, M. S. *Chem. Rev.* **1999**, *99*, 2957.
26. Hering, K.; Cialla, D; Ackermann, K.; Dörfer, T.; Möller, R.; Schneidewind, H.; Mattheis, R.; Fritzsche, W.; Rösch, P.; Popp, J. *Anal. Bioanal. Chem.* **2008**, *390*, 113–124.
27. Tiwari, V. S.; Oleg, T.; Darbha, G. K.; Hardy, W.; Singh, J. P.; Ray, P. C. *Chem. Phys. Lett.* **2007**, *446*, 77–82.
28. Lin, W.; Liao, L.; Chen, Y.; Chang, H.; Tsai, D.; Chaing, H. *Plasmonics* **2011**, *6*, 201–206.
29. Lin, W.; Huang, S.; Chen, C; Chen, C.; Tsai, D. P.; Chiang, H. *Appl. Phys. A* **2010**, *101*, 185–189.
30. Ludemann, M.; Brumboiu, I. E.; Gordan, O. D.; Zahn, D. R. T. *J. Nanopart. Res.* **2011**, *13*, 5855–5861.
31. Aroca, R. F.; Alvarez-Puebla, R. A.; Pieczonka, N.; Sanchez-Cortez, S.; Garcia-Ramos, J. V. *Adv. Colloid Interface Sci.* **2005**, *116*, 45–61.
32. Lakowicz, J. R. *Principles of Fluorescence Spectroscopy*, 3rd ed.; Springer Science + Business Media LLC: New York, 2006; pp 1−25.
33. Yeh, H. C.; Chao, S. Y.; Ho, Y. P.; Wang, T. H. *Curr. Pharm. Biotechnol.* **2005**, *6*, 453–461.
34. Bouhelier, A. *Microsc Res Techniq* **2006**, *69*, 563–579.
35. Zhu, S.; Fischer, T.; Wan, W.; Descalzo, A. B. Rurack, K. *Top. Curr. Chem.* **2011**, 300, 51–91.
36. Lakowicz, J. R. *Principles of Fluorescence Spectroscopy*, 3rd ed.; Springer Science + Business Media LLC: New York, 2006; pp 841−859.
37. Lakowicz, J. R.; Shen, B.; Gryczynski, Z.; D'Aurial, S.; Gryczynski, I. *Biochem. Biophys. Res. Commun.* **2001**, *286*, 875–879.
38. Aslan, K.; Lakowicz, J.; Geddwa, C. D. *Anal. Bioanal. Chem.* **2005**, *382*, 926–933.

39. Sabanayagam, C. R.; Lakowicz, J. R. *Nucleic Acids Res.* **2007**, *35*, e13.
40. Barnes, W. L. *J. Mod. Opt.* **1998**, *45*, 661–669.
41. Anger, P.; Bharadwaj, P.; Novotny, L. *Phys. Rev. Lett.* **2006**, *96*, 113002.
42. Meng, X. K.; Tang, S. C. *J. Mater Sci. Technol.* **2010**, *26*, 487–522.
43. Cao, G. *Nanostructures and Nanomaterials: Synthesis, properties and applications*; Imperial College Press: London, 2004.
44. Nair, L. S.; Laurencin, C. T. *J. Biomed. Nanotechnol.* **2007**, *3*, 301–316.
45. Chou, K.; Ren, C. *Mater. Chem. Phys* **.2000**, *64*, 241–246.
46. He, B.; Tan, J. J.; Liew, K. Y.; Liu, H. *J. Mol. Catal. A: Chem* **2004**, *221*, 121–126.
47. Chen, M.; Wang, L. Y.; Han, J. T.; Zhang, J. Y.; Li, Z. Y.; Qian, D. J. *J. Phys. Chem. B* **2006**, *110*, 11224–31.
48. Dong, X.; Ji, X.; Wu, H.; Zhao, L.; Li, J.; Yang, W. *J. Phys. Chem. C* **2009**, *113*, 6573–6576.
49. Caswell, K. K.; Bender, C. M.; Murphy, C. J. *Nano Lett.* **2003**, *3*, 667–669.
50. Zhou, G.; Lü, M.; Yang, Z.; Zhang, H.; Zhou, Y.; Wang, S.; Wang, S.; Zhang, A. *J. Cryst. Growth* **2006**, *289*, 255–259.
51. Henglein, A.; Giersig, M. *J. Phys. Chem. B* **1999**, *103*, 9533–9539.
52. Qin, Y.; Ji, X.; Jing, J.; Liu, H.; Wu, H.; Yang, W. *Colloids Surf., A* **2010**, *372*, 172–176.
53. Wang, Y.; Camargo, P. H. C.; Skrabalak, S. E.; Gu, H.; Xia, Y. *Langmuir* **2008**, *24*, 12042–12046.
54. Lou, X. W.; Yuan, C.; Archer, L. A. *Chem. Mater.* **2006**, *18*, 3921–3923.
55. Lu, L.; Kobayashi, A.; Tawa, K.; Ozaki, Y. *Chem. Mater.* **2006**, *18*, 4894–4901.
56. Wiley, B.; Sun, Y.; Xia, Y. *Acc. Chem. Res.* **2007**, *40*, 1067–1076.
57. Kan, C.; Zhu, J.; Zhu, X. *J. Phys. D: Appl. Phys.* **2008**, *41*, 155304.
58. Wiley, B.; Herricks, T.; Sun, Y.; Xia, Y. *Nano Lett.* **2004**, *4*, 1733–1739.
59. Wiley, B. J.; Xiong, Y.; Li, Z.; Yin, Y.; Xia, Y. *Nano Lett.* **2006**, *6*, 765–768.
60. Sun, Y.; Gates, B.; Mayers, B.; Xia, Y. *Nano Lett.* **2002**, *2*, 165–168.
61. Cobley, C. M.; Rycenga, M.; Zhou, F.; Li, Z.; Xia, Y. *J. Phys. Chem. C* **2009**, *113*, 16975–16982.
62. Luo, X.; Chen, Y.; Yang, D.; Li, Z.; Han, Y. *Solid State Sci.* **2011**, *13*, 1719–1723.
63. Zhang, Q.; Li, W.; Wen, L.; Chen, J.; Xia, Y. *Chem. Eur. J* **2010**, *16*, 10234–10239.
64. Jana, N. R.; Gearheart, L.; Murphy, C. *J. Chem. Commun.* **2001**, *7*, 617–618.
65. Maillard, M.; Giorgio, S.; Pileni, M. P. *Adv. Mater.* **2002**, *14*, 1084.
66. Yener, D. O.; Sindel, J.; Randall, C. A.; Adair, J. H. *Langmuir* **2002**, *18*, 8692.
67. Sharma, V. K.; Yngard, R. A.; Lin, Y. *Adv. Colloid Interface Sci.* **2009**, *145*, 83–96.
68. Raveendran, P.; Fu, J.; Wallen, S. L. *J. Am. Chem. Soc.* **2003**, *125*, 13940–13941.
69. Eid, K.; Azzazy, H. *Int. J. Nanomed.* **2012**, *7*, 1543–1550.
70. Yoksan, R.; Chirachanchai, S. *Mater. Chem. Phys.* **2009**, *115*, 296–302.

71. Jurasekova, Z.; Sanchez-Cortes, S.; Tamba, M.; Torreggiani, A. *Vib. Spectrosc* .**2011**, *57*, 42–48.
72. Xu, H.; Suslick, K. S. *ACS Nano* **2010**, *4*, 3209–3214.
73. Lengke, M. F.; Fleet, M. E.; Southam, G. *Langmuir* **2007**, *23*, 2694–2699.
74. Mukherjee, P.; Ahmed, A.; Mandal, D.; Senapati, S.; Sainkar, S. R.; Khan, M.; Parishcha, R.; Ajaykumar, P. V.; Alam, M.; Kumar, R.; Sastry, M. *Nano Lett.* **2001**, *1*, 515–519.
75. Ahmad, A.; Mukherjee, P.; Senapati, S.; Mandal, D.; Khan, M.; Kumar, R.; Sastry, M. *Colloids Surf., B* **2003**, *28*, 313.
76. Xia, Y.; Halas, N. J. *MRS Bulletin* **2005**, *30*, 338.
77. Kim, S.; Han, Y.; Lee, B.; Lee, J. *Nanotechnology* **2010**, *21*, 075302.
78. Haynes, C. L.; Van Duyne, R. P. *J. Phys. Chem. B* **2001**, *105*, 5599–5611.
79. Baek, K. H.; Kim, J. H.; Lee, K. B.; Ahnn, H. S.; Yoon, C. S. *J. Nanosci. Nanotechnol.* **2010**, *10*, 3118–22.
80. Sosa, I. O.; Noguez, C.; Barrera, R. G. *J. Phys. Chem. B* **2003**, *107*, 6269–6275.
81. Maayan, G.; Liu, L. *Biopolymers* **2011**, *96*, 679–87.
82. Larguinhoa, M.; Baptistaa, P. V. *J. Proteomics* **2012**, *75*, 2811–2823.
83. Lee, J.; Lytton-Jean, A. K. R.; Hurst, S. J.; Mirkin, C. A. *Nano Lett.* **2007**, *7*, 2112–2115.
84. Tokareva, I.; Hutter, E. *J. Am. Chem. Soc.* **2004**, *126*, 15784–9.
85. Prosperi, D.; Polito, L.; Morasso, C.; Monti, D. Mixed Metal Nanomaterials; Kumar, C. S. R., Ed.; In *Nanomaterials for the Life Sciences*; Wiley VCH Verlag GmbH & Co. KGaA: Weinheim, Germany, 2009; Vol. 3, pp 197−241.
86. Amendola, V.; Polizzi, S.; Meneghetti, M. *Langmuir* **2007**, *23*, 6766–6770.
87. Taton, T. A.; Mirkin, C. A.; Letsinger, R. L. *Science* **2000**, *289*, 1757–1760.
88. Storhoff, J. J.; Elghanian, R.; Mucic, R. C.; Mirkin, C. A.; Letsinger, R. L. *J. Am. Chem. Soc.* **1998**, *120*, 1959–1964.
89. Elghanian, R.; Storhoff, J. J.; Mucic, R. C.; Letsinger, R. L.; Mirkin, C. A. *Science* **1997**, *277*, 1078–1087.
90. Thompson, D. G.; Enright, A.; Faulds, K.; Smith, W. E.; Graham, D. *Anal. Chem.* **2008**, *80*, 2805–2810.
91. Tan, Y. N.; Su, X.; Zhu, Y.; Lee, J. Y. *ACS Nano* **2010**, *4*, 5101–5110.
92. Cao, Y. C.; Jin, R.; Thaxton, C. S.; Mirkin, C. A. *Talanta* **2005**, *67*, 449–455.
93. Xu, X.; Wang, J.; Yang, F.; Jiao, k.; Yang, X. *Small* **2009**, *5*, 2669–2672.
94. Li, H.; Rothberg, L. *Proc. Natl. Acad. Sci. U.S.A.* **2004**, *101*, 14036–14039.
95. Schofield, C. L.; Haines, A. H.; Field, R. A.; Russell, D. A. *Langmuir* **2006**, *22*, 6707–6711.
96. Leesutthiphonchai, W.; Dungchai, W.; Siangprog, W.; Ngamrojnavanich, N.; Chailapakul, O. *Talanta* **2011**, *85*, 870–876.
97. Wang, X.; Wu, L.; Ren, J.; Miyoshi, D.; Sugimoto, N.; Qua, X. *Biosens. Bioelectron.* **2011**, *26*, 4804–4809.
98. Kanjanawarut, R.; Su, X. *Anal. Chem.* **2009**, *81*, 6122–6129.
99. Yuan, Y.; Zhang, J.; Zhang, H.; Yang, X. *Analyst* **2012**, *137*, 496.
100. Maduraiveeran, G.; Ramaraj, R. *J. Nanopart. Res.* **2011**, *13*, 4267–4276.
101. Haes, A. J.; Duyne, R. P. V. *Anal. Bioanal. Chem.* **2004**, *379*, 920–930.
102. McFarland, A. D.; Duyne, R. P. *Nano Lett.* **2003**, *3*, 1057–1062.

103. Haes, A.; Duyne, R. *J. Am. Chem. Soc.* **2002**, *124*, 10596–10604.
104. Haes, A. J.; Chang, L.; Klein, W. L.; Duyne, R. P. *J. Am. Chem. Soc.* **2005**, *127*, 2264–2671.
105. Haes, A. J.; Hall, W. P.; Chang, L.; Klein, W. L.; Duyne, R. P. *Nano Lett.* **2004**, *4*, 1029–1034.
106. Yonzon, C. R.; Jeoung, E.; Zou, S.; Schatz, G. C.; Mrksich, M.; Duyne, R. P. V. *J. Am. Chem. Soc.* **2004**, *126*, 12669–12676.
107. Endo, T.; Ikeda, R.; Yanagida, Y.; Hatsuzawa, T. *Anal. Chim. Acta* **2008**, *611*, 205–211.
108. Zhu, S.; Du, C.; Fu, Y. *Opt. Mater.* **2009**, *31*, 769–774.
109. Zhu, S.; Li, F.; Du, C.; Fu, Y. *Sens. Actuators, B* **2008**, *134*, 193–198.
110. Hall, W. P.; Ngatia, S. N.; Duyne, R. P. *J. Phys. Chem. C* **2011**, *115*, 1410–1414.
111. Zhou, W.; Ma, Y.; Yang, H.; Ding, Y.; Luo, X. *Int. J. Nanomed.* **2011**, *6*, 381–386.
112. Lai, T.; Hou, Q.; Yang, H.; Luo, X.; Xi, M. *Acta Biochim. Biophys. Sin.* **2010**, *42*, 787–792.
113. Zhu, S.; Du, C.; Fu, Y. *Opt. Mater.* **2009**, *31*, 1608–1613.
114. Huang, T.; Nallathamby, P. D.; Xu, X. *J. Am. Chem. Soc.* **2008**, *130*, 17095–17105.
115. Vo-Dinh, T.; Yan, F.; Wabuyele, M. B. Surface-Enhanced Raman Scattering – Physics and Applications; Kneipp, K., Moskovits, M., Kneipp, H., Eds.; In *Topics in Applied Physics*; Springer-Verlag: Berlin-Heidelberg, Germany, 2006; Vol. 103, pp 409–426.
116. Kneipp, K.; Wang, Y.; Kneipp, H.; Perelman, L. T.; Itzkan, I. *Phys. Rev. Lett.* **1997**, *78*, 1667–1670.
117. Futamata, M.; Maruyama, Y.; Ishikawa, M. *Vib. Spectrosc.* **2002**, *30*, 17–23.
118. Xu, H.; Bjerneld, E. J.; Käll, M.; Börjesson, L. *Phys. Rev. Lett.* **1999**, *83*, 4357–4360.
119. Zhang, W. C.; Wu, X. L.; Kan, C. X.; Pan, F. M.; Chen, H. T.; Zhu, J.; Chu, P. K. *Appl. Phys. A* **2010**, *100*, 83–88.
120. Zhang, X.; Duyne, R. P. V. *MRS Online Proc. Libr.* **2005**, *876*, 207–212.
121. Zhang, X.; Young, M. A.; Lyandres, O.; Duyne, R. P. V. *J. Am. Chem. Soc.* **2005**, *127*, 4484–4489.
122. Lyandres, O.; Shah, N. C.; Yonzon, C. R.; Walsh, J. T., Jr.; Glucksberg, M. R.; Duyne, R. P. V. *Anal. Chem.* **2005**, *77*, 6134–6139.
123. Zhang, X.; Shah1, N. C.; Duyne, R. P. V. *Vib. Spectrosc.* **2006**, *42*, 2–8.
124. Zhang, X.; Zhao, J.; Whitney, A. V.; Elam, J. W.; Duyne, R. P. V. *J. Am. Chem. Soc.* **2006**, *128*, 10304–10309.
125. Ji, X.; Xu, S.; Wang, L.; Liu, M.; Pan, K.; Yuan, H.; Ma, L.; Xu, W.; Li, J.; Bai, Y.; Li, T. *Colloids Surf., A* **2005**, *257–258*, 71–175.
126. Luo, Z.; Chen, K.; Lu, D.; Han, H.; Zou, M. *Microchim. Acta* **2011**, *173*, 149–156.
127. Cui, Y.; Ren, B.; Yao, J.; Gu, R.; Tian, Z. *J. Phys. Chem. B* **2006**, *110*, 4002–4006.
128. Lee, S.; Kim, S.; Choo, J.; Shin, S. Y.; Lee, Y. H.; Choi, H. Y.; Ha, S.; Kang, K.; Oh, C. H. *Anal. Chem.* **2007**, *79*, 916–922.

129. Zhang, Z.; Wen, Y.; Ma, Y.; Luo, J.; Jiang, L.; Song, Y. *Chem. Commun.* **2011**, *47*, 7407–7409.
130. Wang, H.; Vo-Dinh, T. *Nanotechnology* **2009**, *20*, 065101.
131. Vo-Dinh, T. *IEEE J. Sel. Top. Quantum Electron.* **2008**, *14*, 198–205.
132. Wong-Ek, K.; Chailapakul, O.; Eiamchai, P.; Horpratum, M.; Limnonthakul, P.; Patthanasettakul, V.; Sutapan, B.; Tuantranont, A.; Chindaudom, P.; Nuntawong, N. *Biomed. Tech.* **2011**, *56*, 235–240.
133. Langlet, M.; Sow, I.; Briche, S.; Messaoud, M.; Chaix-Pluchery, O.; Dherbey-Roussel, F.; Chaudouët, P.; Stambouli, V. *Surf. Sci.* **2011**, *605*, 2067–2072.
134. Gong, J.; Liang, Y.; Huang, Y.; Chen, J.; Jiang, J.; Shen, G.; Yu, R. *Biosens. Bioelectron.* **2007**, *22*, 501–1507.
135. Sun, L.; Sung, K.; Dentinger, C.; Lutz, B.; Nguyen, L.; Zhang, J.; Qin, H.; Yamakawa, M.; Cao, M.; Lu, Y.; Chmura, A. J.; Zhu, J.; Su, X.; Berlin, A.; Chan, S.; Knudsen, B. *Nano Lett.* **2007**, *7*, 351–356.
136. Geddes, C. D.; Parfenov, A.; Roll, D.; Gryczynski, I.; Malicka, J.; Lakowicz, J. R. *J. Fluoresc.* **2003**, *13*, 119–122.
137. Stears, R. L.; Getts, R. C.; Gullans, S. R. *Physiol. Genomics* **2000**, *3*, 93–99.
138. Nath, N.; Chilkoti, A. Radiative Decay Engineering; Lakowicz, J.; Geddes, C. D., Eds.; In *Topics in Fluorescence Spectroscopy*; Springer Science+Business Media, Inc.: New York, 2005; Vol. 8, pp 405−448.
139. Malicka, J.; Gryczynski, I.; Lakowicz, J. R. *Anal. Chem.* **2003**, *75*, 4408–4414.
140. Malicka, J.; Gryczynski, I.; Gryczynski, Z.; Lakowicz, J. R. *Anal. Biochem.* **2003**, *315*, 57–66.
141. Fu, Y.; Zhang, J.; Lakowicz, J. R. *Chem. Phys. Lett.* **2007**, *447*, 96–100.
142. Aslan, K.; Gryczynski, I.; Malicka, J.; Matveeva, E.; Lakowicz, J. R.; Geddes, C. D. *Curr. Opin. Biotechnol.* **2005**, *16*, 55–62.
143. Lakowicz, J. R.; Malicka, J.; D’ Auria, S.; Gryczynski, I. *Anal. Biochem.* **2003**, *320*, 13–20.
144. Gryczynski, I.; Matveeva, E. G.; Sarkar, P.; Bharill, S.; Borejdo, J.; Mandecki, W.; Akopova, I.; Gryczynski, Z. *Chem. Phys. Lett.* **2008**, *462*, 327–330.
145. Li, J.; Wang, Z.; Gryczynski, I.; Mandecki, W. *Anal. Bioanal. Chem.* **2010**, *398*, 1993–2001.
146. Lukomska, J.; Malicka, J.; Gryczynski, I.; Lakowicz, J. R. *J. Fluoresc.* **2004**, *14*, 417–423.
147. Aslan, K.; Lakowicz, J. R.; Szmacinski, H.; Geddes, C. D. *J. Fluoresc.* **2004**, *14*, 677–679.
148. Aslan, K.; Wu, M.; Lakowicz, J. R.; Geddes, C. D. *J. Fluoresc.* **2007**, *17*, 127–131.
149. Aslan, K.; Grell, T. A. J. *Clin. Chem.* **2011**, *57*, 746–752.
150. Aslan, K.; Geddes, C. D. *Plasmonics* **2006**, *1*, 53–59.
151. Aslan, K.; Malyn, S. N.; Geddes, C. D. *Biochem. Biophys. Res. Commun.* **2006**, *348*, 612–617.
152. Lakowicz, J. R.; Kuśba, J.; Shen, Y.; Malicka, J.; D’Auria, S.; Gryczynski, Z.; Gryczynski, I. *J. Fluoresc.* **2003**, *13*, 69–77.

153. JianYu, J.; XiangYuan, O.; JiShan, L.; JianHui, J.; Hao, W.; YongXiang, W.; RongHua, Y. *Sci. China: Chem.* **2011**, *54*, 1266–1272.
154. Shang, L.; Dong, S. *Nano Today* **2011**, *6*, 401–418.
155. Sengupta, B.; Ritchie, C. M. *J. Phys. Chem.* **2008**, *112*, 18776–18782.
156. Gwinn, E. G.; O'Neill, P. *Adv. Mater.* **2008**, *20*, 279–283.
157. Sengupta, B.; Springer, K. *J. Phys. Chem.* **2009**, *113*, 19518–19524.
158. Sharma, J.; Yeh, H. *Chem. Commun.* **2010**, *46*, 3280–3282.
159. Huang, Z.; Pu, F. D. *Chem. Eur. J.* **2011**, *17*, 3774–3780.
160. Yeh, H. C.; Sharma, J.; Han, J. J.; Martinez, J. S.; Werner, J. H. *Nano Lett* **2010**, *10*, 3106–3110.
161. Yang, S. W.; Vosch, T. *Anal. Chem.* **2011**, *83*, 6935–6939.
162. Wong, K. K. Y.; Liu, X. *Med. Chem. Commun.* **2010**, *1*, 125–131.

Subject Index

A

- AD. *See* Alzheimer's disease (AD)
- α-fetoprotein, 188
- Agarose gel electrophoresis, 126*f*
- Ag@Au NPs, 332, 333*f*, 333*t*, 341*f*, 349*f*
  - acrylate-capped, 333, 334*f*, 341
  - citrate-capped, 334
  - Mie modeling, 339, 340*f*
- Alzheimer's disease (AD), 178
- Amyloid-β peptides, 178, 179*f*
- Au@Ag NPs, 335, 336*f*, 338*t*, 345*f*, 350*f*, 354*f*, 355*f*
  - electronic properties, 342
  - electronic structure, 343
- Au@Ag@Au double shell NPs, 335
  - Ag@Au NP synthesis, 339
  - Au@Ag$_{3.6}$@Au$_{0.11}$ NPs, 335, 337*f*, 344*f*, 345*f*, 351*f*
  - Au@Ag$_{3.9}$@Au$_{1.2}$ NPs, 337, 338*f*, 345*f*

B

- Biocompatible charged interfaces, gold nanoparticles, 159
  - calf thymus DNA, 167*f*
  - hyper-langmuirian linker-adsorption model, 161
  - immunotherapy, 168
  - lipid-coated nanoparticles, 169
  - molecular dynamics simulations, 165, 166*f*, 167*f*
  - polyamine-capped AuNP nanocarriers, 159, 161*f*, 162*f*
  - RELS spectra, 162*f*, 163*f*, 168*f*
- Biomarker detections
  - AD, 178
  - α-fetoprotein, 188
  - amyloid-β peptides, 178, 179*f*
  - cancer, 180
  - carcinoembryonic antigen, 190, 191*f*
  - cell signaling molecules, 183
  - cell surface receptors, 181, 182*f*
  - electrochemical immunosensor array, 190*f*
  - glycan expression, 181, 182*f*
  - homogeneous immunoassay, 187*f*
  - interleukin-6, 183, 184*f*
  - overview, 177
  - p53, 192, 192*f*
  - platelet-derived growth factor, 193, 194*f*
  - prostate specific antigen, 185, 186*f*, 187*f*
  - SERS-based immunoassay chip design, 195*f*
  - tau protein, 180, 181*f*
  - tumor necrosis factor α, 185
- Biomolecular recognition
  - agarose gel electrophoresis, 126*f*
  - biomolecule-mediated assemblies, 128
    - amino acids, 128, 129*f*, 130*s*, 131*f*, 132*f*
    - peptides, 128
  - DNA strand binding, 122*s*
  - DNA-AuNP assembly, 122*s*, 123*f*, 124*f*
  - luciferase assays, 127*f*
  - magnetic separation, 134, 134*f*
  - microRNA-conjugated gold nanoparticles, 124, 125*s*, 133*s*
  - MM.1S cells, 127*f*
  - overview, 119
  - *p53* recognition, 121
  - proteins, 134
  - silver-coated magnetic particles, 135, 136*s*, 137*f*
- Biomolecule-mediated assemblies, biomolecular recognition, 128
  - amino acids, 128, 129*f*, 130*s*, 131*f*, 132*f*
  - peptides, 128
- Biosensors, silver nanostructures, 377, 381*t*
  - fluorescence modulation-based biosensors, 390, 392*f*
  - LSPR shift-based biosensors, 378, 384*t*
  - SERS-based biosensors, 383, 386*f*, 388*f*, 389*f*, 390*f*, 392*f*, 393*t*
- Building blocks, gold nanoparticles, 169

C

- Carcinoembryonic antigen, 190, 191*f*
- CdTe nanowires, 170*f*
- Cell signaling molecules, biomarker detections, 183
- Cell surface receptors, biomarker detections, 181, 182*f*
- Chemiluminescence resonance energy transfer (CRET), 1
- Chloride electrolytes, 348
- Cocaine, colorimetric detection, 246*f*
- Colorimetric logic gates, 250*f*

Downloaded by 89.163.35.42 on November 27, 2012 | http://pubs.acs.org
Publication Date (Web): November 26, 2012 | doi: 10.1021/bk-2012-1112.ix002

Downloaded by 89.163.35.42 on November 27, 2012 | http://pubs.acs.org
Publication Date (Web): November 26, 2012 | doi: 10.1021/bk-2012-1112.ix002

- Conjugated polymer nanoparticles (CPN), 81
- Coralyne, non-cross-linking colorimetric detection, 380*f*
- Core-shell nanoparticles, electronic properties manipulation
  - Ag@Au NPs, 332, 333*f*, 333*t*, 341*f*, 349*f*
    - acrylate-capped, 333, 334*f*, 341
    - citrate-capped, 334
    - Mie modeling, 339, 340*f*
  - ATT, 352*f*, 353*f*, 354*f*
  - Au@Ag NPs, 335, 336*f*, 338*t*, 345*f*, 350*f*, 354*f*, 355*f*
    - electronic properties, 342
    - electronic structure, 343
  - Au@Ag@Au double shell NPs, 335
    - Ag@Au NP synthesis, 339
    - $Au@Ag_{3.6}@Au_{0.11}$ NPs, 335, 337*f*, 344*f*, 345*f*, 351*f*
    - $Au@Ag_{3.9}@Au_{1.2}$ NPs, 337, 338*f*, 345*f*
  - d-orbital vacancies, 348*f*
  - gold NPs, 331, 332*f*
    - 14 nm, 331
    - 43 nm, 331
  - molecular sensing properties, 352
  - NP stability assessment, 347
    - chloride electrolytes, 348
  - overview, 327
  - R6G, 352*f*, 353*f*
  - silver NPs, 330, 330*f*, 333*f*, 348*f*, 354*f*
    - acrylate-capped, 331
    - citrate-capped, 331
- CP. *See* fluorescent conjugated polymers (CP)
- CPN. *See* conjugated polymer nanoparticles (CPN)
- CRET. *See* chemiluminescence resonance energy transfer (CRET)

D

- Dip-in polymerization, 321*f*
- DNA-AuNP assembly, biomolecular recognition, 122*s*, 123*f*, 124*f*
- DNA biosensor
  - CP conformational effect, 93
  - FRET, 82, 89*f*
- DNA intercalators, 89*f*
- D-orbital vacancies, 348*f*

E

- Electroactive SAM, 307*f*
- Electrochemical immunosensor, 261*f*, 289*f*
- Electrochemical immunosensor array, biomarker detections, 190*f*
- Electrochemical sensors, self-assembled monolayers
  - electroactive SAM, 307*f*
  - ion-channel mimetic mode, 295, 296*f*
  - nanoparticle incorporation, 299, 300*f*
  - overview, 293
  - receptor immobilization, 297*f*
  - redox active monolayers, 304, 305*f*
- Electrode surface modification
  - carbon nanostructured materials, 317
  - composites, 319
  - core-shell materials, 318
  - dip-in polymerization, 321*f*
  - enzyme-assisted recycling, 316*f*
  - glassy carbon, 319*f*
  - graphene, 320*f*
  - magnetic beads, 317*f*
  - metal-compound nanoparticles, 317
  - metallic nanoparticles, 314, 315*f*
  - nanoparticle structure, 323
  - overview, 313
  - oxygen reduction reaction, 322*f*

F

- Fluorescence resonance energy transfer (FRET), 1
- Fluorescent conjugated polymers (CP)
  - A549 cells, 107*f*
  - AChE activity, 97*f*
  - α-thrombin detection, 95*f*
  - bioimaging application, 104
  - biological-revelant molecules, 102
  - cationic, 89*f*
  - charged substrates, 100*f*
  - ConA detection, 98*f*
  - CP 17, 104*f*
  - DNA biosensor
    - conformational effect, 93
    - FRET, 82, 89*f*
  - DNA detection, 88*f*, 89*f*
  - DNA intercalators, 89*f*
  - DNA sequences, 92*f*
  - drug delivery application, 104
  - enzyme assay, 100*f*
  - heterogeneous assays, 101
  - lysozyme detection, 90*f*
  - macrophage cells, 106*f*

- overview, 81
- PFO/PG-Dox complex system, 109*f*
- PNA hybridization, 102*f*
- properties, 103
- protein detection, conformational change, 100
- protein sensors, 96
  - FRET, 96
- PT-COO disassembly reassembly process, 101*f*
- QTL sensor, 97*f*
- SNP assay, 92*f*
- water soluble, 83*s*, 87*f*

Fluorophore-displacement bacterial detection array, 268*f*

FRET. *See* fluorescence resonance energy transfer (FRET)

G

Glassy carbon, 319*f*

Glycan expression, biomarker detections, 181, 182*f*

Gold nanoparticles
- amines, 149*f*
- biocompatible charged interfaces, 159
  - calf thymus DNA, 167*f*
  - hyper-langmuirian linker-adsorption model, 161
  - immunotherapy, 168
  - lipid-coated nanoparticles, 169
  - molecular dynamics simulations, 165, 166*f*, 167*f*
  - polyamine-capped AuNP nanocarriers, 159, 161*f*, 162*f*
  - RELS spectra, 162*f*, 163*f*, 168*f*
- building blocks, 169
- cancer therapy, 157
- CdTe nanowires, 170*f*
- drug carriers, 148
- electronic properties manipulation, 331, 332*f*
  - 14 nm, 331
  - 43 nm, 331
- gene delivery, 149, 150*f*
- image enhancers, 153, 154*f*
- metal ion induced
  - apparatus, 237
  - bonding influence, 225, 227*f*, 228*f*
  - chemicals, 237
  - disassembly, 227
  - DLS characteristics, 233, 234*f*, 235*f*
  - high-affinity assembly, 215
  - HR-TEM images, 233*f*
  - local surface plasmon frequency shifts, 209
  - low- vs high-affinity assembly, 230, 232*s*
  - low-affinity assembly, 212
  - overview, 207
  - procedures, 238
  - resonance elastic light scattering spectra, 218*f*, 219, 221*f*, 222*f*, 223*f*, 231*f*, 232*f*
  - SP absorbance spectra, 211*f*
  - temporal evolution, 224, 224*f*, 226*f*
  - UV-Vis absorbance spectra, 212*f*, 213*f*, 214*f*, 216*f*, 217*f*, 229*f*, 230*f*
- overview, 147
- photodynamic therapy, 151
- photothermal cancer cell destruction, 152*f*
- theranostics, 155, 156*f*
- tumor blood-vessel receptors, 158*t*
- tumor cell-membrane receptors, 158*t*
- UV-Vis absorbance profiles, 34*f*

Graphene, 320*f*

H

Heterogeneous sandwich immunoassay, 283*f*, 284*f*

Histidine-mediated phase transfer protocol, semiconductor quantum dots, 62

Homogeneous immunoassay, biomarker detections, 187*f*

I

Interleukin-6, 183, 184*f*

Ion-channel mimetic mode, 295, 296*f*

L

Luciferase assays, biomolecular recognition, 127*f*

M

Metal-compound nanoparticles, 317

Metallic nanoparticles
- aggregated, 45*f*
- aggregated glucose sensing system, 46*f*

Downloaded by 89.163.35.42 on November 27, 2012 | http://pubs.acs.org
Publication Date (Web): November 26, 2012 | doi: 10.1021/bk-2012-1112.ix002

Downloaded by 89.163.35.42 on November 27, 2012 | http://pubs.acs.org
Publication Date (Web): November 26, 2012 | doi: 10.1021/bk-2012-1112.ix002

- benzotriazole
  - dyes, 40*f*
  - monoazo dyes, 38*f*
- biomolecule detection, 35, 36
  - extrinsic detection, 35
  - intrinsic detection, 35
- characterization, 42
- common dye molecules, 38*f*
- DNA hybridization efficiency quantification, 43*f*
- DNA sequences, 48*f*
- FRET, 6*f*, 8*f*
- functionalization, 36
  - biofunctionalization, 39
  - nanoparticle biosensor assembly, 40
  - reporter molecules, 36
  - stabilization, 37
- functionalized, 47*f*
- gold, UV-Vis absorbance profiles, 34*f*
- IR-792 dye, 37*f*
- localized surface plasmon resonance applications, 45
- optical biosensing, 15, 16*f*, 18*f*, 19*f*, 20*f*, 23*f*
- overview, 1, 33
- polymer dye, 41*f*
- prostate tissue section mapping, 50*f*
- ScFv-antibody functionalized nanotag, 51*f*
- semiconductor quantum dots, bioanalytical application, 2, 4*f*, 6*f*, 7*f*, 8*f*, 10*f*, 11*f*, 13*f*, 14*f*
- SERS nanotag, 49*f*
- surface-enhanced Raman spectroscopy applications, 47
- unaggregated, 45*f*
- unaggregated glucose sensing system, 46*f*

MicroRNA-conjugated gold nanoparticles, 124, 125*s*, 133*s*

Molecular sensing properties, core-shell nanoparticles, 352

N

Nanoparticles, different shapes
- biosensor readout types, 282
  - assay conduct, 286*f*
  - assay proteinase activity, 286*f*
  - colorimetric, 290, 291*f*
  - electrochemical, 288
  - electrochemical immunosensor, 289*f*
  - heterogeneous sandwich immunoassay, 283*f*, 284*f*
  - localized surface plasmon resonance, 284
  - nanoparticle cluster arrays, 284, 285*f*
  - optical biosensing platform, 286*f*
  - silver nanoparticles, 290*f*
  - surface-enhanced Raman spectroscopy, 282
  - ZnO-Au nanocomposite based biosensor, 287*f*
- overview, 281

Nanoparticle stability assessment, 347
- chloride electrolytes, 348

NEANA. *See* nicking endonuclease assisted nanoparticle amplification (NEANA)

Nicking endonuclease assisted nanoparticle amplification (NEANA), 245*f*

NMN. *See* noble metal nanoparticles (NMN)

Noble metal nanoparticles (NMN)
- absorption spectroscopic analysis, 242
  - cocaine, colorimetric detection, 246*f*
  - colorimetric logic gates, 250*f*
  - Cu^{2+} detection, 254*f*
  - DNA-conjugated AgNP, 251*f*
  - enzymatic reactions, 252*f*
  - NEANA, 245*f*
  - thrombin, colorimetric detection, 248*f*
- electrochemical analysis, 256
  - DNA sensing systems, 259*f*
  - electrochemical immunosensor, 261*f*
  - electron transfer, 261*f*
  - hydrolysis, 257*f*
- fluorescent analysis, 264
  - DNA detection, 267*f*
  - fluorophore-displacement bacterial detection array, 268*f*
- overview, 241

O

Oligonucleotide-functionalized Ag/Au core-shell, 379*f*

Oxygen reduction reaction, 322*f*

P

Photothermal cancer cell destruction, 152*f*

Prostate specific antigen, biomarker detections, 185, 186*f*, 187*f*

Downloaded by 89.163.35.42 on November 27, 2012 | http://pubs.acs.org
Publication Date (Web): November 26, 2012 | doi: 10.1021/bk-2012-1112.ix002

Q

QD. *See* semiconductor quantum dots
Quantum dots (QD). *See* semiconductor quantum dots

R

Receptor immobilization, 297*f*
Redox active monolayers, 304, 305*f*
R6G, 352*f*, 353*f*

S

Semiconductor quantum dots, 2, 4*f*
  absorption spectra, 69*f*
  biofunctionalization, 66
  2D NMR, 65*f*
  FRET, 67*f*, 68*f*, 70*f*
  functionalization, 63*s*
    firefly proteins, 70
    histagged proteins, 69
  histagged streptavidin, 66*f*, 68*f*
  histidine-mediated phase transfer protocol, 62
  ^{1}H-NMR, 64*f*
  ligand exchange, 60*t*
  overview, 59
  PL emission, 69*f*
  spectral properties, 67*f*
  TEM micrographs, 70*f*, 71*f*
Silver-coated magnetic particles, biomolecular recognition, 135, 136*s*, 137*f*
Silver nanoparticles, 290*f*
  electronic properties manipulation, 330, 330*f*, 333*f*, 348*f*, 354*f*
    acrylate-capped, 331
    citrate-capped, 331
Silver nanostructures
  biosensors, 377, 381*t*
    fluorescence modulation-based biosensors, 390, 392*f*
    LSPR shift-based biosensors, 378, 384*t*
    SERS-based biosensors, 383, 386*f*, 388*f*, 389*f*, 390*f*, 392*f*, 393*t*
  characterization, 376
  cooperative binding properties, 377*f*
  coralyne, non-cross-linking colorimetric detection, 380*f*
  functionalization, 376
  oligonucleotide-functionalized Ag/Au core-shell, 379*f*
  optical properties
    local field enhancement, spectroscopic signals, 365
    surface plasmon resonance, 360, 361*f*
    UV-Vis extinction spectra, 364*f*
  overview, 359
  SIF substrate, BSA-avidin monolayer, 394*f*
  synthesis, 370
    colloidal dispersions, 370
    substrate-immobilized, 375

T

Tau protein, 180, 181*f*
Thrombin, colorimetric detection, 248*f*
Tumor blood-vessel receptors, 158*t*
Tumor cell-membrane receptors, 158*t*
Tumor necrosis factor α, 185

Z

ZnO-Au nanocomposite based biosensor, 287*f*